

Technical Report 19-03

**Bentonite backfill performance in a
high-level waste repository:
a geochemical perspective**

October 2019

A. Jenni, P. Wersin, T. Thoenen, B. Baeyens,
A. Ferrari, T. Gimmi, U. Mäder, P. Marschall,
W. Hummel & O. Leupin

**National Cooperative
for the Disposal of
Radioactive Waste**

Hardstrasse 73
CH-5430 Wettingen
Switzerland
Tel. +41 56 437 11 11

www.nagra.ch

Technical Report 19-03

Bentonite backfill performance in a high-level waste repository: a geochemical perspective

October 2019

A. Jenni¹, P. Wersin¹, T. Thoenen², B. Baeyens²,
A. Ferrari³, T. Gimmi^{1,2}, U. Mäder¹, P. Marschall⁴,
W. Hummel² & O. Leupin⁴

¹ University of Bern

² PSI

³ EPFL

⁴ Nagra

**National Cooperative
for the Disposal of
Radioactive Waste**

Hardstrasse 73
CH-5430 Wettingen
Switzerland
Tel. +41 56 437 11 11

www.nagra.ch

ISSN 1015-2636

"Copyright © 2019 by Nagra, Wettingen (Switzerland) / All rights reserved.

All parts of this work are protected by copyright. Any utilisation outwith the remit of the copyright law is unlawful and liable to prosecution. This applies in particular to translations, storage and processing in electronic systems and programs, microfilms, reproductions, etc."

Abstract

Bentonite is a widely used natural material with many applications. Owing to its good sealing properties, compacted bentonite is foreseen as a backfill material for deposition tunnels in high-level waste repositories in several countries. The main safety functions of the bentonite backfill are (i) to protect and isolate the canisters containing the waste and (ii) to retain and retard radionuclides once the canisters have breached.

In the current repository concepts, compacted bentonite is used (based on Nagra 2016):

- in the form of compacted bentonite blocks and granular bentonites as a buffer surrounding the SF and HLW canisters
- in the form of a sand/bentonite mixture in the Engineered Gas Transport System (EGTS)
- in the form of granular bentonite and/or blocks in other repository sealing and closure structures

The main objective of the present report is to assess the impact of repository-induced geochemical processes and phenomena on the safety-relevant properties of bentonite. These safety-relevant properties must fulfil requirements which are formulated in terms of safety-relevant buffer attributes and preferred values for the parameters that quantify these attributes.

The report concludes that there is ample scientific evidence that the bentonite buffer is an efficient hydraulic, mechanical and chemical barrier that will protect the canister and attenuate the release of radionuclides. In the last decades, the properties of bentonite have been thoroughly investigated in small- to large-scale laboratory experiments, under realistic conditions in rock laboratories, in natural analogue studies and based on theoretical considerations by a large international community. Based on the review of these findings, it can be concluded that, under the expected repository conditions, the required properties such as high swelling pressure, low hydraulic conductivity etc. will generally persist.

It is expected that the bentonite performance might be impaired at the interfaces to the cementitious liner and to the canister. Based on today's understanding, this will however not call into question the use of bentonite as a buffer or sealing material.

The present status report also lists recommendations for further reducing remaining uncertainties related to the evolution of the bentonite barrier under repository-relevant conditions.

Résumé

La bentonite est un matériau naturel largement utilisé dans les contextes les plus divers. Ses bonnes propriétés d'étanchéité font de la bentonite compactée un matériau privilégié par plusieurs pays pour le remblayage des tunnels destinés au stockage des déchets de haute activité. Au sein du système de sûreté du dépôt, le remblai de bentonite a pour principales fonctions (i) de protéger et d'isoler les conteneurs contenant les déchets et (ii) de retenir et de retarder les radionucléides suite à la perte d'intégrité des conteneurs.

Les concepts actuels de dépôt mettent en œuvre la bentonite compactée sous diverses formes (selon Nagra 2016) :

- des blocs et des granulés de bentonite compactée comme matériau de comblement autour des conteneurs d'éléments combustibles usés et de déchets de haute activité
- un mélange sable-bentonite dans le système ouvragé de transport des gaz (Engineered Gas Transport System ou EGTS)
- des granulés et/ou des blocs de bentonite dans d'autres structures assurant l'étanchéité et la fermeture du dépôt.

L'objectif principal du présent rapport est d'étudier dans quelle mesure les propriétés de la bentonite peuvent être affectées par les processus et phénomènes géochimiques induits par le dépôt. A cet effet, on utilise une série d'attributs qui reflètent les exigences posées au remblayage en matière de sûreté, ainsi que des valeurs préférentielles pour les paramètres qui quantifient ces attributs.

Le rapport conclut que l'efficacité du remblai de bentonite en tant que barrière hydraulique, mécanique et chimique, en mesure de protéger le conteneur et de ralentir le relâchement des radionucléides, est largement attestée sur le plan scientifique. Au cours des dernières décennies, les propriétés de la bentonite ont fait l'objet d'études approfondies de la part d'une vaste communauté internationale, dans le cadre d'expériences de laboratoire à petite et à grande échelle, dans des conditions réalistes dans les laboratoires souterrains, par le biais d'analogues naturels et sur la base de considérations théoriques. Les résultats de ces études permettent de conclure que, dans les conditions de dépôt prévues, la bentonite conservera d'une façon générale les propriétés requises, telles qu'une pression de gonflement élevée, une faible conductivité hydraulique, etc.

On s'attend à ce que les performances de la bentonite soient affectées aux interfaces, soit avec le revêtement en ciment, soit avec le conteneur. Dans l'état actuel des connaissances, ceci ne remet toutefois pas en question l'usage de la bentonite en tant que remblai ou matériau de fermeture.

Le présent rapport contient également des recommandations relatives aux études nécessaires pour réduire encore les incertitudes qui subsistent quant à l'évolution de la barrière de bentonite dans les conditions du dépôt.

Zusammenfassung

Bentonit ist ein häufig verwendetes Naturmaterial, das sich vielfältig einsetzen lässt. Aufgrund seines guten Abdichtungsvermögens ist kompaktierter Bentonit in mehreren Ländern als Verfüllmaterial für Lagerstollen in Tiefenlagern für hochaktive Abfälle vorgesehen. Die wichtigsten Sicherheitsfunktionen der Bentonitverfüllung sind (i) Schutz und Isolierung der Endlagerbehälter, die die radioaktiven Abfälle einschliessen, und (ii) Rückhaltung und Verzögerung der Radionuklide nach Behälterversagen.

Aktuelle Lagerkonzepte verwenden kompaktierten Bentonit (Grundlage: Nagra 2016):

- in Form von kompaktierten Bentonitblöcken und Bentonitgranulaten als BE/HAA-Endlagerbehälter umschliessende Verfüllung
- in Form einer Sand-/Bentonitmischung im "Engineered Gas Transport System" (EGTS)
- in Form von Bentonitgranulat und/oder -blöcken in weiteren Versiegelungs- und Verschlussbauwerken des Lagers

Das Hauptziel des vorliegenden Berichts ist es, die Auswirkungen der lagerbedingten geochemischen Prozesse und Phänomene auf die sicherheitsrelevanten Eigenschaften des Bentonits zu beurteilen. Der Bentonit muss Anforderungen erfüllen, die anhand sicherheitsrelevanter Verfüllungseigenschaften und der bevorzugten Parameterwerte, die diese Eigenschaften quantifizieren, formuliert werden.

Der Bericht hält abschliessend fest, dass es umfangreiche wissenschaftliche Nachweise gibt und dass die Bentonitverfüllung eine effiziente hydraulische, mechanische und chemische Barriere bildet, die die Endlagerbehälter schützen und die Freisetzung der Radionuklide verringern wird. In den letzten Jahrzehnten sind die Eigenschaften von Bentonit gründlich untersucht worden: in klein- bis grossmasstäblichen Laborexperimenten, unter realistischen Bedingungen in Felslaboren, in Naturanalogstudien sowie basierend auf theoretischen Erwägungen einer grossen internationalen Fachwelt. Nach Prüfung dieser Ergebnisse lässt sich zusammenfassend sagen, dass unter den erwarteten Lagerbedingungen die geforderten Eigenschaften wie hoher Quelldruck, geringe hydraulische Durchlässigkeit etc. in der Regel erhalten bleiben.

Eine eventuelle Beeinträchtigung des Bentonitverhaltens an den Übergängen zum Zementausbau und zum Endlagerbehälter lässt sich nicht ausschliessen. Basierend auf den heutigen Erkenntnissen wird Bentonit deswegen als Verfüll- oder Versiegelungsmaterial jedoch nicht in Frage gestellt.

Der vorliegende Statusbericht führt auch Empfehlungen für die weitere Reduktion verbleibender Ungewissheiten auf, die die Entwicklung der Bentonitbarriere unter lagerrelevanten Bedingungen betreffen.

Table of Contents

| | |
|--|-----------|
| Abstract | I |
| Résumé | II |
| Zusammenfassung..... | III |
| Table of Contents | V |
| List of Tables..... | IX |
| List of Figures | X |
| 1 Introduction | 1 |
| 2 The role of bentonite in Nagra's repository concept | 3 |
| 2.1 Nagra's repository concept..... | 3 |
| 2.2 Current Nagra RD&D programme on bentonite..... | 9 |
| 2.2.1 Bentonite-based barriers (buffer, backfill, seals)..... | 9 |
| 2.2.2 The SF/HLW near-field..... | 12 |
| 2.2.3 Buffer material evaluation for HLW emplacement drifts..... | 14 |
| 2.2.4 Buffer emplacement technology..... | 14 |
| 2.3 Expected evolution of bentonite buffer water saturation, swelling pressure, temperature, chemical interactions, coupled processes | 16 |
| 2.3.1 Description of the near-field evolution..... | 16 |
| 2.3.2 Evolution of the repository | 19 |
| 3 Bentonite characteristics | 23 |
| 3.1 Mineralogy..... | 23 |
| 3.1.1 The role of montmorillonite..... | 23 |
| 3.1.2 Structural iron in smectites | 28 |
| 3.1.3 Accessory minerals..... | 30 |
| 3.1.4 Conceptual uncertainties of bentonite mineralogy relevant for the Nagra concept..... | 32 |
| 3.2 Kinetic and thermodynamic treatment of clays | 33 |
| 3.2.1 Solubility data for clay minerals..... | 33 |
| 3.2.1.1 Solubility of kaolinite | 34 |
| 3.2.1.2 Solubility of illite..... | 35 |
| 3.2.1.3 Solubility of smectites | 38 |
| 3.2.2 Calorimetric data for smectites..... | 41 |
| 3.2.3 Estimation methods for thermodynamic data for smectites..... | 42 |
| 3.2.4 Kinetic data for smectites | 43 |
| 3.2.5 Conclusions | 48 |

| | | |
|---------|--|-----|
| 3.3 | Concepts of microstructure and their implications for clay-water interactions..... | 49 |
| 3.3.1 | Porosity concepts for transport modelling..... | 50 |
| 3.3.2 | Montmorillonite microstructure..... | 52 |
| 3.3.3 | Accessory minerals and related porosity..... | 52 |
| 3.3.4 | Pore size distribution and ion distribution in pores..... | 53 |
| 3.3.5 | Experimental evidence for the different porosity concepts..... | 55 |
| 3.3.6 | Conceptual uncertainties of microstructural understanding relevant for the Nagra concept..... | 60 |
| 3.4 | Porewater chemistry..... | 60 |
| 3.4.1 | Equilibrium models..... | 60 |
| 3.4.2 | Buffering processes..... | 66 |
| 3.4.3 | High pH stability..... | 67 |
| 3.4.4 | Thermodynamic considerations regarding smectites..... | 68 |
| 3.4.5 | Interactions with metal ions..... | 69 |
| 3.4.6 | Redox conditions..... | 70 |
| 3.4.7 | Conceptual uncertainties of porewater chemistry relevant for the Nagra concept..... | 72 |
| 3.5 | Solute transport properties..... | 73 |
| 3.5.1 | Advection..... | 73 |
| 3.5.2 | Diffusion..... | 75 |
| 3.5.3 | Conceptual uncertainties of transport in bentonite relevant for the Nagra concept..... | 79 |
| 3.6 | Conceptual understanding of gas transport in bentonite..... | 80 |
| 3.7 | THM properties..... | 81 |
| 3.7.1 | Saturation of granular bentonite under non-isothermal conditions..... | 81 |
| 3.7.2 | Bentonite homogenisation: microstructural insight..... | 84 |
| 3.7.3 | Hydration mechanisms..... | 92 |
| 3.7.4 | Triaxial mechanical response under unsaturated non-isothermal conditions..... | 93 |
| 3.7.4.1 | Response under isotropic loading..... | 94 |
| 3.7.4.2 | Deviatoric behaviour at ambient temperature..... | 96 |
| 3.7.4.3 | Influence of temperature on triaxial response..... | 99 |
| 3.7.5 | Impact of salinity on strength..... | 101 |
| 3.7.6 | Relevant conceptual uncertainties of the bentonite THM behaviour for the Nagra concept..... | 105 |
| 3.8 | CMH coupling..... | 106 |
| 3.8.1 | Porosity, accessory minerals and swelling pressure..... | 106 |
| 3.8.2 | Porewater chemistry and exchanger population..... | 109 |
| 3.8.3 | Coupling of ionic strength to swelling pressure and porosity at constant volume/dry density and constant exchanger population..... | 110 |

| | | |
|----------|---|------------|
| 3.8.4 | Coupling of exchanger population with swelling pressure and porosity at constant volume/dry density and ionic strength..... | 117 |
| 3.8.5 | Conceptual uncertainties of CMH coupling relevant for the Nagra concept | 120 |
| 3.9 | Impact of high temperatures on the performance of montmorillonite..... | 121 |
| 4 | Reactive transport and thermo-hydro-mechanical modelling..... | 123 |
| 4.1 | Justification and applicability of coupled codes considering charged clay surfaces | 124 |
| 4.2 | Equilibrium calculations..... | 125 |
| 4.2.1 | Aqueous – solid equilibria | 125 |
| 4.2.2 | Consideration of clay surface charge..... | 126 |
| 4.3 | Ion transport..... | 127 |
| 4.4 | CMH coupling | 129 |
| 4.5 | Gas transport modelling..... | 130 |
| 4.6 | THM coupling | 131 |
| 4.6.1 | Equilibrium and balance equations..... | 132 |
| 4.6.2 | Constitutive relations | 133 |
| 4.6.3 | ACMEG-TS model..... | 136 |
| 4.6.3.1 | Mechanical constitutive model | 137 |
| 4.6.3.2 | Water retention constitutive model..... | 139 |
| 4.7 | Conceptual uncertainties in reactive transport modelling of bentonite relevant for the Nagra repository scenario..... | 140 |
| 5 | Evaluation of the impact of processes and phenomena affecting the safety-relevant properties of bentonite..... | 143 |
| 5.1 | Assessment of repository-induced effects on the bentonite buffer considering homogenisation aspects..... | 143 |
| 5.1.1 | Driving processes..... | 144 |
| 5.1.2 | Modelled and measured density and saturation distributions and remaining uncertainties..... | 145 |
| 5.1.2.1 | Results for a cool section during the first dismantling | 145 |
| 5.1.2.2 | Results for a hot section during the first dismantling | 145 |
| 5.1.2.3 | Predicted results for a cool section during the second dismantling | 146 |
| 5.1.2.4 | Predicted results for a hot section during the second dismantling..... | 147 |
| 5.1.2.5 | Remaining modelling uncertainties | 148 |
| 5.1.2.6 | Consequences for the early repository evolution..... | 149 |
| 5.1.3 | Influence of porewater chemistry on homogenisation..... | 149 |
| 5.1.4 | Significance of remaining uncertainties of buffer homogenisation..... | 150 |
| 5.2 | Interaction of host rock porewaters and bentonite, changes in salinity and Ca-Na exchanger occupancy..... | 151 |
| 5.2.1 | Swelling pressure and hydraulic conductivity of bentonite in equilibrium with different host rock porewaters..... | 151 |
| 5.2.2 | Influence of host rock porewater on the bentonite cation occupancy..... | 153 |

| | | |
|--|--|------------|
| 5.2.3 | Dissolution of bentonite accessory minerals | 155 |
| 5.2.4 | Montmorillonite reactivity..... | 156 |
| 5.2.5 | Significance of host rock – bentonite interaction for the Nagra concept..... | 159 |
| 5.3 | Interaction of cementitious tunnel support structures and bentonite | 159 |
| 5.3.1 | Experimental data constraining cement – bentonite interaction..... | 161 |
| 5.3.2 | Modelling approaches predicting cement – bentonite interaction | 164 |
| 5.3.3 | Significance of cement – bentonite interaction for the Nagra concept..... | 165 |
| 5.4 | Interaction of steel and bentonite..... | 165 |
| 5.4.1 | Recent modelling studies..... | 167 |
| 5.4.2 | Recent in-situ experiments | 170 |
| 5.4.3 | Competitive sorption of Fe(II)..... | 174 |
| 5.4.4 | Significance of iron – bentonite interaction for the Nagra concept..... | 178 |
| 5.5 | Interaction between copper and bentonite | 179 |
| 5.6 | Observed microbial activity in various experiments and its consequences for repository conditions..... | 183 |
| 5.7 | Geochemical processes during saturation derived from experiments..... | 186 |
| 5.8 | Relevance of higher temperatures for the performance of the bentonite backfill..... | 191 |
| 5.8.1 | Montmorillonite alteration..... | 191 |
| 5.8.2 | Cementation..... | 191 |
| 5.8.3 | Support from laboratory and in-situ experiments | 192 |
| 5.8.4 | Significance of higher temperatures for the Nagra concept..... | 193 |
| 5.9 | Gas transport in bentonite..... | 193 |
| 5.10 | Coupling and integration of different processes for assessment..... | 195 |
| 5.10.1 | Saturation phase (0 – 100 y after emplacement)..... | 195 |
| 5.10.2 | Porewater equilibration phase (100 – 10,000 y after emplacement) | 197 |
| 5.10.3 | Quasi-steady state (10^4 – 10^6 years after emplacement) | 199 |
| 5.10.4 | Safety-relevant coupling of processes | 201 |
| 6 | Synthesis of scientific evidence and its significance for repository safety | 203 |
| 6.1 | Current understanding of geochemical evolution in the bentonite buffer and remaining uncertainties..... | 203 |
| 6.1.1 | Processes during saturation..... | 203 |
| 6.1.2 | Processes after saturation..... | 206 |
| 6.2 | Suggestions for mitigating uncertainties..... | 208 |
| 7 | References..... | 211 |
| Appendix: Bentonite requirements..... | | A-1 |
| A.1 | Desired properties of bentonite – safety functions | A-1 |
| A.2 | Specific Nagra-required properties – safety functions..... | A-1 |

List of Tables

| | | |
|-----------|---|-----|
| Tab. 2-1: | Post-closure safety requirements | 4 |
| Tab. 3-1: | Mineralogy of Wyoming MX-80 bentonite (wt.-%) | 30 |
| Tab. 3-2: | Compositions of smectites used in solubility experiments | 40 |
| Tab. 3-3: | Compositions of clay minerals used in calorimetry..... | 42 |
| Tab. 3-4: | Fractions of different porosity types in bentonite backfill for the Olkiluoto case (IL: interlayer; DDL: diffuse double layer, "free") estimated from relationships given in the text for salinity conditions (saline & dilute) | 63 |
| Tab. 3-5: | Relative humidity and total suction values resulting from saturated and partially saturated salt solutions..... | 82 |
| Tab. 5-1: | Predicted results for a cool section (section G) during the second dismantling | 147 |
| Tab. 5-2: | Predicted results for a hot section (section F2) during the second dismantling | 148 |
| Tab. 5-3: | Summary of the 2SPNE SC/CE model parameters, the hydrolysis and surface complexation and cation exchange reactions together with the thermodynamic constants used to calculate the Fe sorption on montmorillonite | 175 |
| Tab. 5-4: | MX-80 bentonite porewaters taken from Bradbury et al. (2014) | 177 |
| Tab. 5-5: | Summary of the hydrolysis and surface complexation and cation exchange reactions together with the thermodynamic constants for calculating the Cu(II) sorption on montmorillonite..... | 181 |
| Tab. A-1: | Compilation of attributes for the buffer material around the canister for the different repository designs and concepts | A-4 |

List of Figures

| | | |
|------------|---|----|
| Fig. 2-1: | Illustration of the barrier system for SF along with the properties and processes of the individual barriers that contribute to post-closure safety..... | 7 |
| Fig. 2-2: | Illustration of the barrier system for HLW along with the properties and processes of the individual barriers that contribute to post-closure safety | 8 |
| Fig. 2-3: | The backfilling machine in the FE tunnel (left) and a detail of the emplaced granular bentonite (right) and the contact with the liner (FE experiment)..... | 15 |
| Fig. 2-4: | Overview of the expected evolution of the main processes in a HLW repository based on a compilation of modelling reports and experimental data..... | 17 |
| Fig. 2-5: | Time-history of gas saturation (top), temperature (middle), and pressure (bottom) at selected locations of the HLW repository in the base case | 18 |
| Fig. 3-1: | Sketch of the montmorillonite structure | 24 |
| Fig. 3-2: | Variation of free swelling index of some bentonites with layer charge of smectites | 25 |
| Fig. 3-3: | Smectite contents compiled for selected bentonites | 25 |
| Fig. 3-4: | Layer charge (equivalent per half formula unit (phfu) of different commercial bentonites | 26 |
| Fig. 3-5: | Correlation of layer charge and CEC (a) and smectite content and CEC (b) for a variety of bentonitic materials | 27 |
| Fig. 3-6: | Swelling pressure as a function of average d-spacing for pyrophyllite, low-charge montmorillonite (layer charge: -0.5 eq./unit cell) and high-charge beidellite (-1.0 eq./unit cell)..... | 27 |
| Fig. 3-7: | Compositions of dioctahedral smectites in the ternary Al-Fe-Mg plot..... | 28 |
| Fig. 3-8: | Redox profiles of (a) MX-80 montmorillonite (SWy-2) and (b) nontronite (SWa-1) collected over a series of applied redox potentials (Eh)..... | 29 |
| Fig. 3-9: | SEM backscatter electron image of a polished section through dry MX-80 embedded in resin demonstrating a relatively large mineralogical heterogeneity..... | 31 |
| Fig. 3-10: | SEM backscatter electron image of a polished section of dry MX-80 embedded in resin showing a celestite grain (white)..... | 32 |
| Fig. 3-11: | Miscibility gaps in the system triethylamine–water and in the system $K_2O-Al_2O_3-SiO_2-H_2O$ | 34 |
| Fig. 3-12: | Approach to equilibrium solubility for 5 % suspensions of Dry Branch kaolinite, from over- and undersaturation..... | 35 |
| Fig. 3-13: | Synopsis of experimental data for illite at 25 °C | 36 |
| Fig. 3-14: | Synopsis of experimental data for illite at 100 °C | 36 |
| Fig. 3-15: | Synopsis of experimental data for illite at 200 °C | 37 |

| | | |
|------------|--|----|
| Fig. 3-16: | Composition-temperature phase diagram calculated along the pyrophyllite-muscovite binary..... | 37 |
| Fig. 3-17: | Mg-saturated Belle Fourche montmorillonite equilibrated with gibbsite and goethite..... | 41 |
| Fig. 3-18: | Conceptual view of bentonite micro/nanostructure and its porosity types..... | 50 |
| Fig. 3-19: | Schematic illustration of sodium and chloride concentration profiles in the interlayer, together with the electrostatic potential $-\phi$ | 53 |
| Fig. 3-20: | X-ray diffraction profiles for distilled water-saturated, compacted, Na-montmorillonite with different dry densities | 56 |
| Fig. 3-21: | Reported basal spacings for clay samples saturated from the aqueous phase under confined conditions | 57 |
| Fig. 3-22: | Interparticle porosity as a function of dry density calculated from average interlayer distance | 57 |
| Fig. 3-23: | MX-80 water volumes determined by SAXS plotted against the zero-time magnetisation (short relaxation times) at different densities..... | 58 |
| Fig. 3-24: | Hydraulic conductivity of MX-80 bentonite at different dry densities..... | 59 |
| Fig. 3-25: | Comparison of different porosity domains estimated from different measurements | 59 |
| Fig. 3-26: | Sketch showing the bentonite–water system and main chemical reactions..... | 61 |
| Fig. 3-27: | Effect of acid (HCl) and base (NaOH) titration on pH and calcite concentration of compacted bentonite at $p\text{CO}_2 = 10^{-2.2}$ bar | 66 |
| Fig. 3-28: | Experimental dissolution rates of K-montmorillonite, normalised to initial mass, and calculated rates | 67 |
| Fig. 3-29: | Activity ratio diagram in the Si-Al-K-O-H ₂ O system at 25 °C | 68 |
| Fig. 3-30: | Major redox-reactive phases in the EBS of the SF/HLW repository (not to scale) | 71 |
| Fig. 3-31: | Correlation between permeability and threshold hydraulic gradient (I)..... | 73 |
| Fig. 3-32: | Breakthrough curves of different non-reactive anions and deuterium..... | 74 |
| Fig. 3-33: | Hydraulic conductivity during infiltration of an artificial OPA porewater (APWOPA) followed by a Portland cement porewater (APWOPC, left) or a low-pH cement porewater (APW _{ESDRED} , right) through an MX-80 core | 75 |
| Fig. 3-34: | Schematic of an experimental diffusion set-up resulting in seemingly uphill diffusion | 76 |
| Fig. 3-35: | Effective diffusion coefficient of ³⁶ Cl ⁻ in compacted bentonite as a function of the diffusion-accessible porosity..... | 78 |
| Fig. 3-36: | Sketches of different species moving through a monomineralic claystone | 78 |
| Fig. 3-37: | Water retention behaviour determined at temperatures of 22 °C and 40 °C | 81 |
| Fig. 3-38: | Schematic cross-section of the sorption bench..... | 82 |

| | | |
|------------|--|-----|
| Fig. 3-39: | Evolution of degree of saturation of the sample inside the Micro-cell in a sorption bench at $T = 80\text{ }^{\circ}\text{C}$ | 83 |
| Fig. 3-40: | Influence of temperature on the retention behaviour of bentonite combining Micro-cell and sorption bench..... | 84 |
| Fig. 3-41: | Influence of temperature on the water retention behaviour of FEBEX bentonite with a dry density of 1.65 Mg m^{-3} | 84 |
| Fig. 3-42: | Different microstructural levels in poured and compacted MX-80 granular bentonite..... | 85 |
| Fig. 3-43: | SEM photographs of MX-80 grains with $e = 0.28$ ($\rho_d = 2.13\text{ Mg m}^{-3}$)..... | 86 |
| Fig. 3-44: | SEM photomicrographs of MX-80 granular bentonite in a compacted state with $e = 0.53$ ($\rho_d = 1.80\text{ Mg m}^{-3}$); (a),(b) bentonite grains coated by aggregates composing the assemblages; (c),(d) bentonite aggregate arranged in inter-assemblage space..... | 87 |
| Fig. 3-45: | Hysteresis water retention curve of highly compacted MX-80 granular bentonite..... | 88 |
| Fig. 3-46: | Microstructural evolutions during wetting paths based on the results of the MIP..... | 89 |
| Fig. 3-47: | Microstructural evolutions during drying paths based on the results of the MIP..... | 90 |
| Fig. 3-48: | SEM micrographs of MX-80 granular bentonite after wetting-drying cycle corresponding to Point G in Fig. 3-47..... | 91 |
| Fig. 3-49: | a), b) Average inter-particle distance in smectite mineral and number of sheets per particle versus total suction; c) water retention behaviour of highly compacted bentonite in constant volume condition..... | 92 |
| Fig. 3-50: | a) Visual aspect of the granular bentonite before and after sample preparation; b) Compaction path to the target dry density (1.5 Mg m^{-3})..... | 94 |
| Fig. 3-51: | Evolution of radial and axial stress and the measured pore volume change during the swelling phase in a triaxial cell..... | 94 |
| Fig. 3-52: | Isotropic compression tests performed in saturated and unsaturated samples: (a) change in void ratio and (b) saturation degree (c) stress path (A-B) in the water retention plane..... | 95 |
| Fig. 3-53: | Deviatoric response of MX-80 bentonite under triaxial stress path for a total suction of 100 MPa (a) – (b) and 50 MPa (c) – (d)..... | 97 |
| Fig. 3-54: | Deviatoric response of MX-80 bentonite under triaxial stress path for a total suction of 20 MPa (a) – (b) and saturated state (porewater pressure of 50 kPa) (c) – (d)..... | 98 |
| Fig. 3-55: | Deviatoric behaviour of granular bentonite samples subjected to triaxial stress paths under different values for total suction..... | 98 |
| Fig. 3-56: | Influence of total suction and mean total stress on the deviatoric stress at failure of MX-80 granular bentonite..... | 99 |
| Fig. 3-57: | Influence of temperature on the volumetric strain behaviour of MX-80 granular bentonite under controlled suction conditions..... | 100 |

| | | |
|------------|---|-----|
| Fig. 3-58: | Influence of temperature on the deviatoric behaviour of MX-80 bentonite under controlled suction..... | 101 |
| Fig. 3-59: | Schematic representation of the press used for the specimen compaction (right) and compaction of a specimen inside the oedometric ring (left)..... | 102 |
| Fig. 3-60: | Specimen compaction phases | 102 |
| Fig. 3-61: | Comparison between the swelling pressure developed with distilled water, synthetic water and sodium chloride solutions (left) and between the maximum swelling strain of the S/B mixture wetted with distilled water and synthetic water as a function of the initial dry density (right) | 103 |
| Fig. 3-62: | Evolution of the swelling pressure of the S/B mixture along a wetting-path under quasi-constant volume conditions for specimen compacted to two different dry densities..... | 104 |
| Fig. 3-63: | SEM image of MX-80 granular bentonite wetted to $w = 55\%$ with (a) distilled water and (b) 4M sodium chloride | 104 |
| Fig. 3-64: | Comparison of selected published data on dry density vs. swelling pressure for different bentonites | 107 |
| Fig. 3-65: | Measured swelling pressures plotted against montmorillonite content (X_{mont}) and water content at full water saturation (w_{sat})..... | 108 |
| Fig. 3-66: | Swelling pressure of Na-montmorillonite in NaCl and of Ca-montmorillonite in CaCl ₂ solutions of different ionic strengths at 1,306 kg m ⁻³ dry density | 111 |
| Fig. 3-67: | Swelling pressure of Na-montmorillonite in NaCl and of Ca-montmorillonite in CaCl ₂ solutions of different ionic strengths at different dry density values | 112 |
| Fig. 3-68: | XRD profiles of Na-montmorillonite at 1,000 kg m ⁻³ dry density equilibrated at different NaCl concentrations..... | 113 |
| Fig. 3-69: | Fluxes of tracer ³⁶ Cl ⁻ through Na-montmorillonite (1.9 Mg m ⁻³) in equilibrium with electrolytes of different ionic strengths..... | 114 |
| Fig. 3-70: | Diffusion-accessible porosity of Cl ⁻ in bentonite (ε_{Cl}) as a function of the ionic strength of the porewater for different bulk dry densities | 114 |
| Fig. 3-71: | Hydraulic conductivities of Na-montmorillonite in NaCl solutions and of Ca-montmorillonite in CaCl ₂ solutions of different ionic strengths at different dry densities | 116 |
| Fig. 3-72: | Evolution of swelling pressure and hydraulic conductivity of a compacted MX-80 bentonite disc of 1,470 kg m ⁻³ dry density during infiltration of different electrolytes..... | 117 |
| Fig. 3-73: | XRD profiles of Na-Ca-montmorillonite at 1,000 kg m ⁻³ dry density with different Na/Ca occupancies..... | 118 |
| Fig. 3-74: | XRD profiles of Ca-, Na-montmorillonite and MX-80 | 119 |
| Fig. 3-75: | Comparison of basal spacings derived from XRD of Na- and Ca-montmorillonite saturated from vapour phase under unconfined conditions, and confined saturated with 1 mM NaCl (WyNaCl)..... | 119 |

| | | |
|------------|---|-----|
| Fig. 4-1: | Fluxes and cumulative activities of HTO and $^{36}\text{Cl}^-$ in a through-diffusion experiment..... | 124 |
| Fig. 4-2: | One-dimensional representation of two cells (x , $x+1$) containing clay or clay interfaces in a dual-porosity finite element approach..... | 129 |
| Fig. 4-3: | Graphical visualisation of the yield surface evolution with temperature (left) and suction (right)..... | 138 |
| Fig. 4-4: | Conceptual model of the adopted water retention model | 140 |
| Fig. 5-1: | Layout of the FEBEX in-situ experiment..... | 143 |
| Fig. 5-2: | Comparison of measured dry density and water content data during dismantling and simulation results for a cool section (section 15)..... | 145 |
| Fig. 5-3: | Comparison of measured dry density and water content values during the first dismantling and simulation results for a hot section (section 27) | 146 |
| Fig. 5-4: | Predicted results for a cool section (section G) | 147 |
| Fig. 5-5: | Predicted results for a hot section (section F2)..... | 148 |
| Fig. 5-6: | Hydraulic conductivity of MX-80 montmorillonite and MX-80 at different NaCl and CaCl ₂ ionic strengths and dry densities | 150 |
| Fig. 5-7: | Swelling pressure of Na-montmorillonite in NaCl and of Ca-montmorillonite in CaCl ₂ solutions of different ionic strengths at 1,306 kg m ⁻³ dry density | 152 |
| Fig. 5-8: | Hydraulic conductivities of Na-montmorillonite in NaCl and of Ca-montmorillonite in CaCl ₂ solutions of different ionic strengths at 1,306 kg m ⁻³ dry density | 152 |
| Fig. 5-9: | Chemical composition of the main species in the outflow of a bentonite column as a function of time..... | 154 |
| Fig. 5-10: | Exchangeable Ca and Na profiles across bentonite | 155 |
| Fig. 5-11: | Alteration of Na-montmorillonite by a 0.1 M KCl solution at different porosities (mass ratio) in a closed system (equilibrium calculations) | 157 |
| Fig. 5-12: | Mineralogical evolution at 100 °C of MX-80 in contact with COX porewater (left boundary) and with the modelling cell of the steel overpack corrosion (right boundary) | 158 |
| Fig. 5-13: | Cement-bentonite interaction as a coupled non-linear system | 161 |
| Fig. 5-14: | Evolution of a reaction plume based on CT images and analysed by image processing | 163 |
| Fig. 5-15: | Schematic diagram of the coupled hydraulic/mechanical/chemical analysis approach employed..... | 164 |
| Fig. 5-16: | Schematic illustration showing the HLW near-field without bentonite backfill for better visualisation of steel-containing materials such as rock bolts, mesh, rails and canisters | 166 |
| Fig. 5-17: | Activity diagrams displaying smectite 1:1 clay stability fields for Na ₂ O-Al ₂ O ₃ -FeO-Fe ₂ O ₃ -H ₂ O-SiO ₂ at 25 °C (A) and 80 °C (B) as a function of SiO ₂ (aq) activity..... | 168 |

| | | |
|------------|---|-----|
| Fig. 5-18: | Simulations of Fe-bentonite interactions for KBS-3H (Wersin & Birgersson 2014): spatial distribution of solids and pH away from the Fe/bentonite contact..... | 169 |
| Fig. 5-19: | MX-80 pellets emplaced in steel cage around a steel heater in the ABM2 test before (left) and after (right) the experiment | 171 |
| Fig. 5-20: | Fe/Al profiles perpendicular to Fe contact of different blocks in the ABM2 test measured by SEM/EDX (Hadi et al. 2017a)..... | 172 |
| Fig. 5-21: | Contact zone between the steel liner and bentonite in the FEBEX-DP test (photo) and Fe/Al profiles perpendicular to contact in the same contact zone (blue line) and in a nearby sample (red line) where no interaction was observed (graphic)..... | 173 |
| Fig. 5-22 | (a) Sorption edge for Fe(II) on Na-STx-1 in 0.1 M NaClO ₄ . Fe _{TOT} < 3 × 10 ⁻⁸ M; S ~ 1 g L ⁻¹ and (b) Sorption isotherm for Fe(II) on Na-STx-1 in 0.1 M NaClO ₄ at pH = 6.2. (●) experimental data and (—) modelled curve | 175 |
| Fig. 5-23: | Examples illustrating the competitive sorption behaviour of elements with similar and different valences..... | 176 |
| Fig. 5-24: | Modelling the sorption of trace Ni(II) on MX-80 bentonite in the reference porewater composition (Tab. 5-4, CON-BPW-221sa) as a function of increasing Fe concentration under the assumption that Ni(II) and Fe(II) are mutually competitive | 178 |
| Fig. 5-25: | Modelling of the Ni(II) trace sorption (log R _d Ni) on MX-80 in the reference porewater composition as a function of increasing Cu(II) concentrations under the assumption that Ni(II) and Cu(II) are mutually competitive | 182 |
| Fig. 5-26: | Bentonite water uptake from host rock immediately after emplacement: a) suction-dominated, b) advection-dominated | 187 |
| Fig. 5-27: | Major anion contents in aqueous extracts in MX-80 core after the LOT experiment, and after subsequent equilibration with Äspö porewater | 188 |
| Fig. 5-28: | Photograph of freeze-dried saturated bentonite, emplaced in the form of pellets in a steel cage (inset)..... | 189 |
| Fig. 5-29: | Water and gas injection experiments with compacted granular bentonite..... | 194 |
| Fig. 5-30: | Coupling of different processes in the canister – bentonite – concrete – OPA system during saturation..... | 197 |
| Fig. 5-31: | Coupling of different processes in the canister – bentonite – concrete – OPA system during porewater equilibration | 198 |
| Fig. 5-32: | Coupling of different processes in the canister – bentonite – concrete – OPA system during quasi-steady state..... | 200 |

1 Introduction

Bentonite is a widely used natural material with many applications. Owing to its good sealing properties, compacted bentonite is foreseen as a backfill material for deposition tunnels in high-level waste repositories in a number of countries (Nagra 2002a, SKB 2011, Villagran et al. 2011, NEA 2013, Posiva 2013). The main safety functions of the bentonite backfill are (i) to protect and isolate the canisters containing the waste and (ii) to retain and retard radionuclides once the canisters have breached.

In view of the important role of bentonite backfill as a safety barrier, considerable research on this material has been carried out during the last 30 years. Nagra launched an extensive R&D programme in the 1980s to study the mineralogical, chemical and hydro-mechanical properties of bentonites and their ability to serve as a backfill material. In this context, it is worth mentioning the early review of Grauer (1990), who summarised the geochemical properties of bentonite and pinpointed a number of safety-relevant issues and uncertainties related to this material. Since then, the number of studies has increased, also because of extensive programmes of other waste management organisations and international collaboration (e.g. various EC projects). An important reason for this large effort is the complex nature of compacted bentonite leading to complex and coupled thermo-hydro-mechanical-chemical behaviour. Such couplings render experimental investigations challenging. For example, the intimate association of water and clay make it difficult to obtain reliable porewater chemistry data without inducing disturbances, and porewater compositions of the bentonite backfill are therefore usually estimated from modelling (e.g. Curti & Wersin 2002).

During its lifetime in a repository, the bentonite backfill will experience loads, i.e. conditions which potentially may offset its favourable properties (e.g. swelling capacity), for example:

- elevated temperatures due to heat transfer from the canister during the initial stages after repository closure
- interaction with alkaline leachates from cementitious materials adjacent to or near the backfill
- interaction with iron species and transport of hydrogen gas released from the corroding steel canister and other steel components
- interaction with the host rock porewater and changes in salinity in the surrounding host rock
- uneven swelling during saturation leading to density gradients and low-density areas
- development of microbial activity in low-density areas triggering sulphate reduction and sulphide generation

Many of these loads are related to *geochemical processes*, such as mineral dissolution/precipitation and cation exchange reactions. Key issues in this regard are the dissolution of the main mineral montmorillonite and its transformation to a non-swelling clay, as well as cementation via mineral precipitation. Furthermore, the stability and longevity of montmorillonite in a repository environment – even without "external" loads – has been questioned (Savage et al. 2010a).

Despite the considerable literature on bentonite in the context of HLW¹ repositories, a comprehensive document synthesising the current knowledge and associated uncertainties is lacking. The overall objective of this report is to fill this gap and to provide a state-of-the-art knowledge base for Nagra's HLW repository concept. The main focus is on the loads and underlying *geochemical* processes which may affect the barrier performance of the bentonite backfill. Hydro-mechanical aspects are included in light of their coupling with geochemical processes. Radionuclide retention in bentonite is described only in cases where it competes with other geochemical processes, as this topic has been discussed in detail in other reports (e.g. Van Loon 2014, Baeyens et al. 2014 etc.). The report includes the latest findings and developments from Nagra's bentonite programme (e.g. Leupin et al. 2015) as well as from international projects, such as the SKB-managed ABM project (Svensson et al. 2011, Svensson 2015), the FEBEX-DP project (Villar et al. 2018, Wersin & Kober 2017), or the EC project PEBS (Schäfers et al. 2014). An important component of the report is the description of coupled modelling developments, including thermo-hydro-mechanical (THM) and reactive transport modelling. In this context, the engineered barrier system (EBS) Task Force (a joint project managed by SKB and including several international research teams) has played an import role.

The general framework is provided in Chapter 2 where Nagra's HLW repository concept and the role of bentonite in the repository are described. The safety functions of each barrier are listed. The expected evolution of the bentonite boundary conditions and of the bentonite backfill is summarised based on current understanding.

Important basic information on bentonite is given in Chapter 3. This includes mineralogical data, thermodynamic and kinetic treatments, concepts on microstructure (porosity), porewater chemistry, solute transport, gas transport, THM properties, chemical-mechanical coupling and thermal effects on bentonite. Uncertainties related to these different aspects are highlighted with regard to Nagra's concept.

Chapter 4 is dedicated to the modelling of coupled processes. Current concepts on reactive transport modelling with the focus on the electrical double layer are summarised. The possibilities for coupling chemical with hydro-mechanical processes are explored and the status of gas and THM modelling is provided. Again, uncertainties related to these modelling approaches are highlighted with regard to Nagra's concept.

In the central Chapter 5, the impact of the different processes in the repository on the bentonite backfill performance is evaluated. Specifically, it focuses on homogenisation aspects and then on the impacts of salinity, cementitious leachates, corroding metals (Fe and Cu) and hydrogen gas. Also, the relevant processes and their effects during saturation and the period of elevated temperatures are discussed. Finally, an attempt is made to couple and integrate the different processes during the different stages in the repository.

A synthesis of scientific evidence is documented in Chapter 6. It presents the current understanding of the geochemical evolution of the bentonite backfill and pinpoints the remaining uncertainties. Suggestions for mitigating safety-relevant uncertainties are provided.

¹ HLW refers to vitrified high-level waste as well as spent fuel.

2 The role of bentonite in Nagra's repository concept

2.1 Nagra's repository concept

Overview

The concepts for implementing deep geological disposal currently considered in Switzerland are the result of many years of RD&D, as well as of safety, design, cost, site evaluation and other studies performed by Nagra (e.g. Nagra 1988, 1994a,b, 2002a,b, 2005, 2008a,b, 2011a,b,c,d, 2013a,b,c,d, 2014a,b) and the reviews of these reports by the authorities (e.g. HSK 1986, 1996, 2004, 2005, Nagra 2008b, ENSI 2015). These concepts also take into account the relevant national legal and regulatory guidance (e.g. KEG 2003, KEV 2004, ENSI 2009), as well as input from international developments.

This section provides a brief overview of the concepts currently under investigation, focusing on concepts for the major facilities, their operation and closure of the deep geological repositories, as well as on concepts for the barrier systems that provide post-closure safety. Where pertinent alternatives exist, these are mentioned explicitly.

Post-closure safety concepts

The protection objective for deep geological disposal states that *deep geological disposal of radioactive waste has to ensure the long-term protection of humans and the environment from the effects of ionising radiation, without imposing undue burdens and obligations on future generations*. This objective, and thus the safe disposal of the waste, must be ensured by multiple safety barriers along with additional protective and preventive measures.

The following paragraphs describe the safety concepts for the post-closure phase based on the necessary requirements on post-closure safety and the currently proposed implementation. A more detailed description is given in Nagra (2008b) and in Nagra (2014a).

Requirements

The requirements on post-closure safety of a deep geological repository refer to the overall protection objective and the relevant legal and regulatory guiding principles. An additional requirement of the post-closure phase arises from environmental protection legislation, i.e. the release of chemo-toxic substances from the barrier system after closure of the repository should not exceed regulatory threshold values. The complete set of post-closure safety requirements is given in Tab. 2-1.

Tab. 2-1: Post-closure safety requirements

Note that some of the listed requirements have been extended, merged and/or refined with respect to the original sources. Nagra (2016)

| Title | Requirement | Source/ Motivation |
|--|---|---|
| Protection criteria | Quantitative protection criteria are used until at the most one million years after repository closure to determine whether the protection objective has been fulfilled. | ENSI-G03 Sections 4.3 and 7.2.2 |
| Classification of scenarios | The variants for future evolution of a closed repository that are realistically conceivable are to be classified into likely and less likely and the selected classification has to be justified. | ENSI-G03 Section 4.3.2 |
| Protection criterion 1 | For each future evolution classified as likely, the release of radionuclides may not lead to an individual dose exceeding 0.1 mSv per year. | ENSI-G03 Section 4.3.2 |
| Protection criterion 2 | Future evolutions classified as less likely that are not considered under protection criterion 1 may not, taken together, constitute an additional individual radiological risk of health detriment exceeding one in a million per year. | ENSI-G03 Section 4.3.2 |
| Period of concern | The period during which the multiple barrier system has to provide its safety functions is determined by the radiological hazard potential of the emplaced waste and the predictability of long-term geological evolution. After this period, radiological impacts may not be significantly higher than natural radiological exposure. | ENSI-G03 Section 7.2.2 |
| Protection from natural events and processes | The safety functions of the multiple barrier system must not be impaired to a significant extent by natural events and processes (e.g. erosion, decompaction, seismicity). | SGT ENSI-G03 Sections 4.1 & 4.2 KEG Art. 5.1 |
| Protection from repository-induced effects | The safety functions of the multiple barrier system must not be impaired to a significant extent by repository-induced effects (e.g. thermal load, chemical interactions, gas production, mechanical processes, radiation-induced effects). | SGT ENSI-G03 Section 5.1.3 KEG Art. 5.1 |
| Protection from inadvertent future human actions | The safety functions of the multiple barrier system must not be impaired to a significant extent by foreseeable future activities related to the exploration or exploitation of the geological environment (e.g. drilling and other investigations from the surface, mining activities, geothermal exploitation, extraction of mineral and geothermal water). | ENSI-G03 KEG Art. 4.2 SGT |
| Protection from direct human access | The emplaced radioactive waste must be protected sufficiently and permanently from direct human access. | KEG Art. 5.3 |

Proposed implementation

The individual sub-elements (components) of the post-closure barrier system are:

- the overall geological situation
- the waste matrices
- the SF/HLW disposal canisters
- the backfill of the emplacement drifts
- the backfill of other underground structures and individual seals
- the host rock and possibly additional confining rock units with substantial barrier efficiency that together form the containment-providing rock zone

Interactions between the different barriers are influenced by the spatial arrangement of the waste and the barriers, which is basically given by the repository architecture. Each barrier has its specific evolution, although all barriers are expected to provide significant contributions to the overall barrier effect with regard to the release of radionuclides throughout the respective time frames for safety assessment.

The time frames for safety assessment – or periods of concern – were derived in Nagra (2008b) in the context of the Sectoral Plan for Deep Geological Repositories, based on the guidance set out in ENSI (2009), and considering the radiotoxicity of the allocated wastes and its evolution. The time frame for safety assessment is 100,000 years for the L/ILW repository and 1 million years for the HLW repository.

Each barrier performs one or several post-closure safety functions, which are (Nagra 2008b, 2010, 2014a):

- **Physical isolation of the waste from the human environment and assurance of long-term stability of the barrier system:** The safety and security of the waste, including fissile material, is ensured by placing it deep underground, with all access routes backfilled and sealed, thus isolating it from the human environment and reducing the likelihood of any undesirable intrusion and misapplication of the materials. This also protects the repository from processes and events taking place at the earth's surface that could jeopardise the safety of a near-surface repository (e.g. war, civil unrest, future glaciations, erosion etc.). Furthermore, it is assessed whether the extraction and use of natural resources affects the barrier function of the host rock or directly affects the repository itself.
- **Confinement of radionuclides:** Much of the activity initially present decays while the waste is totally contained within the primary waste containers, particularly in the case of SF and HLW, for which the high integrity canisters are expected to remain unbreached for several thousand years due to the favourable geochemical and geomechanical conditions. Even after the SF/HLW canisters are breached, they still provide a barrier for radionuclide transport because they limit water access to the SF and HLW and because of the favourable radionuclide retention properties of canister corrosion products for many radionuclides.

- **Slow release of radionuclides from the waste matrix:** After canister breaching, the rate at which radionuclides are released from the waste matrix is low, due to favourable geochemical conditions (specifically due to the prevailing reducing conditions). This applies specifically to SF (stable UO₂/MOX matrix) and to HLW (stable glass matrix), but also to some long-lived ILW and L/ILW where a large fraction of radionuclides is incorporated in slowly corroding steel.
- **Retention of radionuclides in the near-field and geosphere:** After release from the waste matrices, radionuclides are transported only very slowly through the further near-field barriers (backfill/seals) and through the host rock and the confining units due to a number of favourable properties of the engineered and geological barriers (e.g. favourable geochemical conditions in the engineered barriers, in the near-field and in the geosphere, low water flow in the engineered barriers, in the host rock and in the confining units). During transport, further radioactive decay takes place, further reducing radionuclide release from the repository to the human environment.

A number of additional processes attenuate releases during transport towards the human environment and limit the concentrations of radionuclides in that environment. These include spreading due to diffusion and hydrodynamic dispersion and also dilution.

Fig. 2-1 and Fig. 2-2 illustrate the barrier systems for the different waste types and describe how the properties and processes of the individual elements of the barrier system contribute to meeting the (safety) functions and the additional safety requirements.

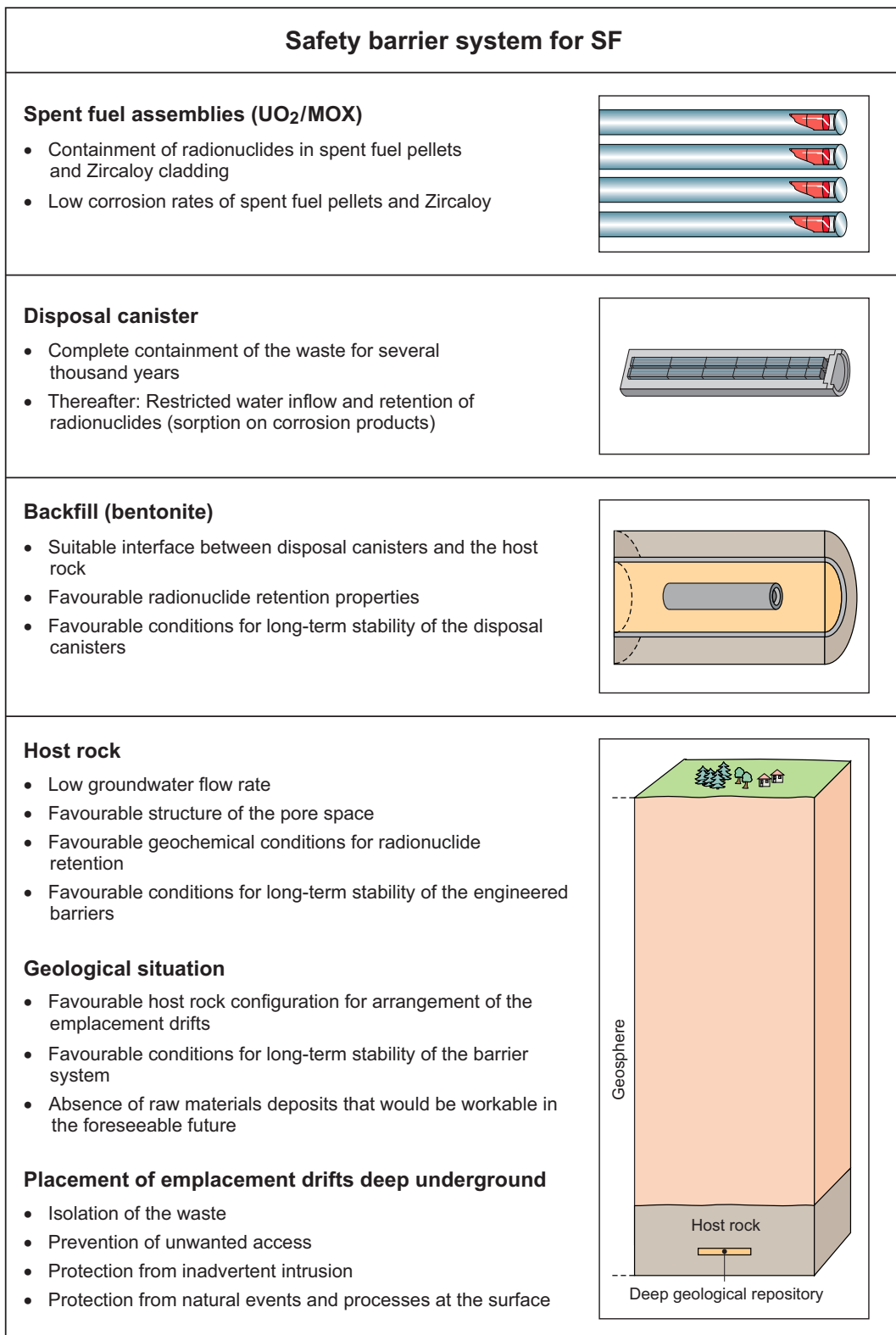


Fig. 2-1: Illustration of the barrier system for SF along with the properties and processes of the individual barriers that contribute to post-closure safety

Not drawn to scale, the backfill of other underground structures and the various seals are omitted.

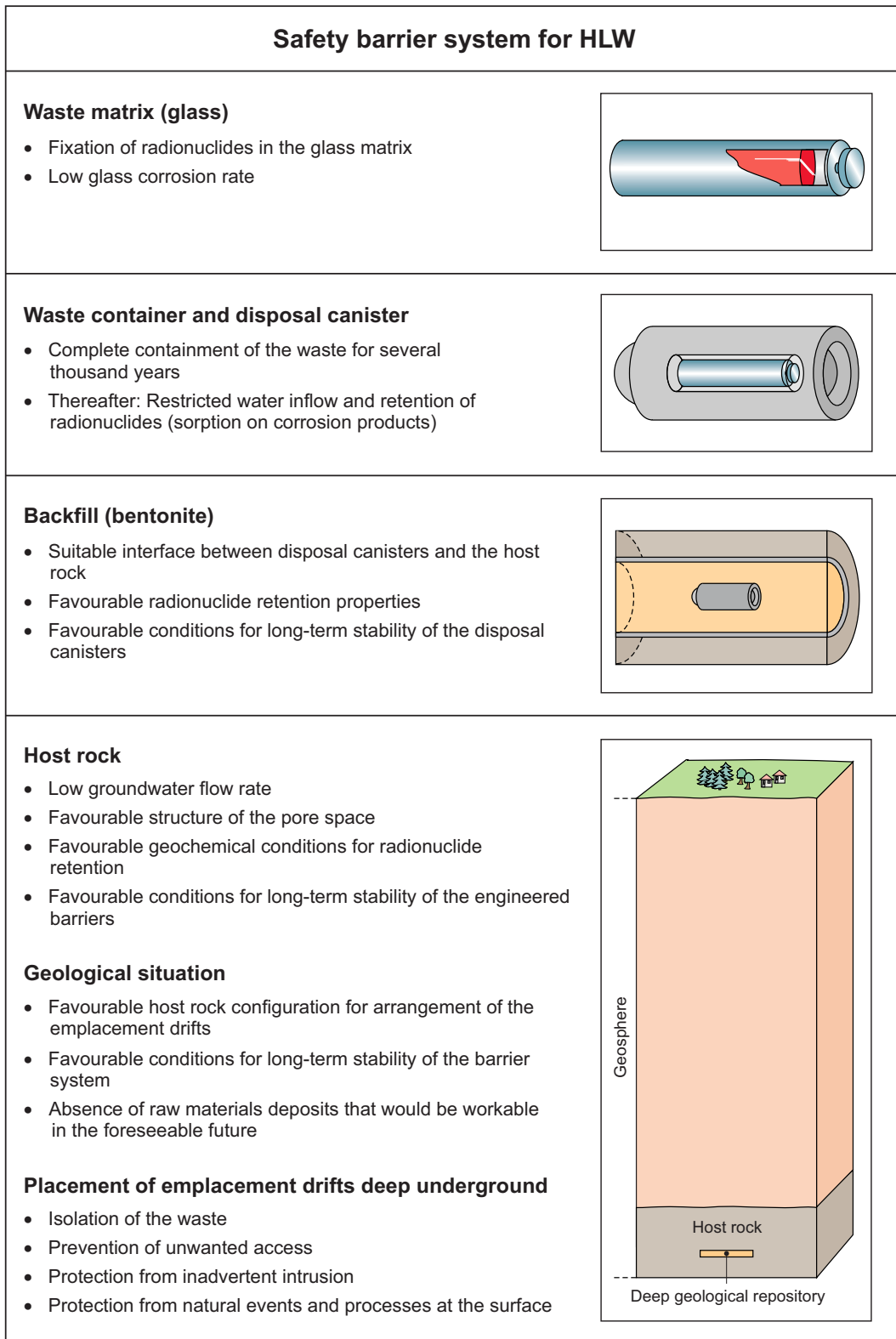


Fig. 2-2: Illustration of the barrier system for HLW along with the properties and processes of the individual barriers that contribute to post-closure safety

Not drawn to scale, the backfill of other underground structures and the various seals are omitted.

2.2 Current Nagra RD&D programme on bentonite

2.2.1 Bentonite-based barriers (buffer², backfill³, seals⁴)

In the current repository concepts, compacted bentonite is used (based on Nagra 2016):

- in the form of compacted bentonite blocks and granular bentonites as a buffer surrounding the SF and HLW canisters
- in the form of a sand/bentonite mixture in the Engineered Gas Transport System (EGTS) in the L/ILW repository
- in the form of granular bentonite and/or blocks in other repository sealing and closure structures

The main objective of the work described below is the development of an improved understanding of the processes occurring in the course of repository evolution that may affect the capacity of these components to fulfil their safety-related requirements over the timescales for which these components have to fulfil their safety functions (e.g. as set out in Leupin et al. 2015). These requirements are formulated in terms of safety-relevant attributes and preferred values of the parameters that quantify these attributes (see Appendix).

Based on the evaluation made in Nagra (2016), specific areas where improved understanding and modelling capabilities will be sought are:

- THM evolution of the bentonite buffer and backfill barriers
- stability of the bentonite buffer at elevated temperatures
- chemical and microbiological processes that might affect the safety functions of the bentonite buffer and backfill barriers, including interactions with other engineered materials
- the migration of repository-generated gases through the bentonite buffer and backfill barriers

Furthermore, a continuing RD&D objective is to support the development of models and data used to evaluate radionuclide retention and transport in the bentonite buffer and backfill barriers in support of safety assessment.

² The term "buffer" refers to the engineered barrier around the SF/HLW canisters that consists of compacted bentonite.

³ The term "backfill" refers to the bentonite-based material used for backfilling the underground structures.

⁴ The term "seals" refers to the repository elements made of bentonite-based materials that seal off the emplacement tunnels from the rest of the underground structures.

TH/THM processes and modelling

TH modelling is required to analyse temperature evolution within a repository, as well as to investigate saturation behaviour and the fate of gases. The HE-E experiment at the Mont Terri underground rock laboratory (URL) was designed and constructed as part of the recent 7th EURATOM PEBS (Long-term Performance of Engineered Barrier Systems) project, which has provided a first large-scale test (1:2 scale with temperatures up to 140 °C) aimed at improving the understanding of TH behaviour of the Nagra near-field concept (Gaus et al. 2014). It included:

- comparing THM model predictions for water uptake by a bentonite buffer against experimental observations as part of PEBS (Johnson et al. 2014)
- measurements of the thermal conductivity of granular bentonite, bentonite blocks and bentonite/sand mixtures at ETHZ (Plötze & Valter 2011)
- updated numerical analyses of combined heat transport, saturation and gas release from an SF/HLW emplacement room into the surrounding host rock using a non-isothermal two-phase flow and transport model (Senger et al. 2014)

Temperature and saturation evolution were found to be well described with current models, at least up to the time that maximum canister and buffer temperatures are reached. The Euratom PEBS project has shown that current models can predict the saturation process well until around 90 % saturation is achieved. Thereafter, uncertainties are greater, but since the safety-relevant attributes of the buffer are already attained at 90 % saturation, these are not so relevant to long-term safety (Johnson et al. 2014). Nonetheless, improved accuracy in predicting temperatures and saturation in time and space is desirable and will be an objective when interpreting the FE experiment, a 1:1 full-scale test of the Nagra concept that started in early 2015 at the Mont Terri URL. THM modelling is used to assess swelling pressure development and buffer homogenisation.

Thermal stability

A review of the current understanding of the thermal stability of montmorillonite⁵ is given in Leupin et al. (2015). A comprehensive understanding of the impact of temperatures above 100 °C on THM properties, similar to that available at temperatures below 100 °C, is not yet available. Nonetheless, there is clear evidence that reasonable swelling pressure and low hydraulic conductivity are likely to be maintained during and after the thermal transient period. In particular, since the RD&D Plan (Nagra, 2009), several laboratory and field investigations of the changes in swelling, plasticity and hydraulic properties of thermally altered bentonite have been performed, including several long-term heater-buffer experiments that have been evaluated as part of the PEBS project (Johnson et al. 2014) and laboratory investigations performed at ETHZ at temperatures above 100 °C under partially saturated conditions (Plötze & Valter 2011). Evaluation of the combined data from these and other studies indicates marginal effects on swelling pressure and an increase in hydraulic conductivity of less than one order of magnitude for exposure of bentonite to partially saturated conditions at temperatures up to 125 °C. It can thus be concluded that the impact on the performance of the bentonite will be minimal over the long term, considering the short duration of the temperature peak and the limited amount of bentonite affected by temperatures over 100 °C when the requirement of maximum heat output of 1,500 W per canister is in place (section 5.8).

⁵ Montmorillonite is a swelling clay from the smectite group and the predominant mineral in bentonite.

The spectrum of experimental conditions described in Leupin et al. (2015) encompasses the range of thermo-hydro-chemical conditions in a HLW repository and in fact goes beyond it. The overall experimental findings confirm that montmorillonite is sufficiently stable over the transient thermal period to fulfil the safety requirements of the bentonite buffer. The repository near-field is designed to have a low water-to-solid ratio, which leads to a lower degree of alteration than observed in the high water-to-solid ratio experiments typically performed.

Chemical and microbial processes

Potential chemical interactions of bentonite with engineered components (canister metals, concrete tunnel liner, steel support mesh, and arches, plus transport rails) in a geological repository for SF/HLW in Opalinus Clay (OPA) have been assessed in Savage (2014). The current status is described below.

The main focus of Nagra's work regarding interactions with metal corrosion products has been on the effects of adsorbed Fe(II) on retention of radionuclides as well as an assessment of impacts on hydraulic and swelling properties. The latter includes work carried out in the context of PEBS and also collaborative work involving PSI and ETHZ (Hofstetter et al. 2014). Fe(II) migration and mineral transformation of the buffer due to Fe(II) have been found to proceed slowly; experiments of up to 6 years duration analysed in the context of the PEBS project indicate that no new iron silicates are formed and a penetration depth of Fe into the bentonite of only a few mm. Indications from models are that the interaction zone may be 1 – 10 cm after some tens of thousands of years (Bradbury et al. 2014).

Potential impacts of interactions with cementitious materials on the long-term properties of clay have been assessed using simple bounding assumptions, such as limitation by mass balance, kinetics, and/or mass transport (Leupin et al. 2015). More detailed reaction-transport simulations have also been carried out (Bradbury et al. 2014, Kosakowski & Smith 2014). These and similar calculations carried out in the context of PEBS (Johnson et al. 2014) show that alteration of the bentonite due to an ordinary Portland cement (OPC) concrete liner is quite limited, extending some 10 cm into the bentonite after a few tens of thousands of years. Bradbury et al. (2014) also showed that the interfaces between the concrete liner and both the OPA and the bentonite have a strong tendency to clog after a few thousand years. However, it remains difficult to predict long-term behaviour and material properties from short-term experimental data. A careful check of mechanistic models by experimental data is required to increase confidence in model predictions. A PhD project at LES/PSI (Shafizadeh 2019) is investigating alterations at montmorillonite – OPC interfaces. Specifically, changes in porosity resulting from dissolution and precipitation reactions and their effect on diffusion properties across the interfaces are observed by tracer diffusion experiments and neutron imaging. Such data can be used to check or to better constrain model simulations.

In order to limit the extent of chemical alterations in both the host rock and backfill material, a shotcrete liner with lower portlandite content, resulting in a reduced pH, can be used. For this material, a conservative mass balance model suggests that a maximum of only 4 cm of bentonite would be altered (Savage 2014). The specific pH value in porewater in low pH shotcrete has been determined (Cloet et al. 2014) and methods to study the interaction with clays have been developed. An integrated assessment of the knowledge of cement-bentonite interactions has been performed at the University of Bern (Dolder 2015). A low-pH shotcrete is the preferred option in view of long-term safety, provided that it also fulfils the operational safety requirements (section 5.3).

Microbial activity in compacted bentonite with a dry density of more than 1.45 Mg m^{-3} is known to be low in Wyoming bentonite, due to the small size of the pores, their poor interconnectivity and the restricted availability of water (e.g. Masurat et al. 2010, Stroes-Gascoyne et al. 2011). However, microbial activity at interfaces, especially those between SF/HLW canisters and the bentonite buffer, or within the excavation damaged zone (EDZ), remains a concern because of the potential for microbes to promote corrosion. Studies of microbially induced effects are being performed at Mont Terri and in laboratories at EPFL to improve understanding of the conditions under which microbial activity can occur (rock pore sizes, availability of nutrients etc.) and to assess possible implications for repository performance (ongoing work).

Migration of repository-generated gas

Nagra has participated in comprehensive laboratory and in-situ experiments in the 7th EURATOM FORGE (Fate of Repository Gases) project (Shaw 2014), which contributed significantly to the understanding of gas flow through bentonite. As described in Villar et al. (2012b), two-phase flow is expected to be the dominant gas transport mechanism in unsaturated or partially saturated bentonite. Strongly confined experiments have, however, shown that, at degrees of saturation of $\sim 80 - 90 \%$ or higher, no gas flow takes place unless the applied pressure is equal to or greater than the total stress, at which pressure dilatant pathways form that transport gas through the bentonite by advection. These pathways self-seal once the gas pressure falls, as has been demonstrated in small-scale experiments and large-scale mock-ups (Shaw 2014).

Two-phase flow is expected to be the dominant gas transport mechanism in the sand-bentonite mixtures used in the EGTS. The ongoing 1:1 scale GAST experiment at the Grimsel Test Site (GTS) represents a sand/bentonite seal and examines water and gas migration through the sand/bentonite. It is described below under planned RD&D leading up to the general licence application. The possibility that interactions between sand/bentonite porewater and high-pH porewater in the ILW and L/ILW emplacement rooms could lead to pore clogging and reduced gas permeability has been investigated in Kosakowski & Smith (2014). This research used qualitative reasoning and quantitative illustrative analyses which indicated that, for an appropriately chosen EGTS design, the EGTS should function as required over a 100 ka time frame.

2.2.2 The SF/HLW near-field

The buffer safety function in the SF/HLW emplacement rooms should provide a well-defined interface between the disposal canisters and the host rock, strong retention of radionuclides and a suitable environment for the disposal canisters and the waste forms over the considered time period, and it should be compatible with the favourable conditions in the host rock. The main objective of studies is to further investigate the impact of the thermal pulse and the resaturation of the SF/HLW near-field on some of the key parameters describing the performance of the buffer and the host rock with respect to its safety function. Because of the coupled nature of the processes involved, an understanding of resaturation requires an understanding of temperature evolution, gas transport and geomechanical evolution and self-sealing of the surrounding excavation damaged zone (EDZ).

Particular focus is on the understanding of the temporal evolution of the conditions anticipated in the repository. Given the scale and time frames involved, numerical (THM) modelling is an important aspect, but it needs to be underpinned by targeted laboratory and URL experiments. The ultimate objective is a reliable description of the evolution of the SF/HLW near-field in terms of safety-relevant parameters so that safety function indicators for the near-field can be derived and demonstrate how the derived criteria can be met.

The resaturation of the SF/HLW near-field has been a high priority for more than a decade. A synopsis of early experimental investigations and numerical studies as part of the Project OPA was given in Nagra (2002a) and Nagra (2004), providing an early quantitative assessment of the hydro-thermal evolution of the repository near-field. Long-term monitoring of saturation, pore-pressure evolution and swelling pressure provided an important new database for the evaluation of HM processes. Some studies of the EU NF-PRO Project were dedicated to the THM evolution of the SF/HLW near-field, ranging from the non-isothermal early post-closure phase to the processes and phenomena occurring at late times (Huertas et al. 2008). As an outcome of the project, a comprehensive document on the state-of-the-art was compiled, addressing phenomenology, conceptualisation and quantitative assessment of SF/HLW near-field evolution for a variety of repository concepts.

More recent work includes the follow-up project PEBS ("Long-Term Performance of Engineered Barrier Systems"), launched as part of the 7th EU Framework Programme, which concentrated on the prediction and evaluation of THM processes in the SF/HLW near-field during the early and late resaturation phases. The experimental work included the dismantling of the Mont Terri EB experiment, which demonstrated that dense bentonite pellets evolve to a swelled material that was not *a priori* distinguishable from swelled block material from a hydro-mechanical perspective. It also demonstrated effective sealing through swelling of blocks and pellets with large initial density differences even under non-optimum emplacement conditions (Mayor & Velasco 2014). In a numerical benchmark exercise, different THM codes and models were evaluated by using them to extrapolate the short-term evolution of the SF/HLW near-field to the long term. The evolution of the relative impacts of different THM processes was examined, as was the propagation of uncertainties. An important insight was thus gained into the capabilities and limitations of the different THM codes and models to capture the evolution of the SF/HLW near-field in terms of temperature, pore pressure and stress. Benchmark exercises with different THM codes and different modelling groups revealed that the thermal evolution of the near-field was modelled consistently, and the thermo-hydraulic properties of the bentonite buffer could be constrained within narrow uncertainty ranges. However, significant discrepancies were seen in the simulation of pore pressure, water saturation and stress, indicating that the existing THM codes do not capture the full spectrum of relevant hydro-mechanical couplings needed for a reliable prediction of the hydro-mechanical evolution of the SF/HLW near-field.

Nagra-specific modelling studies focusing on thermo-hydraulic (TH) near-field behaviour after repository closure have been carried out using a 3D model of a SF/HLW emplacement room (Senger & Ewing 2008). These dedicated sensitivity studies addressed the impact of resaturation, heat, gas transport and physico-chemical processes (Papafotiou & Senger 2014b, Senger & Papafotiou 2014, Senger et al. 2014). Estimates of resaturation time, pressure recovery time and maximum temperature at the canister surface and at the tunnel wall were achieved for a broad spectrum of geological settings. First attempts were undertaken to simulate the impact of hydro-mechanical couplings on the evolution of stress and deformation in the repository near-field, including canister movements in response to the buffer saturation process (Dupray & Laloui 2016).

2.2.3 Buffer material evaluation for HLW emplacement drifts

MX-80 bentonite has been chosen as a reference material by various waste management organisations and characterisation and investigations of this material are therefore correspondingly advanced. It is recognised, nonetheless, that bentonites other than MX-80, with similarly high montmorillonite contents, are likely to be used ultimately in the final repository for reasons related to availability and cost. The objective of the work is thus to identify various suitable bentonite materials to be used as buffer material around SF/HLW canisters according to the necessary requirements (e.g. swelling, hydraulic conductivity) and to demonstrate how the knowledge base on MX-80 bentonite can be transferred to these materials. A reference material will be selected for the general licence application, while additional options will continue to be evaluated. The final decision on the material to be used will be taken in anticipation of the construction licence.

MX-80 sodium bentonite from Wyoming (USA) has been broadly studied over the last decades (e.g. Madsen 1998, Karnland et al. 2006) and is presently considered as a reference material. However, other natural bentonites are also available and could be an alternative to MX-80 (Karnland et al. 2006, Laine & Karttunen 2010, Svensson et al. 2011, Wilson et al. 2011).

The requirements for the buffer material in the Swiss concept are described in Leupin & Johnson (2013) and Leupin et al. (2015). These requirements are related to safety-relevant properties (such as swelling capacity and hydraulic conductivity). Quantitative criteria have been established for several safety-relevant properties independently of the material used.

Cuevas et al. (2013) developed a method for the comparison of different bentonite materials by defining the bentonite properties to be measured. In Cuevas et al. (2014), the database available for the characterisation of 19 bentonites in order to establish a basis for their comparison with respect to MX-80 bentonite was documented. It was concluded that a simple test for the assessment of bentonites and their adequacy to substitute for MX-80 bentonite as a buffer material in a HLW repository is not trivial, mainly because the safety-relevant properties of the bentonite result from a variety of parameters (e.g. octahedral charge, type and amount of accessory minerals, type of charge-compensating cation etc.) and the interpretation of the results of standard methods (e.g. establishing the relevance of the amount and type of accessory minerals measured by X-ray diffraction (XRD) on the long-term stability of the bentonite). Nonetheless, an important conclusion from both Cuevas et al. (2013) and Karnland et al. (2006) is that there are bentonites of different origins that are likely to be appropriate for use as buffer material.

2.2.4 Buffer emplacement technology

Objectives

A buffer includes granular bentonite material as well as pedestals made from pre-compacted bentonite blocks, the latter being emplaced together with the canisters.

The buffer emplacement technology is an integral part of the waste emplacement concept, which envisions that the emplacement of each SF/HLW disposal canister on its bentonite support blocks is directly followed by filling the open space around it with buffer material. There is no industrial reference technology available from which basic technical feasibility can be justified. Hence, the objective of the work consists of technology development to demonstrate that the bentonite emplacement density satisfies long-term safety requirements for the buffer in SF/HLW emplacement tunnels.

Further objectives, to be addressed mainly beyond the general licence application, will concern prototype development and optimisation aspects with regard to industrial application, quality control and quality improvement, as well as operational safety and radiological protection.

The buffer emplacement concept for SF/HLW focuses on the use of granular bentonite material to be backfilled around the disposal canisters and the pedestals. The major requirements relate to the completeness of the backfilling around, in front of and behind each disposal canister allowing for:

- a target dry density of 1.45 Mg m^{-3} for the entire bentonite backfill, a value that ensures the relevant requirements from a long-term safety point of view (Leupin & Johnson 2013)
- a reasonably homogeneous distribution of the backfilled granular bentonite material and thus of its dry density

Moreover, in choosing an appropriate backfilling method, the following engineering requirements must be ensured:

- continuous backfilling process in a retreating mode for each disposal canister with high reliability and availability
- a smooth interaction sequence with the emplacement of disposal canister units incorporating pedestals made of highly compacted bentonite blocks
- sufficient backfilling quality accounting for an irregular tunnel radius due to gallery excavation deviations and support elements (e.g. shotcrete lining, steel ribs, breakouts etc.).

A screw conveyance technique has been identified as the most suitable method for granular bentonite backfilling with the desired quality, in comparison to pneumatic, tube drag conveyance, slinger stowing, belt conveyance methods and manual backfilling (Kennedy & Plötze 2004, Plötze & Weber 2007, Müller et al. 2017).

Major progress has been achieved with the implementation of the Full-scale Emplacement (FE) experiment at the Mont Terri Rock Laboratory and corresponding pre-tests (Müller et al. 2017). To demonstrate the feasibility of the emplacement of the granular bentonite, a prototype machine for emplacing the bentonite was constructed and successfully deployed (Fig. 2-3).



Fig. 2-3: The backfilling machine in the FE tunnel (left) and a detail of the emplaced granular bentonite (right) and the contact with the liner (FE experiment)

Foto left: Comet

The main conclusions from this project are as follows:

- The sectional dry density values in the FE tunnel at the Mont Terri URL assessed by mass-volume balance varied between 1.444 Mg m^{-3} (where low-quality material was backfilled unintentionally) and 1.555 Mg m^{-3} . With an average dry density of $1.489 \pm 0.003 \text{ Mg m}^{-3}$, the target dry density of 1.45 Mg m^{-3} for the entire backfill was clearly met under conditions that were challenging compared to a representative repository environment, due to the presence of the instruments in the buffer and the fact that care had to be taken to avoid damage. This was achieved by ensuring:
 - optimisation of the buffer material production (highly compacted granular bentonite mixture)
 - optimisation of backfilling technology using a machine with five screw conveyors
- Segregation during horizontal backfilling of granular material was observed. Approaches to suppress this effect have been evaluated qualitatively. Flexible slope coverage seems to be most promising in this regard.
- There seems to be potential for further optimisation of the density of horizontal buffer emplacement with the horizontal screw conveyance method. Approaches to increase dry density have been evaluated (Behl & Bunge 2016), but making conclusive statements is not possible at this stage.

Various methods for local dry density assessment were applied, especially in pre-tests at a surface industrial facility where access from outside to a dummy tunnel tube was possible. The tests comprised dielectric and gamma-gamma probe measurements as well as horizontal cone penetration tests (CPT). The resulting profiles of local dry density indicate higher values near the roof section and in the close vicinity of the screw conveyor positions. Lower density was observed near the invert. Although certain open questions persist, e.g. regarding boundary effects with dielectric measurements of density, in general the results show good consistency with the average dry density derived from sectional mass-volume balance calculations (1.48 to 1.55 Mg m^{-3} in the pre-test).

2.3 Expected evolution of bentonite buffer water saturation, swelling pressure, temperature, chemical interactions, coupled processes

2.3.1 Description of the near-field evolution

As an introduction to the following sections, an overview of some of the main coupled processes that govern the evolution of the SF and HLW emplacement tunnels in a HLW repository is given in Fig. 2-4.

After waste emplacement, the development of the safety-relevant properties of the SF/HLW tunnel near-field is essentially controlled by the interplay of various thermal, hydraulic, mechanical and chemical (THMC) processes, including saturation of the backfilled emplacement rooms, heat and gas production from the waste, as well as the swelling of the bentonite buffer and the reconsolidation of the surrounding host rock.

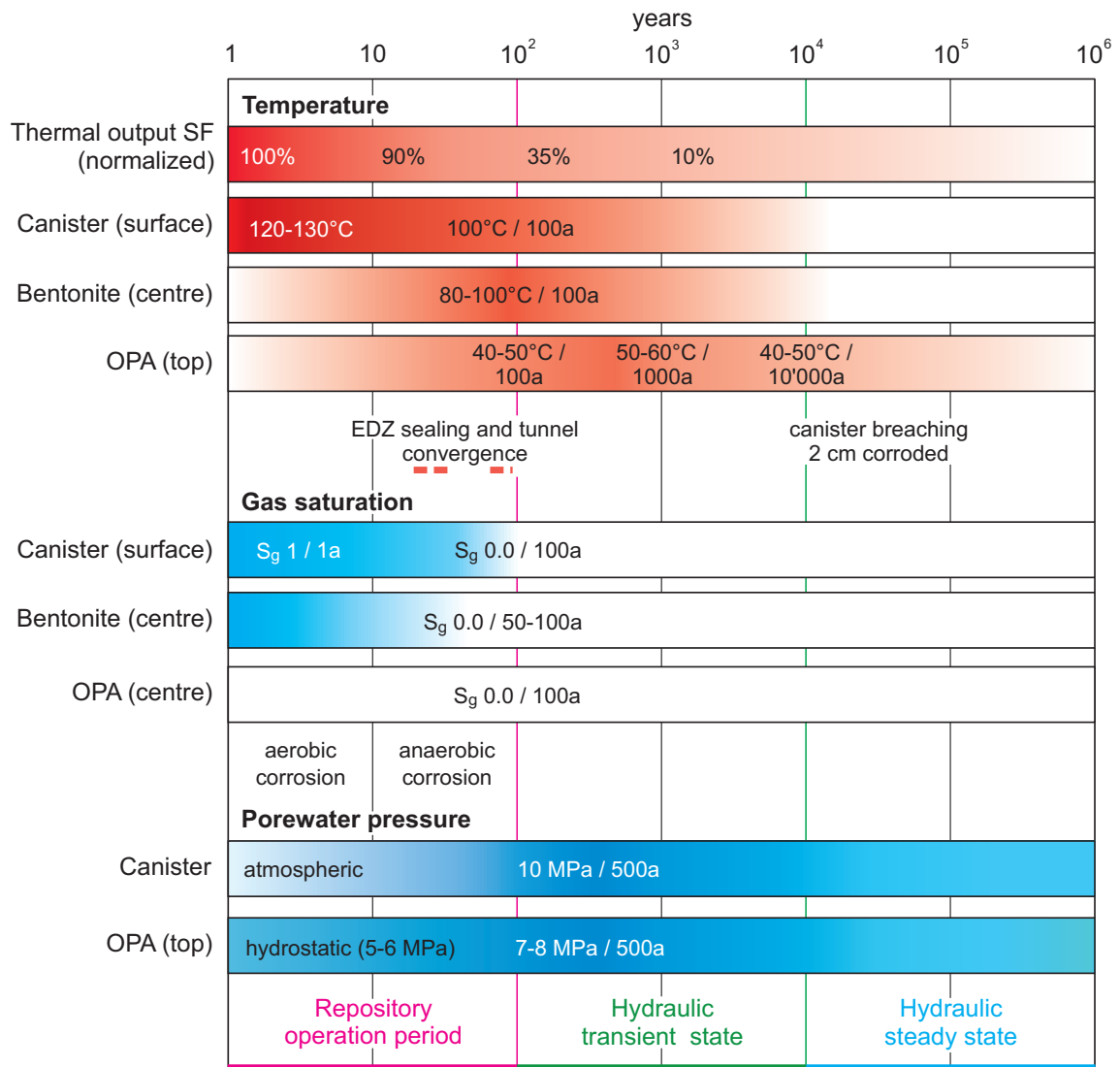


Fig. 2-4: Overview of the expected evolution of the main processes in a HLW repository based on a compilation of modelling reports and experimental data

The colour intensity indicates in a qualitative manner the expected evolution over time. From Leupin et al. (2016a). More detailed figures of TH process description can be found e.g. in Diomidis et al. (2016).

Decay heat from SF and HLW will increase temperatures within and around the repository for long periods of time. The effects of this heat on the engineered and geological barriers cannot be completely eliminated but can be kept low by ensuring a sufficient duration of interim storage and suitable waste emplacement density. The bentonite backfill will become saturated within about 50 to 200 years (depending on the host rock properties), after which pore pressure in the buffer will increase to that in the surrounding host rock. Gas is generated through corrosion of the steel used in tunnel support and the canisters and migrates in the gas and water phase through the engineered barriers or into the rock. The gas transport capacity of the OPA is expected to be sufficient to release the gas generated by corrosion of the SF/HLW canisters and tunnel installation materials into the surrounding host rock without causing rock damage (Diomidis et al. 2016). Fig. 2-5 in this report shows the evolution of temperature, pressure, and gas saturation at different locations in the HLW repository based on TH modelling.

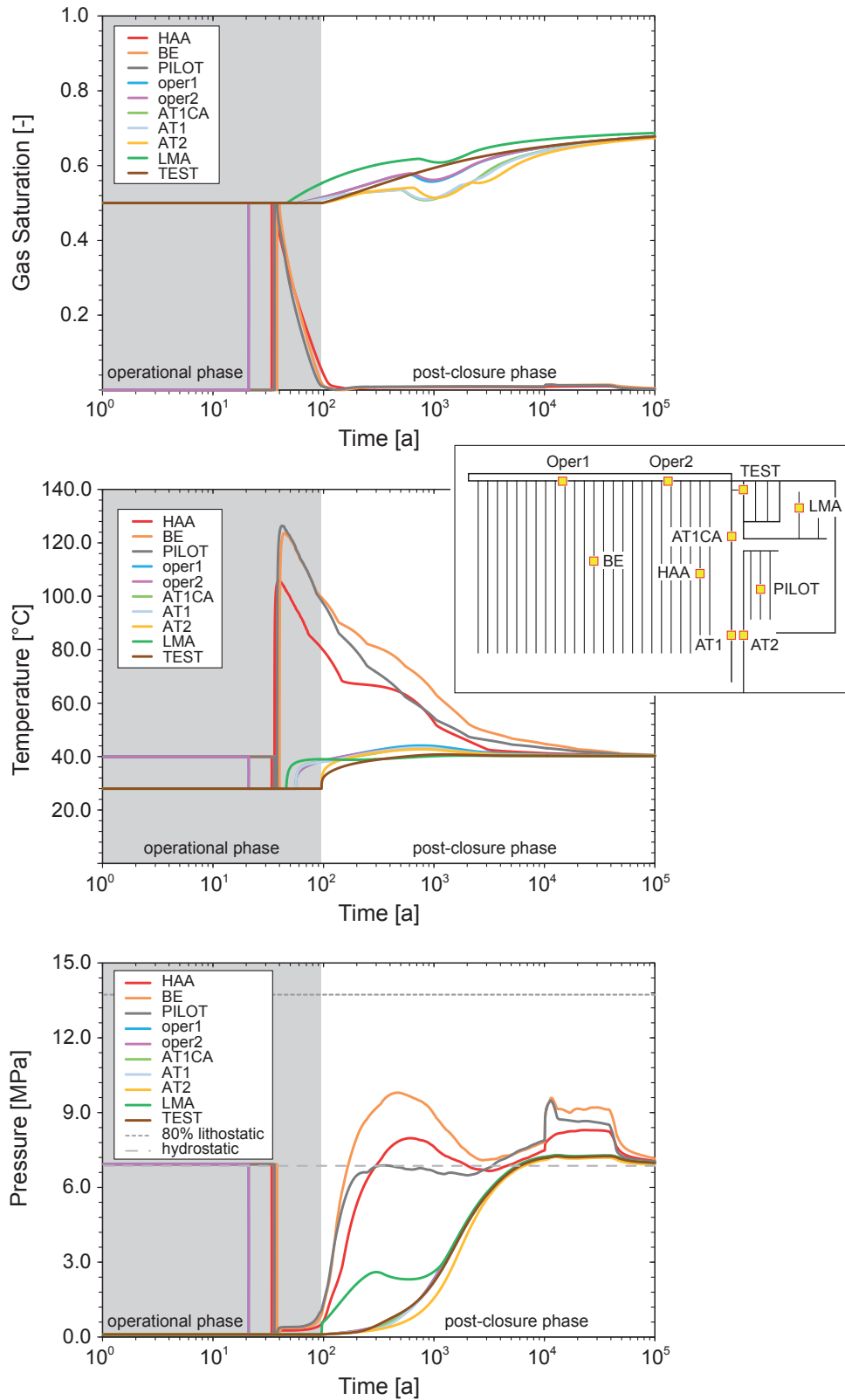


Fig. 2-5: Time-history of gas saturation (top), temperature (middle), and pressure (bottom) at selected locations of the HLW repository in the base case
 The locations of the various points are shown in the plan view of the model.
 Diomidis et al. (2016)

Other potentially significant processes include:

- degradation of the cementitious tunnel liner, migration of high-pH porewater affecting a thin section of the adjacent host rock and bentonite, where chemical interactions can occur (not shown in the figure)
- canister breaching due to corrosion

Overall, it is argued that the repository-induced effects can be adequately described based on present understanding and that the effects will remain below the identified criteria in Tab. 2-1. (Leupin et al. 2016a,b). However, further RD&D activities are foreseen to refine the assessment of the repository-induced effects, while new data and findings are being integrated into the understanding of the near-field evolution. This will also contribute to the refinement and justification of the performance criteria.

2.3.2 Evolution of the repository

In the following sections, a brief overview is given of the expected evolution of conditions in a HLW repository in OPA. The main references are Senger & Papafotiou (2014), Savage (2014) and Bradbury et al. (2014). The evolution of the ILW repository is assumed to be analogous to the L/ILW repository (Leupin et al. 2016a,b).

The pre-excavation phase

The undisturbed in-situ conditions of the host rock domain, geosphere and biosphere in the candidate siting regions will be investigated/assessed in an extensive field campaign prior to the excavation of the underground structures. For the OPA, much of the understanding already exists based on studies summarised in the *Entsorgungsnachweis* feasibility study (Nagra 2002b) and through ongoing field investigations and studies at the Mont Terri URL.

Safety-relevant parameters of the undisturbed system provide a baseline for evaluating all host rock and coupled host rock/near-field processes.

During the construction of the access tunnel and shafts, rock parameters are continuously collected to update safety analysis models. Host rock properties and THM state conditions (pore pressure stress, temperature, and saturation) are finally assessed in a test area. This facility allows for an extensive experimental programme and for a final set of host rock parameter values to be determined. The test area is also used to study aspects such as excavation damage, tunnel support techniques and interaction of backfill with the host rock.

A pilot repository is excavated and instrumented, and waste canisters are emplaced followed by backfilling. Instrumentation of the pilot repository allows monitoring of the evolution of the main repository analogue after closure.

The excavation and waste emplacement phase

The excavation phase starts with the excavation of the access to the HLW repository, followed by the construction of operations tunnels. Waste emplacement rooms are then constructed, including installation of the necessary tunnel support measures. Each room remains open for only a short period of time (up to 1 – 2 years) until waste emplacement and backfilling are complete. A continuing sequence of excavation, waste emplacement and backfilling ensures that a limited number of emplacement rooms are open at any given time. This phase is characterised by excava-

tion-related perturbations such as formation of an EDZ, desiccation of the surface region of the EDZ and cooling of the rock as a result of ventilation, the creation of a high hydraulic gradient, the potential importance of bacteria, oxidation of exposed minerals, mineral precipitation within the open pore space and initiation of corrosion and alteration of materials used for tunnel support.

The excavation phase is important with regard to long-term safety as several safety-relevant parameters are defined or can be modified during excavation, operation, emplacement of the waste and backfilling operations, although these changes to the host rock are restricted to the few metres around the excavation.

The thorough baseline characterisation – description of the initial state of the host rock – is instrumental for understanding the evolution of safety-relevant parameters and processes during the monitoring phase. Important aspects include:

- During excavation, breakouts and EDZ formation must be minimised and need to be carefully observed in order to limit damage to the host rock.
- Tunnel support must limit further EDZ formation but should comply with long-term safety principles.
- The bentonite buffer must have a density high enough to generate a sufficient swelling pressure, thus contributing to EDZ self-sealing under fully saturated conditions, providing sufficient sorption capacity for radionuclide retention upon canister breaching and a low enough swelling pressure that gas generated by canister corrosion can migrate through the buffer.
- Seals and plugs must comply with the hydraulic requirements.
- The emplacement rooms may be supported by a shotcrete liner and steel arches after construction.

The process of waste emplacement begins with the emplacement of the first canister together with its bentonite pedestal. The granular bentonite buffer material (water content about 5 %) is emplaced around the canister and these steps are repeated. If a shotcrete liner has been installed, intermediate seals are installed between every tenth canister and the emplacement of canisters, backfilling and sealing continues until the tunnel is filled. A bentonite seal and temporary plug is placed at the entrance to the tunnel.

The resaturation phase (0 to 100 years after emplacement)

For SF/HLW canisters, the initial heat output is limited to 1350 W, which will result in a temperature at the canister interface with the backfill of about 130 °C within about ten years (Senger et al. 2014). The temperature of the rock at the emplacement room boundary will reach its maximum (about 90 °C) after about 100 years. The bentonite buffer will become saturated within about 50 to 100 years, when porewater pressures within the backfill are much lower compared to those in the surrounding host rock. The chemical composition of the saturation water is expected to be similar to that of the host rock porewater (ionic strength 0.229 – 0.762 mol/kg H₂O, Cloet et al. 2014). Reactions between cementitious materials in the near-field and the saturation water can lead to very different chemical compositions, plug porosity and prolong saturation (section 5.3).

Heat transport to the far-field rock will increase the temperature to a maximum value of ~ 75 °C at a distance of 20 m above the tunnels. The porewater pressure in the rock within about 20 m of the tunnels will increase to as much as 70 % of the lithostatic pressure above the initial host rock value after about 100 years as a result of the thermal expansion of porewater and rock and the low hydraulic conductivity. After full saturation of the buffer, pore pressures in the buffer will increase to those in the surrounding host rock.

Corrosion of the steel used in the tunnel support and the canisters will lead to gas generation, although most of the gas produced in the first hundred years will dissolve (Papafotiou & Senger 2014a).

As defined here, this phase ends with the close-to-full saturation of the buffer (a residual gas saturation of 1 – 2 % is expected in the buffer at the end of the resaturation phase). By then, all construction and operations tunnels are backfilled and sealed. During this phase, the access tunnel and shafts are kept open. The resaturation phase largely coincides with the monitoring phase of the pilot repository, which is thoroughly characterised to identify any deviation from the expected evolution. Only the pilot repository will be monitored.

After complete saturation⁶ of the near-field (100 to 1,000 years after emplacement)

Between 100 and 1,000 years, the canister surface temperature will decline from 80 °C to 60 °C. By about 1,000 years, the near-field rock temperature will also decrease to about 60 °C. Porewater pressure in the near-field will reach its maximum of about 5 MPa above the initial formation pressure as a result of the coupled effects of gas generation (dominated by corrosion of tunnel support materials) and thermal expansion. In the far-field (20 m from tunnels and beyond), the porewater pressure will further increase (up to about 500 years) and then begin to decline and, in the confining units, an insignificant increase in pore pressure will have occurred. The thermal expansion of the rock sequences above the repository footprint will result in a heave of the ground surface in the 0.2 m range (Senger et al. 2014).

Anaerobic corrosion of the canister and the steel materials used for tunnel support will continue.

The end of the thermal period (1,000 to 10,000 years after emplacement)

Temperatures in the near-field will decline from about 60 °C to about 50 °C from 1,000 to 10,000 years and, in the far-field rock, temperatures will decrease to 10 °C above ambient rock values. Corrosion of steel materials used for tunnel support will be completed after a few thousand years, although gas generation from the thick-walled disposal canisters will continue. The gas production rate is thus reduced and porewater pressure will drop by several MPa in the near- and far-field rock due to the combined thermal and gas production effects.

Based on current understanding, compaction of the bentonite around the canister is not expected to occur as the adjacent rock reconsolidates. The EDZ is expected to be largely self-sealed, although increased gas pressures may keep pathways open.

The cementitious liner will eventually degrade due to the resaturation with porewater and precipitates might invade pores at the interface with OPA and bentonite (skin formation). A high-pH plume is expected to affect a few centimetres of the host rock and bentonite (Savage 2014).

Corrosion of the canister will produce mobile iron species that migrate through the bentonite and form iron-rich clay minerals or Fe(II) precipitates around the canisters.

⁶ Note that a residual gas saturation of 1 – 2 % remains in the buffer at the end of the resaturation phase.

Canister breaching and radionuclide transport period (10,000 years and beyond)

Beyond 10,000 years, the temperatures will decline gradually from 50 °C back to ambient rock values. Although some of the canisters are now expected to be locally breached, corrosion and gas production will continue for tens of thousands of years. As a result, hydrogen will continuously be transported through the backfill into the EDZ and host rock and mobile Fe(II) will diffuse into the bentonite. The porewater pressure in the rock surrounding the rooms will increase again slightly as canister corrosion continues, until corrosion is complete after about 50,000 – 100,000 years.

The chemical composition of the bentonite porewater will be similar to the host rock porewater (saturation water of the resaturation phase, defined above), assuming complete cement reaction, no full plugging of the transport porosity, and an unlimited host rock porewater reservoir.

Eventually, the canister will be breached and porewater will contact the waste matrix and radionuclides will diffuse through the saturated buffer and into the host rock. Depending on the chemical forms and half-lives of the radionuclides, the transport distances into the rock will vary. Safety analysis calculations show that negatively charged non-sorbing long-lived nuclides (such as ¹²⁹I, ³⁶Cl and ⁷⁹Se) might migrate as far as the biosphere after several hundred thousand years.

3 Bentonite characteristics

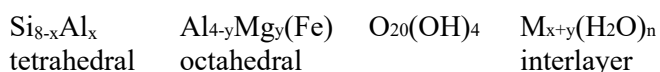
This section gives only a short description of the basic bentonite characteristics and concentrates rather on progress of understanding and increased data quality in the last decade. Not all of the described properties are equally important in the repository concept. Therefore, remaining uncertainties and their relevance for the repository concept are discussed for each group of properties.

3.1 Mineralogy

The main mineral in most commercial bentonites is montmorillonite, a prominent member of the smectite group. The properties of this swelling mineral largely determine the properties of bentonite, for example its swelling capacity, its CEC or its osmotic properties. Typical accessory minerals are quartz, cristobalite, feldspars, calcite and pyrite.

3.1.1 The role of montmorillonite

Smectites have a layered mineral structure consisting of a central sheet of octahedrally coordinated cations (e.g. Al^{3+} , Fe^{3+} , Mg^{2+}) which are sandwiched between two sheets of tetrahedrally coordinated cations (e.g. Si^{4+} , Al^{3+}). The octahedral sheets are linked by shared oxygens to the tetrahedral ones, forming tetrahedra-octahedra-tetrahedra (TOT) layers of about 1 nm thickness. Smectites can be divided into dioctahedral and trioctahedral subgroups (Güven 1988). In dioctahedral smectites, two out of three sites are occupied in the octahedral units by mainly trivalent cations (Al^{3+} , Fe^{3+}), whereas in trioctahedral units all three sites are occupied by mainly divalent cations (Mg^{2+} , Fe^{2+}). Smectites may incorporate variable amounts of water and cations into their structure between the TOT layers (interlayer) to charge balance the permanent negative layer charge of the TOT sheets. This layer charge is mainly induced by substitutions of Al^{3+} by divalent cations (e.g. Mg^{2+}) in the octahedral layer, and of a minor fraction of Si^{4+} by trivalent cations (e.g. Al^{3+}). The net negative charge in smectite (ranging between 0.2 and 0.6 equivalents per half unit cell) is compensated by exchangeable cations (e.g. Na^+ , Ca^{2+} , Mg^{2+}). Montmorillonite, a prominent member of the dioctahedral smectite subgroup, has the idealised structural formula:



where $x+y$ with $0.4 < x+y < 1.2$ and $y > x$. M represents exchangeable cations. The structure is sketched in Fig. 3-1.

The layer charge of montmorillonite is induced primarily by cationic substitution in the octahedral sheet and, to a far lesser extent, by substitution of Si^{4+} by Al^{3+} in the tetrahedral sheet. A typical example of the mineral formula of montmorillonite in an MX-80 bentonite is $(\text{Si}_{7.89}\text{Al}_{0.11})(\text{Al}_{3.10}\text{Ti}_{0.02}\text{Fe}_{0.38}\text{Mg}_{0.49})\text{O}_{20}(\text{OH})_4$ (Karnland et al. 2006). On the other hand, beidellite, another dioctahedral smectite mineral with higher iron content than montmorillonite, is characterised by a layer charge whose main contribution arises from substitution of Si^{4+} by Al^{3+} in the tetrahedral sheets (hence $y > x$).

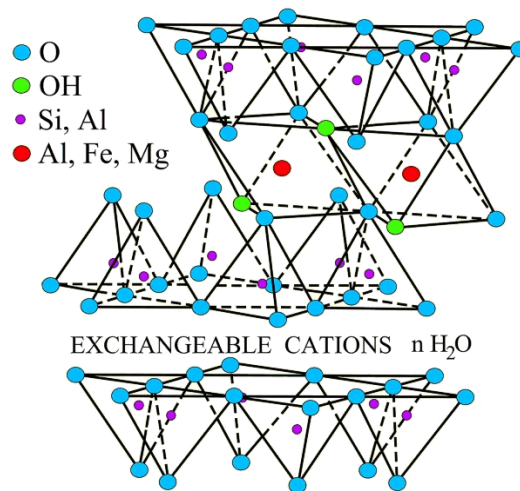


Fig. 3-1: Sketch of the montmorillonite structure
Grim (1968)

Relationship between layer charge, cation exchange capacity (CEC) and swelling properties

For structural reasons, the charges in the tetrahedral sheets are more localised and the electrostatic potential is higher than that in the octahedral sheets. This has implications with regard to the swelling properties, which are more favourable for montmorillonite than for beidellite (Güven 1990). More generally, the swelling properties (free swelling capacity and swelling pressure at confined constant volume) of smectites depend on (Güven 1988, Meunier 2005, Christidis et al. 2006): (i) the layer charge, (ii) the proportions of octahedral and tetrahedral charges, (iii) the nature of the charge-compensating cations, (iv) the presence of fine-grained accessory minerals (e.g. silica), and (v) by the solution conditions (ionic strength, pH). The effect of layer charge on free swelling was studied and discussed for a variety of bentonites (Christidis et al. 2006). The free swelling index (Christidis & Scott 1996) for Na-exchanged bentonite suspensions at solid liquid ratios of 1:10 showed a linear negative correlation with layer charge. Thus, low charge smectites generally have a higher free swelling capacity and also more favourable rheological properties like gel strength, yield strength and thixotropic behaviour (Christidis et al. 2006). The study by Christidis et al. (2006) further highlighted that, for bentonites with a large contribution of beidellitic smectite (i.e. large contribution of tetrahedral layer charge), the swelling index was lowered compared to "normal" bentonites, i.e. with a dominant montmorillonite fraction. Laird (2006) discusses further structural processes that control swelling of smectites and agrees with the findings stated above.

Most commercial bentonites have smectite contents between 70 – 90 % and contain montmorillonite (thus a low tetrahedral charge) as the main mineral component. Bentonites with a large beidellitic component, however, are not uncommon (for example: Rokle (CZ) or Ashapura (India)). The smectite contents and the nature of accessory minerals may vary between different locations and also within a quarry (also see section 3.1.3 for MX-80). The range of smectite contents for selected bentonites has been compiled by Cuevas et al. (2013) and is illustrated in Fig. 3-3.

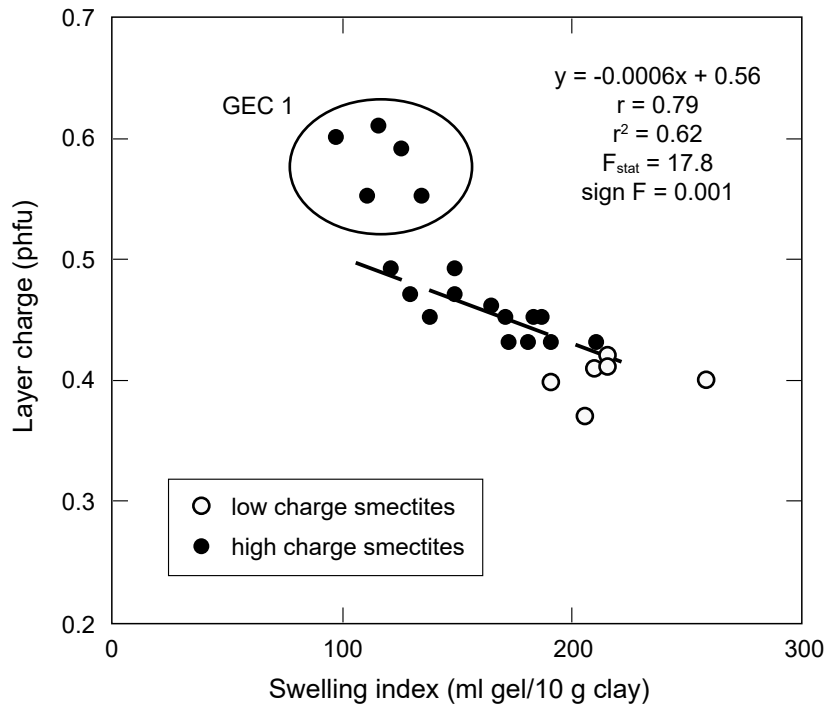
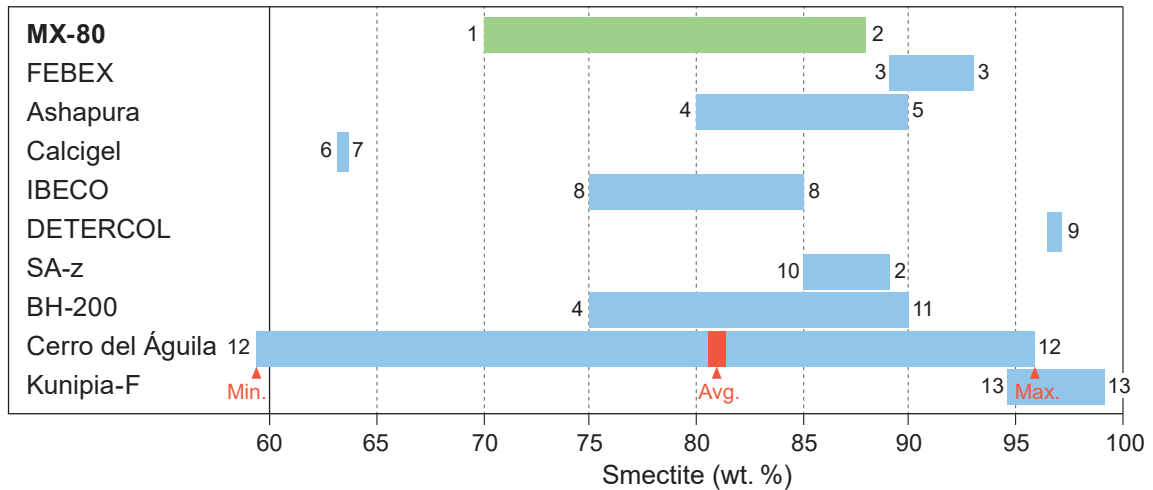


Fig. 3-2: Variation of free swelling index of some bentonites with layer charge of smectites
 Open symbols refer to smectites with a layer charge > -0.50 equivalent per half formula unit (PHFU) which do not follow the trend of high charge smectites.
 Christidis et al. (2006)



- | | | |
|--|---|---------------------------------------|
| 1: Pusch (1999, 2001) | 6: Plötze <i>et al.</i> (2002) | 10: Metz <i>et al.</i> (2005) |
| 2: Christidis <i>et al.</i> (2006) | 7: Steudel (2009) | 11: SP-Minerals/Black Hills Bentonite |
| 3: Linares <i>et al.</i> (1993) | 8: Koch (2008) | 12: Cuevas <i>et al.</i> (1993) |
| 4: Carlson (2004) | 9: Storaro <i>et al.</i> (1996), Geatti <i>et al.</i> (1997) | 13: Sato <i>et al.</i> (1992). |
| 5: Ashapura Minechem Ltd. in Keto (2004) | | |

Fig. 3-3: Smectite contents compiled for selected bentonites
 Range reflects variation in mineralogy of the commercial bentonites and uncertainty of XRD data.
 After Cuevas et al. (2013)

Most of the bentonites are in the region of low- to intermediate-charge smectites, thus displaying favourable swelling properties and rheological properties, as shown by Cuevas et al. (2013). As indicated in Fig. 3-4, exceptions include FEBEX bentonite, DETRECOL (a Moroccan bentonite) and SA-z (a Ca-bentonite from Arizona, USA), all of which display a high layer charge. It is noted that the relationship presented above was derived for a low bentonite/water ratio and the bentonites were normalised to their smectite content.

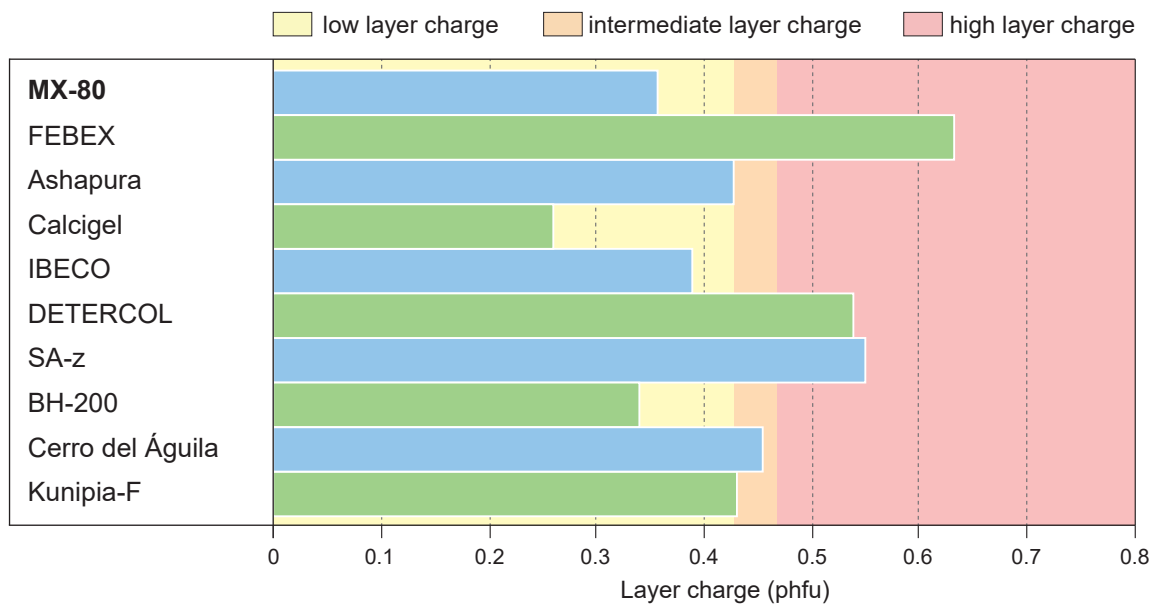


Fig. 3-4: Layer charge (equivalent per half formula unit (phfu) of different commercial bentonites

Background colours show range of low (yellow), intermediate (light orange) and high layer charge smectites (dark orange).

After Cuevas et al. (2013)

The CEC, the capacity to host exchangeable cations, relates to the layer charge via the structural formula shown for montmorillonite above. The good agreement between smectite layer charge from the structural formula and measured CEC was shown by Srodon & McCarty (2008). The CEC of bulk bentonite further relates to the smectite content. These relationships are illustrated in Fig. 3-5 which is based on data of Karnland et al. (2006) who studied a variety of bentonitic materials in terms of different properties. Thus, the CEC data show the expected positive correlation with smectite content over a range of 20 – 90 %, and with the (normalised) layer charge (Fig. 3-5). The data of Cuevas et al. (2013) compiled for a selection of bentonites follow the same trend but display a considerable scatter for the high-smectite samples with a corresponding high layer charge. This scatter may be related to differences in charge localisation in these materials (Güven 1988) or simply reflect data uncertainty (these data represent "average" values compiled from various sources).

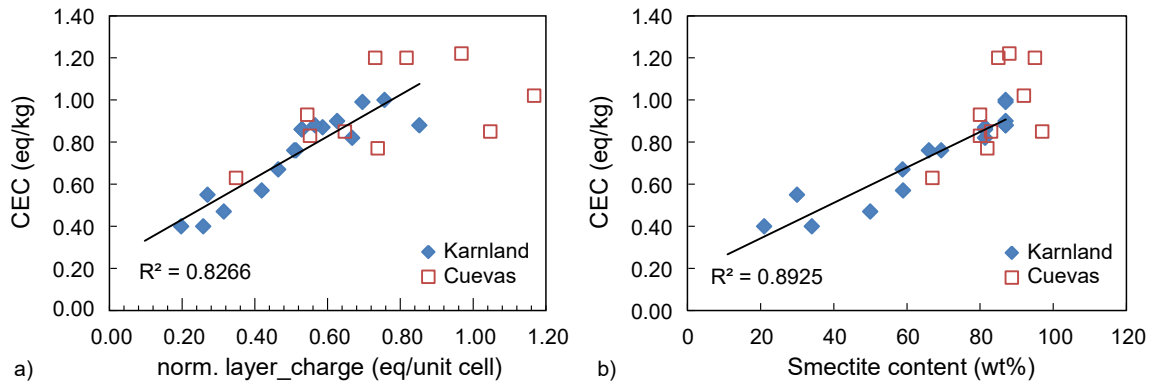


Fig. 3-5: Correlation of layer charge and CEC (a) and smectite content and CEC (b) for a variety of bentonitic materials

Data from Karmland et al. (2006) (diamonds) and Cuevas et al. (2013) (squares); r^2 value given for data of Karmland et al. (2006).

The relationship between layer charge, layer charge localisation and swelling pressure has recently been analysed by molecular dynamics (MD) simulations (Sun et al. 2016). For Na-smectites, these authors showed an inverse relationship between layer charge in the range of -0.5 and -1.0 charge equivalents per unit cell and swelling pressure (Fig. 3-6). Furthermore, at fixed layer charge, the swelling pressure was found to increase with increasing octahedral charge contribution. This finding is in line with the macroscopic data of Christidis et al. (2006). For Ca-smectites, the simulations indicated no swelling beyond three water layers, in contrast to Na-smectites.

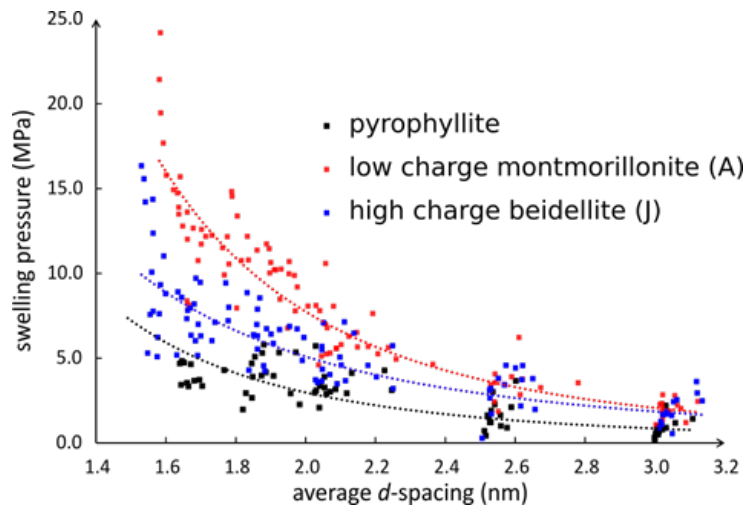


Fig. 3-6: Swelling pressure as a function of average d-spacing for pyrophyllite, low-charge montmorillonite (layer charge: -0.5 eq./unit cell) and high-charge beidellite (-1.0 eq./unit cell)

Sun et al. (2016)

Swelling pressure at constant clay layer composition, but under different external conditions such as equilibration fluid composition (and therefore different cation occupancy), volume, and pressure, are discussed in section 3.8.

3.1.2 Structural iron in smectites

Smectites contain variable amounts of Fe which, for structural reasons, occur predominantly in the Fe^{3+} oxidation state and in the octahedral layer. The Fe content in montmorillonites is generally fairly low, typically 2 – 3 wt.-%, whereas in beidellites it may reach larger contents. The Fe content is highest in nontronites, which may contain a considerable amount of Fe in the tetrahedral layer. The compositional range of smectites is illustrated in the Al-Mg-Fe plot (Fig. 3-7).

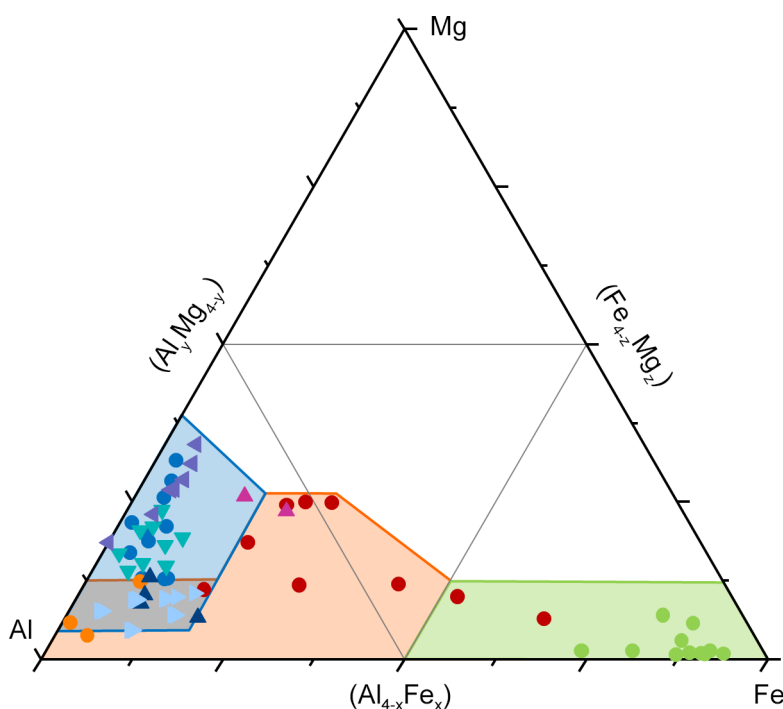


Fig. 3-7: Compositions of dioctahedral smectites in the ternary Al-Fe-Mg plot

Data based on Gates (2005) (circles), Grim & Kulbicki (1961) (triangles); coloured areas represent approximate range of montmorillonite (blue), beidellite (red) and nontronite (green).

Hadi (personal communication)

There is abundant literature on the reduction of structural Fe^{3+} in smectites. Most of this work has focused on Fe-rich smectites, particularly nontronite, sometimes referred to as ferruginous smectite. The reduction process was generally triggered by strong chemical reductants such as dithionite (e.g. Stucki et al. 1984a,b, Stucki et al. 2000, Hadi et al. 2013), but was also induced by microbial activity (Kostka et al. 1996, 1999, Li et al. 2004, Zhang et al. 2012). The Fe^{3+} reduction was reported to induce changes in layer charge, CEC, swelling pressure and also to promote illitisation (Liu et al. 2012, Zhang et al. 2012). The charge deficit resulting from Fe^{3+} reduction has been shown to be – at least partially – compensated by adsorption of exchangeable cations and dehydroxylation of structural OH (Stucki et al. 1984a). The detailed mechanism, however, remains a matter of controversy (Heller-Kallai 1997, Drits & Manceau 2000). Hadi et al. (2013) proposed that, upon a certain level of reduction, lattice destabilisation leads to Fe^{2+} migration and formation of trioctahedral domains. Redox properties of nontronites have also been studied by electrochemical methods. A useful coulometric method involving chemical redox mediators to study redox properties in clays was developed by Hofstetter and co-workers (Hofstetter et al. 2014 and references therein). These authors could determine electron-donating and electron-accepting capacities of Fe-rich smectites (Gorski et al. 2012a) and show that these clays were redox-active over a large range of redox potentials (Gorski et al. 2012b, Hofstetter et al. 2014).

There is comparatively much less information on the reduction of structural Fe^{3+} and redox properties in montmorillonites and bentonites. The reduction mechanism is unclear and has, to the best of our knowledge, not yet been studied in detail. Electrochemical measurements on Wyoming montmorillonite and MX-80 revealed that complete reduction and re-oxidation of structural Fe^{3+} is possible by applying a sufficiently large electrical potential (Gorski et al. 2013, Hofstetter et al. 2014). As illustrated in Fig. 3-8a, the reduction/oxidation is partly reversible, and the hysteresis effect is small compared to nontronite (SWa-1 in Fig. 3-8b). This suggests only minor irreversible structural Fe arrangements (Hofstetter et al. 2014). The electrochemical data obtained are difficult to interpret with regard to natural redox conditions more representative of a SF/HLW repository. Moreover, the electrochemical data were obtained from clay suspensions and their extrapolation to compacted conditions is not straightforward.

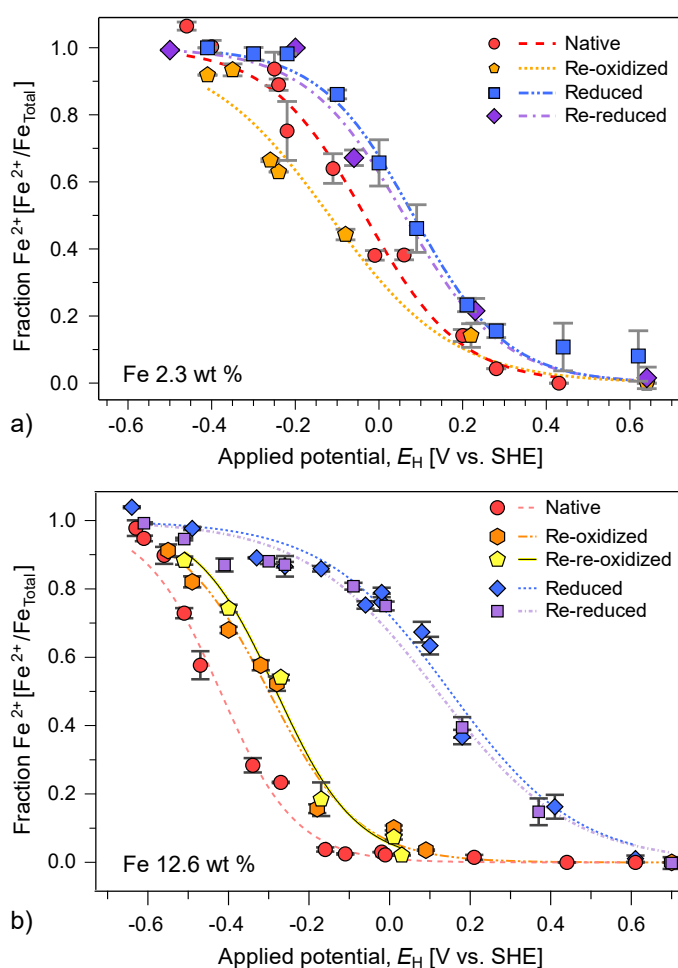


Fig. 3-8: Redox profiles of (a) MX-80 montmorillonite (SWy-2) and (b) nontronite (SWa-1) collected over a series of applied redox potentials (E_h)

Each data point represents the average of several replicate smectite spikes, with error bars showing standard deviations. All experiments were conducted in a pH 7.5 buffer with 0.1 M NaClO_4 as the background electrolyte.

Hofstetter et al. (2014)

It is commonly assumed in safety assessment that structural Fe in the clay fraction is non-redox-active (e.g. Wersin et al. 2003) and redox conditions in the bentonite buffer are constrained by Fe-bearing accessory minerals (e.g. Fe oxyhydroxides, siderite) and/or corrosion products from the adjacent metal surface (section 3.4.6). This assumption is presently not invalidated by the electrochemical data of Hofstetter and co-workers or other literature data, but considerable uncertainties remain. This issue is further discussed in section 3.4.6.

3.1.3 Accessory minerals

The mineralogical composition of bentonite can be measured by XRD and quantified by the Rietveld method. The grain size separation (Atterberg) decreases the clay content and therefore diminishes the accuracy of determining accessories. In turn, readily soluble minerals such as gypsum are lost during the separation process. Karnland (2010) found constant phase assemblages in Wyoming MX-80 batches delivered in the period 1980 – 2001 but points out some differences in fractions of the minerals present (Tab. 3-1). These values agree with other XRD measurements (e.g. Montes-H et al. 2005a, Malfoy et al. 2007, Fernández et al. 2014a, Kaufhold et al. 2015b) or wet chemical methods (Müller-Vonmoos & Kahr 1983, gypsum missing). Precise mineral determination within the feldspar group is rarely done due to their complex XRD patterns. Both quartz and its high-temperature polymorph cristobalite are present, and some authors additionally report tridymite.

The 10 Å mica reflection is commonly interpreted as illite, muscovite, phlogopite or biotite. A more precise analysis based on XRD only is impossible due to the small fractions of these micas. Alternative approaches attempt to distinguish between the separate illite phase and illite in illite/smectite mixed layers and indicate the presence of illite in mixed layers below the sensitivity of the method (Karnland et al. 2006). The same authors evaluated the charge location in the basal sheet by the Greene-Kelly test and further CEC measurements, but found very low beidellite contents, possibly below the sensitivity of the approach.

Tab. 3-1: Mineralogy of Wyoming MX-80 bentonite (wt.-%)

Results from the XRD/Rietveld analyses of five consignments of Wyoming MX-80. The consignments were delivered around 1980 (WySt), 1995 (WyL1), 1999 (WyL2), 2001 (WyR1 and WyR2). Wym denotes the mean value of the six analysed samples. Plus and minus denote the maximum deviations from mean values (Karnland 2010).

| Phase | WySt | WyL1 | WyL2 | WyR1 | WyR1m | WyR2 | Wym | Plus | Minus |
|-----------------|------|------|------|------|-------|------|------|------|-------|
| Montmorillonite | 82.5 | 79.5 | 79.8 | 82.7 | 83.9 | 80.0 | 81.4 | 2.5 | 1.9 |
| Illite | 0.7 | 0.8 | 0.7 | 0.8 | 0.8 | 0.7 | 0.8 | 0.1 | 0.1 |
| Calcite | 1.3 | 0.0 | 0.0 | 0.1 | 0.0 | 0.0 | 0.2 | 1.2 | 0.2 |
| Cristobalite | 0.2 | 1.4 | 2.5 | 0.6 | 0.7 | 0.0 | 0.9 | 1.6 | 0.9 |
| Gypsum | 1.4 | 0.7 | 0.9 | 0.7 | 0.8 | 1.1 | 0.9 | 0.5 | 0.2 |
| Muscovite | 2.4 | 5.1 | 2.6 | 3.5 | 4.4 | 2.5 | 3.4 | 1.7 | 1.0 |
| Plagioclase | 4.6 | 2.4 | 4.0 | 3.2 | 2.3 | 4.7 | 3.5 | 1.2 | 1.2 |
| Pyrite | 0.8 | 0.6 | 0.6 | 0.6 | 0.3 | 0.9 | 0.6 | 0.3 | 0.3 |
| Quartz | 2.6 | 2.5 | 3.8 | 3.0 | 2.8 | 3.2 | 3.0 | 0.8 | 0.5 |
| Tridymite | 1.7 | 5.0 | 3.8 | 3.9 | 3.1 | 5.1 | 3.8 | 1.3 | 2.1 |

Alternative methods can determine accessories near or below XRD sensitivity: a combination of chemical, structural, and scanning electron microscopy (SEM see figures 3.9 and 3.10) analyses further reveals ankerite (1.0 wt.%), iron oxides (0.4 wt.%), and phosphates (0.6 wt.%) in MX-80 (Montes-H et al. 2005a). Minerals containing heavy elements in particular can be easily identified in the SEM, and fractions far below XRD sensitivity (0.1 – 1.0 wt.-%) can be chemically characterised if grains $> 1 \mu\text{m}$ are present. An unpublished feasibility study (A. Jenni) revealed Mg-rich ankerite, iron oxide, celestite ($\text{Sr}_{0.94}\text{Ba}_{0.06}\text{SO}_4$), and possibly small-grained clinopyroxene in MX-80. The presence of iron oxides agrees with selective extraction approaches indicating 0.1 wt.-% Fe_2O_3 present in so-called free iron (hydro-) oxides or possibly in siderite.

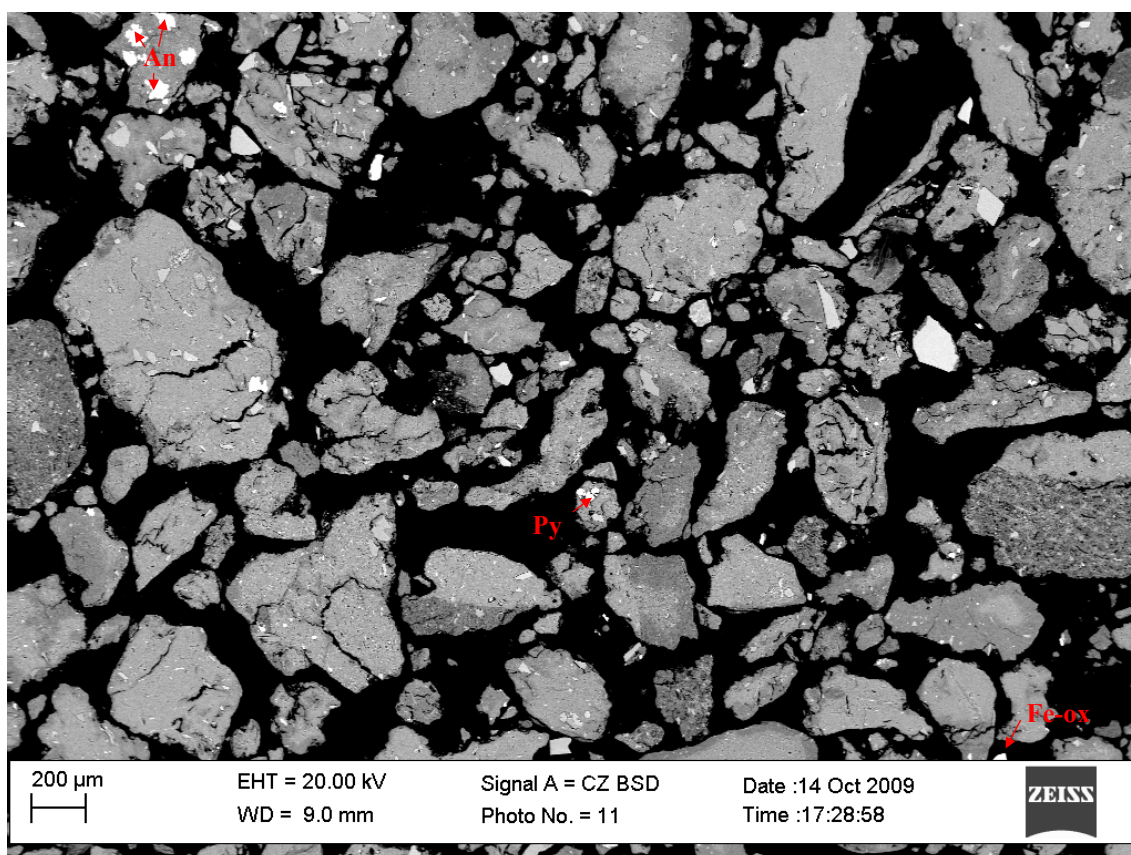


Fig. 3-9: SEM backscatter electron image of a polished section through dry MX-80 embedded in resin demonstrating a relatively large mineralogical heterogeneity

Resin in black, bright colours represent minerals containing heavy elements. An: ankerite, Py: pyrite, Fe-ox: iron oxide

Jenni (unpublished)

Müller-Vonmoos & Kahr (1983), Karnland et al. (2006) and others report a fairly high organic carbon content of 0.2 – 0.4 wt.-%, but more recent studies also report bentonites with lower carbon content (e.g. Kumpulainen & Kiviranta 2010). Little is known about the form of this organic carbon or the organic matter in which it is assumed to be contained. Decomposition and dissolution lead to the presence of organic acids in the porewater. A more detailed study of Marshall et al. (2015) characterises the natural organic matter in MX-80. They conclude that organic matter from vascular plants predominates over organics of microbial origin, and the organic matter has undergone advanced diagenetic alteration. In addition, nuclear magnetic resonance (NMR) indi-

cates the presence of black carbon or some other non-extractable aromatic-rich material. In general, the compounds identified are hypothesised to be recalcitrant; no study connects these recent findings with organic acids found in bentonite porewater. It is unclear if the organic compounds described may serve as a microbial substrate. Alternative bentonites are, in general, lower in organic content, which might have different origins than that found in MX-80.

The mechanical effect of accessory minerals on swelling pressure is reviewed in section 3.8.1.

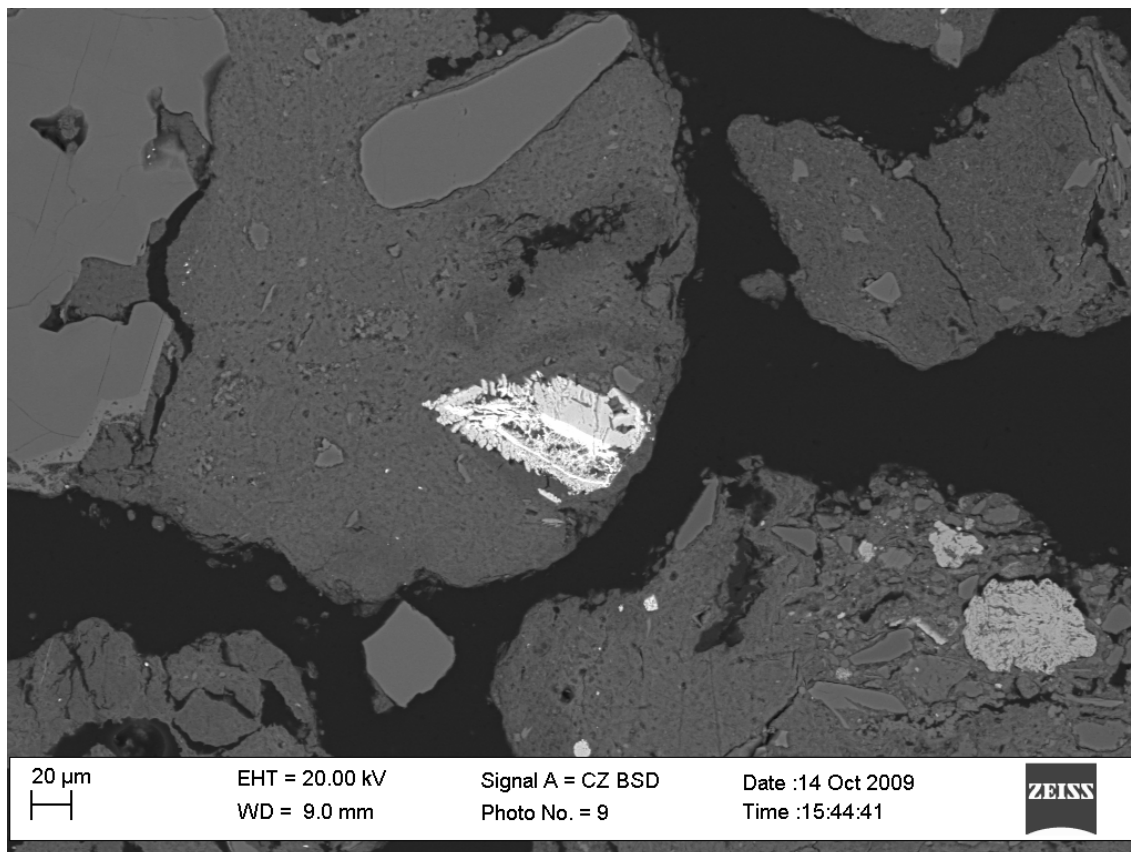


Fig. 3-10: SEM backscatter electron image of a polished section of dry MX-80 embedded in resin showing a celestite grain (white)

Resin in black, bright colours represent minerals containing heavy elements

Jenni (unpublished)

3.1.4 Conceptual uncertainties of bentonite mineralogy relevant for the Nagra concept

The crystal structure and chemistry of MX-80 montmorillonite are well characterised. Uncertainties arising from montmorillonite interaction with its porewater are covered in the sections below.

All solids present in the bentonite react with water at different rates and therefore control the porewater composition, although each to a different extent. Therefore, mineralogical composition, also including minor compounds, is essential for predicting or understanding porewater chemistry. For example, the presence of celestite should lead to a significant Sr content also affecting

the exchanger population. Many species in the porewater, especially organic acids, can interact with radionuclides (e.g. sorption, complexation) in the bentonite, which is not explicitly treated in this report.

The nature of the organic matter in bentonites is not well known. It is generally considered to be recalcitrant to microbial degradation (Stroes-Gascoyne et al. 2007), but this still needs confirmation, especially under conditions of higher temperatures (Stroes-Gascoyne et al. 1996).

3.2 Kinetic and thermodynamic treatment of clays

Smectite provides most of the crucial bentonite properties in a repository context, and smectite stability is therefore of the highest relevance. Reactions of clays are slow in general. Experimental evidence for such reactions is scarce, especially under chemical conditions close to host rock porewater. This section discusses the quality of available thermodynamic and kinetic data and provides the basis for related topics: the interaction of porewater and smectite in general is discussed in section 3.4. Sections 5.2.4, 5.3, 5.4, and 5.8.1 discuss smectite stability under the different geochemical conditions expected during the evolution of the repository.

3.2.1 Solubility data for clay minerals

Friedrich Lippmann discussed the thermodynamic status of clay minerals in a seminal paper (Lippmann 1982). He started with the observations that (1) illites, montmorillonites and related interstratifications show solid solution to an extent which is unusual at room temperature, and (2) they do not grow into coarser crystals through dissolution-precipitation cycles (Ostwald ripening). Solid solution systems in petrology are generally characterised by an upper critical point (UCP) in temperature. Above the UCP, total miscibility is observed, while below the UCP a miscibility gap opens up and increases towards room temperature. For the wide range of solid solutions of illites and smectites to represent thermodynamically stable phases, one might consider a solubility diagram characterised by a lower critical point (LCP), as known for binary systems of certain organic compounds with water, e.g. triethylamine-water (Fig. 3-11, left). For an LCP to exist, chemical thermodynamics requires that the mixing be exothermic, but in all solid solutions for which the heat of mixing is known the sign is endothermic. The crucial point for determining the heat of mixing of clay minerals is knowledge of their heat of hydration. However, experimental heat of hydration values always contains the heat evolved by water adsorption on the external surface of the nanocrystals, and models based on assumptions are needed to separate the different effects. Although hydration explains why expandable minerals form at all, hydration appears not to be sufficient to render the mixing outright exothermic and to lead to a distinct increase in equilibrium miscibility towards low temperature. Lippmann (1982) concluded that virtually all clay minerals are somehow metastable or even completely unstable. From the fine grain size, he concluded that they precipitate at considerable super-saturation. They then persist over geological times but never reach stable or metastable thermodynamic equilibrium.

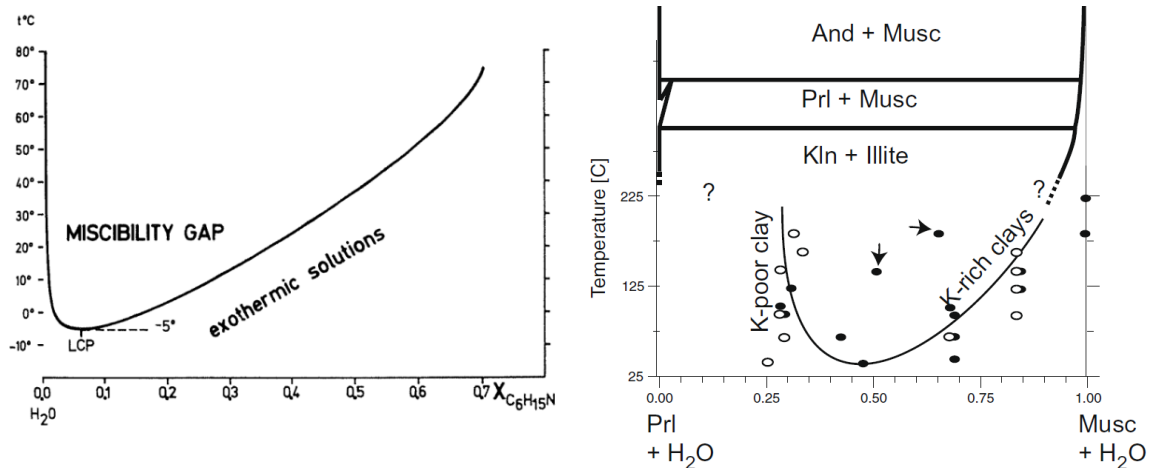


Fig. 3-11: Miscibility gaps in the system triethylamine–water and in the system K_2O – Al_2O_3 – SiO_2 – H_2O

Left: The system triethylamine–water showing a miscibility gap characterised by a lower critical point (LCP). In a system of this type, the mixing process is exothermic. Taken from Lippmann (1982). Right: Phase relations in the system K_2O – Al_2O_3 – SiO_2 – H_2O proposed at high temperature by Loucks (1991) (thick lines, no quantitative scale) and interpreted at low temperature (thin line) from the composition of clay (circles) inferred from the experiments of Rosenberg et al. (1990) and Aja et al. (1991a). The arrows indicate the composition of possible illite/smectite phases.

Vidal & Dubacq (2009)

Essene & Peacor (1995) criticised the use of clay minerals as thermometers (e.g. illite and chlorite crystallinity, chlorite thermometry based on correlations between natural chlorite compositions and temperature). They supported the conclusions of Lippmann (1982) and noted that transmission electron microscopy (TEM) studies of pelitic rocks commonly reveal the presence of heterogeneous detrital clay minerals that coexist with diagenetic clay minerals. Such mineral associations violate the phase rule and equilibrium would require phase homogeneity. They further argued that the ubiquitous presence of local composition variation, stacking disorder and other features observed by TEM are inconsistent with the requirements of homogeneity. In addition, they remarked that the prograde evolution of clay minerals from diagenesis to low grade metamorphism is characterised by increasing homogeneity. This suggests that homogenisation compatible with equilibrium is kinetically hindered at low temperatures.

3.2.1.1 Solubility of kaolinite

In the case of kaolinite, equilibrium solubility data have been published (Kittrick 1970, May et al. 1986). As is obvious from the experimental data of May et al. (1986) shown in Fig. 3-12, equilibrium was attained both from under- and oversaturation. In addition to solubility data, kinetic data for dissolution and precipitation are available, e.g. Marty et al. (2015a) or http://www.thermochimie-tdb.com/pages/kinetic_models.php. Last but not least, calorimetric data provide evidence that kaolinite is the stable phase and the polymorph dickite is metastable (Fialips et al. 2003). Hence, stable chemical equilibrium of kaolinite in aqueous solutions is well established.

3.2.1.2 Solubility of illite

Perhaps motivated by the initial success of the kaolinite precipitation study (Kittrick 1970), Kittrick & Rosenberg of the Washington State University, Pullman, Washington, ran a long-term project that they later termed the "Illite Project" (e.g. Kittrick 1984, Sass et al. 1987, Aja et al. 1991b, Yates & Rosenberg 1996). In all these equilibrium studies, natural illites were used. No changes in solid phases were detected by X-ray powder diffraction in samples before and after the long-term experiments. Hence, interpretation of the experiments relied on aqueous chemistry only. In all theses and publications related to the "Illite Project", the authors tried to fit phase boundaries to their specific data. However, synopses of all data measured at a certain temperature (Fig. 3-13 to Fig. 3-15) are largely featureless. Hence, the tremendous efforts of the "Illite Project" do not give any evidence of (meta)stable chemical equilibria in aqueous solutions.

In a more recent modelling effort, Vidal & Dubacq (2009) re-invented Lippmann's hypothetical LCP phase diagram (Fig. 3-11, left) based on (selected?) experimental data from the "Illite Project" (Fig. 3-11, right). These seem to be the only experimental data they found to support their various calculated LCP phase diagrams (Fig. 3-16).

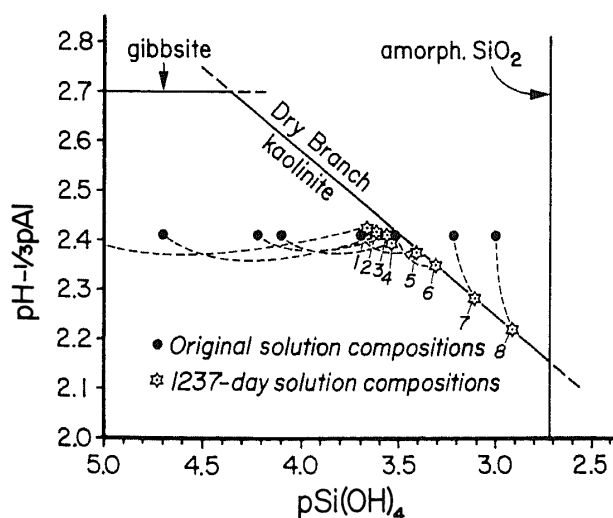


Fig. 3-12: Approach to equilibrium solubility for 5% suspensions of Dry Branch kaolinite, from over- and undersaturation

Dashed lines connecting points of initial and final solution composition show general compositional trends and are curved in some instances to avoid unintended intersection with unrelated points. Undersaturated conditions are on the left of the kaolinite saturation line, oversaturated conditions on the right.

May et al. (1986)

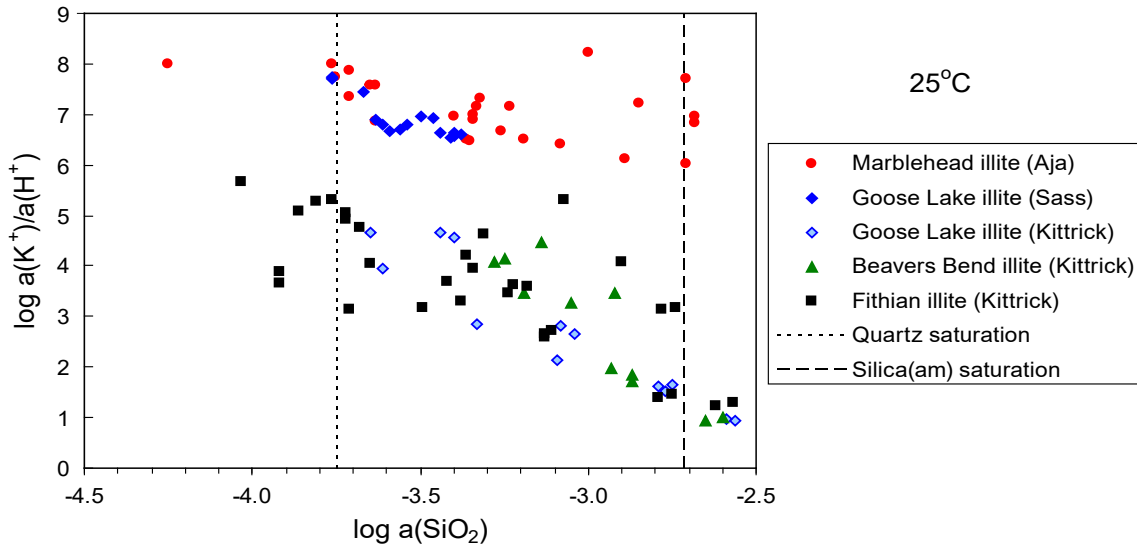


Fig. 3-13: Synopsis of experimental data for illite at 25 °C

Data from to Table A1 in Aja et al. (1991b), Table in Appendix A in Sass et al. (1987), and Table 1 in Kittrick (1984). The symbol "a()" denotes the activity of the species in brackets.

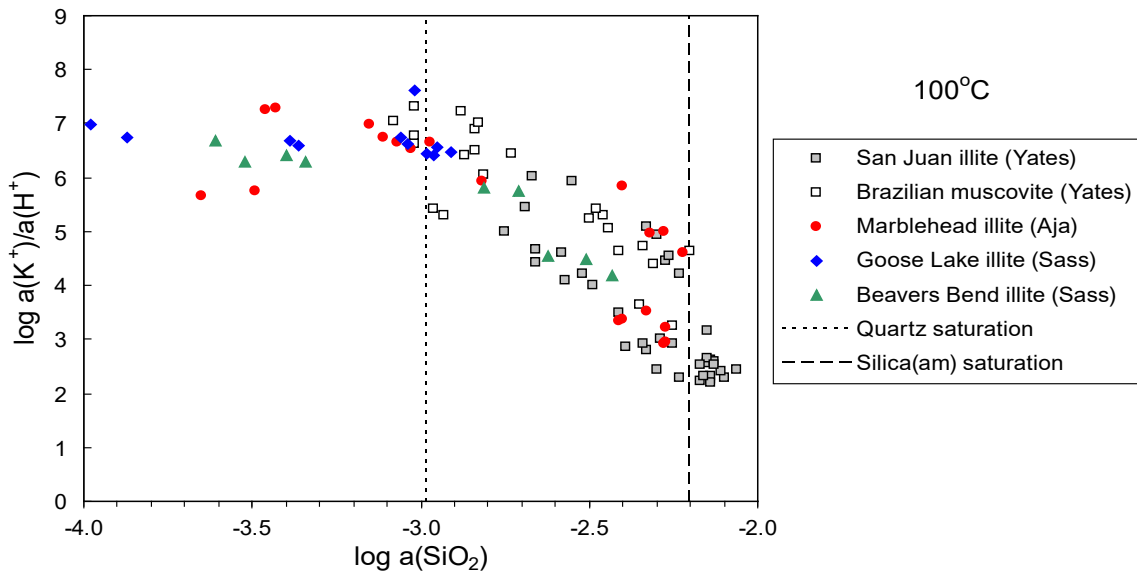


Fig. 3-14: Synopsis of experimental data for illite at 100 °C

Data from Table B1 in Yates & Rosenberg (1996), Table A1 in Aja et al. (1991b), and Table in Appendix A (90 °C) in Sass et al. (1987). The symbol "a()" denotes the activity of the species in brackets.

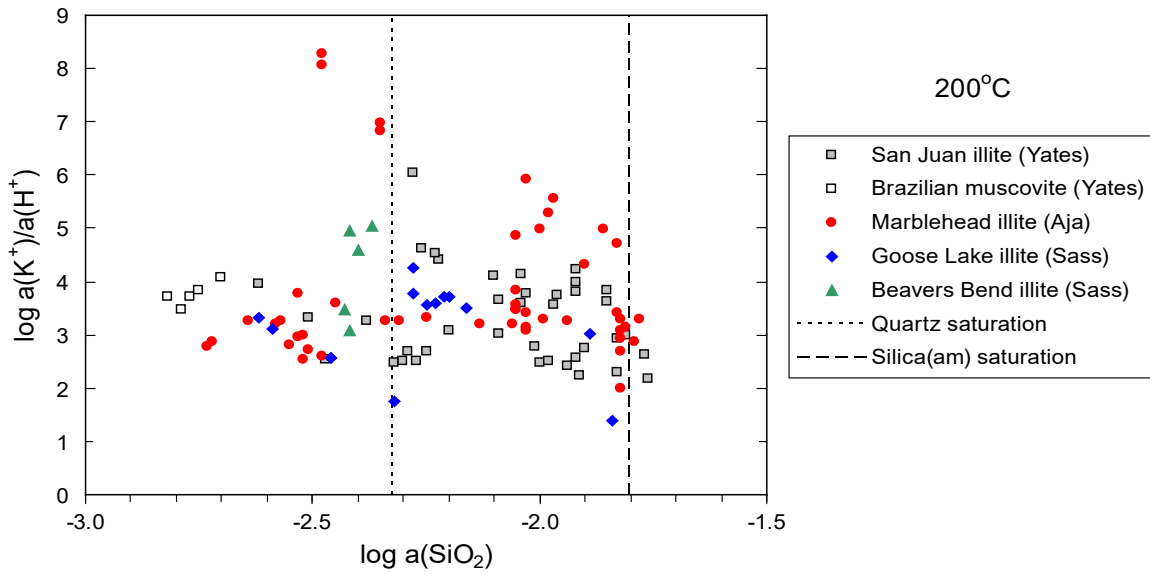


Fig. 3-15: Synopsis of experimental data for illite at 200 °C

Data from to Table B1 in Yates & Rosenberg (1996), Table A1 in Aja et al. (1991b), and Table in Appendix A in Sass et al. (1987). The symbol "a()" denotes the activity of the species in brackets.

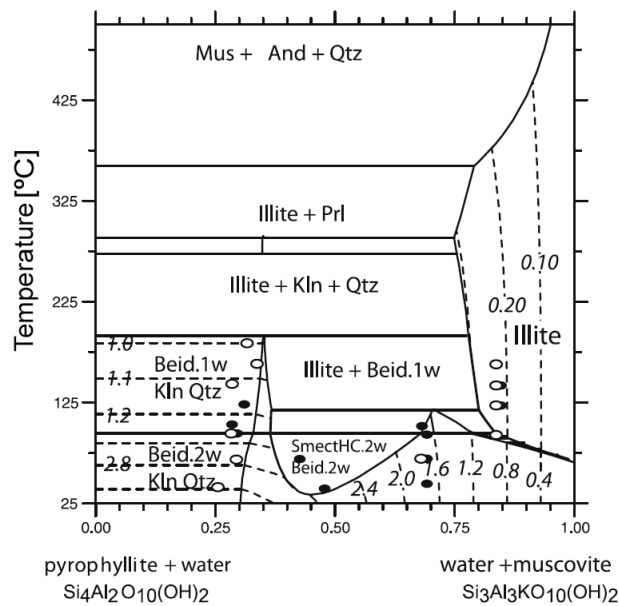


Fig. 3-16: Composition-temperature phase diagram calculated along the pyrophyllite-muscovite binary

The continuous lines show the limits of the stability fields, and the dashed lines show the interlayer water content (the numbers of moles H₂O per O₁₀(OH)₂ are in italics). High-charge smectite (SmectHc), andalusite (And), beidellite (Beid), kaolinite (Kln), muscovite (Mus), pyrophyllite (Prl), quartz (Qtz). The circles show the composition of clay inferred from the experiments of Aja (1991) and Aja et al. (1991a) (see Vidal & Dubacq 2009)

3.2.1.3 Solubility of smectites

There are only a few publications known to us that have dealt with the experimental determination of the solubility of smectite minerals, all of which were carried out at room temperature.

In a study concerned with the solubilities of high-alumina and clay minerals, Reesman & Keller (1968) also investigated the solubilities of Cheto and Clay Spur montmorillonites (see Tab. 3-2 for their compositions). Clay suspensions were shaken in distilled water for 3 up to 1,000 days. The authors argued that their experiments had reached equilibrium since they observed very high initial solubilities which declined for a period of time, but declined too rapidly, according to the authors, to have dissolved all of the clay particles that were structurally disordered during the grinding process. They interpreted the rapid decline in solubility as being caused "by restoration or 'rehealing' of disrupted crystal edges and faces, and further interpreted this effect to mean that saturation equilibrium had been reached between clay crystals and liquid". In the case of their montmorillonites, Reesman & Keller (1968) remarked that "the montmorillonites used in this study seem to be rather unstable with respect to kaolinite and quartz" and that "apparent instability of these montmorillonites may result from inferior analytical values because of incomplete removal of ultra-fine colloidal material from solution".

Kittrick (1971a) determined the solubilities of Belle Fourche and Clay Spur montmorillonites and, in a later study (Kittrick 1971b), the solubility of Panther Creek (Aberdeen) montmorillonite (see Tab. 3-2 for the compositions of these montmorillonites). The experiments were carried out at $\text{pH} < 3.48$. It was later shown by Churchman & Jackson (1976) and May et al. (1986), see below, that montmorillonites do not reach an equilibrium state with such acid solutions.

Huang & Keller (1973) performed dissolution experiments with Cheto and Clay Spur montmorillonites (see Tab. 3-2 for their compositions) in distilled water and reported that solution compositions approached nearly constant values after 102 days, deriving "apparent" solubilities from the data.

Churchman & Jackson (1976) showed that, in dissolution experiments with three montmorillonites (see Tab. 3-2 for their compositions) carried out for up to 432 days in acid aqueous solutions over the pH range 1.5 to 4.2 (these conditions were chosen in order to ensure that Al^{3+} is not hydrolysed), montmorillonite is not in a unique state of equilibrium. Rather, a secondary unidentified solid phase enriched in Si relative to montmorillonite controls the activities of solutes, as well as another unidentified secondary Al-enriched phase. This was deduced from the lack of congruency in the dissolution of montmorillonite and by the dependence of the concentrations of some, but not all, of the constituents of montmorillonite on each other. Churchman & Jackson (1976) explicitly mentioned that the experiments by Kittrick (1971a,b) suffered from the same shortcoming.

In their study demonstrating equilibrium of kaolinite with aqueous solutions from both under- and oversaturation (see section 3.2.1.1), May et al. (1986) also investigated the solubility of five different smectites (see Tab. 3-2 for their compositions) in the pH range 5 to 8. After running the experiments for up to 419 days, there were no signs that equilibrium had been attained by any of the smectites. Most of the Upton and Panther Creek smectite suspensions evolved towards aqueous compositions, suggesting the control of Al solubility by gibbsite, while the suspensions involving the soil clays from Hawaii evolved towards aqueous compositions, suggesting Al control by amorphous $\text{Al}(\text{OH})_3$.

According to Peryea & Kittrick (1986), two conventions can be used to represent the composition of smectites with exchangeable cations in the interlayer for the interpretation of solubility experiments. The first convention includes interlayer cations as part of the smectite phase (monophase model). The second convention treats the interlayer cations and the structurally charged smectite structure as two separate phases (charged structure model). Kittrick & Peryea (1989) considered the former as a solid solution with variable composition on the timescale of laboratory experiments, and the latter as a solid solution of fixed composition on the same timescale. In order to investigate which of the two models is supported by experimental data, Peryea & Kittrick (1986) carried out solubility experiments with Belle Fourche montmorillonite (see Tab. 3-2 for composition). After pre-treatment of montmorillonite with KCl solutions, mixtures of montmorillonite, kaolinite, goethite, and magnesite were brought into contact with 0.01, 0.1, and 1.0 M KCl solutions for up to 54 days at low solution/solid ratios and $\text{pH} = 8.7$ to ascertain the structural integrity of montmorillonite. Addition of kaolinite and goethite served to constrain the activities of Al^{3+} and Fe^{3+} , respectively, since their concentrations were too low for accurate measurement. Magnesite of known solubility was assumed to serve as an internal equilibrium monitor, with equilibrium with respect to magnesite indicating system-wide meta-equilibrium. Montmorillonite dissolution and precipitation were assumed to be congruent. Peryea & Kittrick (1986) acknowledged that true chemical equilibrium cannot be attained, citing Lippmann (1982), but assumed that the investigated mineral system was capable of attaining a metastable equilibrium state that is reproducible and characteristic of the system. Direct validation of this assumption was not obtained. Constant values of the calculated Gibbs free energies of montmorillonite formation over 24 solubility determinations was interpreted as an indication that a characteristic metastable equilibrium had been attained. The results, however, did not permit validation of either the monophase or the charged structure model. Peryea & Kittrick (1986) concluded that alternative criteria must be found for selecting the more appropriate model. Based on a re-evaluation of the experimental data by Peryea & Kittrick (1986), ascertaining that the montmorillonite was actually saturated with K^+ , Kittrick & Peryea (1988) favoured the monophase model. Kittrick & Peryea (1989) performed additional solubility experiments. This time, gibbsite and goethite were added to the Belle Fourche montmorillonite pre-treated with MgCl_2 (see Tab. 3-2 for composition) and 36 samples put in contact with MgCl_2 solutions with pH varying from 2.08 to 7.55. After equilibration, pH values varied from 3.26 to 8.16. Kittrick & Peryea (1989) claimed that their solubility experiments had reached equilibrium, since "during the course of equilibration some individual samples increased and some decreased with regard to the pSi(OH)_4^0 , pH , pMg^{2+} , and $2\text{pH}-\text{pMg}^{2+}$ of initial solutions. Thus, equilibrations from both undersaturation and supersaturation were well presented". A look at Fig. 3-17 reveals, however, that this bold assertion is not at all supported by their experimental data.

To summarise, there does not appear to be a single solubility experiment with smectites that has convincingly shown that equilibrium was attained.

Tab. 3-2: Compositions of smectites used in solubility experiments

Types, origins and compositions as taken from references. Abbreviations: beid beidellite, mont montmorillonite, nont nontronite, AZ Arizona, CO Colorado, HI Hawaii, MS Mississippi, SD, South Dakota, WY Wyoming.

| Reference | Type | Origin | Composition |
|----------------------------|------|---|---|
| Reesman & Keller (1968) | Mont | Bentonite, Cheto, AZ | Not indicated, but see Huang & Keller (1973) below |
| Reesman & Keller (1968) | Mont | Bentonite, Clay Spur, WY | Not indicated, but see Huang & Keller (1973) below |
| Kittrick (1971a) | Mont | Bentonite, Belle Fourche, SD | $M_{0.56}(Si_{7.87}Al_{0.13})(Al_{3.03}Mg_{0.58}Fe_{0.45})O_{20}(OH)_4$ |
| Kittrick (1971a) | Mont | Bentonite, Clay Spur, WY | Not indicated, „essentially identical to Belle Fourche" |
| Kittrick (1971b) | Mont | Bentonite, Panther Creek (Aberdeen), MS | $M_{0.83}(Si_{7.64}Al_{0.36})(Al_{2.58}Fe_{0.67}Mg_{0.89})O_{20}(OH)_4$ |
| Huang & Keller (1973) | Mont | Bentonite, Cheto, AZ | $(Ca_{0.38}Na_{0.04}K_{0.04})(Al_{3.04}Fe_{0.28}Mg_{0.66})(Si_{7.86}Al_{0.14})O_{20}(OH)_4$ |
| Huang & Keller (1973) | Mont | Bentonite, Clay Spur, WY | $(Na_{0.54}Ca_{0.20}K_{0.04})(Al_{3.04}Fe_{0.38}Mg_{0.44})(Si_{7.88}Al_{0.12})O_{20}(OH)_4$ |
| Churchman & Jackson (1976) | Mont | Bentonite, Colony, WY | $M_{0.80}(Si_{7.60}Al_{0.40})(Al_{3.16}Fe_{0.40}Mg_{0.52})O_{20}(OH)_4$ |
| Churchman & Jackson (1976) | Mont | Bentonite, Castle Rock, CO | $M_{0.48}(Si_{7.36}Al_{0.64})(Al_{3.04}Fe_{0.42}Mg_{0.92})O_{20}(OH)_4$ |
| Churchman & Jackson (1976) | Mont | Bentonite, Panther Creek, MS | $M_{0.83}(Si_{7.64}Al_{0.36})(Al_{2.58}Fe_{0.67}Mg_{0.89})O_{20}(OH)_4$ |
| May et al. (1986) | Beid | Bentonite, Upton, WY | $Mg_{0.36}(Si_{7.10}Al_{0.90})(Al_{3.36}Fe_{0.34}Mg_{0.54})O_{20}(OH)_4$ |
| May et al. (1986) | Mont | Bentonite, Panther Creek, MS | $Mg_{0.415}(Si_{7.64}Al_{0.36})(Al_{2.58}Fe_{0.67}Mg_{0.89})O_{20}(OH)_4$ |
| May et al. (1986) | Mont | Soil clay, Lualualei, HI | $Mg_{0.61}(Si_{7.64}Al_{0.36})(Al_{2.20}Fe_{1.20}Mg_{0.47})O_{20}(OH)_4$ |
| May et al. (1986) | Beid | Soil clay, St. Louis Heights, HI | $Mg_{0.42}(Si_{7.12}Al_{0.88})(Al_{2.44}Fe_{1.44}Mg_{0.20})O_{20}(OH)_4$ |
| May et al. (1986) | Nont | Soil clay, Kokokahi, HI | $Mg_{0.39}(Si_{6.78}Al_{1.22})(Al_{1.80}Fe_{2.26}Mg_{0.13})O_{20}(OH)_4$ |
| Peryea & Kittrick (1986) | Mont | Bentonite, Belle Fourche, SD | $K_xMg_{(0.92-x)/2}(Si_{7.57}Al_{0.43})(Al_{3.15}Mg_{0.61}Fe_{0.28})O_{20}(OH)_4$ |
| Kittrick & Peryea (1988) | Mont | Bentonite, Belle Fourche, SD | $K_{0.92}(Si_{7.57}Al_{0.43})(Al_{3.15}Mg_{0.61}Fe_{0.28})O_{20}(OH)_4$ |
| Kittrick & Peryea (1989) | Mont | Bentonite, Belle Fourche, SD | $Mg_{0.47}(Si_{7.55}Al_{0.45})(Al_{3.15}Mg_{0.61}Fe_{0.28})O_{20}(OH)_4$ |

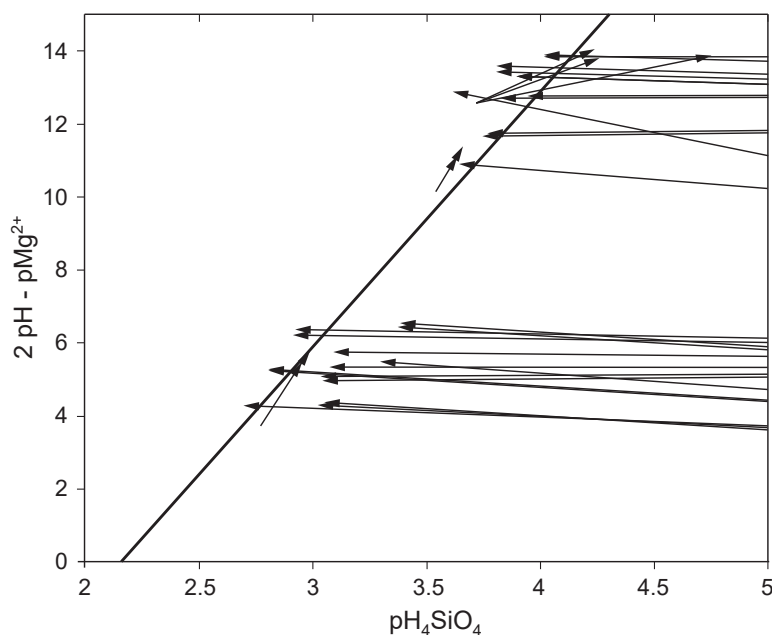


Fig. 3-17: Mg-saturated Belle Fourche montmorillonite equilibrated with gibbsite and goethite

The line represents equilibrium of the reaction $\text{montmorillonite} + 2.16 \text{H}^+ + 17.56 \text{H}_2\text{O}(\text{aq}) = 3.6 \text{gibbsite} + 0.28 \text{goethite} + 1.08 \text{Mg}^{2+} + 7.55 \text{H}_4\text{SiO}_4(\text{aq})$. Gibbsite: $\text{Al}(\text{OH})_3$, goethite: FeOOH , Montmorillonite: $\text{Mg}_{0.47}(\text{Si}_{7.55}\text{Al}_{0.45})(\text{Al}_{3.15}\text{Mg}_{0.61}\text{Fe}_{0.28})\text{O}_{20}(\text{OH})_4$. Arrows connect points of initial and final solution. Undersaturated conditions are to the right of the equilibrium curve. The slope of the equilibrium curve is given by the reaction stoichiometry, the position was fitted by Kittrick & Peryea (1989) to the final solution compositions.

Kittrick & Peryea (1989)

3.2.2 Calorimetric data for smectites

In a series of calorimetric studies, Gailhanou and co-workers produced thermodynamic data for several clay minerals (see Tab. 3-3 for their compositions). Low temperature adiabatic calorimetry and differential scanning calorimetry were used for deriving standard entropies, heat contents, and heat capacity functions for montmorillonite MX-80, illite IMt-2, and illite-smectite mixed-layer ISCz-1 (Gailhanou et al. 2007), chlorite CCa-2 (Gailhanou et al. 2009), and smectite MX-80, illite IMt-2, and beidellite SBId-1 (Gailhanou et al. 2012). The thermodynamic parameters for montmorillonite MX-80, illite IMt-2, and beidellite were complemented by Gailhanou et al. (2012) with standard enthalpies of formation derived from solution-reaction calorimetry at 298.15 K, permitting the calculation of standard Gibbs free energies of formation and of equilibrium constants, and thus providing a complete thermodynamic parameter set. Similarly, Blanc et al. (2014) performed complementary solution-reaction calorimetry for chlorite CCa-2. Additionally, they determined the complete set of thermodynamic parameters for berthierine ISGS. Finally, Gailhanou et al. (2013) obtained the complete thermodynamic parameter set for saponite Sap-Ca-1, nontronite NAu-1, and Santa Olalla vermiculite.

The hydration/dehydration energetics of montmorillonite MX-80 were determined by Tajeddine et al. (2015) by measuring dehydration enthalpies using thermogravimetric and differential thermal analysis. Gailhanou et al. (2017) developed a methodology for extracting the thermodynamic hydration properties of clay minerals from water adsorption isotherms by removing the contribution of non-interlayer water (capillary and multilayer water) and considering only the contribution of the cation hydration in the interlayer. This removal was done by suitably adapting a solid solution model for clay water.

Tab. 3-3: Compositions of clay minerals used in calorimetry

| Reference | Type | Composition |
|-------------------------|---------------------------|---|
| Gailhanou et al. (2007) | Montmorillonite MX-80 | $\text{Na}_{0.435}\text{K}_{0.026}\text{Ca}_{0.010}(\text{Si}_{3.612}\text{Al}_{0.388})(\text{Al}_{1.593}\text{Fe}^{3+}_{0.184}\text{Mg}_{0.228}\text{Fe}^{2+}_{0.038}\text{Ti}_{0.011})\text{O}_{10}(\text{OH})_2$ |
| Gailhanou et al. (2007) | Illite imt-2 | $\text{Na}_{0.044}\text{K}_{0.762}(\text{Si}_{3.387}\text{Al}_{0.613})(\text{Al}_{1.427}\text{Fe}^{3+}_{0.292}\text{Mg}_{0.241}\text{Fe}^{2+}_{0.084})\text{O}_{10}(\text{OH})_2$ |
| Gailhanou et al. (2012) | | |
| Gailhanou et al. (2007) | Mixed-layer iscz-1 | $\text{Na}_{0.135}\text{K}_{0.530}(\text{Si}_{3.565}\text{Al}_{0.435})(\text{Al}_{1.709}\text{Fe}^{3+}_{0.051}\text{Mg}_{0.218}\text{Fe}^{2+}_{0.017}\text{Ti}_{0.005})\text{O}_{10}(\text{OH})_2$ |
| Gailhanou et al. (2009) | Chlorite cca-2 | $(\text{Si}_{2.633}\text{Al}_{1.367})(\text{Al}_{1.116}\text{Fe}^{3+}_{0.215}\text{Mg}_{2.952}\text{Fe}^{2+}_{1.712}\text{Mn}_{0.012}\text{Ca}_{0.011})\text{O}_{10}(\text{OH})_8$ |
| Blanc et al. (2014) | | |
| Gailhanou et al. (2012) | Smectite MX-80 | $\text{Na}_{0.409}\text{K}_{0.024}\text{Ca}_{0.009}(\text{Si}_{3.738}\text{Al}_{0.262})(\text{Al}_{1.598}\text{Fe}^{3+}_{0.173}\text{Mg}_{0.214}\text{Fe}^{2+}_{0.035})\text{O}_{10}(\text{OH})_2$ |
| Tajeddine et al. (2015) | | |
| Gailhanou et al. (2012) | Beidellite sbid-1 | $\text{Ca}_{0.185}\text{K}_{0.104}(\text{Si}_{3.574}\text{Al}_{0.426})(\text{Al}_{1.812}\text{Fe}^{3+}_{0.112}\text{Mg}_{0.09})\text{O}_{10}(\text{OH})_2$ |
| Gailhanou et al. (2013) | Saponite Sap-Ca-1 | $\text{Na}_{0.394}\text{K}_{0.021}\text{Ca}_{0.038}(\text{Si}_{3.569}\text{Al}_{0.397}\text{Fe}^{3+}_{0.034})(\text{Mg}_{2.948}\text{Fe}^{2+}_{0.021}\text{Mn}_{0.001})\text{O}_{10}(\text{OH})_2$ |
| Gailhanou et al. (2013) | Nontronite nau-1 | $\text{K}_{0.020}\text{Ca}_{0.247}(\text{Si}_{3.458}\text{Al}_{0.542})(\text{Al}_{0.268}\text{Fe}^{3+}_{1.688}\text{Mg}_{0.066}\text{Ti}_{0.007})\text{O}_{10}(\text{OH})_2$ |
| Gailhanou et al. (2013) | Vermiculite, Santa Olalla | $\text{Ca}_{0.445}(\text{Si}_{2.778}\text{Al}_{1.222})(\text{Al}_{0.192}\text{Fe}^{3+}_{0.226}\text{Mg}_{2.468}\text{Fe}^{2+}_{0.028}\text{Ti}_{0.018}\text{Mn}_{0.007})\text{O}_{10}(\text{OH})_2$ |
| Blanc et al. (2014) | Berthierine, ISGS | $(\text{Si}_{1.332}\text{Al}_{0.668})(\text{Al}_{0.975}\text{Fe}^{3+}_{0.182}\text{Mg}_{0.157}\text{Fe}^{2+}_{1.422}\text{Li}_{0.035}\text{Mn}_{0.002})\text{O}_{10}(\text{OH})_2$ |

3.2.3 Estimation methods for thermodynamic data for smectites

Many methods for estimating thermodynamic properties of minerals have been developed and only a small number of these can be discussed here. A widely used method is based on the assumption that the thermodynamic properties of silicate minerals can be modelled as the linear combination of the contributions of coordination polyhedra, which build the structural framework of minerals. Examples are Chermak & Rimstidt (1989, 1990), who estimated Gibbs free energies and enthalpies of formation for a wide variety of silicate minerals at 25 °C and higher temperatures, and Van Hinsberg et al. (2005a,b), who extended the polyhedral method and provided enthalpies of formation, entropies, molar volumes, heat capacities, compressibilities and thermal expansions for 35 different types of polyhedra to be used in the estimation of corresponding thermodynamic parameters for silicate minerals and some double-layered oxides.

A number of other methods were specifically developed for estimating thermodynamic properties of phyllosilicates, or clay minerals in particular. Tardy & Garrels (1974) estimated Gibbs free energies of formation of montmorillonites, illites, chlorites and micas by assuming that such silicates can be represented by oxide and hydroxide components in the silicate structure with fixed Gibbs free energies of formation that may differ from those of the components as separate phases. Noting that this estimation method for phyllosilicates could not be applied to other silicates or to hydroxides, Tardy & Garrels (1976) found an empirical parameter, ΔO_2^- that could be used for correlations with the Gibbs free energies of formation of other types of silicates and hydroxides. ΔO_2^- is defined as the difference between the Gibbs free energy of formation from the elements of a crystalline oxide and the Gibbs free energy of formation from the elements of its cation in aqueous solution (per O_2^- in the oxide), which is a function of the electronegativity of the cation. For silicates, the Gibbs free energies of formation from the oxides were shown to be linear functions of ΔO_2^- of their constituent cations. These linear functions can then be used to estimate the Gibbs free energies of formation for silicates.

Tardy & Fritz (1981) refined this method by directly correlating solubility products of phyllosilicates with the ΔO_2^- parameter. This correlation was used to estimate solubility products for 36 ideal clay mineral end members, which can be used to estimate the solubility product of a clay mineral with a specific composition by combining appropriate end members into an ideal solid solution.

Tardy & Duplay (1992) devised a method for estimating the Gibbs free energies of hydrated and dehydrated clay minerals based on the ideal solution model of Tardy & Fritz (1981), estimates of the Gibbs free energies of formation of the clay mineral end members based on the ΔO_2^- parameter, and assuming that hydration energies of clay minerals are proportional to the layer charge and, for a specific layer charge and a specific interlayer cation, also proportional to ΔO_2^- .

Vieillard (1994a,b) estimated enthalpies of formation based on ΔO_2^- parameters and refined crystal structures for a multitude of silicate minerals.

Vieillard (2000) and Vieillard (2002) improved the Gibbs free energy estimation methods for phyllosilicate based on ΔO_2^- parameters by considering ΔO_2^- for a specific cation to be different in interlayer, octahedral, and tetrahedral sites.

Several more recent studies estimated thermodynamic data for montmorillonites with different cation occupancies and/or different degrees of hydration (Marty et al. 2011, Vieillard et al. 2011, Tajeddine et al. 2015). The different mono-cationic occupancies as well as different hydration states can be seen as solid solution end members. Such a solid solution can then describe any montmorillonite with a given sheet structure, following the approach of Tardy & Fritz (1981). A solid solution with constant degree of hydration was successfully applied in a reactive transport simulation (Berner et al. 2013), where a Gibbs free energy minimisation program (GEMS) predicted the phase equilibria including the solid solution.

Finally, Blanc et al. (2015a) presented a generalised model for estimating the enthalpies of formation, the entropies, the heat capacities and the volumes of dehydrated phyllosilicates. Entropies and heat capacities were estimated using the polyhedral method, and enthalpies of formation were estimated based on the method developed by Vieillard (1994a,b).

In order to complement the so called "ThermoChimie"-database with thermodynamic data for clay minerals, Blanc et al. (2015b) used such estimation methods to extend the results of calorimetric measurements to other compositions.

3.2.4 Kinetic data for smectites

In contrast to the scarcity of solubility data for smectites, the dissolution kinetics of dioctahedral (montmorillonite, beidellite, and nontronite) and trioctahedral smectites (hectorite and saponite) have been extensively studied. Cama & Ganor (2015) provided a thorough review of the dissolution kinetics of clay minerals (kaolinite, smectite, vermiculite, chlorite, and the micas illite, muscovite, biotite and phlogopite), and this section on smectite kinetics is largely based on their review. However, there appear to be no data on the precipitation kinetics of clay minerals. Marty et al. (2015a), for example, developed a kinetic model for the dissolution and precipitation of clay minerals. They provided a database of selected parameters for their dissolution and precipitation rate model and reported dissolution rate parameters, but no precipitation rate parameters, for montmorillonite.

Cama & Ganor (2015) identified various factors that influence dissolution rates of clay minerals:

a) pH

In the absence of organic ligands, the main species attacking the surfaces of clay minerals are protons (acid region), water molecules (near neutral region) and hydroxyl ions (basic region), leading to a typical U-shape of dissolution rates as a function of pH, with a minimum at near-neutral conditions, as seen, e.g., by the dissolution rate experiments by Golubev et al. (2006) on Na-montmorillonite (Wyoming Swy-2) at 25 °C and pH from 1 to 12. Si-based dissolution rates decreased from $1 < \text{pH} < 8$ with a slope close to -0.2 and increased from $9 < \text{pH} < 12$ with a slope close to 0.3. Release of Mg was non-stoichiometric and showed a weak decrease from $1 < \text{pH} < 12$.

Zysset & Schindler (1996) carried out dissolution experiments with K-montmorillonite under acid conditions ($1 < \text{pH} < 5$) and 25 °C. Dissolution was found to be nearly congruent, dissolution rates to be linearly dependent on $[\text{H}^+]$ and dissolution to be taking place preferentially at particle edges.

Dissolution of the smectite-rich bentonites SAz-1, STx-1, and Swy-1, containing significant amounts of accessory silica phases (quartz, cristobalite and/or amorphous silica), was studied by Metz et al. (2005a) at 50 °C and pH 2 and 3. Dissolution was highly incongruent during the first few hundred to thousand hours, resulting in large initial release rates of Si, Mg, Ca, and Na which then underwent a distinct transition to significantly lower release rates at steady-state. The rapid release of Mg, Ca, and Na was interpreted as being due to ion exchange in the interlayer, while that of Si was attributed to the dissolution of accessory amorphous silica. Al initially showed low release rates that gradually increased to the steady-state value. At steady-state, the ratio of released Al to Si was nearly constant and independent of experimental conditions, suggesting congruent smectite dissolution. The initial low release rates of Al were interpreted by Metz et al. (2005a) as the result of coating or cementation of smectite aggregates by amorphous silica. Upon dissolution of the latter, the smectite aggregates fell apart, exposing more smectite surfaces, leading to the steady-state of congruent smectite dissolution.

Rozalen et al. (2008) and Rozalen et al. (2009a) studied the dissolution of K-montmorillonite at 25, 50, and 70 °C as a function of pH in KNO_3 solutions with pH ranging from 1 to 13.5 under far-from-equilibrium conditions. Dissolution rates were measured based on the release of Al and Si at steady-state. Dissolution was incongruent between pH 5 and 10, due to adsorption/precipitation of Al. At low pH, dissolution rates are probably controlled by positively charged aluminol sites ($< \text{AlOH}_2^+$) and at basic pH probably by negatively charged aluminol sites ($< \text{AlO}^-$).

Bauer & Berger (1998) investigated the dissolution of kaolinite and two industrial smectites, one a nearly pure Na-montmorillonite and the other a Ca-smectite with significant beidellitic charge, under very basic conditions (0.1 – 4 M KOH) at 35 °C and 80 °C. It was found that, under the experimental conditions, it is likely that the octahedral Al sites are more reactive than the tetrahedral Si sites. Since octahedral layers in smectites are bounded by tetrahedral layers, the dissolution of octahedral sites is limited to edge surfaces until the tetrahedral layers are dissolved. Since the edge surface area is much smaller than the surface of the basal planes, dissolution of octahedral and tetrahedral layers can be considered as serial processes, where the dissolution of the tetrahedral layers is the slower process and therefore rate-limiting.

Nakayama et al. (2004) investigated the dissolution rates of montmorillonite in compacted sand-bentonite mixtures under simulated highly alkaline groundwater conditions at pH 13 to 14 and temperatures from 90 °C to 170 °C. Dissolution of montmorillonite was linear with time and rates were lower than those commonly obtained from far-from-equilibrium batch dissolution experiments.

Ueta et al. (2013) used novel in-situ phase-shift interferometry combined with internal refraction interferometry to observe bulk montmorillonite dissolution under alkaline conditions (23 °C, NaOH, pH = 8.2 – 14). Molecular resolution was achieved during the optical observation of the dissolution processes in real time and in situ. The molar dissolution fluxes obtained gave larger dissolution rates than those previously determined by solution analysis of batch dissolution experiments.

b) Temperature

The temperature dependence of dissolution rates generally follows an Arrhenius-type law, $\text{rate} = A \exp(-E_a/RT)$, where A is the pre-exponential factor which takes account of all other experimental factors besides temperature that influence rates, E_a is the apparent activation energy of the overall dissolution reaction, R is the gas constant and T the temperature in K. Cama & Ganor (2015) emphasised that the pH effect on dissolution is controlled by protons sorbed on the surface of the dissolving mineral and not directly by pH. Therefore, it is essential that, in order to keep the pre-exponential factor constant in experiments, one should keep the surface concentration of protons constant and not necessarily the pH.

c) Inhibition and catalytic effects

It was shown by Oelkers et al. (1994) that, under very far-from-equilibrium conditions at 150 °C and pH = 2, the dissolution rate of kaolinite shows a strong inverse dependence on the concentration of dissolved Al (they observed the same phenomenon with albite at 150 °C and pH = 9). These authors proposed that the dissolution of Al-silicates is controlled by an Al-deficient/Si-rich surface precursor complex formed by the exchange of Al for protons at the surface.

Zysset & Schindler (1996) observed that Al^{3+} inhibits the dissolution reaction of K-montmorillonite at pH < 3 and attributed this inhibition to sorption of Al^{3+} on particle edge sites.

Metz (2001), however, found that, under far-from-equilibrium conditions, the dissolution rates of smectites are independent of both Al and Si concentrations. This observation was also supported by dissolution experiments with SAz-1 Cheto montmorillonite by Amram & Ganor (2005).

Van Rompaey et al. (2002) studied the influence of acid type on the dissolution rate of hectorite. Not unexpectedly, the rate of dissolution increased with increasing acid concentration. At the same molar concentration of acid, dissolution rates decreased in the order of acid strength $\text{H}_2\text{SO}_4 > \text{HNO}_3 > \text{HCl}$.

d) Organic matter

Ganor et al. (2009) reviewed the effect of organic matter on the dissolution rates of minerals. As different types of minerals differ in their surface properties, there is a significant variability in their capacity to adsorb organic matter. The most effective adsorbents are clay and oxide minerals. Organic matter may enhance or inhibit dissolution rates. In the case of kaolinite and montmorillonite, low molecular mass organic acids, such as oxalate, malonate, citrate, salicylate, ortho-

phthalate and gluconate, have been shown to enhance dissolution through ligand-promoted dissolution at the mineral surfaces (see references in Cama & Ganor 2015). However, Golubev et al. (2006) observed that acetate, gluconate, alginate, glucosamine, and glucuronate may also inhibit dissolution of montmorillonite. In any case, Golubev et al. (2006) remarked that, in contrast to framework silicates whose dissolution is greatly enhanced by the presence of minor amounts of organic acids forming strong surface complexes, comparatively high concentrations of organic ligands are needed in order to significantly increase dissolution rates of smectite.

e) Deviation from equilibrium state

Several mechanistic models have been developed over the past 40 years to account for the influence of the deviation from equilibrium (degree of saturation) on dissolution rates of minerals. Cama & Ganor (2015) discussed the following three models: The first and most widely used was derived from transition state theory which was developed for elementary reactions and may be applied to overall dissolution reactions (see Cama & Ganor 2015 for references). It relates the variation in solution composition with the rates of mineral dissolution or precipitation and may only be applied if dissolution kinetics are not influenced by crystal defects such as dislocations. The second model of Lasaga & Luttge (2001) links the surface reactivity of minerals directly to their dissolution kinetics. With the third model, finally, of Dove et al. (2005), the dissolution kinetics of quartz, aluminosilicate minerals, kaolinite, and K-feldspar can be described by the same mechanistic theory of nucleation as developed for mineral growth. According to Cama & Ganor (2015), most of the descriptions and interpretations of clay dissolution kinetics are, at the moment, only based on transition state theory.

Cama et al. (2000) reported stoichiometric dissolution at 80 °C and pH = 8.8 of randomly inter-layered illite-montmorillonite (I/M) from Cabo de Gata, southern Spain, in far-from-equilibrium experiments. The observed dissolution rates reflected the dissolution of the montmorillonite layers and were not influenced by Al. Since the degree of saturation was varied by changing the concentration of Si, the observed decrease of dissolution rates with increasing Si concentrations can be due to the effect of deviation from equilibrium or to silicon inhibition. Consequently, Cama et al. (2000) expressed the observed reaction rates by two different rate laws, one as a function of the deviation from equilibrium and the other as a function of Si concentration. However, on the basis of these experiments alone, it is not possible to decide between these two cases.

Marty et al. (2011) carried out dissolution experiments with synthetic Na-montmorillonite at pH 7 and 9, and 25 and 80 °C. At 25 °C, preferential release of Mg over Al and Si was observed, while at 80 °C dissolution was stoichiometrically congruent. Analysis of the solid after the experiment at 25 °C revealed the presence of a newly formed unidentified Si-rich phase. The reduced solubility of Al remained uncertain. A rate law as a function of the deviation from equilibrium was formulated by Marty et al. (2011) based on the steady-state release of Mg at pH 9 and 25 °C.

f) Surface area and reactivity

The reactive surface area is one of the most important parameters for describing the kinetics of mineral dissolution. Its determination is not trivial in the case of clay minerals, since they possess both internal and external surface areas, and dissolution is often controlled by processes tied to the edge surfaces.

Marty et al. (2011) could not detect any etch pits formed on basal planes of powdered synthetic Na-montmorillonite that had reacted at pH around 9 and 80 °C by atomic force microscopy (AFM) observations, suggesting that dissolution takes place at edge sites.

In-situ AFM observations by Yokoyama et al. (2005) on montmorillonite dissolving under highly alkaline conditions (pH = 13.3, I = 0.3, and 30, 50, and 70 °C) indicated that dissolution occurred at edge surfaces. Etch pits formed on basal planes of a few particles, but these did not appear to be the dominant dissolution sites.

Likewise, Kuwahara (2006) showed by means of in-situ AFM that Na-montmorillonite (Kunipia-P) particles dissolved at 25 °C and pH = 11.2 and 11.8 with retreating edge surfaces and that the basal planes remained essentially unreactive.

Satoh et al. (2013) measured montmorillonite dissolution rates at 70 °C and pH 12.1 as a function of compaction pressure (0.04 to 10 MPa). Observed dissolution rates were 1 to 2 orders of magnitude lower than those observed for dispersed montmorillonite at the same temperature and pH. This rate reduction was explained by limited water flow in nanopores adjacent to the grain surfaces where dissolution takes place, and by limited exposure of such grain surfaces under compaction.

In experimental kinetics studies, dissolution rates are often normalised to surface areas measured by the BET method, which measures the total surface area. Metz et al. (2005b) showed with AFM measurements on SAz-1 montmorillonite that there is no correlation between surface areas measured by BET and the more relevant edge surface areas measured with AFM and suggested the use of AFM measurements of the specific edge surface area as a more reliable proxy for the reactive surface area than surface areas determined by BET.

In the case of nontronite, Grybos et al. (2010) demonstrated that, in contrast to montmorillonite, acid dissolution takes place by leaching of Fe³⁺ from octahedral sites on the edge sites and also by leaching from tetrahedral sites on basal planes. Lack of correlation between the extent of Fe³⁺ dissolution and the decrease in particle size (implying an increase in edge surface area) suggested that reactive surface sites are evenly distributed on basal planes, and that the contribution of basal planes to the dissolution of nontronite is significant.

g) Ionic strength

Transition state theory predicts that the rate constant of an elementary reaction depends on the activity coefficients of the aqueous species and therefore also on the ionic strength. Amram & Ganor (2005) investigated the effect of variable ionic strength on the pH dependence of the dissolution rate of SAz-1 Cheto montmorillonite. In a first series of experiments, the pH was varied (4.5 > pH > 1) by adding only HNO₃ to the experimental solution, resulting in a concomitant variation of ionic strength from 3.2×10^{-5} M to 0.1 M. In the second series, the same variation of pH was produced by adding HNO₃, the ionic strength, however, was maintained at 0.32 M by adding suitable amounts of NaNO₃. No significant differences could be found between the two series of experiments.

Marty et al. (2015a) set up a database of dissolution and precipitation rates for clay minerals to be used in geochemical codes such as PhreeqC3, CrunchFlow, and ToughReact. Three types of experimental kinetic data were considered

- a) data dependent on pH
- b) data dependent on temperature
- c) data dependent on the saturation ratio (deviation from the equilibrium state)

The selected data were used to derive kinetic rate equations based on transition state theory. Two types of regression models were used: a linear regression model and a regression curve model. Linear regression of logarithmic reaction rates as a function of pH leads to three straight segments, with a negative slope in the acid range, a horizontal slope in the near-neutral range and a positive slope in the basic range. With the regression curve model, a continuous curve was fitted to the experimental data. Kinetic parameters for dissolution rates were provided by Marty et al. (2015a) for albite, biotite, celestite, chlorite, C-S-H, cristobalite, dolomite, gibbsite, illite, kaolinite, microcline, portlandite, quartz, siderite, and montmorillonite. Kinetic parameters for precipitation could only be derived for calcite, celestite, C-S-H, cristobalite, dolomite, gibbsite, kaolinite, quartz, and siderite. No such parameters could be provided by Marty et al. (2015a) for albite, biotite, chlorite, illite, microcline, portlandite, and montmorillonite.

3.2.5 Conclusions

Besides the principal objection put forth by Lippmann (1982) that clay minerals are most probably not equilibrium phases and that the results of solubility experiments are not representative of thermodynamic equilibrium, there are numerous experimental problems that impede the straightforward interpretation of solubility experiments with clay minerals:

- In the ideal case, equilibrium must be attained from over- and undersaturation. Equilibrium from oversaturation, however, can often not be reached, since nucleation of a mineral phase is characterised by an activation energy barrier which is difficult to overcome at room temperature (Blanc et al. 2013).
- Equilibration times at low temperature may often exceed reasonable experimental timescales. The quartz solubility experiment by Rimstidt (1997), e.g., lasted for more than 13 years.
- Smectites commonly show incongruent dissolution behaviour, however the nature and crystallinity of the secondary minerals controlling the solubility of Al and Si are usually not known (Tardy & Fritz 1981).
- Even purified clays are in fact mixtures of several phases with different size or compositions, reacting as different phases and dissolving at different rates (Tardy & Fritz 1981).
- Kittrick & Peryea (1989) identified the most difficult aspect of their solubility experiments as the requirement for an exact correspondence between the bulk composition of the montmorillonite sample (which is all that can be analysed) and the composition that actually controls the solubility. Also, impurities such as other smectite phases may be difficult to detect. Kittrick & Peryea (1989) declared that, with respect to their experiments, "in retrospect, it appears that obtaining a sample with the required composition correspondence was a matter of good fortune".

In their review on the thermodynamics of clay minerals, Blanc et al. (2013) make an important statement: "In spite of the large number of studies aiming to determine the solubility of clay minerals by solution equilibrium experiments, these types of data are not often used in geochemical calculations. The reason lies in the uncertainty concerning equilibrium attainment. One way to overcome this problem would be to assess equilibrium experiments by calorimetric measurements performed on the same clay mineral, since calorimetry is independent of any equilibrium in aqueous solution". It is certainly true that calorimetry is independent of any equilibrium in solution, but that does not mean that thermodynamic data obtained with calorimetry for a structurally and compositionally heterogeneous smectite are in any way useful for true equilibrium calculations. Similar considerations hold for estimated thermodynamic data. However, they may well be used in combination with kinetic data for modelling the dissolution of a specific smectite.

In summary, Lippmann's conclusions have not yet been falsified. What are the consequences in the case of illites and smectites? Calorimetric data may indicate the chemical driving force towards dissolution or precipitation of a clay phase in a certain aqueous system. But actual equilibrium reactions are kinetically inhibited. Kinetic data can be used to model dissolution. At this point, the reliability of models including precipitation is strongly questioned.

Yet, a large body of modelling literature exists about studies including clay stability, dissolution, and precipitation (e.g. Savage et al. 2002, Gaucher et al. 2004, Montes-H et al. 2005b, Yamaguchi et al. 2007, De Windt et al. 2008, Fernández et al. 2009a, Gaucher et al. 2009, Savage et al. 2010b, Beaucaire et al. 2012, Berner et al. 2013, Kosakowski & Berner 2013, Savage 2013, Marty et al. 2015b, Savage & Liu 2015). Some of these studies use thermodynamic data of clays to calculate porewaters, which generally agree with measurements. Many studies predict dissolution of clays under alkaline conditions, which are consistent with observed processes (e.g. buffering of pH). Verification of dissolution rates with observations from in-situ experiments (e.g. the Mont Terri CI (cement clay interaction) experiment) is often non-trivial due to the slow reaction (amount of dissolved clay is within the error of the clay quantification method). Also, clay precipitation predicted by modelling is rarely supported by observations for the same reason. Often, similarly structured phases (e.g. layered double hydroxides) cannot be distinguished from clay, or amorphous precursors are hard to detect at low amounts. Furthermore, the quality of thermodynamic data is generally too low to properly predict the nature of the precipitate. Model predictions of the nature of the precipitate are often an overinterpretation of the thermodynamic data (e.g. Dautères et al. 2016). However, the model prediction of unspecified precipitation and its influence on transport can already provide valuable information for the understanding of interaction processes at an interface.

In the repository context, uncertainties in thermodynamic and kinetic data of clay minerals affect the understanding of the behaviour of the bentonite barrier. In view of this, additional arguments from natural analogues have been invoked (e.g. Karnland & Birgersson 2006). In fact, natural bentonites formed under a variety of environmental conditions have been stable for millions of years. Another argument is related to the transport restriction which considerably slows down montmorillonite transformation processes (Leupin et al. 2015). These arguments add additional support to the long-term stability of montmorillonite.

3.3 Concepts of microstructure and their implications for clay-water interactions

The spatial arrangement of montmorillonite, accessory minerals and porosity defines the microstructure in a saturated bentonite, as illustrated in Fig. 3-18, a schematic visualisation frequently replicated in many publications. It should be kept in mind that the comprised elements are not to scale: accessory minerals are three orders of magnitude larger than montmorillonite grains that have a much more bladed habit (~ 40 times wider than thick) and consist of fewer sheets than shown in this figure. Furthermore, the thickness of the double layer (light blue) and free water layer (dark blue) is exaggerated compared to the interlayer water (green) at repository-relevant dry densities of around 1.5 Mg m⁻³ or above.

Unsaturated systems imply the presence of a gas phase, which is considered in section 3.6.

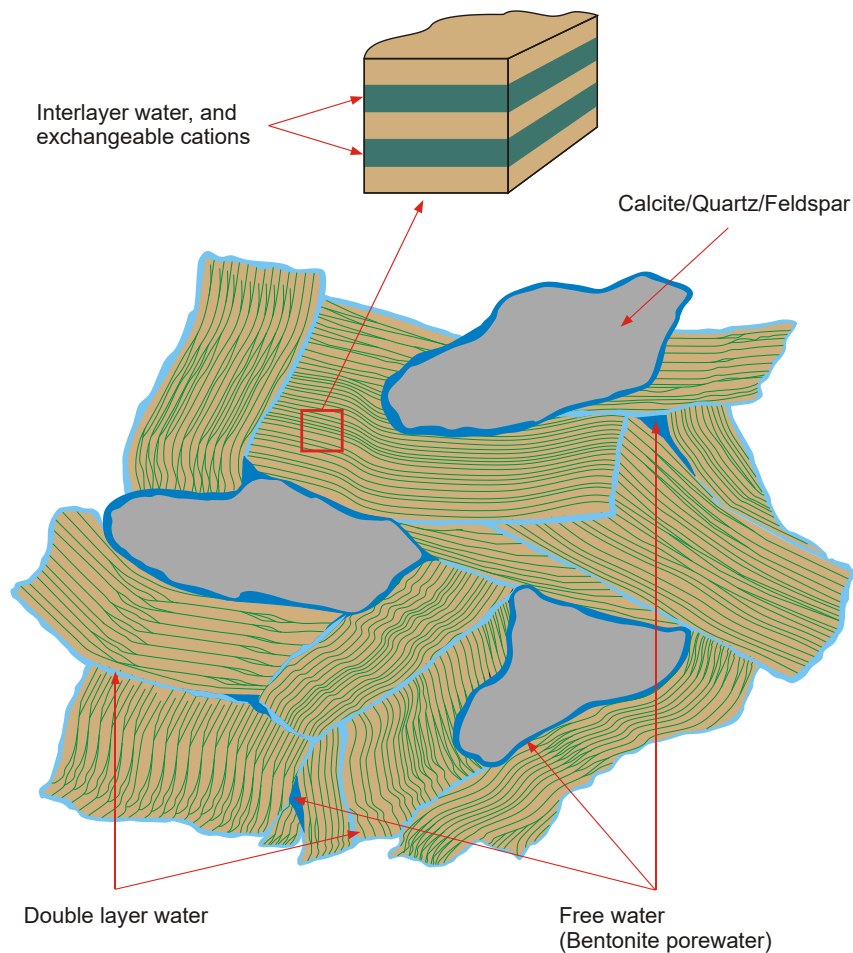


Fig. 3-18: Conceptual view of bentonite micro/nanostructure and its porosity types
Bradbury & Baeyens (2002)

3.3.1 Porosity concepts for transport modelling

Different arrangements and simplifications of accessory minerals and montmorillonite, including its electrostatic effect, lead to different porosity concepts, which provide the basis for various modelling approaches (outlined below). Section 3.4.1 elaborates on the consequences of the different concepts for porewater composition.

- *Single intergranular porosity concept:* the interlayer water is seen as crystalline water in the classical montmorillonite formula, and the cations attracted to the clay sheet surfaces are seen as exchangeable cations as part of the CEC (section 3.1.1). The intergranular water is unaffected by the negative surface charges of the clay and therefore charge-balanced. This concept cannot explain differences in breakthrough curves of anion and neutral tracers observed during advective transport through bentonite (Alt-Epping et al. 2015). In diffusive transport set-ups, the observed differences in steady-state fluxes $J_{\text{cation}} > J_{\text{neutral}} > J_{\text{anion}}$ (Glaus et al. 2010, Tachi & Yotsuji 2014) cannot be explained (Tournassat & Steefel 2015). Some modelling approaches partially overcome such inconsistencies by using different porosities for anions and for other species in the transport equations (anion-accessible/total porosity, Berner et al. 2013, Kosakowski et al. 2014). Furthermore, these two approaches simulate cation exchange with an ideal solid-solution of Na-, Ca-, Mg-, K-montmorillonite end members. However,

such a modified single porosity concept cannot describe certain experimental observations (e.g. different effects of pore clogging on anion and tritiated water (HTO) diffusion in illite; Chagneau et al. 2015). It is not possible to link such a concept to hydromechanical processes and swelling.

- *Single Donnan porosity concept*: the charged clay sheet surface influences the entire porewater, and no charge-balanced water in a free porosity exists. The model approach of Birgersson & Karnland (2009) is based on this concept, applying Donnan equilibrium between the entire clay porewater (assumed to be homogeneous) and the solution in an external reservoir. This elegant approach holds for simple electrolytes and non-reactive transport in highly compacted clays. Tinnacher et al. (2016) applied the single Donnan approach to data on diffusion in montmorillonite of 0.8 Mg m^{-3} dry density and showed the need to increase anion diffusivities without good arguments. Furthermore, it is difficult or even impossible to account for complex pore clogging effects on transport with such a concept. A distinct advantage is the small number of parameters required.
- *Dual porosity concept*: this approach lumps together the Donnan porosity on clay grain surfaces and in interlayers as described further in section 3.3.3, because both porewaters are influenced in a similar way by the negatively charged clay sheet surfaces. This often includes the simplification of the Donnan porosity on the clay surface having a layer thickness of half of the interlayer distance. Applications of this concept can describe advective/diffusive transport through bentonite with two geometric factors (Donnan and free porosity) used for all species, but assuming advection in the free porosity only (Alt-Epping et al. 2015). The comparatively simple concept allows for the simulation of complex reactive transport problems across interfaces (Jenni et al. 2017). The model uses comparably fewer additional parameters than some other models, namely for pore size distribution, which partly can be derived from experimental data.
- *Triple porosity concept*: free porosity, interlayer porosity, and Donnan porosity on clay surfaces are distinguished. Experimental data on cation tracer diffusion can be described by this concept (Kozaki et al. 2008). The presence of additional parameters (fractions of the three porosity domains, transport properties within the domains) enables the models based on this concept to describe most of the data available. The approach of Appelo & Wersin (2007) and Appelo et al. (2010) considers diffusion in the free porosity and in the Donnan porosity on clay surfaces (called diffuse double layer) only. Interlayer water and cations are static and the latter undergo cation exchange with the free water. Similar approaches are used in equilibrium considerations (Wersin et al. 2004, 2016). In order to predict diffusion of differently charged tracer species in OPA, it has been necessary to consider individual geometrical factors for the species. The corresponding values were justified in a heuristic way by different paths according to species charge (although different accessible porosities were already considered) and differences in ion-pairing influencing diffusion (e.g. between mono- and divalent cations). In the examples mentioned, surface complexation describes cation exchange in interlayers, and Donnan equilibrium defines the porewater composition in the Donnan porosity on clay surfaces. Such complex approaches comprise a variety of non-uniquely defined and correlated parameters.

The above concepts can be extended by considering a more specific distribution of ions in the pore space, or a more detailed distinction of surface sites:

- The *Stern layer* describes cations close to the clay sheet surfaces, situated in inner-sphere and outer-sphere complexes, which can be seen as covalently bonded and electrostatically bonded, respectively (Lee et al. 2010). The Stern model is a combination of the Helmholtz and the Gouy-Chapman models. The Stern layer screens a fraction of the surface charge, and the ions in the Donnan porosity balance the remaining charge. Modelling approaches often

simulate the Stern layer with surface complexation. The sum of the complexed cations and the cations in the Donnan porosity must be seen as exchangeable cations. Tinnacher et al. (2016) describe different approaches following this concept.

- *Edge sites* are situated at the lateral borders of the clay stacks and have a capacity of approximately 10 % of total CEC (Bradbury & Baeyens 2002). They can protonate and deprotonate according to pH, and sometimes are further subdivided into weak and strong sites (e.g. Bradbury & Baeyens 2002). If they are considered in reactive transport modelling, the net charge must be compensated in the Donnan porosity composition or by other means (Berner et al. 2013). The characteristics of these sites are expected to be influenced by interlayer distance (dry density), (internal) layer charge, and others such as pH (Avena et al. 2003, Tournassat et al. 2016b). In addition, species-specific sorption on edge sites is described. These sites offer flexibility to model species that show relatively strong sorption compared to what would be expected from simple ion-exchange behaviour in clay interlayers (e.g. Cs, Th(OH)₄).

3.3.2 Montmorillonite microstructure

The properties of montmorillonite crystals, such as their small size, their large internal and external specific surface area, and their capacity to absorb water into their interlayer structure determine the microstructure in bentonites to a large extent. In contact with water, platelets with a lateral extent of 50 – 200 nm are formed (Tournassat & Appelo 2011, citing Pusch 2001 and others) with a layered structure comprising the TOT sheets and interlayer water. Based on specific surface area measurements and simple geometric and crystallographic relationships, the same studies, as well as Cases et al. (1992), state stacking numbers of 3 - 7 in compacted Na-montmorillonite (equal to the number of unit cells in the 001 direction, n_c). Furthermore, $n_a = n_b = 200$ (number of unit cells in the 100 and 010 direction) is derived, leading to internal and external surface areas of 608 m²/g and 163 m²/g, respectively. The fact that $n_c \ll n_a, n_b$ indicates a relatively small contribution of the edge surface to the external surface area.

3.3.3 Accessory minerals and related porosity

The low content of rigid accessory minerals in MX-80 (about 20 %) situated in a swelling clay matrix implies that the microstructure is not accessory-grain supported. This is in contrast to certain bentonite-sand mixtures with added sand. In general, it is assumed that the water layer between a strongly charged clay surface and an accessory mineral surface measures half of the thickness of an interlayer, where both opposing surfaces are charged (Evans & Wennerström 1999). This has recently been supported by molecular dynamic simulations (Hsiao & Hedström 2017). A collapse of the interlayer and the close contact of two clay sheets, or of a clay sheet and accessory grains (mentioned in Tournassat & Appelo 2011) seems unlikely to occur at the densities expected in a repository (< 2.0 Mg m⁻³ dry density). Single-porosity approaches assign the entire porosity to interlayers, which certainly holds for parallel plates. Selected TEM images of flexibly bent montmorillonite stacks in the vicinity of edge surfaces of adjacent stacks support these approaches. However, small-scale surface roughness of accessory minerals might lead to an irregular surface water layer, as even flexible montmorillonite flakes are unable to be perfectly parallel to a rough surface. The resulting pore size larger than half the interlayer distance is ignored in the interlayer-only approach. The comprehensive study of Keller et al. (2014) concludes that, up to 1.5 Mg m⁻³ dry density, a porous clay gel forms preferentially in the pressure shadow of larger accessory minerals, which also questions the homogeneous approach.

Very likely, intergranular porosity occurs at lower densities at rough accessory surfaces or grain triple points, creating porosities too small to be filled by bending clay stacks. Interlayer-like conditions can be expected along parallel grain boundary settings and at higher densities. In the latter case, chemical conditions similar to the interlayer might occur at an accessory mineral or also at the canister surface. Classical corrosion or other phase stability approaches assume an intergranular type of porewater reacting with such surfaces. Predictions based on intergranular porewater reactions with other materials or accessories generally match experimental observations (sections 3.4 and 5.4).

The influence of an inert filler on swelling pressure is discussed in section 3.8.1, in the context of coupling between microstructural and mechanical properties.

3.3.4 Pore size distribution and ion distribution in pores

Pore size distribution is the main point of interest of the microstructure, because it governs solute transport and influences porewater chemistry. A part of the porewater is influenced by the negative surface charge of the montmorillonite sheets and is therefore depleted in anions. Due to the large internal surface area of the montmorillonite, this porosity fraction dominates at higher compaction. The influence of a charged surface on the spatial ion distribution can be estimated with the Poisson-Boltzmann equation. If it is applied to an outer clay surface, the electric field is zero only at an (infinitely) large distance from the surface, and an analytical solution exists for 1:1 electrolytes and planar surfaces (Gouy 1910, Chapman 1913). The solution at infinite distance from the surface, not affected by the surface potential, is denoted as external solution. In the case of two equally charged clay surfaces (interlayer), the electric field neutralises at the midplane (Fig. 3-19) and no analytical solution exists (Hedström & Karnland 2011).

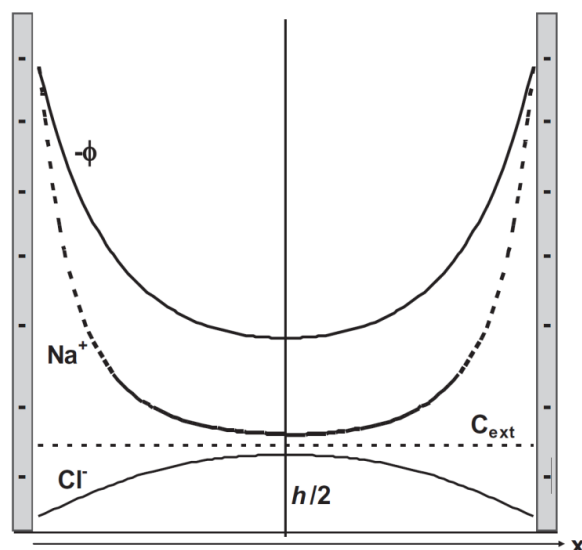


Fig. 3-19: Schematic illustration of sodium and chloride concentration profiles in the interlayer, together with the electrostatic potential $-\phi$

The horizontal dashed line indicates the equilibrium external NaCl concentration. h represents the interlayer distance. Due to symmetry, the electric field, $-\phi/dx$, vanishes at the midplane $x = h/2$.

Hedström & Karnland (2011)

The calculation of the ion distribution near surfaces with complex geometry with the Poisson-Boltzmann equation is difficult. Furthermore, the detailed pore geometry is generally not known. Thus, the pore solution affected by the negatively charged clay sheets is commonly treated as homogeneous. Its composition can then be predicted by the Donnan equation, which defines the equilibrium between porewater in the range of the electric field and the water not affected by the surface field (Donnan & Guggenheim 1932, Tournassat & Steefel 2015) using the mean field potential. Porewater not affected by electrostatics is termed external water. It can be located outside a clay sample (e.g. in an external reservoir) or in pores of the sample not affected by any surface charges (often denoted as "free" porewater). The porosities comprising the Donnan and the "free" porewaters are referred to as "Donnan porosity" and "free porosity" below. Following this definition, the Donnan porosity typically includes the interlayer water as well as porewater on external clay grain surfaces. The free porewater in the free porosity is charge-balanced, in contrast to the Donnan porewater in the Donnan porosity, where the total positive charge of all species balances the negative charge of the clay sheets (CEC). The terminology found in the literature can be misleading:

- "Double layer", "diffuse double layer", or "electric(al) double layer" are often used to describe the Donnan porosity on external clay grain surfaces only. But, especially at high bulk densities, layers with similar structure also occur in the interlayer. Furthermore, "double layer" in fact refers to the charged solid surface with the counterions and the water layer influenced by it, and "diffuse double layer" also to a distance-dependent ion distribution as given for instance by the Poisson-Boltzmann equation.
- "Surface water (porosity)" is sometimes used as a general term for water near clay sheet surfaces. It is thus related to the Donnan porosity. Similarly, surface diffusion of sorbed cations (Gimmi & Kosakowski 2011) can be related to cation diffusion in the Donnan porosity, but the exact relationship is not completely clear because of the relatively large differences in surface diffusion for certain cations of equal charge.
- "Anion-free, -excluded, -restricted porosity" and "anion-accessible porosity" are often used as synonyms for Donnan and free porosity, respectively. The former terms imply an anion-free domain, which contradicts chemical compositions predicted by the Poisson-Boltzmann and Donnan equations (shown schematically in Fig. 3-19), as well as certain MD simulations (Hedström & Karnland 2012, Hsiao & Hedström 2015).
- "Diffuse ion swarm" is sometimes used as synonym for ions in the Donnan porosity but tends to imply a distance-dependent ion distribution, as in a diffuse double layer.
- "Intergranular porosity" is partly used as a synonym for free porosity. This interferes with the fraction of Donnan porosity situated on clay grain outer surfaces. In this sense, free porosity has to be smaller than or equal to the intergranular porosity (assuming that all interlayer porosity is Donnan porosity).
- "Bulk water porosity" is often used as a synonym for free porosity but can be mistaken for total porosity.

3.3.5 Experimental evidence for the different porosity concepts

Only total porosity can be accurately derived from water content and grain density measurements, and the density of the porewater (Pusch 2002). Measurement of the pore size distribution is far more complex because most of the methods have to be applied to dry material but drying modifies the microstructure of the bentonite.

Keller et al. (2014) qualitatively showed the presence of a few small ice-filled pores by cryo-focused ion beam nanotomography (high-pressure shock-frozen MX-80 bentonite with 1.5 Mg m^{-3} dry density). Heating of the sample causes sublimation of this water, but also the opening of cracks "probably formed during drying of the fine-grained matrix, which led to delamination cracks between rigid grains and shrinkage of the clay matrix." Furthermore, a "clay gel" was observed in the frozen and dried state, which fills the intergranular pore space at 1.24 and 1.46 Mg m^{-3} but is absent at 1.7 Mg m^{-3} dry density. Confined samples were saturated with water via the gas phase, but full saturation could not be shown. Interlayer distances could not be assessed because the resolution of the method is limited to $> 10 \text{ nm}$ pores.

The relevance of mercury intrusion porosimetry (MIP) data is highly questionable, other than for systematic/nomenclature purposes: normally, such samples are not as carefully frozen as done in Keller et al. (2014) and Keller et al. (2015), and drying should also lead to cracks as observed in Keller et al. (2014). MIP pore size distributions (Delage et al. 2006, Seiphoori et al. 2014) consistently show peaks at $10 - 20 \text{ nm}$ pore radius, as well as a significant fraction of pores below 4 nm (mismatch between total MIP values and total porosity known from sample preparation). Such pore ranges might correspond to the drying cracks with an approximate width of 100 nm found by Keller et al. (2014). Mercury does not intrude into the interlayer porosity, which is often seen as a fraction of the so-called nanostructural porosity, together with the intra-stack porosity. It has collapsed during drying and is therefore not assessed by this method.

XRD analysis on wet clay shortly after removal from confinement and protected from drying (e.g. X-ray transparent foil, climate chamber) is the most promising approach to measure the interlayer distance (position of the 001 reflection, Fig. 3-20). Alternatively, Muurinen (2009) and later studies of the same author present basal spacings derived from small-angle X-ray scattering (SAXS) measurements, generally in agreement with XRD measurements. Half of the average basal spacing multiplied by the specific surface area of the montmorillonite sheet faces results in the interlayer porosity. The difference between the interlayer and the total porosity can be interpreted as interparticle or free porosity (e.g. Holmboe et al. 2012, Bestel et al. 2018a, 2018b). The absolute pore size distribution and geometry are the main parameters constraining solute transport in the clay. Therefore, porosity parameters are crucial for predictions of interactions with other EBS materials during the repository lifetime, if their influence on transport is significant (section 3.8).

Basal spacing, and therefore interlayer porosity, depends mainly on dry density (Fig. 3-20 and Fig. 3-21). Following the procedure outlined above, Holmboe et al. (2012) calculated the intergranular porosity from their own and literature data and also found a dependence on dry density (Fig. 3-22). The scattering of the data in the latter two figures demonstrates the relatively large errors. Also, Bestel (2014) and Bestel et al. (2018a) conclude, based on neutron scattering measurements, that only interlayer and surface water exist in Na-montmorillonite denser than approximately 1.65 Mg m^{-3} dry density.

Historically, X-ray diffraction was first applied to clays saturated at different humidity levels under unconfined conditions (Mooney et al. 1952). The subsequently assembled extensive data base is not comparable with data from confined samples: Devineau et al. (2006) conclude that the partitioning of the hydration water between interlayer and intergranular porosity is different under

free and confined conditions. Especially at high humidity, the interlayer swells at the expense of the intergranular porosity under confined conditions, which is not observed under unconfined conditions. Furthermore, the unconfined samples might not have been fully saturated. Also, Holmboe et al. (2012) find differences in basal spacings between confined and unconfined saturated clays. However, unconfined saturation data might, nevertheless, reveal general mechanisms, such as differential hydration of different cations in the interlayer, which are also valid in a confined system (discussed below).

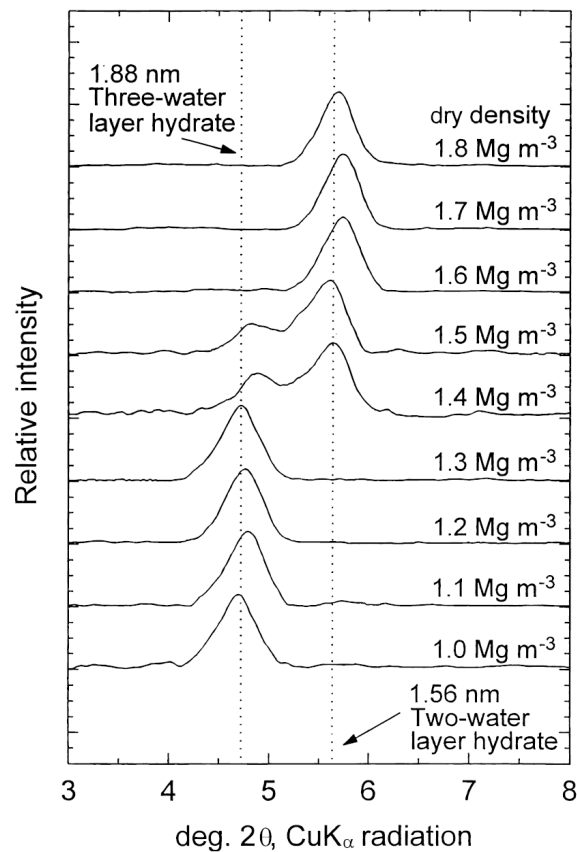


Fig. 3-20: X-ray diffraction profiles for distilled water-saturated, compacted, Na-montmorillonite with different dry densities

Kozaki et al. (1998)

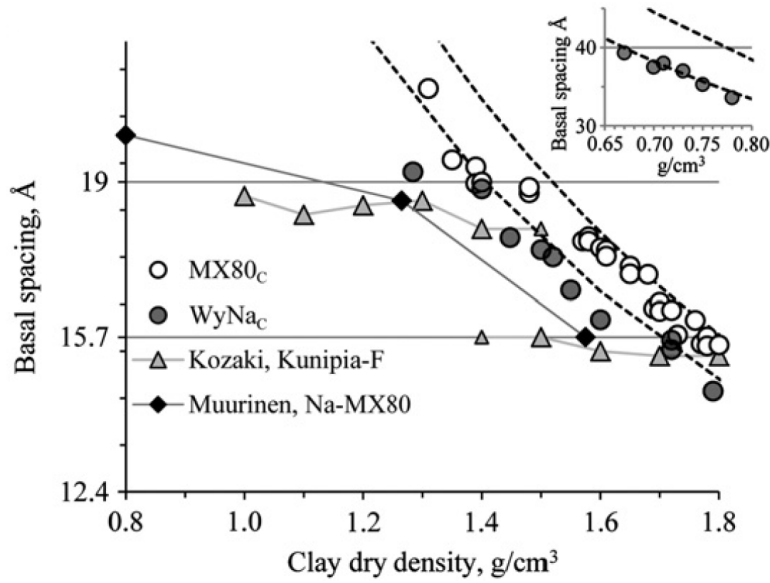


Fig. 3-21: Reported basal spacings for clay samples saturated from the aqueous phase under confined conditions

MX80_C represents values from MX-80 bentonite, WyNa_C and Na-MX80 from washed Na-montmorillonite (MX-80), Kunipia-F values from washed Na-montmorillonite (Kunipia bentonite).

Holmboe et al. (2012)

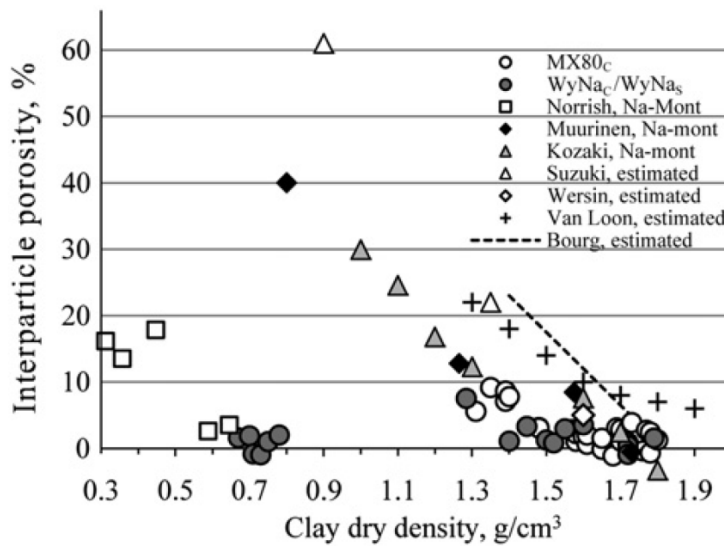


Fig. 3-22: Interparticle porosity as a function of dry density calculated from average interlayer distance

MX80_C, WyNa_{C/S}: MX-80 bentonite and Na-montmorillonite saturated under confined (C) or unconfined (S) conditions.

Holmboe et al. (2012)

Interpretation of ^1H NMR relaxation time measurements reveals information about the pore structure. Muurinen et al. (2013) observed decay curves, which can be split into two different exponential curves, each associated with a different relaxation time. With the help of reference measurements on dry samples and SAXS measurements, these two curves are interpreted as two distinguishable water phases located in two different types of pores. Furthermore, it is proposed that the zero-time magnetisation of each curve, which can be seen as a scaling factor, is proportional to the relative amount of each water phase. Indeed, the zero-time magnetisation of the short relaxation time curve corresponds to the interlayer water determined by SAXS (Fig. 3-23).

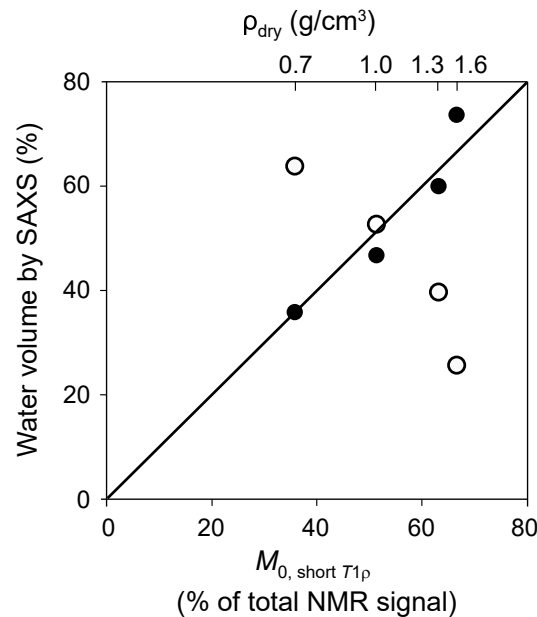


Fig. 3-23: MX-80 water volumes determined by SAXS plotted against the zero-time magnetisation (short relaxation times) at different densities

MX-80 saturated with deionised water under confined conditions. Filled symbols: interlayer water, open symbols: non-interlayer water.

Muurinen et al. (2013)

Hydraulic conductivity reveals information about porosity and pore geometry. In general, conductivity decreases with higher dry density and lower porosity (Fig. 3-24). Unfortunately, the measurement error is large (personal communication Ola Karnland and Jenni & Mäder 2018), and the conductivity possibly results from the sum of different flow paths, or certain porosity regions are not part of a flow path (see sections 3.3 and 3.5). Therefore, interpretation of hydraulic conductivity measurements requires a microstructural model.

Natural claystones represent a material with a known significant fraction of free porosity in addition to the Donnan porosity. Experimental data from such materials help to understand the dense bentonite system, which represents an extreme case with a very small free porosity. Porosity of claystones is commonly divided into anion-accessible and anion-non-accessible porosity. Observed differences in transport behaviour of anions, cations, and neutral species through claystones can be explained by the presence of different porosity domains with different ion concentrations and transport properties (sections 3.4 and 3.5). The discrimination of only two domains, with one of them being free of anions, is an enormous but powerful simplification: this concept can explain most of the data on solute transport through claystone. The two porosity

volumes can be derived from diffusion experiments, and/or aqueous leaching of clays equilibrated with an external reservoir (Glaus et al. 2011, Jenni et al. 2014a). Muurinen et al. (2013) showed that chloride-accessible porosity in bentonite derived by this approach is slightly lower than non-interlayer water estimated from SAXS and NMR measurements (Fig. 3-25).

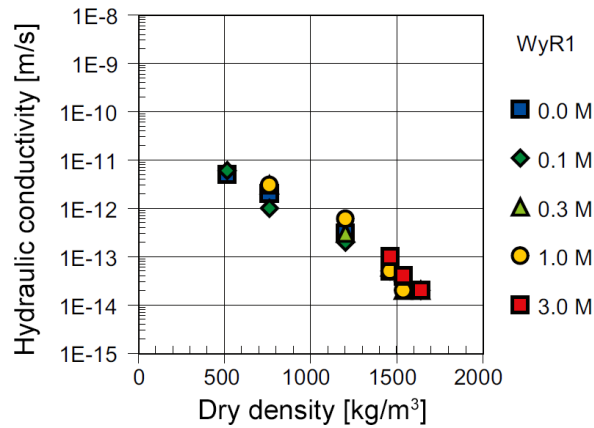


Fig. 3-24: Hydraulic conductivity of MX-80 bentonite at different dry densities
Different symbols refer to different NaCl concentrations of the equilibrating electrolyte.
Karnland et al. (2006)

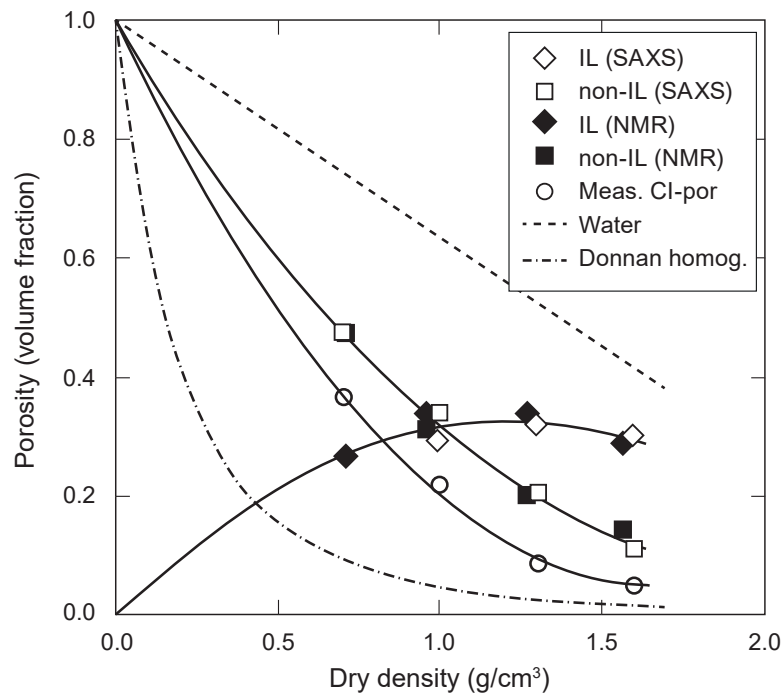


Fig. 3-25: Comparison of different porosity domains estimated from different measurements
Interlayer (IL) and non-interlayer porosities based on SAXS and NMR data, chloride-accessible porosity, total water porosity, and calculated Donnan-only porosity. The solid lines represent mathematical fits of the data.
Muurinen et al. (2013)

It is difficult to summarise the partially contradicting data presented in this section. At dry densities below $1.4 - 1.5 \text{ Mg m}^{-3}$, much evidence exists for the existence of a free porosity domain. Here, a single Donnan porosity concept cannot describe all observed processes (e.g. free swelling). At higher densities, most of the measurements of free porosity volumes are below 4 vol.-% and within the error of the approach. Such low fractions of free porosity are either not interconnected in the case of large pores or occur in pore sizes similar to the interlayer porosity if an interconnected network is assumed (Holmboe et al. 2012). Therefore, the free porosity, if present at all, does not significantly influence transport in high density bentonite. This argument supports the application of the single Donnan porosity concept to high density bentonites.

3.3.6 Conceptual uncertainties of microstructural understanding relevant for the Nagra concept

The main dispute in the literature about microstructure in bentonite concerns the distribution between free and Donnan porosity. Birgersson & Karnland (2009) claim that considering any free porosity is unnecessary to explain transport in bentonite to dry densities as low as 1.2 Mg m^{-3} . In contrast, extensive independent experimental evidence shows that free porosity exists up to at least 1.5 Mg m^{-3} . Ignoring free porosity or Donnan porosity leads to different approaches for interpreting experimental data, or for conducting different reactive transport calculations. Consequently, different porewater chemistries are derived (section 3.4), or different transport properties arise (section 3.5). For much of the existing work, there is a concept-dependence of what appear to be the same properties or parameters.

Several approaches estimating reactive transport in bentonite in a Nagra-type concept use a single-porosity approach with different transport porosities for anions and other species (Bradbury et al. 2014, Kosakowski et al. 2014, Savage 2014). Such approaches do not consider explicit diffusion in the Donnan porosity and assume complete anion exclusion and will predict incorrect transport in materials with variable Donnan porosity and across interfaces where free porosity is present (e.g. in a filter) or clogging occurs (Jenni et al. 2017, see section 3.5). However, single-porosity approaches are practical for constant transport conditions, e.g. prediction of radionuclide transport without simultaneous reactions at interfaces.

3.4 Porewater chemistry

It has been shown in the previous section that, due to the intrinsic properties of montmorillonite, a large part of water in compacted bentonite is located in the interlayer and in the close vicinity of the mineral surfaces. This intimate association between water and clay makes it difficult to extract and analyse the porewater without creating disturbances (Sacchi et al. 2001). Therefore, the derivation of the porewater chemistry relies to a large extent on modelling and on assuming a state of equilibration in experimental work. There are a number of different modelling approaches which have been used to derive porewater chemistry in saturated compacted bentonite and these have evolved over time.

3.4.1 Equilibrium models

"Sorption" models

The classical models put forward more than 20 years ago (Wanner et al. 1994, Wieland et al. 1994, Bradbury & Baeyens 1997, Curti & Wersin 2002, Wersin 2003) accounted for the surface properties and surface reactions at the clay-water interface. They were based on batch experiments

carried out with bentonite suspensions in simple electrolyte solutions. The main reactions considered were (i) dissolution reactions of reactive accessory minerals (e.g. gypsum, calcite), (ii) cation exchange at interlayer sites and (iii) protonation/deprotonation at edge surface sites of the clay (Fig. 3-26). These modelling approaches imply two important assumptions:

- The montmorillonite fraction is assumed to be inert; Si and Al concentrations are constrained by equilibrium with the accessory phases quartz and kaolinite.
- All the water in the pores is assumed to be "free", i.e. electrically balanced, including the interlayer water. In the model of Wanner et al. (1994), the surface charge of the external edge sites is considered for proton exchange reactions, but no explicit electrical double layer composition is calculated.

Two different sorption models with regard to protonation/deprotonation at the clay edge sites were proposed. The model described by Wanner et al. (1994) and Wieland et al. (1994) considers a single amphoteric surface site and a (electrostatic) diffuse layer formulation based on Dzombak & Morel (1990). The other model, proposed by Bradbury & Baeyens (1997, 2003a,b), considers two surface sites (strong and weak sites) and a non-electrostatic surface complexation formulation. Application of these two sub-models for deriving bentonite porewater compositions indicated minor to negligible differences in the results (Wersin 2003, Bradbury et al. 2014, Wersin & Birgersson 2014).

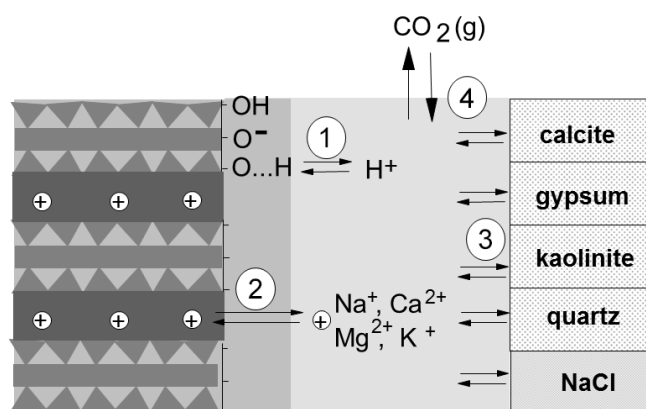


Fig. 3-26: Sketch showing the bentonite–water system and main chemical reactions

(1) protonation/deprotonation of surface hydroxyls, (2) cation exchange, (3) precipitation/dissolution of minor solids, and (4) gas exchange.

Wersin et al. (2004)

The classical models have been refined by distinguishing between different porosity types. The relative proportions of the interlayer water, diffuse double layer water (DDL) and remaining "free" water were estimated based on electrostatic and crystallographic considerations (Wersin et al. 2004, Tournassat & Appelo 2011). These water types are illustrated in Fig. 3-18. The interlayer porosity of a compacted bentonite is derived from the relationship (Tournassat & Appelo 2011, Appelo 2013):

$$\varepsilon_{IL} = \frac{A_{int}}{2} \cdot h_{IL} \cdot w_{mm} \cdot \rho_d \quad (1)$$

where A_{int} (m^2/kg) is the internal surface area of montmorillonite, h_{IL} (m) the interlayer distance, w_{mm} (-) the mass fraction of montmorillonite, and ρ_d the (bulk) dry density (kg m^{-3}). The internal surface area A_{int} depends on the stacking number (n_c) of the montmorillonite stacks, which were taken to be in the range of 5 – 25 (Tournassat & Appelo 2011), based on microscopic observations (e.g. Melkior et al. 2009). The interlayer distance h_{IL} depends on the expansion of montmorillonite in contact with water and is derived from XRD data (Kozaki et al. 1998, Kozaki et al. 2008, Holmboe et al. 2012), and involves 2-3 water layers for the compaction degrees of interest. The DDL porosity induced by the external surface charge of the montmorillonite particles is dependent on the DDL thickness (d_{DDL}) and the external surface area (A_{ext}):

$$\varepsilon_{\text{DDL}} = A_{\text{ext}} \cdot d_{\text{DDL}} \cdot w_{\text{mm}} \cdot \rho_d \quad (2)$$

The parameter d_{DDL} is a function of ionic strength (I), commonly expressed by:

$$d_{\text{DDL}} = \frac{3.09 \cdot 10^{-10}}{\sqrt{I}} f_{\text{DDL}} \quad (3)$$

with f_{DDL} being a multiplier for Debye lengths. This parameter cannot be directly assessed and needs to be estimated using indirect methods (e.g. structural estimates) or considered as a fitting parameter.

The remaining "free" porosity is then:

$$\varepsilon_{\text{free}} = \varepsilon_{\text{tot}} - \varepsilon_{\text{IL}} - \varepsilon_{\text{DDL}} \quad (4)$$

An example of the pore size distribution for a bentonite backfill in contact with two different groundwaters (saline and dilute) for the planned Finnish spent fuel repository is provided in Tab. 3-4 (Wersin et al. 2016). The values were derived from the relationships above.

Once the pore size distribution is derived, the equilibrium modelling is carried out using the same thermodynamic concept as established in the classical models. The main difference in the three-porosity model (e.g. Wersin et al. 2004, Wersin & Birgersson 2014) is that anions are completely excluded from the interlayer where only exchangeable cations may reside. This modelling approach is sometimes referred to as the anion-free interlayer model (Tournassat & Appelo 2011).

More recently, a double porosity model, including a "free" and diffuse double layer, has been advocated (Alt-Epping et al. 2015, Tournassat & Steefel 2015) and applied for solute diffusion through the bentonite backfill (see Chapter 3). It is based on equal electro-chemical potential for each aqueous species in the Donnan and the free porosities. In the model, the interlayer porosity and external DDL porosity are lumped together and considered as DDL, sometimes referred to as Donnan porosity. The pore size distribution for this model type is shown for the Finnish porewater example in Tab. 3-4. In the Donnan space, the negatively charged montmorillonite surface is compensated by a surplus of cations according to the Donnan approximation in which surface potentials and ion concentrations are averaged according to:

$$c_{\text{D},i} = c_{\text{free},i} \exp\left(\frac{-z_i F \psi_{\text{D}}}{RT}\right) \quad (5)$$

where $C_{D,i}$ and $c_{\text{free},i}$ is the concentration of species i in the Donnan space and the "free" solution (mol/L), respectively, z_i is the charge of species i , and ψ_D is the Donnan mean potential. Eq. (5) is theoretically valid only for activities, and not for concentrations (Appelo & Wersin 2007, Tournassat & Steefel 2015). Therefore, eq. (5) assumes equal activity coefficients in Donnan and free porosity, which may not be the case. The sum of ions in the Donnan space counterbalances the surface charge (q):

$$\sum_i z_i c_{D,i} + q = 0 \quad (6)$$

Thus, the Donnan potential is calculated from the condition imposed by eq. (6). The Donnan porosity will also contain surplus electrolyte (anions) in equilibrium with the "free" porewater potentials.

Most recently, this ion partitioning between the two porosity domains was modelled implicitly by diffusion and electrochemical migration (Nernst-Planck equations) between the free porosity and the Donnan porosity, the latter containing immobile anions representing the CEC. The resulting ion compositions of the two equilibrated porosities agree with the concentrations predicted by the Donnan equilibrium, as shown in case studies (Gimmi & Alt-Epping 2018).

Cations located very close to clay sheet surfaces (Stern layer) might behave differently than more distant cations. A fraction of the CEC balanced by the Stern layer can be allocated to surface sites. So far, no experimental data exist constraining this fraction and the selectivity coefficients required for the surface complexation involved. However, explicit consideration of the Stern layer influences modelled solute transport, but equilibration modelling to a lesser extent.

There are two main differences between the three-porosity or anion-free interlayer model (AFI) and the double porosity or Donnan pore space (DS) model (Tournassat & Appelo 2011):

1. The interlayer porosity is devoid of anions in the AFI model, whereas these are present in the DS and defined according to Donnan equilibrium with the external "free" solution.
2. In the AFI model, the negative layer charge is entirely screened by exchangeable cations in the interlayer, whereas in the DS the charge compensation occurs by a surplus of cations in the Donnan space. It is to be noted in the latter models surface charge, screening by both cations in the Donnan and fixed cation exchange complexes can be defined (e.g. Tournassat & Steefel 2015).

Tab. 3-4: Fractions of different porosity types in bentonite backfill for the Olkiluoto case (IL: interlayer; DDL: diffuse double layer, "free") estimated from relationships given in the text for salinity conditions (saline & dilute)

Wersin et al. (2016)

| Modelling approach | Contacting groundwater | % IL | % DDL | % "free" |
|--------------------|------------------------|------|-------|----------|
| AFI | Saline type | 61.1 | 7.7 | 31.2 |
| AFI | Dilute type | 63.1 | 32.6 | 4.3 |
| DS | Saline type | 0 | 78.8 | 31.2 |
| DS | Dilute type | 0 | 95.7 | 4.3 |

AFI: anion-free interlayer; DS: Donnan space

A comparison exercise between the two modelling approaches has recently been carried out (Wersin et al. 2016). This showed only very minor differences in the composition of the "free" water, which was a priori not expected in view of the very different constraints for cations. This "free" water is commonly used as so-called reference porewater to derive radionuclide solubilities and sorption values in safety assessment (Wersin & Schwyn 2004, Altmann 2008, Wersin et al. 2014b). The similar results obtained from the two models with very different assumptions regarding their microstructural properties is reassuring in this context and supports the use of the reference porewater concept. Differences in the model results are obvious in the compartments affected by the surface charge, which reflects the large difference with regard to surface charge screening inherent in the two modelling approaches. This difference is expected to have consequences in transient porewater chemistry evolution as discussed in Wersin et al. (2016).

In the context of solute transport in clay, the question about anion exclusion from interlayers is of great importance: at high densities, where interlayer porosity strongly dominates free porosity, or with precipitations and clogging in the free porosity, anion transport would virtually decrease to zero if anions were completely excluded from the interlayer and diffuse double layer. Several MD simulations addressed this open issue and agree on the presence of Cl^- within interlayers of 9.1 Å thickness (3 water layers) and above. At higher densities, MD simulations show contradictory results (mainly Hedström & Karnland 2012, Hsiao & Hedström 2015 vs. Rotenberg et al. 2007). Tournassat et al. (2016a) compared and partly recalculated the published MD approaches of interest. They conclude that, at a thickness of two water layers, Cl^- does not enter the interlayer in realistic MD simulations. These findings question Gouy-Chapman models, or Poisson-Boltzmann and Donnan approximations frequently used to approximate anion concentrations in the interlayer. In a dual porosity concept (anion transport in the Donnan and free porosity), the minor or zero anion content in the Donnan porosity impacts total transport marginally compared to uncertainties in transport parameters (e.g. tortuosities in the two domains) or the fundamental question about the existence of complete clogging of one domain. In turn, the single Donnan porosity concept (only interlayer porosity) fails to describe the observed anion transport at high densities in the case of complete anion exclusion from the Donnan porosity.

Activities in a dual porosity approach

The few dual porosity concepts described in literature generally assume activity coefficients in the Donnan porosity equal to those in the free porosity. Recently, Birgersson (2017) showed that this assumption leads to significant divergence from an approach where the Donnan equilibrium takes into account activities instead of concentrations. The author denies the presence of a free porosity in bentonite and applies the Donnan equilibrium to the relationship between an external solution and the Donnan porewater. The Stern layer is not explicitly considered but included in the total CEC and the compensating Donnan porewater, making cation exchange or surface complexation obsolete. There is no argument against transferring Birgersson's considerations to the relationship between the Donnan porewater and the internal free porewater, which is in equilibrium with the external solution. Birgersson demonstrated that, in several simple chemical systems, ignoring the activity coefficient calculation in the Donnan porewater leads to an unrealistic ion distribution between the two domains, and certain diffusive transport data also cannot be explained. It is postulated to use the mean salt method for deriving activity coefficients in the Donnan porewater, treating the structural charges in the bentonite as monovalent anions, also entering the ionic strength calculation. The Donnan porewater and the immobile CEC anions are therefore considered as a conventional salt solution. This leads to relatively manageable analytical solutions for Donnan equilibrium concentrations in the case of 1:1, 1:2, and 2:1 salt electrolytes, when minor terms are ignored. Implementation in geochemical codes requires numerical methods. The question remains whether an approach considering activities in the Donnan porewater can predict different fluxes at different ionic strengths of the free porewater (or external

solution as named by Birgersson 2017), as shown by numerous experiments. The recently presented Donnan implementation in the code Flotran (Gimmi & Alt-Epping 2018) can consider different activities in free and Donnan porewater, as also demonstrated in Alt-Epping et al. (2018), and this may be used to further explore such issues.

Solid solution models

This family of models has been used less frequently for deriving porewater compositions in bentonite. Contrary to the "sorption" models described above, the thermodynamics of the main montmorillonite fraction is considered as a multiple end members ideal solid solution (Tardy & Fritz 1981, Tardy et al. 1987, Tardy & Duplay 1992). In that approach, cation exchange reactions have been re-formulated within the framework of ideal solid solutions. These are thus regarded as rapidly reacting solids that continuously change composition (including the structural tetrahedral-octahedral units) as a function of the composition of the contacting solutions. Recently, this approach has been re-assessed and applied to the problem of deriving the porewater composition for the backfill in Nagra's SF/HLW disposal concept (Berner et al. 2013). The results from the solid solution model were compared (Bradbury et al. 2014, Appendix B) with the "sorption" model applied in Curti & Wersin (2002). Only minor differences were found in spite of the strongly differing thermodynamic descriptions.

An important feature of these solid solution models is that the interlayer water is considered to be part of the crystal structure and thus not part of the porosity, in contrast to the models described above. This difference has large implications for the treatment of diffusion and solute transport, as discussed in section 3.3.1. Transport occurs only in the small free porosity fraction, and transport parameters must be adapted to describe experimental data. Further considerations on describing smectites as solid solutions are presented in section 3.4.4.

Modelling smectites as discrete mineral phases

Standard thermodynamic data on montmorillonite describe the pure dehydrated end members containing one type of exchangeable cation and structural water. If cation exchange sites are plugged into such a model phase, the CEC is doubled: dissolution would liberate double the number of exchangeable cations, generating a charge imbalance in the porewater. Furthermore, the degree of montmorillonite hydration influences the thermodynamic properties. If montmorillonite and cation exchange are treated as solid solutions, further end members representing different hydration states might be introduced, based on data available in the literature (Vidal & Dubacq 2009, Vieillard et al. 2011, Tajeddine et al. 2015). This leads to a calculation-intensive multi-end member solid solution, and is normally avoided by selecting the most appropriate hydration state for the system (Berner et al. 2013). However, such concepts considering the Donnan porewater as crystal water cannot describe transport in this porosity.

In an alternative approach, resulting from the dual porosity concept described in section 3.3.1, the montmorillonite hydration water is present as Donnan porosity containing the exchangeable cations. Therefore, the only remaining montmorillonite sub-phase should describe the charged TOT sheets. No thermodynamic descriptions matching this approach have been found in the literature. Ignoring the Al substitution in the octahedral layer and the surface charge, pyrophyllite can be used as a proxy (Jenni & Mäder 2014, Jenni et al. 2017).

3.4.2 Buffering processes

Owing to its intrinsic properties, such as a large CEC, the presence of soluble minerals (e.g. calcite, gypsum) and slow transport despite the high solid/liquid ratio, compacted bentonite has a large buffering capacity. This means that variations in the porewater compositions and ionic strength will be fairly small, even in case of large variations of the external water contacting the clay (Wersin 2003, Bradbury et al. 2014). This particularly holds true for the solutes controlled by cation exchange reactions (total cationic load, although proportions of cations will vary) and dissolution of gypsum and calcite (sulphate, bicarbonate). In addition, the low hydraulic conductivity and the slow diffusive transport (especially of anions) increase the buffering capacity.

Besides buffering with respect to salinity changes, bentonite is an effective pH buffer. This buffering occurs via protonation/deprotonation reactions and dissolution/precipitation of carbonate minerals (mainly calcite). The influence of these reactions on the pH is illustrated by acid-base titration curves. An example is shown in Fig. 3-27 depicting the large acid and base neutralising capacity of compacted bentonite due to these concomitant reactions. At high acid loading when calcite is completely dissolved, significant buffering is still provided by surface protonation reactions.

The solubility of montmorillonite and accessory silicate phases is low over a large pH range (4 – 10). Therefore, the contribution of the silicate fraction under these conditions is expected to be small, although at present not well characterised. The reasons for this are the slow reaction kinetics and the uncertainties related to the thermodynamic and kinetic data for the clay minerals. These characteristics render meaningful experiments for exploring the role of clay mineral dissolution/precipitation on pH buffering at near-neutral pH difficult (section 3.2).

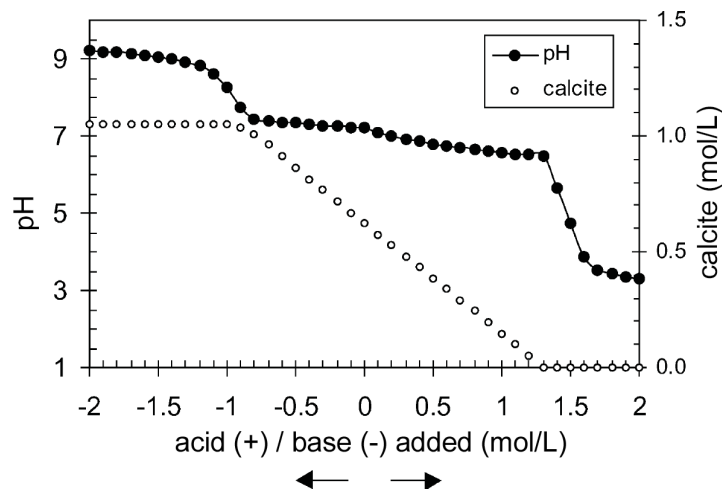


Fig. 3-27: Effect of acid (HCl) and base (NaOH) titration on pH and calcite concentration of compacted bentonite at $p\text{CO}_2 = 10^{-2.2}$ bar

Wersin (2003)

3.4.3 High pH stability

The impact of alkaline leachates released from cementitious components is of concern because it may affect the stability of the clay fraction. At pH values above 10, the dissolution rate of montmorillonite and its solubility are enhanced, parallel to the increased SiO₂ solubility. The increase in dissolution rate of montmorillonite above 10 has been shown experimentally by a number of studies (Cama et al. 2000, Huertas et al. 2006, Rozalen et al. 2008, 2009a, 2009b, Savage & Cloet 2018, Marty et al. 2011). As illustrated by the data of Rozalen et al. (2009b) (Fig. 3-28), the dissolution rates of montmorillonite are enhanced at low and high pH as well as with increased temperature, as is known for many other aluminosilicates.

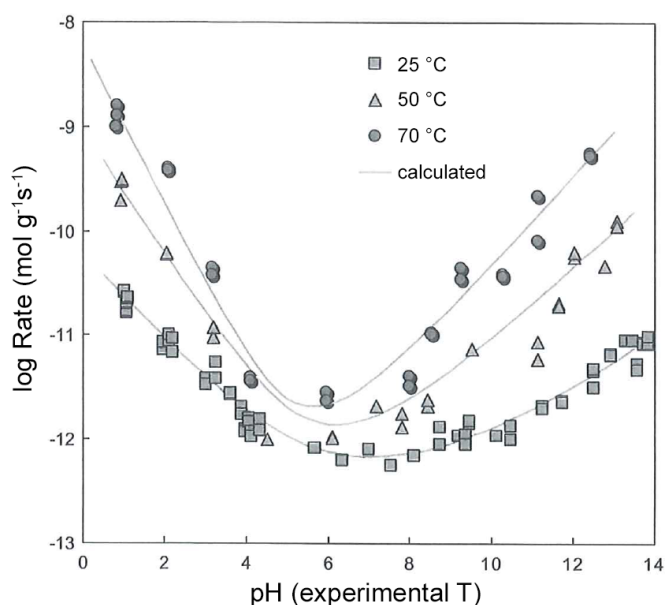


Fig. 3-28: Experimental dissolution rates of K-montmorillonite, normalised to initial mass, and calculated rates

Rozalen et al. (2009b)

It should be noted that these and most other dissolution rate data reflect conditions far from equilibrium, tailored to maximise rates and to inhibit secondary phase precipitation. In fact, incongruent dissolution and secondary phase formation are more common under more realistic conditions. As suggested from experimental evidence (Bouchet et al. 2004, Mosser-Ruck & Cathelineau 2004, Karnland et al. 2007), montmorillonite dissolution in contact with high pH fluids is generally incongruent, leading to an increased Al/Si ratio and an increase in tetrahedral charge and the formation of beidellite. Cation exchange properties are thus modified and, depending on the availability of K⁺, high-charge smectite is further converted to illite (Eberl et al. 1993, Bauer & Velde 1999), which is shown to occur at elevated temperature. However, transformation to zeolites without illite formation has also been observed under alkaline conditions (Fernández et al. 2006), even in the presence of high K⁺ concentrations but at high temperatures of 150 °C.

Dolder (2015) infiltrated bentonite with different cementitious fluids under repository-like conditions (confining pressure, density) at ambient temperature. Apart from gypsum and calcite, mineral reactions occurred only very locally and at slow rates. Data indicate montmorillonite and cristobalite dissolution, and precipitation of saponite and possibly brucite, talc, or a related Mg layered hydroxide.

3.4.4 Thermodynamic considerations regarding smectites

The thermodynamic properties of clay minerals in general have been a debated issue, and large uncertainties still exist (see e.g. Aja & Rosenberg 1996, Essene & Peacor 1995 and references therein, as well as section 3.2). A notable exception is kaolinite, for which well-established solubility data exist. However, for smectites, the chemical equilibrium assumption has been questioned (section 3.2), based both on measurements of solubilities (May et al. 1986) and theoretical arguments (Lippmann 1982).

In addition to fundamental issues mentioned in section 3.2, the complex smectite chemistry complicates a thermodynamic description (Leupin et al. 2015): (1) the mineral displays a large compositional range and does not have a unique stoichiometry, (2) the variable amount of interlayer water may have to be considered in the thermodynamic formulation, and (3) the specific set of ions which compensates the layer charge is variable and controlled by the geochemical environment. Nevertheless, there have been various attempts to describe the thermodynamic properties of smectites. Concerning the structural variability, two types of treatment have been considered: (1) phases with discrete chemical compositions (e.g. Giggenbach 1981, Sass et al. 1987, Rai & Kittrick 1989, Vieillard 2000) and (2) solid solutions (e.g. Lippmann 1977, 1980, Aagaard & Helgeson 1983, Tardy et al. 1987).

Conveniently, the stability of smectites relative to other phyllosilicates is illustrated in stability diagrams. Because adequate thermodynamic data are lacking, idealised compositions (e.g. in the Si-Al-K-H₂O system) have generally been considered. An example of a stability diagram is given by Aagaard & Helgeson (1983) in Fig. 3-29 who applied a solid solution model based on ideal mixing of atoms on homological sites for smectite, illite/smectite mixed layers and illite.

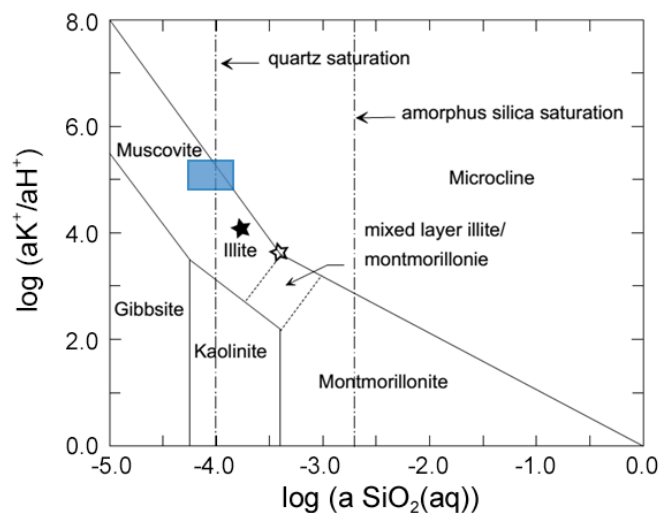


Fig. 3-29: Activity ratio diagram in the Si-Al-K-O-H₂O system at 25 °C

The blue square indicates the range of values for seepage waters at the Mont Terri Rock Laboratory. The filled and unfilled stars indicate representative values for present-day groundwater at Forsmark (Arcos et al. 2006) and Olkiluoto (Birgersson & Wersin 2014), respectively.

Aagaard & Helgeson (1983)

Unfortunately, the usefulness of such diagrams is limited due to the large uncertainty in the underlying thermodynamic constants. This is particularly true for activity diagrams displaying varying Na^+ , K^+ or Ca^{2+} activity since cation exchange reactions are not accounted for (Gaucher et al. 1998). Moreover, the variable hydration state in smectites is commonly ignored, although it is shown to strongly influence thermodynamic properties (Vidal & Dubacq 2009, Dubacq et al. 2010). Notwithstanding the drawbacks of thermodynamic considerations, activity diagrams such as those presented in Fig. 3-29 suggest the importance of SiO_2 , K^+ activities and pH in the stability of montmorillonite. As indicated from the study of marine sediments (Abercrombie et al. 1994), higher Si activity in porewaters stabilises montmorillonite. Low Si and high pH, on the other hand, favour the formation of beidellite and illite. For the latter mineral to form, a sufficiently high K^+ activity is required, and likely high-pH conditions or elevated temperature. Fig. 3-29, which includes representative groundwater compositions at Forsmark and Olkiluoto, shows that the composition of waters with which repository bentonite is expected to interact are typically outside the stability field of montmorillonite. Particularly, the SiO_2 activity of these waters is below the expected stability limit.

3.4.5 Interactions with metal ions

Bentonites contain trace elements and in particular metals in variable concentrations (Vogt & Köster 1978, Curti & Wersin 2002). Bentonites are, in fact, efficient scavengers for metals and thus also for many radionuclides. Interaction of dissolved metals with bentonite and clays in general may involve surface sorption, precipitation/co-precipitation and/or incorporation into the lattice (Charlet & Manceau 1994).

Interactions of metals with bentonite are of interest for safety assessment, primarily because of their role as a sorbent for radionuclides. Therefore, sorption of radioelements (e.g. Cs, Sr, Ni, Eu) to bentonite and montmorillonite surfaces has been extensively studied and documented in the literature. Notably, the research of Bradbury and Baeyens within Nagra's programme has contributed significantly to the understanding of sorption processes (e.g. Baeyens & Bradbury 1997, Bradbury & Baeyens 1997, Bradbury & Baeyens 2003a, Bradbury & Baeyens 2011, Tournassat et al. 2013). It is beyond the scope of this report to dwell on this topic in detail, but a brief summary of the main findings is given: The work of Bradbury and Baeyens and others revealed the importance of two fundamental sorption processes: cation exchange at interlayer sites and surface complexation at amphoteric edge sites of the montmorillonite surface. Whereas the cation exchange process leads to moderate sorption and is strongly dependent on salinity but not on pH, the surface complexation process is strongly dependent on pH but very little dependent on ionic strength and generally leads to strong sorption for the conditions of interest for safety assessment. This behaviour can be fairly well modelled with a simple thermodynamic cation exchange/surface complexation model, which in fact corresponds to the porewater chemistry models described in section 3.4.1.

A further issue is the interaction of corroding metals with the bentonite backfill. This particularly concerns the corrosion of the adjacent carbon steel canister which releases Fe(II) species and hydrogen. The effect of corroding Fe on the integrity of bentonite backfill is an active research field. This topic has been reviewed, for example, by Wersin et al. (2007a) and Bradbury et al. (2014). Recent findings are presented and discussed in section 5.4. Besides carbon steel, Nagra is also considering copper as a coating for steel canisters. Copper released from the corrosion process may also react with bentonite, but the lower anoxic corrosion rate is the main advantage compared to steel. Data on this process are scarcer and are summarised in section 5.5.

3.4.6 Redox conditions

It is commonly assumed that the structural iron in the clay fraction is non-redox-reactive (section 3.1.2). Under these conditions, the redox capacity (i.e. the capacity to reduce or oxidise redox-active species) in most bentonites is fairly low. This is because of the generally low amount of iron-bearing minerals (e.g. iron oxides/hydroxides, pyrite, siderite) and organic matter. On the other hand, in a repository environment, corrosion of metal components and in-diffusion of redox-active species from the reducing host rock will affect redox conditions in the bentonite backfill (Wersin et al. 2003).

Evolution of redox conditions in backfill

After emplacement, the backfill pores will be partially air-filled and thus oxidising. Molecular oxygen will be rapidly consumed by reactions with Fe-bearing minerals in the bentonite, such as pyrite or siderite, corrosion of the adjacent canister metal and diffusion into the host rock (Wersin et al. 2003, Bradbury et al. 2014). Hereafter, the conditions in the buffer will remain reducing. As stated above, redox-active species from the clay host rock (e.g. Fe^{2+} , HS^-) will diffuse into the buffer. Moreover, on the inner side, steel corrosion will release hydrogen and Fe^{2+} . Thus, the buffer porewater will be reducing, but the redox-buffering capacity in the bentonite is limited. Furthermore, microbial activity in compacted bentonite is strongly restricted (Stroes-Gascoyne et al. 2007, Masurat et al. 2010, Pedersen 2010), and thus microbially-mediated redox reactions such as sulphate reduction are negligible.

On the basis of the above considerations, the redox conditions in the bentonite backfill in Nagra's HLW repository concept have been assumed to be controlled by corrosion products (magnetite, green rust) and dissolved Fe(II) (Wersin et al. 2003, Bradbury et al. 2014). The latter species in turn is assumed to be constrained by equilibrium with siderite, present in the OPA host rock (Fig. 3-30). This mineral phase may also occur in minor amounts in bentonite, such as MX-80 (Müller-Vonmoos & Kahr 1983). Hydrogen, produced by steel corrosion, is generally assumed to be non-reactive in the near-field. Experimental data on the interaction of H_2 with clay are scarce and so far not conclusive with regard to redox reactivity. Didier (2012) showed significant H_2 sorption on dry synthetic montmorillonite at temperatures of 90 and 110 °C. Furthermore, it was shown that a minor part of the structural Fe was reduced during this interaction process. Experiments performed under saturated conditions showed less H_2 sorption and were not conclusive with regard to Fe(III) reduction (Didier 2012). Pyrite, an accessory mineral, reacts with H_2 to form pyrrhotite at high temperatures and H_2 partial pressures (Truche et al. 2009, Truche et al. 2010). Under more repository-relevant conditions, such a reaction appears to be unlikely according to the data of Truche et al. (2013), except at $p\text{H}_2 > 10$ bar and $T > 90$ °C. In summary, hydrogen is not expected to react to any large extent with mineral phases in the bentonite backfill, although uncertainties on this issue persist. In contrast, H_2 will be strongly redox-active after canister breaching and reaction with spent fuel (not discussed in this report).

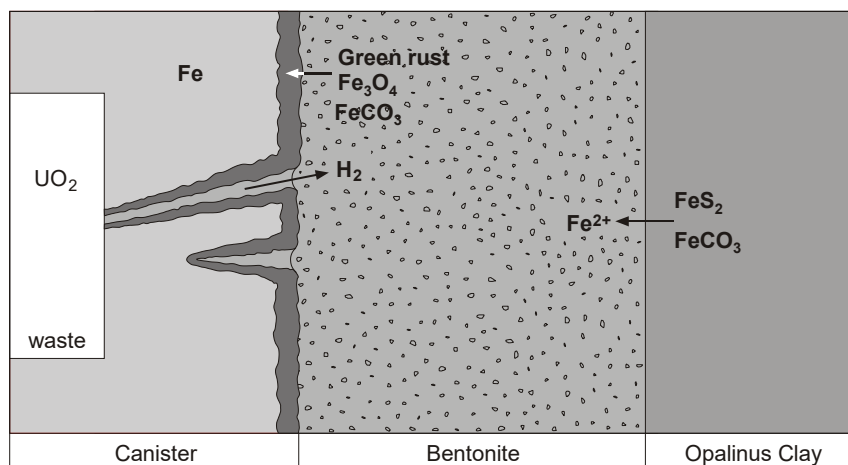


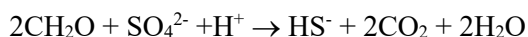
Fig. 3-30: Major redox-reactive phases in the EBS of the SF/HLW repository (not to scale)
Wersin et al. (2003)

Influence of microbial sulphate reduction in the EDZ

Hydrogen, on the other hand, may be reactive in the adjacent EDZ if this zone contains sufficiently large secondary porosity to enable microbial activity and if this secondary porosity remains accessible for a long enough time period. In a such a scenario, hydrogen may be used as an electron donor to reduce sulphate (Vinsot et al. 2014a):



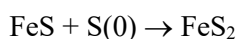
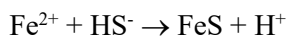
Alternatively, organic carbon released from the bentonite and/or from the clay host rock (e.g. low-molecular weight organic acids) may be degraded by the sulphate reduction process:



where " CH_2O " is used as a proxy for dissolvable organic matter.

The microbial sulphate reduction process in the EDZ may be favoured by dissolution of gypsum present in the backfill and out-diffusion of sulphate (Wersin & Birgersson 2014, Wersin et al. 2016).

The produced sulphide will then react with Fe(II) released from the rock to precipitate FeS and FeS_2 :



These reactions were observed, for example, in a borehole at the Mont Terri Rock Laboratory, albeit under conditions not representative of a repository environment (Stroes-Gascoyne et al. 2011, Wersin et al. 2011b).

Reactivity of structural Fe

The above considerations are based on the assumption that structural Fe(III) in smectite is non-reactive. Support is provided by observations in natural bentonites and claystones formed in reducing environments, where iron in smectites occurs predominantly in the Fe³⁺ form. Strong chemical reductants, such as dithionite, or an induced electrical current are generally required to experimentally reduce structural Fe(III) (section 3.1.2). It should be noted, however, that recent data from Latta et al. (2017) suggest that, under specific conditions, considerable reduction of structural Fe(III) by dissolved Fe(II) can occur.

From the extensive electrochemical work outlined in section 3.1.2, Hofstetter et al. (2014) could derive redox properties of smectite minerals. They concluded that "structural Fe can in fact buffer the Eh over an enormous potential range", which was explained by the structural modifications induced during the reduction/oxidation process of their experiments. These structural modifications were found to be large for high-Fe smectite (nontronite), but these were not observed in the case of montmorillonite. The discrepancy between the large apparent redox buffering (*cf.* Fig. 3-8) and the absence of structural modification could not be resolved. On a more general level, it remains unclear to what extent the electrochemical data can be applied to bentonite clay under repository conditions. Based on observations from natural environments, it appears that the redox reactivity of structural Fe is restricted by kinetic constraints.

3.4.7 Conceptual uncertainties of porewater chemistry relevant for the Nagra concept

Modelling bentonite porewater with a single free porosity in combination with cation exchange cannot explain numerous transport measurements (Gimmi & Kosakowski 2011). The recommended Donnan equilibrium describes the relationship between the interlayer/clay surface water composition (water in the "Donnan porosity") and the bulk-type water far from the clay particles ("free water") with sufficient accuracy. Several studies disagree about the presence of free water within MX-80 of 1,500 Mg m⁻³ and apply the Donnan equilibrium to the entire clay porewater and an external solution. This leads to a slightly lower anion content compared to approaches that consider free porewater within the clay (equal to the external solution at equilibrium), which is in Donnan equilibrium with the Donnan water in the clay. At high densities and low free porosity, the disagreement between the porewaters predicted from the two concepts is small, especially keeping in mind that the rigorous Donnan equilibrium is based on activities and not on concentrations and uses a mean potential approximation to the Poisson-Boltzmann equation, which adds another conceptual uncertainty.

Consideration of activities in the clay porewater is relevant for many processes (Birgersson 2017), e.g. different CECs measured for cations of the same valence cannot be explained with the Donnan equilibrium based on concentrations instead of activities. Keeping in mind the overwhelming volume of the Donnan porosity, its porewater might contact reactive surfaces in the repository (e.g. the canister surface). In the context of corrosion, activities and, strongly connected, pH are of great relevance. Therefore, the activity coefficients in the Donnan water should not be set equal to the coefficients in the free porosity, which is a common practice. But it is as yet unclear how activities can be derived, especially how the contribution of the charged surface is considered.

The Donnan equilibrium predicts an average Donnan porewater composition, which is close to the integration of the Poisson-Boltzmann ion distribution. The gap between the canister surface and the montmorillonite grain surface is expected to be at least half an interlayer distance (see section 3.3.3). The chemistry predicted at this location by Poisson-Boltzmann (see section 3.3.4)

is closer to the free water composition compared to the average Donnan chemistry. Thus, the common practice of using free water activities for any phase reaction modelling does not seem unreasonable. Very likely, reactive surfaces are even further apart from montmorillonite due to geometrical reasons (section 3.3.3).

The multi-porosity model approaches require volumes for each porosity fraction. The calculations presented above are based on a linear relationship between the Donnan porosity fraction and Debye length. This very simplified assumption still requires a multiplier, which is often taken from measurements. However, direct measurements of porosity fractions in clay are scarce and inaccurate, and indirect derivations involve large uncertainties and conceptual assumptions. Such uncertainties propagate to porewater compositions and, to a larger extent, to transport modelling. This adds another uncertainty in the timing of reactions between different materials in the near-field, generally connected via porosity.

Reactivity of structural iron in montmorillonite, e.g. in a reducing porewater, appears to be restricted by kinetic constraints. Observations are scarce, and reduction of structural iron under repository conditions could not be shown beyond doubt.

3.5 Solute transport properties

3.5.1 Advection

Despite the high water content of bentonite, its hydraulic conductivity can be extremely low (as low as 5×10^{-14} m/s for 1.5 Mg m^{-3} dry density and strongly decreasing towards higher density (Karlund et al. 2006, Fig. 3-24). Most simulations of advective transport in bentonite assume that the Darcy law is valid. Liu (2014) postulates very large threshold hydraulic gradients ($I > 10^4$ m/m) for very low-permeability rocks (Fig. 3-31). The hydraulic gradient threshold I refers to the intersection between the hydraulic gradient axis (zero water flux) and the linear part of the hydraulic gradient – water flux relationship. Below this threshold, the behaviour is non-linear towards zero. The few data points at lowest permeability are all from compacted bentonite, where accurate measurement is non-trivial.

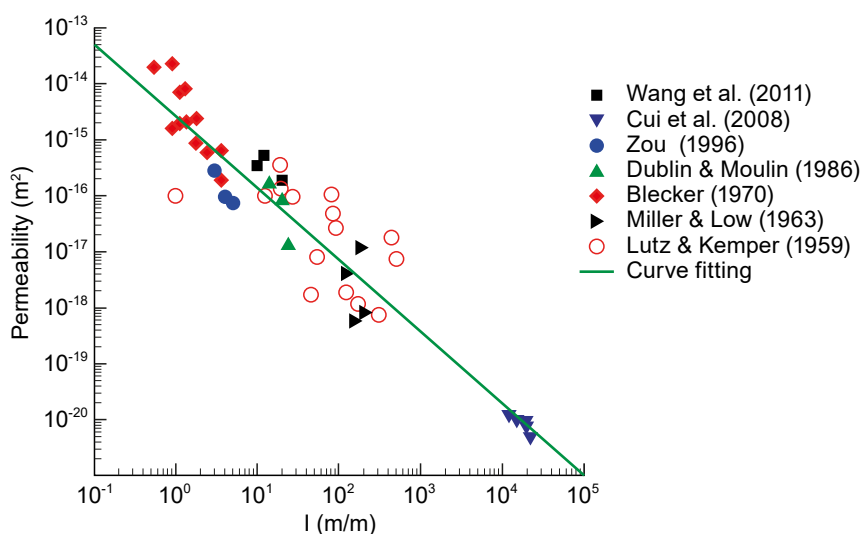


Fig. 3-31: Correlation between permeability and threshold hydraulic gradient (I)
After Liu (2014) and references therein

Non-reactive negatively charged and neutral species show different breakthrough curves in advection-dominated transport through bentonite (Fig. 3-32). This can be explained by the presence of a Donnan porosity with (very) low anion concentration, where advection is supposedly negligible. Because Donnan equilibrium predicts equal concentrations of neutral species in Donnan and free porewater, a water tracer such as deuterium is retarded in the Donnan porosity. Transport modelling following this dual porosity concept (Alt-Epping et al. 2015) can explain the experimental data of Jenni et al. (2014a, Fig. 3-32).

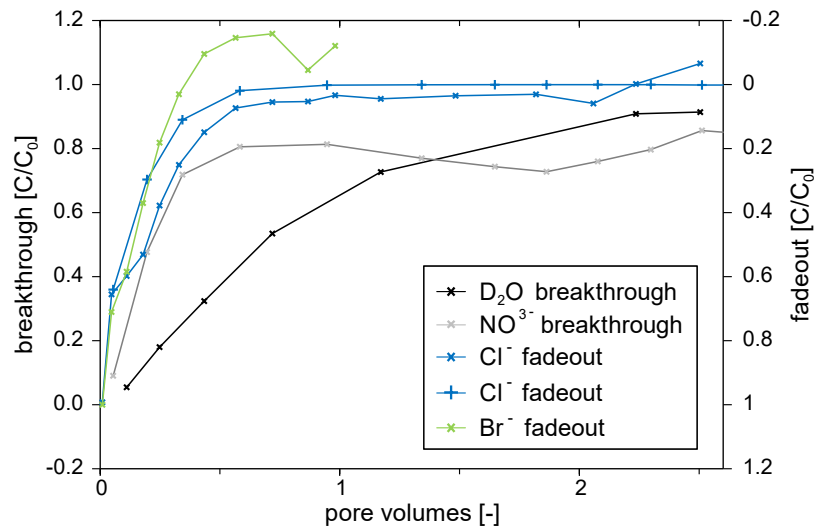


Fig. 3-32: Breakthrough curves of different non-reactive anions and deuterium

Breakout (right axis) applies to Cl⁻ shown as + signs.

Jenni et al. (2014a)

In a repository concept with a bentonite buffer, advection occurs during bentonite saturation. Apart from many THM processes, mineral dissolution/precipitation in the bentonite (and in the surrounding material, depending on its nature) influences advection. The situation at the interface can be mimicked with advective infiltration of an external porewater into a saturated bentonite core at lab-scale. In the case of cementitious porewater infiltration, mineral precipitation occurs and hydraulic conductivity drops (Dolder 2015). Although precipitates have been found in the filter, pore clogging in the bentonite also contributes to the decrease in hydraulic conductivity (Fig. 3-33). The decreasing hydraulic conductivity during OPA porewater infiltration is attributed to the compaction of the core (-1 vol.-% for left, -4 vol.-% for right graphs) under a confining pressure higher than during saturation (before day zero).

Bentonites equilibrated with different ionic strength electrolytes and with different cation occupancies have different hydraulic conductivities. This can be explained with different pore size distributions of the different bentonites (see section 3.8). In the case of a single porosity (interlayer-only) approach under constant volume and water content, interlayer distance must be constant. In this case, the response of advection to porewater composition might be explained by an interplay of the charged clay surfaces, the ions in solution, and the polar water molecules. The resulting effect on the flow might differ at different solute composition. However, there is no literature on this topic.

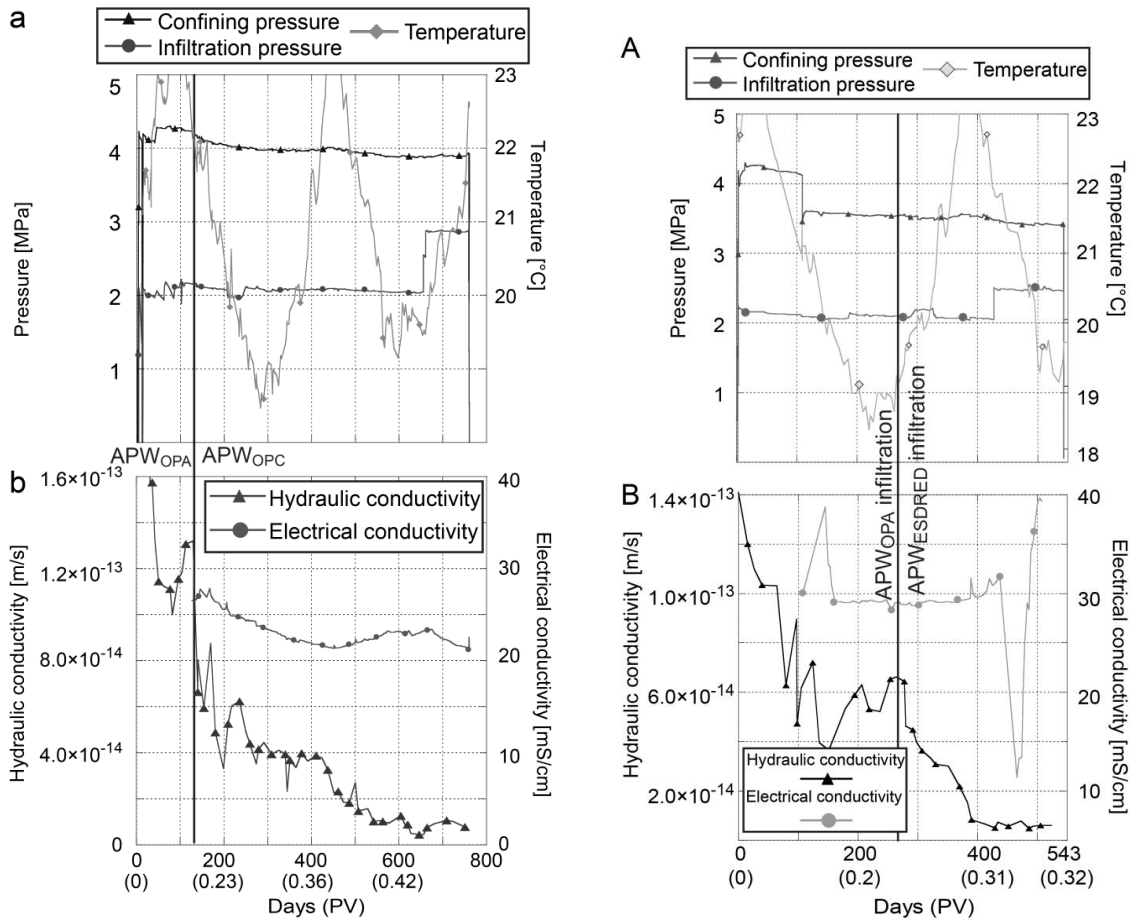


Fig. 3-33: Hydraulic conductivity during infiltration of an artificial OPA porewater (APW_{OPA}) followed by a Portland cement porewater (APW_{OPC}, left) or a low-pH cement porewater (APW_{ESDRED}, right) through an MX-80 core

X-axes show time and number of pore volumes in parentheses.

Dolder (2015)

3.5.2 Diffusion

Numerous diffusion experiments through bentonite or montmorillonite result in different diffusion coefficients for different species. Tournassat & Steefel (2015) conclude, based on a wide range of literature data cited therein, that: $(D_e/D_0)_{\text{Cs}^+} > (D_e/D_0)_{\text{Na}^+} > (D_e/D_0)_{\text{HTO}} > (D_e/D_0)_{\text{I}^-}$, D_e and D_0 being the effective and self-diffusion coefficient, respectively. Such observations clearly indicate that the classic Fickian diffusion theory, where independent diffusion of different species is considered, does not hold for swelling clays. As pointed out by Birgersson (2017), D_e calculated from steady-state fluxes across bentonite and externally imposed concentration differences are assumed to quantify diffusion only in a general way. But the D_e dependence on external concentrations is complex: Glaus et al. (2013) describe a set-up where the classic diffusion approach applied to clay fails, because electrostatics substantially change ion concentrations in the clay compared to the concentrations in the external reservoirs (Fig. 3-34). However, the numerous available experimental diffusion data are very valuable, as long as not only the calculated D_e is given, but also the underlying species fluxes. Bourg & Tournassat (2015) review and compile diffusion data for water tracers, anions and cations in bentonite and clay rock.

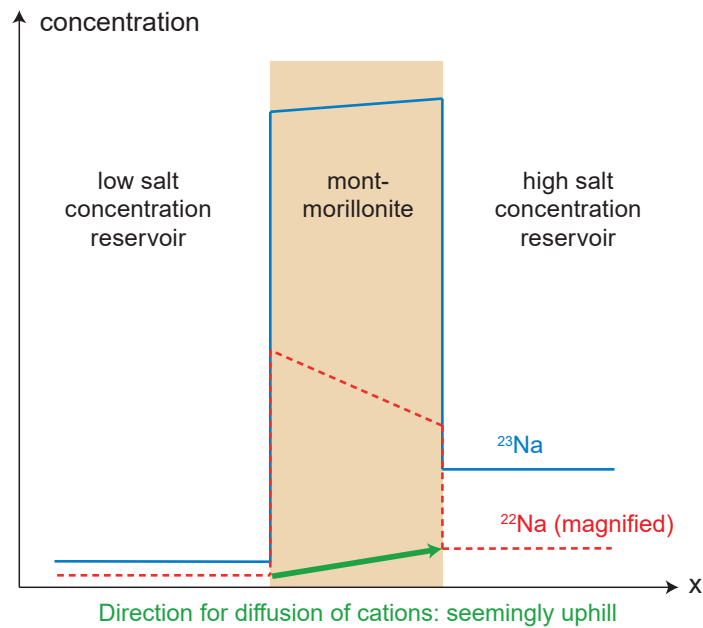


Fig. 3-34: Schematic of an experimental diffusion set-up resulting in seemingly uphill diffusion Concentrations across external solution reservoir – clay – external solution reservoir (x-axis). Glaus et al. (2013)

Wallis et al. (2016) described the fast equilibration of a mixed Ca- and Na-bentonite set-up (ABM1, Äspö, Sweden) with classic Fickian diffusion in a single, charge-balanced porosity (free porosity) combined with cation exchange, and attributed the resulting high diffusion coefficients to the elevated temperature in this experiment. Even though the concept seems too simple or incorrect for bentonite (e.g. total bentonite porosity of 0.47 available for anion diffusion), they could fit the experimental data (also introducing inhomogeneous boundary conditions), because other effects such as solid phase reactions were negligible. Fast equilibration of Na and Ca within the clay can be attributed to surface diffusion of sorbed cations according to the terminology of Gimmi & Kosakowski (2011), or similarly to diffusion of cations in the Donnan porosity (following the definition in section 3.3.1), but the two concepts are not completely equivalent.

The Donnan-porosity-only concept assumes that the entire species transport occurs in the Donnan porosity. It can describe the ABM1 cation equilibration and other phenomena in high density bentonite set-ups (e.g. Glaus et al. 2013), but some specific adjustments of species diffusion coefficients or tortuosities may be required. The single Donnan porosity model is applicable to high density bentonite, because the free porosity fraction is insignificant compared to the dominating Donnan porosity, in agreement with observations (section 3.3.5). Also, it is often only possible to fit the data, but not to predict them based on independently estimated parameters. The single Donnan porosity approach is challenged in the case of systems with lower densities and fails in the case of dispersions in clay rocks and when mineral reactions occur. Here, the explicit consideration of diffusion and phase reactions in the free porosity, including subsequent porosity changes, is inevitable to explain many observations (e.g. Navarro et al. 2014, Chagneau et al. 2015, Navarro et al. 2015, Idiart & Pekala 2016, Jenni et al. 2017). Estimating parameters independently for this more complex approach remains of course an issue.

The relationship between diffusion and porosity plays a key role in the numerical description of diffusive transport in clay. Conceptually, it can be written as (e.g. Flury & Gimmi 2002):

$$D_e = G n D_0 \quad (7)$$

with D_e being the effective diffusion coefficient, D_0 the diffusion coefficient in free water, n the porosity, and G the geometric factor that includes constrictivity and tortuosity effects. In the case of clays, n is the porosity accessible for the specific species (Tinnacher et al. 2016, where G is defined reciprocally). G is material-dependent, but often assumed to be constant for different non-reactive tracers. It varies for different bentonite densities or porosities (or, more generally, for different bentonite microstructures).

Very often, Archie's relation is used to relate D_e/D_0 directly to n (Boving & Grathwohl 2001, after Archie 1942):

$$D_e = n^m D_0 \quad (8)$$

with m being an empirical factor. Van Loon et al. (2007) could satisfactorily fit their own and literature Cl^- diffusion data for different bentonite densities with this equation ($m = 1.9$, Fig. 3-35). Glaus et al. (2010) found a similar relationship for both HTO and Cl^- in Na-montmorillonite with $m = 1.81$, but interpreted D_0 as a fitting parameter (9.8×10^{-11} for both tracers). The calculation of the diffusion-accessible porosity was done based on the $^{36}\text{Cl}^-$ inventory (post-mortem analysis), assuming complete anion exclusion in the remaining porosity. The free/Donnan porosity (as defined in section 3.3.1) can be calculated from the same measurements assuming only partial anion exclusion from the Donnan porosity (anion content defined by the Donnan equilibrium). The resulting free porosity is smaller than the diffusion-active (or anion-accessible) porosity. The free/Donnan porosity is expected to be closer to the porosities estimated geometrically from XRD interlayer distances multiplied by the montmorillonite specific surface area (Holmboe et al. 2012).

In CrunchFlowMC, and in Jenni et al. (2017), two Fickian diffusion transport paths are used in the free and Donnan porosity, whose chemical compositions are in Donnan equilibrium (Fig. 3-36c). During the diffusive transport of a species according to the external concentration gradient (Fig. 3-36a), it can access both porosities (Fig. 3-36b).

A D_e - n relationship is used for the diffusive fluxes in both free and Donnan porosity independently in Jenni et al. (2017). This requires different parameters G_{free} , G_{Donnan} or m_{free} , m_{Donnan} (eq. 7 or 8). The sum of the two fluxes allows calculation of an overall D_e , which can be compared with values derived with a classical diffusion model from experimental data. Applying this concept to diffusion data of different species available in the literature (done in a similar way by Van Loon et al. (2007) for Cl^- assuming an anion-free Donnan porosity) might shed light on the nature of the D_e - n relationship, and, if a single parameter G or m can describe the transport of all species, in one porosity domain.

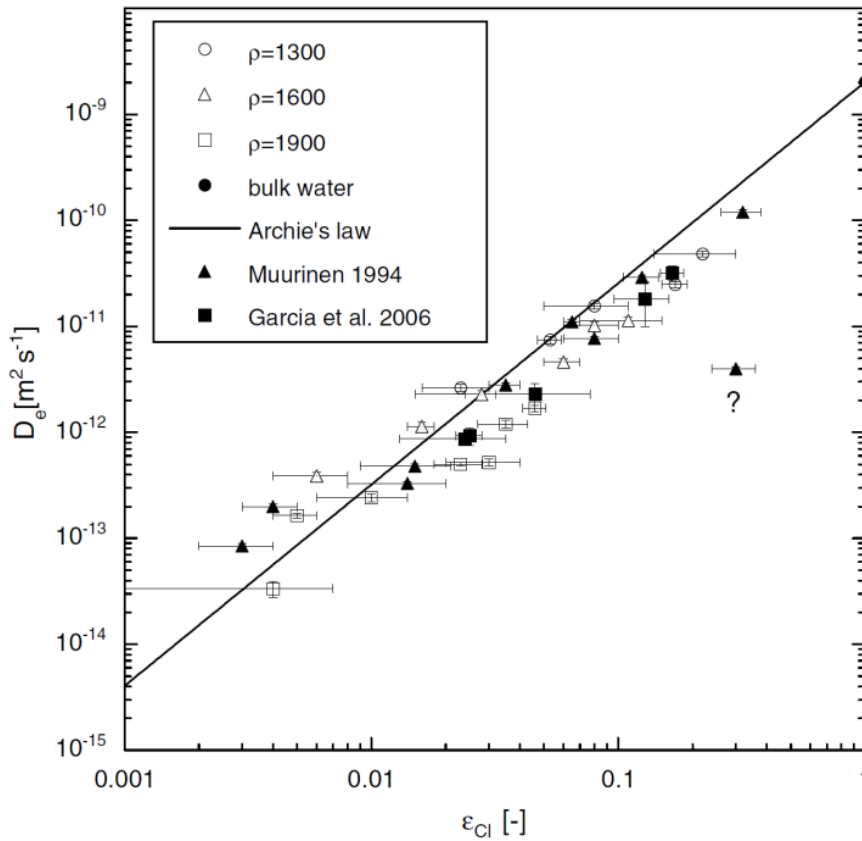


Fig. 3-35: Effective diffusion coefficient of ³⁶Cl⁻ in compacted bentonite as a function of the diffusion-accessible porosity
 Van Loon et al. (2007)

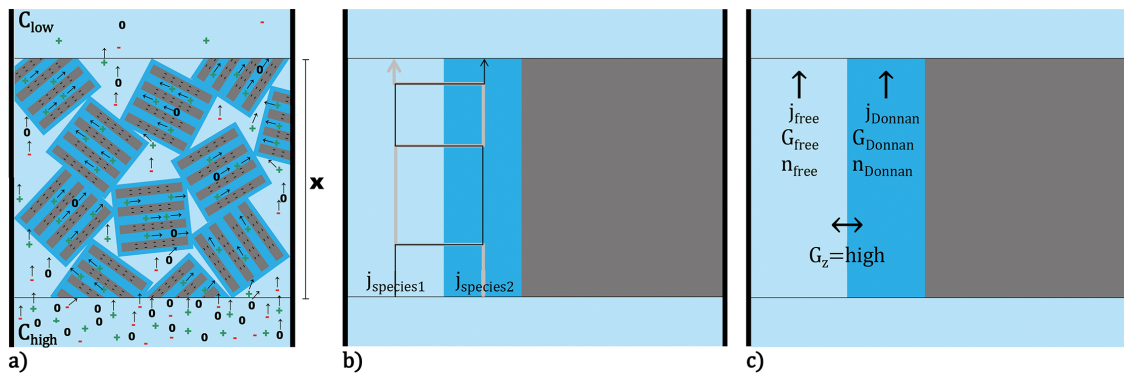


Fig. 3-36: Sketches of different species moving through a monomineralic claystone

Free porosity shown in light blue, Donnan porosity in dark blue, clay sheets within clay particles in grey. a) Arrows indicate movements of neutral species (0), cations (+), and anions (-) from a high ionic strength (bottom) to a low ionic strength reservoir (top). b) Diffusion- and electromigration-controlled transport paths of two species. If a species changes from free into Donnan porosity, other species have to compensate for this change following the equilibrium relationships between the two domains. These domain changes are considered as instantaneous. c) Diffusive transport can be treated as two parallel fluxes in two separate porosity domains, which are in chemical and electrostatic equilibrium. The fluxes j depend on the corresponding geometric factors G and the porosities n (linear D_e - n relationship).

Jenni et al. (2017)

At interfaces between clay represented as either a double-porosity medium or single-porosity medium (e.g. filters, crystalline host rock), the connectivity between the different domains on the two sides is unclear, due to the lack of physical evidence. Different possible scenarios are described in Tournassat & Steefel (2015), and numerical solutions for modelling exist (Jenni et al. 2017). The latter split the single porosity proportionally into free and Donnan porosity in the clay and connect the free porosity with the appropriate part of the single porosity, and the Donnan porosity with the other part of the single porosity.

Similarly to advective transport, diffusion is different in bentonites equilibrated with different ionic strength electrolytes and with different cation occupancies. This can be related to the double layer characteristics that are dependent on the composition of the equilibrium solution, which may lead to different pore size distributions of the different bentonites (see section 3.8).

3.5.3 Conceptual uncertainties of transport in bentonite relevant for the Nagra concept

Pore size distribution governs both advective and diffusive transport. Therefore, the uncertainties described in section 3.3.1 propagate to the transport calculations, and lead to conceptually different understandings of transport in bentonite.

Literature evaluation in this and the two preceding sections suggests that only a multi-porosity conceptual model can explain all experimental data on transport in bentonite. Transport or equilibrium codes that can handle multi- (or at least dual-) porosity transport are still under development. Basic transport properties within the different porosities are not well constrained; it is difficult or even impossible to derive all necessary parameters independently at present. Bourg & Tournassat (2015) suggest that "Future studies should focus particularly on determining the mobility of water and ions as a function of distance from clay mineral surfaces..." and consider the pore scale structure important for understanding density or ionic strength effects on diffusion. Pioneering reactive dual-porosity transport models for bentonite partially assume hypothetical transport properties (e.g. D_e - n relationship with geometric factors of 1 for free (G_{free}) and 0.001 for Donnan porosity (G_{Donnan}) in Fernández et al. 2014b, and in Alt-Epping et al. 2015). In a first stage, available literature data on diffusion of different species through bentonite should be used in order to better consolidate the transport parameters. Data on diffusion under different ionic strengths or for different cation occupancies are scarce.

In the dual-porosity approach, advection in the Donnan porosity of clay is commonly ignored (Kosakowski & Berner 2013, Alt-Epping et al. 2015), without any direct experimental proof. But at high dry densities with free porosities expected to be below 5 % (section 3.3.5), the interconnection of the free porosity becomes more unlikely and advection must occur in the Donnan porosity. This remains to be shown, because if different aqueous species are expected to move in the interlayer, water molecules should also be mobile. Birgersson & Karnland (2009) model water transport in the interlayer (which is not described in detail in their publication).

Saturation of initially undersaturated bentonite is based on advective two-phase flow and is commonly explained and modelled with THM approaches. However, chemical issues such as pore clogging can substantially influence the saturation, especially at reactive interfaces (e.g. skin formation between cement – bentonite). The underlying conceptual model can again strongly influence the prediction of transport mechanisms. If clogging occurs only in the free porosity of the bentonite, the Donnan porosity remains open, but its permeability is still under debate. However, after full saturation of the bentonite buffer in the repository (hydraulic steady-state, Fig. 2-4), advective transport is negligible. It is still unclear at this moment when and if full saturation is achieved.

3.6 Conceptual understanding of gas transport in bentonite

Various gases may be produced in both the HLW and L/ILW repositories, principally as a result of the corrosion of metals and (microbial) degradation of organic matter (Diomidis et al. 2016). Gases will be dissolved in the porewater and eventually, when the solubility limit is exceeded, a separate phase may form. The principal impacts of gas are expected to be increased pore pressures and thus changes in effective stress in the compacted bentonite. Effects on the integrity of compacted bentonite may involve a change in the pore structure by the creation of gas release pathways (impact on pore size distribution by increasing the fraction of macropores) and the expulsion of porewater from the bentonite into the host rock (e.g. Romero & Gonzales-Blanco 2017 and 2018). Thus, compacted bentonite in SF/HLW emplacement drifts is expected to transport gas from the canisters to the rock via discrete pathways. However, limited impacts are expected on the performance of the bentonite as a diffusive barrier for solutes, because the fraction of macropores remains limited as compared to the meso- and micropores (see definition of pore sizes in Nagra 2002c). Furthermore, the plasticity of bentonite may result in pathways sealing once gas pressure decreases (Shaw 2014).

The complexity of the coupled THMC processes associated with gas transport in bentonite gives rise to a multitude of phenomena, which seem hard to predict by means of existing numerical simulation tools (see also section 4.5). For these phenomena, Nagra has launched a research initiative within SKB's Task Force on Engineered Barriers, aimed at modelling gas transport processes in bentonite (Dieudonne et al. 2017). The modelling benchmark and the associated experimental programme (Romero & Gonzales-Blanco 2017 and 2018) give emphasis to a number of phenomena and processes, which have not received major attention in previous research programmes, even though they are of potential significance for long-term safety as they could exhibit adverse effects on the performance of a bentonite-based EBS:

- The procedure applied for compaction of the bentonite specimen together with the actual wetting path during bentonite saturation shows an impact on the aggregation of the bentonite particles and on the pore network, which may affect the percolation process during subsequent gas invasion events (breakthrough pressure/percolation threshold, fragmentation/spreading of gas path). Undesired modifications of the bentonite density and swelling pressure by the presence of a "residual" gas phase in the bentonite cannot be excluded;
- Long-term percolation of gas through the bentonite may be associated with the creation of preferential transport paths for gas and radionuclides, and chemical alteration of the bentonite (incl. Fe-bentonite interactions, impacts such as ex-solution, biochemical processes) by excessive gas pressures. Undesired modifications of the bentonite density, swelling pressure and chemical retention capacity along the preferential gas pathways in the bentonite cannot be excluded;
- The mobilisation of bentonite aggregates (colloids) by gas invasion may affect the micro-fabric and the macroscopic properties of the buffer material on the long term. It is likely that such colloidal processes are controlled by the breakthrough conditions downstream. Undesired modifications of the bentonite density, swelling pressure and hydraulic conductivity as a result of long-term mobilisation of bentonite particles over 10,000s of years cannot be excluded.

The assessment of the relevance of the aforementioned phenomena and development of adequate process models for these hydro-mechanical and chemical couplings is being carried out as part of a new research initiative within the framework of the EURATOM WP2018 call ("Mechanistic understanding of gas transport in clay materials").

The anaerobic corrosion of metals in the near-field produces hydrogen. Hydrogen could react with montmorillonite and reduce ferric iron in octahedral sites (Libert et al. 2011), thus increasing the surface charge in the clay and thereby potentially reducing the swelling pressure and increasing the hydraulic conductivity of the buffer (section 3.1.1). However, Didier et al. (2012) showed that hydrogen is not likely to affect the clay properties under repository-like conditions (section 3.4.6).

3.7 THM properties

It is well known that the mechanical response (e.g. deformation, swelling pressure) of bentonite is affected by environmental factors such as changes in humidity, temperature and porewater composition. This section summarises some of the experimentally observed coupled phenomena such as the influence of temperature on water retention and mechanical response, the changes in microstructure due to a hydration process and the shear strength under different environmental conditions.

3.7.1 Saturation of granular bentonite under non-isothermal conditions

The influence of temperature on the hydration process has been analysed under constant-volume conditions up to 40 °C, using a specially designed cell, named Micro-cell (see Seiphoori et al. 2014 for a detailed description of the experimental procedure). The water retention curves of MX-80 granular bentonite at a void ratio of $e = 0.83$ were determined for two temperatures of 22 °C and 40 °C (Fig. 3-37). The influence of temperature in this range was found to be negligible. The cell containing the granular bentonite was kept in a temperature-controlled, humid chamber at 40 °C and, after each step of the wetting and drying cycle, the total suction was measured using a chilled-mirror psychrometer device (WP4C).

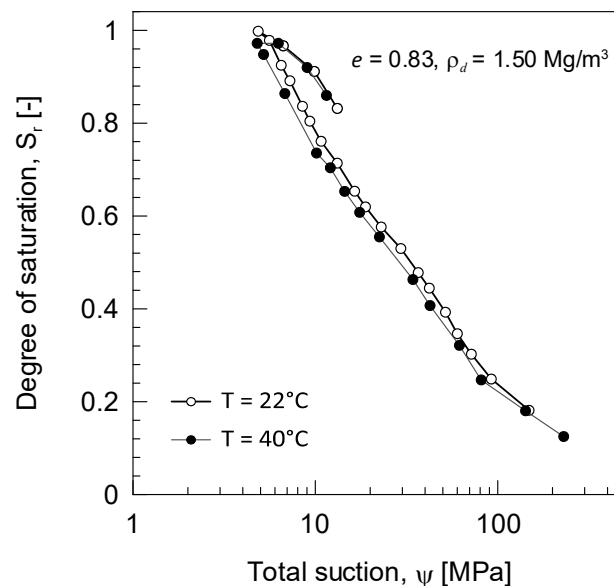


Fig. 3-37: Water retention behaviour determined at temperatures of 22 °C and 40 °C
Seiphoori (2016)

In order to determine the retention curve of the material at higher temperatures, a sorption bench device was used (Salager et al. 2011). The Micro-cell was used in combination with the sorption bench to apply a constant volume condition to the material during the experiment. Fig. 3-38 shows

the general scheme of the sorption bench system. The system enables testing of several samples at eight different suction-controlled desiccators to impose a certain relative humidity at a given temperature. The relative humidity values were controlled using saturated salt solutions inside the desiccators. The desiccators were immersed in a controlled temperature bath. A precision balance is located on the top of the frame, allowing continued weighting of the hanging samples without disturbing the system. Tab. 3-5 lists the different salt solutions used in this study to determine the water retention curve of bentonite at 80 °C.

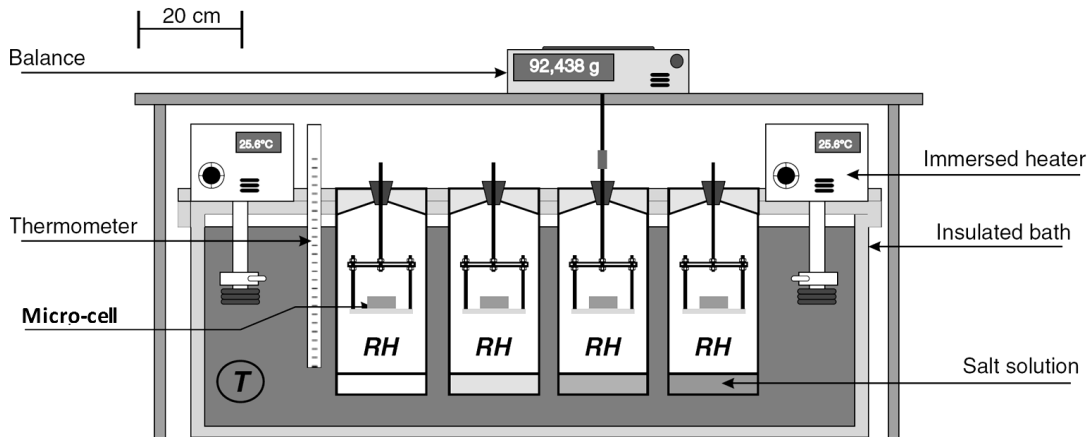


Fig. 3-38: Schematic cross-section of the sorption bench
Salager et al. (2011)

Tab. 3-5: Relative humidity and total suction values resulting from saturated and partially saturated salt solutions
Romero (2001)

| | Salt | Compound | a [%] | b [K] | RH [80° C] | ψ [80° C] |
|---|--------------------|-----------------------------------|-------|-------|------------|-----------|
| 1 | Lithium Chloride | LiCl | 14.53 | -75 | 0.117 | 349.31 |
| 2 | Magnesium Chloride | MgCl ₂ | 29.26 | 34 | 0.322 | 184.77 |
| 3 | Magnesium Nitrate | Mg(NO ₃) ₂ | 25.28 | 220 | 0.471 | 122.70 |
| 4 | Potassium Iodide | KI | 29.35 | 254 | 0.603 | 82.65 |
| 5 | Sodium Chloride | NaCl | 69.2 | 25 | 0.743 | 48.51 |
| 6 | Potassium Chloride | KCl | 49.38 | 159 | 0.775 | 41.66 |
| 7 | Potassium Sulphate | K ₂ SO ₄ | 86.75 | 34 | 0.955 | 7.48 |

The dependence of relative humidity on temperature is expressed with $RH = a \exp(b/T)$, where a and b are tabulated parameters (Tab. 3-5; Romero 2001). Total suction values ψ were calculated using:

$$\psi = -\frac{\rho_w RT}{M_w} \ln(RH)$$

where R is the universal gas constant, ρ_w is water density, M_w is the molecular mass of water, RH is the relative humidity and T is absolute temperature.

In order to determine the water adsorption at this temperature, a Micro-cell containing a sample of granular bentonite with $e = 0.83$ was first rested in desiccator number 2 to perform a wetting path. After the material reached an equilibrium state, the Micro-cell was moved to the next desiccator with lower suction, (see Tab. 3-5).

The evolution of the degree of saturation of the sample with respect to time is depicted in Fig. 3-39. When the material reached the maximum attainable degree of saturation, a drying path was initiated by moving the Micro-cell to desiccators with higher total suction. The water retention curve obtained at 80°C is compared with the one at 22°C in Fig. 3-40.

In Fig. 3-40b, the retention behaviour in terms of the degree of saturation was plotted along the whole drying path at 80°C , whereas this was not possible for the curve at 22°C . In fact, the sample can reach a fully saturated state at the lower temperature. This way, the sample would experience a shrinkage followed by the loss of lateral contact in the drying path, hence the degree of saturation cannot be determined. This was not the case for the sample at 80°C where the contact with the cell was maintained during the test duration.

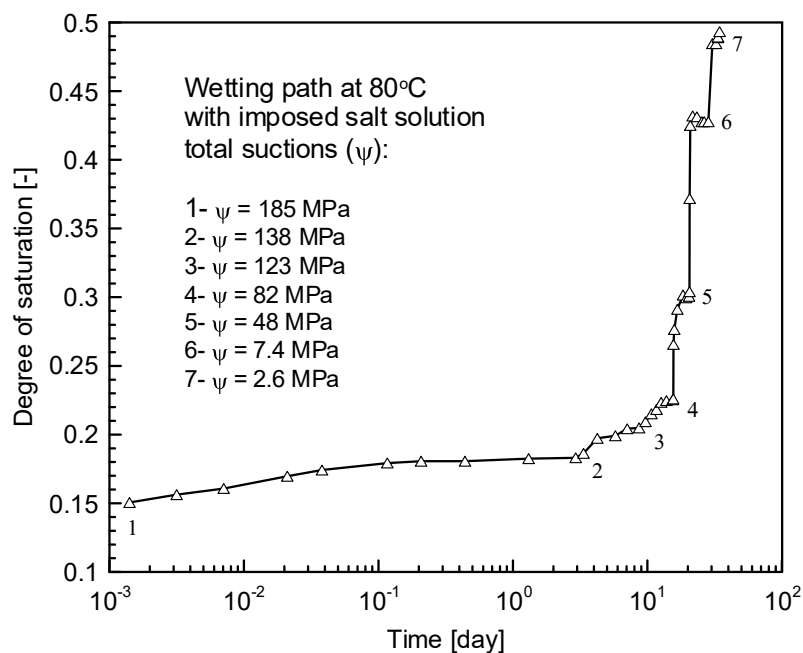


Fig. 3-39: Evolution of degree of saturation of the sample inside the Micro-cell in a sorption bench at $T = 80^\circ\text{C}$

Seiphoori (2016)

As seen in Fig. 3-40, the retention capacity of the material was decreased by around 50 % when increasing the temperature from 22°C to 80°C . Villar & Lloret (2004) and Villar et al. (2010) also observed a decrease in retention capacity due to a temperature increase from suction-controlled cells for FEBEX bentonite (Fig. 3-41). This decrease in retention properties is commonly attributed to the loss of hydration capacity of the smectite mineral (e.g. Pusch & Yong 2014).

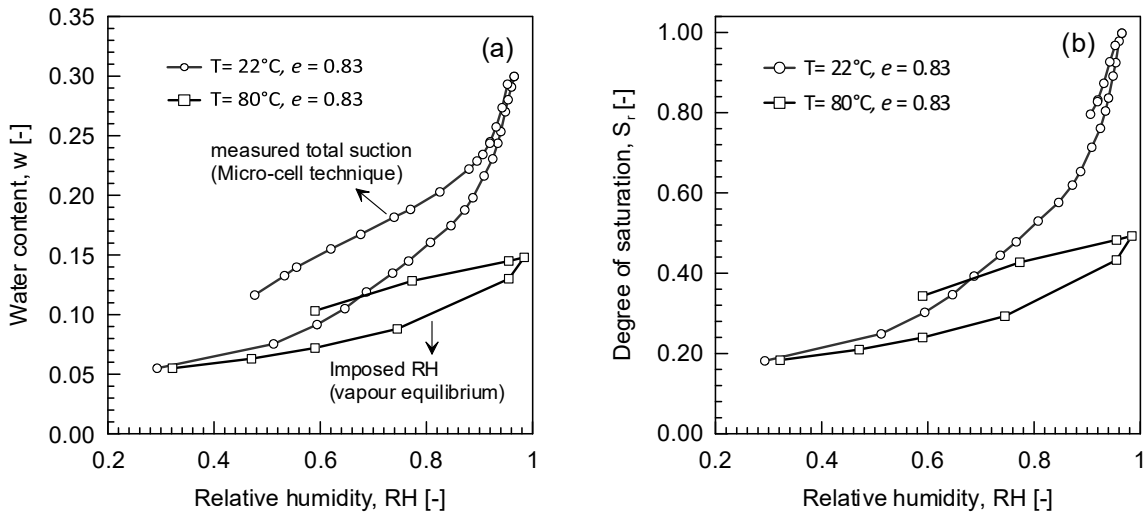


Fig. 3-40: Influence of temperature on the retention behaviour of bentonite combining Micro-cell and sorption bench

From Seiphoori (2016)

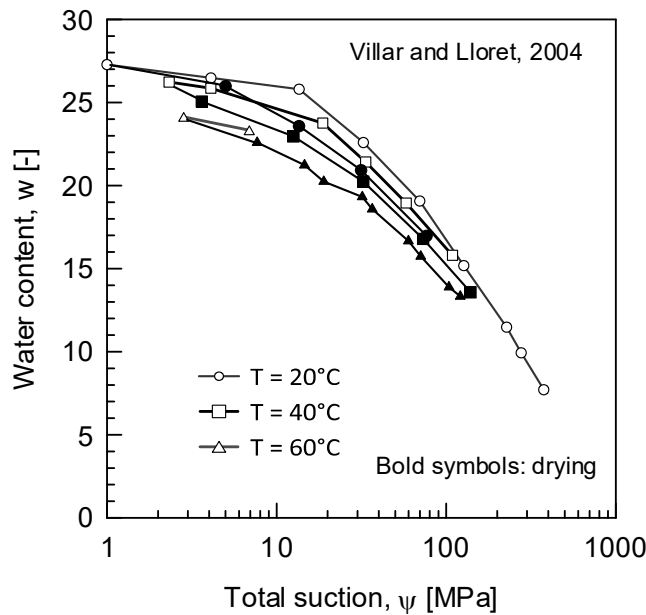


Fig. 3-41: Influence of temperature on the water retention behaviour of FEBEX bentonite with a dry density of 1.65 Mg m^{-3}

Seiphoori (2016), after Villar & Lloret (2004)

3.7.2 Bentonite homogenisation: microstructural insight

Seiphoori et al. (2014) reported microstructural features of granular samples of compacted MX-80 bentonite. These were investigated combining MIP analysis and SEM observations. All specimens for these analyses were prepared at the same water content of 5%.

For preparing each specimen, different grain size fractions were selected and mixed in order to always obtain the same apparent grain size distribution. Specimens were prepared at different void ratios. The highest void ratio, which is attainable by simply pouring the material with the selected grain size distribution, is 0.83 (corresponding to a dry density $\rho_d = 1.50 \text{ Mg m}^{-3}$). Specimens with lower void ratios were obtained by static compaction to $e = 0.66$ ($\rho_d = 1.65 \text{ Mg m}^{-3}$) and $e = 0.53$ ($\rho_d = 1.80 \text{ Mg m}^{-3}$).

In Fig. 3-42, the pore size diameter (PSD) of the material in the poured state ($e = 0.83$) and compacted state ($e = 0.53$) are compared along with the PSD function of a single grain. It is seen that the grain presents a single mode porosity with modal value $d = 12 \text{ nm}$; the PSD of the single grain would suggest that there is no inter-aggregate porosity within the grains; in contrast, this inter-aggregate porosity was reported by Hoffmann et al. (2007) for bentonite pellets. This difference is easily explained by considering the difference in production between pellets and the granular bentonite. In particular, they are both prepared from powder, but the lower water content used for the production of pellets facilitates the formation of aggregates (Pusch 1992). From Fig. 3-42, the different PSD function suggest that an indicative pore size diameter of 50 nm can be selected as the maximum intra-grain pore diameter.

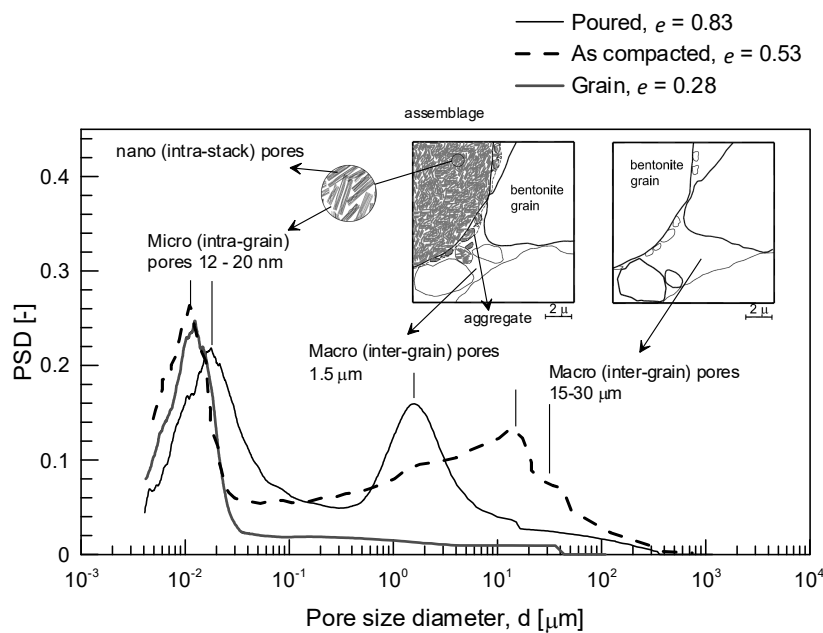


Fig. 3-42: Different microstructural levels in poured and compacted MX-80 granular bentonite
Seiphoori (2016)

The poured material exhibits a well-distributed pore size dimension (Fig. 3-43); the peak corresponding to the intra-grain porosity is still well visible. Dominant pores with mode value in the range of 15 – 30 μm represent inter-grain pores; the pores with diameters between the modal value for the intra- and the inter-grain porosity are associated with pores within assemblages created during the specimen preparation and constituted by the finest fraction and the smaller inter-grain pores.

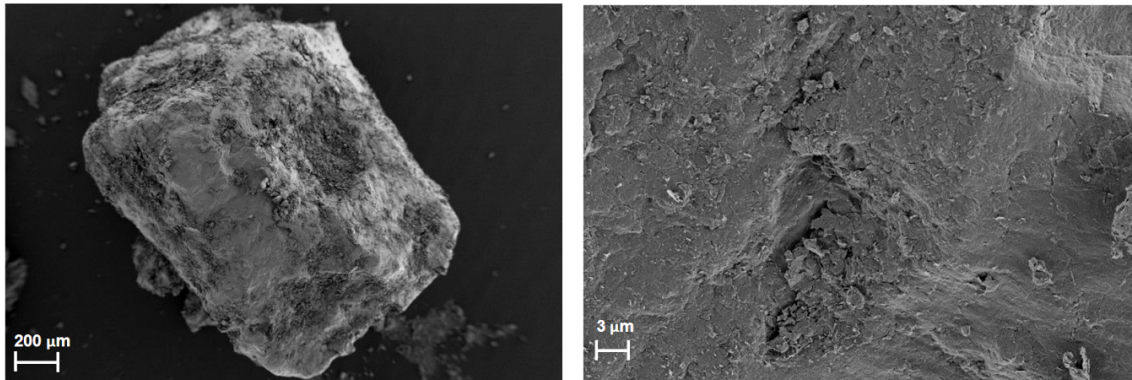


Fig. 3-43: SEM photographs of MX-80 grains with $e = 0.28$ ($\rho_d = 2.13 \text{ Mg m}^{-3}$)

From Seiphoori et al. (2014)

Seiphoori et al. (2014) observed that the compacted specimen presented a clear bimodal distribution. Pores with characteristic diameters in the range of $300 \text{ nm} - 400 \text{ μm}$ were clearly detected. The modal value of this family of pores is directly related to the compaction effort and was measured at $d = 1.5 \text{ μm}$ for $e = 0.53$ (Fig. 3-42) and at $d = 15 \text{ μm}$ for $e = 0.83$. The modal value for the peak observed for the lower pore dimension is situated at $d = 20 \text{ nm}$ and the characteristic diameters for these pores are in the range of $d < 300 \text{ nm}$. In this range, the compacted granular bentonite shows a wider distribution of pore diameters with respect to the single grain. Interestingly, within this peak, a local maximum can be recognised for the diameter corresponding to the modal value of the grain PSD ($d = 12 \text{ nm}$).

SEM photomicrographs help to understand the increased range for these pores. Fig. 3-44a and b show an overview of the compacted material ($e = 0.53$). Grains are well visible as distinct units; they are mostly coated by aggregates composed of the finer clay particles; these aggregates fully occupy the inter-grain space (Fig. 3-44c). Fig. 3-44d shows a photomicrograph of the material in another close-up with clear pores of the frequency size of 1.5 μm within the bentonite aggregates. The micropores are defined here as pores between bentonite particles within grains and aggregates. Inter-particle porosity within bentonite aggregates seems to prevail with respect to the inter-particle porosity within the grains (Fig. 3-42).

To study the microstructural features and their evolution along the wetting and drying paths, Seiphoori et al. (2014) performed a series of MIP and SEM tests on specimens at different steps of the retention analysis. Both analyses require dry specimens; to preserve the structural features due to dehydration, freeze-drying was carried out by immersing the Micro-cell containing the specimen directly in liquid nitrogen (boiling point -196 °C) in order to instantaneously freeze the microstructure and the specimen and subsequent sublimation under applied vacuum (0.06 mbar) to eliminate the frozen porewater at a controlled temperature of -52 °C . This feature of the Micro-cell allows freezing the structure at a given swelling pressure, reached during the hydraulic path, and avoids porosity changes due to stress release upon opening of the cell; this feature is particularly of interest for fully saturated specimens that may reach very high swelling pressures. MIP and SEM tests were carried out at different stages of the hydraulic path depicted in Fig. 3-45. Since MIP is a destructive technique, several specimens were prepared at the same initial conditions ($e = 0.53$, $w_0 = 0.05$) and used in this investigation which followed the same wetting and drying history until the conditions were reached for an MIP test.

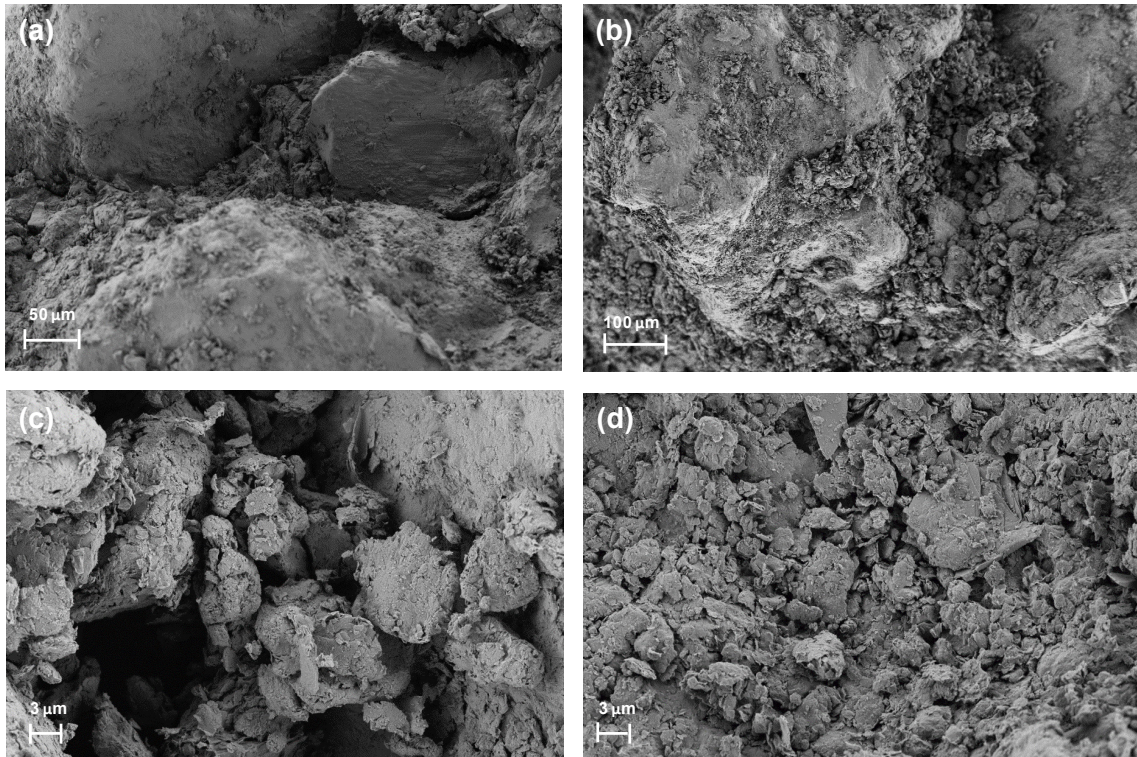


Fig. 3-44: SEM photomicrographs of MX-80 granular bentonite in a compacted state with $e = 0.53$ ($\rho_d = 1.80 \text{ Mg m}^{-3}$); (a),(b) bentonite grains coated by aggregates composing the assemblages; (c),(d) bentonite aggregate arranged in inter-assembly space
Seiphoori et al. (2014)

Freeze-drying removes virtually all water from the montmorillonite interlayers, which have to shrink accordingly. At the densities described here, the major fraction of water is located in the interlayers. At constant outer volume of the sample, freeze-drying must therefore lead to structural changes within the sample, as observed by Keller et al. (2014) and as already reasoned in section 3.3.5. It is therefore not possible to use MIP to quantify pore sizes. Furthermore, mercury does not intrude into the interlayer porosity, which is often seen as part of the nanostructural porosity. It is therefore not assessed by this method, as illustrated in Fig. 3-46b and Fig. 3-47b: The MIP cumulative void ratios go down to $4 \times 10^{-3} \mu\text{m}$ pore size diameter, where cumulative void ratios of 0.3 – 0.45 (porosity of 0.23 – 0.31) are reached. The difference between these values and total porosity (known from sample preparation, shown as dashed horizontal line) cannot represent interlayer porosity, because this porosity mostly collapsed during drying. Most likely, the porosity below $4 \times 10^{-3} \mu\text{m}$ represents drying artefacts, which open up to compensate the shrinking interlayers during drying (intra-stack porosity). For these same reasons, qualitative interpretation of SEM micrographs of dried material can also be misleading. However, careful comparison of MIP data might reveal systematic changes during homogenisation of bentonite, which are described below.

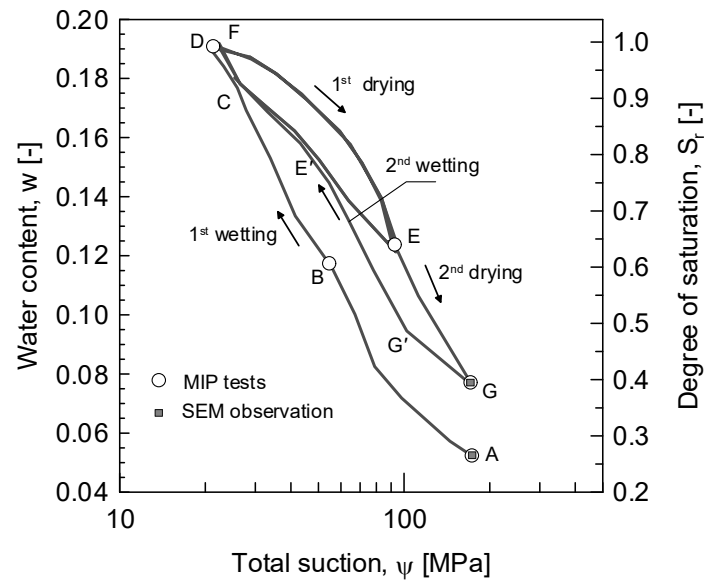


Fig. 3-45: Hysteresis water retention curve of highly compacted MX-80 granular bentonite
Seiphoori et al. (2014)

Fig. 3-46a shows the hydration states on the main wetting path for which MIP tests were performed, while Fig. 3-46b and c present the corresponding cumulative void ratio (intruded void ratio by mercury) and the PSD, respectively. The compacted state (A) exhibits a clear bimodal pore size distribution; two peaks with modal values of approximately 20 nm and 1.5 μm are observed. Pores with sizes in the range of 1.5 μm denote the inter-bentonite assemblage pores which constitute the macropores. For granular bentonite, as mentioned above, the bentonite grains and the coating aggregates form bentonite assemblages. The peak at 20 nm is generally observed in compacted granular bentonites and is associated with intra-grain porosity and intra-aggregates (micropores). The PSD function at Point B, where the bentonite specimen has reached a degree of saturation of 0.62, shows a decrease in the volume of macropores without a change in the modal value with respect to the initial state (Point A); micropores exhibit negligible change. The cumulative void-ratio curve and the PSD function of the material in a fully saturated condition (plot D in Fig. 3-46b and c) indicate a significant reduction of the macropores due to the further hydration of the bentonite assemblages. The micropore cumulative volume and PSD value at the peak were also increased for Point D. The total porosity measured by MIP decreases from A to D, which indicates an increase in intra-stack porosity (compensating interlayer shrinkage during drying), not assessed by the method (total porosity must remain constant). This again suggests an increase in interlayer porosity with ongoing homogenisation.

The states of the material during the drying path for which microstructural analyses were done are shown in Fig. 3-47a. Fig. 3-47b and c present the cumulative void ratio and the PSD functions, respectively. The PSD function at Point E, when the specimen has reached a degree of saturation of 0.64, exhibits a single pore size distribution similar to that obtained at full saturation (Point D). The cumulative void ratio of Point E remains almost identical to that obtained at Point D. This observation indicates a similar structure for the material at Points D and E.

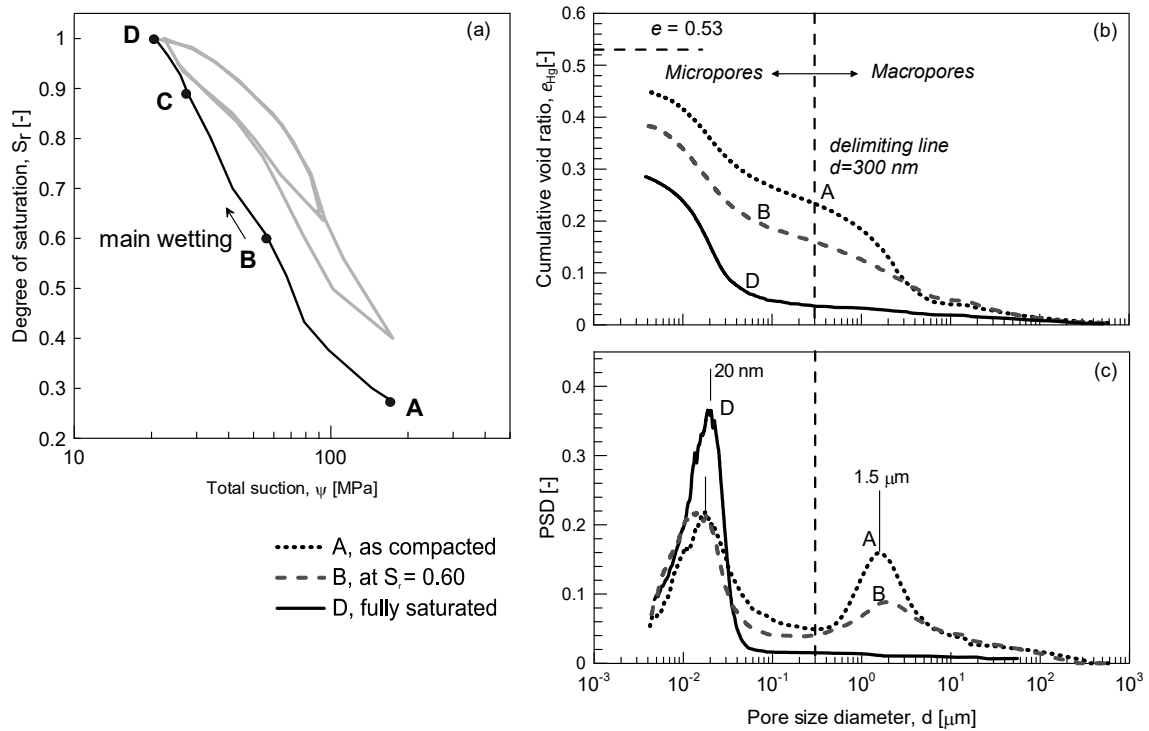


Fig. 3-46: Microstructural evolutions during wetting paths based on the results of the MIP Seiphoori et al. (2014)

Point G (Fig. 3-47a) describes the state at the end of the last drying path after wetting and drying cycles. Fig. 3-47c shows that the material at Point G still exhibits a single-porosity structure which is analogous to those obtained at points D and E. However, a slight increase in the intruded volume can be seen as presented in Fig. 3-47b. In Fig. 3-48, SEM photomicrographs of the bentonite sample at Point G are presented. As seen in Fig. 3-48a, the bentonite grains are still detectable, while the aggregates have expanded with respect to the compacted state of the material. A further observation at the inter-assemblage space (Fig. 3-48c) shows that the expanded aggregates are now filling the macropores and form a more homogeneous structure. Apparently, this structural modification occurs due to smectite hydration and it becomes permanent when the material approaches a fully saturated state (Point D), without recovering its initial state during the next wetting and drying cycles.

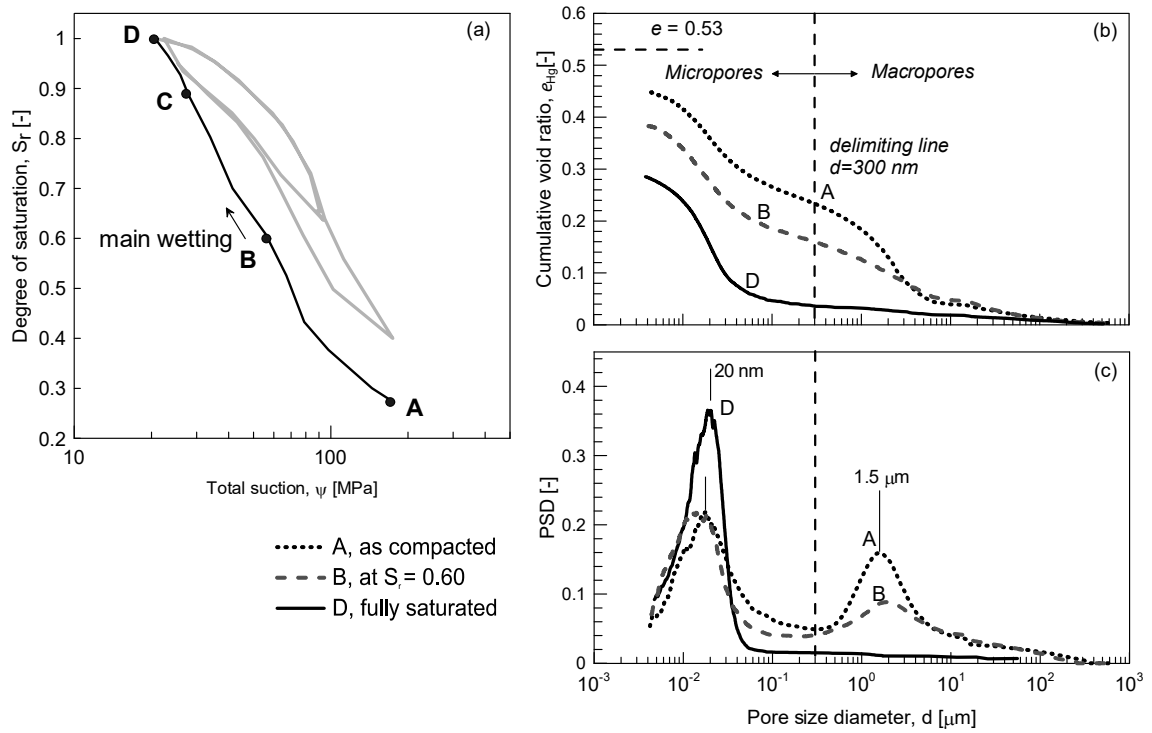


Fig. 3-47: Microstructural evolutions during drying paths based on the results of the MIP
Seiphoori et al. (2014)

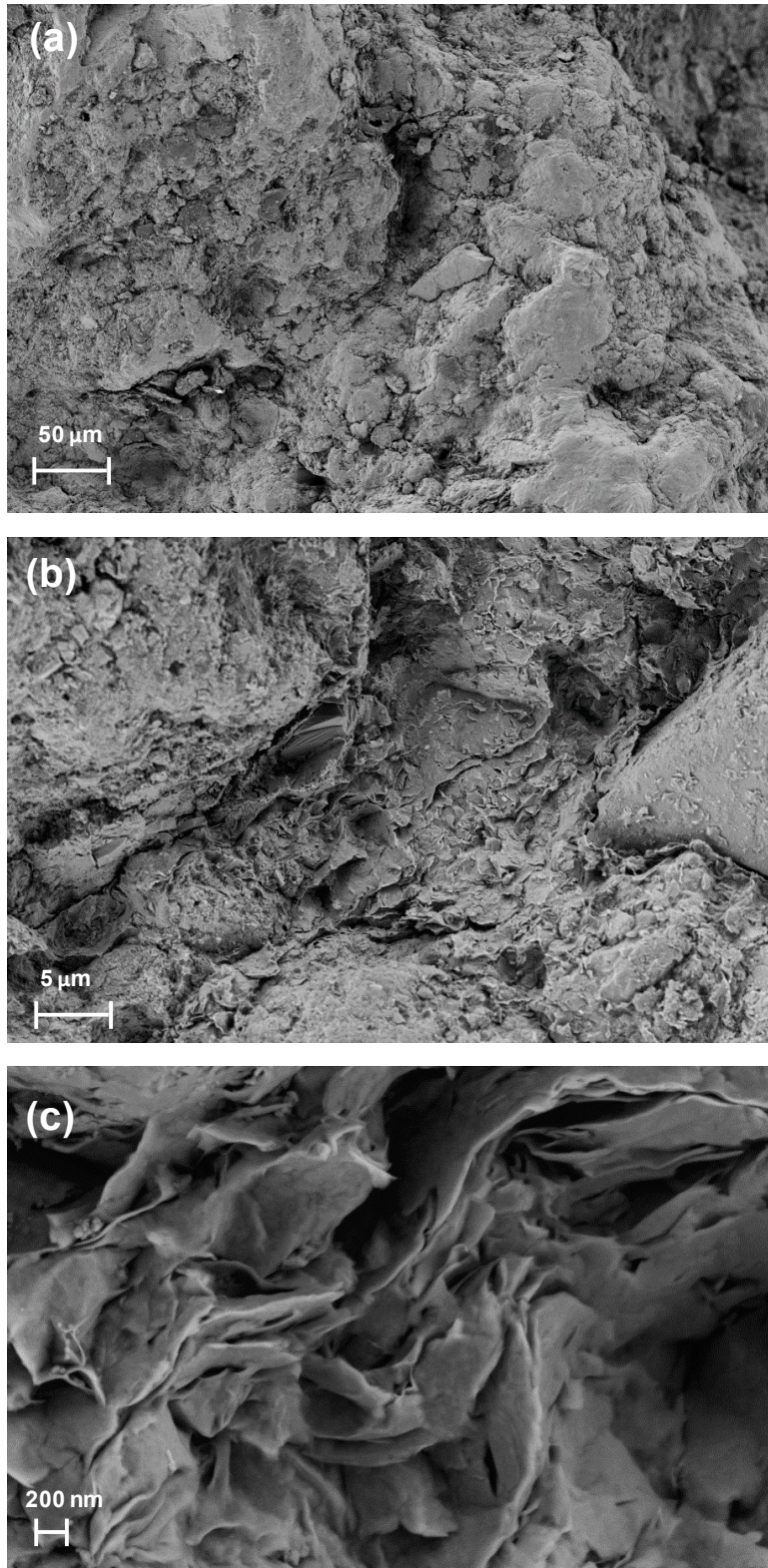


Fig. 3-48: SEM micrographs of MX-80 granular bentonite after wetting-drying cycle corresponding to Point G in Fig. 3-47

Seiphoori et al. (2014)

3.7.3 Hydration mechanisms

In smectite minerals, the hydration is governed by the progressive placement of water molecule layers along the surface of the elementary smectite platelets, initiating from one layer in dry conditions and reaching a maximum of four layers for very low suctions (Saiyouri et al. 1998, Bestel 2014). Saiyouri et al. (1998) analysed the hydration mechanism of the smectite particles in compacted MX-80 bentonite wetted in an unconfined condition using the X-ray diffraction technique. The evolution of the average interlayer distance, the corresponding interlayer water, and the number of elementary sheets per smectite particle were described as a function of the total suction (Fig. 3-49a and b).

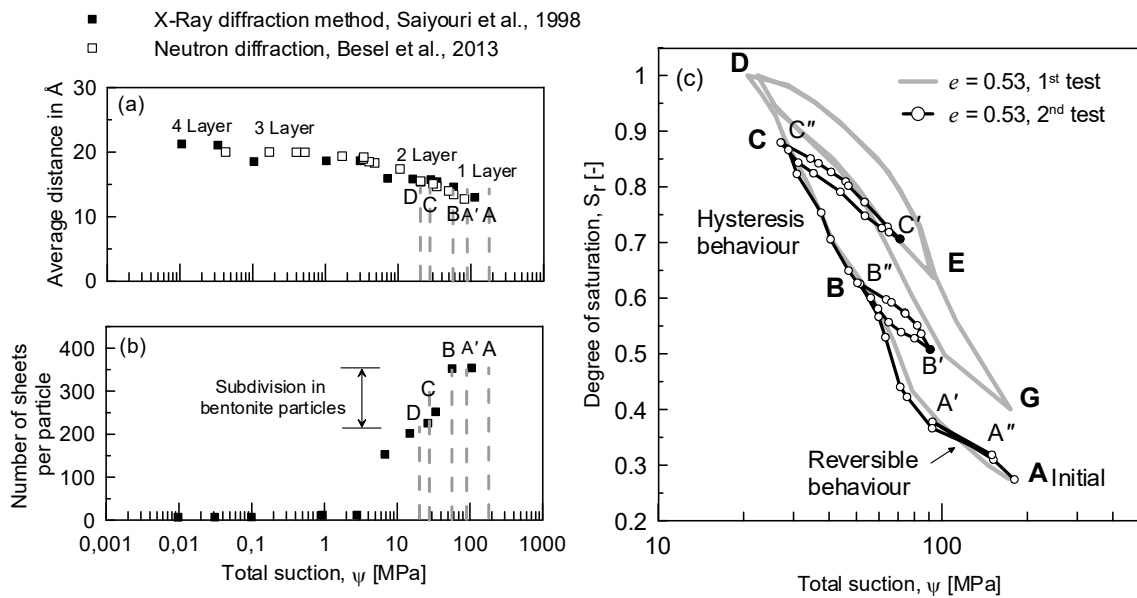


Fig. 3-49: a), b) Average inter-particle distance in smectite mineral and number of sheets per particle versus total suction; c) water retention behaviour of highly compacted bentonite in constant volume condition

Seiphoori et al. (2014)

It is seen that the smectite mineral has only one water layer above about 50 MPa of total suction. The second water layer is absorbed at lower suctions, and the third water layer is added at suction values lower than 7 MPa. At the same time, the number of layers per particle decreases from some hundreds to 10, when the total suction decreases below 3 MPa. Bestel (2014) also measured the evolution of the interlayer distance with water content using neutron diffraction analysis. These results are plotted in Fig. 3-49a in terms of total suction. In order to specify the domain at which the hydration mechanism at particle scale could impose structural modifications, Seiphoori et al. (2014) performed a water retention test on a specimen compacted to the same void ratio of $e = 0.53$ as presented in Fig. 3-49c. The results of the previous test (Fig. 3-45) are also shown in this plot. This water retention test aims at evaluating the hysteresis response of the material at three different points along the first wetting path.

When the material reached degrees of saturation of 0.38, 0.62 and 0.88 (points A', B and C), a drying-wetting path was carried out, which resulted in a scanning path. It is seen that the material exhibits totally reversible retention behaviour in the path A-A'-A'' without a hysteresis cycle. The corresponding positions of Point A' in Fig. 3-49a and b show that the smectite particles have only one layer of water on average with a maximum number of sheets per particle. This initial hydra-

tion was believed to occur on the mineral surface and around the exchangeable cations (Na^+ for MX-80 bentonite) in the interlayer space (e.g. Sposito & Prost 1982). Later at Point B where the material reached a degree of saturation of 0.62, a drying and wetting cycle was performed. It is observed that the scanning curve reaches the initial wetting path by exhibiting hysteresis behaviour in the B-B'-B'' path.

The interlayer state of the material at Point B shown in Fig. 3-49a and b indicates that the material is near a transition to two layers of water, while the number of sheets per particle is still similar to the as-compacted state. The preservation of the main wetting path, despite the reduction in fraction of macropores, implies that the water retention behaviour in this suction domain is exclusively controlled by the micropores.

Finally, a drying and wetting path was performed at Point C where the material reached a degree of saturation of 0.88. The scanning path again reached the initial wetting path with a hysteresis loop (path C – C' – C'' Fig. 3-49a and b), which shows that the material has adsorbed the second water layer at Point C, and a subdivision of the smectite particle may have occurred due to the further hydration.

However, the confined configuration here could have prevented the subdivision of the particles during the hydration. Note that the results from Saiyouri et al. (1998) correspond to hydration in an unconfined condition, while the bentonite specimens in the current study are confined under constant volume. Villar et al. (2012a) also reported the influence of confinement on the interlayer distance at lower suctions.

Further hydration led to a fully saturated state of the material, followed by a permanent structural modification and the creation of a new wetting path as detailed in section 3.7.2. Another subdivision in the material particles from Point C to D can also be observed in Fig. 3-48b.

Further subdivision is prevented at Point D by applying a constant volume condition, despite the tendency for more hydration. As a result, total suction remains at 20.6 MPa, and the swelling pressure reaches its maximum value.

3.7.4 Triaxial mechanical response under unsaturated non-isothermal conditions

The results presented in the following were reported in Seiphoori et al. (2014). The tested material is MX-80 bentonite in granular form as shown in Fig. 3-50a.

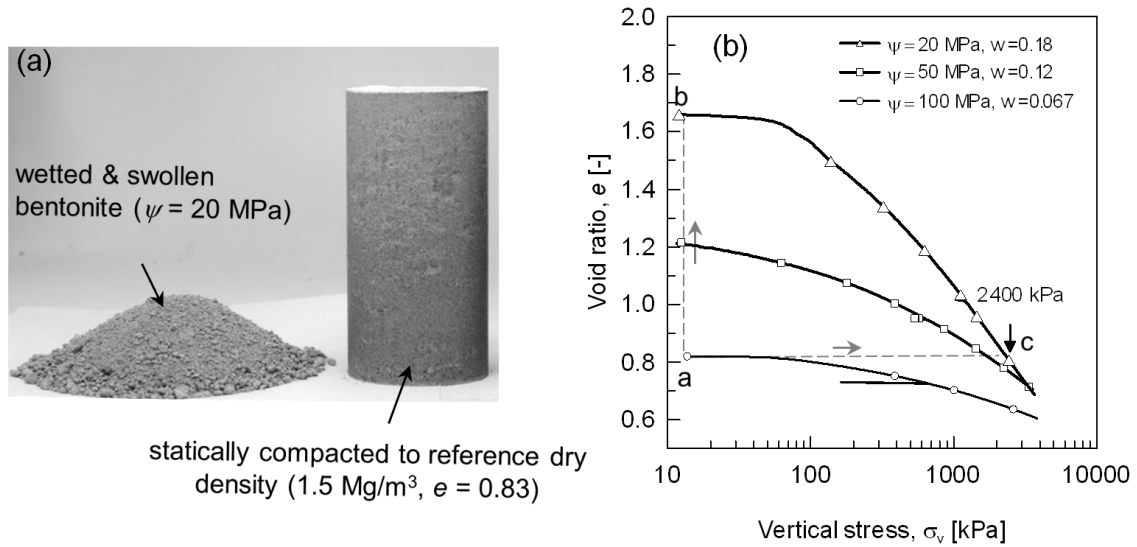


Fig. 3-50: a) Visual aspect of the granular bentonite before and after sample preparation; b) Compaction path to the target dry density (1.5 Mg m^{-3})
Seiphoori et al. (2014)

3.7.4.1 Response under isotropic loading

For the triaxial testing, a first step involves isotropic compression. The samples for unsaturated testing presented in the following were prepared by means of static compaction of the swollen material, which induced a given pre-consolidation pressure to the material. After installation of the samples in a triaxial cell, they were subjected to an isotropic confining stress. An over-consolidation ratio (OCR) is then assumed based on the applied isotropic stress during the consolidation phase. Seiphoori et al. (2014) calculated the OCR values for the vertical component of the mean total stress as $\text{OCR} = \sigma_1 / \sigma_{st}$, which is the ratio of the vertical stress in a triaxial condition with respect to the vertical compaction stress during the sample preparation as presented in Fig. 3-51. The OCR of the samples at total suction of $\psi = 20$ and 50 MPa were computed following this assumption.

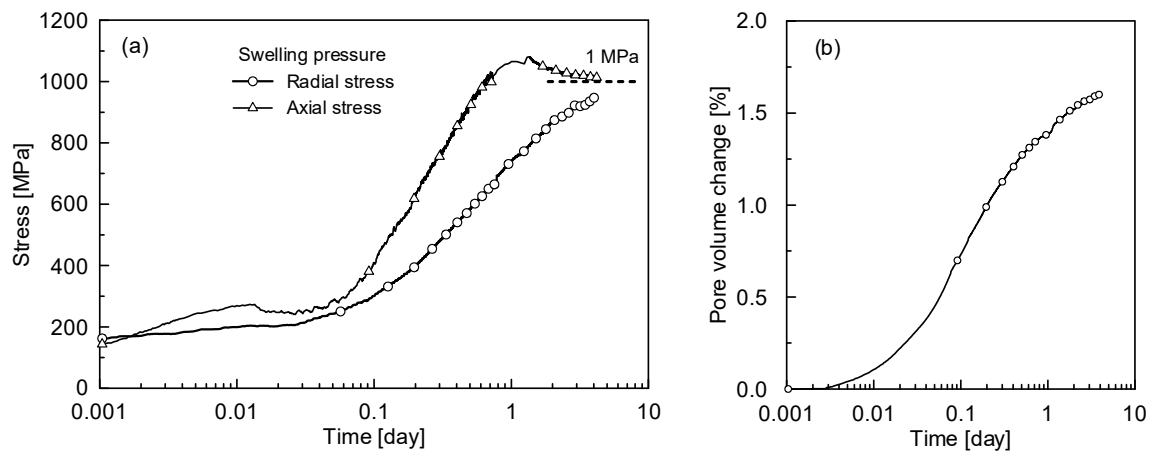


Fig. 3-51: Evolution of radial and axial stress and the measured pore volume change during the swelling phase in a triaxial cell
Seiphoori et al. (2014)

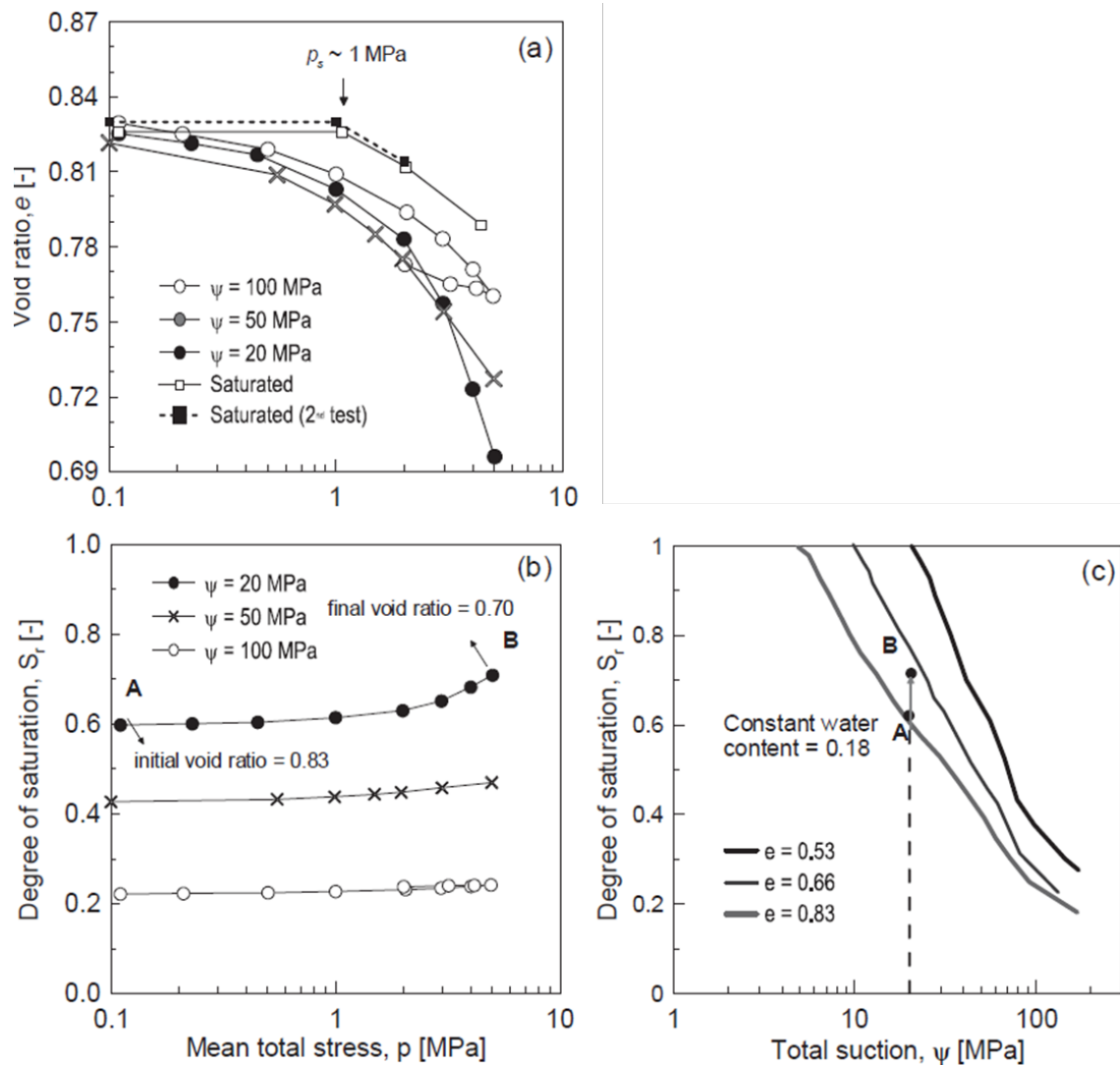


Fig. 3-52: Isotropic compression tests performed in saturated and unsaturated samples: (a) change in void ratio and (b) saturation degree (c) stress path (A-B) in the water retention plane

Seiphoori et al. (2014)

To evaluate the influence of the OCR on the deviatoric behaviour of the material at this suction, a sample was first isotropically loaded up to 5,000 kPa and then unloaded to 2,000 kPa, inducing an OCR of 2.5.

The isotropic behaviour of the material for different values of suction, including saturated conditions, is presented in Fig. 3-52 as reported by Seiphoori et al. (2014). As seen in Fig. 3-52, the compressibility of the material in unsaturated tests increases when total suction decreases. In the case of the saturated sample, the volume change was prevented up to a confining pressure of 1 MPa, which refers to the swelling equilibrium phase where the volume of the sample is kept constant. The pore volume change registered during this step (Fig. 3-51) was associated with the uptake of water by the sample and the lateral drainage (filter paper and geotextile layer). Possibly, the sample could become slightly desaturated after extraction from the saturation mould and during the installation inside the triaxial cell.

A change in the degree of saturation for unsaturated tests with a constant water content is due to the reduction of the void ratio as depicted in Fig. 3-52b. This process is depicted in the plane of the water retention curve, where it can be appreciated how the stress point moves between two water retention curves measured at constant void ratio.

The resulting compressibility is higher for the unsaturated state than for the saturated state. This could be explained by the difference in the microstructural features between an initially compacted sample under partial saturation which differs from the after-saturated state. As discussed in Keller et al. (2014), analysis of the compacted unsaturated samples indicated a marked dual porosity network. This structure consists of macropores filled with partially expanded smectite particles. Such structures are expected to be more developed for granular bentonite samples that swelled after a suction reduction. This implies that inter-aggregate pores are more sensitive to volume changes induced by total stress. However, in an initially saturated sample, due to the hydration and expansion of the particles during saturation, macropores or inter-aggregate pores are practically non-existent. Saturated bentonite thus results in subdivided stacks and fully hydrated smectite particles (up to 4 layers of water adsorbed, Saiyouri et al. 1998, Bestel 2014). In these circumstances, volume changes are related mainly to changes in microporosity, hence such samples present a higher stiffness than those in which macropores are also present. A similar discussion on the compressibility behaviour of initially saturated and compacted saturated bentonite samples is given in Baille et al. (2014).

3.7.4.2 Deviatoric behaviour at ambient temperature

Conventional triaxial tests were performed by Seiphoori et al. (2014) on samples with a total suction applied of 100, 50, 20 and 0 MPa. The deviatoric behaviour of the material under controlled total suction for different confining conditions is presented in Fig. 3-53 and Fig. 3-54.

The influence of the confining stress on the deviatoric behaviour of the material is presented in Fig. 3-53a. A decrease of the elastic domain of the overconsolidated sample at $\psi = 100$ MPa can be observed. Fig. 3-53b presents the volumetric behaviour at the same suction, and the dilatant behaviour is seen for the overconsolidated sample starting from about 6 % of the axial strain. The samples show a tendency to dilate after failure. Fig. 3-53c indicates that the sample at $p = 500$ kPa exhibits ductile behaviour with deviatoric stress remaining constant after failure. Similar behaviour was reported by Blatz & Graham (2003) for a sand/Na-bentonite mixture (50/50 percent in terms of dry weight) during constant water content conditions and initial total suction of 4.5 MPa.

The influence of the OCR can be seen at a low confining stress of $p = 500$ kPa. The dilatant behaviour of the sample is also seen in Fig. 3-54a and b, which presents the deviatoric response of the material at 20 MPa of total suction. A repetition test was also performed at confining stress of $p = 500$ kPa to check the reproducibility of the tests. The second test shows good correspondence with the first test, which proves the reproducibility of the results obtained from the triaxial cell.

The effect of the confining stress p on the deviatoric behaviour of the saturated granular bentonite can be seen in Fig. 3-54c and d. The tests were carried out at $p = 1,150, 2,000$ and $3,000$ kPa. When the sample reached about 1 MPa swelling pressure, the mean total stress was increased to 1,150 kPa (while the back pressure of 50 kPa was still applied). After a given time for the equilibrium under this condition, the deviatoric loading was applied. It is seen that the material shows negligible volume change behaviour.

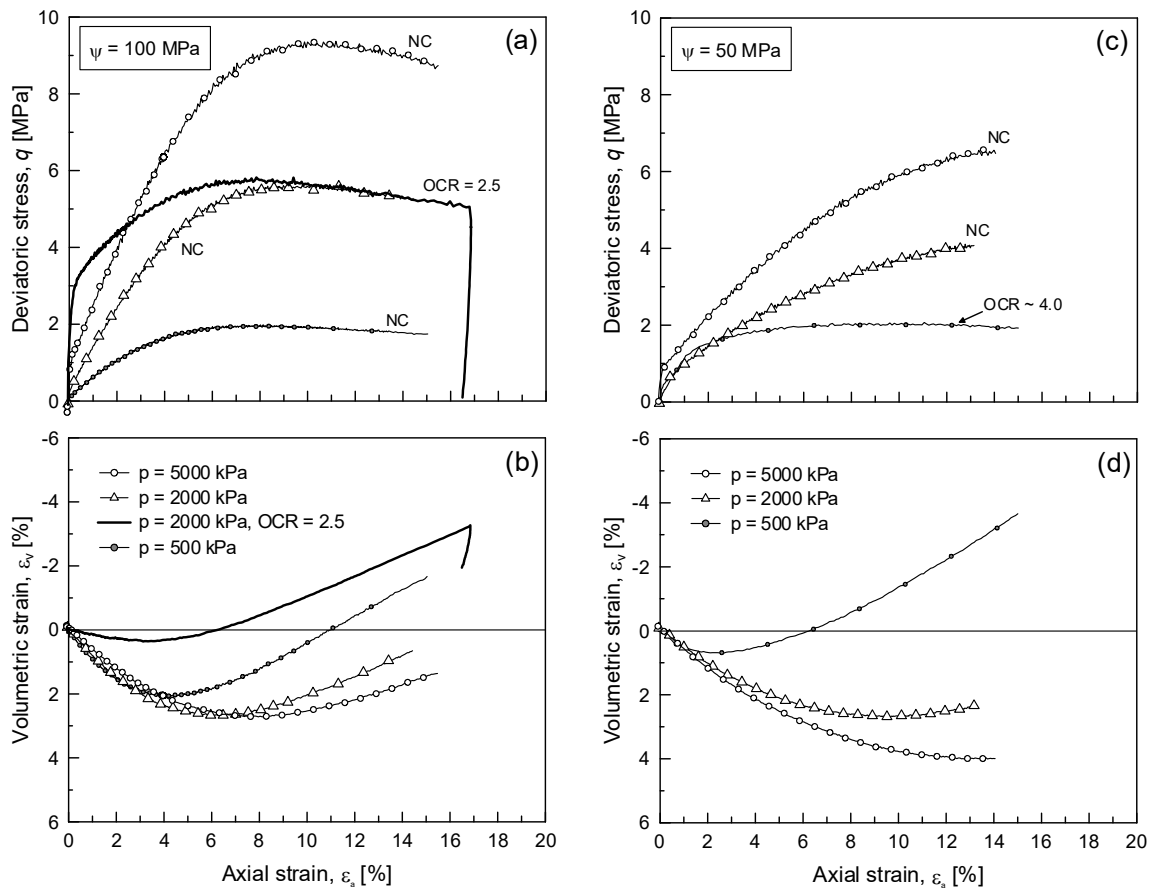


Fig. 3-53: Deviatoric response of MX-80 bentonite under triaxial stress path for a total suction of 100 MPa (a) – (b) and 50 MPa (c) – (d)

Seiphoori et al. (2014)

The volumetric strains of the saturated samples were obtained from the pore volume data assuming that the solid part of the saturated material is incompressible. For the case of $p = 1,150$, the volume strain computed from the inner-cell data (as performed for unsaturated tests) is also presented in Fig. 3-54. The good agreement between the records of the inner-cell and the pore volume confirms the accuracy of the inner-cell volume measurements. It is observed that an increase in confining stress by 2,000 kPa or 3,000 kPa has a negligible influence on the shear strength of the saturated material.

Similar behaviour was observed in Fig. 3-54a for a total suction of 20 MPa. This implies that the influence of the confining stress on the shear resistance is higher under high suction values. The influence of total suction on the deviatoric behaviour is presented in Fig. 3-55 for a mean total stress of $p = 2,000$ kPa, where the decrease in shear strength with decreasing suction can be observed.

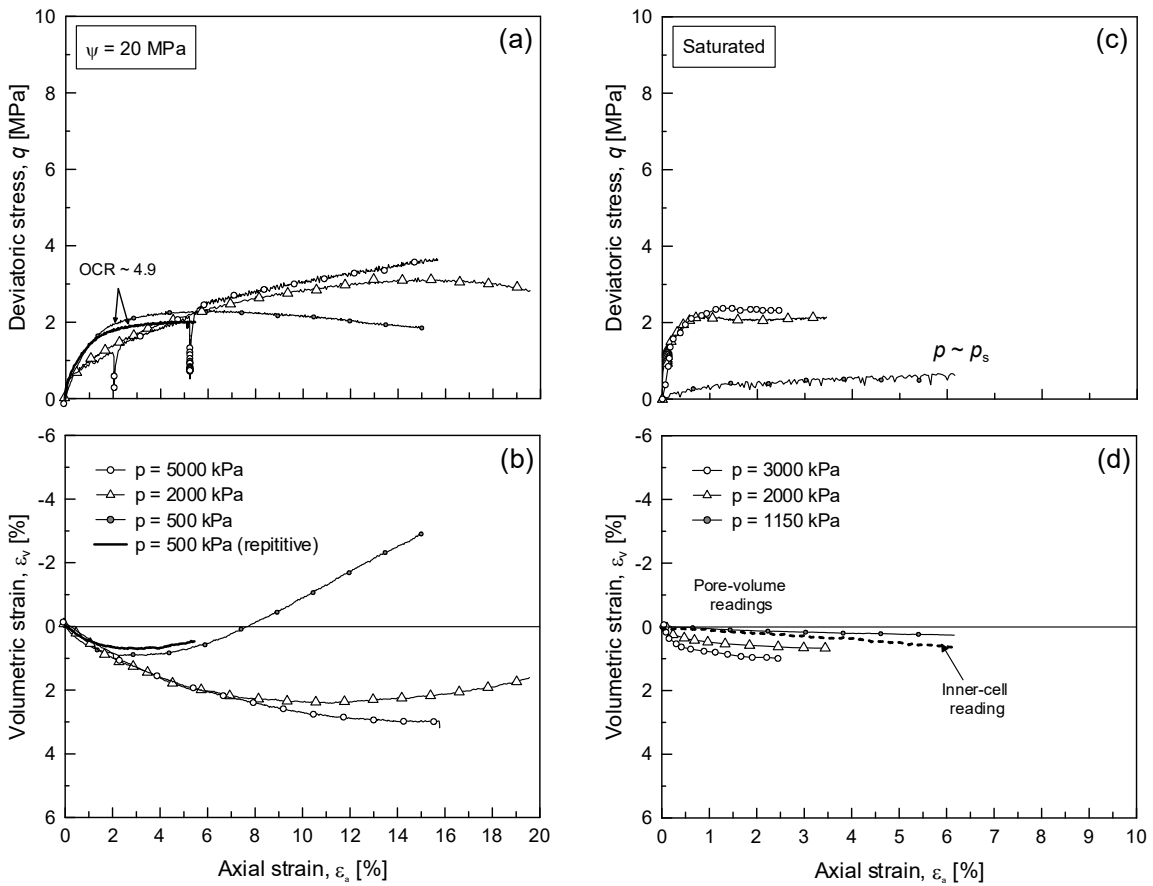


Fig. 3-54: Deviatoric response of MX-80 bentonite under triaxial stress path for a total suction of 20 MPa (a) – (b) and saturated state (porewater pressure of 50 kPa) (c) – (d)
Seiphoori et al. (2014)

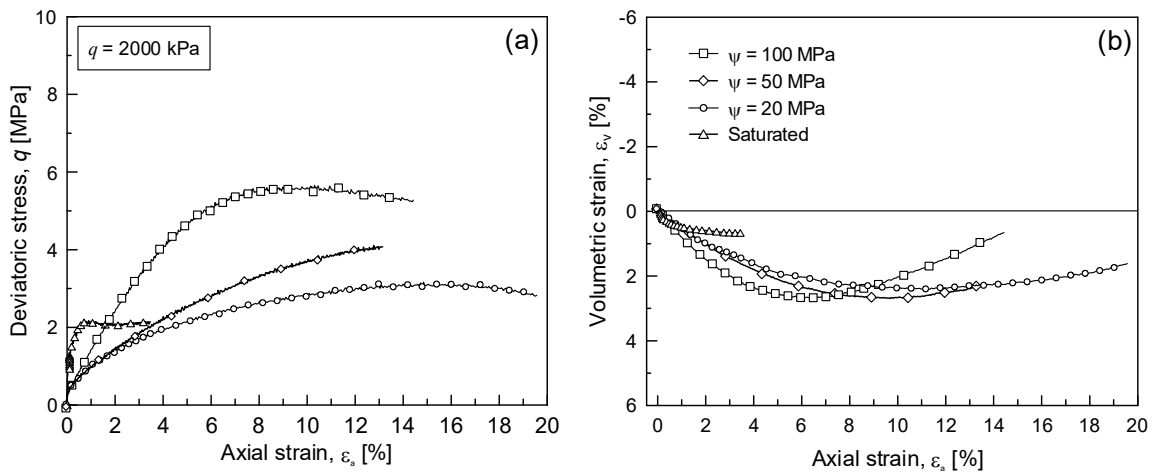


Fig. 3-55: Deviatoric behaviour of granular bentonite samples subjected to triaxial stress paths under different values for total suction
Seiphoori et al. (2014)

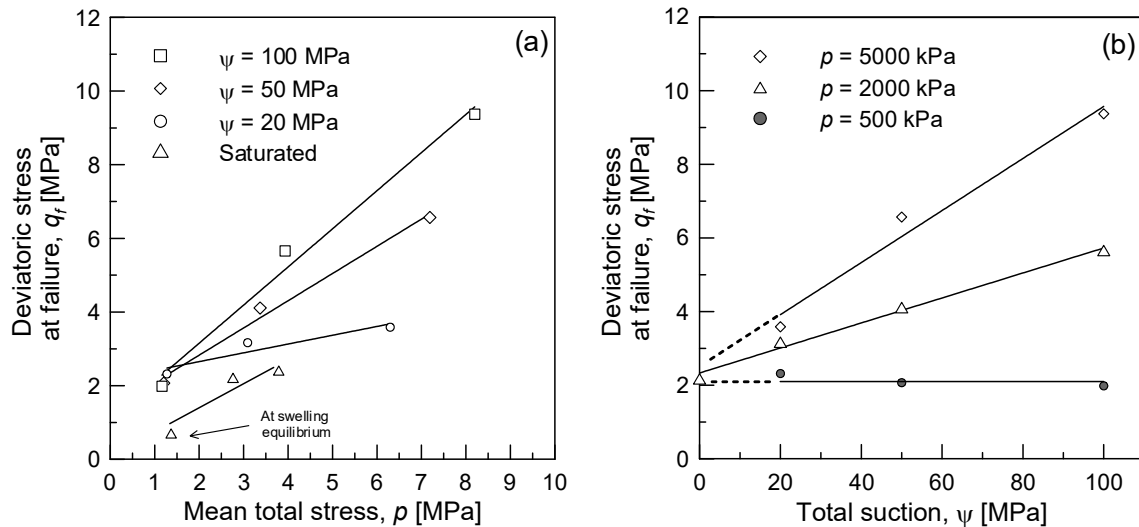


Fig. 3-56: Influence of total suction and mean total stress on the deviatoric stress at failure of MX-80 granular bentonite

Seiphoori et al. (2014)

In unsaturated samples, an increase in shear strength ratio can be seen with an increase in total suction. Despite the deviatoric response of the saturated sample at swelling equilibrium, this trend can include the saturated samples as well. Fig. 3-56b shows that the evolution of the peak strength with total suction increase is negligible under lower confining stress. In general, an increase in resistance due to an increase in total mean stress and total suction is observable in the performed tests. This can be explained for instance by the Cam-Clay model and its extensions to unsaturated states such as the Barcelona Basic Model (Alonso et al. 1990) or the ACMEG-TS (Francois & Laloui 2008). Based on the critical state and elasto-plasticity theories, such models consider that, with increasing preconsolidation stress, the range under which elastic response is obtained also increases. Likewise, the elastic range also increases with increasing matric suction. Details on the ACMEG-TS formulation are given in section 4.6 of the present report.

3.7.4.3 Influence of temperature on triaxial response

This section addresses the influence of temperature on the thermal volumetric strains and deviatoric behaviour of unsaturated granular bentonite samples (at total suction of 20 MPa) which were reported in Seiphoori et al. (2014). For these tests, heating was applied after the isotropic consolidation of the samples at the desired stress level. Once the desired temperature was attained, a deviatoric stress path was applied. The non-isothermal isotropic behaviour of the material was not investigated in these thermal analyses. Nevertheless, a negligible influence of temperature on the compressibility behaviour of MX-80 bentonite material was found by Tang et al. (2008).

The variation of thermal volumetric strains with respect to temperature of the sample at different mean total stresses of $p = 500$, 2,000, and 5,000 kPa is presented in Fig. 3-57. The sample at $p = 500$ kPa exhibited dilatant behaviour, whereas the sample tested under mean total stress of $p = 2,000$ kPa showed contractive behaviour. In oedometric conditions, and also for the MX-80 bentonite, Tang et al. (2008) reported a dilatant behaviour for high values of OCR, whereas contraction was observed for slightly overconsolidated samples.

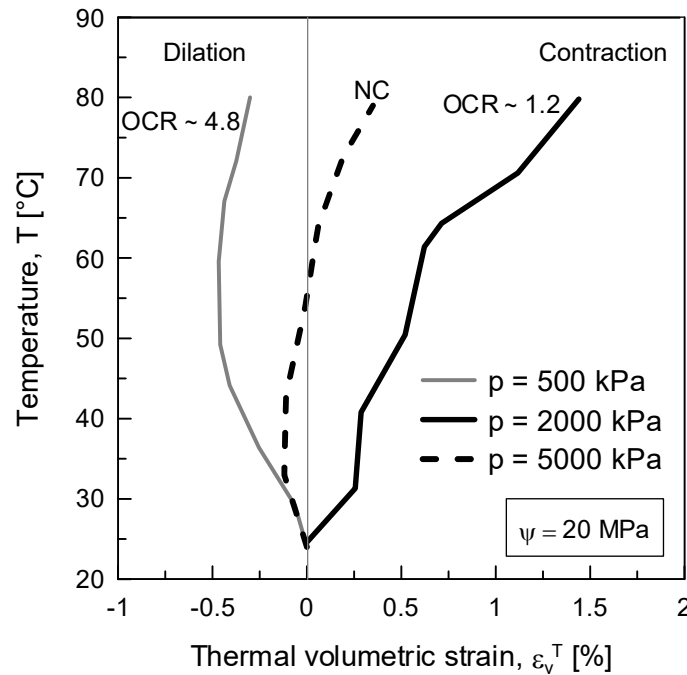


Fig. 3-57: Influence of temperature on the volumetric strain behaviour of MX-80 granular bentonite under controlled suction conditions
 Seiphoori et al. (2014)

The material exhibits small thermal volumetric strains at high confining stress ($p = 5,000$ kPa, Fig. 3-58). This could be associated with reduction in the voids during the mechanical loading, which prevents further change of the void ratio due to an increase in temperature. At this confining stress, the material exhibits an initial expansion followed by a small contraction. The deviatoric behaviour of the samples consolidated at $p = 500$ and $2,000$ kPa at two temperatures of 24 and 80 °C are presented in Fig. 3-58. It is observed that, at low confining stress ($p = 500$ kPa, Fig. 3-57 (a, c) where the material is overconsolidated, a dilatant behaviour is obtained. Under higher temperature, the material shows a contractive response. The yield locus also seems to be diminished at higher temperature for a mean stress of 500 kPa, whereas the change in deviatoric behaviour under different temperatures is negligible at $p = 2,000$ kPa.

These results imply that a stress-strain model for the analysis of bentonite subjected to non-isothermal conditions must take into account the change in behaviour with respect to isothermal conditions. An interpretation of this behaviour using the critical state concept is given in section 4.6 by means of the ACMEG-TS constitutive model.

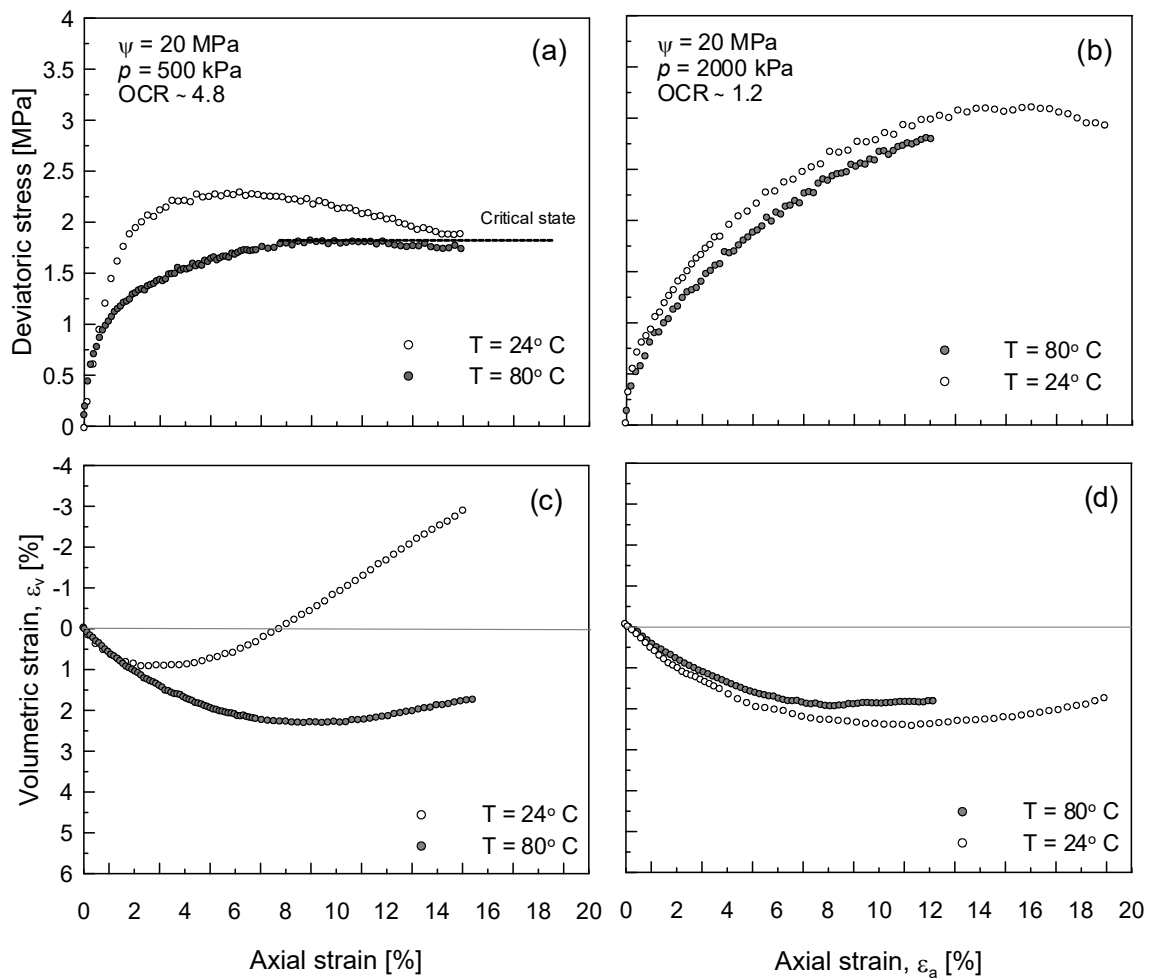


Fig. 3-58: Influence of temperature on the deviatoric behaviour of MX-80 bentonite under controlled suction

Seiphoori et al. (2014)

3.7.5 Impact of salinity on strength

Manca et al. (2016) presented the results of an experimental campaign on sand (80 % of dry weight) – MX-80 bentonite (20 % of dry weight) mixtures with the objective of determining the effects of porewater salinity on the swelling pressure of the material. Specimens were prepared by mixing sand and bentonite then adding different water types to reach the optimum water content for the dry density. Four types of water were studied: distilled water⁷ to allow the maximum swelling of bentonite; synthetic water similar to OPA porewater to reproduce the in-situ chemistry; 1M sodium chloride; and 4M sodium chloride to compare with the results of synthetic water. The wet mixture was compacted statically inside the testing cells at a constant rate of 0.5 mm/min. Fig. 3-59 and Fig. 3-60 illustrate the compaction phases and the device used.

⁷ Note that distilled water mixed with untreated bentonite will develop a notable salinity from the inventory of soluble salts. In fact, this salinity will be distinct. Thus, the effect of "true" distilled water conditions will be even more pronounced.

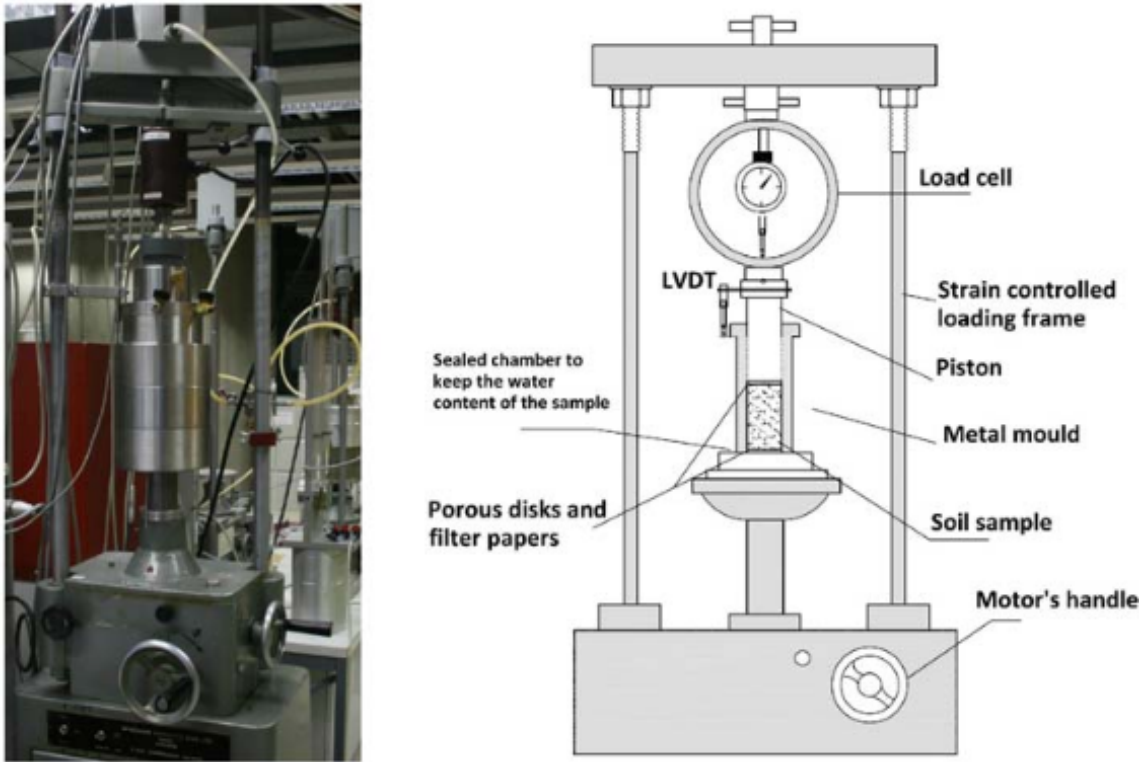


Fig. 3-59: Schematic representation of the press used for the specimen compaction (right) and compaction of a specimen inside the oedometric ring (left)

Manca (2015)

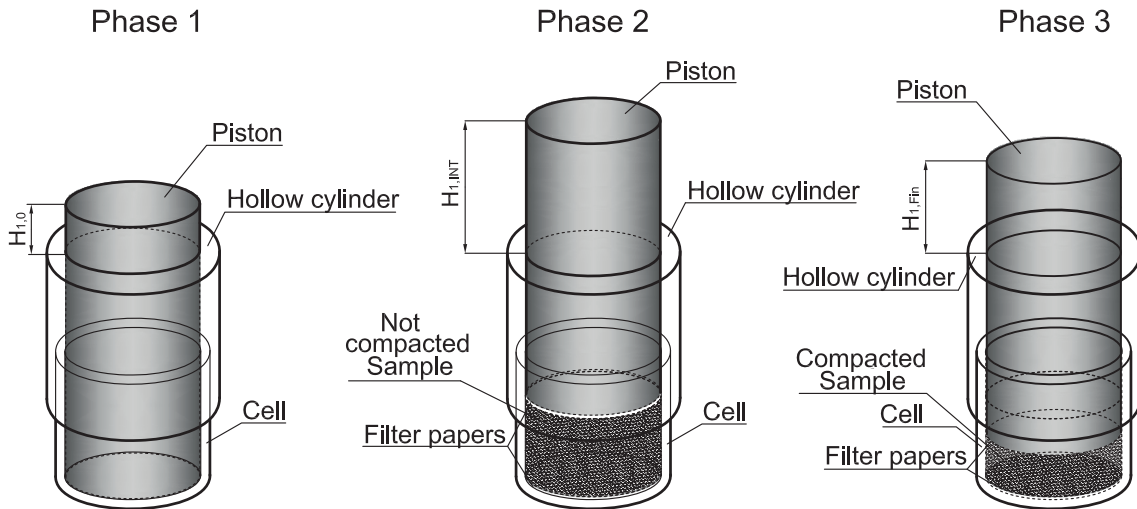


Fig. 3-60: Specimen compaction phases

Manca (2015)

Specimens were wetted to the target water content under isochoric conditions with a syringe so that the injected water flowed preferentially through the largest pores and distributed homogeneously in the sample. Then, the cell was wrapped in paraffin for 15 days for internal moisture equilibration.

Conventional free and swelling tests were then performed. For the conventional swelling test, the cells used consisted of a thick-walled stainless steel oedometric cell 79 mm in diameter and 15 mm high that was inserted inside a highly rigid frame. For the free swelling tests, the sample was allowed to expand vertically, and the vertical displacements were measured by a linear variable differential transformer (LVDT).

Finally, for the controlled suction swelling tests, the cell used allowed the matric suction to be imposed by preserving a constant air pressure and modifying the porewater pressure to reach the target matric suction value. A rigid frame was used to ensure isochoric conditions. Each matric suction step was maintained until equilibrium conditions were achieved. Swelling pressure was measured with a load cell placed at the top of the specimen. The undesirable change in volume was measured by an LVDT and was less than 0.1 %. The results (Fig. 3-61 and Fig. 3-62) showed that the tested material exhibits low swelling capacity compared with other bentonite-based materials prepared with higher bentonite contents. The compaction of the mixture caused compression and closure of the macropores.

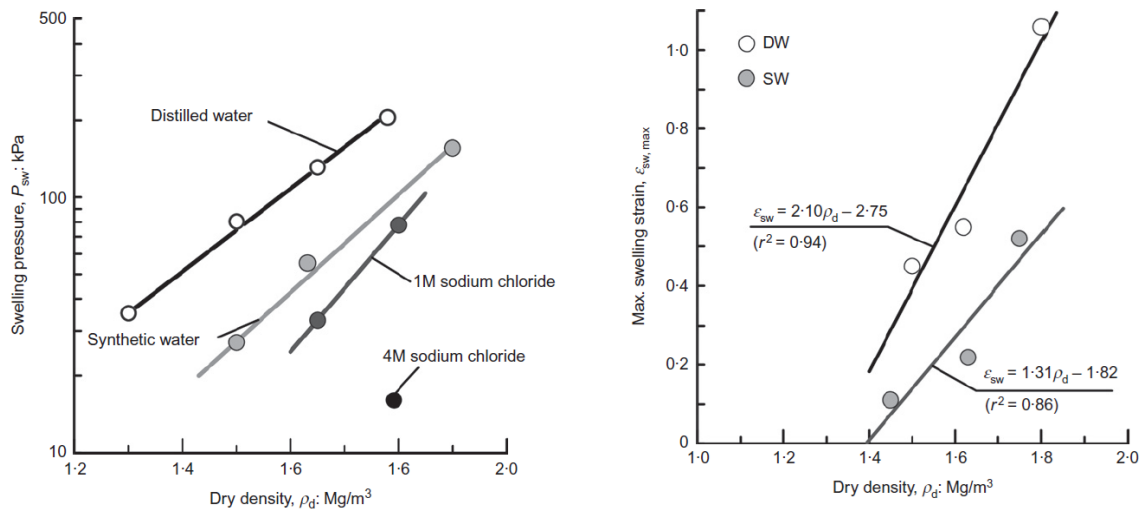


Fig. 3-61: Comparison between the swelling pressure developed with distilled water, synthetic water and sodium chloride solutions (left) and between the maximum swelling strain of the S/B mixture wetted with distilled water and synthetic water as a function of the initial dry density (right)

Manca (2015)

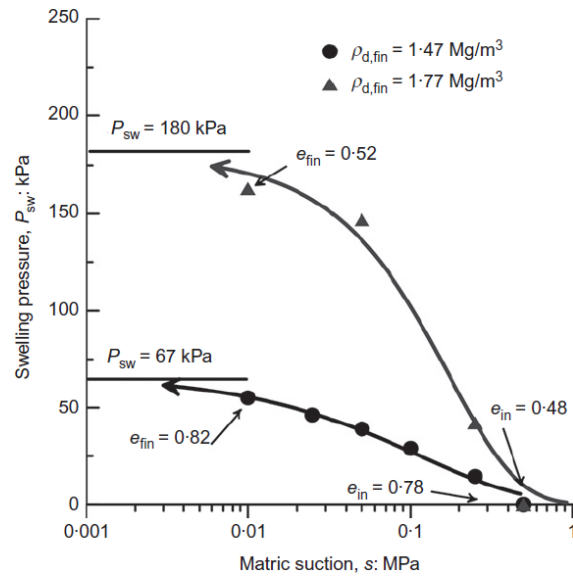


Fig. 3-62: Evolution of the swelling pressure of the S/B mixture along a wetting-path under quasi-constant volume conditions for specimen compacted to two different dry densities

The initial and final void ratios of the specimen are indicated in the figure.
Manca (2015)

Manca (2015) argued that the hydration of the mixture is marked by the delamination of the quasicrystals until the macropores are completely closed (Fig. 3-63). For low densities, the process leads to a progressive decrease of nanopores and to uniform pore size distribution. The macroscopic swelling is caused for the case of low density by the development of the DDL and the splitting of quasicrystals.

An increase in the dry density led to the closure of macropores and therefore a decrease of available volume for the development of the electrostatic double layer. Thus, the potential of the bentonite to sustain chemical loadings is improved.

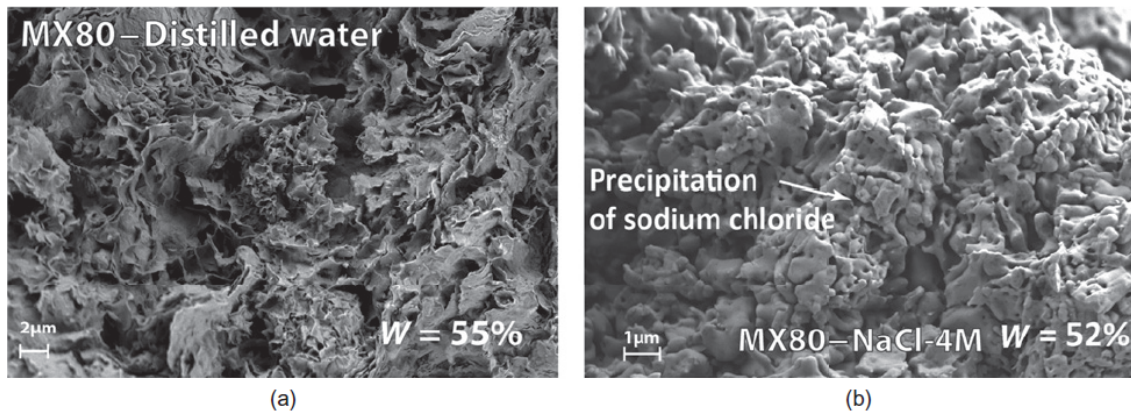


Fig. 3-63: SEM image of MX-80 granular bentonite wetted to $w = 55\%$ with (a) distilled water and (b) 4M sodium chloride

Manca (2015)

3.7.6 Relevant conceptual uncertainties of the bentonite THM behaviour for the Nagra concept

In the Swiss disposal concept, bentonite is used as (i) a sealing buffer for the isolation of the emplacement drifts and (ii) a buffer material as part of the near-field around the SF/HLW canisters.

Bentonite-based seal sections

After their emplacement, the bentonite-based repository seals will not be subjected to major changes in temperature. However, significant hydraulic gradients may act on the seals when the repository starts to saturate after closure. In this context, the potential erosion of the bentonite due to high flow velocities of the imbibing water is a safety-relevant risk that needs to be addressed. Most likely, erosion occurs along discrete flow channels at the interface between the bentonite seal and the concrete liner or the host rock, respectively. The magnitude of bentonite erosional processes is strongly controlled by the local conditions along the discrete flow paths and, consequently, their predictability is limited. Therefore, engineering measures must be taken to avoid any conditions that create strong hydraulic gradients during the early post-closure phase (e.g. removable interim seals).

After 100s – 1,000s of years, gases may accumulate in the backfilled repository structures due to anaerobic corrosion of metals and degradation of organic wastes. The gas-induced pressure build-up in the repository drifts may give rise to gas percolation through the bentonite seals. The mobilisation of bentonite colloids by gas invasion has been studied at the phenomenological level (Romero & Gonzalez-Blanco 2017, Mancha 2015); however, the possible effects of gas-induced mobilisation of bentonite on the long-term performance of the seal sections have not yet been assessed in detail. Special design measures of the seal abutments may be required to avoid the mobilisation of bentonite colloids.

Bentonite in the near-field of the HLW repository

In the HLW near-field, the unsaturated bentonite must sustain temperatures of more than 120 °C during the first few decades after canister emplacement. Limited experimental evidence is available to date concerning the THM(-C)-behaviour of bentonite at high temperature (> 100 °C). Aspects of particular interest are the long-term mechanical behaviour of granular bentonite subjected to high temperature ("creep" phenomena, role of granulometry of the bentonite), thermo-chemical alterations of the bentonite (impact on swelling pressure) and the evolution of void ratio and pore size distribution during the non-isothermal resaturation phase. These uncertainties related to THM(-C) processes impact the underlying assumptions made regarding homogeneity of the buffer and the barrier integrity.

In the long term (100s to 10,000s of years), a free gas phase may develop at the canister surface, giving rise to the build-up of gas overpressures. The percolation of the gas phase through the buffer into the excavation damaged zone depends strongly on the granulometry and the loading history of the bentonite. Furthermore, bentonite colloids may be mobilised to a small extent by the gas invasion (Romero & Gonzalez-Blanco 2017 and 2018). The impact of gas percolation on the long-term safety functions of the bentonite buffer (isolation/confinement of waste canisters) requires further evaluation. Local losses of the buffer density could be associated with a reduced long-term performance thereof.

3.8 CMH coupling

The interdependence of bentonite porewater or equilibration fluid Chemistry, cation occupancy, and Hydro-Mechanical properties is qualitatively well known (Rutqvist 2015). Swelling pressure is the major dependent parameter of the latter, coupled with microstructural characteristics such as pore size distribution and geometry. The key parameters and their dependence on intrinsic bentonite properties are first discussed individually, before examining their coupling.

3.8.1 Porosity, accessory minerals and swelling pressure

Pore size distribution in bentonite, the different porosity concepts, and experimental approaches for assessing porosity have been discussed in section 3.3. Because swelling pressure and pore size distribution both depend primarily on dry density, pressure and porosity are also coupled. Here we concentrate on the effect of porewater chemistry on both properties.

Swelling pressure and swelling capacity of bentonite are well known and are key properties of the EBS functionality (Bradbury et al. 2014). Madsen & Müller-Vonmoos (1989) distinguish inner-crystalline swelling and osmotic swelling, which both contribute to the swelling behaviour, or to the swelling pressure if the material is confined. Hydration of the interlayer cations leads to a widening of the interlayer space and causes the inner-crystalline swelling. The driving force for the osmotic swelling is the large difference in ion concentration between the ions electrostatically held close to the clay surface and the ions in the water outside the clay grains. The clay (grain) surface can be seen as a membrane separating two electrolytes with different concentrations. The osmotic (swelling) pressure is caused by the water penetrating through the semi-permeable membrane, driven by a gradient in water potential, giving rise to a hydrostatic pressure which eventually prevents the further intrusion of water (Tinker 1916). In general, crystalline swelling dominates at high density/low water contents, whereas above approximately 19 Å basal spacing (for Na-montmorillonite), osmotic swelling takes over (Norrish 1954, and later studies reviewed in Holmboe et al. 2012).

At full saturation, a positive correlation between swelling pressure and density can be measured (Fig. 3-64). Empirical relationships between swelling properties of bentonite and density have been shown in a number of studies (Low 1980, Karnland 1997). This correlation becomes more pronounced when the density is normalised to the montmorillonite content, for example to the effective montmorillonite dry density (EMDD) (Dixon et al. 2002, Jenni & Mäder 2018):

$$EMDD = \frac{m_{mont}}{V_{mont} + V_{pores}} = \frac{f_{mont} \cdot \rho_{dry}}{1 - ((1 - f_{mont}) \cdot \rho_{dry} / \rho_{acc})}$$

where m and V are masses and volumes, f_{mont} is the mass fraction of montmorillonite, ρ_{dry} is the dry density of the bentonite and ρ_{acc} is the grain density of the accessory minerals. An empirical relationship between EMDD (range $\sim 1.0 - 1.5 \text{ Mg m}^{-3}$) and swelling pressure was established for a number of bentonitic materials by Kumpulainen & Kiviranta (2011). A similar type of relationship was derived by Karnland (2010), who related the variable f_{mont}/w_{sat}^2 (the montmorillonite mass fraction divided by the square of the water content at full saturation) to the swelling pressure. This relationship is shown in Fig. 3-65 for the same type of materials as presented in Karnland et al. (2006) and Fig. 3-5. At lower f_{mont}/w_{sat}^2 and lower densities, Na-rich materials (within the red circle) deviate from this trend, showing higher swelling pressures than their Ca counterparts (Karnland 2010). This is explained by the different osmotic swelling behaviours of Na-montmorillonite and Ca-montmorillonite at lower densities. At higher densities, this difference largely vanishes, and the small variations noted may be due to other factors such

as charge localisation or simply measurement uncertainty (Karnland 2010). From the evaluation of the empirical relationship shown in Fig. 3-65, Karnland (2010) deduced that accessory minerals had a non-negligible effect on the swelling pressure and that the common assumption of treating them as "inert filler" is not entirely correct. However, the figure includes materials with different dry densities and, therefore, also different EMDD, in addition to the different montmorillonite fraction.

More recently, the same author revisited the filler issue. A test programme included samples with different MX-80/inert filler ratios, but the EMDD was also varied, which makes the data interpretation more difficult. Plotting the EMDD against swelling pressure defined a single curve, regardless of accessory content (presentation Ola Karnland, EBS Task Force Meeting autumn 2016, Oxford UK). The author concluded that the swelling pressure is unaffected up to 40 – 50 % of homogeneously distributed filler. As soon as the filler grains agglomerate and build an inter-filler porosity (grain-supported fabric), the EMDD is changed and therefore also swelling pressure. Furthermore, the author demonstrated theoretically that, based on the Poisson-Boltzmann equation, the inhomogeneous agglomeration of the filler in the form of a layer or column in a bentonite plug must influence the swelling pressure. This can only occur at high filler contents but may be relevant for sand/bentonite seal constructions.

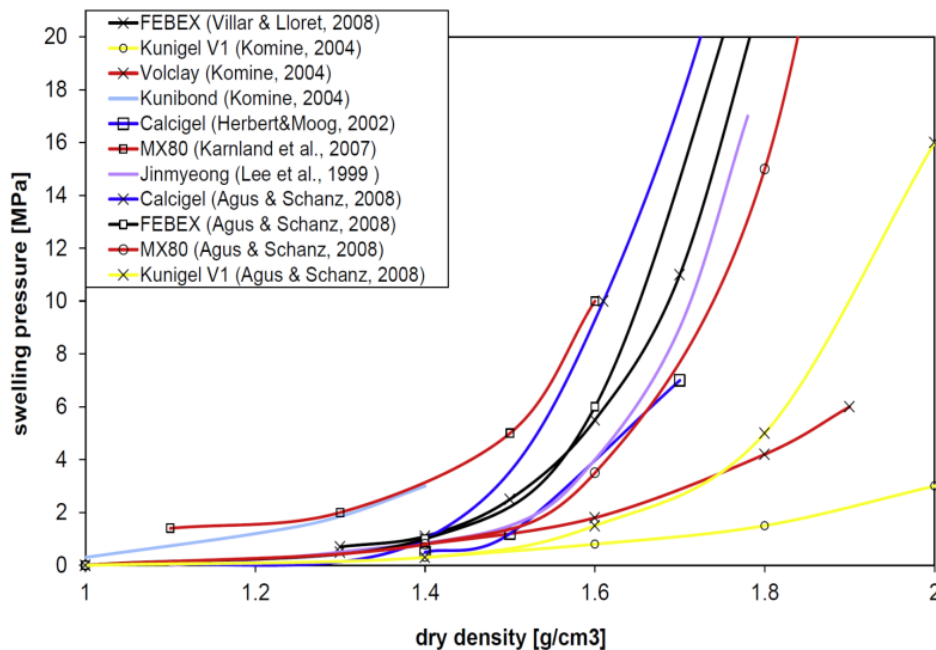


Fig. 3-64: Comparison of selected published data on dry density vs. swelling pressure for different bentonites

Kaufhold et al. (2015a)

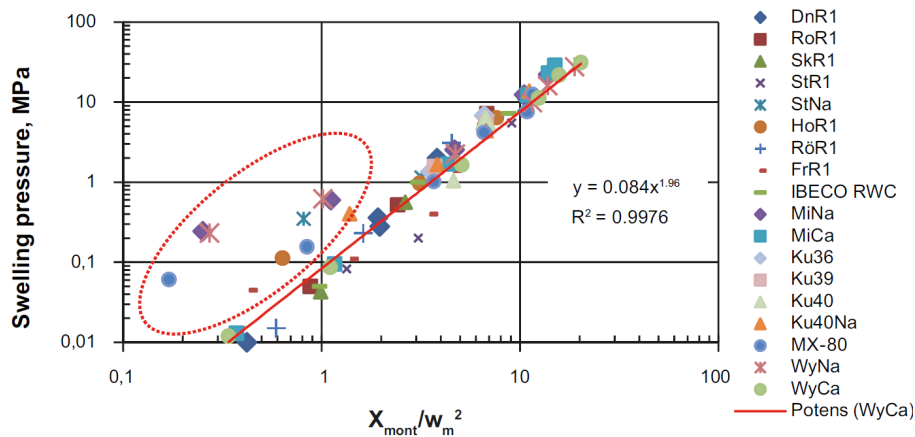


Fig. 3-65: Measured swelling pressures plotted against montmorillonite content (X_{mont}) and water content at full water saturation (w_{sat})

w_{sat} is called w_m in this figure taken from Karnland (2010) and equals solid mass over water mass at full saturation.

Several studies use the Gouy-Chapman diffuse double-layer theory to theoretically derive swelling pressures of bentonite (Tripathy et al. 2004, Schanz & Tripathy 2009, and citations therein). Following this theory, the interaction force of the double layers of two parallel clay platelets depends on the ion concentration at the mid-plane and can be seen as osmotic pressure at the mid-plane (Bolt 1956). For any given separation distance between two clay platelets, the osmotic pressure can be determined from the theory by knowing the concentration of the ions in the mid-plane (and knowing the external "bulk" concentration). Similarly, for any given osmotic pressure and known concentration of the ions in the central plane between two clay platelets, the separation distance between the clay platelets can be determined from the theory. But Tripathy et al. (2004) doubt the applicability, especially at small interlayer distances where the effect of ion and surface hydration becomes more relevant. Empirical modifications have been implemented, and the weighted average valency of exchangeable cations was used in the calculations to account for the co-existence of mono- and bivalent cations in the interlayer. Still, swelling pressures above $1,500 \text{ kg m}^{-3}$ dry density were predicted to be below the measured values. Schanz et al. (2013) claim that the diffuse double-layer theory underestimates interlayer porosity at low densities, but overestimates at high density, based on comparison with total porosity from measurements and assuming that interlayer porosity is the only existing porosity. The authors introduce an empirical, bentonite-specific correction function for porosity. The new porosity values are then used for the swelling pressure calculations following the diffuse double-layer theory. The pressure predictions match experimental data from different bentonites and different studies. Although the osmotic effect is included in the diffuse double-layer theory (ionic strength of the bulk solution), the authors did not verify the consistency of experimental swelling pressures at different bulk ionic strengths and values derived from the diffuse double-layer theory. Furthermore, the approach taking into account mixed cation occupancy (weighted average valency) was not verified by comparing calculated pressures with measurements from one bentonite at different cation occupancies.

Karnland et al. (2003) present swelling pressure predictions based on osmotic considerations and the Poisson-Boltzmann equation, assuming thermodynamic equilibrium between the internal and external solution. The osmotic pressure is calculated based on the mid-plane concentrations (derived from Poisson-Boltzmann), and comparison of predicted pressures agree well with measurements in the osmotic region ($< 1,500 \text{ kg m}^{-3}$ dry density). At higher densities, the misfit is explained by the increasing influence of crystalline swelling. The authors cite Viani et al.

(1983), who proposed an exponential pressure dependence on interlayer distance based on measurements on various clays. This empirical formulation also fits measurements at higher densities. However, the approach is only applied to deionised water as an equilibrating fluid. Further predictions based on the equilibrium between the chemical potentials in the external solution and in the clay disagree at high salt concentrations. The misfit is explained by substantial amounts of ions entering the clay (interlayer), influencing the potentials on both sides. Consequently, the Donnan equilibrium is used to calculate the activity of Na^+ in the clay, and the swelling pressure can then be recalculated. This approach leads to an improvement of the fit, but a significant disagreement at higher salt concentrations at high densities persists.

The porosity – swelling pressure correlation can be investigated by MD simulations, even under consideration of different ionic strengths outside the interlayer or different cations within the interlayer. The swelling pressure is quantified by holding a montmorillonite sheet with a spring, and measuring the force applied by the water and cations in the interlayer (Sun et al. 2015). Different spring constants and/or initial interlayer distances can be transformed into a density – swelling pressure dataset at different cation occupancy and external water concentration. The results show decreased swelling pressures at higher external concentrations and with exchanged Ca for Na, in qualitative agreement with observations.

3.8.2 Porewater chemistry and exchanger population

The porewater chemistry in the clay equilibrates with the outer solution, e.g. the host rock porewater. This can happen within days for discs in the cm range diffusively exposed to reservoirs if no soluble minerals are present and the exchanger population is not altered (Karnland et al. 2003, Karnland et al. 2006). In contrast, advective-diffusive infiltration of host rock porewater can require years for dissolution and removal of gypsum from a compacted bentonite core in the 5 cm range, and decades for complete equilibration of the cation occupancy (Jenni et al. 2014a). In this case, the infiltrating solution equilibrates with the mineralogy present, and the exchanger. The exchanger can be seen as cation exchange sites, surface complexation sites, or as Donnan porosity where the Donnan equilibrium constrains its chemical composition representing the cation occupancy. Furthermore, combinations of these approaches are used for numerical modelling. The different approaches mainly influence transport properties but have a minor influence on the equilibrium condition if set up properly. This means that the equilibrium condition has to agree with cation occupancy measurements, from which the constraining parameters (e.g. selectivity coefficients) have been derived (Bradbury & Baeyens 2002, Bradbury & Baeyens 2003b).

In highly compacted bentonite, certain approaches assume the absence of a free porosity (Birgersson & Karnland 2009). The Donnan equilibrium is then valid between the Donnan porosity and an external solution. Thus, exchangeable cations are essentially treated as mobile cations.

In the repository context, porewater composition and cation occupancy evolve after full saturation is attained (constant infiltrating chemistry of external reservoir assumed):

- Immediately after bentonite saturation, the bentonite porewater represents a mixture of the external hydration water and the initial bentonite exchanger occupancy, additionally controlled by the kinetically rapidly dissolving minerals (e.g. gypsum). This ion pool is distributed between free and Donnan porosity, or between free porosity and cation exchanger, depending on the concept used. Anion exclusion during saturation increases ionic strength in the bentonite (section 5.7).
- Assuming an infinite external reservoir interacting until full equilibrium: all unstable bentonite minerals in the reservoir chemistry have been dissolved, the free porewater chemistry equals the reservoir, and the cation occupancy is in equilibrium with the reservoir/

free porewater. Model calculations for the KBS-3 design and the Olkiluoto case predict equilibrium conditions after 60 – 90 years in systems without mineral reactions, but far above 500 years if gypsum and calcite are considered reactive (Yustres et al. 2017). The external reservoir with constant chemistry represents the host rock, its transport properties are ignored.

Therefore, a saturated bentonite (including cation occupancy and porewater composition) is not unambiguously defined by the composition of the saturation water. In addition, the degree of equilibration with the external water (depending on interaction time and nature of the interface) must be indicated. In many experiments with saturated bentonite, this information is missing, and the bentonite porewater and cation occupancy at the onset of the experiment is not known (e.g. sections 3.7.5 and 3.8.3).

3.8.3 Coupling of ionic strength to swelling pressure and porosity at constant volume/dry density and constant exchanger population

Changes in ionic strength of porewaters adjacent to the bentonite during the lifetime of a repository will influence the porewater in the bentonite. For example, the dilution of the external water infiltrating the bentonite during a glaciation period provides a possible underlying scenario for this case. Although a simultaneous alteration of the exchanger population is likely in a real scenario, the exchanger should be kept constant in experimental set-ups to avoid overlapping effects from two mechanisms. For the same reason, dry density/total volume is also kept constant for all experimental data shown below.

Literature studies of swelling pressure or basal spacing of bentonite equilibrated with electrolytes of specified ionic strength often ignored the controlling effect of soluble minerals present in the sample. The contribution of mineral dissolution or even equilibration with atmospheric CO₂ should not be ignored, especially for external solutions intended to impose low ionic strength. If it is assumed that no free porosity is present, then ionic strength is expected to increase at the clay - external solution interface, e.g. in the filter, which then has the same osmotic effect on swelling pressure as in a Donnan/free porosity concept. For example, a 1 mM NaCl solution infiltrated into bentonite by Holmboe et al. (2012) leads to a free porewater ionic strength of 44 mM in equilibrium with the known accessory minerals gypsum, calcite, and atmospheric CO₂. The steep slope of the swelling pressure-ionic strength curve close to zero ionic strength (Fig. 3-66) increases the significance of this issue (swelling pressure expected to be approximately 80 kPa lower at 44 mM NaCl than at 0 M for 1,500 kg m⁻³ dry density). In contrast, a sufficiently long equilibration time with near-constant reservoir chemistry removes all soluble accessory minerals, and the internal chemistry of the free porewater equals that of the external reservoir. But in this case, dry density is slightly decreased due to mineral dissolution, which may significantly decrease swelling pressure, especially at high densities (Fig. 3-64, example given in section 3.8.1). Performing measurements on purified bentonite or pure montmorillonite avoids this issue. For a comparison of swelling pressure data at constant densities, the EMDD is relevant instead of total dry density.

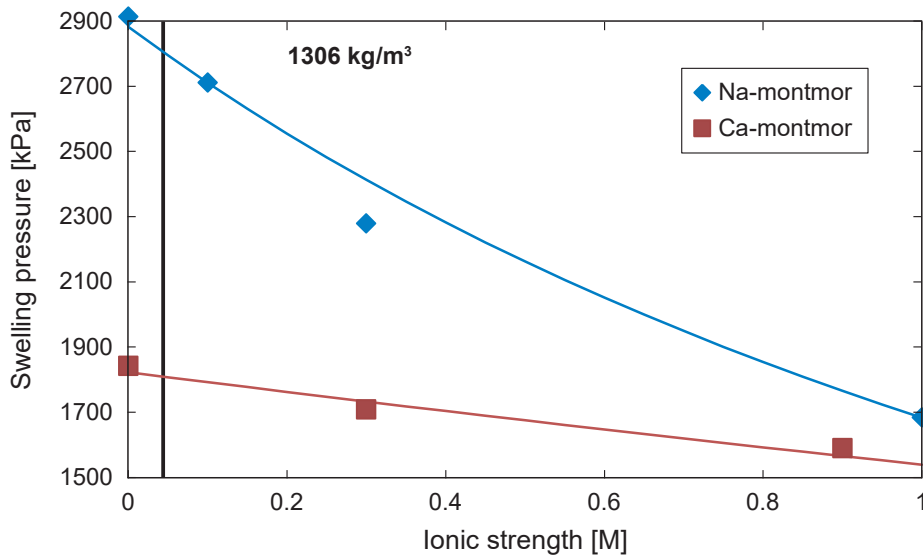


Fig. 3-66: Swelling pressure of Na-montmorillonite in NaCl and of Ca-montmorillonite in CaCl₂ solutions of different ionic strengths at 1,306 kg m⁻³ dry density

The montmorillonite dry density approximately corresponds to MX-80 dry density of 1,500 kg m⁻³ (calculated from the EMDD above). Data from Karland et al. (2006) were interpolated with exponential fit functions to estimate swelling pressures of Na- and Ca-montmorillonite at the desired density (data were originally measured at different densities). Lines represent best fits of a hyperbolic arc tangent function. The vertical line marks 44 mM ionic strength.

Changes in ionic strength of the external solution influence osmotic swelling, which is assumed to occur only at low density (above approximately 19 Å interlayer distance). Therefore, the strongest effects of changes in ionic strength on swelling pressures are measured at low densities (large interlayer distances) as shown in Fig. 3-67. However, ionic strength also influences swelling pressures of dense clays: Na-montmorillonite at 1,690 kg m⁻³ still shows a clear dependence on ionic strength, whereas Ca-montmorillonite swelling pressure seems to remain constant (basal spacing around 15 Å after Fig. 3-21). The influence of ionic strength on crystalline swelling, which is assumed to be responsible for swelling at this basal spacing, is not discussed in the literature. The different behaviour of Na-montmorillonite and Ca-montmorillonite during purification and homoionic treatment questions a direct comparison of the two forms: the Ca form flocculates in dispersion, in contrast to the homogeneous dispersion of the Na form. This might lead to different grain or agglomerate sizes still affecting the microstructure after compaction. Therefore, not only the cation present in the Donnan porosity is responsible for the observed differences between the Na and Ca form, but also a possibly different microstructure. In-situ cation exchange can overcome such preparation artefacts (example in section 3.8.4).

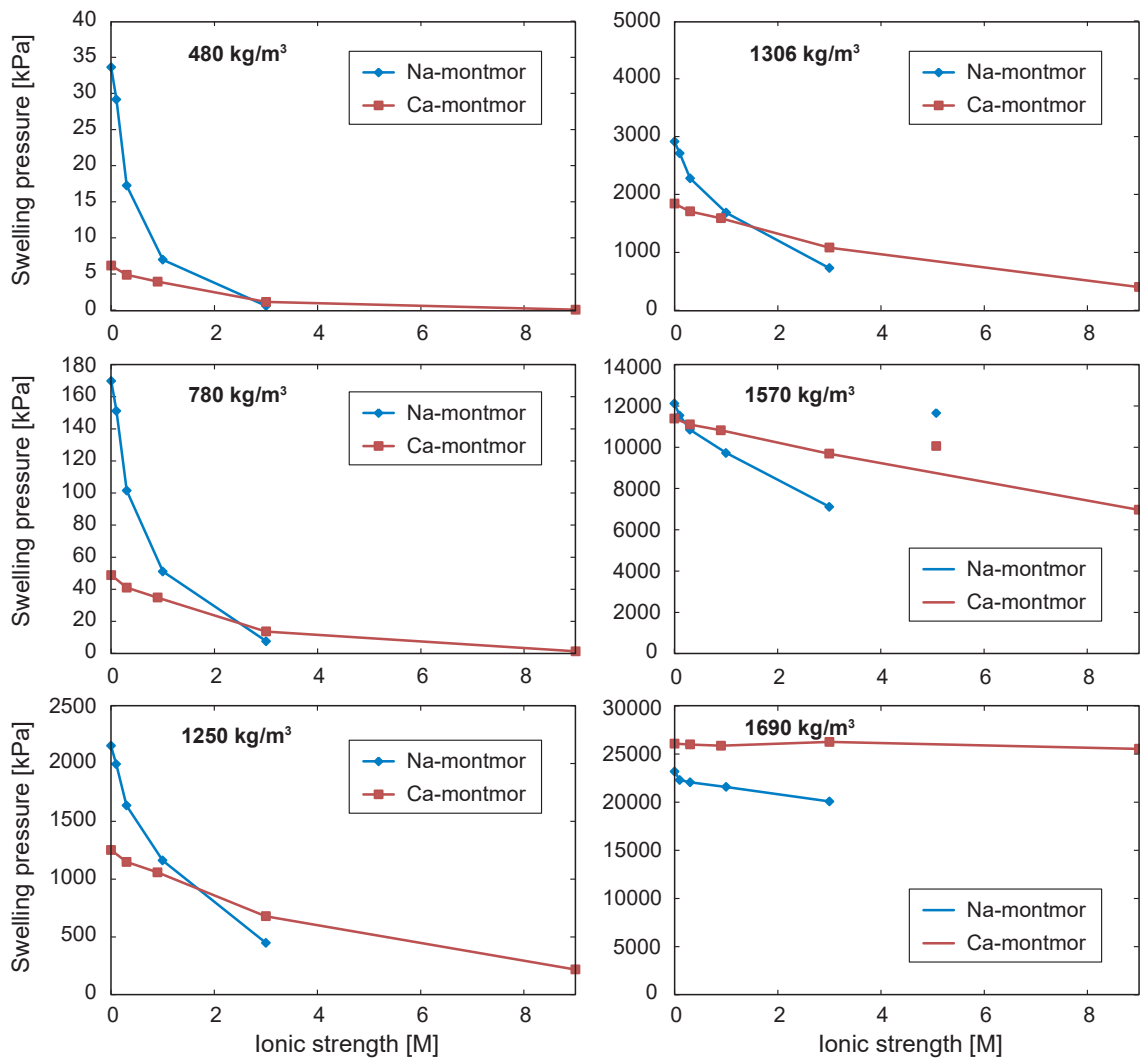


Fig. 3-67: Swelling pressure of Na-montmorillonite in NaCl and of Ca-montmorillonite in CaCl₂ solutions of different ionic strengths at different dry density values

The montmorillonite dry densities approximately correspond to MX-80 dry densities of 600, 945, 1,445, 1,500, 1,757, and 1,870 kg m⁻³ (calculated from the EMDD above). Data from Karnland et al. (2006) were fitted exponentially to estimate swelling pressures of Na- and Ca-montmorillonite at equal densities (data were originally measured at different densities). Lines are shown for better readability only.

Direct observations of pore size distributions at different ionic strength but constant dry density are scarce. The XRD measurement of basal spacings in montmorillonite equilibrated with different NaCl concentrations (Fig. 3-68) clearly shows the presence of 15.6 Å basal spacings above 0.08 M NaCl (Kozaki et al. 2008). The corresponding peak increases with increasing concentration up to 0.5 M NaCl. At 0.08 M NaCl or below, only basal spacings near 18.8 Å are observed at the low constant dry density of 1,000 kg m⁻³ (corresponding to approximately 1,185 kg m⁻³ MX-80 dry density). More recent measurements and elaborated data processing result in larger basal spacings of more than 30 Å at this density (Holmboe et al. 2012). The latter authors justify this large discrepancy of more than 10 Å with the data processing approach of Kozaki (simple use of Bragg's law instead of profile fitting), problems in water content determination, or material differences (larger particle size). However, the appearance of the two water layers basal distance at higher ionic strength cannot be explained by these or other artefacts.

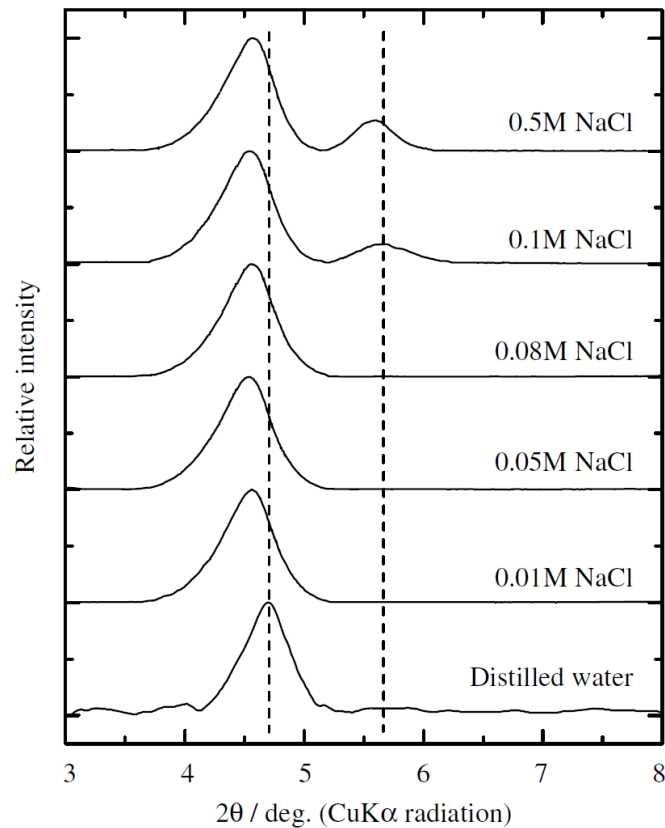


Fig. 3-68: XRD profiles of Na-montmorillonite at 1,000 kg m⁻³ dry density equilibrated at different NaCl concentrations

Left dotted line corresponds with 18.8 Å basal spacing, right line with 15.6 Å.
Kozaki et al. (2008)

Ionic strength significantly influences the diffusion through clay materials. For example, Glaus et al. (2010) report higher tracer Cl⁻ fluxes through Na-montmorillonite (1.9 Mg m⁻³ dry density) at higher ionic strengths (Fig. 3-69). In line with the findings above, basal spacing in the montmorillonite decreases with higher ionic strength, and the decreasing Donnan porosity has to be compensated with a larger proportion of free porosity (constant total volume). The increasing volume of free porewater is fully accessible to anions and must lead to a flux increase. Consistently, Van Loon et al. (2007) derive higher Cl⁻ diffusion-accessible porosities for higher ionic strengths (Fig. 3-70). This interpretation attests to the presence of a free porosity even at a high dry density of 1.9 Mg m⁻³. However, it is based on a dual porosity assumption in the data evaluation with a completely anion-free and a homogeneous and connected charge-balanced porosity accessible for anion diffusion. The underlying data of Fig. 3-70 (aqueous extracts of bentonite after the diffusion experiments) can also be explained with a partly Cl⁻ accessible Donnan porosity and a charge-balanced free porosity, which leads to a smaller ϵ_{Cl} than shown in the figure. Although the fluxes shown in Fig. 3-69 can be explained with this approach, it involves diffusive transport parameters for both Donnan and free porosities (see section 3.5.2). Representing cation diffusion, Kozaki et al. (2008) derive higher apparent self-diffusion coefficients for ²²Na⁺ for higher ionic strength. Again, the authors explain this measurement with an increasing free porosity providing a faster pathway than the Donnan porosity. The authors further divided Donnan porosity water into montmorillonite grain surface water (often called DDL) and the inter-layer water.

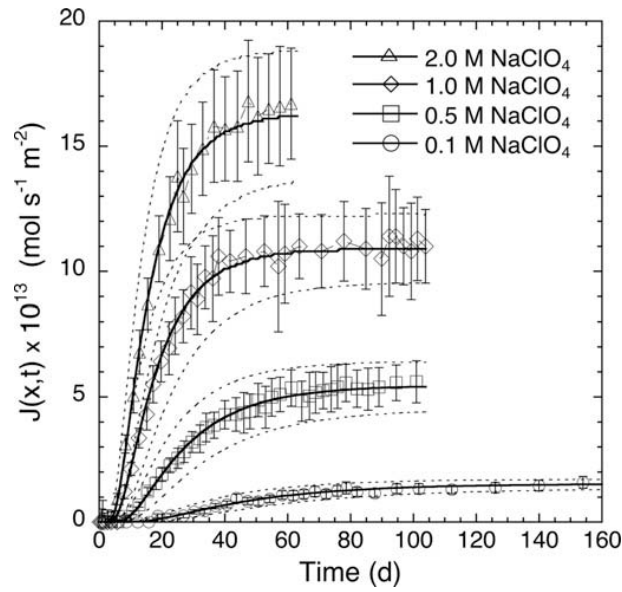


Fig. 3-69: Fluxes of tracer ^{36}Cl through Na-montmorillonite (1.9 Mg m^{-3}) in equilibrium with electrolytes of different ionic strengths
 The symbols represent the measurements.
 Glaus et al. (2010)

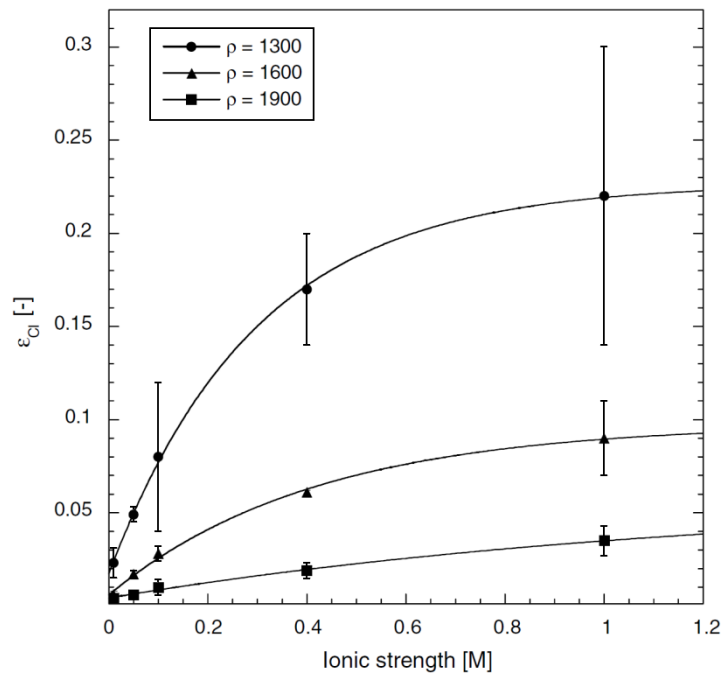


Fig. 3-70: Diffusion-accessible porosity of Cl^- in bentonite (ϵ_{Cl}) as a function of the ionic strength of the porewater for different bulk dry densities
 Van Loon et al. (2007)

Ionic strength clearly influences hydraulic conductivity in montmorillonite (Fig. 3-71, Karnland et al. 2006), and is confirmed by several additional studies (Zhu et al. 2013, Chen et al. 2015, Jenni & Mäder 2017). In general, conductivity increases with higher ionic strength at constant dry densities up to around $1,400 \text{ kg m}^{-3}$. At higher densities, and also in the case of Ca-montmorillonite, this effect is less obvious or within the error of the method, which increases drastically at high densities (errors not stated by the author). This behaviour may also be explained with an interlayer distance decrease at higher ionic strengths, which has to be compensated with an increasing free porosity. Permeability within the Donnan porosity can be expected to be several orders of magnitudes smaller or even negligible compared to that in the free porosity (section 3.5). Alternative unpublished explanations argue that the clay surface – porewater interaction is influenced by its chemical composition. This interaction certainly influences the movement of polar water molecules along the charged clay sheet surface and might be significant enough to influence hydraulic conductivity as a function of the carried ions. This should lead to an additional term in any kind of transport equation, and Darcy's law should no longer be valid.

Hydraulic conductivity correlates exponentially with dry density (Fig. 3-24). Only in Ca-montmorillonite at very low swelling pressures (low dry densities and/or high ionic strengths) does conductivity increase beyond this correlation. Coagulation possibly leads to preferential flow paths, and the material resembles a slurry rather than a compacted bentonite (e.g. hydraulic conductivities of $1\text{E-}8 \text{ m/s}$ in 800 kg m^{-3} Ca-montmorillonite in 3 and 9 M ionic strength CaCl_2 solution, with swelling pressures below 20 kPa, possibly below the pressure sensor sensitivity with respect to friction forces).

The exclusive dependence of osmotic swelling of clay on ionic strength has not been shown theoretically or experimentally. The data shown above indicate differences in various properties between the Na and Ca forms also at low densities and high ionic strengths, where osmotic swelling is expected to govern swelling.

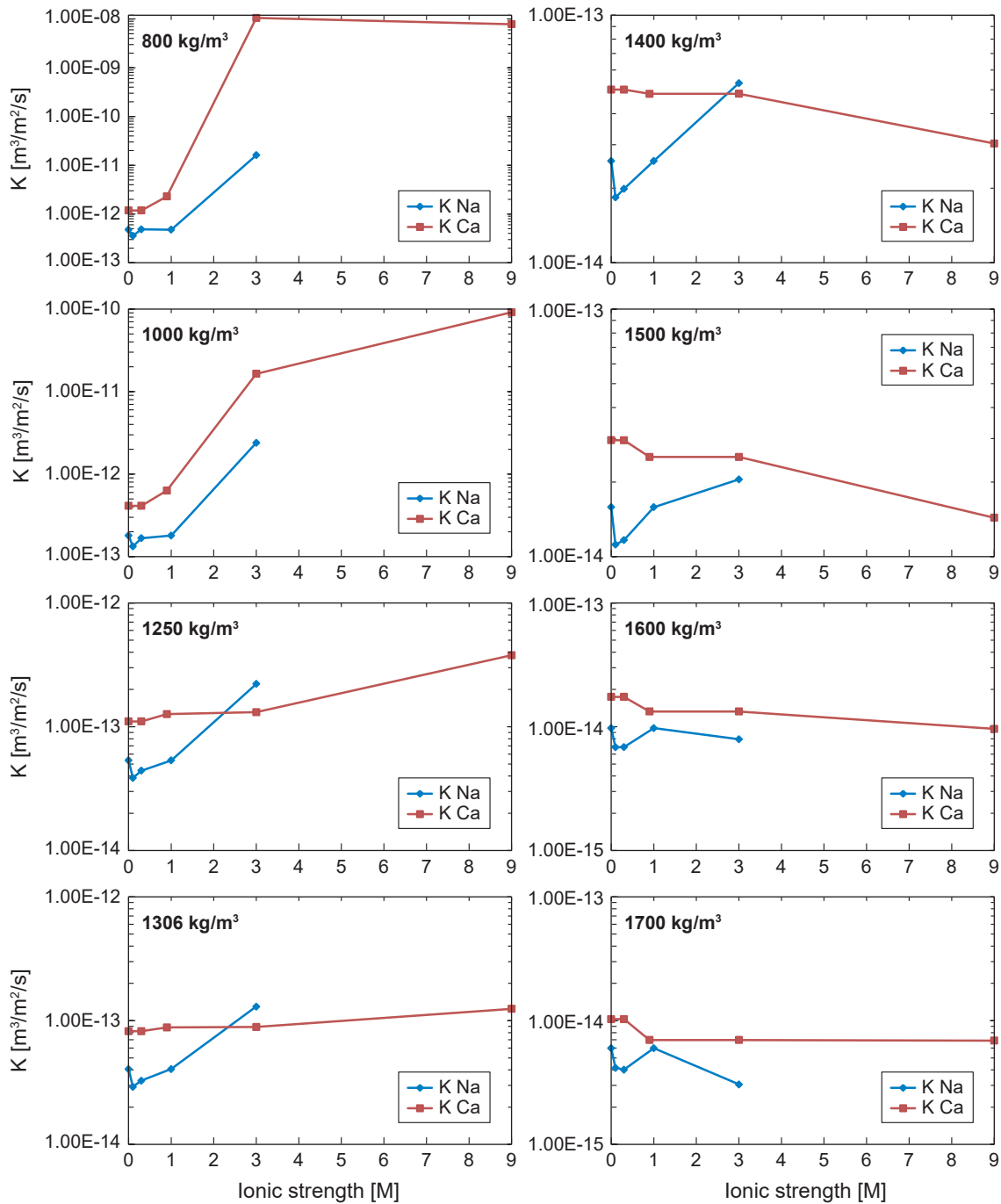


Fig. 3-71: Hydraulic conductivities of Na-montmorillonite in NaCl solutions and of Ca-montmorillonite in CaCl_2 solutions of different ionic strengths at different dry densities

The montmorillonite dry densities approximately correspond to MX-80 dry densities of 970, 1,185, 1,445, 1,500, 1,595, 1,690, 1,785 and 1,880 kg m^{-3} (calculated from the EMDD above). Data from Karnland et al. (2006) were fitted to estimate conductivities of Na- and Ca-montmorillonite at equal densities (data were originally measured at different densities). Lines are shown for better readability only.

3.8.4 Coupling of exchanger population with swelling pressure and porosity at constant volume/dry density and ionic strength

Differences in swelling pressures between Na- and Ca-bentonites are well known and are attributed to differences in crystalline swelling, e.g. different hydration behaviour of the cations. Rapidly dissolving accessory minerals influence cation occupancy, and only data from purified bentonites or from montmorillonite should be compared at equal ionic strength. In most studies comparing swelling pressures or pore size distributions of Na- and Ca-montmorillonite, a homo-ionic treatment was done in suspension, where flocculation occurs in the Ca form only and microstructural differences are to be expected also in the compacted form produced from treated material. The cation exchange of a confined sample (by diffusion or by advection/diffusion) is time-consuming due to the comparably large CEC and small transport rates. The required long-term measurement of hydraulic conductivity and swelling pressure is therefore tedious and rather demanding. Most likely, short tests did not reach geochemical equilibrium and thus they average a complex transient process. However, data of an ongoing long-term experiment (MX-80 at $1,470 \text{ kg m}^{-3}$) show an increase in swelling pressure after the change from 3 M ionic strength NaCl to 3 M ionic strength CaCl_2 in agreement with Fig. 3-67 (Jenni & Mäder 2018, Fig. 3-72). Simultaneously, hydraulic conductivity decreased from $4.2 \times 10^{-13} \text{ m/s}$ (NaCl) to $2.1 \times 10^{-13} \text{ m/s}$ (CaCl_2) within the confined constant volume sample. Similar to the ionic strength effect, the exchange of cations might alter the pore size distribution (at constant total porosity), which again changes conductivity.

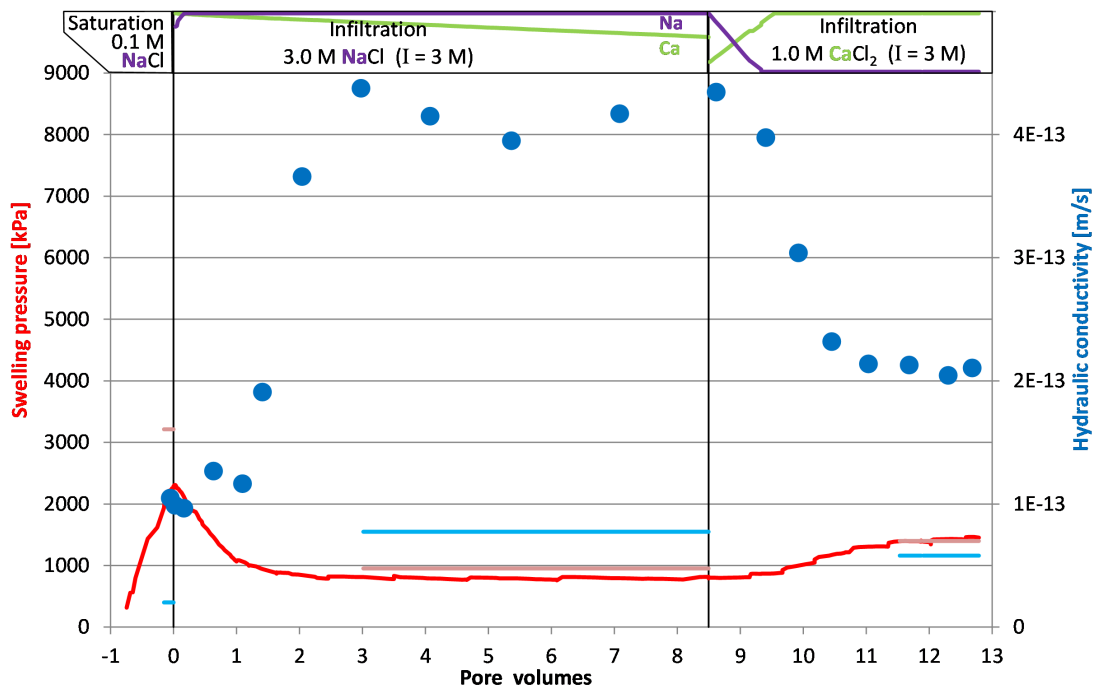


Fig. 3-72: Evolution of swelling pressure and hydraulic conductivity of a compacted MX-80 bentonite disc of $1,470 \text{ kg m}^{-3}$ dry density during infiltration of different electrolytes

Swelling pressure in red, conductivity in blue, infiltration solutions indicated at the top. The pale red and pale blue lines indicate values measured at equal EMDD by Karnland et al. (2006). The top graph indicates Na and Ca fractions of the total cation pool at equilibrium, estimated from simple mass balance considerations. One pore volume refers to the total water content in the bentonite disc; the 14 pore volumes required 3.25 years of infiltration at infiltration pressures in the range of 100 – 600 kPa.

Jenni & Mäder (2018)

Fig. 3-67 shows higher swelling pressures in Na-montmorillonite than in Ca-montmorillonite at densities below 800 kg m^{-3} and below 3 M ionic strength. Pressures are higher in the Ca form at high ionic strength. This trend continues with increasing densities, and at densities above $1,600 \text{ kg m}^{-3}$ Ca-montmorillonite swelling pressures are higher at all ionic strengths considered (MX-80).

A dual porosity concept implies that swelling pressure influences the pore size distribution. In contrast, Fig. 3-73 suggests equal interlayer spacings for Na- and Ca-montmorillonite at $1,000 \text{ kg m}^{-3}$ dry density, as well as for mixed Na-Ca occupancies. Holmboe et al. (2012) found the same interlayer spacing (18.8 \AA , three water layers) in both forms (700 kg m^{-3}) but detected an additional low-angle reflection at $35 - 40 \text{ \AA}$ thanks to an improved XRD set-up (Fig. 3-74). This basal spacing is explained by the formation of repulsive diffuse double layers (osmotic swelling). The density at which the transition from crystalline to osmotic swelling occurs depends on the cation. If basal spacings of 40 \AA are considered as interlayer, Fig. 3-74 suggests that the average interlayer distance of Na-montmorillonite is considerably higher than that of the Ca form (at a density of 700 kg m^{-3}). Measurements from the same authors on unconfined samples (Fig. 3-75) also indicate larger basal spacings in Na-montmorillonite. This again agrees with lower hydraulic conductivities observed in Na-montmorillonite at this density (Fig. 3-71), caused by a lower advection-relevant free porosity fraction.

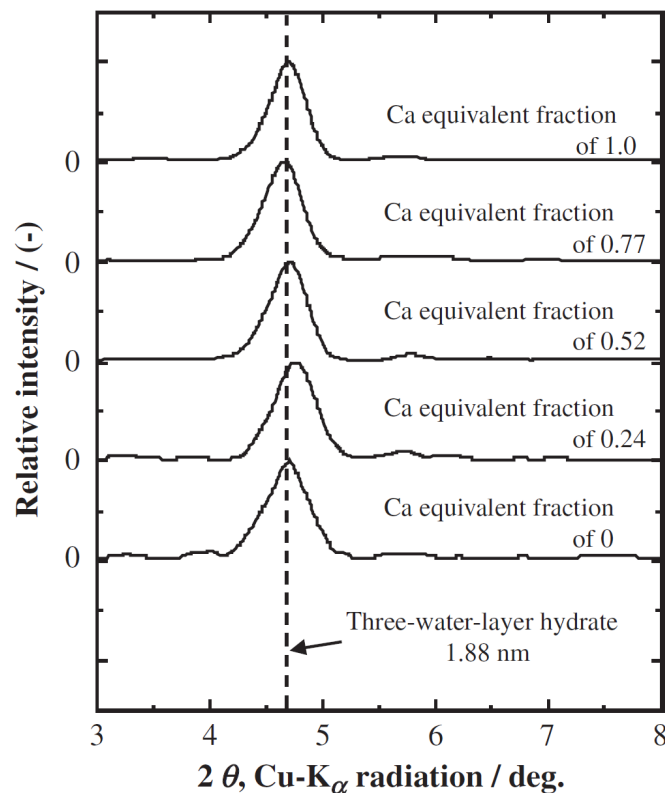


Fig. 3-73: XRD profiles of Na-Ca-montmorillonite at $1,000 \text{ kg m}^{-3}$ dry density with different Na/Ca occupancies

Saturated with distilled water.

Kozaki et al. (2010)

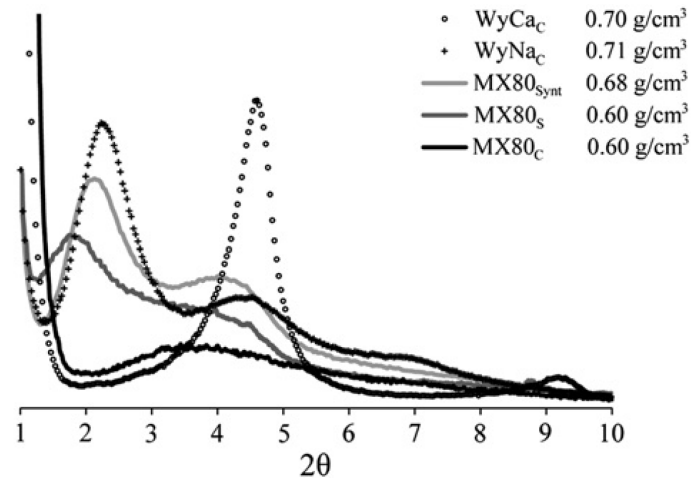


Fig. 3-74: XRD profiles of Ca-, Na-montmorillonite and MX-80

Subscripts: C: confined saturation, S: unconfined saturation, Synt: mixture of 80 % WyNa_C and 20 % WyCa_C. Measured with Cu K α radiation.

Holmboe et al. (2012)

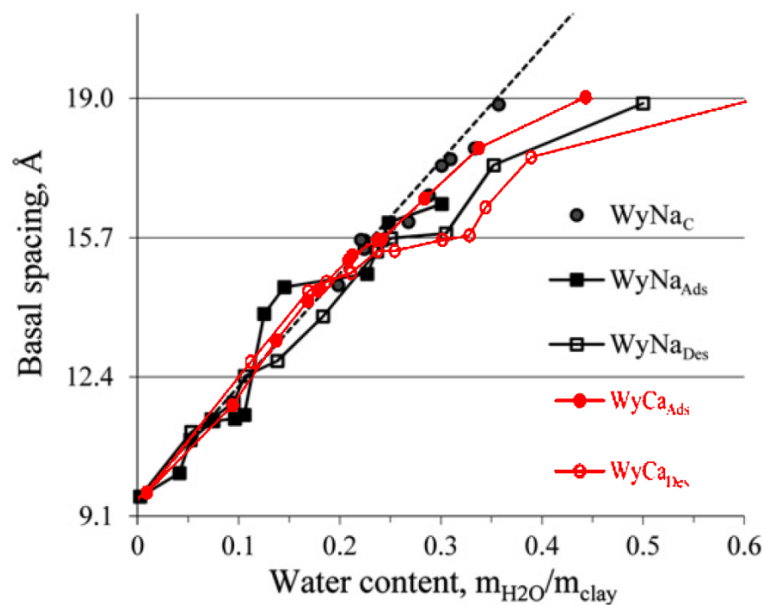


Fig. 3-75: Comparison of basal spacings derived from XRD of Na- and Ca-montmorillonite saturated from vapour phase under unconfined conditions, and confined saturated with 1 mM NaCl (WyNa_C)

Subscripts Ads and Des: measured after adsorption and desorption.

Holmboe et al. (2012)

Choi & Oscarson (1996) consistently measured higher HTO, I, and Sr²⁺ diffusive fluxes across purified Ca-exchanged Avonlea bentonite than across the Na form (both at 1,300 kg m⁻³ dry density). They attribute these differences to the larger particle size and therefore greater portion of larger pores in Ca-bentonite. This interpretation is supported by MIP, which shows an accumulation of 1 μ m pores in Ca-bentonite that is missing in the Na form. Kozaki et al. (2010) derived

apparent diffusion coefficients for HTO and $^{45}\text{Ca}^{2+}$ across Na- and Ca-montmorillonite mixtures with different ionic equivalent fractions of Ca^{2+} ions at a dry density of $1,000 \text{ kg m}^{-3}$. The apparent diffusion coefficient of HTO increased slightly with an increase in the ionic equivalent fraction of Ca^{2+} , but the coefficients for $^{45}\text{Ca}^{2+}$ remained in the same range. An increase in the faster free porosity pathway with higher ionic strength could explain the HTO behaviour, whereas additional processes like $\text{Ca}^{2+}/\text{Na}^{+}$ redistribution between Donnan/free porosity or in the Stern layer may complicate the interpretation in the case of $^{45}\text{Ca}^{2+}$.

No direct measurements of Na-/Ca-montmorillonite (or other) basal spacings at higher densities (crystalline swelling) could be found. However, differences in hydraulic conductivity and swelling pressure at high densities suggest an effect of the cation population on pore geometry.

Li^{+} occupancy can lead to a substantial decrease in swelling pressure, especially at elevated temperatures. This phenomenon is not caused by the presence of Li^{+} in the interlayer but is attributed to the incorporation of Li^{+} into octahedral vacancies in the smectite TOT layer, which then decreases layer charge, CEC, and therefore swelling pressure (section 3.1.1). This mechanism can be used to determine the smectite content (Greene-Kelly 1953, 1955).

3.8.5 Conceptual uncertainties of CMH coupling relevant for the Nagra concept

Clear evidence exists for the influence of ionic strength on swelling pressure of bentonite, on the pore space distribution, and transport properties in bentonite. Internal chemical influences such as cement degradation lead to changes in ionic strength and cation occupancy during and after the thermal period of a repository. Elevated ionic strength leads to an unknown increase in the free porosity fraction, which will accelerate diffusive transport, especially of anions. Furthermore, advection and gas transport will also increase. CM coupling is qualitatively acknowledged in Cloet et al. (2014), but swelling pressures are only roughly estimated based on Karnland et al. (2006) in that study.

Changes in swelling pressure with ionic strength can roughly be estimated based on literature data, although only for pure Na and Ca bentonites. No quantitative basis exists for the influence on pore size distribution. In the range of 0 – 3 M ionic strength, hydraulic conductivity is expected to rise from $3 \times 10^{-14} \text{ m/s}$ to above $1 \times 10^{-13} \text{ m/s}$ (Na-montmorillonite at $1,500 \text{ kg m}^{-3}$) but always remains near $1 \times 10^{-13} \text{ m/s}$ for Ca-montmorillonite.

Various literature data suggest a significant influence of cation occupancy on swelling pressure, pore size distribution, and transport properties in bentonite in the osmotic density range. The effect is unclear at higher density. Preparation artefacts impair the comparability of Na and Ca bentonites. Furthermore, consistent data exist only for pure Na and Ca forms and are very limited for other cations or mixed cation occupancies.

Certain studies postulate the non-existence of free ("bulk-like") water in bentonites even with dry densities as low as $1,450 \text{ kg m}^{-3}$: in a freezing experiment, confined bentonite behaves similar to an ordinary salt solution, and no sign of free water freezing is observed (Birgersson et al. 2008). This and other evidence imply that interlayer spacing must remain constant at constant total volume, because there is no free porosity volume that could compensate for a change in basal spacing. However, no unambiguous measurement so far shows if interlayer distance in montmorillonite at constant total volume responds to chemical changes. Therefore, transport properties in bentonite in varying chemical conditions cannot be predicted without considerable uncertainties.

The possible variation of pore size distribution and the subsequent effect on ion transport has not yet been considered in any report about interactions of bentonite with adjacent materials (Bradbury et al. 2014, Kosakowski et al. 2014, Savage 2014).

Karnland et al. (2006) provide the only consistent swelling pressure and hydraulic conductivity data for bentonite equilibrated with different ionic strengths and cation occupancies. More fragmentary alternative data scatter considerably (e.g. Agus & Schanz 2008, shown in Fig. 3-64, or Kaufhold et al. 2015a).

No effect of filler contents below 40 % on swelling pressure has been postulated. The swelling pressure of a montmorillonite-accessory mixture is claimed to depend only on the EMDD (at constant montmorillonite structure, CEC, cation occupancy, saturation solution). More data are required to underpin this assumption, especially regarding the use of sand-bentonite mixtures with high sand contents.

3.9 Impact of high temperatures on the performance of montmorillonite

The impact of higher temperatures on the stability of montmorillonite during the initial stage after repository closure has been an issue of concern in the past (Grauer 1990). This aspect has recently been elaborated in detail by Leupin et al. (2015), where literature findings were reviewed, and new data were discussed. Here the most relevant aspects are summarised.

Smectites generally form in low temperature environments, but under favourable conditions may also form at temperatures > 100 °C. The stability of smectites is still not well established because of high uncertainty of the underlying thermodynamic data (section 3.2). Nevertheless, these suggest the important role of Si, pH and K^+ in constraining smectite stability, besides temperature.

The most common alteration of montmorillonite in nature is its transformation to illite. This process depends primarily on time, temperature and potassium activity, but also on SiO_2 activity, pH, layer charge, nature of exchangeable cations, pressure and water activity. The transformation reaction is complex and still not fully understood. Strongly variable kinetic rates, rate expressions and activation energies have been reported in the literature. Reviews of these studies in the context of repository conditions (Karnland & Birgersson 2006, Leupin et al. 2015) lend support to experimentally determined reaction rates pointing to high activation energies (~ 30 kcal/mol) such as that by Huang et al. (1993). Using the rate expression proposed by these authors leads to negligible illitisation for Nagra's or the KBS-3 repository concepts. It is noted that mass transfer limitation of K^+ supply and the fact that the thermal period will occur to a significant extent under unsaturated conditions will further limit the transformation reaction.

Another transformation process is chloritisation, which is less common for dioctahedral smectites and expected to occur at higher temperatures than illitisation.

A further temperature-related process is the transformation to beidellite occurring via preferential release of Si and increase of tetrahedral layer charge. This process has been observed in some sediments as the initial process of illitisation (Meunier et al. 1998), sometimes accompanied by the formation of saponite (Beaufort et al. 2001). Saponite formation at the expense of montmorillonite has also been based on thermodynamic considerations (Wilson et al. 2006, Wilson et al. 2015) and observations from in-situ experiments (Svensson 2015, section 5.8). It should be noted that saponite is also a swelling smectite mineral. A saponite formation reaction is thus expected to have a much smaller effect on the bentonite barrier compared to illitisation.

4 Reactive transport and thermo-hydro-mechanical modelling

Experiments including bentonite saturation and performance under various chemical conditions provide valuable information, but the observations are short-term relative to the repository lifetime. In addition, the high costs, particularly of real-scale experiments, limit the number of experiments and therefore the variability of experimental parameters (bentonite type, dry density, host rock, type of saturation water, geometry). These limitations emphasise the importance of predictive modelling. In addition, coupled processes in the complex EBS can be difficult to understand, and modelling can help to reveal or verify the processes.

The first part of this section is limited to reactive transport studies and codes that consider the charged clay surface. Reactive transport modelling approaches combine equilibrium concepts (discussed in section 3.4.1) and transport mechanisms (section 3.5) within an n-dimensional grid (Steeffel et al. 2014). Several codes include, and can often solve, both phase equilibria and transport within one global matrix (global implicit reactive transport mode, option in CrunchFlow, Flotran). If a reaction and a transport code are coupled ("coupled codes"), phase equilibria and transport equations must be solved sequentially, which is generally more time-consuming and/or involves larger numerical errors. For "externally" coupled codes, an interface between the chemical and the transport code is required to provide the data transfer (codes that are coupled "internally" include this interface, e.g. option in CrunchFlow, Flotran). Particularly externally coupled codes often allow for complex grid geometries and parallelisation, normally limited in all-in-one codes. Wissmeier & Barry (2011) pioneered this development by coupling PhreeqC and COMSOL Multiphysics[®] (copied and applied to other codes by Amphos21). Further examples are the GEMS – OpenGeosys coupling (Kosakowski & Berner 2013), and very recent couplings of CrunchFlow chemistry with various transport codes for commercial use by Amphos21.

Interactions between the porewaters of bentonite and other materials present in a repository setting go beyond simple tracer transport that might be handled by groundwater flow codes. Charge balance must be considered, and a multicomponent transport concept is indispensable, where the transport of all solutes is explicitly coupled. Diffusive transport has to be combined with electromigration (Nernst-Planck equation) if different species diffusion coefficients are used (e.g. Tournassat & Steeffel 2015). This is also required if charged clay surfaces are to be included explicitly in the model, which allows for an implicit consideration of Donnan behaviour (Gimmi & Alt-Epping 2018). Approaches not considering clay sheet surface charge fail to predict transport of differently charged species in clay correctly (Alt-Epping et al. 2015). Only an explicit consideration of charge balance allows coupled reactive transport simulations to be performed. Simplified approaches, such as attributing species-specific porosities (e.g. to anions), fail when it comes to coupled reactive transport considering all porosity domains.

The few and limited modelling approaches that couple hydro-mechanical processes in bentonite with geochemical processes are described in section 4.4. Numerical modelling of gas transport and THM processes are discussed in sections 4.5 and 4.6, mainly to reveal if, and to what extent, geochemical processes are considered.

4.1 Justification and applicability of coupled codes considering charged clay surfaces

The influence of negatively charged clay sheet surfaces on bentonite porewater is widely accepted. The static charge leads to a fractionation of aqueous species in the porewater based on their valence. Single-porosity codes assign equal transport properties for all species, or different but constant transport properties to individual species (e.g. diffusion-accessible or advection-active porosities, tortuosities). Both approaches may hold for static microstructures but fail in the case of porosity changes: in this case, the transport properties should change individually for the species. In the experiment described by Chagneau et al. (2015), the diffusion-accessible porosity of anions in a compacted illite should approach zero after celestite precipitation, because the Cl flux stops. In contrast, HTO flux continued at a lower value (Fig. 4-1). Such a species-dependent coupling of transport and porosity changes is generally not implemented in single-porosity transport codes, with the exception of the recent example of Flotran (Gimmi & Alt-Epping 2018). No transport simulations have been done so far with Flotran considering a single Donnan porosity and precipitation. Idiart & Pekala (2016) compared the performance of single-porosity (only free porosity) and dual-porosity approaches by predicting measured anion and cation concentrations in the ABM1 experiment. They concluded that only multi-porosity models can account for the multi-physical coupling expected in the near-field and that such models are invaluable for the understanding of radionuclide diffusion through bentonite.

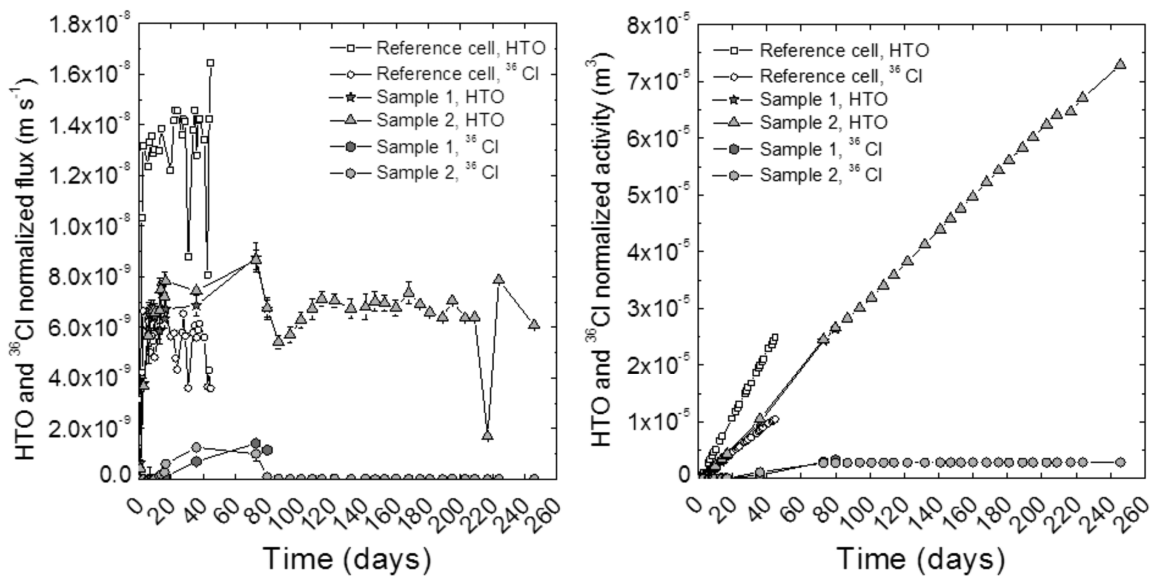


Fig. 4-1: Fluxes and cumulative activities of HTO and ³⁶Cl⁻ in a through-diffusion experiment
 Reference cell: no celestite precipitation, samples 1 + 2: celestite precipitation induced by SrCl₂ and Na₂SO₄ diffusion from opposite sides starting at 0 d, sample 1: stopped at 80 d for post-mortem analysis.
 Chagneau et al. (2015)

4.2 Equilibrium calculations

4.2.1 Aqueous – solid equilibria

Most reactive transport codes define the solid-liquid equilibria with equilibrium constants ($\log K$). In contrast to the generally well-established data of most bentonite secondary minerals, thermodynamic properties for smectites are controversial (section 3.2). Solubility experiments indicate that equilibrium cannot be attained. This questions the thermodynamic equilibrium approach, the basis for reactive transport modelling. Uncertainties propagate to the outcome of numerical simulations and question the predictions of smectite stability, especially at high temperature or extreme pH conditions.

Reaction among aqueous species is treated as instantaneous, whereas most codes allow for kinetically controlled solid-liquid reactions. Again, reaction kinetics of secondary minerals are better constrained than those of smectites. Bentonite accessory minerals such as gypsum and calcite influence porewater chemistry in MX-80. Dissolution of these minerals is often controlled by the slow transport in compacted bentonite, and the accuracy of reaction kinetic data is less crucial. In the case of smectites, data on reaction kinetics are controversial. Due to slow dissolution rates, it is uncertain in many cases if smectite dissolution is controlled by reaction rates (porewater undersaturated with respect to smectite) or controlled by transport in the case of interaction of bentonite with another material. However, the relationship between dissolution and transport defines the evolution at an interface (e.g. porosity clogging or propagation of a reaction plume into a material).

Both the thermodynamic and kinetic data mentioned in section 3.2 describe montmorillonite consisting of a basal sheet and cations balancing its negative charge and sometimes include the hydration water in the interlayer. In the dual porosity approach, both cations and water are located in the Donnan porosity and do not belong to the solid phase representing the montmorillonite basal sheets. In theory, thermodynamic and kinetic data are required that describe only these negatively charged sheets. In turn, cation occupancy and hydration state should influence the sheet dissolution/precipitation as indicated by experiments. However, the thermodynamic data of the sheet will not depend on the composition of the Donnan porewater, which is required to evaluate experimental data. Up to now, no efforts have been undertaken to solve these issues. Therefore, dual porosity reactive transport modelling cannot accurately predict the stability of montmorillonite at present. Reaction rates can be assumed to be equal for both the basal sheet and the entire mineral, including Donnan porosity.

Many of the well-established reactive transport codes derive changes in porosity from the mole balance and molecular volumes of precipitated or dissolved minerals. If hydrates are involved, this water should also be balanced. If this is not done (as in most codes except for free energy minimisation approaches), a water imbalance will arise. In the case of cement (clinker) hydration, for example, the decrease of free water in the porosity should increase concentrations of non-reacting K and Na species. Therefore, such approaches fail to predict concentration changes of non-reactive species, which can significantly influence pH in the case of cement hydration. Such a water consumption or release by hydrates should also lead to additional advective fluid fluxes in or out of a modelling domain (e.g. for compensation of so-called chemical shrinkage during cement hydration).

Alternatively, a Gibbs free energy minimisation routine determines the phase assemblage in the equilibrium code GEMS. Here, water as well as gas are treated as phases entering all reaction equations. Therefore, no water imbalance builds up and porewater composition adapts to implied

changes in porosity. In this non-kinetic approach, however, minimal changes in total chemistry of the system can lead to a completely different phase assemblage, which is not consistent with observations. A kinetic control of mineral reactions in GEMS is in preparation.

4.2.2 Consideration of clay surface charge

Recently, the influence of the negatively charged clay sheet surfaces was included in several transport codes. This static charge influences either the entire porewater or parts of it. The concepts are described in sections 3.3.1 and 3.4.1.

The transport model of Birgersson & Karnland (2009) assumes that the static charge influences the entire porewater. The Donnan equilibrium defines the chemical composition of this charge-imbalanced porewater as a function of the water chemistry outside the bentonite (reservoir, porous rock or filter). Implementing the Donnan equilibrium in a reactive transport code and following the single (Donnan) porosity approach (e.g. Gimmi & Alt-Epping 2018) allows handling of complex reactive transport including different activity calculation options, aqueous speciation, and mineral dissolution/precipitation. However, no such calculations have been done so far.

Various approaches segment total porosity into different domains, such as interlayer porosity, porosity on clay grain surfaces (DDL), and free porewater (section 3.3.1). Wersin et al. (2016) compare the two approaches in equilibrium systems without transport, calculated in PhreeqC:

- The triple porosity concept distinguishes free, interlayer and DDL (grain surface) porewater. The interlayer water is considered as anion-free and its cation content is simulated via cation exchange reactions. The Donnan equilibrium with the free water defines the DDL water composition (section 3.4.1). Interlayer and DDL volumes are derived from crystallographic considerations (stacking number, interlayer thickness, sheet and grain dimensions of montmorillonite, mostly rather speculative). In theory, PhreeqC can simulate diffusive transport in all three porosity domains, although interlayer and DDL diffusion options are not straightforward to implement in a simulation and often require interaction with the author of the code.
- The dual porosity concept lumps together interlayer and DDL porosity into Donnan porosity, as both compositions are controlled by the negative clay sheet surface. Equal interlayer and DDL thicknesses are assumed. Again, the Donnan equilibrium defines the chemical composition of the Donnan porosity. This approach is implemented in PhreeqC and CrunchFlowMC (Alt-Epping et al. 2015), allowing for diffusive transport in both porosity domains (next section). Gimmi & Alt-Epping (2018) present an alternative approach of the same concept: the Donnan porosity contains immobile anions representing the CEC. Relatively fast diffusion/electromigration (Nernst-Planck equations) of remaining aqueous species leads to a close to instantaneous equilibrium between Donnan and free porosity. Virtually any multi-component transport code containing Nernst-Planck can simulate a dual porosity system with this approach. The fast transport between the two porosity domains relative to the transport across the entire system (e.g. under a concentration or pressure gradient) requires short time-stepping, which leads to extensive calculation times. Nevertheless, this approach was already successfully applied to a clay-cement interface (Jenni et al. 2017).

It is worth noting that, depending on the (external) equilibrium solution, the Donnan approach predicts a considerable amount of anions in the Donnan porosity. This agrees with molecular dynamic simulations of interlayer porewater in contact with free porewater or with an external reservoir (e.g. Tinnacher et al. 2016). The anion accessibility of the Donnan porosity depends on the anion concentration in the free water, the Donnan potential (representing the CEC), the valence of the anion, and on the volumes of the two porosity domains, as they influence concen-

trations. From this it follows that the volume distribution between Donnan and free porosity (mainly controlled by the interlayer distance) is an important parameter with respect to the degree of anion exclusion.

PhreeqC and CrunchFlowMC simplify the Donnan equilibrium (strictly valid for activities only) by applying the activity coefficient calculated for the free porosity species to the Donnan porosity species. Under this assumption, the Donnan equilibrium can be written for concentrations (eq. 5). This simplification is questionable (Birgersson 2017). In the Nernst-Planck Donnan approach, the diffusive flux of aqueous species between Donnan and free porosity should strictly also depend on activity gradients between these domains, and not on concentrations. Then, it is possible to consider different activity models in the Donnan and the free porewater. At present, nothing is known about activities in the Donnan porosity, but such activities can significantly influence the calculated ion distributions. Alt-Epping et al. (2018) numerically evaluated the influence of different activity definitions with the Nernst-Planck approach in a double porosity simulation of MX-80. Birgersson (2017) suggests the mean salt method for calculation of activity coefficients in the interlayer and demonstrates that the activities can then be used for calculation of the Donnan equilibrium.

In addition, a Stern layer or edge sites can be taken into account explicitly. Surface complexation sites are then implemented to represent more specific sorption (e.g. inner-sphere complexes). Selectivity coefficients and site densities of three different sites derived from experimental data are reported by Bradbury & Baeyens (2002) for MX-80. In turn, selectivity coefficients reported by the same authors and others describe the total cation exchange, which is the sum of exchange at Stern layer surface sites plus the (ion) exchange between Donnan and free porosity. Therefore, the reported site densities and selectivity coefficients must be considered as model-specific (Gimmi & Alt-Epping 2018), and the site density and selectivity coefficients describing the Stern layer surface complexes are not known independently. The sum of the negative charge compensated by the Stern layer and by the Donnan porosity should equal the CEC.

The Donnan – free porewater equilibrium is considered as instantaneous and as such implemented in PhreeqC and CrunchFlowMC. Only the Nernst-Planck approach allows for a kinetically controlled Donnan equilibrium by slowing down diffusion/electromigration between Donnan and free porosity. However, little research has been done on this issue.

4.3 Ion transport

In most codes, Darcy's law describes *advective transport*. So far, it is widely assumed that, in a dual-porosity approach, advection is restricted to the free porosity. This assumption is questionable (see section 3.3.5, last paragraph) and a point for further investigation, but it reduces advective transport through clays to a mono-porosity advection case extensively described in the literature. Numerical model set-ups make use of two different modes:

- The water flux is known from measurements, e.g. a constant hydraulic gradient column experiment. The water flux, or its evolution with time, is imposed as a boundary condition. Therefore, porosity changes of any kind do not affect the water flux.
- A more sophisticated approach calculates the water flux based on hydraulic head gradient and permeability. The latter can be input as an initial condition but can also be updated with changing porosity using some empirical relationship (e.g. Kozeny-Carman) as done in CrunchFlowMC.

Changing porosity due to mineral precipitation/dissolution in a specific cell will alter porewater pressure. Local pressure gradients towards neighbouring cells cause local advective flow that adds to the overall advection. Most of the well-known reactive transport codes ignore this process, because the water phase is not included in the overall water balance (similar to reactions including solid hydrates, described in section 4.2.1). This inconsistency is insignificant in the case of small porosity changes but violates the mass conservation law substantially if pore clogging occurs. An updated version of CrunchFlowMC considers this effect, presently in a beta version.

Diffusion of aqueous species is expected to dominate transport in a clay-dominated, saturated repository set-up in the long term. If extreme bounding waters such as low ionic strength melt waters, cementitious fluids or brines contact the bentonite buffer, a multicomponent transport code is required to predict the interactions. In addition, the involvement of the static charge of the clay and multicomponent species transport requires the inclusion of electromigration. The Nernst-Planck equation combines diffusion (Fick's law) and electromigration, and is implemented in PhreeqC, CrunchFlowMC, and Flotran. Diffusive transport depends in principle on activity gradients, and not on concentration gradients. However, only PhreeqC can include the activity terms in diffusive transport, whereas CrunchFlow and Flotran ignore them (an extended version of Flotran exists that includes them). In any case, activities also have an indirect influence on transport via aqueous speciation or solid reactions, both being calculated with the activities of the phases.

Typically, effective diffusion coefficients are calculated in the codes for each species (multicomponent transport) from the well-known diffusion in water (D_0) and properties of the porous media. Most codes assume a linear relationship with porosity and a constant multiplier (geometric factor or tortuosity, section 3.5.2), but this latter parameter in fact also depends on porosity. Archie's law, additionally implemented in Flotran and PhreeqC, assumes an empirical exponential function of porosity involving the exponent m (section 3.5.2). In an approach considering transport in a single porosity only (e.g. Berner et al. 2013), different transport-active porosities are chosen for anions and other species. This approach fails if pore clogging occurs. In an approach containing free porosity and Donnan porosity, the two diffusive fluxes add up (Fig. 3-36). Each flux of aqueous species requires the domain volume and the porosity characteristics (geometric factor, or m of Archie's law).

The dual porosity approach leads to the issue of pore connectivity between two materials with different pore size distributions (e.g. clay-filter interface, discussed in section 3.5.2). Very recently, an attempt was made to solve this issue in CrunchFlowMC and PhreeqC, and a modelling benchmark is planned (Christophe Tournassat, Carl Steefel). In Flotran, harmonic averaging is applied for diffusion between cells in the main transport direction. The concentration-averaging procedure in the electromigration term as implemented in Flotran was adapted to ensure consistency with the Donnan calculation. The default implementation of an arithmetic mean of neighbouring concentrations (as is typically implemented in multicomponent transport codes including electromigration) leads to major errors under certain conditions. In an example of a clay-filter contact, the free porosity in the filter is split into the proportion of free and Donnan porosity in the clay (rightmost case in Fig. 4-2). The free porosity is connected with the appropriate part of the single porosity, and the Donnan porosity with the other part of the single porosity. This connectivity is based on geometric considerations only, and, as stated by Tournassat & Steefel (2015), "... the priority that should be given to the connectivity between diffuse layer or bulk water volumes (or interlayer porosity) is not clear and the convention that is chosen must then be seen as arbitrary."

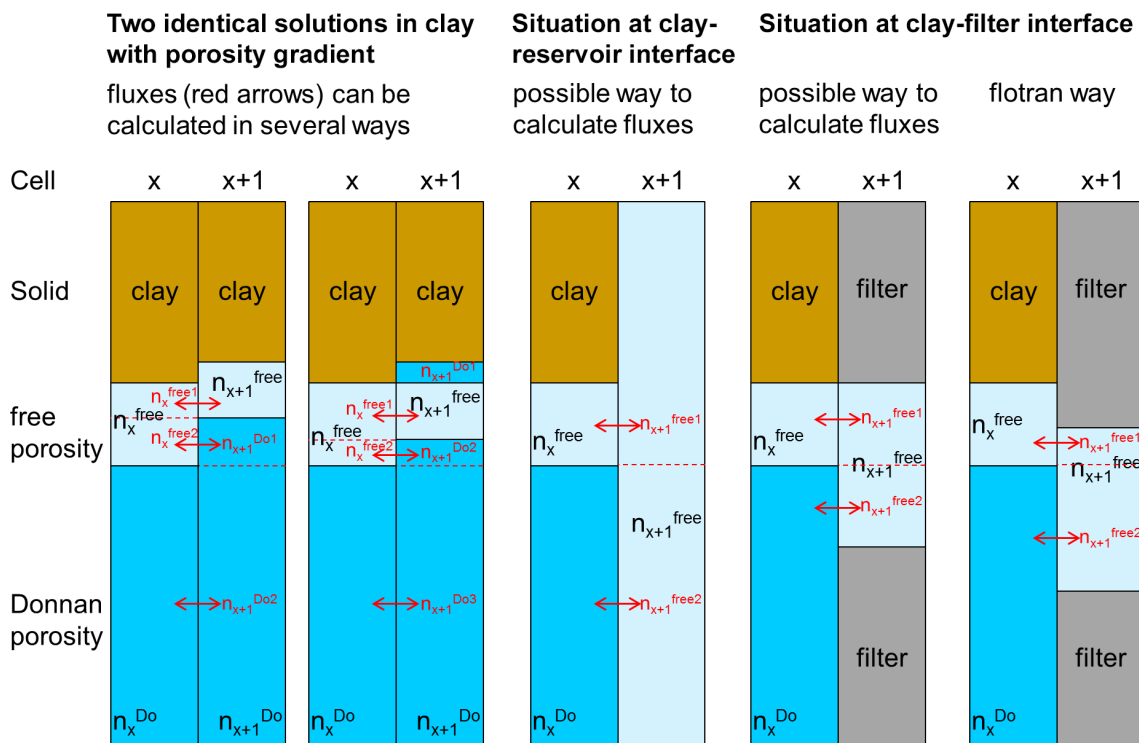


Fig. 4-2: One-dimensional representation of two cells (x , $x+1$) containing clay or clay interfaces in a dual-porosity finite element approach

Different connections between the porosity domains can be chosen to calculate fluxes.

Red arrows represent sub-fluxes between the sub-porosity domains. Volumes n are divided and rearranged for visualisation (dashed red separators, resulting sub-volumes in red). The connectivity on the very right represents the solution chosen in the Flotran approach. This figure served as the basis for the connectivity chapter in Tournassat & Steefel (2015).

4.4 CMH coupling

The coupling of chemical and mechanical issues is tackled from two different directions:

- Chemical processes such as diffusion or cation exchange are implemented into classical (T)HM codes, which then allows for the description of certain HMC interactions. Navarro et al. (2017) describe a THM model approach that accounts for salinity effects on clay swelling, based on a dual-porosity concept. The approach was applied to a saturated bentonite layer (1D) exposed to low and high ionic strength infiltrates (Yustres et al. 2017). At the current stage of code development, no mineral reactions can be modelled, and the chemistry is restricted to a Na-Ca-Cl system.
- Rudimentary mechanical properties are implemented into reactive transport codes. In a single porosity model under constant saturated volume, the effect of chemistry on pore size distribution cannot be considered: porosity is treated as a continuum, and transport properties within the porosity (e.g. tortuosity) describe pore space heterogeneities in a very simplified way. Therefore, only multiporosity approaches can take into account chemically induced changes in pore size distribution. At the moment, only a beta version of CrunchFlowMC and PhreeqC can redistribute Donnan and free porosity according to chemistry. The thickness of the DDL situated on the clay sheets is calculated by the product of a constant multiplier and the Debye length (fitting parameter, section 3.4.1). The Donnan porosity volume equals this thickness

times the total clay surface. In compacted bentonites, the DDLs in the interlayer overlap, and the multiplier is < 1 . The multiplier can be derived from diffraction measurements revealing an average interlayer distance at a given dry density and porewater ionic strength. Therefore, the multiplier, a best fit of the diffraction data, is only valid for the specific compaction (dry density) but responds to changes in ionic strength. Effects of cation occupancy on Donnan porosity volume are not yet implemented, as available data are scarce (section 3.8.4). In general, the described response to ionic strength overestimates the amplitude of Donnan porosity if compared with the few data available (section 3.8.3). In most scenarios, the total volume of the bentonite can be assumed to be constant (e.g. confined space in a repository, or constant volume diffusion cell). Then, total porosity is constant (apart from mineral reactions, section 4.2.1), and the free porosity volume equals the difference between Donnan and total porosity. Less frequently, total bentonite volume is unconfined, but the confining pressure (related to swelling pressure) is constant (Fernández et al. 2011, Jenni et al. 2014a). CrunchFlowMC can handle such saturated swelling, where total porosity and therefore total volume varies (only in 1D). The free porosity does not compensate for a change in the Donnan porosity. This approach requires the implementation of pore pressures and advective fluxes, supplying/removing the volumes arising from porosity changes (analogously to mineral reactions, section 4.2.1). However, the full implementation of this bentonite swelling would require solid fluxes across cell boundaries, or flexible grid approaches.

Presently, the coupling of chemical with hydro-mechanical properties is still in its infancy, probably due to a divide between the chemistry (reactive transport modellers) and engineering (THM modellers) communities. Primarily, however, a lack of experimental data impedes the definition of the coupling mechanisms, even on an empirical level.

Bentonite resaturation after its emplacement and repository closure involves two-phase flow and temperatures above 100 °C. Swelling pressure build-up and porosity redistribution are key processes at this stage and strongly influence solute transport and therefore also chemical reactions. Reactive transport codes that do not consider hydro-mechanical changes might reveal general processes but cannot precisely predict chemical observations related to this stage (e.g. redox behaviour and chemical inhomogeneities of bentonites as seen for example in the ABM experiments). At the moment, however, no numerical approach can handle all these processes simultaneously.

4.5 Gas transport modelling

In Nagra's repository post-closure scenarios, the phenomena and processes associated with gas transport in a bentonite-based EBS (see section 3.5) will be strongly dependent on the prevailing repository setting in terms of geological conditions (hydrogeology, geomechanics), general repository layout and detailed EBS design (bentonite emplacement density), but also on the waste inventory, which governs the gas invasion regime (e.g. rapid/slow loading). Evidence from laboratory experiments (Romero & Gonzalez-Blanco 2018) suggests that transport in bentonite is strongly controlled by both the ambient stress state and the saturation history of the material. Repeated gas flow through fully saturated bentonite gives further evidence of a certain degree of memory of the bentonite, indicating that distinct pathways are established when gas percolates through saturated bentonite. It is likely that these pathways are caused by microstructural modifications of the material as a result of capillary forces associated with the invasion of the gas phase.

As part of SKB's Task Force on Engineered Barriers, Nagra is leading a task aimed at modelling gas transport processes in bentonite along stress paths and hydration paths that are relevant for the repository post-closure phase (Dieudonné et al. 2017). Different conceptual approaches will

be used for modelling localised gas transport through saturated bentonite samples. Romero & Gonzalez-Blanco (2017), for example, proposed an embedded fracture model. Pre-defined fracture traces need to be implemented in the model. Fracture aperture depends on gas pressure, allowing for high gas transport capacity of the fracture at elevated gas injection pressure. A fracture closure pressure is specified to switch between a fracture-dominated flow regime and matrix flow. Another modelling approach is based on a workflow proposed by Senger & Marschall (2008). The stochastic approach makes use of subscale information on property distributions and mimics mechanical processes along the gas path by introducing a pore pressure-dependent permeability. A dual-porosity microstructure of the bentonite with a stochastic permeability distribution is assumed by conditioning the model with data from microstructural analyses (MIP, focused ion beam nanotomography FIB-nt). Single-phase hydraulic tests and repeated gas injection events were modelled with a conventional two-phase flow simulator. A third modelling approach draws on a fully coupled THM formulation of multiphase flow in double-structured porous media (Madaschi & Laloui 2018). A probabilistic workflow is applied for parameter estimation and uncertainty assessment. A verification and validation exercise has been specified to assess the performance of the three different approaches for their capacity to simulate gas transport processes in compacted granular bentonite.

4.6 THM coupling

Numerical modelling is used to assess the long-term performance of HLW repositories. Multi-physical processes take place in a buffer and therefore numerical codes that can cope with thermo-hydro-mechanical phenomena are essential in order to make reliable predictions. This section provides an overview of the relevant equations that govern the physical processes in a HLW repository. The THM framework presented corresponds to the one implemented in the finite element modelling software Lagamine (Charlier 1987, Collin 2003). An example of model performance is reported in section 5.1.

In the context of the SF/HLW programme, a supported argumentation needs to be developed to demonstrate that repository-induced effects (RIE) will not compromise the safety functions of the EBS and the geological barriers. In particular, the numerical studies must show that heat emission of the SF/HLW due to radioactive decay processes will not affect the long-term performance of the bentonite buffer. Phenomena and processes of potential relevance are assessed for their impact on the evolution of the HLW near-field, particularly addressing THM couplings as a consequence of heat emission, tunnel convergence in response to the excavation process, resaturation of the drifts and pore pressure recovery, the build-up of swelling pressures of the bentonite buffer and the reconsolidation of the EDZ. The complexity of the associated THM processes and interactions calls for the use of numerical models. Model-supported analyses of the THM evolution of the HLW near-field were conducted by Senger et al. (2014) and Dupray et al. 2014 as a contribution to SGT Stage 2 (SGT: Sectoral Plan for Deep Geological Repositories) in Switzerland. In the context of Nagra's RD&D programme, a multitude of modelling initiatives were accomplished as part of the FEBEX experiment (Olivella et al. 2012, Sanchez et al. 2012a, Sanchez et al. 2012b, Papafotiou et al. 2017), within the framework of the EU-funded PEBS Project (Czaikowski et al. 2012, Gaus et al. 2014, Kuhlmann et al. 2015), in the FE Experiment (Nagra 2019) and in the HotBENT Pre-study (Kober et al. 2018, Zheng et al. 2018). In the context of the EBS Task Force, Nagra participated in two THM benchmarks called "THM Sensitivity Analyses" and "Homogenisation Processes in Bentonite" (Dupray et al. 2013, Dieudonné et al. 2017).

4.6.1 Equilibrium and balance equations

Buffer and host rock materials are modelled as porous media. To describe the diffusive processes in such media, the theory of mixtures (Bowen 1982) is used. The porous media are assumed to be composed of a solid matrix and voids filled with liquid and gas phases. The liquid phase contains liquid water and dissolved air, whereas the gas phase is composed of dry air and water vapour. The equilibrium between liquid water and water vapour is controlled by temperature. To uniquely describe the state of the material, four primary state variables are required, namely gas pressure p_g , water pressure p_w , temperature T , and displacement vector u . The intrinsic solid phase component is assumed to be incompressible (incompressible grains), while the water phase is compressible. The solid, liquid and water phases are assumed to be in thermal equilibrium and a unique temperature is defined for the whole medium. This assumption is justified by the relatively slow kinematics of the governing processes which allows a continuous thermal equilibrium between phases.

The compositional approach (Panday & Corapcioglu 1989, Collin et al. 2002) is adopted to formulate the mass balance equations; thus, mass balance is described for the species rather than for the phases. Therefore, mass conservation of each chemical species (water and air) is imposed. Using this approach, the phase exchange terms cancel in the balance equations. In the following equations, the subscripts l , g , w , da , a , and v are related to the liquid phase, the gas phase, the liquid water, the dissolved air in water, the dry air, and the water vapour, respectively. An extended description of the governing equations can be found in Collin (2003), Collin et al. (2002, 2006).

The equilibrium and balance equations, as well as the water and heat flows, are expressed in the moving current configuration through an updated Lagrangian formulation (Charlier 1987). According to these assumptions, the mass balance equation of the solid skeleton is necessarily met. For a given mixture volume V , the mass balance equation reads (Collin et al. 2006):

$$\frac{\partial \rho_s (1-n)V}{\partial t} = 0 \quad (9)$$

where ρ_s is the density of solid grains, n the soil porosity, and t the time.

The mass conservation equations for the water and gas species are, respectively:

$$\underbrace{\frac{\partial}{\partial t}(\rho_w n S_r) + \text{div}(\rho_w \mathbf{f}_l)}_{\text{Liquid water}} - Q_w + \underbrace{\frac{\partial}{\partial t}(\rho_v n (1-S_r)) + \text{div}(\mathbf{i}_v + \rho_v \mathbf{f}_g)}_{\text{Water vapour}} - Q_v = 0 \quad (10)$$

$$\underbrace{\frac{\partial}{\partial t}(\rho_a n (1-S_r)) + \text{div}(\rho_a \mathbf{f}_g + \mathbf{i}_a)}_{\text{Dry air in gas phase}} - Q_a + \underbrace{\frac{\partial}{\partial t}(\rho_a H_s n S_r) + \text{div}(\rho_a H_s \mathbf{f}_l)}_{\text{Dissolved air in water}} - Q_{da} = 0 \quad (11)$$

where ρ_w , ρ_v , and ρ_a are the bulk density of liquid water, water vapour, and dry air; \mathbf{f}_l and \mathbf{f}_g are the macroscopic velocity of the liquid and gas phases, respectively; \mathbf{i}_v and \mathbf{i}_a are the non-advective flux of water vapour and dry air; S_r is the degree of saturation; H_s is Henry's coefficient, defining the proportion of dissolved air in the liquid phase, taken as equal to 0.017; and Q_w , Q_v , Q_a , and Q_{da} are volumetric sources of liquid water, water vapour, dry air, and dissolved air in water, respectively.

The energy balance equation of the mixture has the following form:

$$\underbrace{\frac{\partial S_T}{\partial t} + L \frac{\partial}{\partial t} (\rho_v n (1 - S_r))}_{\text{Heat storage}} + \underbrace{\text{div}(\mathbf{f}_T) + L \frac{\partial}{\partial t} (\mathbf{i}_v + \rho_v \mathbf{f}_g)}_{\text{Heat transfer}} - Q_T = 0 \quad (12)$$

where \mathbf{f}_T is the heat flow; Q_T is a volume heat source; L is the latent heat of water vaporisation; and S_T is the enthalpy of the system given by:

$$S_T = \rho C_p (T - T_0) \quad (13)$$

where ρ and C_p are the density and the specific heat of the mixture (solid matrix with voids filled by gas and liquid), respectively. These parameters are deduced from the properties of each phase:

$$\rho C_p = n S_r \rho_w c_{p,w} + (1 - n) \rho_s c_{p,s} + n (1 - S_r) \rho_a c_{p,a} + n (1 - S_r) \rho_v c_{p,v} \quad (14)$$

where ρ_s is the soil grain bulk density and $c_{p,w}$, $c_{p,s}$, $c_{p,a}$, and $c_{p,v}$ are the specific heat of liquid water, solid, dry air, and water vapour respectively.

The equilibrium equation is given by:

$$\text{div}(\boldsymbol{\sigma}) + \mathbf{b} = 0 \quad (15)$$

where $\boldsymbol{\sigma}$ is the total (Cauchy) stress tensor, with compressive stress taken as positive, and \mathbf{b} is the body force vector which is equal to $\rho \mathbf{g}$ as the only body force is gravity.

4.6.2 Constitutive relations

The conservation equations governing the THM equilibrium of the system (Equations 1 to 7) are expressed in terms of the primary state variables (u , p_w , p_g , and T), after introduction of the constitutive relationships. The liquid water bulk density depends on the porewater pressure p_w and temperature T through the water bulk modulus χ_w and the volumetric water thermal expansion coefficient β_w' :

$$\rho_w = \rho_{w0} \left(1 + \frac{p_w - p_{w0}}{\chi_w} - \beta_w' (T - T_0) \right) \quad (16)$$

where ρ_{w0} , p_{w0} , and T_0 are the initial values of water bulk density, porewater pressure, and temperature, respectively. The bulk density of the water vapour is determined through the following equation:

$$\rho_v = \exp \left(\frac{(p_w - p_g) M_v}{R T \rho_w} \right) \frac{p_{v,0} M_v}{R T} \quad (17)$$

where p_w and p_g are the liquid water and gas pressures, respectively, M_v is the vapour molar mass (= 0.018 kg/mol), T is temperature expressed in Kelvin, and $p_{v,0}$ is the saturated vapour pressure given by an empirical expression as a function of temperature (Gerard et al. 2008):

$$p_{v,0} = a \exp(-b/T) \quad (18)$$

with $a = 112'659$ MPa and $b = 5'192.74$ K for the temperature range between 273 K and 373 K.

The bulk density of dry air can be deduced considering that the gas phase is an ideal gas to which the Dalton law can be applied:

$$p_g = p_a + p_v \quad (19)$$

Consequently, the bulk density of dry air is:

$$\rho_a = \frac{p_a M_a}{R T} = \frac{(p_g - p_v) M_a}{R T} = \frac{p_g M_a}{R T} - \frac{\rho_v M_a}{M_v} \quad (20)$$

where M_a is the dry air molar mass (= 28.8×10^{-3} kg/mol).

The liquid phase motion is governed by Darcy's law:

$$\mathbf{f}_l = -\frac{\mathbf{k}_w}{\mu_w} (\mathbf{grad}(p_w) + g \rho_w \mathbf{grad}(y)) \quad (21)$$

where \mathbf{k}_w is the tensor of intrinsic water permeability; g the gravity acceleration; y the vertical upward directed coordinate; and μ_w the dynamic viscosity of the water. The water permeability, assumed to be isotropic ($\mathbf{k}_w = k_w \mathbf{I}$, \mathbf{I} being the identity matrix), depends on the degree of saturation S_r according to the following equation:

$$k_w = k_{w,sat} S_r^{CKW1} \quad (22)$$

where $CKW1$ is a material parameter and $k_{w,sat}$ is the saturated permeability, which depends on the soil porosity n through the Kozeny-Carman relation:

$$k_{w,sat} = k_{w0,sat} \frac{n^{EXPN} (1-n_0)^{EXPM}}{(1-n)^{EXPM} n_0^{EXPN}} \quad (23)$$

where $k_{w0,sat}$ is the saturated water permeability, corresponding to the reference porosity n_0 ; and $EXPN$ and $EXPM$ are material parameters of the Kozeny-Carman relation.

The dynamic viscosity of the water is assumed to vary with temperature according to the following form:

$$\mu_w = 0.6612(T - 229)^{-1.562} \quad (24)$$

In eq. (13), it is assumed that the ρ_w , \mathbf{k}_w , and μ_w are unaffected by the amount of dissolved air in the liquid phase.

Similar to water flow, gas flow is governed by the generalised Darcy's law for a multiphase medium:

$$\mathbf{f}_g = -\frac{\mathbf{k}_g}{\mu_g} \left(\mathbf{grad}(p_g) + g\rho_g \mathbf{grad}(y) \right) \quad (25)$$

where \mathbf{k}_g is the tensor of intrinsic gas permeability and μ_g is the dynamic viscosity of the gas, which is assumed to be linearly dependent on the temperature according to

$$\mu_g = \mu_{g0} \left(1 - \alpha_{g,T} (T - T_0) \right) \quad (26)$$

where μ_{g0} is the dynamic viscosity of the gas at initial temperature, T_0 , and $\alpha_{g,T}$ is a material parameter.

Water vapour movement is governed by diffusion and is related to the air bulk density gradient:

$$\mathbf{i}_v = n(1 - S_r) \tau D \rho_g \mathbf{grad} \left(\frac{\rho_a}{\rho_g} \right) \quad (27)$$

where τ is the tortuosity of the material and D is the air diffusion coefficient expressed according to the work of Philip & de Vries (1957):

$$D = 5.893 \cdot 10^{-6} \frac{T^{2.3}}{p_g} \quad (28)$$

where D , T , and p_g are expressed in m²/s, Kelvin, and Pascal, respectively.

Heat transport is governed by conduction and convection:

$$\mathbf{f}_T = -\Gamma \mathbf{grad}(T) + c_{p,w} \rho_w \mathbf{f}_w + c_{p,a} (\mathbf{i}_a + \rho_a \mathbf{f}_g) + c_{p,v} (\mathbf{i}_v + \rho_v \mathbf{f}_g) \quad (29)$$

where Γ is the thermal conductivity of the mixture as deduced from the thermal conductivity of each phase:

$$\Gamma = \lambda_s (1 - n) + \lambda_w n S_r + \lambda_g n (1 - S_r) \quad (30)$$

where λ_s , λ_w , and λ_a are the thermal conductivity of the solid, liquid water, and gas phase respectively. Note that since the current configuration is defined following the skeleton movement, the thermal convection effect is implicitly taken into account.

The behaviour of the solid matrix is assumed to be governed by the generalised effective stress tensor $\boldsymbol{\sigma}'$, which is based on a volume-averaged equivalent pressure as (Nuth & Laloui 2008):

$$\boldsymbol{\sigma}' = \boldsymbol{\sigma} - p_g \mathbf{I} + S_r (p_g - p_w) \mathbf{I} \quad (31)$$

In this Lagrangian approach, the Cauchy strain tensor is used:

$$\boldsymbol{\varepsilon} = \frac{1}{2} (\mathbf{L} - \mathbf{L}^T) \quad (32)$$

where $\mathbf{L} = \frac{\partial \mathbf{u}}{\partial \mathbf{X}}$ is the displacement (\mathbf{u}) gradient defined in the global axis (\mathbf{X}) in the moving current configuration.

The strain tensor is related to the generalised effective stress tensor through the mechanical constitutive model:

$$d\boldsymbol{\sigma}' = \mathbf{C} : d\boldsymbol{\varepsilon} \quad (33)$$

where \mathbf{C} is the mechanical constitutive tensor. The equation is written in incremental form in order to accommodate the non-linear behaviour of geomaterials.

4.6.3 ACMEG-TS model

The ACMEG models (Advanced Constitutive Models for Environmental Geomechanics) have been developed during the last decades at EPFL in order to deal numerically with the behaviour of geomaterials under several environmental conditions. These models are relevant for multiple geoenvironmental applications, including the performance of radioactive waste repositories.

In particular, the ACMEG-TS version (Francois & Laloui 2008) provides a stress-strain formulation suitable for implementation in boundary value codes, such as finite element, dealing with non-isothermal conditions and transitions from saturated to unsaturated states. It has been used to analyse the behaviour of geomaterials in the context of nuclear waste disposal (e.g. Dupray et al. 2013) and energy geostructures (e.g. Di Donna & Laloui 2015).

The response of the material is dependent on the Bishop's effective stress using a volume-averaged pore pressure, leading to a direct dependence of the mechanical response on the hydraulic state. In addition, the increase in apparent preconsolidation pressure with capillary suction and temperature is taken into account, defining a loading collapse curve.

The mechanical model is complemented with a water retention model that accounts for hysteresis and the mechanical and temperature effects on the hydraulic behaviour. This provides a two-way coupling between mechanics and hydraulics.

4.6.3.1 Mechanical constitutive model

The model is formulated using an elasto-plastic framework based on Hujeux's critical state model (Hujeux 1979). In order to accommodate behaviour in an unsaturated state, Bishop's effective stress and suction are used as constitutive variables. Bishop's coefficient is taken as equal to the degree of saturation (Schrefler 1984, Nuth & Laloui 2008), leading to:

$$\boldsymbol{\sigma}' = \boldsymbol{\sigma} - [S_r u_w + (1 - S_r) u_a] \mathbf{I} = \boldsymbol{\sigma}^n - S_r s \mathbf{I} \quad (34)$$

where $\boldsymbol{\sigma}'$ is the effective stress tensor, $\boldsymbol{\sigma}$ is the total stress tensor, S_r is the degree of saturation, u_w is water pressure, u_a is air pressure, $s = u_a - u_w$ is suction and $\boldsymbol{\sigma}^n = \boldsymbol{\sigma} - u_a \mathbf{I}$ is the net stress tensor.

Changes in effective stress are related to the deformation of the material as:

$$d\boldsymbol{\varepsilon} = \mathbf{C} : d\boldsymbol{\sigma}' \quad (35)$$

where $\boldsymbol{\varepsilon}$ is the strain tensor and \mathbf{C} is the secant compliance tensor. To allow for irreversible deformation, the strain tensor is divided as (isothermal conditions):

$$d\boldsymbol{\varepsilon} = d\boldsymbol{\varepsilon}^e + d\boldsymbol{\varepsilon}^p \quad (36)$$

where $d\boldsymbol{\varepsilon}^e$ is the elastic strain increment and $d\boldsymbol{\varepsilon}^p$ the plastic strain increment.

Elastic strains will be induced as long as the stress increment lies inside the yield surface. In such cases, the response will be governed by the elastic compliance \mathbf{C}^e :

$$\mathbf{C}^e = C_{ijkl}^e = 2G \delta_{ik} \delta_{jl} + \left(K - \frac{2}{3} G \right) \delta_{ij} \delta_{kl} \quad (37)$$

where G is the shear modulus and K the bulk modulus. These moduli depend on the confining stress p' as:

$$G = G_{ref} \left(\frac{p'}{p'_{ref}} \right)^{n^e} \quad K = K_{ref} \left(\frac{p'}{p'_{ref}} \right)^{n^e} \quad (38)$$

where G_{ref} and K_{ref} are the shear and bulk modulus respectively at a reference pressure p'_{ref} and n^e is a parameter controlling the non-linear behaviour.

In non-isothermal conditions, additional elastic strains are induced by temperature changes according to:

$$d\boldsymbol{\varepsilon}^e = \mathbf{C}^e : d\boldsymbol{\sigma}' - \left(\frac{1}{3} \beta_s \mathbf{I} \right) dT = \mathbf{C}^e : d\boldsymbol{\sigma}' - \boldsymbol{\beta}_T dT \quad (39)$$

where $\boldsymbol{\beta}_T$ is the thermal expansion coefficient tensor and β_s is given by:

$$\beta'_s = \beta'_{s0} \left(1 - \frac{T-T_0}{100} \right) \frac{p'_{cro}}{p'} \quad (40)$$

where β'_{s0} is the thermal expansion coefficient at a reference temperature T_0 and p'_{cro} is the initial critical state pressure at the reference temperature.

If the effective stress state reaches the yield surface, plastic strains will develop. These might be induced by two mechanisms, namely isotropic $d\epsilon_{iso}^p$ and deviatoric $d\epsilon_{dev}^p$ plastic strains. Or:

$$d\epsilon^p = d\epsilon_{iso}^p + d\epsilon_{dev}^p \tag{41}$$

Each mechanism corresponds to a different yield surface f whose expressions are respectively:

$$f_{iso} = p' - p'_c r_{iso} = 0 \tag{42}$$

$$f_{dev} = q - Mp'[1 - b \ln(\frac{p'd}{p'_c})]r_{dev} \tag{43}$$

Where p'_c is the preconsolidation pressure, q is the deviatoric stress, M is the slope of the critical state line in the $(p' - q)$ plane; b is a material parameter defining the shape of the deviatoric yield surface; $d = \frac{p'_c}{p'_{cr}}$ where p'_{cr} is the critical state pressure; r_{iso} and r_{dev} correspond to the degrees of plastification for each mechanism, allowing for plastic strains within the yield limits. It can be readily observed that both mechanisms are coupled by means of the preconsolidation pressure p'_c .

Preconsolidation pressure depends on the volumetric plastic strain, temperature and suction as follows:

$$p'_c = \begin{cases} p'_{c0} \exp(\beta \epsilon_v^p) [1 - \gamma_T \log(T/T_0)] & \text{if } s < s_e \\ p'_{c0} \exp(\beta \epsilon_v^p) [1 - \gamma_T \log(T/T_0)] [1 + \gamma_s \log(s/s_e)] & \text{if } s > s_e \end{cases} \tag{44}$$

where β is the plastic compressibility modulus (slope of the $\epsilon_v^p - \ln p'_c$ relation); s_e is the air entry suction value; and γ_T and γ_s account for the increase/decrease of the elastic domain with suction and temperature. Fig. 4-3 shows the influence of temperature and suction on the size of the yield surface, which decreases when temperature increases and increases when suction increases above the air entry suction.

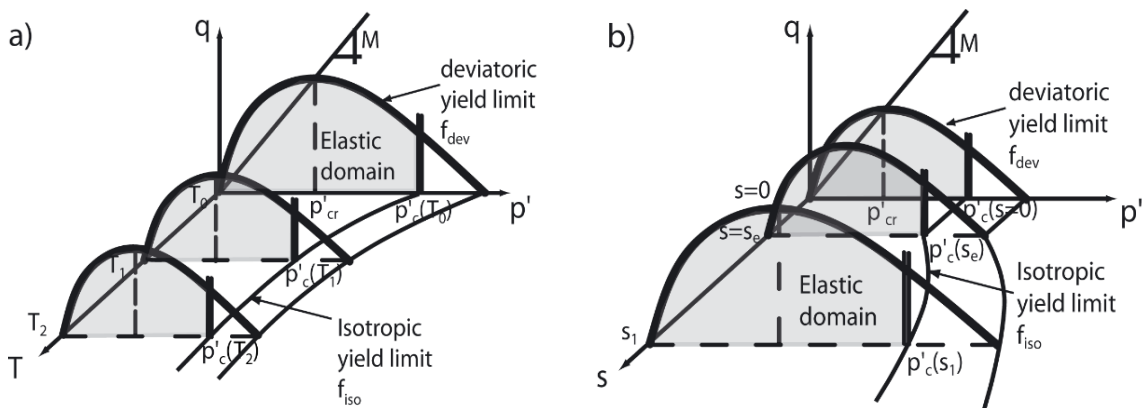


Fig. 4-3: Graphical visualisation of the yield surface evolution with temperature (left) and suction (right)

The flow rule of the isotropic mechanism is associated, whereas that for the deviatoric mechanism can be non-associated. Thus, the plastic potentials have the following form:

$$g_{iso} = p' - p'_c r_{iso} = 0 \quad (45)$$

$$g_{dev} = q - \frac{\alpha}{\alpha-1} M p' \left[1 - \frac{1}{\alpha} \left(\frac{p' d}{p'_c} \right)^{\alpha-1} \right] = 0 \quad (46)$$

where α is a non-associativity parameter. The magnitude of plastic strains depends on the derivatives of these potentials as follows:

$$d\boldsymbol{\varepsilon}_{iso}^p = d\lambda_{iso}^p \frac{\partial g_{iso}}{\partial \boldsymbol{\sigma}'} \quad (47)$$

$$d\boldsymbol{\varepsilon}_{dev}^p = d\lambda_{dev}^p \frac{\partial g_{dev}}{\partial \boldsymbol{\sigma}'} \quad (48)$$

where λ_{iso}^p and λ_{dev}^p are the plastic multipliers which are determined following Prager's consistency condition extended to multi-dissipative materials (Rizzi et al 1990):

$$d\mathbf{F} = \frac{\partial \mathbf{F}}{\partial \boldsymbol{\sigma}'} : d\boldsymbol{\sigma}' + \frac{\partial \mathbf{F}}{\partial \boldsymbol{\pi}} \cdot \frac{\partial \mathbf{F}}{\partial \boldsymbol{\pi}} \cdot d\boldsymbol{\lambda}^p \leq 0, d\boldsymbol{\lambda}^p \geq 0, d\mathbf{F} \cdot d\boldsymbol{\lambda}^p = 0 \quad (49)$$

where $\mathbf{F} = (f_{iso} \ f_{dev})$ is the yield surface vector; $\boldsymbol{\pi} = (p'_c \ r_{iso} \ r_{dev})$ is the internal variable vector; and $\boldsymbol{\lambda}^p = (\lambda_{iso}^p \ \lambda_{dev}^p)$ is the plastic multiplier vector.

4.6.3.2 Water retention constitutive model

In order to account for unsaturated conditions, a relationship between degree of saturation and suction is introduced (Francois & Laloui 2008). An elastoplastic approach is used to model water retention. This includes hysteretic behaviour controlled by two yield surfaces corresponding to drying and wetting paths. The conceptual model is represented in Fig. 4-4. Desaturation (or saturation) is induced when suction reaches either the wetting limit or the drying limit, satisfying respectively:

$$f_{dry} = s - s_d, f_{wet} = s_d s_{hys} - s \quad (50)$$

where f_{dry} and f_{wet} stand for the yield activated during a wetting or drying process respectively, s_d is the drying yield limit which during a desaturation/saturation process (i.e. $f_{dry} = 0$ or $f_{wet} = 0$) remains equal to the actual value of s ; and s_{hys} a material parameter controlling the size of the water retention hysteresis.

If the initial state is saturated, s_{d0} is equal to the air entry suction s_{e0} and increases when suction exceeds this value according to the following hardening law:

$$s_d = s_e \exp(-\beta_h \Delta S_r) \quad (51)$$

where β_h is the slope of the retention curve in the $(S_r - \ln s)$ plane (see Fig. 4-4). The same process is activated for a wetting path in the opposite way (eq. 50). Thus, eq. (51) describes the hardening process that leads to changes in S_r . A limiting condition is imposed so that when S_r reaches the residual degree of saturation s_d is kept constant.

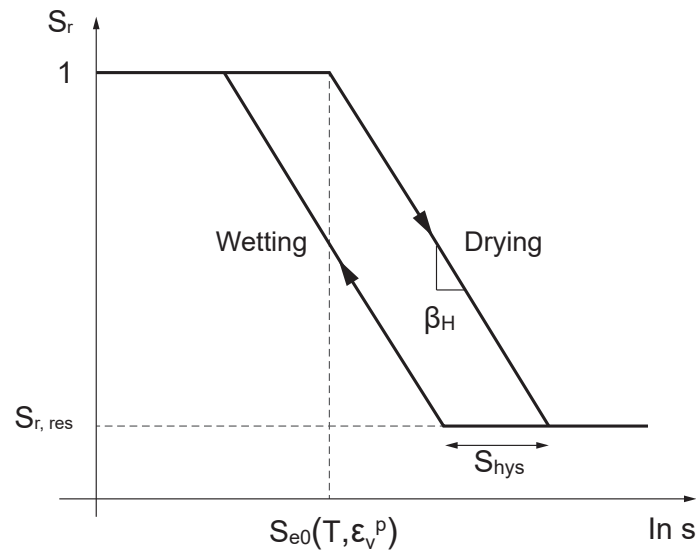


Fig. 4-4: Conceptual model of the adopted water retention model

Parameters defined in the text.

To account for the dependence of water retention on dry density and temperature, s_e is taken as a function that depends on the material state as:

$$s_e = s_{e0} \left[1 - \theta_T \log\left(\frac{T}{T_0}\right) - \theta_E \log(1 - \varepsilon_v) \right] \quad (52)$$

where s_{e0} is the initial air entry suction, and θ_T and θ_E describe the evolution of air entry suction with temperature and volumetric strain respectively.

Based on the same framework, more advanced models have been developed in Nuth & Laloui (2008) and Salager et al. (2013). Changes respond mainly to a more progressive slope approaching the air entry suction and the assumption that a common asymptotic behaviour for low saturation states exists regardless of dry density (or void ratio).

4.7 Conceptual uncertainties in reactive transport modelling of bentonite relevant for the Nagra repository scenario

Any model approach suffers from uncertainties in crucial input parameters or ignoring important processes or couplings. In general, the thermodynamic and kinetic properties of the bentonite accessory minerals are well established. Larger uncertainties exist in montmorillonite data, especially at extreme temperature or pH. During interaction of bentonite with cement or steel at high temperatures, Mg-rich or Fe-precipitations are observed at the interface, and the reactivity of montmorillonite is still unclear. Such interactions are the subject of ongoing research (Lothenbach et al. 2015, Dauzères et al. 2016, Nied et al. 2016, Hadi et al. 2017a, Hadi et al. 2017b). As long as the interaction processes are unknown, they cannot be included in numerical models.

Many studies investigated diffusive transport of trace and major species in bentonite. Effective diffusion coefficients, combined with diffusion-active porosities, characterise overall diffusion through bentonite rather well. In most studies, transport or the presence of anions in the Donnan porosity is ignored. In the case of porosity increase or clogging (mineral reactions), or chemically

induced changes in pore size distribution (CM coupling), only a multiporosity concept can accurately predict transport (Chagneau et al. 2015, Jenni et al. 2017). The available beta versions of multiporosity reactive transport codes must be further developed and established (e.g. benchmarks similar to Alt-Epping et al. 2015). Based on available experimental data, transport parameters in the different porosity domains should be systematically evaluated. They can then be used to predict transport across the three major interfaces of the bentonite barrier (bentonite – OPA, bentonite – cement, bentonite – steel).

The impact of the infiltrate's chemical composition on swelling pressure and transport properties is indisputable. Ignoring this CM coupling may lead to biased estimates of transport properties, equilibration time and swelling pressure. Fully coupled modelling of THMC processes is impeded by the lack of suitable modelling frameworks and also by the limited databases for adequate description of the chemical components of the aqueous system. For the same reason, it is presently difficult to gauge what the uncertainties are in applying the more simplistic approaches now available.

5 Evaluation of the impact of processes and phenomena affecting the safety-relevant properties of bentonite

5.1 Assessment of repository-induced effects on the bentonite buffer considering homogenisation aspects

FEBEX (Huertas et al. 2006) was a large-scale in-situ experiment conducted at the Grimsel Test Site with the objective of increasing the knowledge of the physical processes that take place in a bentonite barrier under thermo-hydro-mechanical actions representative of an actual HLW repository. The experiment started in 1998 and was dismantled in two parts, one in 2005 and the rest in 2015. A scheme of the layout, including the sections analysed, is shown in Fig. 5-1. The modelling results of the FEBEX experiment regarding thermo-hydro-mechanical processes are summarised hereafter. The mathematical formulation employed for the simulations can be consulted in section 4.6 of the present report.

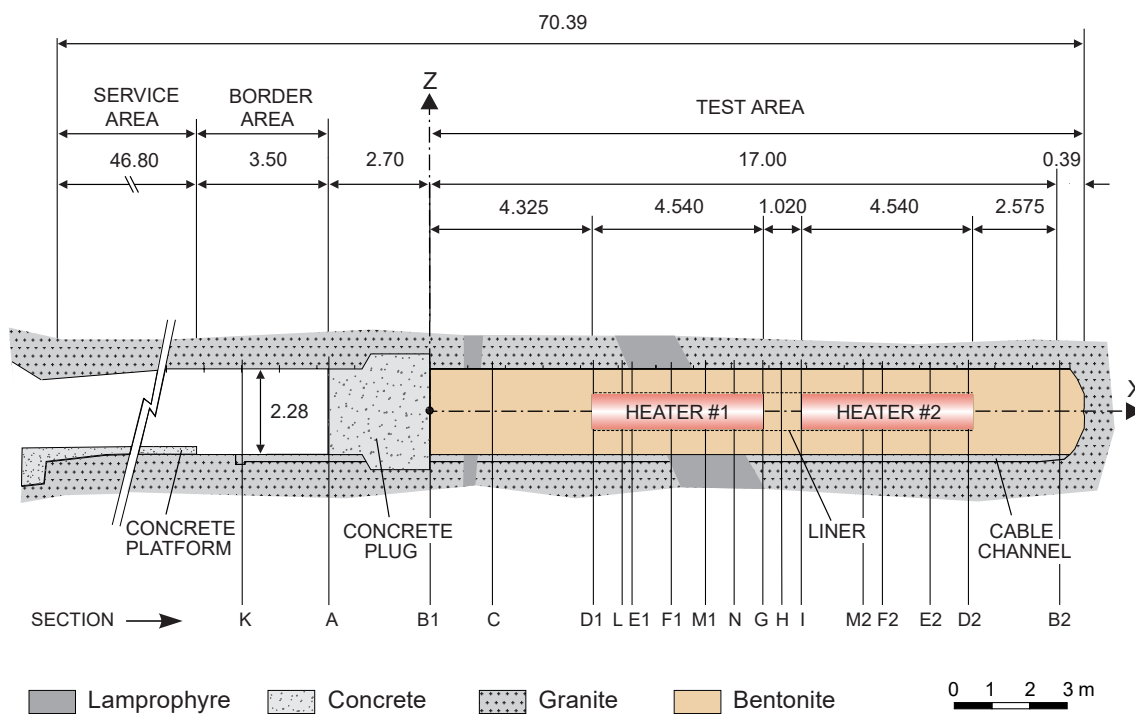


Fig. 5-1: Layout of the FEBEX in-situ experiment

Extensive homogenisation laboratory experiments have been carried out by Ann Dueck (Dueck et al. 2016, Dueck et al. 2017). They consisted of either bentonite blocks and water-filled gaps in different geometries, or bentonite in different forms (blocks, pellets) with different initial dry densities at isothermal conditions. In all experiments, a relatively small dry density gradient remains also after full saturation (generally the density decrease is smaller than 15 % of the average density), which does not seem to further homogenise with time. These data complement findings from in-situ experiments (e.g. FEBEX-DP), where full saturation is often not reached at termination. Therefore, the laboratory experiments are generally more representative for the full saturation state after the thermal phase than large-scale in-situ tests.

5.1.1 Driving processes

Complex THM coupling processes occurred in the buffer region during the experiment. The significant phenomena that affect the bentonite region are the heating from heaters and hydration from the surrounding granite.

During the ventilation phase, the temperature is homogeneous and no thermally induced stresses or deformations occur. The only driving force is the hydraulic gradient between the buffer and the surrounding granite. Due to the high initial suction in the buffer region, the water flows into the bentonite from the high-water pressure zone. During this process, the mechanical behaviour is also affected due to the high swelling capacity of bentonite. Owing to some construction gaps between the blocks, and between blocks and the drift surface, the initial swelling of bentonite will induce a higher porosity. As a result, a higher intrinsic conductivity will be generated. Also considering that the degree of water saturation increases with absorbing water, the water flow rate will increase during this phase. This fast water flow will be neutralised by the decrease in hydraulic gradient with time. However, the drift will constrain the swelling deformation and swelling pressure will be generated.

During the heating phase, one additional driving force is the thermal gradient. At the inner boundary of the buffer system, heat flows from the heater to the bentonite. This heat flux will generate a thermal gradient in the buffer system as well as in the granite zone. Due to the high temperature, the inner part of buffer system will have a strong water evaporation, which leads to the drying of bentonite. Thus, the degree of saturation will decrease, and suction will increase in this region. This vapour will flow outwards and will condense in the cooler region, leading to an increase in water content in the middle region. However, it is also due to this process that there is an increase in suction in the middle part during the cooling phase. This means that a sudden water flow occurs from the middle part to the inner part, while the middle part cannot absorb enough water from the outer part. Vapour diffusion is a significant mechanism of water transfer and it also contributes to heat transport. Owing to this vapour flux, the water transfer is much more complex under a thermal gradient condition.

Because of thermal loading, the bentonite will shrink, causing an increase in dry density. However, the mechanical response of bentonite under thermal loading needs to be investigated further. One interesting point is that, whether or not this thermally induced shrinking is recoverable, Laloui et al. (2009) pointed out that the thermal loading can cause some plastic deformation for normally consolidated clays. The initial stress state of FEBEX blocks can be assumed to be highly overconsolidated. Therefore, no thermal plasticity is considered in this work. However, owing to the presence of montmorillonite, the fabric of bentonite can be modified during the water-absorbing process, and this may change the bentonite consolidation state from overconsolidation to normal consolidation. If this is true, an irreversible thermal deformation would occur in the inner part of buffer system. Moreover, the coupling effects of thermal loading and hydraulic loading on the mechanical response also need further investigation.

5.1.2 Modelled and measured density and saturation distributions and remaining uncertainties

5.1.2.1 Results for a cool section during the first dismantling

Fig. 5-2 shows both modelling results and measured data for dry density and water content as a function of the distance to the drift axis for a section far away from the heater (section 15 in the first dismantling; near to section C in Fig. 5-1). The good agreement between experimental results and (partly blind) modelling results indicates that the THM framework can capture the complex coupling process very well. A decrease in dry density in the part next to the granite is expected due to the swelling deformation of bentonite. The swelling of the outer region will compress the inner part, causing it to increase in density. However, the modelling underestimates the decrease in dry density in the outer part. Two reasons are responsible for this deviation. One is that the mechanical law adopted in the simulation has a limit in terms of modelling the high swelling potential of bentonite for a degree of saturation close to one. The other reason could be related to the fact that the construction gaps between the buffer system and the granite can also lead to a greater decrease in dry density in the outer part next to granite. As stated in the previous section, the outer part is almost fully saturated. The underestimation of the swelling deformation will also lead to an underestimation of the water content in the outer part of the buffer system (see Fig. 5-2b). It is clear that the water content at all radial distances increases during five years, although the increase in the inner part is only between 3 % to 5 %. This is related to the thickness of the buffer and the low water permeability of bentonite.

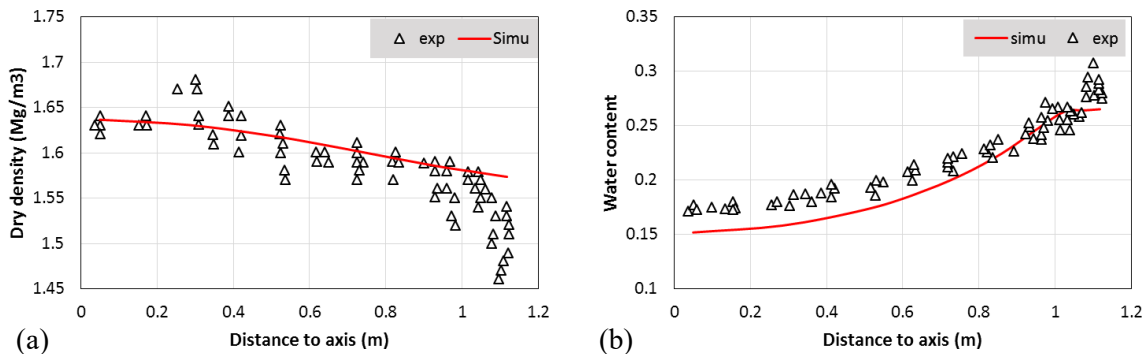


Fig. 5-2: Comparison of measured dry density and water content data during dismantling and simulation results for a cool section (section 15)

a) dry density, b) water content.

5.1.2.2 Results for a hot section during the first dismantling

Fig. 5-3 shows both modelling results and measured data for dry density and water content as a function of the distance to the drift axis for a section near Heater #1 (section 27 in the first dismantling; near to M1 in Fig. 5-1). The dismantling effect on the dry density distribution is also plotted. The modelling results show a good agreement with experimental results for the inner 2/3 part, while a deviation for the outer 1/3 part is observed. This deviation could be explained in a similar manner as in the previous section.

Comparing to the results for the cool section, it is noticeable that a larger increase in dry density occurs in the inner part. This is due to thermal loading. The high temperature causes the drying of bentonite, leading to a shrinking of that region. Looking at the water content results, it is

obvious that there is a decrease in water content in the inner part of the buffer system. This thermally induced drying effect cannot be compensated for by the hydraulic flow, not even after five years.

The dry density decreases after dismantling because of the unloading that occurs during the dismantling or coring processes. The reduction foreseen by the simulation is about 0.02 Mg m^{-3} . Based on the measured dry density after dismantling, an average dry density can be calculated to be 1.57 Mg m^{-3} , which is about 0.03 Mg m^{-3} smaller than the initial average dry density of 1.60 Mg m^{-3} . Thus, the simulation can reproduce the dismantling effects in the inner 2/3 part. However, other parameters that can also lead to the decrease in the dry density are the coring technology and field test technology.

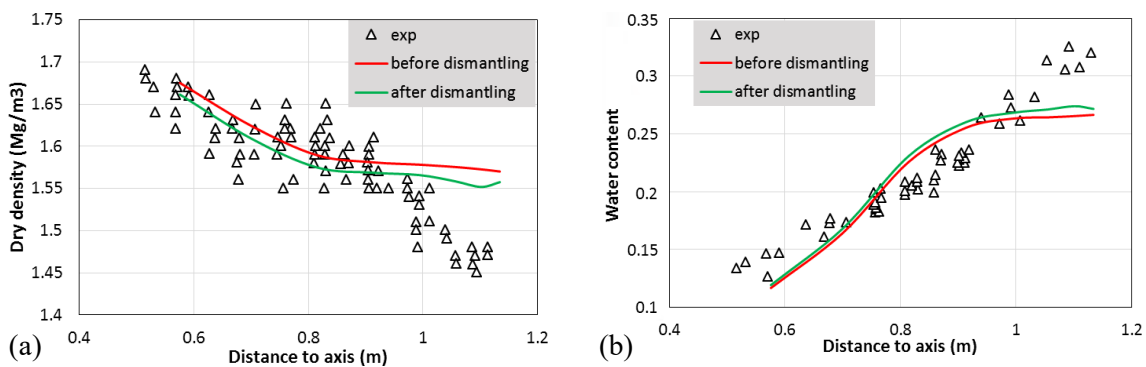


Fig. 5-3: Comparison of measured dry density and water content values during the first dismantling and simulation results for a hot section (section 27)

a) dry density, b) water content.

5.1.2.3 Predicted results for a cool section during the second dismantling

This simulation work aimed at predicting dry density and water content for a cool section (section G) and the results are presented in Fig. 5-4 and Tab. 5-1. After 18 years, the whole section G is almost fully saturated, with the degree of saturation in the inner part reaching about 99.4 %. Looking at the suction value, it is noticeable that there is still a suction gradient along the radial direction and the maximum suction, about 4.14 MPa, is in the inner part of the buffer system. Since the air entry value of 4 MPa is used in the simulation, the full section seems to reach the full saturation state. However, if a different air entry value were used, the saturation condition would be shifted. One uncertainty is the effect of fabric modification due to absorbing water on the air entry value.

The dry density at section G is almost homogenised. The reason for this predicted result is that irrecoverable hydraulic swelling deformations are not foreseen by the mechanical law. Therefore, the deformation of the buffer system is assumed to be elastic. Thus, after the buffer system reaches full saturation, the homogenised dry density with the initial value of 1.6 Mg m^{-3} is recovered. This point is also stated by Dixon et al. (2002) where they analysed two large-scale sealing tests conducted at Canada's underground laboratory.

Tab. 5-1: Predicted results for a cool section (section G) during the second dismantling

| Radial distance to axis [m] | Porosity n | Degree of saturation S_r [%] | Suction s [MPa] | Dry density [Mg m^{-3}] | Water content [%] |
|-----------------------------|--------------|--------------------------------|-------------------|------------------------------------|-------------------|
| 0.05 | 0.409 | 99.4 | 4.14 | 1.596 | 25.48 |
| 0.28 | 0.407 | 99.4 | 4.14 | 1.601 | 25.27 |
| 0.50 | 0.406 | 99.9 | 4.02 | 1.603 | 25.29 |
| 0.63 | 0.407 | 100 | 4.00 | 1.601 | 25.42 |
| 0.76 | 0.409 | 100 | 3.94 | 1.596 | 25.63 |
| 0.86 | 0.409 | 100 | 3.89 | 1.596 | 25.63 |
| 0.95 | 0.409 | 100 | 3.76 | 1.596 | 25.63 |
| 1.02 | 0.409 | 100 | 3.34 | 1.596 | 25.63 |
| 1.08 | 0.410 | 100 | 2.65 | 1.593 | 25.74 |
| 1.12 | 0.410 | 100 | 1.82 | 1.593 | 25.74 |

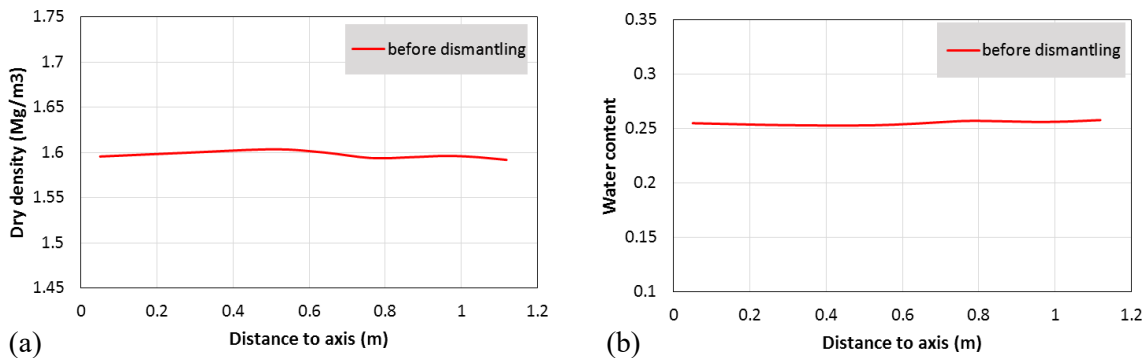


Fig. 5-4: Predicted results for a cool section (section G)

a) dry density, b) water content.

5.1.2.4 Predicted results for a hot section during the second dismantling

Fig. 5-5 shows the predicted dry density and water content for a hot section near Heater #2 (section F2). The detailed results are also given in Tab. 5-2. Owing to the thermal effects, the inner part of section F2 still has high suction, about 12.52 MPa. This means that although a certain amount of water has reached the inner region, it is still insufficient, after 18 years, to make this region fully saturated. One interesting phenomenon is that an increase in suction in the middle part of the buffer system is predicted. This is related to switching off Heater #2 and was analysed in the previous section. Due to the non-saturation of the inner part, a dry density gradient is observed in this section. The maximum difference between the inner and the outer part is about 0.03 Mg m^{-3} . Since neither thermal plasticity nor irrecoverable hydraulic swelling deformation are considered in the simulation, this dry density gradient may be underestimated. The unloading during dismantling cannot be avoided. Thus, a smaller average dry density than the initial value of 1.6 Mg m^{-3} is expected, as stated in the first dismantling.

Tab. 5-2: Predicted results for a hot section (section F2) during the second dismantling

| Radial distance to axis [m] | Porosity n | Degree of saturation S_r [%] | Suction s [MPa] | Dry density [Mg m ⁻³] | Water content [%] |
|-----------------------------|--------------|--------------------------------|-------------------|-----------------------------------|-------------------|
| 0.05 | 0.409 | 99.4 | 4.14 | 1.596 | 25.48 |
| 0.58 | 0.401 | 82.0 | 12.52 | 1.617 | 20.33 |
| 0.71 | 0.406 | 98.9 | 4.28 | 1.604 | 25.04 |
| 0.82 | 0.4065 | 98.5 | 4.39 | 1.602 | 24.99 |
| 0.92 | 0.407 | 98.8 | 4.29 | 1.601 | 25.11 |
| 1.00 | 0.408 | 99.4 | 4.16 | 1.598 | 25.37 |
| 1.06 | 0.408 | 100 | 3.65 | 1.598 | 25.53 |
| 1.10 | 0.409 | 100 | 2.63 | 1.596 | 25.63 |
| 1.13 | 0.411 | 100 | 1.53 | 1.590 | 25.84 |

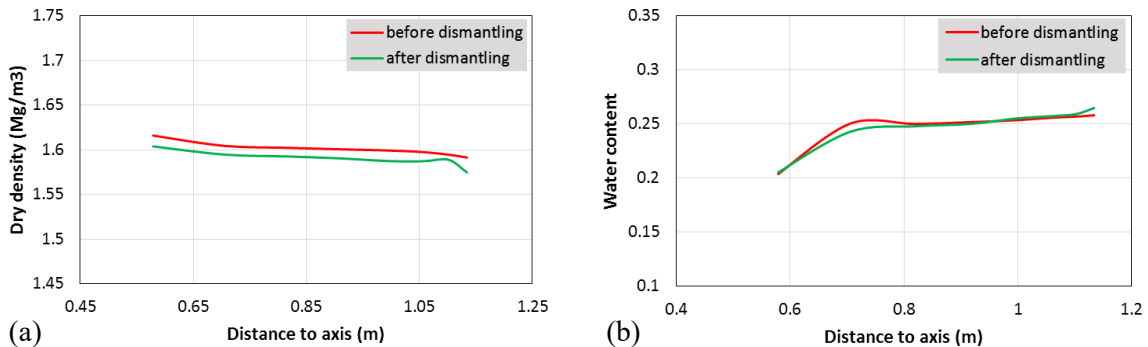


Fig. 5-5: Predicted results for a hot section (section F2)

a) dry density, b) water content.

5.1.2.5 Remaining modelling uncertainties

The main focus of this simulation work is the thermo-hydro-mechanical behaviour of the buffer system. Therefore, a careful calibration and analysis of the experimental results was carried out. A much deeper understanding of the hydraulic swelling mechanism was obtained through this exercise. Based on the simulation results and monitoring results, it can be summarised that both the thermal mechanism and hydraulic mechanism can be well captured by the current EPFL model. However, there are still some remaining uncertainties related to the mechanical response of the bentonite. One uncertainty is whether thermal plasticity exists for the FEBEX bentonite blocks. The other is the mechanism of swelling for the material with very high swelling potential. Behind these two uncertainties, one intrinsic factor is how the fabric of bentonite is modified during the swelling process. This fabric modification happens at both macro- and micro-level and involves interaction between the two. To fill this gap, more laboratory tests should be conducted to investigate the swelling mechanism at both macro- and micro-level.

Another uncertainty of the FEBEX dismantling simulation is related to the effects of the construction gaps on the THM coupling processes. Because of these construction gaps, the mechanical boundaries of the FEBEX blocks vary with time. As an example, one may consider the outer part of the buffer system. At the initial condition, the blocks can be assumed to swell under free swelling conditions due to the gaps between the buffer and the granite. When the gaps are filled by the swelling of blocks, the blocks swell under constant volume conditions and swelling pressure is generated. The construction gaps can also affect the water transfer. As presented in the previous section, the gaps between the buffer and the granite can delay the time to absorb water from granite. Moreover, the gaps in the radial direction and those in the circular direction can also have different effects. Although some tests have already been done to investigate the effect of gaps on hydraulic conductivity, there are not enough results to build a clear concept of the impacts.

5.1.2.6 Consequences for the early repository evolution

After 18 years of testing, the section far from Heater #2 (section G) seems to be fully saturated based on both simulation results and monitoring data. However, for the section near Heater #2 (section F2), the inner part is still unsaturated owing to the thermal gradient along the radial direction. After switching off Heater #2, a fast increase in saturation in the inner part is observed due to a higher hydraulic gradient between the middle and inner part, but no thermal gradient exists any longer to maintain this hydraulic gradient. Thus, it is expected that, in a repository after the canister is beyond the highest thermal peak, the saturation process will become faster and the time to attain full saturation will decrease. Based on the simulation results, the dry density gradient will disappear after the whole buffer system reaches the full saturation state. Based on data from small-scale lab experiments, minor to moderate gradients in dry density also persist after full saturation and after sufficient time for homogenisation.

5.1.3 Influence of porewater chemistry on homogenisation

Swelling pressure is a key parameter for homogenisation. Because swelling pressure of any bentonite depends not only on density but also on porewater ionic strength and cation occupancy, porewater chemistry also affects homogenisation. Most homogenisation lab experiments have been performed with deionised water (Dueck et al. 2016), whereas more recent studies by POSIVA include saline waters for saturation. In general, homogenisation occurs in both set-ups, but a systematic study and comparison is lacking.

In contrast, indications for preferential pathways and therefore inhomogeneities on a micro-structural level can be observed only in the Ca-montmorillonite from MX-80 above 3 M ionic strength and at low densities (Fig. 5-6): the well-defined exponential relationship between hydraulic conductivity and dry density no longer holds for Ca-montmorillonite at 3 M ionic strength below approximately $1,200 \text{ kg m}^{-3}$, and at 9 M below $1,400 \text{ kg m}^{-3}$. Preferential pathways can explain the extreme increase in conductivity under these conditions. The same behaviour can be observed for Milos Deponit CAN, but here the conductivity increases non-exponentially at all ionic strengths (0-9 M) below approximately $1,200 \text{ kg m}^{-3}$. These data suggest that homogenisation is significantly lowered in Ca-montmorillonite at high ionic strengths and low densities, conditions not expected in the buffer.

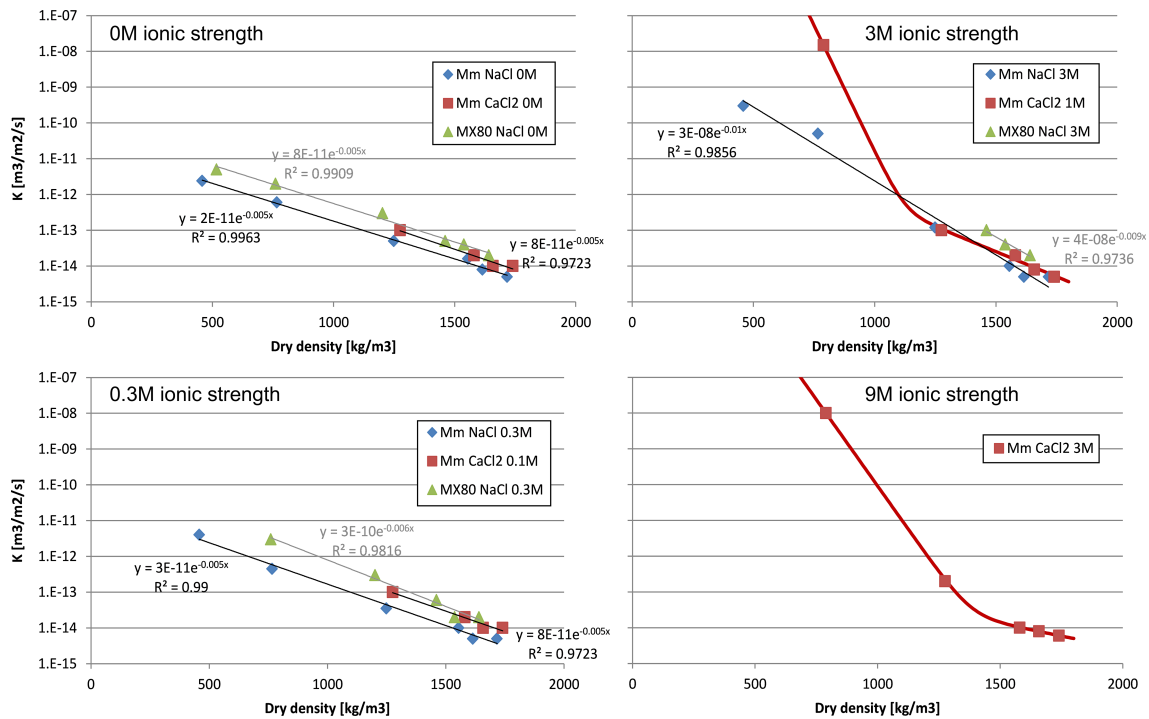


Fig. 5-6: Hydraulic conductivity of MX-80 montmorillonite and MX-80 at different NaCl and CaCl₂ ionic strengths and dry densities
Karnland et al. (2006)

5.1.4 Significance of remaining uncertainties of buffer homogenisation

The assessment of the mechanical evolution of a bentonite barrier and of the resulting performance is challenging. Understanding the evolution from an installed engineered system to a fully functioning barrier must involve design and engineering, science and performance assessment. A model able to fully integrate the above-mentioned information and to simulate density evolution at a larger scale is yet to be developed. Such a model requires a detailed understanding of material properties, the fundamental processes that lead to homogenisation, and the role of scale effects.

Based on information from small-scale laboratory experiments, homogenisation is expected to lead to a moderate material density distribution in the entire buffer. Large-scale experiments such as FE (Müller et al. 2017) have shown that the emplacement technique and the form (bricks or pellets) have a great impact on the initial dry density distribution in the near-field. Upon wetting and the consequent swelling, heterogeneities may gradually disappear (Villar et al. 2018).

If, due to heterogeneities in the backfill, bacteria can thrive for longer time periods, microbial corrosion may become a significant aspect in the assessment of canister corrosion rates. The influence of the chemical environment on homogenisation is likely to be of less importance within the expected range of ionic strength, but systematic data in this context are scarce.

5.2 Interaction of host rock porewaters and bentonite, changes in salinity and Ca-Na exchanger occupancy

In this section, geochemical and coupled chemo-mechanical processes occurring at the contact of the saturated, homogeneous bentonite and claystone host rock are considered. Saturation, homogenisation and the influence of elevated temperature on the bentonite are discussed elsewhere with respect to their geochemical aspects (sections 4.6, 5.1, 5.8, respectively). Very likely, the saturation and equilibration water of the bentonite will not be equal to the undisturbed host rock porewater at first. Its contact with other parts of the EBS will alter its chemical composition, which is not considered here, but is described in sections 5.3 (cement), 5.4 (steel), and 5.5 (copper). However, these materials are of limited volume compared to the host rock porewater reservoir. Depending on the transport properties across the bentonite-host rock interface, bentonite porewater and mineralogy will eventually equilibrate with the host rock porewater. Then, the host rock will dominate the porewater in the EBS. Heat is expected to return to formation temperature within 10,000 y (Fig. 2-4). Consequently, the predominant part of the repository lifetime is expected to be dominated by the host rock porewater at low temperatures.

The host rock porewater infiltrating into the bentonite is not in geochemical equilibrium with the bentonite. This disequilibrium might lead to the alterations described below within the bentonite while the bentonite porewater composition slowly approaches the host rock porewater (assuming an infinite host rock porewater reservoir). Similarly, these alterations must be expected at any time when the equilibrating host rock porewater changes, and the bentonite porewater equilibrates to a new porewater (see also SKB 2010, Section 3.5, and Posiva 2013, Section 7.4):

- change in ionic strength and cation composition (e.g. Na/Ca) of the bentonite porewater leads to changes in swelling pressure and hydraulic conductivity
- the cation population on the montmorillonite exchanger sites adapts to changes in cation composition in the bentonite porewater
- secondary minerals, especially gypsum, dissolve or precipitate, which alters porosity, dry density, and therefore swelling pressure and conductivity of the bentonite
- montmorillonite reacts with the host rock porewater, again altering porosity, dry density and, therefore, swelling pressure and conductivity of the bentonite (minor effect due to slow kinetics)

5.2.1 Swelling pressure and hydraulic conductivity of bentonite in equilibrium with different host rock porewaters

Cloet et al. (2014) discuss the influence of the host rock porewater on the bentonite. They concentrate on the influence of ionic strength and cation occupancy (only pure Na and Ca montmorillonite) on swelling pressure and hydraulic conductivity. Based on Karnland et al. (2006), they conclude that no safety-relevant properties of the bentonite are affected within the expected ionic strength range of the host rock porewater (defined within the same report). A more careful examination of the same data reveals a range of possible swelling pressures within the ionic strength range (1,890 – 2,510 kPa for Na-montmorillonite, 1,600 – 1,750 kPa for Ca-montmorillonite, Fig. 5-7). Hydraulic conductivities deduced from the same data show large uncertainties but imply increasing conductivities for both Na- and Ca-montmorillonite with increasing ionic strength (Fig. 5-8). The montmorillonite dry density considered here equals the EMDD of an MX-80 bentonite with 1,500 kg m⁻³ dry density (see section 3.8.1). No data exist for mixed Na-Ca-montmorillonites.

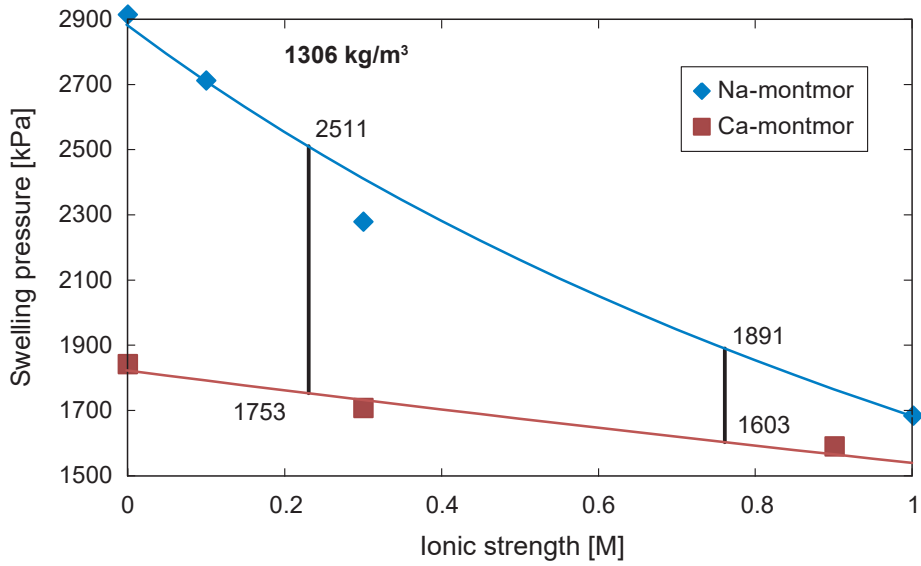


Fig. 5-7: Swelling pressure of Na-montmorillonite in NaCl and of Ca-montmorillonite in CaCl₂ solutions of different ionic strengths at 1,306 kg m⁻³ dry density

Black lines represent the bounding host rock porewater ionic strengths. The montmorillonite dry density corresponds approximately to an MX-80 dry density of 1,500 kg m⁻³. Data from Karnland et al. (2006) were fitted exponentially to estimate swelling pressures of Na- and Ca-montmorillonite at specific density (data were originally measured at different densities). Curves represent best fits of a hyperbolic arctangent function.

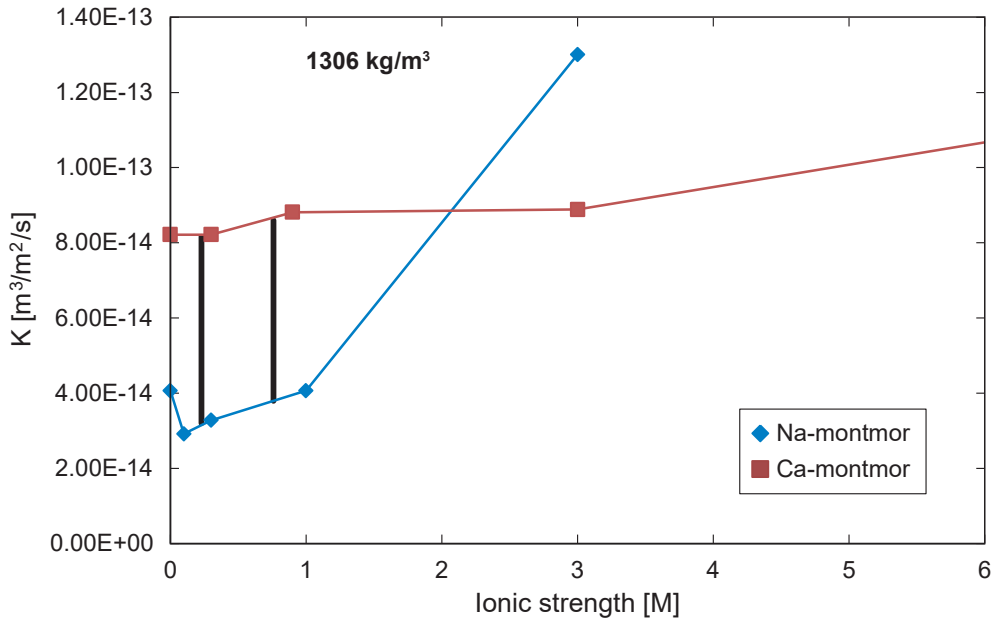


Fig. 5-8: Hydraulic conductivities of Na-montmorillonite in NaCl and of Ca-montmorillonite in CaCl₂ solutions of different ionic strengths at 1,306 kg m⁻³ dry density

Black lines represent the bounding host rock porewater ionic strengths. The montmorillonite dry density corresponds approximately to MX-80 dry density of 1,500 kg m⁻³. Data from Karnland et al. (2006) were fitted to estimate conductivities of Na- and Ca-montmorillonite at equal densities (data were originally measured at different densities). Lines are shown for better readability only.

As discussed in sections 3.8.3 and 3.8.4, systematic data for swelling pressures and hydraulic conductivities at different ionic strengths and different exchanger occupancies are scarce (Karnland et al. 2006), and no systematic data exist for mixed cation occupancies. Data are available from unwashed MX-80 equilibrated with a defined chemical solution (commonly deionised water), but the actual ionic strength and cation occupancy within the bentonite are mostly unknown, because they depend on the equilibration time and method (kinetic dissolution of accessories, supply of cations for exchange). Furthermore, swelling pressures measured by different approaches differ considerably. However, the available data always show swelling pressures of mixed Na-Ca bentonites between the end member swelling pressures (e.g. section 3.8.4).

Large-scale experiments on bentonite saturation are time-consuming: often, full saturation is not achieved within the experiment duration, and the bentonite porewater is far from equilibrium with the host rock porewater. Comparison of swelling pressures or hydraulic conductivities under different chemical conditions within one experiment or across similar experiments is beyond the scope of such set-ups. Laboratory-scale data provide the only source of information.

5.2.2 Influence of host rock porewater on the bentonite cation occupancy

The saturation and subsequent equilibration of bentonite with the host rock porewater leads to a shift in cation occupancy. Such a shift is rarely observed in large-scale experiments. In the Mont Terri EB experiment (EB stands for "engineered barrier" and was an artificially hydrated isothermal, full-scale bentonite emplacement experiment), FEBEX bentonite with a high Mg occupancy was in contact with an artificial OPA porewater with comparatively low Mg content for 10 y. Analogously, MX-80 was in contact with artificial granitic Äspö groundwater for 6 y, which should have led to an increase in Ca at the expense of Na on the exchanger (LOT A2 test parcel, additional heat-induced processes). However, measurements showed no exchanger alteration in the expected direction (Fernandez et al. 2015, Karnland et al. 2009). This indicates the long interaction period necessary to fully equilibrate the large CEC of the bentonite with the host rock porewater. The ABM1 experiment involved various Na and Ca bentonites, which were brought in contact with one another and with Äspö groundwater at high temperatures. Against many expectations, the cation occupancies within the bentonites largely homogenised within the 2.5 y of the experiment. Wallis et al. (2016) could only explain the final cation distribution by taking into account the fracture network of the borehole wall delivering additional Äspö groundwater. Yustres et al. (2017) showed in a modelling exercise that the exchanger (and porewater) equilibration of a 35 cm thick bentonite layer (1,548 kg m⁻³ dry density) with a brine or meltwater-type groundwater requires interaction times in the range of hundreds of years. Such apparent contradictions can be explained with the cations being mobile within the Donnan porosity, which makes up the major porosity fraction. In contrast, anions mainly diffuse through the small free porosity fraction (or are strongly depleted in a single Donnan porosity concept). In addition, cation concentrations in the Donnan porosity (CEC) are extremely high compared to the average concentrations in a host rock porewater. Therefore, internal cation equilibration can be faster than equilibration with external solutions, especially with different anion bases.

Laboratory-scale experiments demonstrated the exchanger equilibration process with a host rock porewater. A confined bentonite cylinder derived from the LOT experiment was infiltrated with almost 8 pore volumes of Äspö groundwater for more than 2.5 y (Jenni et al. 2014a). Throughout the process, the Na outflow concentration was far above, and Ca far below, the infiltration concentrations (Fig. 5-9). Consistently, Na decreased and Ca increased on the exchanger during the experiment (Fig. 5-10). Exchange processes involving Mg, K, and Sr affect concentrations on a scale at least one order of magnitude lower. At the end of the experiment, the exchanger population had not yet attained equilibrium with the infiltration solution.

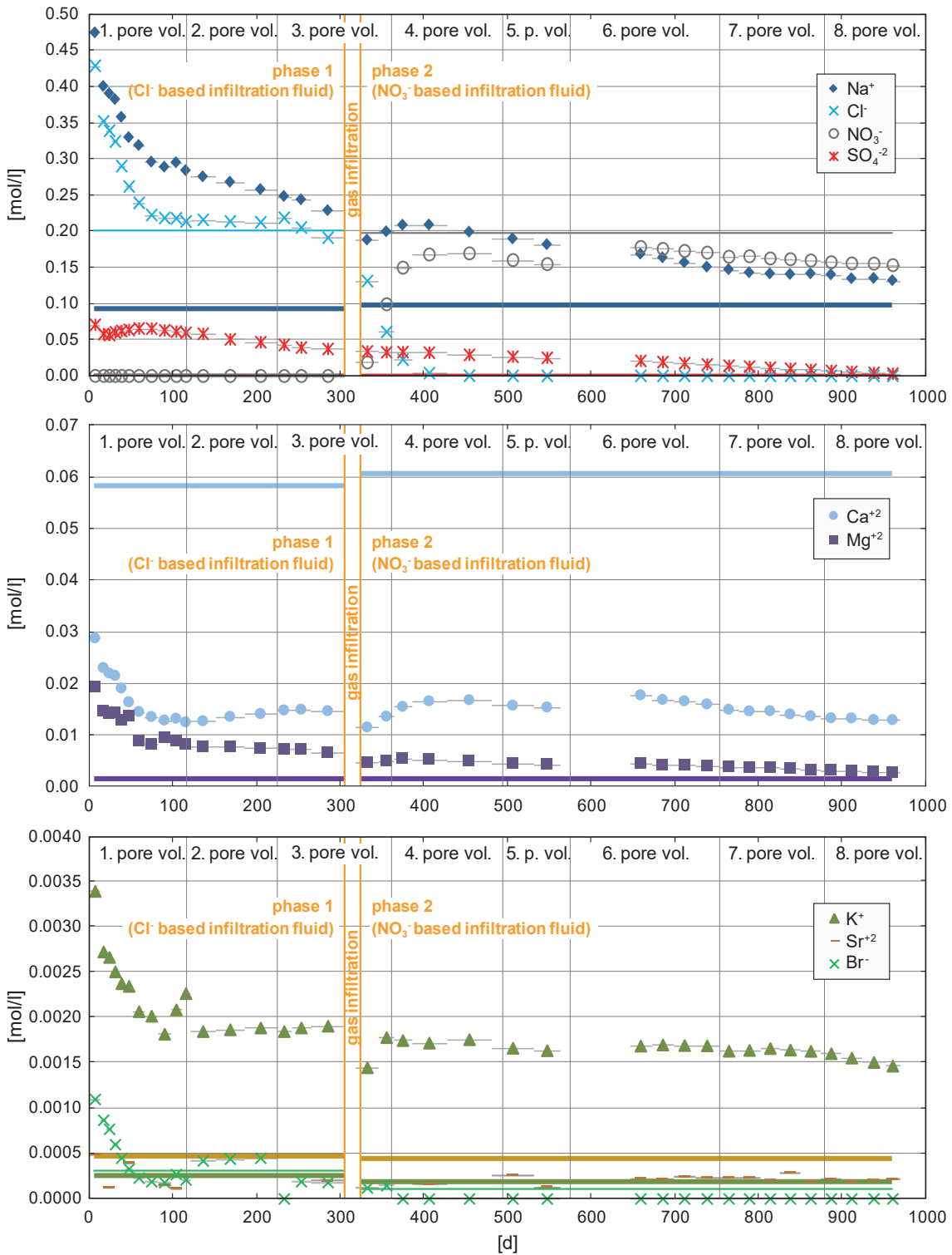


Fig. 5-9: Chemical composition of the main species in the outflow of a bentonite column as a function of time

Pore volumes are also indicated (calculated based on a total water content of 46.75 g at the beginning of the experiment). They are not proportional to time, because the flow rate varies. Compositions of infiltrating fluids are given as horizontal lines.

Jenni et al. (2014a)

An enormous amount of cation exchange sites in a natural bentonite is in equilibrium with an original porewater. If interaction with a host rock porewater alters the bentonite porewater, the original cation occupancy buffers the alteration by cation exchange. Only after the entire CEC has equilibrated with the interacting host rock porewater, can the bentonite free porewater also equilibrate. Thermodynamic stability of montmorillonite differs significantly according to the cation occupancy (section 3.2). This implies that, in all large-scale experiments, montmorillonite reactivity differs from the reactivity after host rock equilibration. For example, K-enriched porewater infiltrating bentonite equilibrates at first with the exchanger, before reaction with the montmorillonite takes place. Hardly any change in cation occupancy is measured in large-scale bentonite experiments due to their relatively restricted interaction with host rock or artificial hydration water. Therefore, the montmorillonite reactivity observed in such experiments does not reflect the reactivity when equilibrated with the host rock porewater, which will be the major part of the repository lifetime.

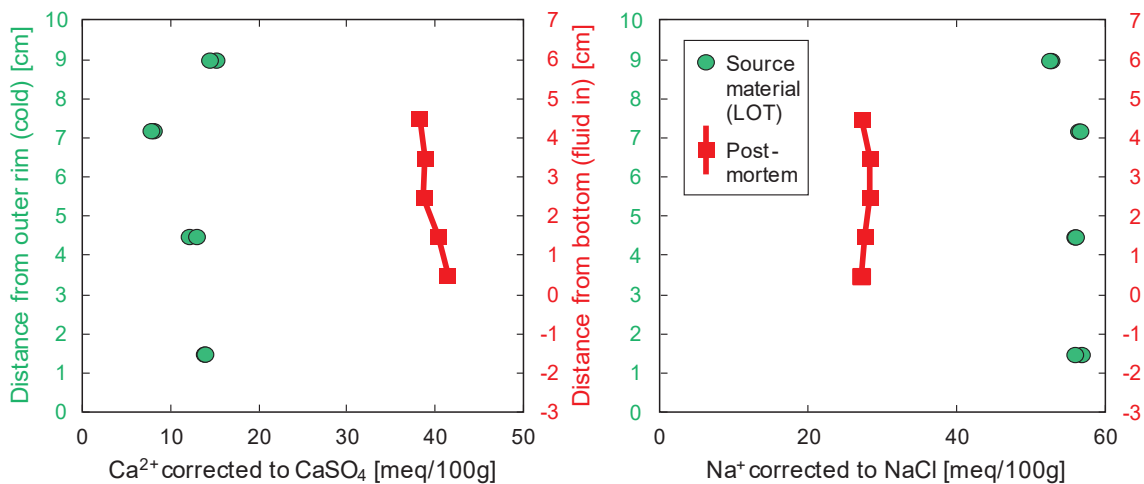


Fig. 5-10: Exchangeable Ca and Na profiles across bentonite

Corrected for mineral dissolution of source material. Before infiltration experiment (green, duplicate measurements) and after 970 d of infiltration (red). Lines connect measurements for increased readability only.

Jenni et al. (2014a)

5.2.3 Dissolution of bentonite accessory minerals

Dissolution of accessory minerals other than gypsum is unlikely, because the OPA porewater is slightly undersaturated with respect to gypsum but saturated with respect to the remaining bentonite mineralogy. Gypsum is the most soluble accessory mineral in MX-80, which leads to high sulphate concentrations in aqueous leachates. Despite the low gypsum content of approximately 1 wt.-%, the outflow of the column experiment mentioned above was saturated with respect to gypsum for almost 6 pore volumes of percolation. The Ca from the gypsum dissolution contributes to the exchange of Na for Ca. After 6 pore volumes, the gypsum saturation index of the outflow drops. Pioneering dual-porosity reactive transport modelling could confirm all these mechanisms and reasonably predict the measurements (Fernández et al. 2014b). The approach was confirmed by a benchmark exercise, modelling the same experimental data (Alt-Epping et al. 2015). The model results are not sensitive to gypsum dissolution kinetics, as long as the hydraulic conductivity is low enough and the free porewater remains saturated in the presence of gypsum. This was the case in the experiment with a constant hydraulic conductivity of 2.3×10^{-9} m/s.

Assuming diffusion as the only transport mechanism, gypsum removal would substantially slow down. Dual-porosity reactive transport calculations, considering the response of the pore size distribution as a function of the ionic strength, predict gypsum dissolution in a 35 cm thick MX-80 layer ($1,548 \text{ kg m}^{-3}$ dry density) within 500 – 1,000 y, depending on the ionic strength of the interacting groundwater (accompanying calculations to Yustres et al. 2017). In this scenario, the bentonite porosity controls diffusion and transport properties in the host rock are equal to a free water reservoir. An unfractured claystone host rock would significantly prolong gypsum dissolution in the bentonite due to its slower transport properties (smaller porosity, higher tortuosity). The lower bounding water sulphate concentration of $21.1 \text{ mmol/kgH}_2\text{O}$ proposed by Cloet et al. (2014) is slightly below gypsum saturation at the given Ca concentration. Considering such bounding water in contact with the bentonite, gypsum dissolution and diffusive sulphate migration into the host rock porewater is again slower. Complete dissolution of gypsum would only decrease the solid volume by 1 vol.-% of the MX-80 at $1,500 \text{ kg m}^{-3}$ dry density, decrease the EMDD from $1,306 \text{ kg m}^{-3}$ to $1,293 \text{ kg m}^{-3}$ and the swelling pressure of Na-montmorillonite from 2.3 MPa to 2.1 MPa (at 0.3 M NaCl), or from 1.7 MPa to 1.5 MPa (at 1.0 M NaCl, estimated from data in Karnland et al. 2006).

Potential sulphate reduction by bacteria in the EDZ of the host rock and diffusion of the sulphide towards the canister may increase canister corrosion. However, gypsum dissolution only contributes to the sulphate pool replenished from the OPA porewater.

Calcite, quartz, and feldspars are abundant in the host rocks considered and are often used to constrain the porewater composition, especially of OPA. Therefore, bentonite interaction with the host rock is not expected to lead to significant dissolution of further accessories at equal pH conditions.

In general, dissolution of MX-80 accessory minerals is not significant due their similarity to the potential host rock mineralogy. Only dissolution of gypsum must be expected in the case of interaction with a slightly undersaturated host rock porewater, which leads to a swelling pressure decrease in the range of only 10 %. Apart from the host rock porewater composition, slow transport of dissolved gypsum limits its dissolution, and not the comparably fast dissolution kinetics. The whole process is well constrained and can be modelled with reactive transport approaches taking into account anion-exclusion properties of the clay. Reaction rates for accessories other than gypsum and calcite are several orders of magnitudes slower and would control their dissolution in the unlikely case of a dilute porewater infiltration.

5.2.4 Montmorillonite reactivity

Dissolution or conversion of the main MX-80 constituent would severely impact all beneficial properties of bentonite. Reactivity of montmorillonite at room temperature in contact with host rock porewater is expected to be extremely slow, which makes it difficult to evaluate from experimental data. As a consequence, data on potential host rock porewater interaction with bentonite at late (low) repository temperature, close to neutral pH, and relevant dry densities are missing (Savage & Liu 2015). A gypsum-free bentonite in equilibrium with OPA porewater has to be expected for the predominant part of the repository lifetime. Thermodynamic data are controversial (section 3.2), which complicates numerical simulations. However, the widespread occurrence of bentonite formed millions of years ago attests to a stability over geological timescales and it is difficult to conceive of significant bentonite dissolution under normal groundwater conditions.

The main driving force for montmorillonite reaction at room temperature is expected to be the potentially relatively high K content in the interacting host rock porewater (1.8 – 2.6 mM) (Cloet et al. 2014). Thermodynamic equilibrium calculations at high K content (100 mM KCl, pH = 7.0) show the general instability of montmorillonite in this environment (Fig. 5-11, Savage & Liu 2015). The reaction products change with increasing solution volume (amount of available K) in the closed system calculated with different porosities. Translating these results to the EBS, the reaction is either controlled by transport of K into the bentonite, or by the reaction rate. These results indicate possible processes during bentonite interaction with high K porewaters but are irrelevant for interaction with low K solutions like OPA porewater. In addition, all modelling studies without careful sensitivity studies suffer from poor thermodynamic data quality for most clays (section 3.2).

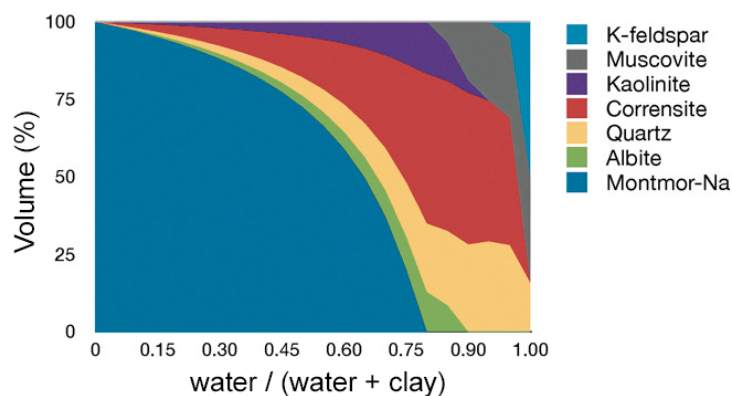


Fig. 5-11: Alteration of Na-montmorillonite by a 0.1 M KCl solution at different porosities (mass ratio) in a closed system (equilibrium calculations)

Only solids are shown, pH = 7.0, 25 °C. Muscovite is used as a proxy for illite, corrensite is a mixed-layer Mg-chlorite-smectite.

Savage & Liu (2015)

Numerical simulations from Marty et al. (2010) take transport and solid phase reaction kinetics into account in a Callovian-Oxfordian argillaceous rock (COX) porewater – MX-80 – steel system, but no spatial temperature gradients (constant at 100 °C). The calculations predict complete montmorillonite dissolution within approximately 25 cm of the bentonite contacting the COX reservoir (7 mM K) within 100,000 y (Fig. 5-12). Precipitations of illite, vermiculite, saponite and quartz reduce total porosity within this alteration zone (1). Obviously, possible reactions within the COX are not considered, and the entire bentonite porosity is treated as free porosity. Nevertheless, such studies imply that clogging of porosity might occur at the bentonite – host rock interface. In the case of total clogging, a closed system approach best represents the bentonite; in the case of remaining porosity, transport across the interface and therefore bentonite – host rock interaction is significantly influenced (considered in Marty et al. 2010). Up to now, no simulation takes into account the influence of the negatively charged montmorillonite sheet surfaces on clogging and transport, although its relevance has been experimentally demonstrated (section 4.1). However, the clay dissolution/precipitation rates and clay stability mostly govern the model outcome. Unfortunately, these data bear the largest uncertainty of all input parameters.

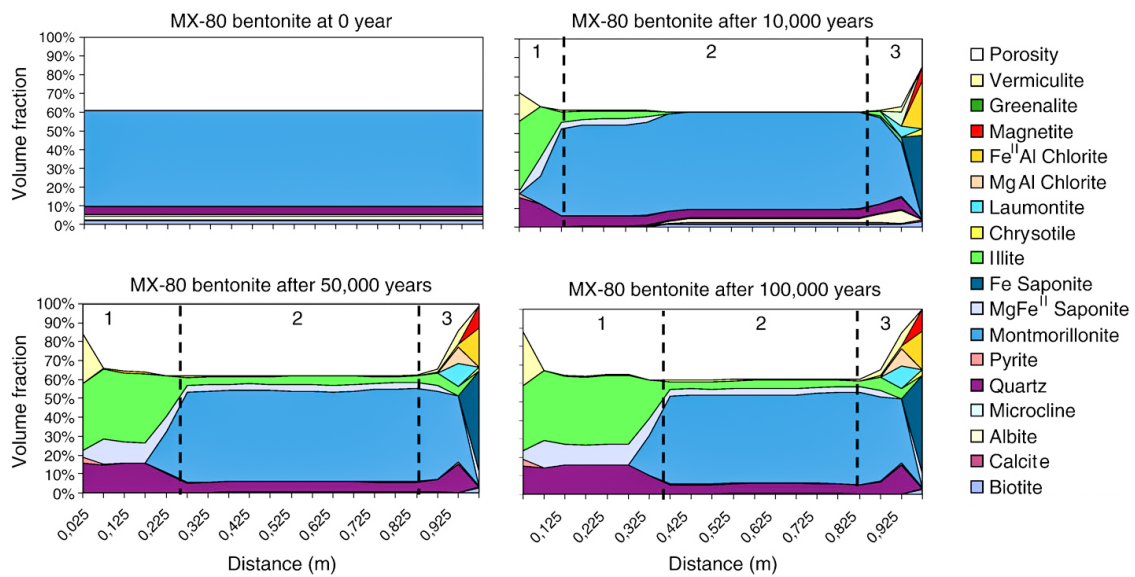


Fig. 5-12: Mineralogical evolution at 100 °C of MX-80 in contact with COX porewater (left boundary) and with the modelling cell of the steel overpack corrosion (right boundary)

Marty et al. (2010)

Leupin et al. (2015) give experimental results for MX-80 and montmorillonite in contact with 0.2 M NaCl, or KCl, and 0.1 M CaCl₂ or MgCl₂ at 20 °C for 2 weeks. In all cases, a dissolution rate of approximately 2.5×10^{-12} mol Si/g clay/s was found at first, when Si activity is well below equilibrium. In addition, an increase in layer charge was measured, and the chemical composition of the resulting solid was determined. All results point towards the alteration of the montmorillonite towards a beidellite, although the presence of cristobalite and amorphous silica may have influenced the experiment, and layer charge measurements are highly error-prone in such systems. The aluminium required for the beidellitisation process seems to be provided by parallel congruent dissolution of the montmorillonite. This process might only occur in low Si solutions, unrealistic for the porewaters from quartz-containing host rocks. No K fixation was observed, in contrast to batch experiments at higher temperatures described in the same report.

At present, no experimental data on montmorillonite stability in host rock porewater at low temperatures exist. Possibly, reactions under such conditions and within reasonable experimental timescales affect volumes and concentrations below the detection limits of any analytical approach. Leupin et al. (2015) recommended using high-temperature data as upper bounding values and for process understanding. They conclude, based on their experiments, that illitisation occurs only at high K activities and elevated temperatures, but not in contact with K-feldspar-saturated solutions or at room temperature. Natural analogues are often regarded as closed systems with restricted K availability, or temperatures are above the long-term repository temperature. However, bentonite-host rock interface samples, or interfaces suitable for sampling, are available from large-scale and rock laboratory experiments (e.g. Mont Terri CI) but have not been investigated so far.

5.2.5 Significance of host rock – bentonite interaction for the Nagra concept

The predominant bentonite porewater composition is not yet exactly known: the limited volumes of readily soluble bentonite secondary phases and other EBS materials compared with the host rock porewater volume suggest dissolution of gypsum, cement, and reaction of steel. In the case of slow transport (e.g. clogging), the entire bentonite will be equilibrated with the resulting porewater different from OPA porewater for the major part of the repository lifetime. In contrast, with ongoing diffusive exchange between bentonite and OPA, the minor dissolved EBS material will diffuse and dilute into the host rock, and the bentonite porewater will resemble the host rock porewater during the remaining time, possibly for the major duration of the planned lifetime. Numerical simulations including the entire EBS and sufficient host rock volume mostly ignore the influence of the charged clay sheet surfaces on transport in the porewater and/or on solid phase reactions. Assuming the predominance of the host rock porewater, the following minor safety-relevant effects of its interaction with bentonite can be expected:

- Extrapolations from literature data suggest swelling pressure differences up to 900 kPa in the ionic strength and Na/Ca ratio ranges of potentially equilibrating host rock porewaters (bentonite dry density $1,500 \text{ kg m}^{-3}$). Along with swelling pressure, hydraulic conductivity also changes, but quantification is difficult due to the poor and scarce reference data available. However, the expected change in hydraulic conductivity is below one order of magnitude. Chemical influences on both swelling pressure and conductivity will not lead to values below the Nagra requirements (Appendix), even accounting for the large uncertainty in underlying data. However, the latter lead to large uncertainties in estimation of saturation time or in understanding of processes.
- Although many studies indicate the instability of montmorillonite in high K solutions, Leupin et al. (2015) and Karnland & Birgersson (2006) classify the montmorillonite transformation as negligible under repository conditions (both mainly based on extrapolation of experimentally derived kinetic data from Huang et al. 1993, as well as natural analogues). Experimental data for bentonite equilibrated with OPA porewater at room temperature are still missing. Montmorillonite dissolution or transformation under these conditions is expected to be either non-existent (too high activation energy), or below the detection limit. In the latter case, montmorillonite reactions might still be relevant within the one million years of interaction (Savage & Liu 2015).

5.3 Interaction of cementitious tunnel support structures and bentonite

Concrete-bentonite interaction was assessed by Savage (2014) and Bradbury et al. (2014) in the context of Nagra's HLW repository concept. The interaction is controlled by the transport of aqueous species in the porewater across the interface, and reactions of the resulting modified porewater with the original solids. Since these reports, additional kinetic and thermodynamic data for montmorillonite have confirmed older measurements, and the list of possible neoformations increased (evidence from batch experiments). At the same time, experimental and modelling approaches combining transport and reactions have evolved significantly. The concept of anion exclusion in the major part of the bentonite porosity must be considered, especially if pore clogging occurs. The figure shown in the reports above summarising cement-bentonite interaction mechanisms and their coupling is extended with recent findings and with cement-specific mechanisms not considered so far (Fig. 5-13).

Cement-clay interaction has been investigated in numerous studies in the context of host rock or barrier interaction with a cementitious tunnel support or waste matrix in case of some L/ILW types. The special case of compacted bentonite differs from most natural claystone formations:

- Montmorillonite represents the predominant clay mineral in bentonite, contrasting to a whole range of sheet silicates generally present in claystone. In many claystones, montmorillonite mainly occurs in the form of illite-smectite mixed layers and may be subordinate to other non-swelling clays/sheet silicates such as kaolinite and chlorite. Therefore, clay stability and dissolution kinetics are expected to be different in bentonite and in claystone, and ion-exchange capacities much larger in bentonite (e.g. a factor of 10 between MX-80 and OPA).
- With respect to the emplacement of the materials in a repository, the application of fresh unhydrated shotcrete onto the partly desaturated claystone host rock (tunnel wall) defines the onset of cement-clay interaction. In contrast, mostly desaturated bentonite (barrier) contacts the hardened shotcrete's carbonated surface of tunnel liners. The bentonite is subsequently saturated by host rock porewater, which flows through the shotcrete barrier, leaches the latter, and picks up the chemical signature of cementitious porewater. The interaction of cement and clay in general leads to porosity clogging, as observed (Dolder et al. 2016) and modelled for comparable systems (Berner et al. 2013, Kosakowski et al. 2014, Marty et al. 2015b). Therefore, gaps in the concrete liner ensure that bentonite saturation may continue after this possible clogging of concrete-bentonite interfaces. The interaction of bentonite with cementitious leachates and porous concrete is therefore a complex multi-stage process.
- Solute transport within compacted bentonite differs substantially from claystones: total porosity is much higher in bentonite (even at high compaction), the anion-accessible porosity fraction in bentonite is much smaller, and Donnan porosity (absolute and in proportion) is higher than in most claystones. Advective and diffusive transport, as well as porosity clogging, differ substantially.

Based on the arguments above, the literature reviewed here is restricted to bentonite on the clay side, including simplifications of the bentonite-cement system. The last two bullet points mentioned above might be irrelevant for the final equilibrium state of a system, but significantly influence the time evolution and transient states. Simple mass-balance calculations (e.g. dissolved volume of bentonite per dissolved volume of cement) cannot predict a hypothetical case of an impermeable clogging zone in thermodynamic equilibrium with the porous media on either side. However, the existence of complete clogging in bentonite is questionable (section 4.1).

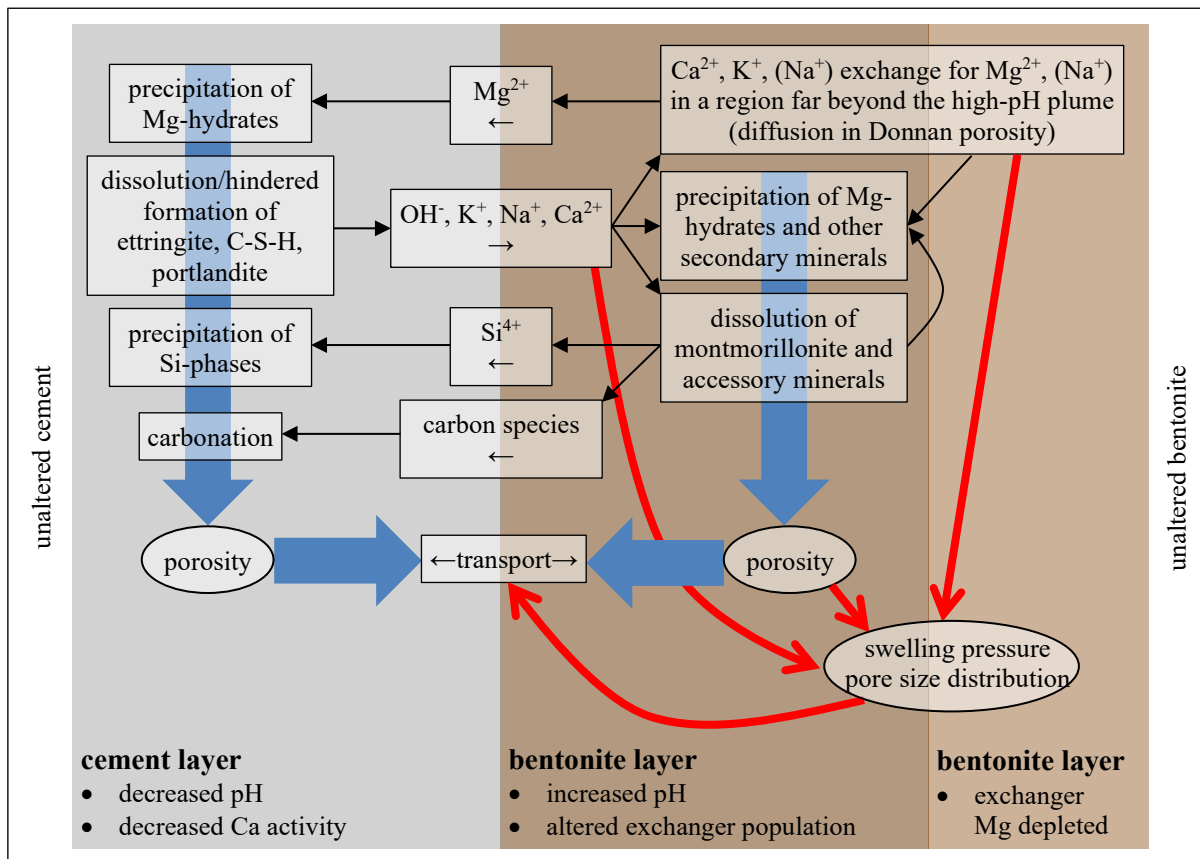


Fig. 5-13: Cement-bentonite interaction as a coupled non-linear system

Takase (2004)

5.3.1 Experimental data constraining cement – bentonite interaction

Smectite stability studies indicate a strong influence of the various substitutions typical of clay minerals. Valuable data on montmorillonite stability at elevated pH exist (e.g. Johnston & Miller 1984), as well as on dissolution kinetics (Rozalen et al. 2009b). All smectites are likely thermodynamically unstable at $\text{pH} > 12$.

Bentonite interaction with alkaline fluids has been widely investigated in unconfined batch experiments (*bentonite dispersions* with low solid-liquid ratio). In many studies, montmorillonite dissolution and precipitation of zeolites was confirmed (De La Villa et al. 2001, Ramírez et al. 2002, Fernández et al. 2010b, Fernández et al. 2014a). Depending on the nature of the bentonite (mainly smectite mineralogy) and temperature, additional neoformations such as feldspar, mixed-layer illite/smectite, and saponite have been detected. These results do not necessarily apply for cement-bentonite interfaces, because the alteration of the alkaline solution during its diffusion into the bentonite is missing in batch set-ups: the diffusion-active porosity is much smaller for anions than for other species in compacted bentonite. Ion-exchange, surface complexation and solid phase reactions (both buffering pH) further alter the porewater composition during its penetration into the bentonite. The complex layering of interaction zones parallel to interfaces observed on both sides of clay-cement interfaces indicates such progressive porewater alterations (e.g. Dolder et al. 2016).

Therefore, interaction of the *alkaline fluid penetrating into a compacted bentonite* is more comparable with the EBS set-up than batch experiments. The filter between the alkaline fluid and the bentonite represents the cement, and precipitations in the filter suggest back-diffusion and interactions. Such filter precipitations are often ignored in experiments or avoided with continuous filter flushing with the original alkaline solution, or reduced with advective infiltration. Karnland et al. (2007) measured changes in swelling pressure during bentonite exposure to NaCl or NaOH (0.1 – 1.0 M) and could relate them to osmotic effects due to changes in ionic strength and volume decrease due to dissolution of accessories (decrease of dry density), but also montmorillonite dissolution (only at 0.3 and 1.0 M NaOH). The associated CEC increase, together with post-mortem XRD data and measured smectite chemistry, indicated a transformation into beidellite (intermediate step only). Nakayama et al. (2004) observed analcime precipitation not only in dispersions, but also in compacted bentonite at 90 – 170 °C. In contrast, alkaline infiltration of a compacted FEBEX Mg-bentonite at 60 °C led to precipitation of hydrotalcite-like structures, gibbsite, and brucite, at the expense of montmorillonite (Fernández et al. 2009b). Interestingly, K exchanged for Mg within the entire core, and the Mg precipitated within a small high-pH zone at the inlet. Therefore, the Donnan porosity in the entire core (interlayer and DDL) provided a fast pathway for cations, allowing for fast Mg transport to the precipitation zone. At elevated temperatures, discrete brucite did not precipitate; this was the main difference between the 60 and 90 °C experiments (Fernández et al. 2013). Spatially resolved density changes in bentonite cores infiltrated with alkaline solution could be detected non-destructively by X-ray computed tomography (CT, Dolder et al. 2016). The resulting reaction plume penetrating the bentonite is shown in Fig. 5-14. With increasing reaction plume, on-line recorded hydraulic conductivity decreased (Fig. 3-33). Although the reaction plume and conductivity drop occurred in bentonite and sand-bentonite during infiltration of both high-pH (OPC) and low-pH (shotcrete) solutions, differences in precipitated minerals, evolution of outflow chemistry, and volume changes of the core have been found (Dolder 2015). The drop in hydraulic conductivity was associated with mineral precipitation within the reaction plume, possibly also influenced by porosity redistribution as a response to changing ionic strength (CM coupling). Also, changes in core size at different distances from infiltration suggested CM coupling effects. Apart from calcite precipitations, mineral reactions were close to the detection limit for the chosen experimental conditions: saponite precipitated in most experiments, whereas barely detectable XRD reflections might indicate the presence of brucite or talc in some cases. Only in one case could cristobalite dissolution be confirmed at the inlet, but all experiments revealed an increased silica outflow, indicating dissolution of silicates. In the low-pH infiltrate, formate initially carried most of the negative charge but was absent in the outflow. This and other indications support the presence of microbes in the filter, but possibly also in the sand-bentonite.

Montmorillonite dissolution rate in sand-bentonite mixtures and the impact of alkaline infiltration on OH⁻ diffusivity and hydraulic conductivity were investigated in Yamaguchi et al. (2007) and Yamaguchi et al. (2013): mineral dissolution led to a lower EMDD, and therefore to an increase in hydraulic conductivity (section 3.8.1). The disagreement with Dolder (2015), who measured decreasing conductivities during infiltration of cementitious solutions, might be caused by the higher temperatures and higher hydraulic conductivities in the former study.

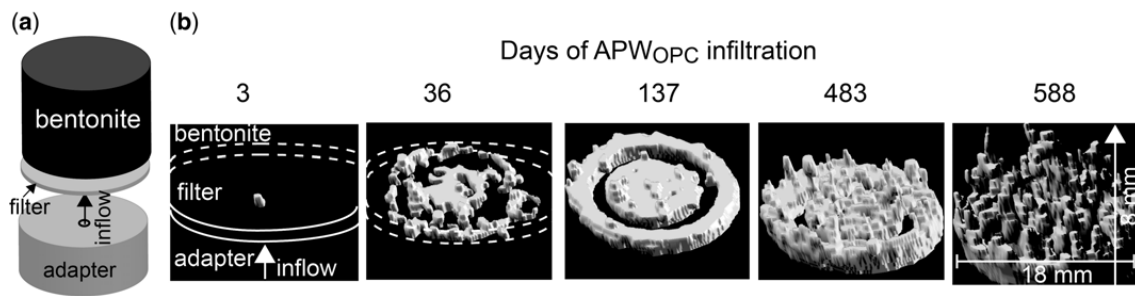


Fig. 5-14: Evolution of a reaction plume based on CT images and analysed by image processing
 (a) Sketch of the analysed section; (b) zone of reaction consisting of an increased X-ray attenuation (time in days after infiltration of OPC artificial porewater APW_{OPC}).
 Dolder et al. (2016)

Laboratory studies involving *entire cement-clay interfaces* are experimentally more demanding and, therefore, limited data exist in the literature. Injecting portlandite-saturated solution (pH 12.6) into cement and adjacent bentonite did not alter the mineralogy at various temperatures (Fernández et al. 2006). In contrast, injection of 0.25 M NaOH solution (pH 13.3) led to precipitation of C-S-H, analcime, and Mg clays, but quartz and feldspar dissolution in the bentonite (mainly at 120 °C). In a zone at the interface enriched in Mg, brucite was found at low temperatures. Cation occupancy measurements indicate the same mechanism as described above: Mg from the exchanger migrated towards the interface and precipitated at elevated pH. Yamaguchi et al. (2016) investigated HTO diffusivity across a high porosity cement paste – bentonite interface. No conclusive alterations in bentonite mineralogy could be found, but portlandite dissolved, and calcite and katoite (a hydrogarnet) precipitated in the cement. Ca from the cement migrated into the bentonite and increased the Ca fraction on the exchanger. The overall decrease of HTO diffusivity is attributed to cement carbonation. Apparently, carbonation decreased porosity to a higher extent than the increase expected from decalcification.

No literature data were found describing cement-bentonite interfaces from *large-scale experiments in rock laboratories*. Especially in Spain and Japan, cement-bentonite (FEBEX) interaction has been extensively investigated, but data from large-scale experiments are missing. Standard core drilling destroys such interfaces, and sophisticated core stabilisation is needed to recover an intact bentonite in contact with concrete (Mäder et al. 2014). Interface characterisation is ongoing in the case of Mont Terri CI samples (Yokoyama et al. 2015), and of Grimsel FEBEX-DP samples (Villar et al. 2018).

Savage et al. (2010b) describe and simulate the alteration of smectite-containing mudstones by fluids in the pH range of 9 – 10 over a three million-year timescale. In this *natural analogue* for low-pH – clay interaction, up to 70 % of detrital clay may be displaced by illite, analcime, and K-feldspar within 100 ka.

CEBAMA is a large EU Project (2015 – 2019) with the focus on cement-clay interfaces and their impact on transport, although the topics covered are rather diverse, and include a reactive transport modelling work package. Bentonite materials examined include FEBEX bentonite (in part from the FEBEX-DP Project mentioned above) and MX-80 bentonite. One approach in the experimental work package combines the core infiltration technique with X-ray CT to monitor reaction progress.

5.3.2 Modelling approaches predicting cement – bentonite interaction

Cement – bentonite interaction is numerically simulated in many *reactive transport modelling* studies and is reviewed in Savage & Cloet (2018). Most approaches concentrate on solid phase reactions and their rates but ignore anion exclusion and resulting effects on diffusive transport (Savage et al. 2002, Gaucher et al. 2004, Watson et al. 2009, Fernández et al. 2009a), as the latter effects can only be simulated with a multicomponent approach. Two different simplifications are commonly made: either the total porosity is treated as free porosity (transport of trace anions is too fast compared to HTO), or only the anion-accessible porosity is treated as free porosity (no transport in the Donnan porosity). Furthermore, large cell sizes at the interface lead to an over-estimation of porosity clogging time (Marty et al. 2009), if the influence of porosity on transport is considered at all. However, Fernández et al. (2010a) predict experimental cement-bentonite interaction well with a multicomponent single-porosity transport approach combined with cation exchange. It was necessary to use much slower diffusion coefficients for anions than for cations. Ishii et al. (2013) realised a remarkable coupled chemical-hydraulic-mechanical modelling approach (Fig. 5-15). Unfortunately, the relationships between chemical and mechanical properties are not explained.

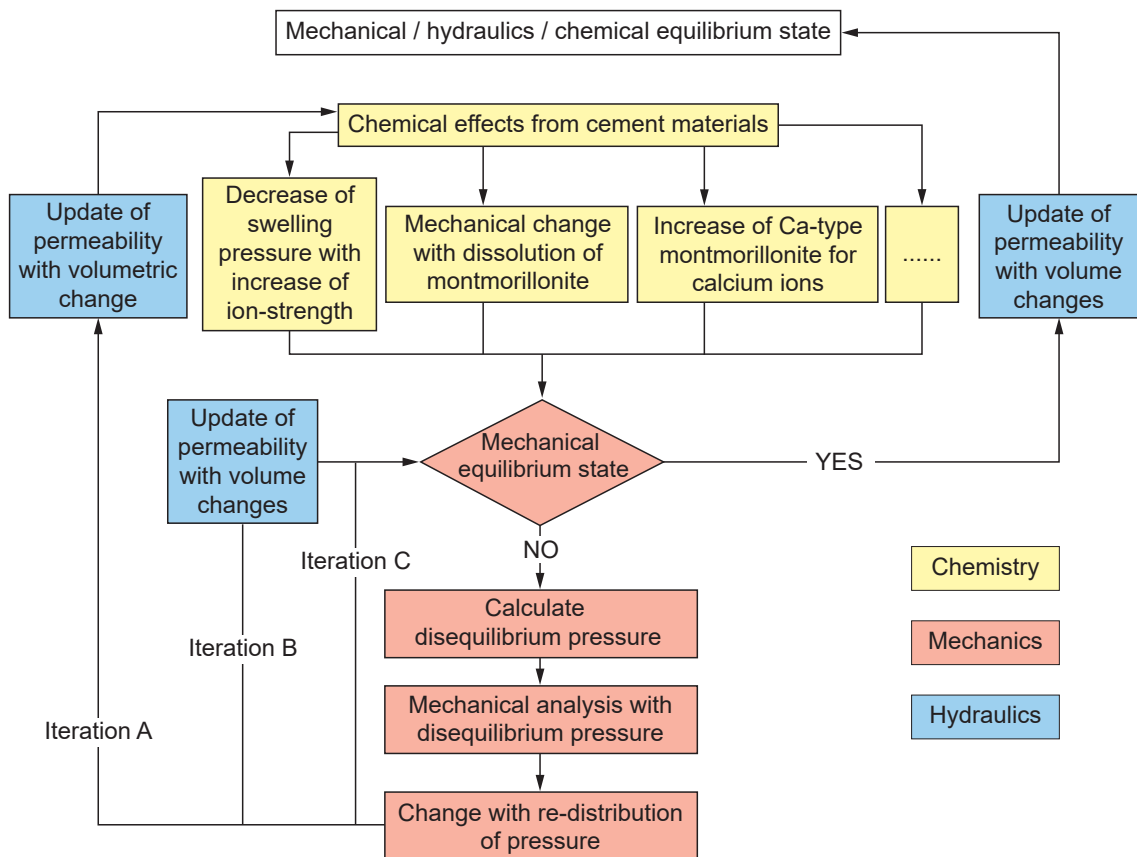


Fig. 5-15: Schematic diagram of the coupled hydraulic/mechanical/chemical analysis approach employed

Ishii et al. (2013)

5.3.3 Significance of cement – bentonite interaction for the Nagra concept

Many laboratory and natural analogue studies strongly indicate dissolution of montmorillonite and precipitation of secondary minerals in bentonite in contact with cementitious material. Uncertainties in reaction rates still exist. The subsequent decrease of swelling pressure is not only attributed to montmorillonite (and accessory mineral) dissolution, but also to osmotic effects: higher ionic strength and Ca exchange for Na lowers swelling pressure (section 3.8). Straight-forward mass balance calculations can estimate the maximum montmorillonite fraction dissolved as a function of the mass of concrete present (Savage 2014). From this, the decrease in swelling pressure can be estimated. Scarce experimental data allow for the estimation of the additional swelling pressure reduction attributed to chemical effects.

Although such calculations can be done, it is still unclear if and how this simplified fully reacted state is attained. Recent studies (e.g. Jenni et al. 2014b, Jenni et al. 2017) show that OPA interaction with certain concrete types can lead to porosity reduction at the interface, affecting the resaturation of the bentonite. Similar effects must be expected at the bentonite – concrete interface. Gaps in tunnel liners might provide resaturation pathways across the host rock – bentonite interface (section 5.2) but could lead to inhomogeneous resaturation with chemical and mechanical inhomogeneities after completed resaturation. At the moment, no data exist on bentonite – cement interfaces from real-scale experiments with bentonite saturation across a concrete liner.

Virtually all reactive transport models simplify the multiporosity properties of bentonite. Therefore, changes in porosity, as well as their effect on transport (including clogging time), cannot be predicted reliably at this stage. Furthermore, CM coupling affects the pore size distribution in bentonite and therefore transport and clogging behaviour as well (section 3.8), but this has not been considered in any numerical simulation so far.

5.4 Interaction of steel and bentonite

There are large amounts of steel in the HLW repository, most of which are contained in the canister contacting the buffer at the inner interface. Furthermore, in the current concept, the support of rock walls in emplacement drifts foresees a cementitious liner, rock bolts and a steel mesh. (Fig. 5-16). Inevitable corrosion of these steel materials in contact with water will occur, leading to oxidised Fe(II, III) species and – once the residual O₂ in the near-field has been depleted – to the production of H₂ gas.

In fact, roughly three corrosion stages can be distinguished: (1) an initial aerobic corrosion stage under hot and variably saturated conditions followed by (2) anaerobic corrosion under hot and variably saturated conditions, and finally (3) anaerobic corrosion under temperate and fully saturated conditions. Stages (1) and (2) will be short (a few decades) compared to stage (3) and therefore the final stage is the most relevant regarding the safety functions of the bentonite backfill (Bradbury et al. 2014).

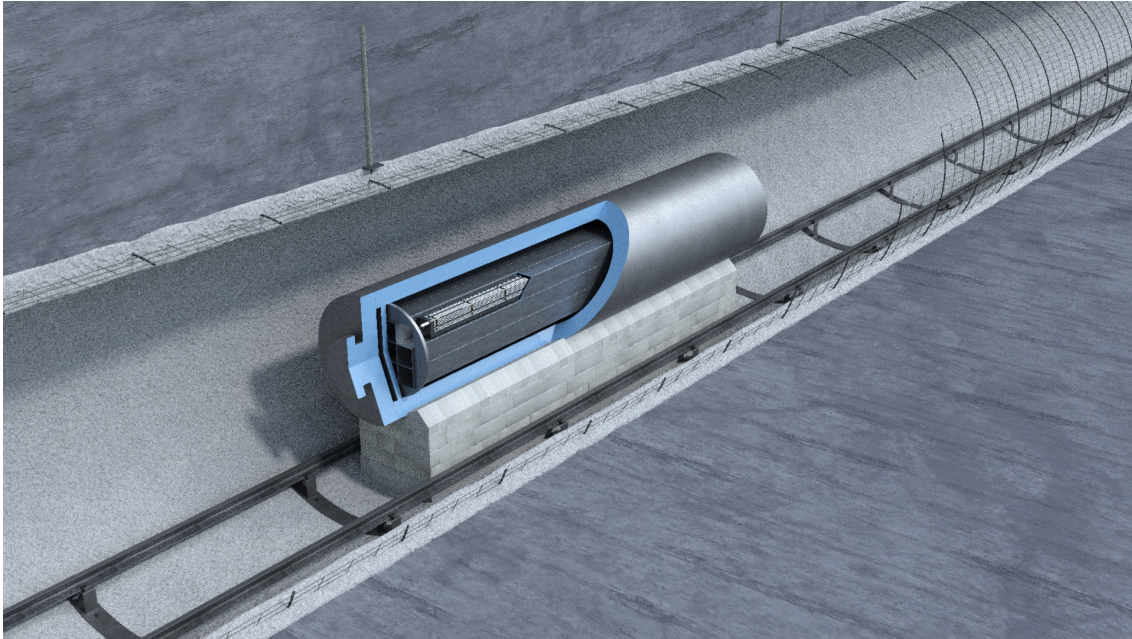


Fig. 5-16: Schematic illustration showing the HLW near-field without bentonite backfill for better visualisation of steel-containing materials such as rock bolts, mesh, rails and canisters

The relevance of iron corrosion for the backfill performance has been recognised only rather recently. A cornerstone in this regard was the workshop initiated jointly by Nagra, Andra and SKB (Wersin & Mettler 2006), where the impact of corroding Fe on bentonite materials was discussed. In principle, various adverse effects may result from Fe-bentonite interaction, including:

- local cementation of the bentonite via precipitation of Fe(II)/(III) oxides and hydroxides
- transformation of montmorillonite to a non-swelling phyllosilicate (e.g. berthierine)
- sorption competition of corrosion-derived Fe(II) with radionuclides
- reduction of structural Fe³⁺ and subsequent destabilisation of the dioctahedral montmorillonite structure
- direct interaction of H₂ with structural Fe³⁺ in the smectite

The following sections are focused on the discussion of the first three points. The last two points have been discussed in section 3.4.6.

Literature reviews on the impact of Fe-bentonite interaction on the backfill were carried out in the context of the Finnish/Swedish KBS-3H concept (Wersin et al. 2007a) and for Nagra's HLW concept (Bradbury et al. 2014). From the conclusions drawn therein, the following are worth noting here:

- Fe-bentonite interaction processes influence steel corrosion and compete with the precipitation of iron (hydr)oxides. The details of this interaction are still not understood entirely.
- The presence of iron, and particularly Fe(II), may destabilise the smectite structure and lead to its alteration, but this process is slow and difficult to investigate experimentally. Two types of transformation products may form: swelling and non-swelling phyllosilicates. The exact

nature of these minerals is challenging to identify, but Fe-rich smectites (e.g. saponite) on the one hand and 1:1 phyllosilicates (especially berthierine) on the other have been found in a number of experiments. Chlorite was not found in experiments at less than 100 °C.

- Based on mass balance considerations, corroding Fe in Nagra's HLW repository has the potential to transform a substantial part, if not all, of the montmorillonite in the backfill. This effect, however, will be attenuated by (i) the precipitation of Fe(hydr)oxides and Fe carbonates, (ii) the slow diffusion rate of Fe(II) and (iii) the slow reaction kinetics of montmorillonite.
- An important drawback preventing more accurate prediction of the interaction processes is the uncertainty related to the thermodynamic and kinetic properties of clay minerals.
- There is a lack of experimental data representing conditions and possible evolution in a repository setting (e.g. variable redox and saturation conditions, elevated temperatures, diffusive mass transfer). In fact, most studies examined idealised laboratory systems, tuned to enhance the effect of Fe-bentonite interaction. Thus, they were generally conducted in dispersed batch systems at high liquid/solid and high Fe/clay ratios.
- Changes in bulk properties (swelling pressure, hydraulic conductivity) of bentonite affected by corroding iron have not been investigated in detail.

In the following, selected recent experimental and modelling data that shed some further light on the Fe-bentonite interaction are presented and discussed.

5.4.1 Recent modelling studies

Thermodynamic relationships

Recently, efforts have been made to improve the thermodynamic data of clay minerals in the context of radioactive waste disposal and to integrate them into consistent thermodynamic databases (Blanc et al. 2012, Giffaut et al. 2014). The data also include minerals relevant for Fe-clay interaction. A specific exercise in this regard was performed by Wilson et al. (2006) and Wilson et al. (2015) who estimated Gibbs free energies of formation for a set of simplified clay mineral compositions. On this basis, Wilson et al. (2015) derived stability diagrams for 1:1 minerals and smectites as illustrated in Fig. 5-17. It shows Fe-rich clay mineral stabilities as a function of SiO_2 activity and the $\text{Fe}^{2+}/\text{H}^+$ activity ratio at 25 and 80 °C. The diagram suggests that Fe-rich 1:1 layer silicates such as berthierine are only stable at low Si activity, below quartz saturation. At higher Si activity, corresponding, for example, to chalcedony or amorphous silica saturation, the data suggest that Fe-smectites are more stable. Also shown in Fig. 5-17 is the range of conditions of OPA porewaters as inferred from measurements at Mont Terri. This suggests that, from a thermodynamic viewpoint, both Fe-smectites and non-swelling 1:1 layer silicates are possible transformation products of Fe-bentonite interactions under repository conditions.

Uncertainties exist about the porewater in contact with the steel surface. If this porewater is still influenced by the negatively charged clay sheets, then pH and activities of solutes in this Donnan porewater differ from the values of a (extractable) free porewater. However, the chemistry of the bentonite free porewater is generally considered in modelling corrosion reactions, based on considerations outlined in section 3.4.7.

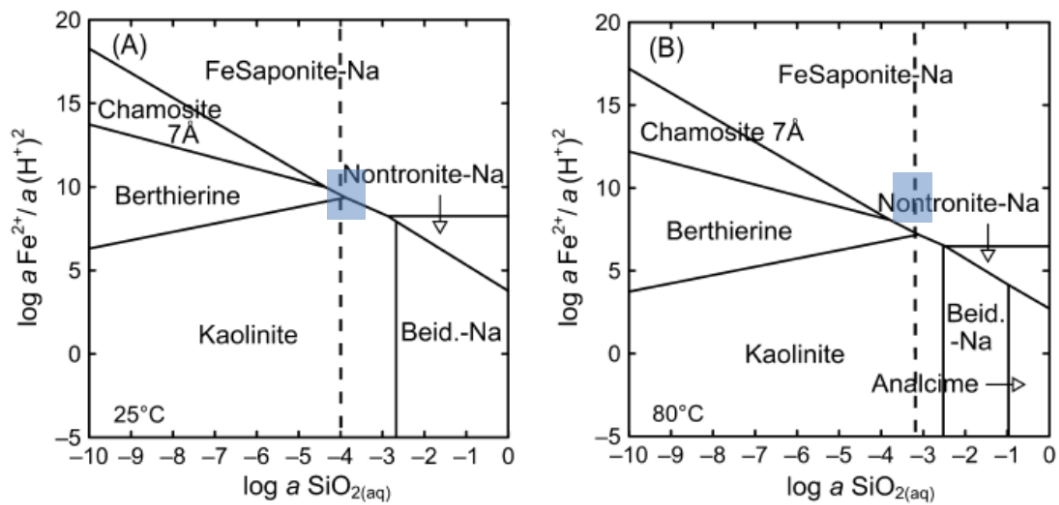


Fig. 5-17: Activity diagrams displaying smectite 1:1 clay stability fields for $\text{Na}_2\text{O}-\text{Al}_2\text{O}_3-\text{FeO}-\text{Fe}_2\text{O}_3-\text{H}_2\text{O}-\text{SiO}_2$ at 25 °C (A) and 80 °C (B) as a function of $\text{SiO}_2(\text{aq})$ activity

Iron oxides not included. Blue field: expected range of conditions of OPA porewaters based on Mont Terri data. Dashed line: quartz solubility.

Wilson et al. (2015)

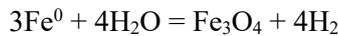
Reactive transport modelling studies

Several corrosion and Fe-bentonite modelling studies in the context of simulating the evolution in the EBS have been carried out for different repository concepts. These have been partly reviewed (Wersin et al. 2007b, Bradbury et al. 2014). The modelling strategies, assumptions and systems considered being quite different, it is not surprising that the predicted impact on the bentonite buffer differs considerably. For example, about 40 % of montmorillonite was predicted to have transformed to illite and, to a lesser extent, to saponite in the study of Marty et al. (2010) (Fig. 5-12). In other studies, such as Savage et al. (2010c), Wersin & Birgersson (2014) or Wilson et al. (2015), the extent of montmorillonite transformation was generally lower, but lower temperatures were assumed and illite formation was not accounted for. Further relevant findings are briefly discussed here:

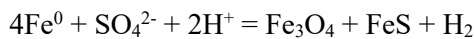
- **Clogging:** Mineral precipitation at the Fe-clay interface resulting in partial or complete clogging was predicted in many long-term simulations (e.g. Bildstein et al. 2006, Savage et al. 2010c, Marty et al. 2010, Wilson et al. 2015). It should be pointed out that the extent of clogging depends on grid size (Marty et al. 2010) and is also related to the type of diffusion model. In fact, models generally assume a single "bulk" porosity and ignore diffusion in the interlayers and electrostatic effects, such as anion exclusion (Wilson et al. 2015). In particular, according to a more advanced double porosity model description (Jenni et al. 2016), transport of cations across a "clogged" interface is possible (supported by experimental findings from Chagneau et al. 2015).
- **Effect of pH:** This parameter strongly affects both corrosion and smectite dissolution. Note that the corrosion reaction itself produces hydroxyl ions. For anaerobic corrosion, the reaction with water can be described as:



Precipitation of corrosion products, such as $\text{Fe}(\text{OH})_2$ or magnetite, will consume OH^- , thus no net pH change will result if all Fe^{2+} is consumed:



However, if precipitation kinetics of corrosion products are slow or slowed down, high pH conditions may persist, leading to enhanced dissolution of montmorillonite. This has been illustrated by a sensitivity analysis of Wersin & Birgersson (2014). In their model, a uniform corrosion rate of $1 \mu\text{m/a}$ was assumed. The largest pH effect was induced by concomitant iron corrosion and sulphate reduction via H_2 oxidation, leading to concomitant iron sulphide and iron oxide formation:



With the high pH induced, the model predicted transformation of montmorillonite to zeolite and hydrotalcite, but no Fe silicate in that case. As illustrated in Fig. 5-18, the spatial extent of montmorillonite alteration is greatly increased after 5,000 years ($\sim 7 \text{ cm}$) for the case of sulphate reduction compared to the base case where sulphate reduction is inhibited ($\sim 1 \text{ cm}$).

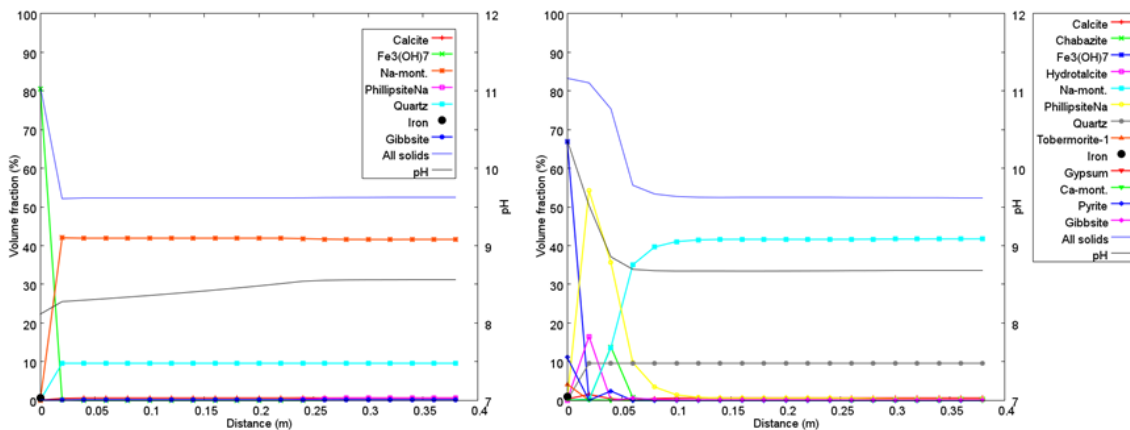


Fig. 5-18: Simulations of Fe-bentonite interactions for KBS-3H (Wersin & Birgersson 2014): spatial distribution of solids and pH away from the Fe/bentonite contact

Left: base case with green rust as the main corrosion product. Right: case with microbial sulphate reduction occurring at Fe/clay contact.

- **Fe(II) sorption process:** Fe(II) is known to strongly react with the smectite surface. From batch experiments under disperse conditions, a fairly complex interaction process was unravelled: cation exchange at interlayer sites, surface complexation at edge sites and electron transfer with structural Fe(III) (Tournassat 2003, Muurinen et al. 2014, Soltermann et al. 2014b, Soltermann et al. 2014a, Latta et al. 2017). The extrapolation of Fe(II) sorption to a compacted diffusive system is at present not straightforward and in fact has not been attempted in the modelling studies mentioned above. One aspect to bear in mind is the possibility of pH change due to the sorption process (Wersin & Birgersson 2014).
- **Clay mineral equilibria and cation exchange:** Cation exchange, an intrinsic property of smectites, has been included in some of the modelling studies (e.g. Bildstein et al. 2006, Wilson et al. 2015), whilst in others it was not (e.g. Savage et al. 2010c; Wersin & Birgersson 2014). It should be kept in mind that consistent thermodynamic description of both ion exchange and solubility for montmorillonite is difficult (e.g. Kittrick 1979). Notably, this regards the issue of "double counting" of cations (exchangeable and structural) when montmorillonite dissolves (Wersin & Birgersson 2014, section 3.2).

- Treatment of corrosion: Generally, constant corrosion rates of one to several $\mu\text{m}/\text{y}$ were assumed (Bildstein et al. 2006, Savage et al. 2010c, Wersin & Birgersson 2014) and a separate iron cell adjacent to the bentonite was considered. Wilson et al. (2015) tested different assumptions for iron corrosion and also considered diffusion-limited corrosion. The latter assumption resulted in a much smaller spatial extent of alteration. Another noteworthy point is that the corrosion reaction consumes water whose supply may be limiting, especially in the initial stages of the repository lifetime. This process is rarely included in the modelling (Bradbury et al. 2014).
- Effect of temperature: This parameter affects corrosion, mineral reactions and diffusion. In general, at higher temperatures, a larger impact on the bentonite is expected. This is qualitatively confirmed by the modelling studies. Thus, the spatial extent of alteration is generally larger in the studies where higher temperatures were considered (Marty et al. 2010, Montes-H et al. 2005c, Wilson et al. 2015) than in the studies assuming 25 °C (Savage et al. 2010c, Wersin & Birgersson 2014). Note that all simulations have so far been carried out assuming isothermal conditions and calculations accounting for the temperature evolution in the EBS are lacking.
- Effect of H₂: Considerable overpressures of H₂ may result from the corrosion reaction, as has been shown (e.g. Wilson et al. 2015, Wersin & Birgersson 2014). The process of gas transport and mechanical impact on the buffer has not been included so far. It should also be noted that build-up of gas pressure could in principle affect transport of water to the metal surface and slow down the corrosion reaction.

5.4.2 Recent in-situ experiments

The impact of corrosion and Fe-bentonite interaction has been investigated in several in-situ experiments. Of particular interest in this regard are ABM1 and ABM2 at the Äspö hard rock laboratory (HRL) and the FEBEX-DP experiment at the Grimsel Test Site (GTS), in which the impact of corroding Fe on heated bentonite was investigated over several years. The advantage of such studies is that conditions reflect repository-type settings. Thus, redox conditions in the above experiments were first oxidising and later reducing; the bentonite materials (inserted as blocks or pellets) were initially unsaturated and reached – at least partially – saturation by natural or artificial wetting in the course of the experiment. Maximum temperatures at the steel/bentonite interface were 100 °C (FEBEX-DP) or even 140 °C (ABM1, ABM2). Contrary to most laboratory experiments, the in-situ tests were run for several years, thus representing the initial stages of a repository.

ABM (Alternative Buffer Materials) experiments

The ABM experiment consists of a series of boreholes in which different bentonite materials were emplaced as ring-shaped blocks (thickness ~ 10 cm) around a steel heater. In the ABM1 and ABM2 boreholes, the bentonite was both saturated with artificial groundwater and heated to temperatures up to 140 °C (Svensson et al. 2011, Svensson 2015) for 2.5 and 5 years, respectively. A preliminary study of an Fe-MX-80 bentonite interface in ABM1 was carried out by Wersin et al. (2014a). More recently, Hadi et al. (2017a) have conducted a systematic geochemical and mineralogical investigation of Fe – clay interfaces in the ABM2 borehole, involving different bentonite materials and positions in the borehole as well as a suite of analytical methods.

Fig. 5-19 (left) depicts highly compacted MX-80 pellets in a steel cage inserted around a steel heater before emplacement in the ABM2 borehole. The same material after a reaction time of 5.5 years exhibited a homogeneous saturated bentonite mass and clearly visible corrosion features (Fig. 5-19, right).



Fig. 5-19: MX-80 pellets emplaced in steel cage around a steel heater in the ABM2 test before (left) and after (right) the experiment

Hadi et al. 2017a

From carefully calibrated SEM/EDX (energy dispersive X-ray spectroscopy) data, spatially resolved elemental profiles perpendicular to the Fe source were acquired. These revealed a systematic strong Fe increase within the first 5 to 10 mm adjacent to the interface (Fig. 5-20)⁸. These Fe profiles could be fitted with an empirical bimodal diffusion model. This yielded apparent diffusion coefficients of $1 - 8 \times 10^{-13} \text{ m}^2/\text{s}$ and $0.4 - 1 \times 10^{-14} \text{ m}^2/\text{s}$ for the fast and slow diffusion coefficient, respectively. It should be noted that this approach is entirely empirical and does not reflect the underlying mechanisms, which, besides diffusion, involve sorption, precipitation and redox reactions (see below). The obtained values are in the same range as those derived by Xia et al. (2005) for Fe(II) diffusion in compacted bentonite, but higher than reported by Muurinen et al. (2014) who estimated D_a values for Fe(II) in the range of 10^{-15} to $10^{-16} \text{ m}^2/\text{s}$. Despite the differences in the estimated diffusion coefficients, they underline that Fe(II) diffusion is strongly retarded compared to an inert tracer.

From the amount of Fe transferred from the metal source to the clay, the corrosion depths were estimated to be $\sim 20 - 30 \text{ }\mu\text{m}$. Considering the total experimental run time, this yields average corrosion rates of roughly $4 - 6 \text{ }\mu\text{m/a}$.

The largest part of the Fe close to the interface could be attributed to Fe(III) oxides, mainly goethite. The corrosion layer at the metal surface in turn was found to be more enriched in Fe(II), sitting in magnetite and siderite. On the clay side adjacent to the Fe(III) oxide enrichment, newly formed Fe(II) which extended deeper into the clay was found. The nature of this diffused Fe(II) in the clay could not be identified. Possibilities discussed by Hadi et al. (2017a) include sorbed Fe(II), reduced structural Fe, amorphous mixed Fe(II)/Fe(III) hydroxides (green rust) or even neo-formation of Fe-rich clay. A phenomenological model for explaining the Fe distribution is summarised below.

⁸ An exception is sample #24, the Rokle bentonite, which naturally contains a much higher amount of Fe than the other analysed bentonites.

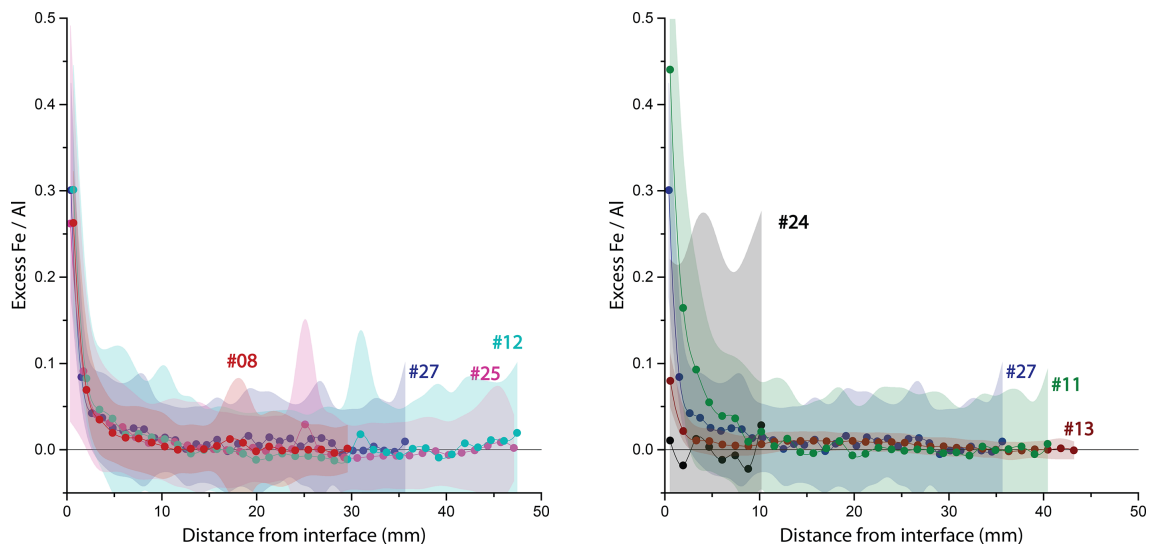


Fig. 5-20: Fe/Al profiles perpendicular to Fe contact of different blocks in the ABM2 test measured by SEM/EDX (Hadi et al. 2017a)

Points represent average values and areas represent standard deviation. Red line: Background Fe/Al concentration determined by X-ray fluorescence (XRF).

Another systematic finding was the enrichment of Mg close to the heater surface. A part of this enrichment was related to a local boiling event in the upper section of the bentonite package resulting in formation of Mg and Ca sulphate salts. Another part of enriched Mg was explained by the higher Mg content on the exchanger. This may have been caused by the precipitation of (unidentified) Mg minerals and concomitant diffusion of Mg^{2+} in the interlayer along the concentration gradient (Hadi et al. 2017a). It is worth noting that Svensson (2015) identified a small amount of trioctahedral saponite at the contact to the steel heater in one sample. Other than this finding, no indications of smectite alteration by the combined heat and corrosion impact could be found. The stability of the originally present smectite is also suggested from the observed absence of changes in CEC and in the constant Al/Si elemental ratios.

FEDEX-DP

The FEBEX experiment was a large-scale in-situ experiment with two heaters surrounded by FEBEX bentonite blocks in crystalline rock (section 5.1). Saturation of the clay occurred via natural inflow (Grimsel groundwater) from the rock. The heat output was regulated to 100 °C at the heater surface. Operations started in 1996 (Huertas et al. 2006), dismantling of the 1st heater section was carried out in 2002 and the remaining section was re-plugged. The 2nd heater section was dismantled in 2015 and since then an extensive investigation programme has been conducted (termed FEBEX-DP). A significant part of this programme included corrosion and Fe-bentonite studies which were compiled in Wersin & Kober (2017 (eds.)). The studied bentonite samples were exposed to 18 years of heat and Fe corrosion under variably saturated conditions.

The results from the Fe-bentonite interaction studies revealed the same type of phenomena and processes as identified in the ABM1 and ABM2 tests. There was, however, a difference in scale of corrosion and interaction features, which in the case of FEBEX could be large and macroscopically visible by reddish and greenish colourations at the contact to steel surfaces. The reasons for the differences are the longer exposure time and, more importantly, the longer timescale of saturation and oxidising conditions. This led to locally massive accumulations of Fe(III) oxides.

An example is shown in Fig. 5-21 (left), which shows an inner reddish and outer blueish Fe-bentonite interaction zone. The Fe front emanating from the corroding steel surface corresponds to the reddish halo, thus extending ~ 50 mm into the bentonite clay. The Fe consists mainly of Fe(III) in the form of goethite. Further on, a weaker second Fe front in the blueish zone up to about 100 mm with Fe contents of about 10 % above background levels could be deduced (Fig. 5-21, right). Therein, the Fe(II)/Fe(III) is slightly increased, suggesting an Fe(II) diffusion process which may however have been accompanied by a complex redox reaction with the clay (see below). It is noted that the Fe-bentonite interactions and the extent of Fe fronts were very heterogeneous in the FEBEX experiment. In fact, a nearby sample displayed essentially no interaction at all (Fig. 5-21, right, red curve). The reason for this heterogeneous behaviour is the spatially variable moisture and O_2 content in the central part close to the heater (Wersin & Kober 2017).

A further finding was the lack of montmorillonite alteration. However, dissolution of some SiO_2 minerals and formation of minor Mg-rich smectite (saponite) close to the heater could be detected.

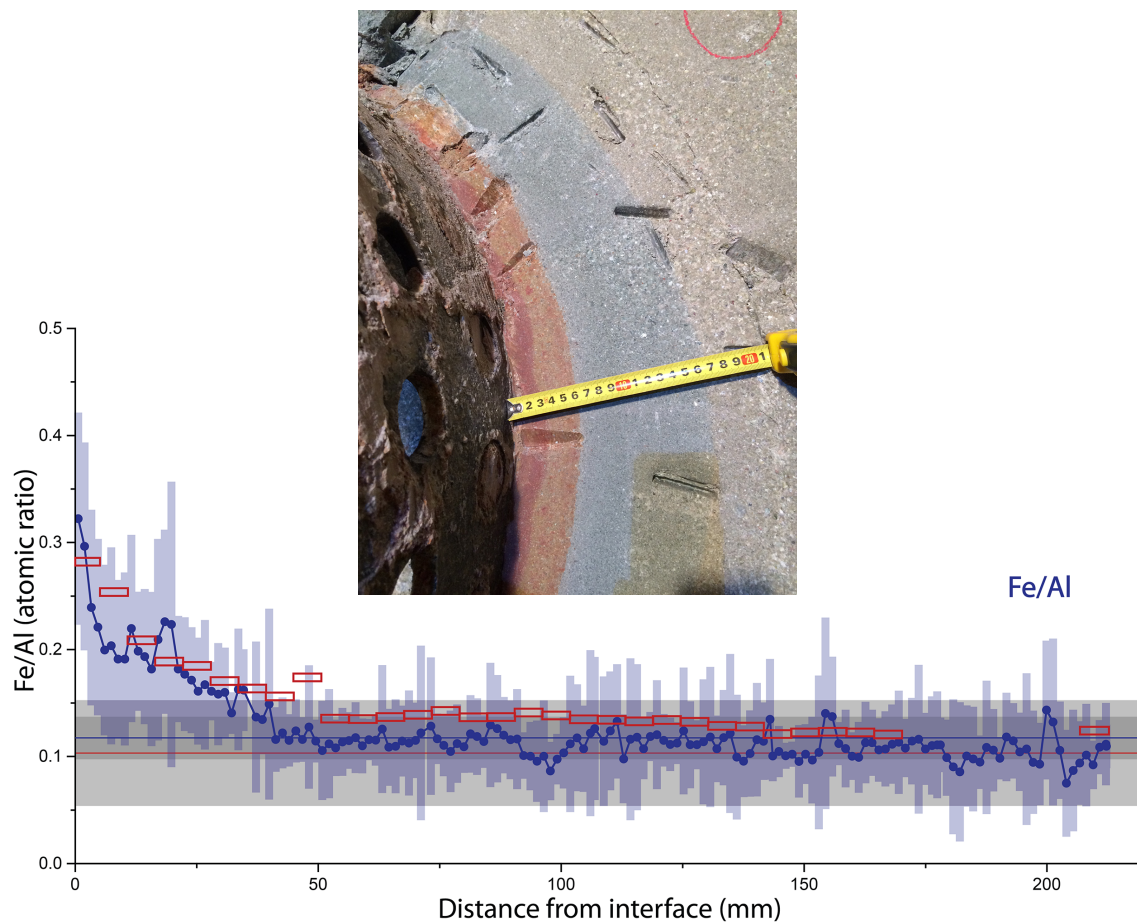


Fig. 5-21: Contact zone between the steel liner and bentonite in the FEBEX-DP test (photo) and Fe/Al profiles perpendicular to contact in the same contact zone (blue line) and in a nearby sample (red line) where no interaction was observed (graphic)

A phenomenological model of Fe-bentonite interaction

Based on analyses of Fe-clay interfaces, a phenomenological model for the redox evolution and Fe(II) diffusion was proposed (Hadi et al. 2017b, Hadi et al. 2017a). This can be summarised by the following stages:

- Initial state: The steel is coated with a thin magnetite layer which is in contact with unsaturated bentonite containing structural Fe(III) in smectite as the main iron pool.
- Phase 1: Aerobic corrosion of steel leads to the formation of Fe(III) oxides. O₂ and H₂O transfer to steel diminishes as corrosion proceeds and the corrosion layer thickens.
- Phase 2: Anaerobic corrosion of steel at the inside of the corrosion layer leads to generation of Fe(II) and formation of magnetite and siderite in the corrosion layer. Furthermore, (rapid) electron transfer across the corrosion layer occurs, generating Fe(II) at the corrosion layer/bentonite interface which reacts with remaining O₂ to further produce Fe(III) oxides.
- Phase 3: Anaerobic conditions everywhere: Continuation of anaerobic steel corrosion, generation of Fe(II) (and magnetite/siderite) and (rapid) electron transfer across the corrosion layer. Diffusion of Fe(II) into bentonite and accumulation of Fe(II) in clay. Further transport of small fluxes of Fe(II) into clay. The mechanism of this transfer process still needs to be established. It probably involves redox reactions with structural Fe(III) and previously formed Fe(III) oxides.

5.4.3 Competitive sorption of Fe(II)

In a deep geological repository for high-level waste (HLW), stable elements originating from many different sources such as porewaters, tunnel backfill materials, the host rock formation, corrosion of the carbon steel canisters, and finally dissolution of the spent fuel and vitrified HLW are ubiquitous. These stable elements and the released radionuclides themselves can potentially compete with one another for the sorption sites on the backfill material and the host rock, and thus reduce their uptake. Such competitive effects may have consequences for the selection of sorption values for sorption databases used in the safety assessment of radioactive waste repositories (Bradbury et al. 2017). In this section, we will focus on the potential competing effects of dissolved ferrous iron Fe(II) (which may arise from the corrosion of the steel canister) on the sorption values of other radionuclides, while in section 5.5 the influence of the cupric ion Cu(II) (which may arise from the corrosion of a copper canister) will be investigated.

Sorption model for ferrous iron on montmorillonite

The sorption of Fe(II) on synthetic iron-free and natural montmorillonites (STx and SWy) has been thoroughly investigated (Soltermann et al. 2013, Soltermann et al. 2014b). The 2-site protolysis non-electrostatic surface complexation and cation exchange (2SPNE SC/CE) sorption model (Bradbury & Baeyens 1997) was applied to model the experimental sorption data on montmorillonite. In this sorption model, there are essentially three types of sorption sites. At the basal planes of montmorillonite, radionuclide uptake is governed by cation exchange with a sorption capacity equal to the CEC. In addition, there are amphoteric functional groups at the edges and broken bonds of montmorillonite where pH-dependent sorption of nuclides occurs via surface complexation. In the model, strong and weak sites have been assumed to explain the non-linear sorption behaviour of radionuclides on these site types.

Fig. 5-22 shows a sorption edge (pH-dependent sorption of trace Fe at fixed ionic strength) and a sorption isotherm (concentration-dependent sorption of Fe at a fixed pH and ionic strength) on a natural montmorillonite (STx-1). The solid curves in Fig. 5-22 are modelled by Soltermann et al. (2014a) with the parameters given in Tab. 5-3.

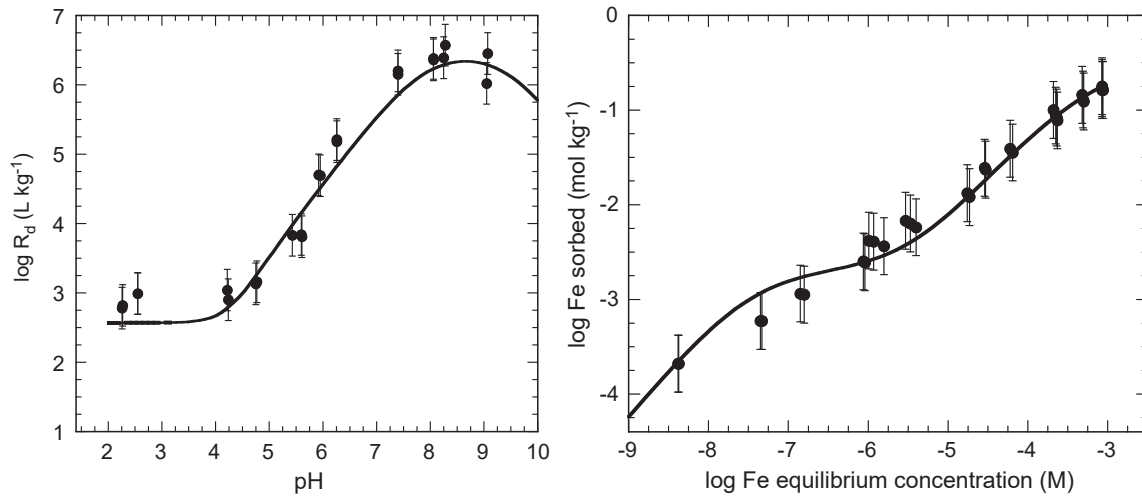


Fig. 5-22 (a) Sorption edge for Fe(II) on Na-STx-1 in 0.1 M NaClO₄. $Fe_{TOT} < 3 \times 10^{-8}$ M; $S \sim 1$ g L⁻¹ and (b) Sorption isotherm for Fe(II) on Na-STx-1 in 0.1 M NaClO₄ at pH = 6.2. (●) experimental data and (—) modelled curve

Soltermann et al. (2014a)

Tab. 5-3: Summary of the 2SPNE SC/CE model parameters, the hydrolysis and surface complexation and cation exchange reactions together with the thermodynamic constants used to calculate the Fe sorption on montmorillonite

| Site types | Site capacities | Source |
|---|---|---------------------------|
| $\equiv S^S OH$ | 2.0×10^{-3} mol kg ⁻¹ | Bradbury & Baeyens (1997) |
| $\equiv S^{W1} OH$ | 4.0×10^{-2} mol kg ⁻¹ | |
| Cation exchange capacity | 8.7×10^{-1} mol kg ⁻¹ | |
| Surface protolysis reactions | log K_{protolysis} | |
| $\equiv S^{S/W1} OH + H^+ \Leftrightarrow \equiv S^S OH_2^+$ | 4.5 | |
| $\equiv S^S OH \Leftrightarrow \equiv S^S O^- + H^+$ | -7.9 | |
| Hydrolysis reactions | log ^{OH}K | |
| $Fe^{2+} + H_2O \Leftrightarrow FeOH^+ + H^+$ | -9.1 | Lemire et al. (2013) |
| $Fe^{2+} + 2H_2O \Leftrightarrow Fe(OH)_2^0 + 2H^+$ | -20.6 | Baes & Mesmer (1976) |
| $Fe^{2+} + 3H_2O \Leftrightarrow Fe(OH)_3^- + 3H^+$ | -34.6 | |
| Surface complexation reaction | log K | |
| $\equiv S^S OH + Fe^{2+} \Leftrightarrow \equiv S^S OFe^+ + H^+$ | 1.9 | Soltermann et al. (2014a) |
| $\equiv S^{W1} OH + Fe^{2+} \Leftrightarrow \equiv S^{W1} Fe^+ + H^+$ | -1.7 | |
| Cation exchange reaction | log K_c | |
| $2Na\text{-mont} + Fe^{2+} \Leftrightarrow Fe\text{-mont.} + 2 Na^+$ | 0.8 | |

Experimental results on competitive and non-competitive sorption on montmorillonite

An extensive experimental programme is ongoing at PSI in which the competitive sorption between elements of various valences on 2:1 type clay minerals (montmorillonite and illite) is being investigated. In Fig. 5-23, four examples are shown where sorption isotherms of a divalent reference metal (Fe or Ni) have been measured in the presence of metals with di-, tri-, tetra- and hexavalent valences at trace concentration (Bradbury et al. 2017). If sorption is competitive, the increasing concentration of the reference element will progressively fill up the strong sites and thereby reduce the sorption of the trace element.

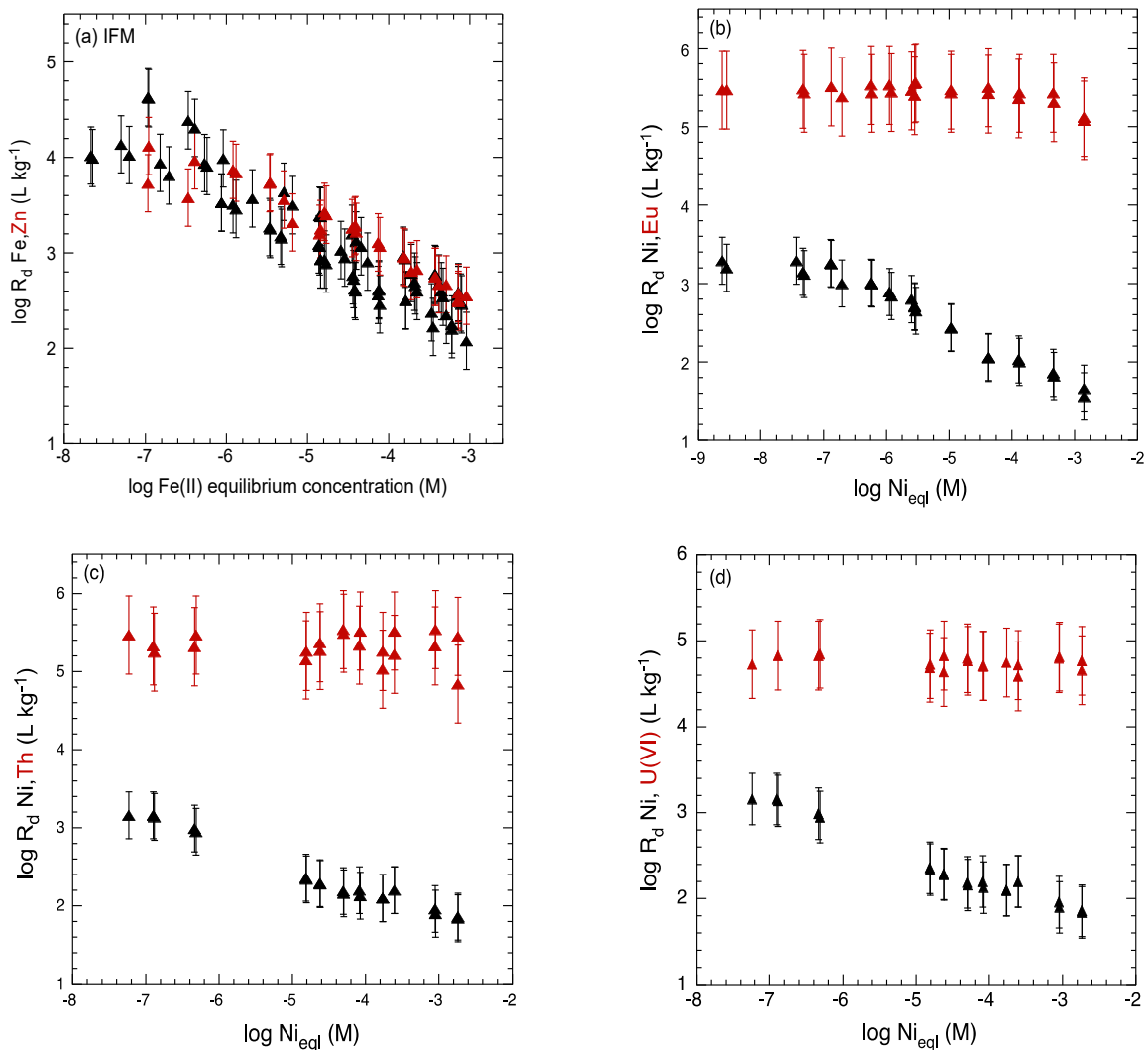


Fig. 5-23: Examples illustrating the competitive sorption behaviour of elements with similar and different valences

Bradbury et al. (2017)

Fig. 5-23a is an example where increasing Fe(II) concentration is competing with trace Zn(II) on a synthetic iron-free montmorillonite. Clearly, the experimental data indicate that Fe(II) is mutually competitive with Zn(II). On the other hand, the experimental data in Fig. 5-23b, c and d show that Ni(II) is not competing with Eu(III), Th(IV) and U(VI) for strong sites. The sorption of trace

Eu(III), Th(IV) and U(VI) remains nearly constant with increasing Ni(II) concentrations up to $\sim 10^{-3}$ M. Under the assumption that Fe(II) behaves similarly to Ni(II), we can assume that ferrous iron will only potentially compete with divalent radionuclides, whereas the sorption of radionuclides with a higher valence (trivalent lanthanides/actinides, tetravalent elements/actinides and hexavalent elements) is not influenced by Fe(II).

Modelling competitive sorption of Fe(II) and Ni(II) in bentonite

The competitive sorption of Fe(II) and Ni(II) is illustrated in the following model calculation. The sorption of trace Ni on MX-80 bentonite with a mineralogical composition (given in Tab. 3-1) in the reference bentonite porewater (Tab. 5-4, CON-BPW-221sa) is calculated in the presence of increasing Fe(II) concentration (from trace concentration (no competition) to a hypothetical high concentration (10^{-2} M)) under the assumption that no iron solid phases precipitate. The 2SPNE SC/CE sorption model is used for Ni (Baeyens & Bradbury *in prep.*) and Fe (see Tab. 5-2) using the bottom-up approach (Bradbury & Baeyens 2011). In this approach, the sorption of both elements is modelled on the montmorillonite component of bentonite in the bentonite porewater composition. A montmorillonite weight content of 81.4 % is taken from Tab. 3-1 (Wym). The auxiliary thermodynamic data required to calculate the aqueous speciation are taken from the PSI/NAGRA TDB (Thoenen et al. 2014). The results are shown in Fig. 5-24 where the calculated curve represents the sorption of Ni (R_d values at trace concentration) as a function of Fe(II) concentration. As can be seen from Fig. 5-24, the presence of Fe, even at very low concentrations, reduces the sorption of Ni. The reference porewater for MX-80 bentonite (Tab. 5-4) has an Fe(II) concentration of 2.1×10^{-5} M. This concentration is determined by the siderite/pyrite solid phases in an undisturbed near-field (indicated by the grey area in Fig. 5-24). The log R_d of Ni s at this Fe concentration is reduced by ~ 1.7 log units. The influence of a further increase of Fe(II) concentration on the sorption of Ni on bentonite can be read from Fig. 5-24.

Tab. 5-4: MX-80 bentonite porewaters taken from Bradbury et al. (2014)

CON-BPW-221sa was used to calculate the trace Ni/Fe sorption isotherm shown in Fig. 5-24.

| Bentonite porewater | | |
|---|-----------------------|-----------------------|
| ID-code | CON-BPW-221sa | NEW-BPW-opt2 |
| pH, ionic strength, redox potential, CO₂ partial pressure | | |
| pH | 7.27 | 7.79 |
| I (m) | 0.365 | 0.239 |
| Eh (V) | -0.167 | -204 |
| pPe | -2.84 | -3.44 |
| log pCO ₂ (bar) | -2.2 | -3.2 |
| Total element concentration [molality] | | |
| [Na] | 3.02×10^{-1} | 1.92×10^{-1} |
| [Ca] | 1.30×10^{-2} | 9.11×10^{-3} |
| [Sr] | 2.10×10^{-6} | 5.63×10^{-5} |
| [Mg] | 9.07×10^{-3} | 5.15×10^{-3} |
| [Ba] | - | 1.13×10^{-5} |
| [K] | 1.56×10^{-3} | 1.56×10^{-3} |
| [Fe] | 2.12×10^{-5} | 3.71×10^{-5} |
| [Al] | 1.08×10^{-8} | 147×10^{-8} |
| [C] _{inorg.} | 2.96×10^{-3} | 8.98×10^{-4} |
| [S] | 7.08×10^{-2} | 3.01×10^{-2} |
| [Cl] | 2.02×10^{-1} | 1.61×10^{-1} |
| [Si] | 1.77×10^{-4} | 1.82×10^{-4} |

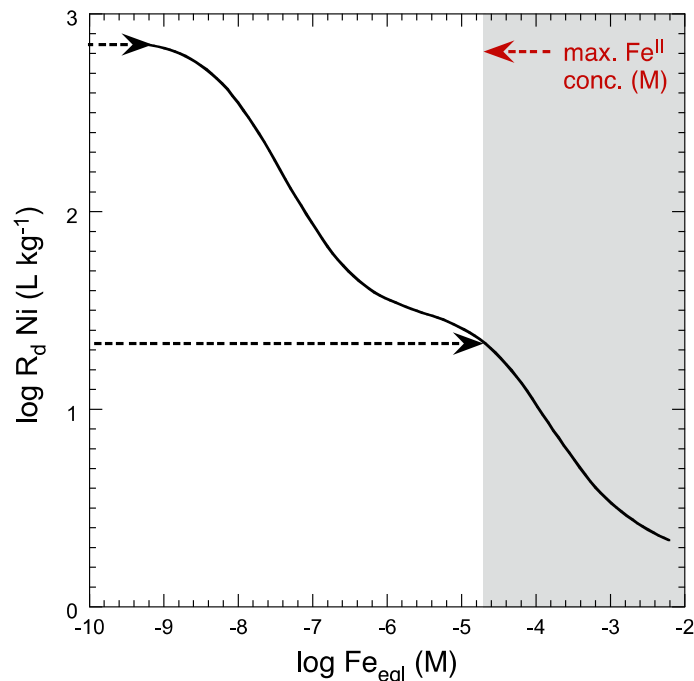


Fig. 5-24: Modelling the sorption of trace Ni(II) on MX-80 bentonite in the reference porewater composition (Tab. 5-4, CON-BPW-221sa) as a function of increasing Fe concentration under the assumption that Ni(II) and Fe(II) are mutually competitive

5.4.4 Significance of iron – bentonite interaction for the Nagra concept

In the past, the impact of corroding iron on the performance of the bentonite buffer has been assessed by simple mass balance considerations in view of the uncertainties related to process understanding. For example, Bradbury et al. (2014) estimated, for Nagra's HLW concept, the amount of montmorillonite that would transform if all Fe in the steel canister reacted with this mineral. This resulted in complete or almost complete conversion to a non-swelling mineral, depending on whether chamosite or berthierine was assumed as the reaction product. A more refined analysis accounting for the source term (i.e. an average corrosion rate of 1 $\mu\text{m}/\text{y}$) yielded complete corrosion of the steel canister in the range of 72,000 – 160,000 years, which means timescales that are of concern for safety analysis.

As pointed out by Bradbury et al. (2014), and also supported by more recent studies cited above, not all corrosion-derived Fe will react with montmorillonite, but a considerable (and likely larger) amount will precipitate as Fe oxides and, to a lesser extent, as Fe carbonates. Moreover, modelling and in-situ data suggest that at least a part of the Fe-bearing silicates formed will be smectites (saponite), which also have a swelling capacity.

A further process attenuating the impact of corrosion is diffusion of Fe(II) in the clay. Empirical fits of Fe profiles from in-situ tests, such as ABM2, could be obtained assuming two parallel diffusion pathways for Fe(II). This yielded apparent diffusion coefficients of $1 - 8 \times 10^{-13} \text{ m}^2/\text{s}$ and $0.4 - 1 \times 10^{-14} \text{ m}^2/\text{s}$ for the fast and slow diffusion coefficient, respectively. Such values can be expected to represent the higher end with regard to repository conditions because they reflect elevated temperatures ($> 100 \text{ }^\circ\text{C}$) and the probable slowing down of the diffusion front in the long run. Fe(II) tracer diffusion experiments at room temperature of Muurinen et al. (2014) suggest

lower apparent diffusivities ($10^{-15} - 10^{-16} \text{ m}^2/\text{s}$). With these diffusion coefficients in mind, the mean diffusion distance of Fe(II) from a corroding iron source can be roughly estimated by the relationship:

$$x \approx 2\sqrt{D_a t}$$

where x represents the mean diffusion distance of a diffusing Fe(II) cation. For a diffusion time of 10^5 years, and assuming D_a to be $10^{-14} \text{ m}^2/\text{s}$, a diffusion distance of 36 cm results. With a D_a value of $10^{-16} \text{ m}^2/\text{s}$, the same calculation yields a mean diffusion distance of 3.6 cm. Thus, assuming the lower D_a value, the Fe front would migrate only a small distance from the Fe/clay interface into the backfill, whereas for the higher value, the front would extend into the major part of the bentonite barrier after 10^5 years. Thus, considering the Fe(II) diffusion data at hand, the issue cannot be closed.

The spatial extent of altered bentonite backfill is likely to be smaller than estimated from mass balance or diffusion considerations. This is because of the very slow kinetics involved in montmorillonite reactions and also the small diffusion gradients of Fe(II) in the backfill as suggested from modelling (e.g. Wersin & Birgersson 2014). However, the reactive transport models applied to date represent the processes in a very simplistic way and do not account for the complex diffusion and retention processes indicated from recent in-situ studies.

The mechanical and transport properties of Fe-affected bentonite have, to the authors' knowledge, not yet been investigated. This relates in particular to the effect of cementation by iron oxides and/or of reduction of structural Fe(III) on swelling pressure and hydraulic conductivity (Hadi et al. 2017a).

The impact of corroding steel at the backfill/rock interface and the EDZ has so far received little attention in Nagra's concept. The production of hydrogen may act as a source favouring microbial sulphate reduction (Cloet et al. 2017). Also, corrosion may affect porewater compositions, in particular pH and Eh conditions.

Fe(II) is a strong sorbate and may weaken the sorption of other divalent metals such as Zn(II). The considerations in section 5.4.3 are based on data for Fe-free montmorillonite. For natural Fe-bearing montmorillonites, Fe(II) sorption is generally accompanied by a redox process, inducing reduction of structural Fe and oxidation of sorbed Fe(II) (Tournassat 2003, Soltermann et al. 2014a, Soltermann et al. 2014b, Latta et al. 2017). This generally results in a stronger sorption of Fe. To what extent this process affects sorption of radionuclides still requires clarification.

5.5 Interaction between copper and bentonite

Copper-coated steel canisters are considered as an alternative to the steel canister concept in Nagra's programme. Copper is a more noble metal than iron and will therefore be less prone to corrosion and to the production of H_2 . Nevertheless, some corrosion will occur, especially in contact with air during the initial phase and by interaction with sulphide (Cloet et al. 2017). Corrosion-released copper may occur a priori as Cu(I) and Cu(II) species, which may interact with bentonite. This interaction process has been reviewed in the context of SKB's and Posiva's KBS-3H concept (King & Wersin 2014). From the outcome of that study and from data analysis on Cu of the in-situ test LOT A2 (Wersin 2013), some relevant statements can be made which are also of interest for Nagra's concept:

- Corrosion under the initial oxic conditions may release Cu(II) species which will strongly interact with the clay by different uptake processes, such as sorption reactions, polymerisation and surface precipitation (Morton et al. 2001, Strawn et al. 2004). Support for uptake of Cu(II)

by montmorillonite under oxic conditions is provided by data from the LOT A2 test, where the clay in the contact area showed significant loading of Cu (Wersin 2013). A similar type of Cu profile in MX-80 bentonite was observed in small-scale long-term laboratory experiments (Kumpulainen et al. 2010).

- Incorporation of Cu(II) into the clay lattice is known to occur at high Cu(II) concentrations at high temperatures (> 200 °C). This leads to irreversible fixation of Cu and a decrease in CEC and swelling capacity (Heller-Kallai & Mosser 1995, Mosser et al. 1997, Madejova et al. 1999, Madejova et al. 2006, Karakassides et al. 1999, Emmerich 2000, He et al. 2001, Shaiek et al. 2003, Karmous et al. 2006, Ouselati et al. 2006, Seiffarth & Kaps 2009). The exact location of Cu^{2+} in the structure is still controversial. Vacant octahedral sites (e.g. Mosser et al. 1997, Shaiek et al. 2003) and the bottom of hexagonal cavities of the tetrahedral sheets (Karakassides et al. 1999, Madejova et al. 2006, Seiffarth & Kaps 2009) or both locations (e.g. Heller-Kallai & Mosser 1995, He et al. 2001) have been proposed. In conclusion, Cu(II) incorporation into the clay lattice is not expected to be a relevant process under repository-type conditions. This is also supported by the lack of indications of transformation of smectite by Cu(II) in natural systems (King & Wersin 2014).
- Under anoxic conditions, much less corrosion will occur, with release of Cu(I) species and precipitation of an insoluble copper sulphide layer. In contrast to Cu(II), the interaction of Cu(I) with the clay is expected to be rather weak (King & Wersin 2014), but very little experimental data are available to support this statement.

Competitive sorption of Cu(I & II)

Berner (2012) made an estimate of the solubility of copper in an MX-80 bentonite porewater (Tab. 5-4, NEW-BPW-opt2), where he assumed that $\text{Cu}^0_{(s)}$ is the limiting solid phase. At an Eh of -204 mV, the speciation calculation indicates that $\text{Cu(I)Cl}_{(aq)}$ and $\text{Cu(I)HS}_{(aq)}$ are the dominant aqueous species with a maximum solubility of 2×10^{-10} [mol/kg H_2O]. It is anticipated that the neutral Cu(I) complexes will not show competitive sorption with other radionuclides in the bentonite near-field.

Berner (2012) also considered a second scenario where he assumed that metallic copper and Cu(I) will not be formed. In this case, copper hydroxides ($\text{Cu(OH)}_2_{(s)}$) or mixed copper-hydroxide-carbonates, malachite/azurite) are the solubility-limiting phases. The maximum solubility of the cupric ion in the bentonite porewater was calculated to be 1.6×10^{-6} [mol/kg]. An estimate of the potential competitive effect of Cu(II) at this concentration is described in the following section.

Sorption model for cupric ion on montmorillonite

Maes et al. (1976) have studied the cation exchange behaviour of Cu^{2+} in Na-montmorillonite and obtained a selectivity coefficient of 3.6 for the Na^+ - Cu^{2+} exchange on the planar sites. This study also showed very similar cation exchange behaviour for other divalent transition metals, i.e. Co, Ni, Zn and Cd.

Sorption studies of cupric ion Cu(II) on smectites have been carried out by Morton et al. (2001) and Strawn et al. (2004). These authors have mainly focused on spectroscopic investigations (X-ray absorption spectroscopy (XAS) and electron paramagnetic resonance (EPR)) to study the structure and mechanism (inner-sphere/outer-sphere) of Cu surface complexes. The macroscopic measurements presented in their studies were interpreted semi-quantitatively and no surface complexation or cation exchange model was used to fit the experimental data. Unfortunately, the macroscopic sorption data contained in these studies did not allow parameterisation of the 2SPNE SC/CE sorption model for Cu uptake on montmorillonite. No other suitable surface complexation studies of Cu on montmorillonite could be found in the open literature.

Baeyens & Bradbury (*in prep.*) have used linear free energy relationships to derive the first surface complexation constants on strong and weak sites which can be used in the 2SPNE SC/CE sorption model. The hydrolysis data together with the surface complexation constants on strong and weak sites and the cation exchange selectivity coefficient are summarised in Tab. 5-5. Because the first hydrolysis constant of Cu(II) is stronger compared to Ni(II) or Fe(II), the surface complexation constant is also stronger for Cu(II).

Tab. 5-5: Summary of the hydrolysis and surface complexation and cation exchange reactions together with the thermodynamic constants for calculating the Cu(II) sorption on montmorillonite

Auxiliary data for speciation calculations in the bentonite porewater are included in this table.

Bradbury et al. (2017)

| Surface complexation reactions | log K | Reference |
|---|---------------------|--|
| $\equiv\text{S}^{\text{S}}\text{OH} + \text{Cu}^{2+} \Leftrightarrow \equiv\text{S}^{\text{S}}\text{OCu}^{+} + \text{H}^{+}$ | 4.2 | Baeyens & Bradbury (<i>in prep.</i>) |
| $\equiv\text{S}^{\text{W1}}\text{OH} + \text{Cu}^{2+} \Leftrightarrow \equiv\text{S}^{\text{W1}}\text{Cu}^{+} + \text{H}^{+}$ | -1.6 | |
| Cation exchange reaction | log K_c | |
| $2\text{Na-mont} + \text{Cu}^{2+} \Leftrightarrow \text{Cu-mont.} + 2 \text{Na}^{+}$ | 0.6 | Maes et al. (1976) |
| Hydrolysis reactions | log $^{\text{OH}}K$ | |
| $\text{Cu}^{2+} + \text{H}_2\text{O} \Leftrightarrow \text{CuOH}^{+} + \text{H}^{+}$ | -7.95 | Powell et al. (2007) |
| $\text{Cu}^{2+} + 2 \text{H}_2\text{O} \Leftrightarrow \text{Cu}(\text{OH})_2^0 + 2\text{H}^{+}$ | -16.2 | |
| $\text{Cu}^{2+} + 3 \text{H}_2\text{O} \Leftrightarrow \text{Cu}(\text{OH})_3^{-} + 3\text{H}^{+}$ | -26.6 | |
| $2 \text{Cu}^{2+} + 2 \text{H}_2\text{O}(\text{l}) \Leftrightarrow \text{Cu}_2(\text{OH})_2^{2+} + 2 \text{H}^{+}$ | -10.43 | |
| Aqueous complexation reactions | log K | |
| $\text{Cu}^{2+} + \text{Cl}^{-} \Leftrightarrow \text{CuCl}^{+}$ | 0.83 | Powell et al. (2007) |
| $\text{Cu}^{2+} + 2\text{Cl}^{-} \Leftrightarrow \text{Cu}(\text{Cl})_2(\text{aq})$ | 0.6 | |
| $\text{Cu}^{2+} + \text{CO}_3^{2-} \Leftrightarrow \text{CuCO}_3(\text{aq})$ | 6.75 | |
| $\text{Cu}^{2+} + 2 \text{CO}_3^{2-} \Leftrightarrow \text{Cu}(\text{CO}_3)_2^{2-}$ | 10.3 | |
| $\text{Cu}^{2+} + \text{HCO}_3^{-} \Leftrightarrow \text{CuHCO}_3^{+}$ | 1.84 | |
| $\text{Cu}^{2+} + \text{SO}_4^{2-} \Leftrightarrow \text{CuSO}_4(\text{aq})$ | 2.35 | |

Modelling competitive sorption between Cu(II) and Ni(II) in bentonite

An identical exercise to that for the Ni-Fe system presented in section 5.4.3 has been performed for the Ni-Cu system. The auxiliary data for Cu(II) are summarised in Tab. 5-5. The sorption of trace Ni on bentonite in the reference bentonite porewater is calculated in the presence of increasing Cu(II) concentration (from trace concentration (no competition) to a hypothetical high concentration ($\sim 10^{-3}$ M)) under the assumption that no copper solid phases precipitate. The modelling results are shown in Fig. 5-25. Compared to the Fe/Ni system (Fig. 5-24), the competing effect of Cu is much more pronounced compared to Fe because of the stronger surface complexation constant. It is noted that this calculation is performed with an estimated surface complexation constant using a linear free-energy relationship and no experimental data exist to verify this surface complexation constant. The maximum solubility of cupric ion in the reference bentonite porewater (Tab. 5-4, CON-BPW-221sa) is 2.5×10^{-6} M (indicated by the grey area in Fig. 5-24). The presence of Cu(II) at this concentration limit leads to a reduction of the $\log R_d$ for Ni by ~ 1.5 log units.

The main conclusion drawn from this exercise is that cupric ion, if present, will reduce the sorption of divalent radionuclides by blocking the strong edge sites of montmorillonite. These radionuclides will sorb mainly on the weak and planar sites of montmorillonite.

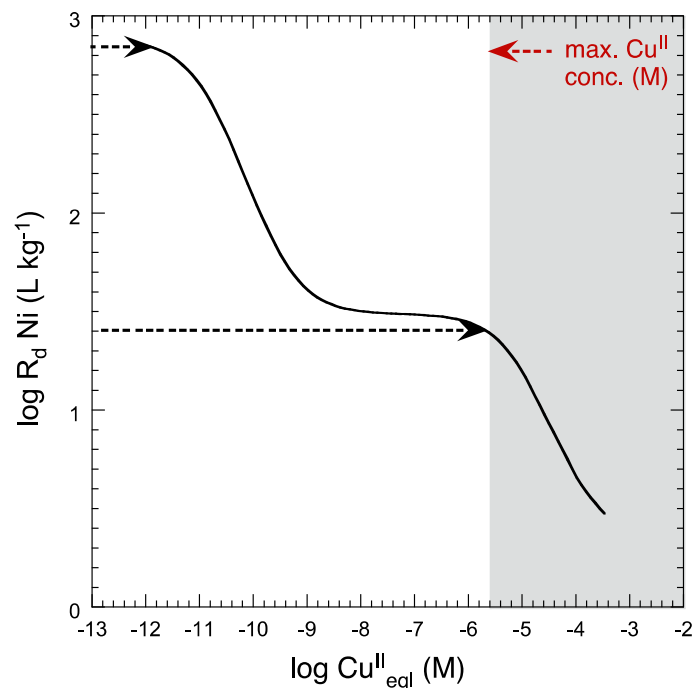


Fig. 5-25: Modelling of the Ni(II) trace sorption ($\log R_d \text{ Ni}$) on MX-80 in the reference porewater composition as a function of increasing Cu(II) concentrations under the assumption that Ni(II) and Cu(II) are mutually competitive

5.6 Observed microbial activity in various experiments and its consequences for repository conditions

The potential for microbial activity in the immediate vicinity of waste containers in a HLW repository is of interest for the long-term integrity of the containers (e.g. Stroes-Gascoyne et al. 1996, Stroes-Gascoyne et al. 2011, Stroes-Gascoyne & Hamon 2014) and the gas pressure evolution. Microbial activity in the near-field, which includes the EBS and those parts of the host rock in contact with, or near, the EBS whose properties have been affected by the presence of the repository, may result potentially in the following processes that are relevant for long-term safety:

- Microbially influenced corrosion (MIC), which could reduce the longevity of the waste containers. MIC would occur through the formation of corrosion-inducing aggressive environments under biofilms or through the production of corrosive metabolites. For the latter, sulphate-reducing bacteria (SRB) that produce sulphide are of specific concern.
- Microbial gas production (mainly CO₂ and CH₄) may contribute to the build-up of a gas phase in a repository, potentially reducing the effectiveness of the bentonite-based barriers and/or natural barriers by partial desaturation of the bentonite and affecting the integrity of the engineered barrier through the creation of pathways for the gas to escape.
- Microbial activity may lead to dissolution of minerals in the clay, or leaching of specific elements from those minerals, with possible deleterious effects on the integrity and the effectiveness of this barrier.
- Microbes may adsorb radionuclides released from breached containers and either immobilise these in biofilms or (mobile) microbes may act as colloids to enhance radionuclide migration through unsealed (or incompletely sealed) fractures in the near-field.
- Microbial activity could reduce the gas pressure build-up resulting from anoxic corrosion of the waste containers by oxidising H₂ gas anaerobically, or possibly by the formation of CH₄ from H₂ and CO₂ which would reduce the volume of gas.

Microbial activity in the buffer or in the remaining part of the near-field depends on the availability of sufficient *pore space*, *nutrients* (micro- and macronutrients, electron acceptors and electron donors) and *water activity*. If one of these conditions fails, microbial activity will come to a halt. During the transient phase, when the buffer is not yet fully saturated, water activity will be too low close to the canister to sustain microbial activity. Under partially saturated conditions, persisting macropores may allow microorganisms to be locally and temporally active. These microorganisms will, however, be competing for water with the bentonite due to the high suction pressure of the swelling clay, which may further limit their activity.

Conditions in the EDZ, however, might be suitable for microbial activity for a limited time period, since, in the EDZ, water activity, pore space and nutrients will be available.

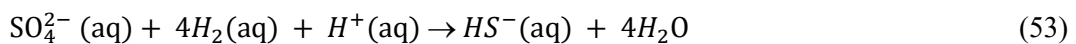
Pore space

As soon as the buffer is saturated, and assuming that the buffer is emplaced with a sufficiently high emplacement density (and the volume remains constant), the swelling pressure will reduce the pore size and thus eliminate microbial activity. The emplacement density and the resulting swelling pressure in the buffer thus play a crucial role in preventing microbial activity close to the canister (Masurat et al. 2010, Pedersen 2010). Masurat demonstrated that, as the wet density of compacted bentonite increases from 1,500 kg m⁻³ to 2,000 kg m⁻³ (corresponding to swelling pressures of 0.1 MPa and 7.8 MPa), the production of sulphide decreases (Masurat et al. 2010). The mineralogy of the buffer material, and especially the clay content, also has an impact on the

obtained swelling pressure. A high swelling pressure may also lower the degree of heterogeneity in the buffer material that may arise from the material itself, from the emplacement procedure or the THM evolution of the bentonite. The threshold value for the dry density of bentonite to limit microbial activity seems to be dependent on the origin of the bentonite as Bengtsson has shown in his recent publication (Bengtsson et al. 2017). The underlying mechanism for limiting the viability of microorganisms in compacted bentonite is not yet fully understood and is currently under debate.

Nutrients

The sulphate flux in the SF/HLW near-field is important for a relevant group of microorganisms: the so-called sulphate-reducing bacteria (SRB). These microorganisms use sulphate as an electron acceptor, and use dissolved organic matter (e.g. lactate, pyruvate, acetate) or hydrogen gas as an electron donor. The latter will be available in large quantities in the repository, originating from the anoxic corrosion of steel components such as the steel canister, rock bolts and steel mesh. Because of the sulphate reduction that is carried out by SRB, sulphide is produced (see eq. 53 for an example with H_2 as electron donor). The fact that SRB are present in OPA porewater has been demonstrated at the Mont Terri rock laboratory (e.g. Stroes-Gascoyne et al. 2011, Bagnoud et al. 2016). Through metagenomics, the activity of the sulphate-reducing metabolism could be demonstrated.



The formation of biofilms is also of importance to the sulphide-assisted corrosion of the canister. Biofilms are assemblages of microbial cells that are attached to a surface and enclosed in an extracellular matrix that is secreted by the microorganisms themselves. Owing to the extracellular matrix, the microorganisms are protected against detachment and the biofilm becomes very resilient. Biofilms tend to occlude the surface and promote the development of an environment which is different from the bulk and which can result in localised corrosion. Copper alloys are generally considered to be unaffected by biofilms since elemental copper has a broad spectrum of antimicrobial activity (Grass et al. 2011, Sato et al. 2012). Nevertheless, it has been reported that SRB can form a biofilm on copper surfaces in anoxic conditions and this can result in the acceleration of corrosion (Chen et al. 2014). Because the impact and outcome of biofilm formation is uncertain and difficult to predict (King 2009), biofilm formation should be prevented in the first place. This is achieved by the high temperature, desiccation, and - depending on the canister specification - the radiation field during the early stages of repository evolution, and by a combination of insufficient pore space, low water activity and swelling pressure of the buffer during the later stages.

Dissolved sulphate is the electron acceptor required by SRB for microbial sulphate reduction. In the near-field of the repository, two main sources of sulphate can be distinguished: gypsum (in the MX-80 buffer) and celestite (in the OPA). Thanks to reliable thermodynamic data on gypsum and celestite, the initial concentration of sulphate in the porewater near the repository can be constrained with reasonable confidence. The initial sulphate concentration in the MX-80 buffer due to gypsum equilibrium is expected to be roughly five to ten times higher (ca. 0.05 – 0.1 mol/L) compared to the initial sulphate concentration in the OPA due to celestite equilibrium (ca. 1 – 2 × 10⁻² mol/L). However, the total volume of the MX-80 buffer is small compared with the volume of the OPA. Therefore, it is expected that, if the microbial reaction can proceed for a sufficiently long time at a sufficiently high rate, all the gypsum in the buffer will be completely consumed. Following this, celestite contained in the OPA will remain the sole source of sulphate for microbial activity.

Various chemical species could serve as electron donor for microbial sulphate reduction, including reactive organic carbon (from dissolution of solid organic matter), methane and higher alkanes or hydrogen gas.

OPA contains 0.6 wt.-% of solid organic matter (SOM), which translates into 14.7 kg m^{-3} rock (or $1,225 \text{ mol m}^{-3}$ assuming the molar mass of pure carbon is 12 g mol^{-1}). MX-80 contains about 0.1 wt.-% of SOM, which equals 1.45 kg m^{-3} or 120.8 mol m^{-3} (making the same assumption about molar mass). This is much more (especially in OPA) than the total inventories of sulphate (see below).

The solid organic matter in bentonite is, generally speaking, recalcitrant, because it has persisted in this natural material for a long time period. A recent study by Marshall et al. (2015) investigated solid organic matter in several bentonites and concluded that the SOM shows signs of advanced diagenesis and appears to be geochemically recalcitrant and, therefore, unlikely to serve as a microbial substrate. However, when exposed to repository conditions, this SOM might become more reactive. For example, it was observed that heating and irradiation of bentonite-based buffer materials followed by leaching in distilled water stimulated microbial growth in granitic groundwaters by up to two orders of magnitude (Stroes-Gascoyne et al. 1996). In the long run, dissolution processes of SOM in the compacted buffer are expected to be small as long as microbial activity is restricted. Thus, the amount of reactive carbon and dissolved organic carbon concentration in the porewater are expected to be low, but these concentrations are so far not well constrained.

The organic matter in OPA consists predominantly of kerogen, a fossilised macromolecular insoluble form of organic matter derived from biomass. Regarding its maturation degree, it can be considered as fairly immature but close to the onset of the oil window (Elie & Mazurek 2008). The dissolved organic fraction is fairly low, a few mg C/L. Courdouan et al. (2007) studied the dissolved organic matter (DOM) in OPA and confirmed that only a small fraction ($< 0.4 \%$) of the total organic C was extractable in synthetic OPA porewater. The concentrations in the anoxic extracts were found to be in the range 4 – 8 mg/L. About 2/3 of this DOM exhibited hydrophilic properties and molecular sizes < 500 Dalton.

Natural methane concentrations in OPA determined at the Mont Terri Rock Laboratory are about 0.3 mmol/L and those of higher alkanes at least a factor of 10 lower (Vinsot et al. 2017). From the available experimental observations at Mont Terri (e.g. PC and BN experiments), there are no indications that alkanes play a role as electron donors in the microbial sulphate reduction process (Stroes-Gascoyne et al. 2011, Wersin et al. 2011a). Thus, anaerobic methane oxidation has so far never been observed in OPA. Hydrogen, on the other hand, strongly impacts sulphate reduction when injected into the rock (Vinsot et al. 2014b). The natural levels of this species however are very low, usually below detection limits (Vinsot et al. 2017). Corrosion of steel materials in the EDZ may produce higher H_2 levels, which could then be utilised by SRB provided that sufficient pore space is available.

Water activity

The results of various studies (e.g. Leupin et al. 2016a,b, Stroes-Gascoyne & Hamon 2014) were interpreted in terms of the effect of low water activity (a_w) on limiting the extent of microbial activity. There is evidence for a limiting a_w of approximately 0.96, below which microbial activity is suppressed. The strongest evidence that a_w controls microbial activity is that a similar effect is observed at high bentonite density saturated with distilled water or a dilute simulated groundwater solution as in low-density bentonite with a high-salinity simulated groundwater solution. Both increasing buffer density and increasing salinity result in a decrease in a_w .

Stroes-Gascoyne et al. (2011) showed that the number of culturable aerobes following 90-days exposure to compacted MX-80 bentonite in a pressure cell as a function of dry density and salinity of the saturating solution clearly evidenced microbial activity at dry densities less than approximately $1.3 - 1.4 \text{ Mg m}^{-3}$ for salinities of 50 g/L or less. At higher dry density, there was no consistent evidence for an increase in microbial population following exposure. However, for a Salinity of 100 g/L or higher, there is no evidence for microbial activity at any dry density as low as approximately 0.7 Mg m^{-3} .

Summary

Based on today's understanding of the phenomena and processes related to microbial activity in a highly compacted bentonite buffer, and considering a canister of carbon steel, the safety-related impact of microbial activity on canister performance is rather limited.

However, uncertainties persist regarding minimum buffer emplacement density. Based on recent findings, Bengtsson et al. (2017) conclude that there are different threshold values for the different bentonites he investigated. The reason for this is unclear and under investigation.

5.7 Geochemical processes during saturation derived from experiments

Only limited data are available on geochemical processes during the bentonite saturation. The chemical impact of the saturating solution on this process and on the barrier performance in the long term is generally ignored. Saturation is mainly treated as a THM process.

OPA porewater is assumed to saturate the bentonite. It may be altered by other materials in the near-field, especially cement and steel. The resulting solution enters the bentonite barrier, whose initial water content is set by the equilibrium with the relative humidity in the atmosphere (approximately 12 wt.-% of dry mass at average room conditions, but lower in the case of compacted pellets). A moist MX-80 with a grain density of $2,750 \text{ kg m}^{-3}$ and $1,500 \text{ kg m}^{-3}$ dry density requires 454.6 L/m^3 water to reach full saturation (0.46 total porosity). Because 180 L/m^3 of initial water (12 wt.-% of $1,500 \text{ kg m}^{-3}$ dry MX-80) are already in place, only an additional 274.6 L/m^3 are needed for full saturation. Depending on water inflow and the form of the bentonite, two different scenarios are envisioned below (Fig. 5-26).

- a) *Slow water inflow into bentonite containing small preferential pathways* (e.g. OPA host rock, compacted bentonite blocks): the bentonite instantly swells, preferential pathways and free porosity in the bentonite decrease to a minor volume fraction and barely contribute to water uptake. In contrast, suction into the interlayers dominates any hydraulic head-driven advection (pore pressure in the host rock). The blue lines in the sketched anion concentration profile of Fig. 5-26a) show the anion concentration in the host rock (e.g. Äspö porewater in this example), and the much lower anion content in the Donnan porosity of the bentonite (anion exclusion). Indeed, the calculated anion concentration in the Donnan porosity matches aqueous extracts from an MX-80 core after equilibration with Äspö porewater (blue dashed line and squares in Fig. 5-27; Donnan equilibrium between the Äspö porewater and the bentonite's Donnan porewater based on eq. (5) and equal activity coefficients in both porewaters is assumed). In contrast, the material from the LOT experiment, saturated with Äspö porewater, shows about twice the anion concentration in aqueous extracts. Because all exchangeable cations in the montmorillonite are already in place, and because only limited amounts of anions can enter the Donnan porosity, only dilute host rock porewater enters the Donnan porosity during saturation and montmorillonite swelling. This leads to a local concentration increase at the interface. The Donnan equilibrium now also predicts higher concentrations in the bentonite Donnan porosity (red lines in the sketched anion concentration profile of

Fig. 5-26a). The Donnan calculation predicts a 1.6-times increase of concentrations at the interface to match the aqueous extracts measurement of LOT MX-80 (red dashed line and circles in Fig. 5-27). Similar elevated concentrations can be observed in bentonite cores saturated advectively in a lab set-up, as well as in other URL experiments (e.g. ABM1). In contrast, no elevated concentrations are expected in bentonite saturated from flushed filters (e.g. Van Loon et al. 2007), because the concentration increase at the bentonite-filter interface is continuously flushed into a large reservoir.

- b) *Fast inflow into bentonite containing large preferential pathways* (e.g. saturation of bentonite pellets via cracks, or artificially): experiments have shown that the water inflow rate determines if the early saturation is suction-dominated, or if the hydraulic head on the inflow leads to an early saturation around the pellets/along an initially large free porosity (Börgesson et al. 2014). In the latter case, the host rock porewater with its original concentration flows into the bentonite, where the concentration increases in the free porosity due to dilute water entering the montmorillonite interlayers (red stars in Fig. 5-26b). The same process described in a) at the interface now leads to an elevated concentration in the free porosity within the bentonite by a factor of 7.7 (assumptions: Donnan porosity of 0.42 and a free porosity of 0.04 at full saturation and homogenisation based on XRD measurements from Holmboe et al. (2012), all initial water in the Donnan porosity, complete anion exclusion from the Donnan porosity).

In reality, a combination of both scenarios must be expected (the presence of free porosity in bentonite after backfilling is undisputed). The interplay of both scenarios is supported by measurements of advectively displaced bentonite porewater, which shows a general anion concentration increase higher than the factor of 1.6 (Donnan equilibrium in the case of Äspö porewater).

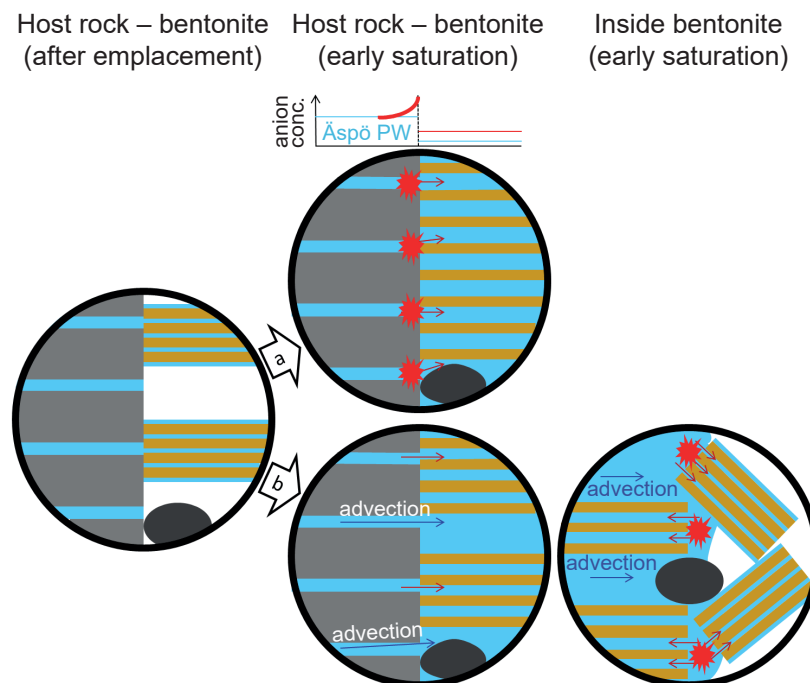


Fig. 5-26: Bentonite water uptake from host rock immediately after emplacement: a) suction-dominated, b) advection-dominated

Grey: host rock; brown: montmorillonite basal sheets; dark grey: accessory mineral; red stars: concentration increase; blue arrows: hydraulic head and suction-driven advection in free porosity; red arrows: suction. Explanation in text.

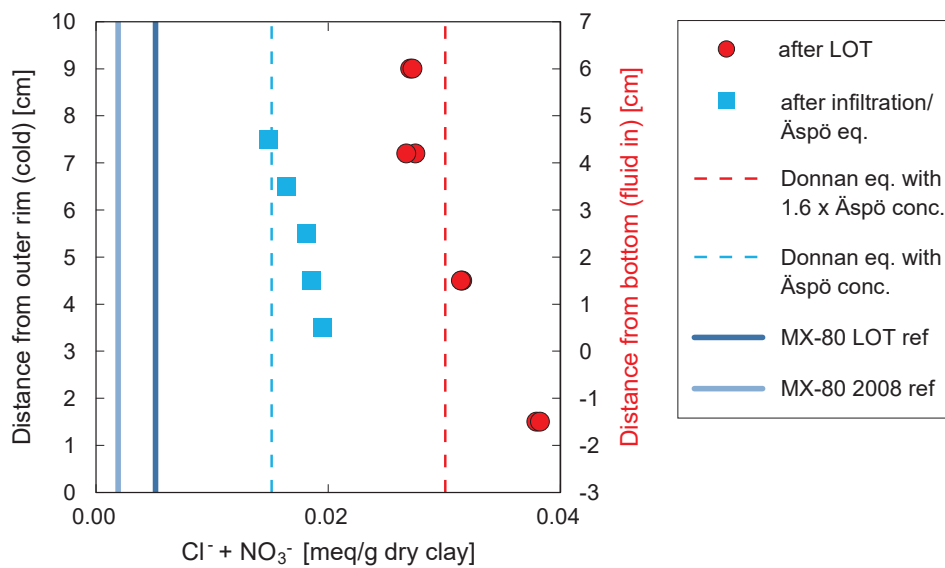


Fig. 5-27: Major anion contents in aqueous extracts in MX-80 core after the LOT experiment, and after subsequent equilibration with Äspö porewater

Lines show measurements of reference material; dashed lines result from calculated Donnan equilibria.

Jenni et al. (2014a)

The preferential pathways described above generally disappear after saturation (homogenisation, section 5.1), thus both full-scale and laboratory-scale saturated bentonites have a macroscopically homogeneous appearance. Exceptions can be found in experiments where boiling occurred, and substantial amounts of minerals precipitate in the preferential pathways; these precipitates do not re-dissolve during consecutive saturation and equilibration. During post-mortem sample preparation, drying cracks open favourably along pre-existing structures, indicating the persistence of certain inhomogeneities. In ABM2, one sample of caged pellets exhibits a network of drying cracks (Fig. 5-28). A red halo borders some of these cracks, indicating the transport of iron from the drying cracks into homogeneous, water-containing bentonite. Such observations indicate the presence of preferential pathways in the form of

- Voids between bentonite pellets/grains at very early saturation: Although the voids must contain water for iron transport, this water needs a certain time to enter the pellets, where it leads to swelling and homogenisation. Advection caused by saturation leads to fast transport of steel corrosion products (from early corrosion or from a pre-existing corrosion layer on the steel surface), along the voids, presumably within hours or days. Pellet swelling and homogenisation close the voids and drastically slow down the transport of iron, which then slowly diffuses into the former pellets.
- Bentonite with lower density between the pellets: These zones allow for faster iron diffusion and fluid advection than within the pellets. These preferential pathways are expected to persist for a longer time compared to water-filled voids but allow for slower transport.

Based on these two explanations, the transport-active time interval of the preferential pathways is unknown. Astonishingly, the rusty iron halo around the voids is larger than the halo around the actual steel parts (ABM2 samples). It must be emphasised that open voids have never been observed in any saturated, confined bentonite sample, and the cracks shown opened during drying. Furthermore, indications for preferential pathways in fully saturated, confined bentonite have exclusively been found in the sample presented here, where the total dry density is expected to be

below $1,400 \text{ kg m}^{-3}$. However, these structures support the geochemical concentrating process described above, although the timescale is not yet clear. Smart et al. (2017) describe similar preferential pathways in saturated bentonite, but only within $100 \mu\text{m}$ from the steel surface. The structures contain iron, calcium sulphate, or calcite (the latter only at $1,450 \text{ kg m}^{-3}$ dry density and below, not found at $1,550 \text{ kg m}^{-3}$). The structures often follow original boundaries of bentonite aggregates and provide a weakness for the formation of shrinkage cracks during post-mortem sample drying. The precipitates and iron accumulation are attributed to steel-bentonite interaction and seem to favour low density regions within the bentonite, again indicating the presence of preferential pathways.



Fig. 5-28: Photograph of freeze-dried saturated bentonite, emplaced in the form of pellets in a steel cage (inset)

MX-80, ABM2 block #08. Steel cage segment (left, flanking the heater) and strut cross-section in grey, approximate width 10 cm.

From Hadi et al. (2017a)

During saturation, the following additional geochemical processes are expected to take place:

- Cation exchange between the free porewater and the Donnan porosity: No significant effect on total ionic strength in the free porewater. Furthermore, saturation even with a Ca-dominated porewater (e.g. from cementitious materials) will not significantly alter the cation occupancy (sodium-dominated in the initial MX-80): the CEC is much higher than the absolute cation content provided by the saturation solution, therefore the initial cation occupancy can be altered only marginally.
- Back-diffusion against the infiltrating water flow: Initially small but becomes the major transport mechanism at decreasing suction and increasing concentration gradient against the host rock. In the long term, back-diffusion will decrease the high concentrations in the free porosity.

- If the saturating solution is saturated with respect to any phase (e.g. calcite in the case of OPA porewater, possibly sulphate phases), the concentrating mechanism described above will lead to precipitation a) at the host rock-bentonite interface, and b) within the free porosity of the bentonite. Although only small volumes are expected, such precipitates might slow down the bentonite saturation. Indications of precipitation are scarce, because of subsequent dissolution and back-diffusion during the equilibration after saturation.
- Microfiltration might also explain increased concentrations at bentonite interfaces. However, the effect of possible microfiltration during saturation cannot be distinguished from the concentrating mechanism described above. Indications of microfiltration, e.g. after saturation in a steady-state advective infiltration, are missing.
- Equilibration of the infiltrated OPA porewater with the bentonite mineralogy, especially with gypsum, increases the sulphate content compared to the initial saturation water concentration. In the long term, the bentonite porewater composition will approach that of the host rock porewater and all unstable minerals will be removed. However, the timescale of this equilibration is uncertain (50 – 200 y, section 2.2.3) and, potentially, full porosity clogging at the bentonite-cement interface may stop equilibration.

The running time of large-scale URL experiments can exceed the saturation period. In this case, local evidence of geochemical processes during saturation is overprinted by processes after saturation, tending to equilibrate the system and to reduce any inhomogeneities. Online measurements are generally focused on THM properties (swelling pressure, moisture content). Geochemical measurements are complex and difficult to implement online, thus data are generally restricted to post-mortem investigations. Dynamic effects of the temperature gradient cannot be studied. The focus of most large-scale bentonite experiments is on THM behaviour and technology demonstration/development, rather than details of geochemical interactions.

Significance of geochemical processes during saturation for the Nagra concept

Porewater concentrations in bentonite higher than the concentrations of the saturating fluid have been observed in many laboratory and large-scale URL experiments, and are explained here for the first time, consistent with additional observations. This major geochemical process during saturation might lead to local mineral precipitations, porosity clogging, and extended saturation times. So far, no case of full clogging has ever been observed, either at large-scale or in laboratory experiments

The increased ionic strength in the bentonite, as well as at the bentonite – host rock interface, will lower the swelling pressure locally. In addition, the supply of Ca from cementitious structures can shift the cation occupancy in the bentonite towards Ca, which also lowers swelling pressure. Simultaneously, hydraulic conductivity increases (section 3.8), which will decrease the saturation period.

The initially elevated concentrations will decrease at the latest when full saturation is achieved, when equilibration with the host rock porewater becomes the governing process. Geochemical processes are expected to only marginally influence the saturation. Subsequent equilibration is expected to eliminate these perturbances, and no influence on the long-term behaviour is expected.

5.8 Relevance of higher temperatures for the performance of the bentonite backfill

The effect of heat during the thermal period will induce changes in porewater chemistry and dissolution/precipitation of minerals (section 3.9). Upon cooling after the thermal period, many of these processes will be reversed. In other words, the porewater will re-equilibrate leading to a re-dissolution/precipitation according to thermodynamic constraints. Some safety-relevant processes occurring during the thermal period are not reversible or will take a long time to reach the new thermodynamic state. These processes can be grouped into montmorillonite alteration and cementation (SKB 2011, Posiva 2013).

5.8.1 Montmorillonite alteration

As partly described in section 3.2, the important findings regarding the thermal stability of montmorillonite under repository conditions have been discussed in Leupin et al. (2015). These are summarised below:

- The thermodynamic stability of smectites is not well established because of uncertainties regarding theoretical issues and experimental gaps (sections 3.4.4, 3.2).
- In spite of the uncertainty regarding kinetic rates, mineralogical transformations to illite or to other non-swelling minerals (e.g. chlorite) up to temperatures of about 120 °C are expected to be very limited under repository conditions, where such temperatures occur for some decades (section 2.3.1). The same conclusion was reached in a previous review study (Wersin et al. 2007b).
- Conversion of montmorillonite to other smectites such as beidellite and/or saponite cannot be ruled out. In experiments ranging from 90 – 150 °C, an increase in the tetrahedral layer charge – the initial process of beidellitisation – was observed, albeit under extreme conditions. The extent of this conversion process under repository conditions is uncertain but, generally speaking, this does not affect the fundamental properties of the bentonite material.
- The effect of steam on the bentonite swelling properties postulated previously by Couture (1985) could not be supported by more recent data. On the contrary, the effects described by Couture could be attributed to sedimentation rather than to swelling properties.
- Loss of structural OH groups (de-hydroxylation) occurs upon heating at temperatures 300 – 800 °C, but no sharply defined lower temperature can be defined (Grim 1968). Thus, such temperatures are far beyond those that are relevant. The de-hydroxylation reaction may also be induced upon structural Fe(III) reduction at low temperatures (Hadi et al. 2013). To what extent this is relevant for repository conditions is still to be clarified.

The stability of montmorillonite under repository-like conditions is supported by findings from the European PEBS (Long-term Performance of Engineered Barrier Systems) project. From the analysis of a variety of experimental data, the authors concluded that thermally induced mineralogical changes will be relevant mainly above 130 °C (Schäfers et al. 2014).

5.8.2 Cementation

Higher temperatures and temperature gradients across the buffer will lead to a redistribution of salts and silicates, induced by the dissolution and re-precipitation of accessory minerals, such as gypsum/anhydrite, carbonates and SiO₂ (quartz, cristobalite, SiO₂(am)). The precipitation of significant amounts of such accessory minerals is referred to here by the term cementation. Generally speaking, the mineral masses converted by temperature effects are rather limited, as

indicated from modelling and/or mass balance considerations (e.g. Savage 2014, Arthur & Zhou 2005). Thus, the effect of cementation on the buffer via dissolution and re-precipitation during the thermal stage is expected to be small.

It is noted that the precipitation of Ca sulphates and carbonates induced by high temperature should be reversible in view of their fairly rapid dissolution kinetics. Thus, after cooling, these cements should re-dissolve, although this process has so far not been studied experimentally. On the other hand, precipitation of silicates (mainly in the form of SiO_2) needs to be considered as irreversible (Wersin et al. 2007a).

In general, as pointed out by Savage (2012), there is still a lack of knowledge on the cementing processes during the thermal phase in which thermal-hydraulic-mechanical and chemical processes are highly coupled and still not properly accounted for in the models.

5.8.3 Support from laboratory and in-situ experiments

Further support of the above statements is provided by in-situ experiments at the Äspö HRL, such as the LOT and ABM experiments. In the tests of LOT A2 (Karnland et al. 2009), ABM1 (Svensson et al. 2011) and ABM2 (Svensson 2015), compacted bentonite blocks were exposed to rather harsh conditions (temperatures up to 130 – 140 °C) and contacted with artificial Äspö water for periods of 2.5 – 5 years. The bentonite materials were found to be fully saturated after dismantling of the tests. In both tests, usually enrichment of Ca at the expense of Na on the exchanger was observed. Otherwise, the general outcome was that very little mineralogical changes occurred, besides some precipitation of gypsum/anhydrite close to the heater. Some minor dissolution of SiO_2 phases was found. In terms of smectite, virtually no changes could be identified with XRD. A slight increase in Mg close to the heater was observed, which was explained in the case of ABM1 and ABM2 as due to the formation of trioctahedral smectite (Kaufhold et al. 2013, Svensson & Hansen 2013, Svensson 2015). The change in CEC, respectively the layer charge behaviour, was not unambiguous, but changes, if encountered, were small.

The FEBEX experiment at the Grimsel Test Site, where bentonite blocks were exposed to a carbon steel heating source at temperatures up to 100 °C for a period of 18 years, also showed very little effect on the montmorillonite (Villar et al. 2018). Similar to LOT and ABM, there were indications of minor formation of trioctahedral Mg smectite. It thus appears that Mg enrichment and formation of trioctahedral smectite is a process that may occur in a repository setting. This is also in line with the modelling study of Wilson et al. (2015) who re-evaluated thermodynamic data of clay minerals in the context of iron corrosion and heat-induced processes. Their findings suggested the stabilisation of Fe-saponite at low $p\text{O}_2$ and Si activities buffered by quartz or higher solubility polymorphs.

Dueck (2010) conducted mechanical testing on saturated and unsaturated bentonite exposed to temperatures of up to 150 °C in order to further study the effect of reduction of strain at failure observed in the A2 parcel in the LOT test (Karnland et al. 2009). They could, to a certain extent, reproduce a brittle behaviour in the short term, an effect which could be reversed, however, by milling and recompacting the bentonite material (in agreement with section 5.8.2).

Valter & Plotze (2013) investigated the effect of temperature (50 – 150 °C) on MX-80 bentonite at variable moisture content in closed cells for periods up to 18 months. Their finding is in general agreement with the other studies mentioned above. Thus, almost no effect on montmorillonite stability was observed in all samples. Only subtle changes in physico-chemical properties occurred up to 120 °C. Above this temperature, however, changes in CEC, specific surface area, and water vapour adsorption ability became more significant.

5.8.4 Significance of higher temperatures for the Nagra concept

The alteration of montmorillonite during the thermal stage is expected to be small or negligible, although process understanding is still incomplete. For example, the processes leading to Mg enrichments close to the heat are still not quite resolved; they are perhaps related to the formation of trioctahedral saponite. It is noted that the latter phase also has a swelling capacity.

The amounts of redistributed salts and re-precipitated minerals will be fairly small and thus the effects of cementation will be limited. The overall knowledge on cementing processes during the complex THMC regime is poor. This relates, for example, to the combined effect of heat and iron corrosion (section 5.10.2).

5.9 Gas transport in bentonite

In a deep geological repository for HLW, the generation and accumulation of gas in the backfilled repository structures accompanied by the build-up of excessive gas pressures may compromise the buffer integrity and reduce its barrier efficiency. The bentonite buffer around the HLW canisters and the bentonite-based repository seals are particularly sensitive to mechanical disruption due to the low mechanical strength of bentonite. On the other hand, it is well known that bentonite exhibits the favourable feature of self-sealing after sustaining mechanical disruption.

During the last 2 decades, transport of gases in bentonite has been the subject of a multitude of international research programmes in the field of nuclear waste disposal (NEA 2001, Hoch et al. 2004, Norris et al. 2013). Substantial insight has been gained into the phenomena of gas transport processes in bentonite for a wide spectrum of thermo-hydro-mechanical and -chemical (THM-C) state conditions. Furthermore, model-based approaches were proposed for the interpretation of the experimental results and for the analysis of gas release scenarios from geological repositories in the context of long-term safety assessment.

Evidence from laboratory experiments suggests that transport in bentonite is strongly controlled by both the ambient stress state and the saturation history of the material (Horseman et al. 1997, Gallé 2000, Graham et al. 2002, Arnedo et al. 2008, Seiphoori et al. 2014). Repeated gas flow through fully saturated bentonite gives evidence of a certain degree of bentonite memory, indicating that distinct pathways are established when gas percolates through saturated bentonite. In 2016, a comprehensive laboratory programme was launched as part of Nagra's RD&D programme, aimed at characterising gas and water transport properties of compacted Wyoming bentonite (Romero & Gonzalez-Blanco 2017 and 2018). For this programme, highly accurate experiments under isotropic and oedometric configurations were performed together with detailed analysis of the microstructural changes of the bentonite when subjected to complex stress paths, including wetting stages and gas invasion. Fig. 5-29 shows a sketch of the oedometer cell and a typical example of a gas injection test on a sample of compacted bentonite (dry density 1.54 Mg m^{-3}). The gas injection pressure (red line in Fig. 5-29b) was limited to 4.5 MPa, whereas the applied vertical stress (green line) corresponded to the pre-consolidation stress of 5 MPa. The experiment reveals three major phases: (A – B) gas pressure build-up in the lower filter section at a constant air injection volumetric rate of 100 ml/min. Essentially no response on the loading process is observed in the sample in terms of outflow or axial strain. In the second stage (B-B'), gas starts to invade the sample and the sample expands (negative axial strain). Towards the end of this stage, a small but measurable outflow is observed in the upper filter. The third stage of the experiment (B'-C) is characterised by the gas breakthrough with a marked drop in gas pressure in the lower filter section, strong increase of outflow volume and compaction of the sample (negative axial strain).

More than 10 gas injection experiments on bentonite samples using different compaction and hydration procedures, different injection rates, different compaction stresses and different gases (air, He) were conducted. The experimental programme formed the database for a modelling benchmark as part of the EBS Task Force, called "Task 7 – Gas Transport in Bentonite" (Dieudonné et al. 2017, Madaschi & Laloui 2018). Different conceptual approaches and model implementations were used to back-analyse the experimental data from previous tests and to predict the hydro-mechanical behaviour of bentonite samples when subjected to new gas injection sequences. All modelling approaches made use of conceptual frameworks that describe the granular bentonite as a double porosity/permeability structure with intra-aggregate and inter-aggregate porosity. The intra-aggregate porosity includes not only interlayer porosity, but also pores up to 20 nm, which differs from the geochemical dual porosity approach (Donnan and free porosity, section 3.3.1). Preliminary results of the benchmark reveal that the applied double structure approaches are well-suited to describe both the combined transport of gas and water in the bentonite and its volumetric behaviour with an initial undrained phase, a phase of expansion during gas invasion and the compaction after gas breakthrough.. After completion of the benchmark in the EBS Task Force, the experimental work and modelling activities will be continued as task of the EURAD project called "Mechanistic understanding of gas transport in clay materials" (EURAD-GAS).

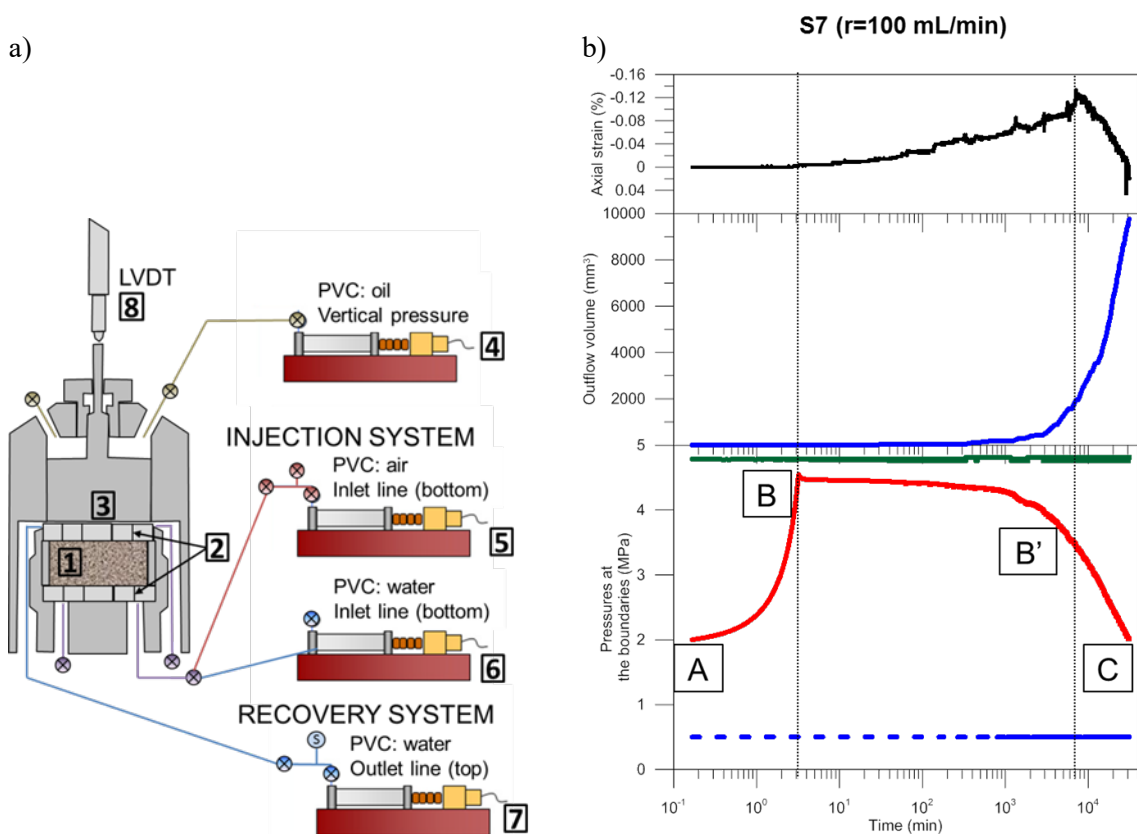


Fig. 5-29: Water and gas injection experiments with compacted granular bentonite

a) Scheme of the oedometer set-up: bentonite sample (1); concentric stainless steel rings with gaps (2); axial loading piston (3); pressure/volume controller (PVC) for vertical stress (4); PVC for air (5); PVCs for water (6 & 7); and linear variable differential transformer for distance measurement (LVDT, 8). b) Transients of pressures at the boundaries, outflow volume and axial deformation of sample S7 ($r = 100$ mL/min).

Romero & Gonzalez-Blanco (2018)

Significance of geochemical influences on gas transport for the Nagra concept

The transport of hydrogen gas generated from steel canister corrosion is simulated in experiments. Results indicate gas release through preferential pathways, which reseal when gas pressure drops. The set-up allows for expansion of the bentonite, as is expected under repository conditions. The difference between Na- and Ca-bentonite, or the influence of ionic strength, have not yet been investigated, but might be insignificant.

5.10 Coupling and integration of different processes for assessment

5.10.1 Saturation phase (0 – 100 y after emplacement)

The time period required to reach full saturation depends on many parameters. The indicated period of 100 y (section 2.3.1) must be seen as a rough estimate. The main processes active during bentonite saturation are shown as white boxes in Fig. 5-30; the numbers in the text below correspond with the numbers on this figure. Water flows either from OPA into the bentonite or crosses a cementitious tunnel reinforcement. The bentonite will be saturated with a concentrated version of the OPA or cementitious porewater. The concentrating process of the porewaters is not explicitly depicted in the figure (described in section 5.7). The advective saturation of the bentonite leads to the build-up of swelling pressure, the most important hydro-mechanical coupling in this phase (1). Swelling pressure build-up leads to structural homogenisation in the long term (2).

The infiltrating concentrated OPA porewater is expected to still be below gypsum saturation and, therefore, the infiltrating water partly dissolves the gypsum present in MX-80 (major OPA porewater – bentonite interaction (3), section 5.2.3). Dissolution of minor amounts of salts slightly increases porewater salinity. The Ca thus freed, in addition to the Ca entering with OPA porewater (section 5.2.2), leads to an increase of Ca on the exchanger (4). The increase of Ca on the exchanger lowers the swelling pressure (5), which is expected to be significant only at high Ca occupancy (section 3.8). In addition, gypsum dissolution frees up space, which lowers the dry density: despite the small volume fraction occupied by gypsum, its dissolution lowers the swelling pressure (6) by as much as 10 % due to the exponential density-pressure relationship (section 5.2). Because the swelling pressure build-up leads to structural homogenisation in the long term (2), all processes that lower swelling pressure prolong homogenisation.

In the case of infiltrating cementitious porewater, similar processes to those described above are expected: the infiltrating high-Ca porewater and accessory dissolution trigger cation exchange (8, 9, 5), the associated density decrease lowers swelling pressure (10). The interaction between high-pH cementitious porewater and bentonite (11) also results in montmorillonite reaction (section 5.3), again lowering swelling pressure (10). The volume that reacts during the limited saturation period is expected to be small. Precipitation of reaction products and calcite decreases the free porosity at the interface (12), and this reduces infiltration (13). Several Mg layered double hydroxides are more stable at elevated pH and precipitate at such interfaces. Mg in the free porosity drops but is refilled from the exchanger (34). The resulting gradient on the exchanger in the bentonite perpendicular to the interface (or in the Donnan porosity) leads to Mg diffusion from the entire bentonite towards the interface, mostly compensated by Ca (Donnan diffusion). Similar processes occur at the concrete-OPA interface (not part of this report).

The temperature effect on the cementitious porewater-bentonite interaction (32) leads to a higher reactivity and permeability in general, as well as different interaction products at the interface. The effect of temperature on the cement itself must also be taken into account: ettringite decom-

poses well below the 100 °C expected at the OPA wall, but C-S-H dehydration just starts at this temperature, and portlandite is still stable. The temperature effect is expected to accelerate the decomposition in the governing OPA porewater environment.

With ongoing saturation, diffusive solute transport also gains in significance at the cement-bentonite interface. Mainly Ca and OH enter the bentonite and interact with it (14), comparable to the advectively transported solutes (11), thereby also clogging porosity (15). Mg enters the cement and precipitates must also be expected here. In turn, the decalcification of the cement opens the porosity (16). Porosity clogging reduces diffusive transport (17), comparable to advective transport (13). Advective transport dominates at the bentonite-OPA interface, diffusion is expected to be smaller due to more limited reactions, which lead to smaller gradients. However, a minor back-diffusion flux of sulphate must be expected at both cement and OPA interfaces, caused by the gypsum-controlled high sulphate content in the bentonite porewater.

With ongoing saturation, the montmorillonite swells, and the Donnan porosity dominates the pore distribution (porosity homogenisation). This significantly limits advection (section 3.5.1), and the infiltration and saturation slow down (18).

The comparatively slow infiltration allows the air present in the emplaced bentonite to be dissolved. Together with the oxygen delivered from the cementitious porewater, the total oxygen reacts fast, mainly with pyrite and the steel canister, consuming only a small fraction of the pyrite inventory (section 3.4.6). These coupled processes depend less on the other processes described here and are not included in Fig. 5-30.

At the canister side, high temperatures prevent the bentonite from reaching saturation (19), boiling at the water front is expected, leading to a steam/air layer around the canister (section 5.1). Calcium sulphate precipitates at this water front (20). In addition, the heating of the saturation water lowers the solubility, especially of calcium sulphate, again leading to precipitation (21); the subsequent clogging (22) impedes saturation (23).

At the canister-bentonite interface, corrosion leads to iron/copper and hydrogen species diffusing into the bentonite (24), accelerated by the high temperature (25). The additional Fe also accesses the exchanger (26) (synonymous with entering the Donnan porosity, which offers an additional transport path away from the canister). Interactions with the partly saturated porous medium bentonite (27) include dissolution of hydrogen in the porewater and diffusion away from the canister (section 5.4), which lowers the gas pressure and enhances saturation (28). Precipitation of iron oxides/hydroxides leads to clogging (29), slowing down further diffusion (30). The extent of reactions with montmorillonite remains unclear, possibly including reduction of structural iron or other reactions that might affect swelling pressure (31). High temperature facilitates such reactions (32) by providing the activation energy and/or increasing the reaction rate.

Mg, and in some cases Ca, are enriched in the bentonite at the canister. The nature of this Mg trap is unclear (33), possibly higher pH values could trigger processes comparable to the cement-bentonite interface. The increased stability of Mg precipitates leads to a Mg gradient and a gradual consumption of the Mg on the exchanger of the entire bentonite layer (34). The associated clogging (29) slows down transport. Experimental observations indicate substantial clogging at cement interfaces, but only limited Mg increase at heater surfaces within the limited laboratory timescales.

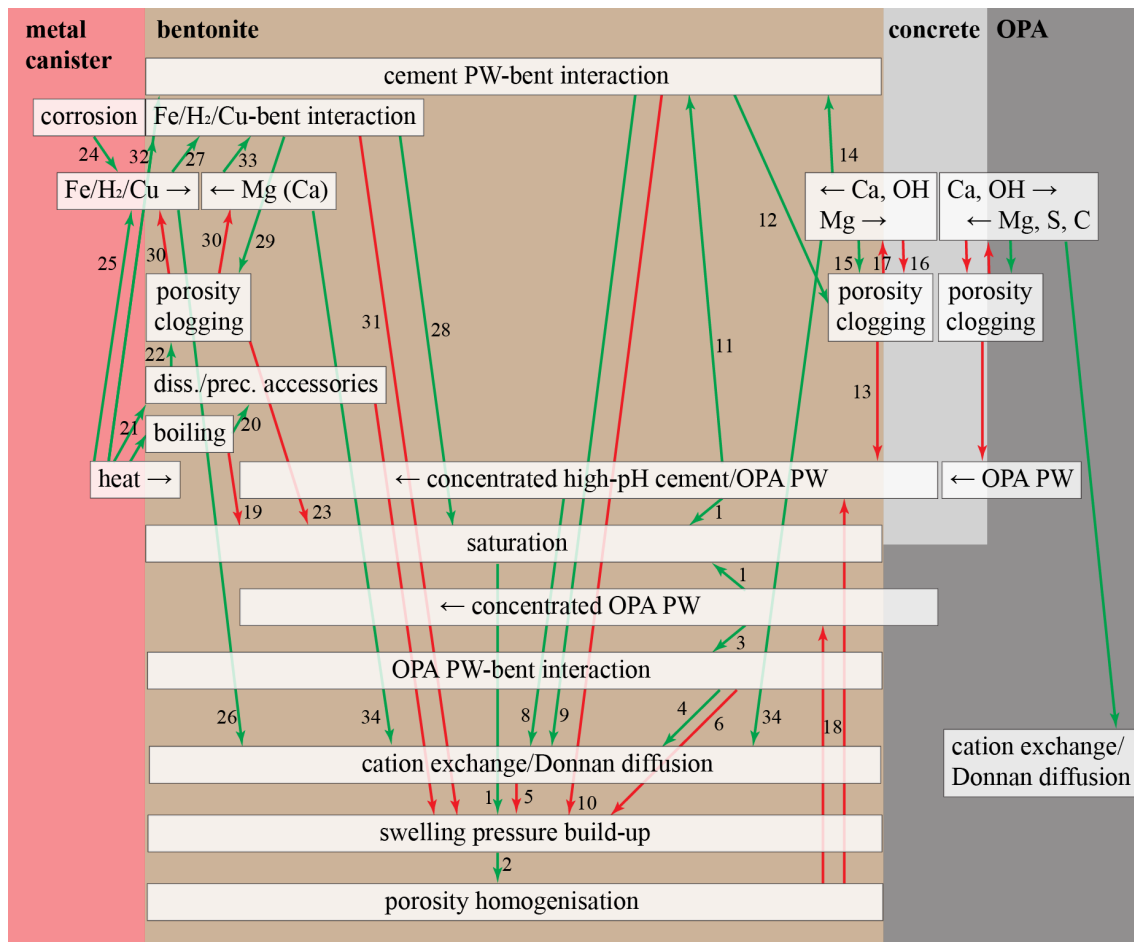


Fig. 5-30: Coupling of different processes in the canister – bentonite – concrete – OPA system during saturation

Dimensions are not to scale. Major processes are shown in boxes, green arrows connect process A enhancing process B, red arrows connect process A impeding process B. The numbers refer to couplings explained in the text. OPA: Opalinus Clay, bent: bentonite, PW: porewater.

5.10.2 Porewater equilibration phase (100 – 10,000 y after emplacement)

The saturation of the bentonite has essentially terminated and Fig. 5-31 thus lacks all advective processes. The porewaters equilibrate with the reactive solids, and diffusion smooths out spatial gradients in porewater chemistry. Temperatures have fallen below 100 °C at any near-field location (section 2.3.1).

Fast advective processes have ceased and the remaining slow diffusion processes govern the near-field evolution during this much longer phase. In general, all diffusive processes and their couplings continue as described above for the saturation phase (numbers still refer to the text above). OPA serves as an unlimited porewater reservoir and buffer for the interaction with high-pH cementitious fluids.

The sulphate from gypsum dissolution diffuses into the OPA (A), which is the main equilibration process between the saturated bentonite and OPA. The Ca freed equilibrates with the exchanger and the OPA porewater, which leads to only very limited diffusion. At the end of the saturation

phase, the porewater in the bentonite is higher in ionic strength than the saturating OPA or cementitious porewaters (section 5.7). This gradient leads to a back-diffusion against the former saturating flow. Possible precipitates formed during this concentrating process dissolve again. The decrease in ionic strength in the bentonite causes a slight increase in swelling pressure (B, section 3.8.3). Furthermore, a lateral equilibration between domains saturated with cementitious porewater and OPA-saturated domains must be expected. This process promotes structural homogenisation within the entire bentonite (C). Diffusion of dissolved hydrogen from steel corrosion follows the gradient from steel outwards into OPA. Any porosity clogging slows down the hydrogen discharge (D). All these diffusive processes already took place during the saturation phase, but had been insignificant compared to the advective transport, or insignificant within the comparably short saturation phase in terms of absolute mass transfer.

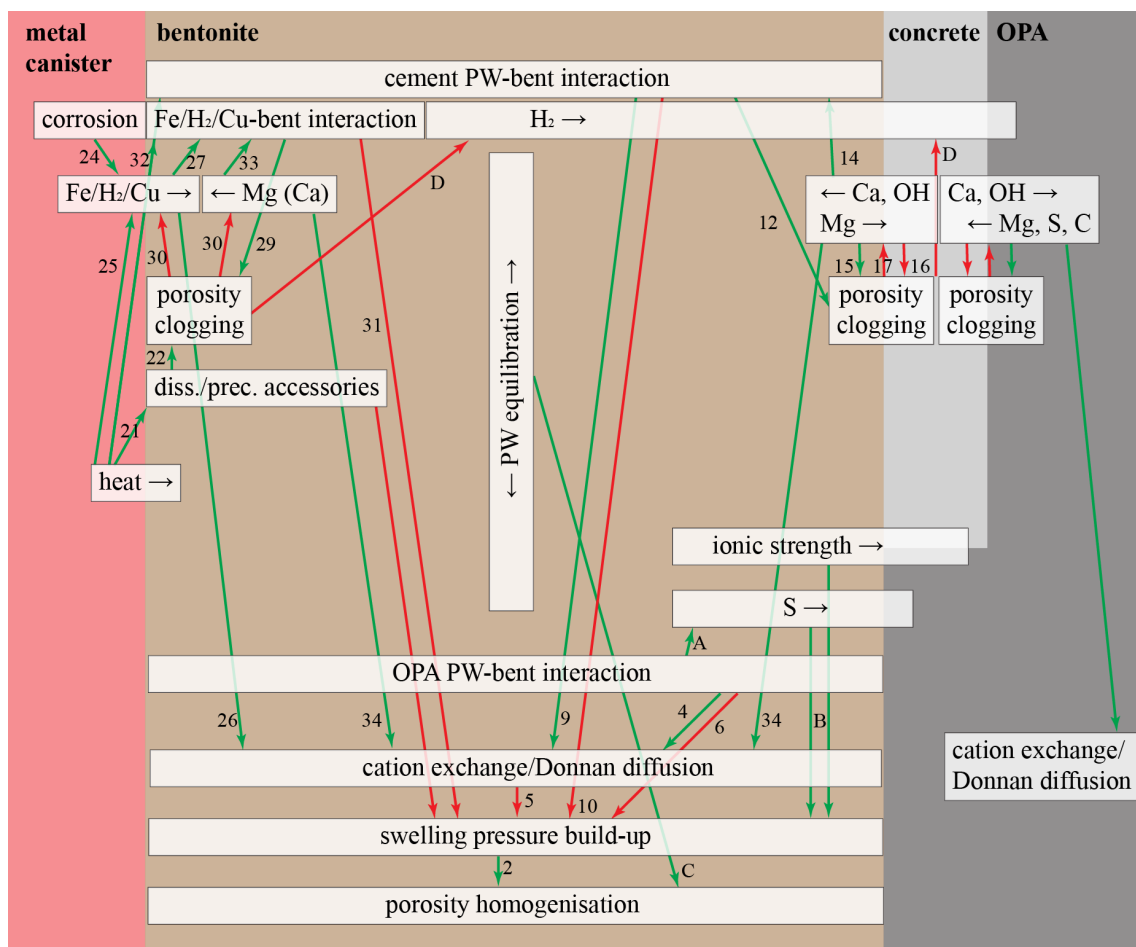


Fig. 5-31: Coupling of different processes in the canister – bentonite – concrete – OPA system during porewater equilibration

Dimensions are not to scale. Major processes are shown in boxes, green arrows connect process A enhancing process B, red arrows connect process A impeding process B. The numbers and letters refer to couplings explained in the text. OPA: Opalinus Clay, bent: bentonite.

At the end of this phase, major porewater gradients are smoothed out and diffusion slows down. Gypsum is expected to be completely removed from the bentonite, whose porewater now equals the OPA porewater far from cement or steel. Steel corrosion, iron-bentonite interaction and hydrogen transport continue, but depend on the degree of porosity clogging (including the formation of a protective corrosion layer). Similarly, the evolution at the cement-bentonite interface strongly depends on clogging: in the case of strong clogging, the bentonite porewater has laterally equilibrated with the OPA porewater, and any cement-bentonite interaction ceases, including montmorillonite dissolution. In the case of insignificant clogging or even porosity increase, cement continues to dissolve or might already have disappeared; the reaction plume spreads into the bentonite and equilibrates with the OPA porewater. In this case, the freed volume (corresponding to the volume of cement in the concrete) is mainly occupied by the swelling bentonite, which lowers dry density and therefore swelling pressure (E).

5.10.3 Quasi-steady state (10^4 – 10^6 years after emplacement)

Reactions have slowed down considerably or stopped (e.g. protective layer on canister surface, clogged concrete interfaces or concrete dissolved). The remaining reactions now limit the overall evolution of the near-field. The resulting small gradients in the porewater are smoothed out by diffusion into the OPA in the same way radionuclides are now transported⁹. The temperature of the bentonite approaches the original formation temperature.

In this phase (Fig. 5-32), anaerobic corrosion (24), diffusion and interaction (27) of corrosion products with the bentonite are the main remaining, slow processes. If the Mg sink was caused by the elevated temperature, back-diffusion of Mg (and Ca) has stopped by now. The main interactions between the corrosion products and the bentonite (27) are precipitation of iron hydroxides or oxides decreasing porosity (29), and possible reduction of structural iron in montmorillonite or other phase transformations. Reactivity of the dissolved hydrogen is expected to be negligible and it continues to diffuse into the OPA. Still, any diffusion may be hindered or even virtually stopped by porosity clogging (30, D).

⁹ Radionuclide transport from the breached container across the near-field is not treated in this report.

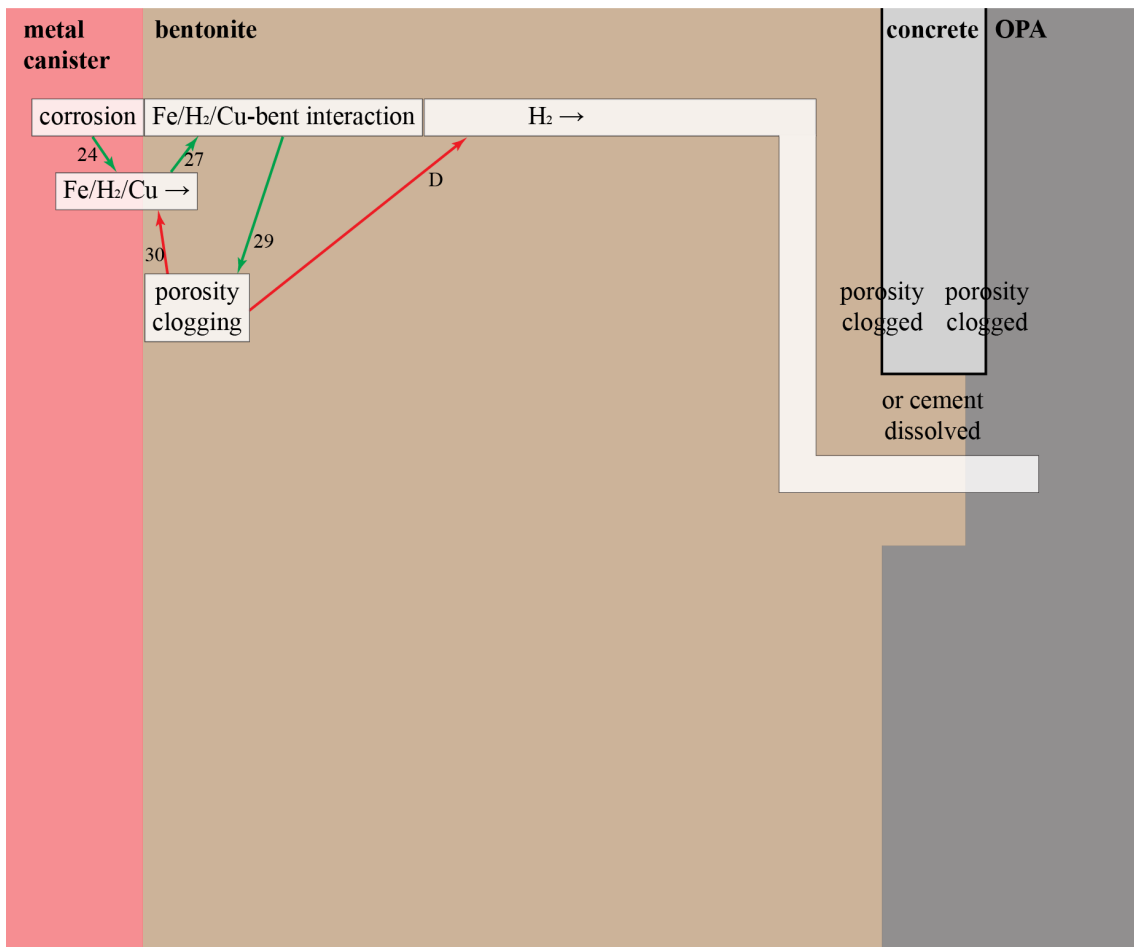


Fig. 5-32: Coupling of different processes in the canister – bentonite – concrete – OPA system during quasi-steady state

Dimensions are not to scale. Major processes are shown in boxes, green arrows connect process A enhancing process B, red arrows connect process A impeding process B. The numbers and letters refer to couplings explained in the text. OPA: Opalinus Clay, bent: bentonite.

5.10.4 Safety-relevant coupling of processes

At any stage of the near-field evolution, mineral reactions, advective and diffusive transport and THM processes are mostly coupled. In the context of the repository, the coupling process affecting the overall safety are:

- Corrosion at the canister interface → clogging of macropores by formation of iron (hydr)oxides → slow-down of hydrogen transport: during the major part of the repository evolution, the hydrogen released from canister corrosion will partly dissolve in the porewater. The resulting gradient will lead to diffusive transport towards the host rock. Precipitation of iron oxides or hydroxides might partly clog the diffusion-active porosity in the bentonite. In this case, gas pressure builds up above values estimated from unclogged material properties. The latest understanding of reactive transport in bentonite suggests clogging only in the macroporosity. The Donnan porosity, which is the dominant fraction of the porosity, is expected to remain open. Many indications exist that diffusion in the Donnan porosity is very efficient. Uncharged species like H₂ enter the Donnan porosity and can therefore bypass the potentially clogged free porosity.
- Corrosion → iron-montmorillonite interaction/montmorillonite alteration → swelling pressure reduction at the interface: the steel corrosion products react with montmorillonite. Although lower temperature and partially clogged porosity prevail for the major part of the repository lifetime, the reaction is expected to continue and propagate into the bentonite. Major uncertainties are related to the reaction, rate, and required activation energy. A decrease of the amount of swelling clay and the swelling pressure must be expected at the interface.
- Cement-clay interaction → clogging of macropores at the interface (skin formation) → slow-down of the saturation → lowered swelling pressure at the interface, or slow-down of chemical equilibration with OPA porewater: clogging of macropores at the cement interfaces will slow down the bentonite saturation. Saturation will preferentially occur where these skins are not continuous (such as joints or gaps in the cementitious liner). Saturation is expected to be prolonged and to occur in an inhomogeneous pattern. Furthermore, equilibration with OPA porewater after saturation will be prolonged and swelling pressure will build up later than expected based on THM considerations only.

The remaining coupled processes are not expected to influence the safety-relevant properties of the bentonite barrier with the major montmorillonite fraction still intact, a homogeneous pore size distribution, swelling pressure in the required range, and porewater close to equilibrium with OPA porewater. But, due to uncertainties related the coupling of all the processes listed above, the predictions of how and when the steady state is attained remains difficult.

6 Synthesis of scientific evidence and its significance for repository safety

6.1 Current understanding of geochemical evolution in the bentonite buffer and remaining uncertainties

Bentonite is a widely used natural material with many applications. Owing to its good sealing properties, compacted bentonite is foreseen as a backfill material for deposition tunnels in high-level waste repositories in several countries. There is ample evidence that the bentonite buffer is an efficient hydraulic, mechanical and chemical barrier that will protect the canister and attenuate the release of radionuclides. The evolution of the repository will induce processes that may impair the safety functions of the buffer:

- processes and loads occurring during saturation of the buffer ("short term")
- processes and loads occurring after saturation ("long term")

6.1.1 Processes during saturation

During the non-isothermal resaturation of the buffer, coupled THMC (thermal, hydraulic, mechanical and chemical) processes are expected in the bentonite. Despite the steady improvement of computational capacities and increased body of experimental evidence, modelling coupled processes remains challenging in terms of conceptualisation and parameterisation.

The thermal and thermo-hydraulic evolution of the bentonite buffer can be reasonably well captured by the current state-of-the-art THM models. However, the capability of these models to predict the mechanical behaviour is less advanced, although qualitative trends observed in the experiments can be captured.

Difficulties in coupling the hydro-mechanical (HM) and chemical-mechanical (CM) behaviour of clay boils down to the conceptualisation of the clay's micro- and nanostructure evolution.

Nevertheless, a dual-porosity framework, which has recently been developed in THM as well as in THC models, appears to offer a robust and consistent framework to represent coupled THMC processes. Within this framework, several different features and observations can be readily explained. A fully coupled coherent THMC model, however, is lacking to date. It is however questionable whether chemo-hydro-mechanical interactions are significant enough regarding their impact on the safety-relevant properties of the buffer to justify the development of such a model framework.

Water saturation

Suction pressure resulting from capillary and osmotic forces in non-saturated bentonite, the thermal gradient of the near-field and the hydraulic head will control the rate at which the near-field resaturates. The expected geochemical processes are outlined below (see: chemical and mineralogical evolution). Saturation of the bentonite close to the hot canister will be delayed, and vapour might form. Evaporation and vapour transport may induce precipitation of soluble salts close to the canister. This effect, however, is expected to be small and reversible.

Gas transport

At the onset of saturation, the unsaturated buffer contains large amounts of air. Many laboratory and large-scale experiments have shown that the increasing pressure of the gas in the partially saturated buffer leads to dissolution of the gas. Minor mineral reactions and diffusion into the host rock reduce the dissolved gas concentration. The redox conditions become anoxic, which is a strong indication for consumption, sorption or out-diffusion of the original gas, paired with the consumption of oxygen by redox reactions. Preferential gas escape pathways from the inner (still undersaturated) buffer through the more saturated and swollen outer part have not been observed in large-scale experiments. At this stage, gas pressure is still low and/or pathways are not preserved during continuing saturation and homogenisation.

Homogenisation

There are numerous experimental observations indicating that homogenisation of density/porosity variations is effective during the saturation and swelling process. However, data also suggest that some inhomogeneity will persist after saturation. Observations from in-situ tests yield valuable but not unambiguous information, partly because they did not reach full saturation after completion, as for example the FEBEX experiment at the GTS. The artificially saturated EB experiment at Mont Terri reached almost complete saturation and showed good homogenisation between the dense blocks and less dense pellets (Villar et al. 2014). In the lowest part of the gallery, however, a low-density zone persisted at densities which were about 17 % lower than average density ($\sim 1,200 \text{ kg m}^{-3}$). The persistence of such low densities should be avoided in the backfill since it may favour microbial activity and linked sulphide generation (Bengtsson et al. 2017).

Preliminary THM modelling (i.e. from the EBS Task Force) indicated, in general, a fairly good description of the homogenisation process, but uncertainties remain, for example related to the mechanical properties of pelletised material. The models include empirical parameters that had been adjusted to the material, and so are not truly predictive in a general sense.

The effect of chemistry (e.g. salinity, nature of interlayer cations) on homogenisation has not yet been studied in detail. Laboratory experiments by Dueck et al. (2016) and Martikainen et al. (in review) suggest small differences in the behaviour of Ca- and Na-bentonite as well as regarding the salinity of contacting solutions. Further studies should be carried out to confirm or deny these preliminary findings.

Chemical and mineralogical evolution

During saturation of the bentonite with host rock porewater, a transient behaviour of the salinity with fairly high chloride concentrations in the "free" porewater due to the clay's osmotic membrane properties is expected. The thermal gradients will induce redistribution of accessory minerals, such as dissolution of gypsum at the "cold" side and re-precipitation of anhydrite/ gypsum at the "hot" side. This effect is enhanced by evaporative processes close to the canister. Overall, the amounts of redistributed salts and minerals are small as shown by reactive transport calculations, mass balance considerations, and large-scale experiments. Cation exchange reactions will also come into play within the thermal gradient, thus generally leading to an increase in Ca/Mg and decrease in Na in the exchange population at the hot side. Montmorillonite alteration due to the heat input from the canister is limited by slow kinetics and the limited supply of reactants (e.g. K^+), particularly at lower degrees of saturation. In-situ tests suggest formation of minor trioctahedral smectite as a result of the thermal gradient, but it is unclear to what extent this phase is formed from the conversion of montmorillonite or from the dissolution of accessory silicate minerals.

Redox conditions in the bentonite, which initially contains residual air in the pores, will turn reducing by reactions with reducing minerals (e.g. pyrite), corrosion reactions with the canister, diffusion of O₂ into the rock, and microbial processes occurring mainly at the buffer/rock interface. Thus, O₂ depletion is expected to occur within a few years or perhaps even faster, as recent data from the FE experiment and from a down-scaled KBS-3 mock-up suggest.

At the interfaces with cement and steel, chemical and mineralogical changes are likely to be larger than those induced by heat alone. Because of strong chemical gradients at the cement/clay interface, diffusion followed by dissolution/precipitation processes will occur on the clay and the cement side. As also indicated from experimental data, this can induce porosity reduction. If such a skin is continuous and effective, it will reduce further solute and water exchange between the two materials and might slow down the buffer saturation across a concrete liner. The exchange process will be affected by the comparatively large interlayer porosity in the clay. Although uncertain at this stage, we envision that solute exchange between the cement and the clay will persist even upon complete clogging of the "free" (intergranular) porosity, operating in the Donnan porosity. Due to slow kinetics and (partial) clogging, the amount of montmorillonite transformed to other minerals during the saturation phase is expected to be small in spite of the locally high pH environment. At OPC-OPA interfaces, the high-pH front is expected to enter the OPA roughly 10 mm in 10 years. In contrast, clogging observed at low pH cement-OPA interfaces seems to slow down the high-pH front entering the OPA. Experimental data still do not clearly define the time evolution of the reaction fronts. Modelling of such interfaces is extremely sensitive to dissolution kinetics of clays and ion transport in the two porosity domains, both bearing rather large uncertainties. It is therefore not possible at present to reliably predict the extent and the timing of clogging.

Corrosion of the steel canister will release iron species which will form a corrosion layer and may also react with the clay. Initially, under oxidising conditions, Fe(III) (hydr)oxides will precipitate. Soon afterwards, anaerobic conditions will prevail and Fe(II)-bearing minerals (e.g. magnetite, siderite) will precipitate in the corrosion layer. Fe(II) will also diffuse into the bentonite and react with clay by sorption/precipitation and redox processes. The details of this interaction process are not well understood. It may involve reduction of structural Fe(III) which may destabilise the montmorillonite structure and possibly also lead to the formation of Fe-rich silicates (Fe smectite, berthierine). The amount formed, however, will be limited during the saturation phase. Porosity reduction, mainly due to formation of Fe (hydr)oxides may occur, but this effect is probably not very large during the saturation phase, as seen from in-situ data. These data also indicate that corrosion-derived Fe(II) may migrate through preferential pathways in low density zones (e.g. former gaps between pellets) and precipitate as iron (hydr)oxides.

Corrosion of a Cu-coated canister will induce interaction of the oxidised Cu(I,II) with the clay. The amounts of released Cu will be small once the oxic period has ceased in view of the low corrosion rates.

Microbial activity

Initially, microbial activity will be limited because of the low water activity in the clay, the limited transport of nutrients and the elevated temperatures. At higher moisture content, it may become more likely because of higher water activity, increased availability of nutrients and more moderate temperatures. On the other hand, due to swelling, the fraction of small pores (interlayer and DDL) will increase at the expense of the larger pores (free porosity), which will limit microbial activity. The main concern is the possibility that microbial sulphate reduction may produce gaseous H₂S which may diffuse towards the canister. This process has so far not been systematically studied in experimental programmes.

6.1.2 Processes after saturation

After the end of the saturation process (about 100 – 200 years), the heat output from the decaying waste will be considerably lower, thus temperatures in the buffer will have decreased well below 100 °C. The initial variations in porosity and density will have largely disappeared and the material will have gained a fairly homogeneous nanopore-dominated structure. Slight differences in density may remain, especially in the interface region with the host rock. Cooling will redistribute reactive accessory minerals, thus re-dissolving anhydrite/gypsum and calcite according to thermodynamic constraints. Also, Fe(III) (hydr)oxides (goethite, lepidocrocite) will continue to re-dissolve and release Fe(II) in the reducing environment. Anoxic steel corrosion will continue and further release Fe(II). The cementing silicate agents, however, having formed during the saturation phase as a result of the thermal transient (e.g. SiO₂) will likely persist, but their amounts will be small (see above). In general, processes with slow reaction kinetics and slow diffusive transport might not lead to significant alteration during the short saturation period, but they might impact the system within the one million years after saturation is achieved.

Gas transport

The transport of gas through saturated bentonite samples, as studied in Nagra's recent experimental programme (section 5.9), considers three stages when gas is continuously added: (i) constant outflow of (dissolved) gas during pressure build-up at the inlet with no effect on strain, (ii) expansion of sample and start of free gas flow and (iii) gas breakthrough together with an increase in water outflow rate, which is accompanied by a pressure drop and sample consolidation. In the repository concept, release of hydrogen from steel corrosion cannot be fully compensated by dissolution and diffusion through the buffer. The uncertainty of additional gas transport processes remains: will the proposed gas escape in flow pathways postulated in stage (iii)? The influence of clogging and cementation at the steel interface, or more significantly at the cement interface, on the gas transport is not fully understood. Further chemical issues are of minor importance: pore-water composition only slightly influences swelling pressure, the main driving force for closure of low-density transport pathways and homogenisation of the entire buffer porosity.

Porewater chemistry

The porewater composition in the buffer will slowly evolve via the diffusive exchange with the surrounding OPA porewater, assuming no, or a completely altered, cement liner. The differences between the two porewaters, in general, will be minor, although there will be a gradient in sulphate if gypsum in the bentonite is not completely dissolved. The porewater will be further influenced by high-pH alkaline leachates from the cement on the outer side and metal corrosion on the inner side. Exactly how all the different materials and processes act together and affect the porewater evolution has not yet been assessed to the full extent. The large pH buffer and CEC of the clay is thought to efficiently buffer the porewater composition for long times. The processes buffering the OPA and cementitious porewaters are expected to affect swelling pressure of bentonite in two ways: increased ionic strength in the porewater and increased Ca on the exchanger lower swelling pressure, and dissolution of any solid phase in the buffer lowers dry density and therefore swelling pressure. Lower swelling pressure decreases homogenisation. It is noted that the two different bounding waters envisaged for buffer saturation or equilibration lead to significantly different swelling pressures (1,890 and 2,510 kPa for Na-bentonite, 1,600 and 1,750 kPa for Ca-bentonite with 1,500 kg m⁻³ dry density).

Cement-bentonite interaction

This interaction process at the buffer/cement interface will continue at a low rate at lower temperatures and also because of potential clogging that reduces mass transfer rates. Suction of the buffer has ceased, and no more saturation water crosses the cementitious liner. Transport is now purely diffusive and slower than in the saturation phase. The timescale of complete dissolution of the concrete liner and out-diffusion into buffer and host rock is unclear, but it is unlikely that this happens within the repository lifetime. A mass-balance calculation can predict the mass of buffer dissolved per mass of cement, but not the spatial distribution and timing. This simplistic but worst-case approach results in insignificant dissolved buffer volumes and ignores the accompanying precipitation. The resulting clogging might decouple the buffer from the liner, which impedes equilibration with OPA porewater and might hinder gas transport. At the moment, too many uncertainties (reaction kinetics and parameters for dual porosity transport in OPA) impede a reliable modelling prediction of the cement-bentonite interaction.

Iron-bentonite interaction

Anaerobic corrosion of steel will continue, but the formation of a protective corrosion layer will decrease corrosion rates to 1 $\mu\text{m/a}$ or less. Fe(II) will continue to diffuse into the clay at a reduced rate. It is unclear if the free porewater or a Donnan-type porewater is relevant for corrosion: at high densities, steel and charged clay sheet surfaces might be close enough to exclude anions and impact activities, which are crucial for quantification of reactions. However, the released Fe(II) will continue to interact with the clay, but the impact on montmorillonite (i.e. reduction of Fe(III) to Fe(II), transformation) is unclear at present. Because of uncertainties in process understanding, modelling predictions are difficult.

Cu-bentonite interaction

Anaerobic corrosion of Cu will occur in the presence of sulphide, but the rates will be very small. Thus, very low corrosion rates and correspondingly low Cu(I) transfer rates to the clay will result. The impact on sorption competition with radionuclides is expected to be very minor except at the direct contact to the metal surface where Cu(II) could be sorbed during the oxic phase.

Radionuclide transport

It is conservatively assumed in safety assessment that the steel canister breaches after 10^4 years and radionuclides are released into the buffer, where their transport is dominated by diffusion. Bentonite acts as an efficient scavenger of many radionuclides by sorption and/or (co)precipitation processes. The presence of sorbed Fe(II) from the Fe-bentonite interaction may weaken the sorption capacity of the clay to some extent, but this effect is likely limited to divalent radionuclides (e.g. Ni(II)). Radionuclide transport is not covered in this geochemical report.

Microbial processes

The compacted saturated bentonite with its high swelling pressure and nanoporous structure is a hostile environment for microbes. Thus, at high densities all microbial activity comes to a halt. There is still uncertainty, however, as to where the upper density limit for microbial activity is. More generally, it is not clear whether there exists a sharp cut-off value above which no microbial activity is possible or whether there is a more gradual relationship between microbial activity and density. Transferring this information to the saturated buffer, essentially no microbial activity is expected for a well-emplaced MX-80 buffer with a dry density of $1,450 \text{ kg m}^{-3}$ (and above). Resulting sulphide generation would be limited to the EDZ around the bentonite or perhaps to low density areas at the buffer/rock interface. In the case of poor buffer emplacement, lower density areas might persist within the buffer, and microbial sulphate reduction in the buffer cannot be ruled out. This process, however, seems to have a limited impact on the canister lifetime as shown by Cloet et al. (2017).

Long-term stability of montmorillonite

The thermodynamic stability of montmorillonite under repository conditions and, more generally, in low-temperature environments, is a difficult issue to resolve in view of the large data uncertainties and also because of theoretical considerations regarding the thermodynamic stability of smectites. Available data, in fact, suggest instability of montmorillonite under near-field conditions. On the other hand, kinetic considerations as well as information from natural analogues suggest that montmorillonite will persist under "normal" (i.e. circumneutral pH) conditions for millions of years. Moreover, transport arguments have been put forward which support a very limited dissolution of the montmorillonite in the buffer as well.

6.2 Suggestions for mitigating uncertainties

Gas transport

Current experimental work should help to reduce uncertainties related to gas transport phenomena in compacted bentonite. Within the framework of the Swedish EBS task forces, initiatives have been taken to conceptualise processes seen in experimental data.

Additional efforts to reduce uncertainties are envisioned in the EURAD-Gas task, in which Nagra has the lead of the tasks related to barrier integrity.

Homogenisation

Currently, considerable effort is dedicated to the better understanding of the homogenisation process and its prediction under repository conditions within the EBS Task Force and within the EC project BEACON. In this regard, a better understanding of hydro-mechanically coupled processes and their conceptualisation is to be expected at the end of the BEACON project.

Iron-bentonite interaction

The main relevant uncertainty regards the long-term interaction of Fe(II) with the clay and potential effects on the smectite stability. This topic is part of the new EURAD Project (EURAD-ACED) where dedicated experiments will be carried out in combination with reactive transport modelling.

Cement-bentonite interaction

Cement-bentonite interaction is addressed in the EU/Euratom Horizon 2020 Cebama Project (Cement-based materials, properties, evolution, barrier functions) and includes a limited number of studies related to aged concrete-bentonite interfaces, including FEBEX-DP. A key issue is that it is extremely difficult to obtain quantitative information on porosity and pore size distribution across such interfaces, and this will likely not be resolved as an outcome of Cebama. Some progress is being made with ^{14}C -MMA impregnation and radiography methods. The Mont Terri CI Experiment (long-term cement-clay interaction) sampled 10-year-old interfaces of MX-80 bentonite and OPC as well as a low-alkali concrete ("low-pH" concrete) in 2017 and these are presently being examined by partner labs of the CI Experiment.

Microbial processes

The conditions and constraints for microbial activity in the bentonite buffer continue to bear uncertainties which need to be unravelled. Currently, several initiatives have been launched to understand the underlying processes affecting the cut-off values relating to the bentonite material density and microbial viability.

7 References

- Aagaard, P. & Helgeson, H.C. (1983): Activity/composition relations among silicates and aqueous solutions: II. Chemical and thermodynamic consequences of ideal mixing of atoms on homological sites in montmorillonites, illites, and mixed-layer clays. *Clays and Clay Minerals* 31, 207-217.
- Abercrombie, H.J., Hutcheon, I.E., Bloch, J.D. & Decaritat, P. (1994): Silica activity and the smectite-illite reaction. *Geology* 22, 539-542.
- Agus, S.S. & Schanz, T. (2008): A method for predicting swelling pressure of compacted bentonites. *Acta Geotechnica* 3, 125.
- Aja, S.U. & Rosenberg, P.E. (1996): The thermodynamic status of compositionally-complex clay minerals: Discussion of "clay mineral thermometry - a critical perspective". *Clays and Clay Minerals* 44, 560-568.
- Aja, S.U. (1991): Illite equilibria in solutions. 3. A reinterpretation of the data of sass et-al (1987). *Geochimica et Cosmochimica Acta* 55, 3431-3435.
- Aja, S.U., Rosenberg, P.E. & Kittrick, J.A. (1991a): Illite equilibria in solutions. 1. Phase-relationships in the system $K_2O-Al_2O_3-SiO_2-H_2O$ between 25 and 250-degrees-C. *Geochimica et Cosmochimica Acta* 55, 1353-1364.
- Aja, S.U., Rosenberg, P.E. & Kittrick, J.A. (1991b): Illite equilibria in solutions. 2. Phase-relationships in the system $K_2O-MgO-Al_2O_3-SiO_2-H_2O$. *Geochimica et Cosmochimica Acta* 55, 1365-1374.
- Alonso, E.E., Gens, A. & Josa, A. (1990): A constitutive model for partially saturated soils. *Geotechnique* 40, 405-430.
- Alt-Epping, P., Gimmi, T., Wersin, P. & Jenni, A. (2018): Incorporating electrical double layers into reactive-transport simulations of processes in clays by using the Nernst-Planck equation: A benchmark revisited. *Applied Geochemistry* 89, 1-10.
- Alt-Epping, P., Tournassat, C., Rasouli, P., Steefel, C.I., Mayer, K.U., Jenni, A., Mäder, U., Sengor, S.S. & Fernández, R. (2015): Benchmark reactive transport simulations of a column experiment in compacted bentonite with multispecies diffusion and explicit treatment of electrostatic effects. *Computational Geosciences*, 1-16.
- Altmann, S. (2008): 'Geo'chemical research: A key building block for nuclear waste disposal safety cases. *Journal of Contaminant Hydrology* 102, 174-179.
- Amram, K. & Ganor, J. (2005): The combined effect of pH and temperature on smectite dissolution rate under acidic conditions. *Geochimica et Cosmochimica Acta* 69, 2535-2546.
- Appelo, C.A.J. & Wersin, P. (2007): Multicomponent diffusion modeling in clay systems with application to the diffusion of tritium, iodide, and sodium in Opalinus Clay. *Environmental Science & Technology* 41, 5002-5007.
- Appelo, C.A.J. (2013): A review of porosity and diffusion in bentonite. WR 2013-29, Posiva, Olkiluoto, Finland.

- Appelo, C.A.J., Van Loon, L.R. & Wersin, P. (2010): Multicomponent diffusion of a suite of tracers (HTO, Cl, Br, I, Na, Sr, Cs) in a single sample of Opalinus Clay. *Geochimica et Cosmochimica Acta* 74, 1201-1219.
- Archie, G.E. (1942): The electrical resistivity log as an aid in determining some reservoir characteristics. *Transactions of the American Institute of Mining and Metallurgical Engineers* 146, 54-61.
- Arcos, D., Grandia, F. & Domenech, C. (2006): Geochemical evolution of the near field of a KBS-3 repository. TR-06-16, SKB, www.skb.se, Stockholm, Sweden.
- Arnedo, D., Alonso, E.E., Olivella, S. & Romero, E. (2008): Gas injection tests on sand/bentonite mixtures in the laboratory. Experimental results and numerical modelling. *Physics and Chemistry of the Earth* 33, S237-S247.
- Arthur, R. & Zhou, W. (2005): Reactive transport model of buffer cementation. 2005:59, SKI, Sweden.
- Avena, M.J., Mariscal, M.M. & De Pauli, C.P. (2003): Proton binding at clay surfaces in water. *Applied Clay Science* 24, 3-9.
- Baes, C.F. & Mesmer, R.E. (1976): *Hydrolysis of cations*. Wiley.
- Baeyens, B. & Bradbury, M.H. (1997): A mechanistic description of Ni and Zn sorption on Namontmorillonite Part I: Titration and sorption measurements. *Journal of Contaminant Hydrology* 27, 199-222.
- Baeyens, B. & Bradbury, M.H. (*in prep.*): The development of a thermodynamic sorption data base (td-sdb) for montmorillonite and the application to bentonite. Nagra Technical Report (*in prep.*).
- Baeyens, B., Marques Fernandes, M. & Bradbury, M.H. (2014): Comparison of sorption measurements on argillaceous rocks and bentonite with predictions using the SGT-E2 approach to derive sorption data bases. Nagra Technical Report NTB 12-05.
- Bagnoud, A., Leupin, O., Schwyn, B. & Bernier-Latmani, R. (2016): Rates of microbial hydrogen oxidation and sulfate reduction in Opalinus Clay rock. *Applied Geochemistry* 72, 42-50.
- Baille, W., Tripathy, S. & Schanz, T. (2014): Effective stress in clays of various mineralogy. *Vadose Zone Journal* 13.
- Bauer, A. & Berger, G. (1998): Kaolinite and smectite dissolution rate in high molar KOH solutions at 35 °C and 80 °C. *Applied Geochemistry* 13, 905-916.
- Bauer, A. & Velde, B. (1999): Smectite transformation in high molar KOH solutions. *Clay Minerals* 34, 259-273.
- Beaucaire, C., Tertre, E., Ferrage, E., Grenut, B., Pronier, S. & Madé, B. (2012): A thermodynamic model for the prediction of porewater composition of clayey rock at 25 and 80 °C – comparison with results from hydrothermal alteration experiments. *Chemical Geology* 334, 62-76.

- Beaufort, D., Berger, G., Lachapagne, J.C. & Meunier, A. (2001): An experimental alteration of montmorillonite to a di plus trioctahedral smectite assemblage at 100 and 200 degrees C. *Clay Minerals* 36, 211-225.
- Behl, M. & Bunge, R. (2016): Abschlussbericht DENSFILL. Nagra Arbeitsbericht NAB 15-11.
- Bengtsson, A., Blom, A., Johansson, L., Taborowski, T., Eriksson, L. & Pedersen, K. (2017): Bacterial sulphide-producing activity in water saturated iron-rich Rokle and iron-poor Gaomiaozi bentonite at wet densities from 1'750 to 1'950 kg m⁻³. TR-17-05, SKB, www.skb.se, Stockholm, Sweden.
- Berner, U. (2012): Abschätzung der Löslichkeit von Kupfer in Zement- und Bentonitreferenzwässern. AN-44-12-10. Paul Scherrer Institute, Villigen, Switzerland.
- Berner, U., Kulik, D.A. & Kosakowski, G. (2013): Geochemical impact of a low-pH cement liner on the near field of a repository for spent fuel and high-level radioactive waste. *Physics and Chemistry of the Earth* 64, 46-56.
- Bestel, M. (2014): Water–montmorillonite systems: Neutron scattering and tracer throughdiffusion studies. PhD Thesis, Institute of Geological Sciences. University of Bern.
- Bestel, M., Gimmi, T., Glaus, M.A., Van Loon, L.R., Zamponi, M., Diamond, L.W. & Juranyi, F. (2018a): Quantification of water distribution in Na- and Cs-montmorillonite based on water mobility. *Clays and Clay Minerals in revision*.
- Bestel, M., Glaus, M.A., Frick, S., Gimmi, T., Juranyi, F., Van Loon, L.R. & Diamond, L.W. (2018b): Combined tracer through-diffusion of HTO and ²²Na through Na-montmorillonite with different bulk dry densities. *Applied Geochemistry* 93, 158-166.
- Bildstein, O., Trotignon, L., Perronnet, M. & Jullien, M. (2006): Modelling iron–clay interactions in deep geological disposal conditions. *Physics and Chemistry of the Earth* 31, 618-625.
- Birgersson, M. & Karnland, O. (2009): Ion equilibrium between montmorillonite interlayer space and an external solution-consequences for diffusional transport. *Geochimica et Cosmochimica Acta* 73, 1908-1923.
- Birgersson, M. & Wersin, P. (2014): KBS-3H. Reactive transport modelling of iron-bentonite interactions, an update for the Olkiluoto case. WR 2013-02, Posiva, Olkiluoto, Finland.
- Birgersson, M. (2017): A general framework for ion equilibrium calculations in compacted bentonite. *Geochimica et Cosmochimica Acta* 200, 186-200.
- Birgersson, M., Karnland, O. & Nilsson, U. (2008): Freezing in saturated bentonite – a thermodynamic approach. *Physics and Chemistry of the Earth, Parts A/B/C* 33, Supplement 1, S527-S530.
- Blanc, P., Gailhanou, H., Rogez, J., Mikaelian, G., Kawaji, H., Warmont, F., Gaboreau, S., Grangeon, S., Greneche, J.M., Vieillard, P., Fialips, C.I., Giffaut, E., Gaucher, E.C. & Claret, F. (2014): Thermodynamic properties of chlorite and berthierine derived from calorimetric measurements. *Physics and Chemistry of Minerals* 41, 603-615.

- Blanc, P., Lassin, A., Piantone, P., Azaroual, M., Jacquemet, N., Fabbri, A. & Gaucher, E.C. (2012): Thermoddem: A geochemical database focused on low temperature water/rock interactions and waste materials. *Applied Geochemistry* 27, 2107-2116.
- Blanc, P., Vieillard, P., Gailhanou, H. & Gaboreau, S. (2013): Chapter 6 - thermodynamics of clay minerals. *In: Bergaya, F. & Lagaly, G. (eds.): Developments in clay science.* Elsevier, pp. 173-210.
- Blanc, P., Vieillard, P., Gailhanou, H., Gaboreau, S., Gaucher, E., Fialips, C.I., Made, B. & Giffaut, E. (2015a): A generalized model for predicting the thermodynamic properties of clay minerals. *American Journal of Science* 315, 734-780.
- Blanc, P., Vieillard, P., Gailhanou, H., Gaboreau, S., Marty, N., Claret, F., Made, B. & Giffaut, E. (2015b): Thermochemie database developments in the framework of cement/clay interactions. *Applied Geochemistry* 55, 95-107.
- Blatz, J. & Graham, J. (2003): Elastic-plastic modelling of unsaturated soil using results from a new triaxial test with controlled suction. *Geotechnique* 53, 113-122.
- Bolt, G.H. (1956): Physico-chemical analysis of the compressibility of pure clays. *Geotechnique* 6, 86-93.
- Börgesson, L., Sandén, T., Dueck, A., Andersson, L., Jensen, V., Nilsson, U., Olsson, S., Åkesson, M., Kristensson, O. & Svensson, U. (2014): Consequences of water inflow and early water uptake in deposition holes – EVA project. SKB Technical Report TR-14-22. Swedish Nuclear Fuel and Waste Management CO, www.skb.se, Stockholm, Sweden.
- Bouchet, A., Casagnabère, A. & Parneix, J.C. (2004): Batch experiments: Results on MX80. (Andra) European contract FIKW-CT-2000-0028, pp. 79-86.
- Bourg, I.C. & Tournassat, C. (2015): Chapter 6 - Self-diffusion of water and ions in clay barriers. *In: Tournassat, C., Steefel, C.I., Bourg, I.C. & Bergaya, F. (eds.): Natural and engineered clay barriers, developments in clay science.* Elsevier, pp. 189-226.
- Boving, T.B. & Grathwohl, P. (2001): Tracer diffusion coefficients in sedimentary rocks: Correlation to porosity and hydraulic conductivity. *Journal of Contaminant Hydrology* 53, 85-100.
- Bowen, R.M. (1982). Compressible porous media models by use of the theory of mixtures. *International Journal of Engineering Science* 20/6, 697-735.
- Bradbury, M.H. & Baeyens, B. (1997): A mechanistic description of Ni and Zn sorption on Namontmorillonite part II: Modelling. *Journal of Contaminant Hydrology* 27, 223-248.
- Bradbury, M.H. & Baeyens, B. (2002): Porewater chemistry in compacted re-saturated MX-80 bentonite: Physico-chemical characterisation and geochemical modelling. Nagra Technical Report NTB 01-08.
- Bradbury, M.H. & Baeyens, B. (2003a): Near-field sorption data bases for compacted MX-80 Bentonite for performance assessment of a high-level radioactive waste repository in Opalinus Clay host rock. Nagra Technical Report NTB 02-18.
- Bradbury, M.H. & Baeyens, B. (2003b): Porewater chemistry in compacted re-saturated MX-80 bentonite. *Journal of Contaminant Hydrology* 61, 329-338.

- Bradbury, M.H. & Baeyens, B. (2011): Predictive sorption modelling of Ni(II), Co(II), Eu(III), Th(IV) and U(VI) on MX-80 bentonite and Opalinus Clay: A "bottom-up" approach. *Applied Clay Science* 52, 27-33.
- Bradbury, M.H., Berner, U., Curti, E., Hummel, W., Kosakowski, G. & Thoenen, T. (2014): The long term geochemical evolution of the nearfield of the HLW repository. Nagra Technical Report NTB 12-01.
- Bradbury, M.H., Marques Fernandes, M. & Baeyens, B. (2017): Estimates of the influence of radionuclide solubility limits and sorption competition on the sorption values in the SDBS of MX-80 bentonite and Opalinus Clay. Nagra Technical Report NTB 17-11.
- Cama, J. & Ganor, J. (2015): Dissolution kinetics of clay minerals. *In*: Tournassat, C., Steefel, C.I., Bourg, I.C. & Bergaya, F. (eds.): Natural and engineered clay barriers, developments in clay science. Elsevier, pp. 101-153.
- Cama, J., Ganor, J., Ayora, C. & Lasaga, C.A. (2000): Smectite dissolution kinetics at 80 degrees C and pH 8.8. *Geochimica et Cosmochimica Acta* 64, 2701-2717.
- Cases, J.M., Berend, I., Besson, G., Francois, M., Uriot, J.P., Thomas, F. & Poirier, J.E. (1992): Mechanism of adsorption and desorption of water-vapor by homoionic montmorillonite .1. The sodium-exchanged form. *Langmuir* 8, 2730-2739.
- Chagneau, A., Tournassat, C., Steefel, C.I., Bourg, I.C., Gaboreau, S., Esteve, I., Kupcik, T., Claret, F. & Schaefer, T. (2015): Complete restriction of $^{36}\text{Cl}^-$ diffusion by celestite precipitation in densely compacted illite. *Environmental Science & Technology Letters* 2, 139-143.
- Chapman, D.L. (1913): A contribution to the theory of electrocapillarity. *The London, Edinburgh, and Dublin Philosophical Magazine and Journal of Science* 25, 475-481.
- Charlet, L. & Manceau, A. (1994): Evidence for the neof ormation of clays upon sorption of Co(II) and Ni(II) on silicates. *Geochimica et Cosmochimica Acta* 58, 2577-2582.
- Charlier, R. (1987): Approche unifiée de quelques problèmes non linéaires de mécanique des milieux continus par la méthode des éléments finis. PhD. Université de Liège.
- Chen, S.Q., Wang, P. & Zhang, D. (2014): Corrosion behavior of copper under biofilm of sulfate-reducing bacteria. *Corrosion Science* 87, 407-415.
- Chen, Y.-G., Zhu, C.-M., Ye, W.-M., Cui, Y.-J. & Wang, Q. (2015): Swelling pressure and hydraulic conductivity of compacted GMZ01 bentonite under salinization–desalinization cycle conditions. *Applied Clay Science* 114, 454-460.
- Chermak, J.A. & Rimstidt, J.D. (1989): Estimating the thermodynamic properties (ΔG_f and ΔH_f) of silicate minerals at 298K from the sum of polyhedral contributions. *American Mineralogist* 74, 1023-1031.
- Chermak, J.A. & Rimstidt, J.D. (1990): Estimating the free-energy of formation of silicate minerals at high-temperatures from the sum of polyhedral contributions. *American Mineralogist* 75, 1376-1380.

- Choi, J.W. & Oscarson, D.W. (1996): Diffusive transport through compacted Na- and Ca-bentonite. *Journal of Contaminant Hydrology* 22, 189-202.
- Christidis, G.E. & Scott, P.W. (1996): Physical and chemical properties of bentonite deposits of Milos island, Greece. *Transactions of the Institution of Mining and Metallurgy Section B-Applied Earth Science* 105, B165-B174.
- Christidis, G.E., Blum, A.E. & Eberl, D.D. (2006): Influence of layer charge and charge distribution of smectites on the flow behaviour and swelling of bentonites. *Applied Clay Science* 34, 125-138.
- Churchman, G.J. & Jackson, M.L. (1976): Reaction of montmorillonite with acid aqueous-solutions – solute activity control by a secondary phase. *Geochimica et Cosmochimica Acta* 40, 1251-1259.
- Cloet, V., Pekala, M., Smith, P., Wersin, P. & Diomidis, N. (2017): An evaluation of sulphide fluxes in the near field of a HLW repository. Nagra Technical Report NTB 17-04.
- Cloet, V., Schwyn, B., Baeyens, B., Curti, E., Diomidis, N., Johnson, L.H., Leupin, O.X., Mibus, J., van Loon, L.R. & Wieland, E. (2014): Einfluss der Salinität des Porenwassers der Wirtgesteine auf die Langzeitsicherheit der Tiefenlager. Nagra Arbeitsbericht NAB 14-09.
- Collin, F. (2003): *Couplages thermo-hydro-mécaniques dans les sols et les roches tendres partiellement saturés*. PhD. Université de Liège.
- Collin, F., Chambon, R. & Charlier, R. (2006). A finite element method for poro mechanical modelling of geotechnical problems using local second gradient models. *International Journal for Numerical Methods in Engineering* 65, No. 11, 1749-1772.
- Collin, F., Cui, Y. J., Schroeder, C. & Charlier, R. (2002). Mechanical behaviour of Lixhe chalk partly saturated by oil and water: experiment and modelling. *International Journal for Numerical and Analytical Methods in Geomechanics* 26/9, 897-924.
- Courdouan, A., Christl, I., Meylan, S., Wersin, P. & Kretzschmar, R. (2007): Isolation and characterization of dissolved organic matter from the callovo-oxfordian formation. *Applied Geochemistry* 22, 1537-1548.
- Couture, R.A. (1985): Steam rapidly reduces the swelling capacity of bentonite. *Nature* 318, 50-52.
- Cuevas, J., Fernandez, R., Ortega, A. & Ruiz, A.L. (2014): Comparison of alternative bentonites for potential use as buffer and sealing materials in the Swiss concept for radioactive waste disposal – part 2: Results. Nagra Arbeitsbericht NAB 14-65.
- Cuevas, J., Ruiz, A.L. & Fernández, R. (2013): Comparison of alternative bentonites for potential use as buffer and sealing materials in the Swiss concept for radioactive waste disposal – part 1: Methodology. Nagra Arbeitsbericht NAB 13-69.
- Curti, E. & Wersin, P. (2002): Assessment of porewater chemistry in the bentonite backfill for the Swiss SF/HLW repository. Nagra Technical Report NTB 02-09.
- Czaikowski, O., Garitte, B., Gaus, I., Gens, A., Kuhlmann, U. & Wiczorek, K. (2012): Design and predictive modelling of the HE-E test. Pebs Project. DELIVERABLE (D-N°: 3.2-1).

- Dauzères, A., Achiedo, G., Nied, D., Bernard, E., Alahrache, S. & Lothenbach, B. (2016): Magnesium perturbation in low-pH concretes placed in clayey environment – solid characterizations and modeling. *Cement and Concrete Research* 79, 137-150.
- De La Villa, R.V., Cuevas, J., Ramírez, S. & Leguey, S. (2001): Zeolite formation during the alkaline reaction of bentonite. *European Journal of Mineralogy* 13, 635-644.
- De Windt, L., Marsal, F., Tinseau, E. & Pellegrini, D. (2008): Reactive transport modeling of geochemical interactions at a concrete/argillite interface, Tournemire site (France). *Physics and Chemistry of the Earth* 33, p. 295-305.
- Delage, P., Marcial, D., Cui, Y.J. & Ruiz, X. (2006): Ageing effects in a compacted bentonite: A microstructure approach. *Geotechnique* 56, 291-304.
- Devineau, K., Bihannic, I., Michot, L., Villiéras, F., Masrouri, F., Cuisinier, O., Fragneto, G. & Michau, N. (2006): In situ neutron diffraction analysis of the influence of geometric confinement on crystalline swelling of montmorillonite. *Applied Clay Science* 31, 76-84.
- Di Donna, A. & Laloui, L. (2015): Numerical analysis of the geotechnical behaviour of energy piles. *International journal for numerical and analytical methods in geomechanics* 39/8, 861-888.
- Didier, M. (2012): Etude du transfert réactif de l'hydrogène au sein de l'argillite intacte. PhD Thesis, Sciences de la Terre. Université de Grenoble.
- Didier, M., Leone, L., Greneche, J.M., Giffaut, E. & Charlet, L. (2012): Adsorption of hydrogen gas and redox processes in clays. *Environmental Science & Technology* 46, 3574-3579.
- Dieudonné, A.C., Qiao, Y.F., Ferrari, A. & Laloui, L. (2017): EBS – task force 2016 activity report. Nagra Arbeitsbericht NAB 17-20.
- Diomidis, N., Cloet, V., Leupin, O., Marschall, P., Poller, A. & Stein, M. (2016): Production, consumption and transport of gases in deep geological repositories according to the Swiss disposal concept. Nagra Technical Report NTB 16-03.
- Dixon, D.A., Chandler, N.A. & Baumgartner, P. (2002): The influence of groundwater salinity and interfaces on the performance of potential backfilling materials. 6th International Workshop on design and Construction of Final Repositories. ONDRAF/NIRAS, Brussels, Belgium.
- Dolder, F. (2015): Experimental characterization and quantification of cement-Bentonite interaction using core infiltration techniques coupled with X-ray tomography. PhD Thesis, Philosophisch-Naturwissenschaftliche Fakultät. Universität Bern.
- Dolder, F., Mäder, U., Jenni, A. & Münch, B. (2016): Alteration of MX-80 bentonite backfill material by high-pH cementitious fluids under lithostatic conditions – an experimental approach using core infiltration techniques. Geological Society, London, Special Publications 443.
- Donnan, F.G. & Guggenheim, E.A. (1932): Exact thermodynamics of membrane equilibrium. *Zeitschrift Für Physikalische Chemie-Abteilung A-Chemische Thermodynamik Kinetik Elektrochemie Eigenschaftslehre* 162, 346-360.

- Dove, P.M., Han, N.Z. & De Yoreo, J.J. (2005): Mechanisms of classical crystal growth theory explain quartz and silicate dissolution behavior. *Proceedings of the National Academy of Sciences of the United States of America* 102, 15357-15362.
- Drits, V.A. & Manceau, A. (2000): A model for the mechanism of Fe³⁺ to Fe²⁺ reduction in dioctahedral smectites. *Clays and Clay Minerals* 48, 185-195.
- Dubacq, B., Vidal, O. & De Andrade, V. (2010): Dehydration of dioctahedral aluminous phyllosilicates: Thermodynamic modelling and implications for thermobarometric estimates. *Contributions to Mineralogy and Petrology* 159, 159-174.
- Dueck, A. (2010): Thermo-mechanical cementation effects in bentonite investigated by unconfined compression tests. SKB Technical Report TR-10-41. Swedish Nuclear Fuel and Waste Management CO, www.skb.se, Stockholm, Sweden.
- Dueck, A., Börgesson, L. & Goudarzi, R. (2017): Homogenisation of bentonite in long steel tubes – laboratory test results and analyses. *In: Nagra (ed.): Book of Abstracts. Clay Conference 24.-27. September 2017, Davos, Switzerland. The 7th international conference on clays in natural and engineered barriers for radioactive waste confinement.*
- Dueck, A., Goudarzi, R. & Börgesson, L. (2016): Buffer homogenisation. Status report 3. SKB Technical Report TR-16-04. Swedish Nuclear Fuel and Waste Management CO, www.skb.se, Stockholm, Sweden.
- Dupray F., Gökök T. & Laloui, L. (2014): Sensitivity analyses of thermohydro-mechanical evolution of the SF/HLW nearfield in the candidate siting regions of Northern Switzerland. *Nagra Arbeitsbericht NAB 14-14.*
- Dupray, F. & Laloui, L. (2016): Numerical analysis of canister movements in an engineered barrier system. *Acta Geotechnica* 11, 145-159.
- Dupray, F., Li, C. & Laloui, L. (2013): Significance of rock thm parameters in geological nuclear waste storage simulation. 47th U.S. Rock Mechanics/Geomechanics Symposium. American Rock Mechanics Association, San Francisco, California.
- Dzombak, D.A. & Morel, F.M.M. (1990): Surface complexation modeling: Hydrous ferric oxide. Wiley – Interscience.
- Eberl, D.D., Velde, B. & McCormick, T. (1993): Synthesis of illite-smectite from smectite at earth surface temperatures and high pH. *Clay Minerals* 28, 49-60.
- Elie, M. & Mazurek, M. (2008): Biomarker transformations as constraints for the depositional environment and for maximum temperatures during burial of Opalinus Clay and Posidonia shale in northern Switzerland. *Applied Geochemistry* 23, 3337-3354.
- Emmerich, K. (2000): Die geotechnische Bedeutung des Dehydroxylierungsverhaltens quellfähiger Tonminerale. PhD thesis, ETH Zurich, Switzerland, 143 pp.
- ENSI (2009): Specific design principles for deep geological repositories and requirements for the safety case. Guideline for Swiss nuclear installations. ENSI-G03/e, Swiss Federal Nuclear Safety Inspectorate (ENSI), Brugg, Switzerland.

- ENSI (2015): Nachforderung zum Indikator "Tiefenlage im Hinblick auf bautechnische Machbarkeit" in Etappe 2 SGT. Aktennotiz 33/476. Swiss Federal Nuclear Safety Inspectorate (ENSI), Brugg, Switzerland.
- Essene, E.J. & Peacor, D.R. (1995): Clay mineral thermometry – a critical perspective. *Clays and Clay Minerals* 43, 540-553.
- Evans, D.F. & Wennerström, H. (1999): *The colloidal domain: Where physics, chemistry, biology, and technology meet*. 2nd ed. Wiley, New York.
- Fernandez, A.M., Sánchez-Ledesma, D.M., Melón, A., Labajo, M.A., Clavero, M.A., Carretero, S., Gutierrez-Nebot, L., González, A.E. & Mayor, J.C. (2015): Geochemical outcome of the dismantling of the EB experiment at Mont Terri (Switzerland). Unpubl. Mont Terri Technical Note. Mont Terri Project, Switzerland.
- Fernández, R., Cuevas, J., Sanchez, L., de la Villa, R.V. & Leguey, S. (2006): Reactivity of the cement-bentonite interface with alkaline solutions using transport cells. *Applied Geochemistry* 21, 977-992.
- Fernández, R., Cuevas, J. & Mäder, U.K. (2009a): Modelling concrete interaction with a bentonite barrier. *European Journal of Mineralogy* 21, 177-191.
- Fernández, R., Mäder, U., Rodríguez, M., Virgil de la Villa, R. & Cuevas, J. (2009b): Alteration of compacted bentonite by diffusion of highly alkaline solutions. *European Journal of Mineralogy* 21, 725-735.
- Fernández, R., Cuevas, J. & Mäder, U.K. (2010a): Modeling experimental results of diffusion of alkaline solutions through a compacted bentonite barrier. *Cement and Concrete Research* 40, 1255-1264.
- Fernández, R., Rodríguez, M., Villa, R.V.d.l. & Cuevas, J. (2010b): Geochemical constraints on the stability of zeolites and C–S–H in the high pH reaction of bentonite. *Geochimica et Cosmochimica Acta* 74, 890-906.
- Fernández, R., Mäder, U. & Jenni, A. (2011): Multi-component advective-diffusive transport experiment in MX-80 compacted bentonite: Method and results of 1st phase of experiment. *Nagra Arbeitsbericht NAB 11-02*.
- Fernández, R., Vigil de la Villa, R., Ruiz, A.I., García, R. & Cuevas, J. (2013): Precipitation of chlorite-like structures during OPC porewater diffusion through compacted bentonite at 90 °C. *Applied Clay Science* 83-84, 357-367.
- Fernández, R., Ruiz, A.I. & Cuevas, J. (2014a): The role of smectite composition on the hyperalkaline alteration of bentonite. *Applied Clay Science* 95, 83-94.
- Fernández, R., Mäder, U. & Jenni, A. (2014b): Modelling a bentonite column experiment with CrunchFlow and comparison of results with PhreeqC, including diffuse double layer features. *Nagra Arbeitsbericht NAB 15-02*.
- Fialips, C.I., Majzlan, J., Beaufort, D. & Navrotsky, A. (2003): New thermochemical evidence on the stability of dickite vs. Kaolinite. *American Mineralogist* 88, 837-845.

- Flury, M. & Gimmi, T. (2002): Solute diffusion. *In*: Dane, J.H. & Topp, G.C. (eds.): *Methods of Soil Analysis, Part 4: Physical Methods*. Soil Science Society of America, Inc., Madison, Wisconsin, USA.
- Francois, B. & Laloui, L. (2008): ACMEC-TS: A constitutive model for unsaturated soils under non-isothermal conditions. *International Journal for Numerical and Analytical Methods in Geomechanics* 32, 1955-1988.
- Gailhanou, H., Blanc, P., Rogez, J., Mikaelian, G., Horiuchi, K., Yamamura, Y., Saito, K., Kawaji, H., Warmont, F., Greneche, J.M., Vieillard, P., Fialips, C.I., Giffaut, E. & Gaucher, E.C. (2013): Thermodynamic properties of saponite, nontronite, and vermiculite derived from calorimetric measurements. *American Mineralogist* 98, 1834-1847.
- Gailhanou, H., Blanc, P., Rogez, J., Mikaelian, G., Kawaji, H., Olives, J., Amouric, M., Denoyel, R., Bourrelly, S., Montouillout, V., Vieillard, P., Fialips, C.I., Michau, N. & Gaucher, E.C. (2012): Thermodynamic properties of illite, smectite and beidellite by calorimetric methods: Enthalpies of formation, heat capacities, entropies and Gibbs free energies of formation. *Geochimica et Cosmochimica Acta* 89, 279-301.
- Gailhanou, H., Rogez, J., van Miltenburg, J.C., van Genderen, A.C.G., Greneche, J.M., Gilles, C., Jalabert, D., Michau, N., Gaucher, E.C. & Blanc, P. (2009): Thermodynamic properties of chlorite cca-2. Heat capacities, heat contents and entropies. *Geochimica et Cosmochimica Acta* 73, 4738-4749.
- Gailhanou, H., van Miltenburg, J.C., Rogez, J., Olives, J., Amouric, M., Gaucher, E.C. & Blanc, P. (2007): Thermodynamic properties of anhydrous smectite MX-80, illite imt-2 and mixed-layer illite-smectite iscz-1 as determined by calorimetric methods. Part I: Heat capacities, heat contents and entropies. *Geochimica et Cosmochimica Acta* 71, 5463-5473.
- Gailhanou, H., Vieillard, P., Blanc, P., Lassin, A., Denoyel, R., Bloch, E., De Weireld, G., Gaboreau, S., Fialips, C.I., Made, B. & Giffaut, E. (2017): Methodology for determining the thermodynamic properties of smectite hydration. *Applied Geochemistry* 82, 146-163.
- Gallé, C. (2000): Gas breakthrough pressure in compacted Fo-Ca clay and interfacial gas overpressure in waste disposal context. *Applied Clay Science* 17, 85-97.
- Ganor, J., Reznik, I.J. & Rosenberg, Y.O. (2009): Organics in water-rock interactions. *In*: Oelkers, E.H. & Schott, J. (eds.): *Thermodynamics and kinetics of water-rock interaction. Reviews in mineralogy & geochemistry*, pp. 259-369.
- Gates, W.P. (2005): Infrared spectroscopy and the chemistry of dioctahedral smectites. *In*: Klopogge, J.T. (ed.): *Application of vibrational spectroscopy to clay minerals and layered double hydroxides*, pp. 125-168.
- Gaucher, E.C., Claude, L., Pitsch, H. & Ly, J. (1998): Influence of temperature on the sorption isotherm of potassium on a montmorillonite. *In*: Arehart, G.B. & Hulston, J.R. (eds.): *Water-rock interaction: Proceedings of the 9th International Symposium on Water-Rock Interaction, WRI-9, Taupo, New Zealand, 30 March 1998 – 3 April 1998. Water-rock interaction 9*, 931-934. Balkema, 9054109424.
- Gaucher, E.C., Blanc, P., Matray, J.-M. & Michau, N. (2004): Modeling diffusion of an alkaline plume in a clay barrier. *Applied Geochemistry* 19, 1505-1515.

- Gaucher, E.C., Tournassat, C., Pearson, F.J., Blanc, P., Crouzet, C., Lerouge, C. & Altmann, S. (2009): A robust model for pore-water chemistry of clayrock. *Geochimica et Cosmochimica Acta* 73, 6470-6487.
- Gaus, I., Garitte, B., Senger, R., Gens, A., Vasconcelos, R., García-Siñeriz, J.-L., Trick, T., Wieczorek, K., Czaikowski, O., Schuster, K., Mayor, J.C., Velasco, M., Kuhlmann, U. & Villar, M.V. (2014): The HE-E Experiment: Lay-out, interpretation and THM modelling. *Nagra Arbeitsbericht NAB* 14-53.
- Gerard, P., Charlier, R., Chambon, R. & Collin, F. (2008). Influence of evaporation on the convergence of a ventilated cavity. *Water Resources Research* 44, W00C02.
- Giffaut, E., Grivé, M., Blanc, P., Vieillard, P., Colàs, E., Gailhanou, H., Gaboreau, S., Marty, N., Madé, B. & Duro, L. (2014): Andra thermodynamic database for performance assessment: Thermochimie. *Applied Geochemistry* 49, 225-236.
- Giggenbach, W.F. (1981): Geothermal mineral equilibria. *Geochimica et Cosmochimica Acta* 45, 393-410.
- Gimmi, T. & Alt-Epping, P. (2018): Simulating Donnan equilibria based on the Nernst-Planck equation. *Geochimica et Cosmochimica Acta* 232, 1-13.
- Gimmi, T. & Kosakowski, G. (2011): How mobile are sorbed cations in clays and clay rocks? *Environmental Science and Technology* 45, 1443-1449.
- Glaus, M.A., Frick, S., Rosse, R. & Van Loon, L.R. (2010): Comparative study of tracer diffusion of HTO, Na-22(+) and Cl-36(-) in compacted kaolinite, illite and montmorillonite. *Geochimica et Cosmochimica Acta* 74, 1999-2010.
- Glaus, M.A., Frick, S., Rosse, R. & Van Loon, L.R. (2011): Consistent interpretation of the results of through-, out-diffusion and tracer profile analysis for trace anion diffusion in compacted montmorillonite. *Journal of Contaminant Hydrology* 123, 1-10.
- Glaus, M.A., Birgersson, M., Karnland, O. & Van Loon, L.R. (2013): Seeming steady-state uphill diffusion of Na-22(+) in compacted montmorillonite. *Environmental Science & Technology* 47, 11522-11527.
- Golubev, S.V., Bauer, A. & Pokrovsky, O.S. (2006): Effect of pH and organic ligands on the kinetics of smectite dissolution at 25 degrees C. *Geochimica et Cosmochimica Acta* 70, 4436-4451.
- Gorski, C.A., Aeschbacher, M., Soltermann, D., Voegelin, A., Baeyens, B., Marques Fernandes, M., Hofstetter, T.B. & Sander, M. (2012a): Redox properties of structural Fe in clay minerals. 1. Electrochemical quantification of electron-donating and -accepting capacities of smectites. *Environmental Science & Technology* 46, 9360-9368.
- Gorski, C.A., Klupfel, L., Voegelin, A., Sander, M. & Hofstetter, T.B. (2012b): Redox properties of structural Fe in clay minerals. 2. Electrochemical and spectroscopic characterization of electron transfer irreversibility in ferruginous smectite, swa-1. *Environmental Science & Technology* 46, 9369-9377.

- Gorski, C.A., Klupfel, L.E., Voegelin, A., Sander, M. & Hofstetter, T.B. (2013): Redox properties of structural Fe in clay minerals: 3. Relationships between smectite redox and structural properties. *Environmental Science & Technology* 47, 13477-13485.
- Gouy, M. (1910): Sur la constitution de la charge électrique à la surface d'un électrolyte. *J. Phys. Theor. Appl.* 9, 457-468.
- Graham, J., Halayko, K.G., Hume, H., Kirkham, T., Gray, M. & Oscarson, D. (2002): A capillary-advective model for gas break-through in clays. *Engineering Geology* 64, 273-286.
- Grass, G., Rensing, C. & Solioz, M. (2011): Metallic copper as an antimicrobial surface. *Applied and Environmental Microbiology* 77, 1541-1547.
- Grauer, R. (1990): The chemical behaviour of montmorillonite in a repository backfill: Selected aspects. Nagra Technical Report NTB 88-24E.
- Greene-Kelly, R. (1953): Irreversible dehydration in montmorillonite. Part II. *Clay Minerals Bulletin* 2, 52-65.
- Greene-Kelly, R. (1955): Dehydration of montmorillonite minerals. *Mineralogical Magazine* 30, 604-615.
- Grim, R.E. & Kulbicki, G. (1961): Montmorillonite: High temperature reactions and classification. *American Mineralogist* 46, 1329-1369.
- Grim, R.E. (1968): *Clay mineralogy*. 2nd ed. McGraw-Hill, New York.
- Grybos, M., Michot, L.J., Skiba, M., Billard, P. & Mustin, C. (2010): Dissolution of anisotropic colloidal mineral particles: Evidence for basal surface reactivity of nontronite. *Journal of Colloid and Interface Science* 343, 433-438.
- Güven, N. (1988): Smectites. *Reviews in Mineralogy* 19, 497-559.
- Güven, N. (1990): Longevity of bentonite as buffer material in a nuclear-waste repository. *Engineering Geology* 28, 233-247.
- Hadi, J., Tournassat, C., Ignatiadis, I., Greneche, J.M. & Charlet, L. (2013): Modelling CEC variations versus structural iron reduction levels in dioctahedral smectites. Existing approaches, new data and model refinements. *Journal of Colloid and Interface Science* 407, 397-409.
- Hadi, J., Wersin, P., Jenni, A. & Grenèche, J.M. (2017a): Redox evolution and Fe-bentonite interaction in the ABM2 experiment, Äspö hard rock laboratory. Nagra Technical Report NTB 17-03.
- Hadi, J., Wersin, P., Serneels, V. & Greneche, J.M. (2017b): Eighteen years of Fe-bentonite interaction in the Febex "in situ" experiment at the grimsel test site in Switzerland. *Clays & Clay Minerals* 67, 111-131.
- He, H.P., Guo, J.G., Xie, X.D. & Peng, J.L. (2001): Location and migration of cations in Cu²⁺-adsorbed montmorillonite. *Environment International* 26, 247-352.

- Hedström, M. & Karnland, O. (2011): Ca/Na selectivity coefficients from the Poisson-Boltzmann theory. *Physics and Chemistry of the Earth* 36, 1559-1563.
- Hedström, M. & Karnland, O. (2012): Donnan equilibrium in Na-montmorillonite from a molecular dynamics perspective. *Geochimica et Cosmochimica Acta* 77, 266-274.
- Heller-Kallai, L. & Mosser, C. (1995): Migration of Cu ions in Cu montmorillonites heated with and without alkali halides. *Clays and Clay Minerals* 43, 738-743.
- Heller-Kallai, L. (1997): Reduction and reoxidation of nontronite: The data reassessed (vol 45, pg 479, 1997). *Clays and Clay Minerals* 45, 903-903.
- Hoch, A.R., Cliffe, K.A., Swift, B.T. & Rodwell, W.R. (2004): Modelling gas migration in compacted bentonite: Gambit club phase 3 final report. Posiva 2004-02. Posiva, Eurajoki, Finland.
- Hoffmann, C., Alonso, E.E. & Romero, E. (2007): Hydro-mechanical behaviour of bentonite pellet mixtures. *Physics and Chemistry of the Earth* 32, 832-849.
- Hofstetter, T.B., Sosedova, Y., Gorski, C., Voegelin, A. & Sander, M. (2014): Redox properties of iron-bearing clays and MX-80 bentonite – electrochemical and spectroscopic characterization. Nagra Technical Report NTB 13-03.
- Holmboe, M., Wold, S. & Jonsson, M. (2012): Porosity investigation of compacted bentonite using XRD profile modeling. *Journal of Contaminant Hydrology* 128, 19-32.
- Horseman, S.T., Harrington, J.F. & Sellin, P. (1997): Gas migration in MX80 buffer bentonite. *In: Gray, W.J. & Triay, I.R. (eds.): Scientific Basis for Nuclear Waste Management XX, Materials Research Society Conference Proceedings, pp. 1003-1010.*
- Hsiao, Y.W. & Hedström, M. (2015): Molecular dynamics simulations of NaCl permeation in bihydrated montmorillonite inter layer nanopores. *Journal of Physical Chemistry C* 119, 17352-17361.
- Hsiao, Y.-W. & Hedström, M. (2017): Swelling pressure in systems with Na-montmorillonite and neutral surfaces: A molecular dynamics study. *The Journal of Physical Chemistry C* 121, 26414-26423.
- HSK (1986): Gutachten zum Projekt Gewähr 1985 der Nationalen Genossenschaft für die Lagerung radioaktiver Abfälle (Nagra). HSK 23/28. Hauptabteilung für die Sicherheit der Kernanlagen (HSK), Villigen, Schweiz.
- HSK (1996): Gutachten zum Gesuch um Rahmenbewilligung für ein SMA-Endlager am Wellenberg. HSK 30/9, KSA 30/11, Hauptabteilung für die Sicherheit der Kernanlagen (HSK), Villigen, Schweiz.
- HSK (2004): Stellungnahme zur Sicherheitsanalyse Kristallin-I der Nagra. HSK 23/73. Hauptabteilung für die Sicherheit der Kernanlagen (HSK), Villigen, Schweiz.
- HSK (2005): Gutachten zum Entsorgungsnachweis der Nagra für abgebrannte Brennelemente, verglaste hochaktive sowie langlebige mittelaktive Abfälle (Projekt Opalinuston). HSK 35/99. Hauptabteilung für die Sicherheit der Kernanlagen (HSK), Villigen, Schweiz.

- Huang, W.H. & Keller, W.D. (1973): Gibbs free-energies of formation calculated from dissolution data using specific mineral analyses. 3. Clay-minerals. *American Mineralogist* 58, 1023-1028.
- Huang, W.L., Longo, J.M. & Pevear, D.R. (1993): An experimentally derived kinetic-model for smectite-to-illite conversion and its use as a geothermometer. *Clays and Clay Minerals* 41, 162-177.
- Huertas, F., Farinia, P., Farias, J., Garcia-Sineires, J.L., Villar, M.V., Fernandez, A.M., Martin, P.L., Elorza, F.J., Gens, A., Sanchez, M., Lloret, A., Samper, J. & Martinez, M.A. (2006): Full-scale engineered barriers experiment. Updated final report 1994-2004. ENRESA Technical Publication 05-0/2006, Madrid 590 pp., ISSN 1134-380X.
- Huertas, F., Villar, M.V., García-Siñeriz, J.L., Sellin, P., Stührenberg, D. & Alheid, H.-J. (2008): Final synthesis report RTD component 3: Thermo-hydro-mechanical (geochemical) processes in the engineered barrier system. Deliverable: D 3.6.2, NF-PRO Contract Number: FI6W-CT-2003-02389, European Commission.
- Hujeux, J.C. (1979): Calcul numérique de problèmes de consolidation élastoplastique. Ph.D. Thesis, Ecole Centrale de Paris,
- Idiart, A. & Pekala, M. (2016): Models for diffusion in compacted Bentonite. SKB Technical Report TR-15-06. Swedish Nuclear Fuel and Waste Management CO, www.skb.se, Stockholm, Sweden.
- Ishii, T., Yahagi, R., Owada, H., Kobayashi, I., Takazawa, M., Yamaguchi, K., Takayama, Y., Tsurumi, S. & Iizuka, A. (2013): Coupled chemical-hydraulic-mechanical modelling of long-term alteration of bentonite. *Clay Minerals* 48, 331-341.
- Jenni, A. & Mäder, U. (2014): CI (cement clay interaction) experiment: Set-up and first results for modelling of concrete/Opalinus Clay interfaces. Unpubl. Mont Terri Technical Note. Mont Terri Project, Switzerland.
- Jenni, A. & Mäder, U. (2017): Coupling of chemical and mechanical properties in bentonite. *In*: Nagra (ed.): Book of Abstracts. Clay Conference 24.-27. September 2017, Davos, Switzerland. The 7th international conference on clays in natural and engineered barriers for radioactive waste confinement.
- Jenni, A. & Mäder, U. (2018): Coupling of chemical and hydromechanical properties in bentonite. *Applied Geochemistry* 97, 147-156.
- Jenni, A., Mäder, U. & Fernández, R. (2014a): Multi-component advective-diffusive transport experiment in MX-80 compacted bentonite: Method and results of 2nd phase of experiment and post mortem analysis. Nagra Arbeitsbericht NAB 14-22.
- Jenni, A., Mäder, U., Lerouge, C., Gaboreau, S. & Schwyn, B. (2014b): In situ interaction between different concretes and Opalinus Clay. *Physics and Chemistry of the Earth, Parts A/B/C* 70-71, 71-83.
- Jenni, A., Gimmi, T., Alt-Epping, P., Mäder, U. & Cloet, V. (2017): Interaction of ordinary Portland cement and Opalinus Clay: Dual porosity modelling compared to experimental data. *Physics and Chemistry of the Earth, Parts A/B/C* 99, 22-37.

- Johnson, L., Gaus, I., Wieczorek, K., Mayor, J.C., Sellin, P., Villar, M.V., Samper, J., Cuevas, J., Gens, A., Velasco, M., Turrero, M.J., Montenegro, L., Martín, P.L. & Armand, G. (2014): Integration of the short-term evolution of the engineered barrier system (EBS) with the long-term safety perspective (deliverable d4.1 of the PEBS project). Nagra Arbeitsbericht NAB 14-79.
- Johnston, R.M. & Miller, H.G. (1984): The effect of pH on the stability of smectite. AECL-8366, Atomic Energy of Canada limited, Pinawa, Manitoba, Canada.
- Karakassides, M.A., Madejova, J., Arvaiova, B., Bourlinos, A., Petridis, D. & Komadel, P. (1999): Location of Li(I), Cu(II) and Cd(II) in heated montmorillonite: Evidence from specular reflectance infrared and electron spin resonance spectroscopies. *Journal of Material Chemistry* 9, 1553-1558.
- Karmous, M.S., Ben, R., H., Naamen, S., Oueslati, W., Ben, H. & Amara, A. (2006): The interlayer structure and thermal behavior of Cu and Ni montmorillonites. *Zeitschrift für Kristallographie, Supplement* 23, 431-436.
- Karland, O. & Birgersson, M. (2006): Montmorillonite stability with special respect to KBS-3 conditions. SKB Technical Report TR-06-11. Swedish Nuclear Fuel and Waste Management CO, www.skb.se, Stockholm, Sweden.
- Karland, O. (1997): Bentonite swelling pressure in strong NaCl solutions. Correlation between model calculations and experimentally determined data. SKB Technical Report TR-97-31. Swedish Nuclear Fuel and Waste Management CO, www.skb.se, Stockholm, Sweden.
- Karland, O. (2010): Chemical and mineralogical characterization of the bentonite buffer for the acceptance control procedure in a KBS-3 repository. SKB Technical Report TR-10-60. Swedish Nuclear Fuel and Waste Management CO, www.skb.se, Stockholm, Sweden.
- Karland, O., Muurinen, A. & Karlsson, F. (2003): Bentonite swelling pressure in NaCl solutions – experimentally determined data and model calculations. *In: Alonso, E.E. & Ledesma, A. (eds.): International Symposium on Large Scale Field Tests in Granite.* Taylor & Francis Group, Barcelona.
- Karland, O., Olsson, S. & Nielsson, U. (2006): Mineralogy and sealing properties of various bentonites and smectite-rich clay materials. SKB Technical Report TR-06-30. Swedish Nuclear Fuel and Waste Management CO, www.skb.se, Stockholm, Sweden.
- Karland, O., Olsson, S., Dueck, A., Birgersson, M., Nilsson, U., Hernan-Håkansson, T., Pedersen, K., Nilsson, S., Eriksen, T. & Rosborg, B. (2009): Long term test of buffer material at the Äspö hard rock laboratory, LOT project. Final report on the A2 test parcel. SKB Technical Report TR-09-29. Swedish Nuclear Fuel and Waste Management CO, www.skb.se, Stockholm, Sweden.
- Karland, O., Olsson, S., Nilsson, U. & Sellin, P. (2007): Experimentally determined swelling pressures and geochemical interactions of compacted Wyoming bentonite with highly alkaline solutions. *Physics and Chemistry of the Earth* 32, 275-286.
- Kaufhold, S., Baille, W., Schanz, T. & Dohrmann, R. (2015a): About differences of swelling pressure – dry density relations of compacted bentonites. *Applied Clay Science* 107, 52-61.

- Kaufhold, S., Dohrmann, R., Klinkenberg, M. & Noell, U. (2015b): Electrical conductivity of bentonites. *Applied Clay Science* 114, 375-385.
- Kaufhold, S., Dohrmann, R., Sanden, T., Sellin, P. & Svensson, D. (2013): Mineralogical investigations of the first package of the alternative buffer material test – I. Alteration of bentonites. *Clay Minerals* 48, 199-213.
- KEG (2003): Kernenergiegesetz (KEG) vom 21. März 2003 [nuclear energy act], Stand am 1. Juli 2016. Switzerland.
- Keller, L.M., Holzer, L., Gasser, P., Erni, R. & Rossell, M.D. (2015): Intergranular pore space evolution in MX80 bentonite during a long-term experiment. *Applied Clay Science* 104, 150-159.
- Keller, L.M., Seiphoori, A., Gasser, P., Lucas, F., Holzer, L. & Ferrari, A. (2014): The pore structure of compacted and partly saturated MX-80 bentonite at different dry densities. *Clays and Clay Minerals* 62, 174-187.
- Kennedy, K. & Plötze, M. (2004): Engineered barrier emplacement experiment in Opalinus Clay (EB). Granular material backfill emplacement methods evaluation. EC contract FIKW-CT-2000-00017. Project Deliverable D4, European Commission.
- KEV (2004): Kernenergieverordnung vom 10. Dezember 2004 (KEV) [nuclear energy ordinance], Stand am 1. Juli 2016. Switzerland.
- King, F. & Wersin, P. (2014): Review of supercontainer copper shell-bentonite interactions and possible effects on buffer performance for the KBS-3H design. Posiva Working Report WR 2013-03.
- King, F. (2009): Microbiologically influenced corrosion of nuclear waste containers. *Corrosion* 65, 233-251.
- Kittrick, J.A. & Peryea, F.J. (1988): Experimental validation of the monophase structure model for montmorillonite solubility. *Soil Science Society of America Journal* 52, 1199-1201.
- Kittrick, J.A. & Peryea, F.J. (1989): The monophase model for magnesium-saturated montmorillonite. *Soil Science Society of America Journal* 53, 292-295.
- Kittrick, J.A. (1970): Precipitation of kaolinite at 25 degrees C and 1 atm. *Clays and Clay Minerals* 18, 261-267.
- Kittrick, J.A. (1971a): Stability of montmorillonites .1. Belle fourche and clay spur montmorillonite. *Soil Science Society of America Proceedings* 35, 140-145.
- Kittrick, J.A. (1971b): Stability of montmorillonites .2. Aberdeen montmorillonite. *Soil Science Society of America Proceedings* 35, 820-823.
- Kittrick, J.A. (1979): Ion exchange and mineral stability: Are the reactions linked or separate? *ACS Symposium Series* 93. *Chemical Modeling in Aqueous Systems* Chapter 20, pp 401-412.
- Kittrick, J.A. (1984): Solubility measurements of phases in 3 illites. *Clays and Clay Minerals* 32, 115-124.

- Kober, F., Vomvoris, S. & Finsterle, S. (2018): HotBENTt – preliminary design study – overview of results. Nagra Arbeitsbericht NAB 17-29.
- Kosakowski, G. & Berner, U. (2013): The evolution of clay rock/cement interfaces in a cementitious repository for low- and intermediate level radioactive waste. *Physics and Chemistry of the Earth* 64, 65-86.
- Kosakowski, G. & Smith, P.A. (2014): Long-term evolution of the engineered gas transport system. Nagra Arbeitsbericht NAB 14-16.
- Kosakowski, G., Berner, U., Wieland, E., Glaus, M. & Degueldre, C. (2014): Geochemical evolution of the L/ILW near-field. Nagra Technical Report NTB 14-11.
- Kostka, J.E., Stucki, J.W., Neelson, K.H. & Wu, J. (1996): Reduction of structural Fe(III) in smectite by a pure culture of *shewanella putrefaciens* strain MR-1. *Clays and Clay Minerals* 44, 522-529.
- Kostka, J.E., Wu, J., Neelson, K.H. & Stucki, J.W. (1999): The impact of structural Fe(III) reduction by bacteria on the surface chemistry of smectite clay minerals. *Geochimica et Cosmochimica Acta* 63, 3705-3713.
- Kozaki, T., Fujishima, A., Sato, S. & Ohashi, H. (1998): Self-diffusion of sodium ions in compacted sodium montmorillonite. *Nuclear Technology* 121, 63-69.
- Kozaki, T., Liu, J. & Sato, S. (2008): Diffusion mechanism of sodium ions in compacted montmorillonite under different NaCl concentration. *Physics and Chemistry of the Earth* 33, 957-961.
- Kozaki, T., Sawaguchi, T., Fujishima, A. & Sato, S. (2010): Effect of exchangeable cations on apparent diffusion of Ca(2+) ions in Na- and Ca-montmorillonite mixtures. *Physics and Chemistry of the Earth* 35, 254-258.
- Kuhlmann, U., Senger, R. & Gaus, I. (2015): Inverse modelling of the HE-E experiment using iTOUGH2. Nagra Arbeitsbericht NAB 15-53.
- Kumpulainen, S. & Kiviranta, L. (2010): Mineralogical and chemical characterization of various Bentonite and smectite-rich clay materials part a: Comparison and development of mineralogical characterization methods part b: Mineralogical and chemical characterization of clay materials. WR 2010-52, B+Tech Oy, Eurajoki, Finland.
- Kumpulainen, S. & Kiviranta, L. (2011): Mineralogical, chemical and physical study of potential buffer and backfill materials from ABM test package 1. WR 2011-41, B+Tech Oy, Eurajoki, Finland.
- Kumpulainen, S., Carlsson, T., Muurinen, A., Kiviranta, L., Svensson, D., Sasamoto, H., Yui, M., Wersin, P. & Rosch, D. (2010): Long-term alteration of bentonite in the presence of metallic iron. Posiva Working Report 2010-71 and SKB Report R-10-52.
- Kuwahara, Y. (2006): In-situ AFM study of smectite dissolution under alkaline conditions at room temperature. *American Mineralogist* 91, 1142-1149.
- Laine, H. & Karttunen, P. (2010): Long-term stability of bentonite. A literature review. WR 2010-53, Posiva, Helsinki, Finland, p. 127.

- Laird, D.A. (2006): Influence of layer charge on swelling of smectites. *Applied Clay Science* 34, 74-87.
- Lasaga, A.C. & Luttge, A. (2001): Variation of crystal dissolution rate based on a dissolution stepwave model. *Science* 291, 2400-2404.
- Latta, D.E., Neumann, A., Premaratne, W. & Scherer, M.M. (2017): Fe(II)-Fe(III) electron transfer in a clay mineral with low Fe content. *Acs Earth and Space Chemistry* 1, 197-208.
- Lee, S.S., Fenter, P., Park, C., Sturchio, N.C. & Nagy, K.L. (2010): Hydrated cation speciation at the muscovite (001)-water interface. *Langmuir* 26, 16647-16651.
- Lemire, R., Berner, U., Musikas, C., Palmer, D., Taylor, P. & Tochiyama, O. (2013): Chemical thermodynamics of iron, part 1. *Chemical Thermodynamics* 13, 1082.
- Leupin, O., Birgersson, M., Karnland, O., Korkeakoski, P., Sellin, P., Mäder, U. & Wersin, P. (2015): Montmorillonite stability under near-field conditions. Nagra Technical Report NTB 14-12.
- Leupin, O., Smith, P., Savage, D., Johnson, L., Marschall, P., Schneider, J. & Senger, R. (2016a): High-level waste repository-induced effects. Nagra Technical Report NTB 14-13.
- Leupin, O., Smith, P., Savage, D., Johnson, L., Marschall, P., Schneider, J. & Senger, R. (2016b): Low- and intermediate-level waste repository-induced effects. Nagra Technical Report NTB 14-14.
- Leupin, O.X. & Johnson, L.H. (2013): Buffer requirements for a SF/HLW repository in Opalinus Clay. Nagra Arbeitsbericht NAB 13-46.
- Leupin, O.X., Bernier-Latmani, R., Bagnoud, A., Moors, H., Leys, N., Wouters, K. & Stroes-Gascoyne, S. (2017): Fifteen years of microbiological investigation in Opalinus Clay at the Mont Terri Rock Laboratory (Switzerland). *Swiss J Geosci.* 110, 343-354.
- Li, Y.L., Vali, H., Sears, S.K., Yang, J., Deng, B.L. & Zhang, C.L. (2004): Iron reduction and alteration of nontronite nau-2 by a sulfate-reducing bacterium. *Geochimica et Cosmochimica Acta* 68, 3251-3260.
- Libert, M., Bildstein, O., Esnault, L., Jullien, M. & Sellier, R. (2011): Molecular hydrogen: An abundant energy source for bacterial activity in nuclear waste repositories. *Physics and Chemistry of the Earth* 36, 1616-1623.
- Lippmann, F. (1977): The solubility products of complex minerals, mixed crystals, and three-layer clay minerals. *N. Jb. Miner. Abh* 130, 243-263.
- Lippmann, F. (1980): Phase diagrams depicting the aqueous solubility of mineral systems. *Neues Jahrbuch Mineralogische Abhandlungen* 139, 1-25.
- Lippmann, F. (1982): The thermodynamic status of clay minerals. *In: van Olphen, H. & Veniale, F. (eds.): Developments in sedimentology.* Elsevier, Amsterdam, pp. 475-485.
- Liu, D., Dong, H., Bishop, M.E., Zhang, J., Wang, H., Xie, S., Wang, S., Huang, L. & Eberl, D.D. (2012): Microbial reduction of structural iron in interstratified illite-smectite minerals by a sulfate-reducing bacterium. *Geobiology* 10, 150-162.

- Liu, H.-H. (2014): Non-darcian flow in low-permeability media: Key issues related to geological disposal of high-level nuclear waste in shale formations. *Hydrogeology Journal* 22, 1525-1534.
- Lothenbach, B., Nied, D., L'Hôpital, E., Achiedo, G. & Dauzères, A. (2015): Magnesium and calcium silicate hydrates. *Cement and Concrete Research* 77, 60-68.
- Loucks, R.R. (1991): The bound interlayer H₂O content of potassic white micas - muscovite-hydromuscovite-hydropyrophyllite solutions. *American Mineralogist* 76, 1563-1579.
- Low, P.F. (1980): The swelling of clay. 2. Montmorillonites. *Soil Science Society of America Journal* 44, 667-676.
- Madaschi, A. & Laloui, L. (2018): EBS – task force: Task 7/gas transport in Bentonite status report 2017. *Nagra Arbeitsbericht NAB 18-03*.
- Madejova, J., Aravaiova, B. & Komadel, P. (1999): FTIR spectroscopic characterization of thermally treated Cu²⁺, Cd²⁺ and Li⁺ montmorillonites. *Spectrochimica Acta Part A* 55, 2467-2476.
- Madejova, J., Palkova, H. & Komadel, P. (2006): Behaviour of Li⁺ and Cu²⁺ heated montmorillonite: Evidence from far-, mid-, and near-IR regions. *Vibrational Spectroscopy* 40, 80-88.
- Mäder, U., Eul, A., Jenni, A., Frieg, B. & Dolder, F. (2014): CI experiment: Sampling by stabilized overcoring for the 2nd campaign (2012). Unpubl. Mont Terri Technical Note. Mont Terri Project, Switzerland.
- Madsen, F.T. & Müller-Vonmoos, M. (1989): The swelling behaviour of clays. *Applied Clay Science* 4, 143-156.
- Madsen, F.T. (1998): Clay mineralogical investigations related to nuclear waste disposal. *Clay Minerals* 33, 109-129.
- Maes, A., Peigneur, P. & Cremers, A. (1976): Thermodynamics of transition metal ion exchange in montmorillonite. *Proc. Int. Clay Conf.*, 319-333.
- Malfoy, C., Fontaine, C., Pantet, A. & Monnet, P. (2007): The effect of mineralogical and cationic heterogeneities on rheological properties of suspensions with Li-smectites, extracted from Volclay MX-80. *Comptes Rendus Geosciences* 339, 960-969.
- Manca, D. (2015): Hydro-chemo-mechanical characterisation of sand/bentonite mixtures - with a focus on the water and gas transport properties. PhD Thesis, Laboratoire de Mécanique des Sols. École polytechnique fédérale de Lausanne.
- Manca, D., Ferrari, A. & Laloui, L. (2016): Fabric evolution and the related swelling behaviour of a sand/bentonite mixture upon hydro-chemo-mechanical loadings. *Geotechnique* 66, 41-57.
- Marshall, M.H.M., McKelvie, J.R., Simpson, A.J. & Simpson, M.J. (2015): Characterization of natural organic matter in bentonite clays for potential use in deep geological repositories for used nuclear fuel. *Applied Geochemistry* 54, 43-53.

- Martikainen, J., Pintado, X. & Mamunul, H.M. (in review): Laboratory tests to evaluate buffer homogenization. Posiva, Olkiluoto, Finland.
- Marty, N.C.M., Cama, J., Sato, T., Chino, D., Villi ras, F., Razafitianamaharavo, A., Brendl , J., Giffaut, E., Soler, J.M., Gaucher, E.C. & Tournassat, C. (2011): Dissolution kinetics of synthetic Na-smectite. An integrated experimental approach. *Geochimica et Cosmochimica Acta* 75, 5849-5864.
- Marty, N.C.M., Claret, F., Lassin, A., Tremosa, J., Blanc, P., Mad , B., Giffaut, E., Cochepin, B. & Tournassat, C. (2015a): A database of dissolution and precipitation rates for clay-rocks minerals. *Applied Geochemistry* 55, 108-118.
- Marty, N.C.M., Fritz, B., Cl ment, A. & Michau, N. (2010): Modelling the long term alteration of the engineered bentonite barrier in an underground radioactive waste repository. *Applied Clay Science* 47, 82-90.
- Marty, N.C.M., Tournassat, C., Burnol, A., Giffaut, E. & Gaucher, E.C. (2009): Influence of reaction kinetics and mesh refinement on the numerical modelling of concrete/clay interactions. *Journal of Hydrology* 364, 58-72.
- Marty, N.M., Bildstein, O., Blanc, P., Claret, F., Cochepin, B., Gaucher, E., Jacques, D., Lartigue, J.-E., Liu, S., Mayer, K.U., Meeussen, J.L., Munier, I., Pointeau, I., Su, D. & Steefel, C. (2015b): Benchmarks for multicomponent reactive transport across a cement/clay interface. *Computational Geosciences* 19, 635-653.
- Masurat, P., Eriksson, S. & Pedersen, K. (2010): Microbial sulphide production in compacted Wyoming bentonite MX-80 under in situ conditions relevant to a repository for high-level radioactive waste. *Applied Clay Science* 47, 58-64.
- May, H.M., Kinniburgh, D.G., Helmke, P.A. & Jackson, M.L. (1986): Aqueous dissolution, solubilities and thermodynamic stabilities of common aluminosilicate clay-minerals – kaolinite and smectites. *Geochimica et Cosmochimica Acta* 50, 1667-1677.
- Mayor, J.C. & Velasco, M. (2014): EB dismantling synthesis report. PEBS deliverable D2.18, European Commission.
- Melkior, T., Gaucher, E.C., Brouard, C., Yahiaoui, S., Thoby, D., Clinard, C., Ferrage, E., Guyonnet, D., Tournassat, C. & Coelho, D. (2009): Na⁺ and HTO diffusion in compacted bentonite: Effect of surface chemistry and related texture. *Journal of Hydrology* 370, 9-20.
- Metz, V. (2001): Dissolution kinetics of smectite and kaolinite. PhD. Ben-Gurion University of the Negev.
- Metz, V., Amram, K. & Ganor, J. (2005a): Stoichiometry of smectite dissolution reaction. *Geochimica et Cosmochimica Acta* 69, 1755-1772.
- Metz, V., Raanan, H., Pieper, H., Bosbach, D. & Ganor, J. (2005b): Towards the establishment of a reliable proxy for the reactive surface area of smectite. *Geochimica et Cosmochimica Acta* 69, 2581-2591.
- Meunier, A. (2005): *Clays*. Springer, Berlin.

- Meunier, A., Velde, B. & Griffault, L. (1998): The reactivity of bentonites: A review. An application to clay barrier stability for nuclear waste storage. *Clay Minerals* 33, 187-196.
- Montes-H, G., Geraud, Y., Duplay, J. & Reuschlé, T. (2005a): ESM observations of compacted bentonite submitted to hydration/dehydration conditions. *Colloids and Surfaces A: Physicochemical and Engineering Aspects* 262, 14-22.
- Montes-H, G., Marty, N., Fritz, B., Clement, A. & Michau, N. (2005b): Modelling of long-term diffusion–reaction in a bentonite barrier for radioactive waste confinement. *Applied Clay Science* 30, 181-198.
- Mooney, R.W., Keenan, A.G. & Wood, L.A. (1952): Adsorption of water vapor by montmorillonite. II. Effect of exchangeable ions and lattice swelling as measured by X-ray diffraction. *Journal of the American Chemical Society* 74, 1371-1374.
- Morton, J.D., Semrau, J.D. & Hayes, K.F. (2001): An X-ray absorption spectroscopy study of the structure and reversibility of copper adsorbed to montmorillonite clay. *Geochimica et Cosmochimica Acta* 65, 2709-2722.
- Mosser, C., Michot, L.J., Villieras, F. & Romeo, M. (1997): Migration of cations in copper(II) exchanged montmoillonite and laponite upon heating. *Clays and Clay Minerals* 45, 789-802.
- Mosser-Ruck, R. & Cathelineau, M. (2004): Experimental transformation of Na,Ca-smectite under basic conditions at 150 °C. *Applied Clay Science* 26, 259-273.
- Müller, H.R., Garitte, B., Vogt, T., Kohler, S., Sakaki, T., Weber, H., Spillmann, T., Hertrich, M., Becker, J.K., Giroud, N., Cloet, V., Diomidis, N. & Vietor, T. (2017): Implementation of the full-scale emplacement (FE) experiment at the Mont Terri rock laboratory. *Swiss Journal of Geosciences* 110, 287-306.
- Müller-Vonmoos, M. & Kahr, G. (1983): Mineralogische Untersuchungen von Wyoming Bentonit MX-80 und Montigel. *Nagra Technischer Bericht NTB* 83-12.
- Muurinen, A. (2009): Studies on the chemical conditions and microstructure in the reference bentonites of alternative buffer materials Project (ABM) in Äspö. WR 2009-42, VTT Technical Research Centre of Finland, Olkiluoto, Finland.
- Muurinen, A., Carlsson, T. & Root, A. (2013): Bentonite pore distribution based on SAXS, chloride exclusion and NMR studies. *Clay Minerals* 48, 251-266.
- Muurinen, A., Tournassat, C., Hadi, J. & Greneche, J.M. (2014): Sorption and diffusion of Fe(II) in bentonite. Posiva 2014-04.
- Nagra (1988): Projekt Gewähr 1985: Endlager für hochaktive Abfälle. *Nagra Gewähr Bericht* NGB 85-05.
- Nagra (1994a): Endlager für kurzlebige Abfälle EL-SMA: Sicherheitsanalyse Betrieb: Technischer Bericht zum generellen Projekt SMA-AB (GRS). Unpubl. Nagra Interner Bericht.
- Nagra (1994b): Funktionen zur Ableitung von Personendosen aus Quelltermen im Rahmen der Sicherheitsanalyse Betrieb (Generelles Projekt EL-SMA Anlagen und Betrieb). Unpubl. Nagra Interner Bericht.

- Nagra (2002a): Project Opalinus Clay – safety report: Demonstration of disposal feasibility for spent fuel, vitrified high-level waste and long-lived intermediate level waste (Entsorgungsnachweis). Nagra Technical Report NTB 02-05.
- Nagra (2002b): Projekt Opalinuston – Konzept für die Anlage und den Betrieb eines geologischen Tiefenlagers. Entsorgungsnachweis für abgebrannte Brennelemente, verglaste hochaktive sowie langlebige mittelaktive Abfälle. Nagra Technischer Bericht NTB 02-02.
- Nagra (2002c): Projekt Opalinuston: Synthese der geowissenschaftlichen Untersuchungsergebnisse – Entsorgungsnachweis für abgebrannte Brennelemente, verglaste hochaktive sowie langlebige mittelaktive Abfälle. Nagra Technischer Bericht NTB 02-03.
- Nagra (2004): Effects of post-disposal gas generation in a repository for spent fuel, high-level waste and long-lived intermediate level waste sited in Opalinus Clay. Nagra Technical Report NTB 04-06.
- Nagra (2005): Entsorgungsprogramm 2005: Lagerkonzepte für ein geologisches SMA-Lager. Bautechnische und betriebliche Grundlagen zur Reevaluation potenzieller Lagerstandorte SMA. Nagra Arbeitsbericht NAB 05-08.
- Nagra (2008a): Vorschlag geologischer Standortgebiete für das SMA- und das HAA-Lager: Darlegung der Anforderungen, des Vorgehens und der Ergebnisse (Hauptbericht). Nagra Technischer Bericht NTB 08-03.
- Nagra (2008b): Vorschlag geologischer Standortgebiete für ein SMA- und ein HAA-Lager: Begründung der Abfallzuteilung, der Barrierensysteme und der Anforderungen an die Geologie (Bericht zur Sicherheit und Machbarkeit). Nagra Technischer Bericht NTB 08-05.
- Nagra (2010): PAMINA RTCD 2 deliverable d2.2.E.1: Fully probabilistic safety assessment. Nagra Arbeitsbericht NAB 10-37.
- Nagra (2011a): Stilllegungsstudie 2011: Radiologische Inventare der aktivierten Grundmaterialien des KKB. Nagra Arbeitsbericht NAB 11-13.
- Nagra (2011b): Stilllegungsstudie 2011: Radiologische Inventare der aktivierten Grundmaterialien des KKG. Nagra Arbeitsbericht NAB 11-14.
- Nagra (2011c): Stilllegungsstudie 2011: Radiologische Inventare der aktivierten Grundmaterialien des KKL. Nagra Arbeitsbericht NAB 11-11.
- Nagra (2011d): Stilllegungsstudie 2011: Radiologische Inventare der aktivierten Grundmaterialien des KKM. Nagra Arbeitsbericht NAB 11-12.
- Nagra (2013a): Sachplan geologische Tiefenlager Etappe 2, Standortareal JO-3+-HAA im Planungssperimeter Jura Ost für die Oberflächenanlage eines geologischen Tiefenlagers HAA, Planungsstudie. Nagra Arbeitsbericht NAB 13-67.
- Nagra (2013b): Sachplan geologische Tiefenlager Etappe 2, Standortareal JO-3+-Kombi im Planungssperimeter Jura Ost für die Oberflächenanlage eines geologischen Tiefenlagers Kombi, Planungsstudie. Nagra Arbeitsbericht NAB 13-68.

- Nagra (2013c): Sachplan geologische Tiefenlager Etappe 2, Standortareal JO-3+-SMA im Planungssperimeter Jura Ost für die Oberflächenanlage eines geologischen Tiefenlagers SMA, Planungsstudie. Nagra Arbeitsbericht NAB 13-66.
- Nagra (2013d): Standortunabhängige Betrachtungen zur Sicherheit und zum Schutz des Grundwassers – Grundlagen zur Beurteilung der grundsätzlichen Bewilligungsfähigkeit einer Oberflächenanlage für ein geologisches Tiefenlager. Nagra Technischer Bericht NTB 13-01.
- Nagra (2014a): SGT Etappe 2: Vorschlag weiter zu untersuchender geologischer Standortgebiete mit zugehörigen Standortarealen für die Oberflächenanlage. Charakteristische Dosisintervalle und Unterlagen zur Bewertung der Barriersysteme. Nagra Technischer Bericht NTB 14-03.
- Nagra (2014b): SGT Etappe 2: Vorschlag weiter zu untersuchender geologischer Standortgebiete mit zugehörigen Standortarealen für die Oberflächenanlage. Sicherheitstechnischer Bericht zu SGT Etappe 2. Sicherheitstechnischer Vergleich und Vorschlag der in Etappe 3 weiter zu untersuchenden geologischen Standortgebiete. Nagra Technischer Bericht NTB 14-01.
- Nagra (2016): The Nagra research, development and demonstration (RD&D) plan for the disposal of radioactive waste in Switzerland. Nagra Technical Report NTB 16-02.
- Nagra (2019): Implementation of the full-scale emplacement experiment in Mont Terri: Design, construction and preliminary results. Nagra Technical Report NTB 15-02.
- Nakayama, S., Sakamoto, Y., Yamaguchi, T., Akai, M., Tanaka, T., Sato, T. & Iida, Y. (2004): Dissolution of montmorillonite in compacted bentonite by highly alkaline aqueous solutions and diffusivity of hydroxide ions. *Applied Clay Science* 27, 53-65.
- Navarro, V., Asensio, L., De la Morena, G., Pintado, X. & Yustres, A. (2015): Differentiated intra- and inter-aggregate water content models of MX-80 bentonite. *Applied Clay Science* 118, 325-336.
- Navarro, V., Asensio, L., Yustres, A., Pintado, X. & Alonso, J. (2014): An elastoplastic model of bentonite free swelling. *Engineering Geology* 181, 190-201.
- Navarro, V., Yustres, A., Asensio, L., De la Morena, G., Gonzalez-Arteaga, J., Laurila, T. & Pintado, X. (2017): Modelling of compacted bentonite swelling that accounts for salinity effects. *Engineering Geology* 223, 48-58.
- NEA (2001): Proceedings of an NEA/EC workshop on gas generation and migration in radioactive waste disposal: Safety-relevant issues. OECD Paris, Reims, France.
- NEA (2013): The safety case for deep geological disposal of radioactive waste: 2013 state of the art. OECD, Paris, France.
- Nied, D., Enemark-Rasmussen, K., L'Hopital, E., Skibsted, J. & Lothenbach, B. (2016): Properties of magnesium silicate hydrates (M-S-H). *Cement and Concrete Research* 79, 323-332.
- Norris, S., Lemy, F., del Honeux, C.-A., Volckaert, G., Weetjens, E., Wouters, K., Wendling, J., Dymitrowski, M., Pellegrini, D., Sellin, P., Johnson, L., Sentis, M. & Harrington, J. (2013): Synthesis report: Updated treatment of gas generation and migration in the safety case. Euratom 7th framework program Project: Forge, Project milestone m68.

- Norrish, K. (1954): Manner of swelling of montmorillonite. *Nature* 173, 256-257.
- Nuth, M. & Laloui, L. (2008): Advances in modelling hysteretic water retention curve in deformable soils. *Computers and Geotechnics* 35/6, 835-844.
- Oelkers, E.H., Schott, J. & Devidal, J.L. (1994): The effect of aluminum, pH, and chemical affinity on the rates of aluminosilicate dissolution reactions. *Geochimica et Cosmochimica Acta* 58, 2011-2024.
- Olivella, S., Gens, A. & Mokni, N. (2012): Modelling the FEBEX in-situ experiment including dismantling operations – incorporating the effect of additional phenomena. *Clays in Natural and Engineered Barriers for Radioactive Waste Confinement*. 5th international Conference, Montpellier, France.
- Ouselati, W., Ben, R., H., Karmous, M.S., Naamen, S., Ben, H. & Amara, A. (2006): Study of the structural evolution and selectivity of Wyoming montmorillonite in relation with concentration of Cu^{2+} and Ni^{2+} . *Zeitschrift für Kristallographie, Supplement* 23, 425-429.
- Panday, S. & Corapcioglu, M.Y. (1989). Reservoir transport equations by compositional approach. *Transport in Porous Media* 4/4, 369-393.
- Papafotiou, A. & Senger, R. (2014a): Sensitivity analyses of gas release from a SF/HLW repository in the Opalinus Clay in the candidate siting regions of Northern Switzerland. *Nagra Arbeitsbericht NAB 14-10*.
- Papafotiou, A. & Senger, R. (2014b): Thermo-hydraulic modelling of the temperature distribution in the siting region Jura Ost. *Nagra Arbeitsbericht NAB 14-39*.
- Papafotiou, A., Li, C. & Kober, F. (eds.) (2017): Pre-dismantling THM modelling of the FEBEX in situ experiment. *Nagra Arbeitsbericht NAB 16-22*.
- Pedersen, K. (2010): Analysis of copper corrosion in compacted bentonite clay as a function of clay density and growth conditions for sulfate-reducing bacteria. *Journal of Applied Microbiology* 108, 1094-1104.
- Peryea, F.J. & Kittrick, J.A. (1986): Experimental evaluation of 2 operational standard states for montmorillonite in metastable hydrolysis reactions. *Soil Science Society of America Journal* 50, 1613-1617.
- Philip, J.R. & de Vries, D.A. (1957). Moisture movement in porous materials under temperature gradients. *Eos, Transactions American Geophysical Union* 38/2, 222-232.
- Plötze, M. & Valter, M. (2011): Bentonite as barrier material – thermal conductivity of compacted bentonite. *Nagra Arbeitsbericht NAB 11-16*.
- Plötze, M. & Weber, H. (2007): ESDRED: Emplacement tests with granular bentonite MX-80 – laboratory results from ETH Zürich. *Nagra Arbeitsbericht NAB 07-24*.
- Posiva (2013): Safety case for the disposal of spent nuclear fuel at Olkiluoto - performance assessment 2012. *Posiva 2012-04*, Posiva, Eurajoki, Finland.

- Powell, K.J., Brown, P.L., Byrne, R.H., Gajda, T., Hefter, G., Sjöberg, S. & Wanner, H. (2007): Chemical speciation of environmentally significant metals with inorganic ligands part 2: The Cu^{2+} -OH, Cl, CO_3^{2-} , SO_4^{2-} , and PO_4^{3-} systems (IUPAC technical report). *Pure and Applied Chemistry* 79, 2425-2476.
- Pusch, R. & Yong, R.N. (2014): *Microstructure of smectite clays and engineering performance*. CRC Press.
- Pusch, R. (1992): Use of bentonite for isolation of radioactive-waste products. *Clay Minerals* 27, 353-361.
- Pusch, R. (2001): The microstructure of MX-80 clay with respect to its bulk physical properties under different environmental conditions. SKB Technical Report TR-01-08. Swedish Nuclear Fuel and Waste Management CO, www.skb.se, Stockholm, Sweden.
- Pusch, R. (2002): The buffer and backfill handbook. Part 1: Definitions, basic relationships, and laboratory methods. SKB Technical Report TR-02-20. Swedish Nuclear Fuel and Waste Management CO, www.skb.se, Stockholm, Sweden.
- Rai, D. & Kittrick, J.A. (1989): Mineral equilibria and the soil system. *In*: Dixon, J.B. & Weed, S.B. (eds.): *Minerals in soil environments*. Soil Science Society of America Book Series. Soil Science Society, Madison, Wisconsin, USA, pp. 161-198.
- Ramírez, S., Cuevas, J., Vigil, R. & Leguey, S. (2002): Hydrothermal alteration of "La Serrata" bentonite (Almeria, Spain) by alkaline solutions. *Applied Clay Science* 21, 257-269.
- Reesman, A.L. & Keller, W.D. (1968): Aqueous solubility studies of high-alumina and clay minerals. *American Mineralogist* 53, 929-942.
- Rimstidt, J.D. (1997): Quartz solubility at low temperatures. *Geochimica et Cosmochimica Acta* 61, 2553-2558.
- Romero, E. (2001): Controlled-suction techniques. *In*: Gehling, W.Y.Y. & Schnaid, F. (eds.): *4º Simpósio Brasileiro de Solos Não Saturados*, Porto Alegre, Brazil, pp. 533-542.
- Romero, E. & Gonzalez-Blanco, L. (2017): Hydro-mechanical processes associated with gas transport in MX-80 bentonite in the context of Nagra's RD&D program. Nagra Arbeitsbericht NAB 17-09.
- Romero, E. & Gonzalez-Blanco, L. (2018): Hydro-mechanical processes associated with gas transport in Wyoming granular bentonite – complementary laboratory experiments carried out at UPC in 2017. Nagra Arbeitsbericht NAB 18-09.
- Rosenberg, P.E., Kittrick, J.A. & Aja, S.U. (1990): Mixed-layer illite smectite - a multiphase model. *American Mineralogist* 75, 1182-1185.
- Rotenberg, B., Marry, V., Vuilleumier, R., Malikova, N., Simon, C. & Turq, P. (2007): Water and ions in clays: Unraveling the interlayer/micropore exchange using molecular dynamics. *Geochimica et Cosmochimica Acta* 71, 5089-5101.
- Rozalen, M., Brady, P.V. & Huertas, F.J. (2009a): Surface chemistry of K-montmorillonite: Ionic strength, temperature dependence and dissolution kinetics. *Journal of Colloid and Interface Science* 333, 474-484.

- Rozalen, M., Huertas, F.J. & Brady, P.V. (2009b): Experimental study of the effect of pH and temperature on the kinetics of montmorillonite dissolution. *Geochimica et Cosmochimica Acta* 73, 3752-3766.
- Rozalen, M.L., Huertas, F.J., Brady, P.V., Cama, J., Garcia-Palma, S. & Linares, J. (2008): Experimental study of the effect of pH on the kinetics of montmorillonite dissolution at 25 degrees C. *Geochimica et Cosmochimica Acta* 72, 4224-4253.
- Rutqvist, J. (2015): Chapter 9 – coupled thermo-hydro-mechanical behavior of natural and engineered clay barriers. *In: Tournassat, C., Steefel, C.I., Bourg, I.C. & Bergaya, F. (eds.): Natural and engineered clay barriers, developments in clay science. Elsevier, pp. 329-355.*
- Sacchi, E., Michelot, J.L., Pitsch, H., Lalieux, P. & Aranyossy, J.F. (2001): Extraction of water and solutes from argillaceous rocks for geochemical characterisation: Methods, processes, and current understanding. *Hydrogeology Journal* 9, 17-33.
- Saiyouri, N., Hicher, P.Y. & Tessier, D. (1998): Microstructural analysis of highly compacted clay swelling. *Second International Congress on Unsaturated Soils. Unsat'98.*
- Salager, S., Nuth, M., Ferrari, A. & Laloui, L. (2013): Investigation into water retention behaviour of deformable soils. *Canadian Geotechnical Journal* 50/2, 200-208.
- Salager, S., Rizzi, M. & Laloui, L. (2011): An innovative device for determining the soil water retention curve under high suction at different temperatures. *Acta Geotechnica* 6, 135-142.
- Sanchez, M., Gens, A. & Guimaraes, L. (2012a): Thermal-hydraulic-mechanical (thm) behaviour of a large-scale in situ heating experiment during cooling and dismantling. *Canadian Geotechnical Journal* 49, 1169-1195.
- Sanchez, M., Gens, A. & Olivella, S. (2012b): THM analysis of a large-scale heating test incorporating material fabric changes. *International Journal for Numerical and Analytical Methods in Geomechanics* 36, 391-421.
- Sass, B.M., Rosenberg, P.E. & Kittrick, J.A. (1987): The stability of illite smectite during diagenesis – an experimental-study. *Geochimica et Cosmochimica Acta* 51, 2103-2115.
- Sato, T., Fujimori, Y., Nakayama, T., Gotoh, Y., Sunaga, Y., Nemoto, M., Matsunaga, T. & Tanaka, T. (2012): Assessment of the anti-biofouling potentials of a copper iodide-doped nylon mesh. *Applied Microbiology and Biotechnology* 95, 1043-1050.
- Satoh, H., Ishii, T. & Owada, H. (2013): Dissolution of compacted montmorillonite at hyper-alkaline pH and 70 degrees C: In situ vsi and ex situ AFM measurements. *Clay Minerals* 48, 285-294.
- Savage, D. & Cloet, V. (2018): A review of cement-clay modelling. *Nagra Arbeitsbericht NAB 18-24.*
- Savage, D. & Liu, J. (2015): Water/clay ratio, clay porosity models and impacts upon clay transformations. *Applied Clay Science* 116, 16-22.
- Savage, D. (2012): Prospects for coupled modelling. *STUK-TR 13, Finland.*

- Savage, D. (2013): Constraints on cement-clay interaction. *Procedia Earth and Planetary Science* 7, 770-773.
- Savage, D. (2014): An assessment of the impact of the degradation of engineered structures on the safety-relevant functions of the bentonite buffer in a HLW repository. Nagra Technical Report NTB 13-02.
- Savage, D., Arthur, R., Watson, C. & Wilson, J. (2010a): An evaluation of models of bentonite porewater evolution. 2010:12, Swedish Radiation Safety Authority, Sweden.
- Savage, D., Benbow, S., Watson, C., Takase, H., Ono, K., Oda, C. & Honda, A. (2010b): Natural systems evidence for the alteration of clay under alkaline conditions: An example from Searles Lake, California. *Applied Clay Science* 47, 72-81.
- Savage, D., Noy, D. & Mihara, M. (2002): Modelling the interaction of bentonite with hyper-alkaline fluids. *Applied Geochemistry* 17, 207-223.
- Savage, D., Watson, C., Benbow, S. & Wilson, J. (2010c): Modelling iron-bentonite interactions. *Applied Clay Science* 47, 91-98.
- Schäfers, A., Gaus, I., Johnson, L., Liu, Y., Mayor, J.C., Sellin, P. & Wieczorek, K. (2014): Pebs (long-term performance of engineered barrier systems) final scientific report. D5-16, European Commission.
- Schanz, T. & Tripathy, S. (2009): Swelling pressure of a divalent-rich bentonite: Diffuse double-layer theory revisited. *Water Resources Research* 45.
- Schanz, T., Khan, M.I. & Al-Badran, Y. (2013): An alternative approach for the use of DDL theory to estimate the swelling pressure of bentonites. *Applied Clay Science* 83-84, 383-390.
- Schreffler, B.A. (1984): The finite element method in soil consolidation (with applications to surface subsidence). Ph.D. Thesis, University College of Swansea, C/Ph/76/84.
- Seiffarth, T. & Kaps, C. (2009): Structural characterization of (Cu²⁺, Na⁺)- and (Cu²⁺, NH⁴⁺)-exchanged bentonites upon thermal treatment. *Clays and Clay Minerals* 57, 40-45.
- Seiphoori, A. (2016): Thermo-hydro-mechanical characterisation and modelling of Wyoming granular bentonite. Nagra Technical Report NTB 15-05.
- Seiphoori, A., Ferrari, A. & Laloui, L. (2014): Water retention behaviour and microstructural evolution of MX-80 bentonite during wetting and drying cycles. *Geotechnique* 64, 721-734.
- Senger, R. & Marschall, P. (2008): Task force on EBS/gas transport in buffer material. Nagra Arbeitsbericht NAB 08-24.
- Senger, R. & Papafotiou, A. (2013): Effects of salt enrichment in SF/HLW tunnels and L/ILW caverns due to water consumption by iron corrosion. Nagra Arbeitsbericht NAB 13-72.
- Senger, R., Papafotiou, A. & Marschall, P. (2014): Thermo-hydraulic simulations of the near-field of a SF/HLW repository during early- and late-time post-closure period. Nagra Arbeitsbericht NAB 14-11.

- Senger, R.K. & Ewing, J.E. (2008): Evolution of temperature and water content in the bentonite buffer: Detailed modelling of two-phase flow processes associated with the early closure period – complimentary simulations. Nagra Arbeitsbericht NAB 08-53.
- Shafizadeh, A. (2019): Neutron imaging study of evolution of structural and transport properties of Cement-Clay interfaces. Inauguraldissertation der Philosophisch-naturwissenschaftlichen Fakultät der Universität Bern. Bern University.
- Shaiek, M., Karmous, M.S., Naamen, S., Ben, R., H., Ben, H., Amara, A. & Plançon, A. (2003): Structural evolution of heated dioctahedral montmorillonite saturated with Cu^{2+} , Ni^{2+} and Cs^+ . Abstracts of the 10th Conference of the European Clay Groups Association, Euroclay 2003, Modena, p. 258.
- Shaw, R.P. (2014): Principal outcomes of the FORGE – fate of repository gases – Project. D0.8-R, European Commission FP7.
- SKB (2010): Buffer, backfill and closure process report for the safety assessment sr-site. SKB Technical Report TR-10-47. Swedish Nuclear Fuel and Waste Management CO, www.skb.se, Stockholm, Sweden.
- SKB (2011): Long-term safety for the final repository for spent nuclear fuel at Forsmark. Main report of the SR-site project. SKB Technical Report TR-11-01, 1 – 3. Swedish Nuclear Fuel and Waste Management CO, www.skb.se, Stockholm, Sweden.
- Smart, N.R., Reddy, B., Rance, A.P., Nixon, D.J., Frutschi, M., Bernier-Latmani, R. & Diomidis, N. (2017): The anaerobic corrosion of carbon steel in compacted bentonite exposed to natural Opalinus Clay porewater containing native microbial populations. *Corrosion Engineering, Science and Technology* 52, 101-112.
- Soltermann, D., Baeyens, B., Bradbury, M.H. & Fernandes, M.M. (2014a): Fe (II) uptake on natural montmorillonites. II. Surface complexation modeling. *Environmental Science & Technology* 48, 8698-8705.
- Soltermann, D., Fernandes, M.M., Baeyens, B., Dähn, R., Miché-Brendlé, J., Wehrli, B. & Bradbury, M.H. (2013): Fe (II) sorption on a synthetic montmorillonite. A combined macroscopic and spectroscopic study. *Environmental Science and Technology* 47, 6978-6986.
- Soltermann, D., Marques Fernandes, M., Baeyens, B., Dähn, R., Joshi, P.A., Scheinost, A.C. & Gorski, C.A. (2014b): Fe (II) uptake on natural montmorillonites. I. Macroscopic and spectroscopic characterization. *Environmental Science & Technology* 48, 8688-8697.
- Sposito, G. & Prost, R. (1982): Structure of water adsorbed on smectites. *Chemical Reviews* 82, 553-573.
- Srodon, J. & McCarty, D.K. (2008): Surface area and layer charge of smectite from CEC and egme/H₂O-retention measurements. *Clays and Clay Minerals* 56, 155-174.
- Steeffel, C.I., Appelo, C.A.J., Arora, B., Jacques, D., Kalbacher, T., Kolditz, O., Lagneau, V., Lichtner, P.C., Mayer, K.U., Meeussen, J.C.L., Molins, S., Moulton, D., Shao, H., Šimůnek, J., Spycher, N., Yabusaki, S.B. & Yeh, G.T. (2014): Reactive transport codes for subsurface environmental simulation. *Computational Geosciences* 18, 1-34.

- Strawn, D.G., Palmer, N.E., Furnare, L.J., Goodell, C., Amonette, J.E. & Kukkadapu, R.K. (2004): Copper sorption mechanisms on smectites. *Clays and Clay Minerals* 52, 321-333.
- Stroes-Gascoyne, S. & Hamon C.J. (2014): Microbial analysis of highly compacted bentonite samples from two large in situ tests at the Äspö Hard Rock Laboratory, Sweden. NWMO TR-2014-15.
- Stroes-Gascoyne, S., Hamon, C.J., Dixon, D.A., Kohle, C.L. & Maak, P. (2007): The effects of dry density and porewater salinity on the physical and microbiological characteristics of compacted 100 % bentonite. *In: Dunn, D., Poinssot, C., Begg, B. (eds.): Materials Research Society Symposium Proceedings. Materials Research Society, p. 505.*
- Stroes-Gascoyne, S., Haveman, S.A. & Vilks, P. (1996): The change in bioavailability of organic matter associated with clay-based buffer materials as a result of heat and radiation treatment. *MRS Proceedings* 465.
- Stroes-Gascoyne, S., Sergeant, C., Schippers, A., Hamon, C.J., Neble, S., Vesvres, M.H., Barsotti, V., Poulain, S. & Le Marrec, C. (2011): Biogeochemical processes in a clay formation in situ experiment: Part D – microbial analyses – synthesis of results. *Applied Geochemistry* 26, 980-989.
- Stucki, J.W., Golden, D.C. & Roth, C.B. (1984a): Effects of reduction and reoxidation of structural iron on the surface-charge and dissolution of dioctahedral smectites. *Clays and Clay Minerals* 32, 350-356.
- Stucki, J.W., Low, P.F., Roth, C.B. & Golden, D.C. (1984b): Effects of oxidation-state of octahedral iron on clay swelling. *Clays and Clay Minerals* 32, 357-362.
- Stucki, J.W., Wu, J., Gan, H.M., Komadel, P. & Banin, A. (2000): Effects of iron oxidation state and organic cations on dioctahedral smectite hydration. *Clays and Clay Minerals* 48, 290-298.
- Sun, L.L., Hirvi, J.T., Schatz, T., Kasa, S. & Pakkanen, T.A. (2015): Estimation of montmorillonite swelling pressure: A molecular dynamics approach. *Journal of Physical Chemistry C* 119, 19863-19868.
- Sun, L.L., Ling, C.Y., Lavikainen, L.P., Hirvi, J.T., Kasa, S. & Pakkanen, T.A. (2016): Influence of layer charge and charge location on the swelling pressure of dioctahedral smectites. *Chemical Physics* 473, 40-45.
- Svensson, D. (2015): The bentonite barrier: Swelling properties, redox chemistry and mineral evolution. PhD. Lund University, Sweden.
- Svensson, P.D. & Hansen, S. (2013): Redox chemistry in two iron-Bentonite field experiments at Äspö hard rock laboratory, Sweden: An XRD and Fe K-edge XANES study. *Clays and Clay Minerals* 61, 566-579.
- Svensson, D., Dueck, A., Nielsson, U., Olsson, S., Sandén, T., Lydmark, S., Jägerwall, S., Pedersen, K. & Hansen, S. (2011): Alternative buffer material - status of the ongoing laboratory investigation of reference materials and test package 1. SKB Technical Report TR-11-06. Swedish Nuclear Fuel and Waste Management CO, www.skb.se, Stockholm, Sweden.

- Tachi, Y. & Yotsuji, K. (2014): Diffusion and sorption of Cs⁺, Na⁺, I⁻ and HTO in compacted sodium montmorillonite as a function of porewater salinity: Integrated sorption and diffusion model. *Geochimica et Cosmochimica Acta* 132, 75-93.
- Tajeddine, L., Gailhanou, H., Blanc, P., Lassin, A., Gaboreau, S. & Vieillard, P. (2015): Hydration-dehydration behavior and thermodynamics of MX-80 montmorillonite studied using thermal analysis. *Thermochimica Acta* 604, 83-93.
- Takase, H. (2004): Discussion on PA model development for bentonite barriers affected by chemical interaction with concrete: Do we have enough evidence to support bentonite stability? International Workshop on Bentonite-Cement Interaction in Repository Environments, Tokyo, Japan, pp. 172-177.
- Tang, A.M., Cui, Y.J. & Barnel, N. (2008): Thermo-mechanical behaviour of a compacted swelling clay. *Géotechnique* 58, 45-54.
- Tardy, Y. & Duplay, J. (1992): A method of estimating the Gibbs free-energies of formation of hydrated and dehydrated clay-minerals. *Geochimica et Cosmochimica Acta* 56, 3007-3029.
- Tardy, Y. & Fritz, B. (1981): An ideal solid-solution model for calculating solubility of clay-minerals. *Clay Minerals* 16, 361-373.
- Tardy, Y. & Garrels, R.M. (1974): Method of estimating Gibbs energies of formation of layer silicates. *Geochimica et Cosmochimica Acta* 38, 1101-1116.
- Tardy, Y. & Garrels, R.M. (1976): Prediction of Gibbs energies of formation .1. Relationships among gibbs energies of formation of hydroxides, oxides and aqueous ions. *Geochimica et Cosmochimica Acta* 40, 1051-1056.
- Tardy, Y., Duplay, J. & Fritz, B. (1987): Stability fields of smectites and illites as a function of temperature and chemical composition. SKB Technical Report TR-87-20. Swedish Nuclear Fuel and Waste Management CO, Stockholm, Sweden.
- Thoenen, T., Hummel, W., Berner, U. & Curti, E. (2014): The PSI/Nagra Chemical Thermodynamic Database 12/07. Nuclear Energy and Safety Research Department, Laboratory for Waste Management (LES). PSI Bericht Nr. 14-04, ISSN 1019-0643. Paul Scherrer Institut, PSI Villigen, Switzerland.
- Tinker, F. (1916): Osmotic pressure or osmotic suction – which? *Nature* 97, 122.
- Tinnacher, R.M., Holmboe, M., Tournassat, C., Bourg, I.C. & Davis, J.A. (2016): Ion adsorption and diffusion in smectite: Molecular, pore, and continuum scale views. *Geochimica et Cosmochimica Acta* 177, 130-149.
- Tournassat, C. (2003): Cations-clays interactions: The Fe(II) case. Application to the problematic of the french deep nuclear repository field concept. University of Grenoble, p. 199.
- Tournassat, C. & Appelo, C.A.J. (2011): Modelling approaches for anion-exclusion in compacted Na-bentonite. *Geochimica et Cosmochimica Acta* 75, 3698-3710.
- Tournassat, C. & Steefel, C.I. (2015): Ionic transport in nano-porous clays with consideration of electrostatic effects. *Reviews in Mineralogy and Geochemistry* 80, 287-329.

- Tournassat, C., Grangeon, S., Leroy, P. & Giffaut, E. (2013): Modeling specific pH dependent sorption of divalent metals on montmorillonite surfaces. A review of pitfalls, recent achievements and current challenges. *American Journal of Science* 313, 395-451.
- Tournassat, C., Bourg, I.C., Holmboe, M., Sposito, G. & Steefel, C.I. (2016a): Molecular dynamics simulations of anion exclusion in clay interlayer nanopores. *Clays and Clay Minerals* 64, 374-388.
- Tournassat, C., Davis, J.A., Chiaberge, C., Grangeon, S. & Bourg, I.C. (2016b): Modeling the acid–base properties of montmorillonite edge surfaces. *Environmental Science & Technology* 50, 13436-13445.
- Tripathy, S., Sridharan, A. & Schanz, T. (2004): Swelling pressures of compacted bentonites from diffuse double layer theory. *Canadian Geotechnical Journal* 41, 437-450.
- Truche, L., Berger, G., Destigneville, C., Pages, A., Guillaume, D., Giffaut, E. & Jacquot, E. (2009): Experimental reduction of aqueous sulphate by hydrogen under hydrothermal conditions: Implication for the nuclear waste storage. *Geochimica et Cosmochimica Acta* 73, 4824-4835.
- Truche, L., Berger, G., Destigneville, C., Guillaume, D. & Giffaut, E. (2010): Kinetics of pyrite to pyrrhotite reduction by hydrogen in calcite buffered solutions between 90 and 180 degrees C: Implications for nuclear waste disposal. *Geochimica et Cosmochimica Acta* 74, 2894-2914.
- Truche, L., Jodin-Caumon, M.C., Lerouge, C., Berger, G., Mosser-Ruck, R., Giffaut, E. & Michau, N. (2013): Sulphide mineral reactions in clay-rich rock induced by high hydrogen pressure. Application to disturbed or natural settings up to 250 degrees C and 30 bar. *Chemical Geology* 351, 217-228.
- Ueta, S., Satoh, H., Kato, H., Ueda, A. & Tsukamoto, K. (2013): A novel technique of in situ phase-shift interferometry applied for faint dissolution of bulky montmorillonite in alkaline solution. *Journal of Nuclear Science and Technology* 50, 731-741.
- Valter, M. & Plotze, M. (2013): Characteristics of variably saturated granular bentonite after long-term storage at near-field relevant temperatures. *Clay Minerals* 48, 343-361.
- Van Hinsberg, V.J., Vriend, S.P. & Schumacher, J.C. (2005a): A new method to calculate end-member thermodynamic properties of minerals from their constituent polyhedra I: Enthalpy, entropy and molar volume. *Journal of Metamorphic Geology* 23, 165-179.
- Van Hinsberg, V.J., Vriend, S.P. & Schumacher, J.C. (2005b): A new method to calculate end-member thermodynamic properties of minerals from their constituent polyhedra II: Heat capacity, compressibility and thermal expansion. *Journal of Metamorphic Geology* 23, 681-693.
- Van Loon L.R. (2014): Effective Diffusion Coefficients and Porosity Values for Argillaceous Rocks and Bentonite: Measured and Estimated Values for the Provisional Safety Analyses for SGT-E2. Nagra Technical Report NTB 12-03.
- Van Loon, L.R., Glaus, M.A. & Müller, W. (2007): Anion exclusion effects in compacted bentonites: Towards a better understanding of anion diffusion. *Applied Geochemistry* 22, 2536-2552.

- Van Rompaey, K., Van Ranst, E., De Coninck, F. & Vindevogel, N. (2002): Dissolution characteristics of hectorite in inorganic acids. *Applied Clay Science* 21, 241-256.
- Viani, B.E., Low, P.F. & Roth, C.B. (1983): Direct measurement of the relation between inter-layer force and interlayer distance in the swelling of montmorillonite. *Journal of Colloid and Interface Science* 96, 229-244.
- Vidal, O. & Dubacq, B. (2009): Thermodynamic modelling of clay dehydration, stability and compositional evolution with temperature, pressure and H₂O activity. *Geochimica et Cosmochimica Acta* 73, 6544-6564.
- Vieillard, P. (1994a): Prediction of enthalpy of formation based on refined crystal-structures of multisite compounds. 1. Theories and examples. *Geochimica et Cosmochimica Acta* 58, 4049-4063.
- Vieillard, P. (1994b): Prediction of enthalpy of formation based on refined crystal-structures of multisite compounds. 2. Application to minerals belonging to the system Li₂O-Na₂O-K₂O-BeO-MgO-CaO-MnO-FeO-Fe₂O₃-Al₂O₃-SiO₂-H₂O – results and discussion. *Geochimica et Cosmochimica Acta* 58, 4065-4107.
- Vieillard, P. (2000): A new method for the prediction of Gibbs free energies of formation of hydrated clay minerals based on the electronegativity scale. *Clays and Clay Minerals* 48, 459-473.
- Vieillard, P. (2002): New method for the prediction of Gibbs free energies of formation of phyllosilicates (10 angstrom and 14 angstrom) based on the electronegativity scale. *Clays and Clay Minerals* 50, 352-363.
- Vieillard, P., Blanc, P., Fialips, C.I., Gailhanou, H. & Gaboreau, S. (2011): Hydration thermodynamics of the SWy-1 montmorillonite saturated with alkali and alkaline-earth cations: A predictive model. *Geochimica et Cosmochimica Acta* 75, 5664-5685.
- Villagran, J., Ben Belfadhel, M., Birch, K., Freire-Canosa, J., Garamszeghy, M., Garisto, F., Gierszewski, P., Gobien, M., Hirschorn, S., Hunt, N., Khan, A., Kremer, E., Kwong, G., Lam, T., Maak, P., McKelvie, J., Medri, C., Murchison, A., Russell, S., Sanchez-Rico Castejon, M., Stahmer, U., Sykes, E., Urrutia-Bustos, A., Vorauer, A., Wanne, T. & Yang, T. (2011): RD&D program 2011 – NWMO's program for research, development and demonstration for longterm management of used nuclear fuel. TR-2011-01, Nuclear Waste Management Organization, Toronto, Ontario, Canada.
- Villar, M.V. & Lloret, A. (2004): Influence of temperature on the hydro-mechanical behaviour of a compacted bentonite. *Applied Clay Science* 26, 337-350.
- Villar, M.V., Gómez-Espina, R. & Lloret, A. (2010): Experimental investigation into temperature effect on hydro-mechanical behaviours of bentonite. *Journal of Rock Mechanics and Geotechnical Engineering* 2, 71-78.
- Villar, M.V., Gomez-Espina, R. & Gutiérrez-Nebot, L. (2012a): Basal spacings of smectite in compacted bentonite. *Applied Clay Science* 65-66, 95-105.

- Villar, M.V., Martín, P.L., Romero, F.J., Barcala, J.M. & Gutiérrez-Rodrigo, V. (2012b): Gas transport through bentonite: Influence of dry density, water content and boundary conditions. *In*: Skoczylas, F., Davy, C.A., Agostini, F., Burlion, N. (eds.): Propriétés de transfert des géomatériaux. Transfert 2012, Actes du Colloque, 379-389.
- Villar, M.V., Campos, R. & Gutiérrez-Nebot, L. (2014): EB experiment laboratory post-mortem analyses report. DMA/2G210/01, CIEMAT.
- Villar, M.V., Fernandez, A.M., Romero, E., Dueck, A., Cuevas, J., Plötze, M., Kaufhold, S., Dohrmann, R., Iglesias, R.J., Sakaki, T., Zheng, L., Kawamoto, K. & Kober, F. (2018): FEBEX-DP post-mortem THM/THC analysis report. Nagra Arbeitsbericht NAB 16-17 Rev. 1.
- Vinsot, A., Appelo, C.A.J., Lundy, M., Wechner, S., Lettry, Y., Lerouge, C., Fernandez, A.M., Labat, M., Tournassat, C., De Canniere, P., Schwyn, B., McKelvie, J., Dewonck, S., Bossart, P. & Delay, J. (2014a): In situ diffusion test of hydrogen gas in the Opalinus Clay. Geological Society London Special Publications 400, 563-578.
- Vinsot, A., Leveau, F., Bouchet, A. & Arnould, A. (2014b): Oxidation front and oxygen transfer in the fractured zone surrounding the Meuse/Haute-Marne URL drifts in the callovian-oxfordian argillaceous rock. *In*: Norris, S., Bruno, J., Cathelineau, M., Delage, P., Fairhurst, C., Gaucher, E.C., Hohn, E.H., Kalinichev, A., Lalieux, P. & Sellin, P. (eds.): Clays in natural and engineered barriers for radioactive waste confinement. Geological Society Special Publication, pp. 207-220.
- Vinsot, A., Appelo, C.A.J., Lundy, M., Wechner, S., Cailteau-Fischbach, C., de Donato, P., Pironon, J., Lettry, Y., Lerouge, C. & De Canniere, P. (2017): Natural gas extraction and artificial gas injection experiments in Opalinus Clay, Mont Terri rock laboratory (Switzerland). Swiss Journal of Geosciences 110, 375-390.
- Vogt, K. & Köster, H.M. (1978): Zur Mineralogie, Kristallchemie und Geochemie einiger Montmorillonite aus Bentoniten. Clay Minerals 13, 25-43.
- Wallis, I., Idiart, A., Dohrmann, R. & Post, V. (2016): Reactive transport modelling of ground-water-bentonite interaction: Effects on exchangeable cations in an alternative buffer material insitu test. Applied Geochemistry 73, 59-69.
- Wanner, H., Albinsson, Y., Karnland, O., Wieland, E., Wersin, P. & Charlet, L. (1994): The acid-base chemistry of montmorillonite. Radiochimica Acta 66/7, 157-162.
- Watson, C., Hane, K., Savage, D., Benbow, S., Cuevas, J. & Fernández, R. (2009): Reaction and diffusion of cementitious water in bentonite: Results of 'blind' modelling. Applied Clay Science 45, 54-69.
- Wersin, P. (2003): Geochemical modelling of bentonite porewater in high-level waste repositories. Journal of Contaminant Hydrology 61, 405-422.
- Wersin, P. (2013): LOT A2 test parcel. Compilation of copper data in the LOT A2 test parcel. SKB Technical Report TR-13-17. Swedish Nuclear Fuel and Waste Management CO, www.skb.se, Stockholm, Sweden.

- Wersin, P. & Birgersson, M. (2014): Reactive transport modelling of iron-bentonite interaction within the KBS-3H disposal concept – the Olkiluoto site as case study. Geological Society, London Special Publication 400, 237-250.
- Wersin, P. & Kober, F. (eds.) (2017): FEBEX-DP. Metal corrosion and iron-bentonite interaction studies. Nagra Arbeitsbericht NAB 16-16 .
- Wersin, P. & Mettler, S. (eds.) (2006): Workshop on Fe-clay interactions in repository environments, a joint initiative by Andra, SKB and Nagra. Basel/Switzerland, 9-10 May 2006. Nagra Arbeitsbericht NAB 06-15.
- Wersin, P. & Schwyn, B. (2004): Integrated approach for the development of geochemical databases used for safety assessment. Nagra Technical Report NTB 03-06.
- Wersin, P., Johnson, L.H., Schwyn, B., Berner, U. & Curti, E. (2003): Redox conditions in the near field of a repository for SF/HLW and ILW in Opalinus Clay. Nagra Technical Report NTB 02-13.
- Wersin, P., Curti, E. & Appelo, C.A.J. (2004): Modelling bentonite-water interactions at high solid/liquid ratios: Swelling and diffuse double layer effects. Applied Clay Science 26, 249-257.
- Wersin, P., Birgersson, M., Olsson, S., Karnland, O. & Snellman, M. (2007a): Impact of corrosion-derived iron on the bentonite buffer within the KBS-3H disposal concept - the Olkiluoto site as case study. Posiva 2007-11, Posiva.
- Wersin, P., Johnson, L.H. & McKinley, I.G. (2007b): Performance of the bentonite barrier at temperatures beyond 100 degrees C: A critical review. Physics and Chemistry of the Earth 32, 780-788.
- Wersin, P., Leupin, O.X., Mettler, S., Gaucher, E.C., Maeder, U., De Canniere, P., Vinsot, A., Gaebler, H.E., Kunimaro, T., Kiho, K. & Eichinger, L. (2011a): Biogeochemical processes in a clay formation in situ experiment: Part A – Overview, experimental design and water data of an experiment in the Opalinus Clay at the Mont Terri Underground Research Laboratory, Switzerland. Applied Geochemistry 26, 931-953.
- Wersin, P., Stroes-Gascoyne, S., Pearson, F.J., Tournassat, C., Leupin, O.X. & Schwyn, B. (2011b): Biogeochemical processes in a clay formation in situ experiment: Part G – key interpretations and conclusions. Implications for repository safety. Applied Geochemistry 26, 1023-1034.
- Wersin, P., Jenni, A. & Mäder, U.K. (2014a): ABM experiment (test package 1): A feasibility study on iron-bentonite interaction in block 3. Nagra Arbeitsbericht NAB 14-24.
- Wersin, P., Kiczka, M. & Rosch, D. (2014b): Safety case for a spent nuclear fuel repository at Olkiluoto. Radionuclide solubility limits and migration parameters for the canister and the buffer. Posiva 2012-39.
- Wersin, P., Kiczka, M. & Koskinen, K. (2016): Porewater chemistry in compacted bentonite: Application to the engineered buffer barrier at the Olkiluoto site. Applied Geochemistry 74, 165-175.

- Wieland, E., Wanner, H., Albinsson, Y., Wersin, P. & Karnland, O. (1994): A surface chemical model of the bentonite-water interface and its implications for modelling the near field chemistry in a repository for spent fuel. SKB Technical Report TR-94-26. Swedish Nuclear Fuel and Waste Management CO, www.skb.se, Stockholm, Sweden.
- Wilson, J., Savage, D., Cuadros, J., Shibata, M. & Ragnarsdottir, K.V. (2006): The effect of iron on montmorillonite stability. (I) background and thermodynamic considerations. *Geochimica et Cosmochimica Acta* 70, 306-322.
- Wilson, J., Savage, D., Bond, A., Watson, S., Pusch, R. & Bennett, D. (2011): Bentonite. A review of key properties, processes and issues for consideration in the uk context. QRS1378ZG-1 Version 1.1, p. 137.
- Wilson, J.C., Benbow, S., Sasamoto, H., Savage, D. & Watson, C. (2015): Thermodynamic and fully-coupled reactive transport models of a steel-bentonite interface. *Applied Geochemistry* 61, 10-28.
- Wissmeier, L. & Barry, D.A. (2011): Simulation tool for variably saturated flow with comprehensive geochemical reactions in two- and three-dimensional domains. *Environmental Modelling & Software* 26, 210-218.
- Xia, X., Idemitsu, K., Arima, T., Inagaki, Y., Ishidera, T., Kurosawa, S., Iijima, K. & Sato, H. (2005): Corrosion of carbon steel in compacted bentonite and its effect on neptunium diffusion under reducing condition. *Applied Clay Science* 28, 89-100.
- Yamaguchi, T., Sakamoto, Y., Akai, M., Takazawa, M., Iida, Y., Tanaka, T. & Nakayama, S. (2007). Experimental and modeling study on long-term alteration of compacted bentonite with alkaline groundwater. *Physics and Chemistry of the Earth, Parts A/B/C* 32, 298-310.
- Yamaguchi, T., Sawaguchi, T., Tsukada, M., Kadowaki, M. & Tanaka, T. (2013). Changes in hydraulic conductivity of sand-bentonite mixtures accompanied by alkaline alteration. *Clay Minerals* 48, 403-410.
- Yamaguchi, T., Sawaguchi, T., Tsukada, M., Hoshino, S. & Tanaka, T. (2016). Mineralogical changes and associated decrease in tritiated water diffusivity after alteration of cement-bentonite interfaces. *Clay Minerals* 51, 279-287.
- Yates, D.M. & Rosenberg, P.E. (1996). Formation and stability of endmember illite.1. Solution equilibration experiments at 100-250° C and P-V, P-Soln. *Geochimica et Cosmochimica Acta* 60, 1873-1883.
- Yokoyama, S., Kuroda, M. & Sato, T. (2005): Atomic force microscopy study of montmorillonite dissolution under highly alkaline conditions. *Clays and Clay Minerals* 53, 147-154.
- Yokoyama, S., Watanebe, Y., Jenni, A. & Mäder, U. (2015): Alteration of compacted bentonite contacted with concrete. *In: ONDRAF (ed.): 6th Meeting on Clays in Natural and Engineered Barrier for Radioactive Waste Confinement*, Brussels, Belgium.
- Yustres, A., Jenni, A., Asensio, L., Pintado, X., Koskinen, K., Navarro, V. & Wersin, P. (2017): Comparison of the hydrogeochemical and mechanical behaviours of compacted bentonite using different conceptual approaches. *Applied Clay Science* 141, 280-291.

- Zhang, J., Dong, H.L., Liu, D., Fischer, T.B., Wang, S. & Huang, L.Q. (2012): Microbial reduction of Fe(III) in illite-smectite minerals by methanogen *methanosarcina mazei*. *Chemical Geology* 292, 35-44.
- Zheng, L., Xu, H. & Birkholzer, J. (2018): THMC modeling in support of an experiment studying the effects of high temperatures on clay buffers/near-field. Nagra Arbeitsbericht NAB 17-32.
- Zhu, C.-M., Ye, W.-M., Chen, Y.-G., Chen, B. & Cui, Y.-J. (2013): Influence of salt solutions on the swelling pressure and hydraulic conductivity of compacted GMZ01 bentonite. *Engineering Geology* 166, 74-80.
- Zysset, M. & Schindler, P.W. (1996): The proton promoted dissolution kinetics of K-montmorillonite. *Geochimica et Cosmochimica Acta* 60, 921-931.

Appendix: Bentonite requirements

A.1 Desired properties of bentonite – safety functions

Overall required properties

The overall safety functions of a nuclear waste repository are confinement and retardation. Confinement is defined as the complete isolation of the waste, while retardation slows down any releases in the case of a failed confinement.

The overall criterion for evaluating repository safety is the risk criterion issued by national regulators, which is usually expressed as a maximum dose, or risk, to a representative individual in the group in the biosphere exposed to the greatest risk.

To evaluate the dose or risk from a repository, a detailed and quantitative understanding of all processes that affect the repository together with the associated uncertainties is needed. Dose and risk are therefore not very practical entities to use for the study of individual repository components. To resolve this, the concept of "safety functions" has been introduced. A safety function is a description of how an individual barrier contributes to the confinement and retardation of radionuclides. Safety functions can be defined based on the understanding of the properties of the components and the long-term evolution of the system.

To safely contain the waste and to be compliant with the overriding safety principles, the key requirements for a buffer material in the case of high-level radioactive waste disposal independently of the host rock are: (1) a low hydraulic permeability/conductivity; (2) a self-sealing ability; and (3) durability of properties on the very long term.

A.2 Specific Nagra-required properties – safety functions

The required properties for the bentonite buffer specific to the Nagra context have been defined and described in more detail in Leupin and Johnson (2013) and Leupin et al. (2015).

The attenuation of radionuclide release from the repository system is strongly dominated by sorption and diffusive transport in the clay-rich rock, which is much thicker than the bentonite engineered barrier. As a result, in a scenario in which diffusion dominates transport in the host rock, bentonite makes a limited contribution to retarding radionuclide transport, but nonetheless provides redundancy and a suitable chemical (low microbial activity) and hydromechanical (isotropic loads on the canister) environment.

Bentonite plays a particularly important role in alternative scenarios or assessment cases. These assessment cases are based on what-if scenarios that investigate the robustness of the disposal system (Nagra 2002a), such as i) unintentional borehole intrusion of the near-field and ii) occurrence of hydraulically transmissive discontinuities intersecting the emplacement tunnels. Both cases incorporate the assumption that the emplacement tunnels, including the bentonite, have low hydraulic conductivity. This attribute contributes to ensuring low dose consequences. As a result, the most important requirement in relation to long-term safety assessment is to maintain overall low hydraulic conductivity in the waste emplacement tunnels. This also requires that all voids are filled by swelling clay, i.e. some swelling pressure must be provided by the bentonite.

In order to achieve the two safety functions (i.e. low hydraulic permeability and self-sealing ability), safety-relevant attributes are defined. The safety-relevant attributes of the buffer include those that contribute to the safety functions of other barriers or those that directly involve the safety functions of the buffer itself.

Low hydraulic conductivity

This requirement supports the buffer safety function "attenuate releases". The hydraulic parameters of the saturated buffer should prevent advective flow through the buffer and therefore result in an effective transport barrier. Possible cracks in the buffer should close due to self-sealing.

Chemical retention of radionuclides

This requirement supports the buffer safety function "attenuate releases" by retarding transport of radionuclides from the buffer.

Sufficient density

This requirement supports the buffer safety function "attenuate releases" by ensuring that the density of the buffer will be high enough that the resulting microporous structure provides an effective barrier for colloid transport.

Sufficient swelling pressure

This requirement supports the rock safety function "attenuate releases". Emplacement tunnels in the Opalinus Clay may be supported with rock bolts and mesh (reference design) or rock bolts and liner (alternative support concept). In either case, the lifetime of the support is designed to provide stable conditions during construction and operation (up to several years). After waste and buffer emplacement, there may be interactions of the support system with other system components (host rock, buffer, canister, waste form). These interactions should not be detrimental to the safety of the system. The support will eventually fail due to corrosion and deformation and allow additional time-dependent deformations of the near-field host rock and compaction of the buffer. The maximum convergence-induced compaction of the buffer, which is controlled by the stress field and the mechanical properties of host rock and swelling pressure of the buffer material, should be limited to avoid significant extension of the EDZ of the host rock. Limited convergence will also enhance the self-sealing capacity of Opalinus Clay in the EDZ. The consequences of such an extension may include significant increases in permeability of the EDZ that are difficult to evaluate quantitatively. In addition, a too high swelling pressure could also initiate fracturing of the rock. Furthermore, an adequate swelling pressure will prevent canister sinking. The canister should be emplaced in such a way that its distance to the tunnel wall is constant and so that it is encased by a thick layer of buffer material to avoid hydraulic short-cuts to the EDZ of the tunnels. Having sufficient swelling pressure also supports the buffer safety function "protect the canister" (Leupin and Johnson 2013). The rheology of the buffer material (viscous material behaviour) should keep deviant stresses and stress inhomogeneity as low as possible to protect the canisters (e.g. avoid point loading of canister). Potential larger deformations of the host rock resulting from tectonic events (e.g. earthquakes) should be attenuated.

Sufficient gas transport capacity

This requirement supports the buffer safety function "attenuate releases". The buffer should transport corrosion gases without significant reduction of its function as a hydraulic barrier.

Minimise microbial corrosion

This requirement supports the buffer safety function "protect the canister". Studies of the reduction of sulphate to sulphide in bentonite indicate that the rate decreases as saturated density increases. Based on an extensive literature review and results of ongoing studies, a value for a saturated density may be defined in order to minimise the viability of microorganisms in the bentonite (Stroes-Gascoyne et al. 2011).

Resist transformation

This requirement supports the buffer safety functions "attenuate releases" and "protect the canister". Mineralogical interactions occurring over time due to elevated temperatures and chemical interactions with other components of the disposal system should not lead to significant alteration and /or loss of the buffer functions.

Suitable thermal conductivity

This requirement supports the buffer safety functions "attenuate releases" and "protect the canister". The buffer should conduct heat sufficiently well that the waste form, canister and buffer do not experience conditions detrimental to the performance of their safety functions.

Tab. A-1: Compilation of attributes for the buffer material around the canister for the different repository designs and concepts

| Safety-relevant attributes | Favours/contributes to ... | Preferred values for Nagra | Favours/contributes to ... |
|--------------------------------------|--|--|---|
| Low hydraulic conductivity | Attenuation safety function of buffer, by ensuring diffusive transport | $K < 10^{-11} \text{ m s}^{-1}$ for buffer around canister | Limits advective transport |
| Chemical retention of radionuclides | Attenuation safety function of buffer, by retarding transport from the buffer | No quantitative criterion ¹⁰ , strong sorption is favoured | - |
| Sufficient density | Attenuation safety function of buffer, by preventing colloid transport | $\rho_s > 1.650 \text{ Mg m}^{-3}$ ¹¹ | Attenuation safety function. Damp shear movement |
| Sufficient swelling pressure | Attenuation safety function of rock, by providing mechanical stabilisation of rooms, and hence avoiding significant extension of EDZ | $0.2 \text{ MPa} < P_s < \text{minimum principal stress}$ | Attenuation safety function of rock, by providing mechanical stabilisation of rooms |
| Mechanical support | Safety function of canister, by ensuring it is surrounded by a protective layer of buffer (stress buffering) | Buffer must be sufficiently viscous to avoid canister displacement ^f | Safety function to prevent canister displacement by a protective layer of buffer (stress buffering) |
| Sufficient gas transport capacity | Attenuation safety function of buffer, by ensuring gas can migrate without compromising hydraulic barrier | No quantitative criterion ¹⁰ , less than the minimum principal stress | - |
| Minimise microbial corrosion | Safety function of canister, by ensuring conditions favorable to slow corrosion. | No quantitative criterion but higher densities are preferred to limit microbial activity ¹⁰ | Safety function of canister, by ensuring conditions favourable to slow corrosion |
| Resistance to mineral transformation | Longevity of other safety-relevant attributes of buffer | No quantitative criterion. | Longevity of other safety-relevant attributes of buffer |
| Mechanical support | Safety function of canister, by providing stress buffering | Not a required property | No quantitative requirement for stress buffering. Canister must be designed to handle variations in swelling pressure |
| Suitable heat conduction | Safety function of canister, by ensuring favorable maximum temperature conditions | $0.4 < T_c < 2 \text{ W m}^{-1} \text{ K}^{-1}$ (for a specific thermal heat load of 1,500 W) | Safety function of canister, by ensuring favorable maximum temperature conditions |
| | Safety functions of buffer and rock, by ensuring favorable maximum temperature conditions | $0.4 < T_c < 2 \text{ W m}^{-1} \text{ K}^{-1}$ (for a specific thermal heat load of 1,500 W) | Safety functions of buffer and rock, by ensuring favorable maximum temperature conditions |

¹⁰ Where no quantitative criterion is indicated, the impacts on safety of the process must nonetheless be evaluated.

¹¹ ρ_s –values are indicative assuming MX-80 is the selected buffer material and are given as saturated densities.